Patterns of Shallow Clouds and Rainfall over the Amazon: Climatic Impacts of Deforestation

by

Frédéric J. F. Chagnon

B.Sc., McGill University (1997)
M.Sc., University of London (1998)
D.I.C., Imperial College of Science, Technology and Medicine (1998)
M.Eng., Massachusetts Institute of Technology (1999)

Submitted to the Department of Civil and Environmental Engineering
in partial fulfillment of the requirements for the degree of

Doctor of Philosophy

at the

Massachusetts Institute of Technology

February 2005

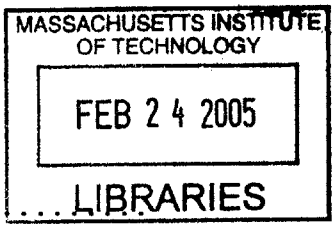

Author .....
Department of Civil and Environmental Engineering
January 7, 2005

Certified by ....
Rafael L. Bras
Edward A. Abdun-Nur Professor
Professor of Civil and Environmental Engineering
Thesis Supervisor

Accepted by .....
Andrew J. Whittle
Chairman, Department Committee on Graduate Students

Patterns of Shallow Clouds and Rainfall over the Amazon: Climatic Impacts of Deforestation

by

Frédéric J. F. Chagnon

Submitted to the Department of Civil and Environmental Engineering
on January 7, 2005, in partial fulfillment of the
requirements for the degree of
Doctor of Philosophy in the Field of Hydrology

Abstract

The climatic impact of the current state of deforestation in the Amazon basin is examined in this thesis. Past modeling studies have shown that complete deforestation of the Amazon basin could result in dramatic decreases in regional rainfall and evaporation leading to desertification (e. g., Salati and Vose [1984], Shukla *et al.* [1990]). Yet, although 15% of the 4,000,000 km^2 Brazilian Amazon has already been deforested [INPE, 2003], current deforestation patterns in the Amazon basin are not uniform, nor do their extents surpass tens of kilometers. Numerical simulations indicate that idealized heterogeneities of land-surface properties could lead to organized mesoscale circulations that enhance convection (e. g., Anthes [1984], Chen and Avissar [1994a], Avissar and Liu [1996], Wang *et al.* [1998]); similar results were found in case-study simulations of actual Amazon deforestation (e. g., Wang *et al.* [2000], Roy and Avissar [2002]). Qualitative observations of enhanced shallow cloud cover over cleared areas have provided preliminary indications of episodic land-cover-driven mesoscale circulations in the Amazon basin (e. g., Cutrim *et al.* [1995], Durieux *et al.* [2003], Negri *et al.* [2004]). Based on these studies, the effects of the "fishbone" patterns of deforestation on shallow convection were thought to occur only episodically during few precious weeks toward the end of the dry season, and were largely accepted as being climatically insignificant. However, through the use of satellite data from the Geostationary Operational Environmental Satellite (GOES) and the Tropical Rainfall Measuring Mission (TRMM), this thesis quantitatively demonstrate that the complex pattern of deforestation in the Amazon has resulted in a climatic shift in shallow cloud, rainfall and, to a lesser extent, cold cloud patterns over the Amazon. Through complex interactions, the results reported in this thesis may have important implications for the local ecosystem dynamics of the Amazon, for the geomorphology of the Amazon river basin, for the flow regimes of the Amazon river, and for global climate.

Thesis Supervisor: Rafael L. Bras
Title: Edward A. Abdun-Nur Professor
Professor of Civil and Environmental Engineering

Acknowledgments

I owe a debt of gratitude to Rafael L. Bras for his generosity, patience and counsel. Rafael has been a supportive advisor, and has afforded me great independence in research. Rafael also deserves much praise for bringing together such a stimulating research group, whose camaraderie I have very much enjoyed. I also wish to thank Dara Entekhabi, Earle Williams and Elfatih Eltahir for serving on my doctoral committee. They have been assiduous in their presence, and their criticism and insight have been invaluable. Jingfeng Wang, Daniele Veneziano and Kevin Amaratunga have always made themselves available, and must also be thanked. Jingfeng has, in particular, been a constant source of help on mathematical and statistical problems.

I am greatly indebted to Professor Donald R. F. Harleman for providing me the opportunity to supervise many masters degree students over the past five years (and I thank Rafael for allowing me to pursue these interests), and most importantly for his friendship. And I must also thank Mrs. Harleman for her immense generosity. Pat Dixon, Sheila Frankel, Donna Hudson, Vicky Murphy, Elaine Pagliarulo and Cynthia Stewart have always been present and helpful beyond any expectation; they are truly the backbone of this laboratory and this department.

I thank the members of the Bras research group, past and present: Bill Bennett, Domenico Capolongo, Daniel Collins, Giacomo Falorni, Jean Fitzmaurice, Homero Flores, Lejo Flores, Fotios Fotopoulos, Nicole Gasparini, Salvatore Grimaldi, Ola Hall, Erkan Istanbulluoglu, Valeri Ivanov, Hanan Karam, Jeffrey Niemann, Valerio Notto, Vanessa Teles, Gregory Tucker, Enrique Vivoni and Jingfeng Wang. The following fellow Parsons Laboratory dwellers are also thanked: Sam Arey, Aaron Chow, Maureen Coleman, Susan Dunne, Kirsten Findell, Paul Fricker, Marco Ghisalberti, Gavin Gong, Marine Herrmann, Anke Hildebrandt, Dana Hunt, Peter Israelsson, Zachary Johnson, Vanja Klepac-Ceraj, Blake Landry, Steven Margulis, Mario Martina, Holly Michael, Jeremy Pal, Elsa Petrelluzzi, Chanathip Pharino, Rolf Reichle, Ramahi Sarma-Rupavtarm, Charlie Stock, Matthew Sullivan, Yoshi Tajima, Janelle Thompson and Erik Zinser.

The following sources of funding are acknowledged: a NASA TRMM grant, a NASA ESS Fellowship, a Martin Family Sustainability Fellowship, many Arthur Ippen Travel Fellowships, and a Ralph M. Parsons Fellowship.

Finalement, je remercie ceux qui m'ont entouré ces cinq dernières années: Erin Hains, Antoine Chagnon, Nicolas Chagnon, Laurent Chagnon, Sengmany Phommachakr, Thomas Lellouche, Rami Bebawi, Kevin Tsui, David Turmel, Sylvia Lee, et tout particulièrement mes parents, Jean et Sylvie Chagnon.

Le chien qui lâche sa proie pour l'ombre

Chacun se trompe ici-bas.
On voit courrir après l'ombre
Tant de fous, qu'on en sait pas
La plupart du temps le nombre.
Au chien dont parle Esope il faut les renvoyer.
Ce chien, voyant sa proie en l'eau représentée,
La quitta pour l'ombre, et pensa se noyer;
La rivière devint tout d'un coup agitée.
A toute peine il regagna les bords,
Et n'eut ni l'ombre ni le corps.

La Fontaine

TABLE OF CONTENTS

LIST OF FIGURES

LIST OF TABLES

CHAPTER 1

INTRODUCTION

Tropical forests around the globe are undergoing major changes in land-use due to human activity [Myers, 1991]. Of all tropical "hot-spots", none is perhaps more notorious than the Amazon rainforest: as of 2001, 15% of the 4,000,000 km^2 Brazilian Amazon has been deforested [INPE, 2003]. Skole and Tucker [1993] showed a three-fold increase in deforestation of the Brazilian Amazon between 1978 and 1988; each year agricultural exploitation claims an estimated 13,000 km^2 of tropical forest through clear-cutting [Achard *et al.*, 2002]. Such dramatic changes have prompted studies to determine their impact; the following section provides a broad review that highlights some of the major findings.

1.1 The Wider Impacts of Tropical Deforestation

Tropical forests are hosts to more than half of all living species [Myers, 1991]. The habitat fragmentation caused by deforestation (Figure 1-1) creates dramatic shifts in biodiversity; for example, Ferraz *et al.* [2003] has documented the disappearance of certain bird species, while Laurance *et al.* [1998] found that tree mortality in fragmented patches is higher than that of undisturbed forests. The conversion of forest to pasture also has profound effects on the chemical and physical properties of the soil [Moraes *et al.*, 1996], determining which species may establish themselves in this changed environment. Erosion occurs more readily in deforested areas, and changes the sedimentary organic loading of the Amazon river [Farella *et al.*, 2001]. In an effort to summarize all of the effects of human activity on natural environment, the United Nation Environmental Program (UNEP) created the map presented in Figure 1-2, where the extent of human encroachment is presented. Most deforestation is concentrated in the "arc of deforstation" that covers the states of Rondônia and Mato Grosso (see Figure 1-4). Perhaps most alarming than the extent of disturbance documented by UNEP is the possibility of

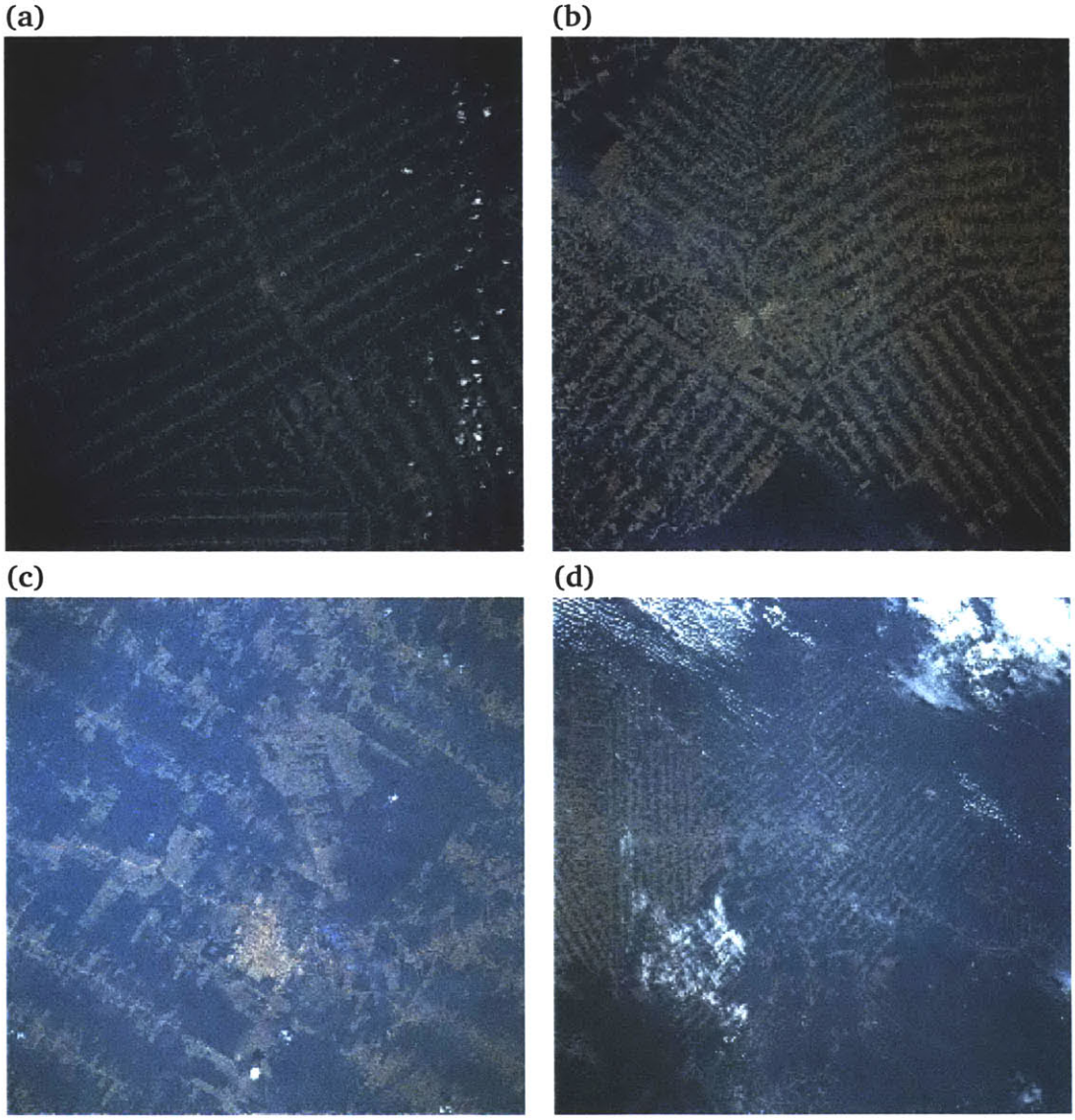

Figure 1-1: Deforestation Patterns in Rondônia from NASA Space Shuttle Missions. These pictures highlight the "fishbone" deforestation patterns, shallow clouds and smoke from biomass burning. **(a)** Date: 06/28/1985; Center: 10.1S 63.1W. **(b)** Date: 08/02/1992; Center: 11.7S 61.8W. **(c)** Date: 08/06/1992; Center: 9.8S 63W. **(d)** Date: 09/25/1995; Center: 10.5S 62.5W

sudden catastrophic shifts in ecosystem states that was documented by Scheffer *et al.* [2001].

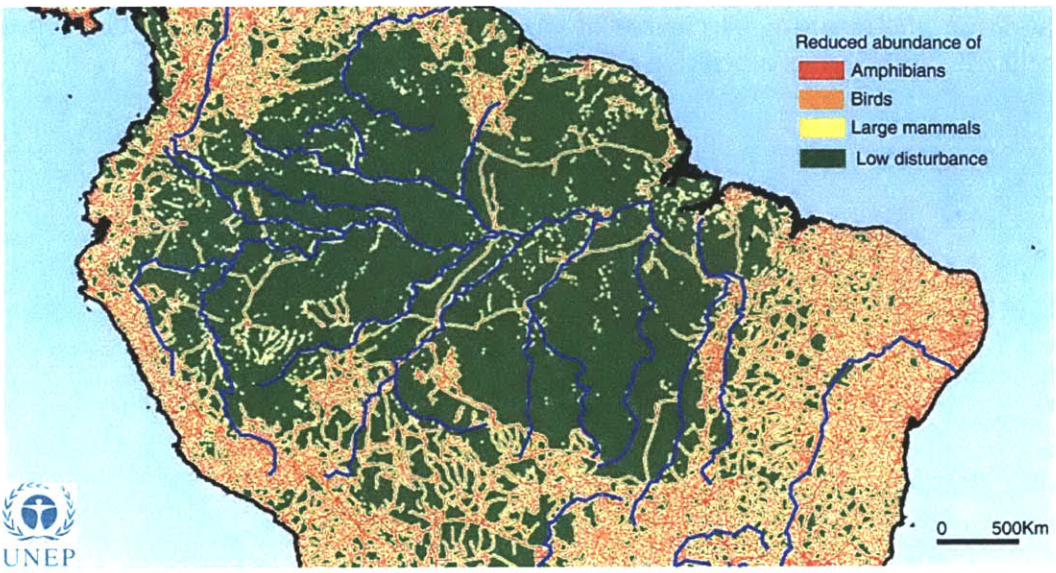

Figure 1-2: Preliminary Assessment of the Amazon Region Impact of Human Activities on Ecosystems around 1980 using the GLOBIO Methodology (UNEP).

The Amazon river (Figure 1-3) represents some 15 to 20% of global runoff [Salati and Vose, 1984]. Runoff is the integrated hydrologic response of a basin; if deforestation has had any significant impact on the local climate, then it could be reflected as a change in river discharge. Runoff is the residual in the balance between rainfall and evaporation, and unless both are equally and synchronously affected by deforestation, runoff will change. Gentry and Lopez-Parodi [1980] examined a time-series of flood crests at Iquitos (Peru) in the upper parts of the Amazon basin, and deduced that intense deforestation had markedly increased river flows. This claim was however disputed by Nordin and Meade [1982] as being possibly caused by an increase in rainfall or by a change in channel geometry. The detailed studies of Sternberg [1987], Richey *et al.* [1989] and Marengo [1995] all agree that while deforestation certainly has effects on the river discharge, these effects are as of yet undetectable, or rather undifferentiable from the inter-annual variability and fluctuations induced by large-scale atmospheric phenomena such as ENSO.

Deforestation also raises questions about the possible changes in the Earth's CO_2 balance. This issue is still not resolved; it is not yet known whether undisturbed tropical forests are net sources or sinks of CO_2 [Houghton *et al.*, 2000; Saleska *et al.*, 2003]. The act of deforestation is widely accepted to result in a net source of CO_2 to the atmosphere [Houghton *et al.*, 2000], but the magnitude of the source is as of yet undetermined [Fearnside, 1996]. The climatic effects, through the greenhouse effect, of deforestation's impact on the CO_2 balance is hence still unresolved.

Complicating the carbon accounting exercises further is the fact that much of the deforestation is accomplished by burning, which is estimated to have released the carbon equivalent of 40% of worldwide fossil fuel use in 1997-98 [Cochrane, 2003]. In addition, the resulting patchwork of vegetation is much more susceptible to fire [Cochrane, 2003], thus a positive reinforcement is possible.

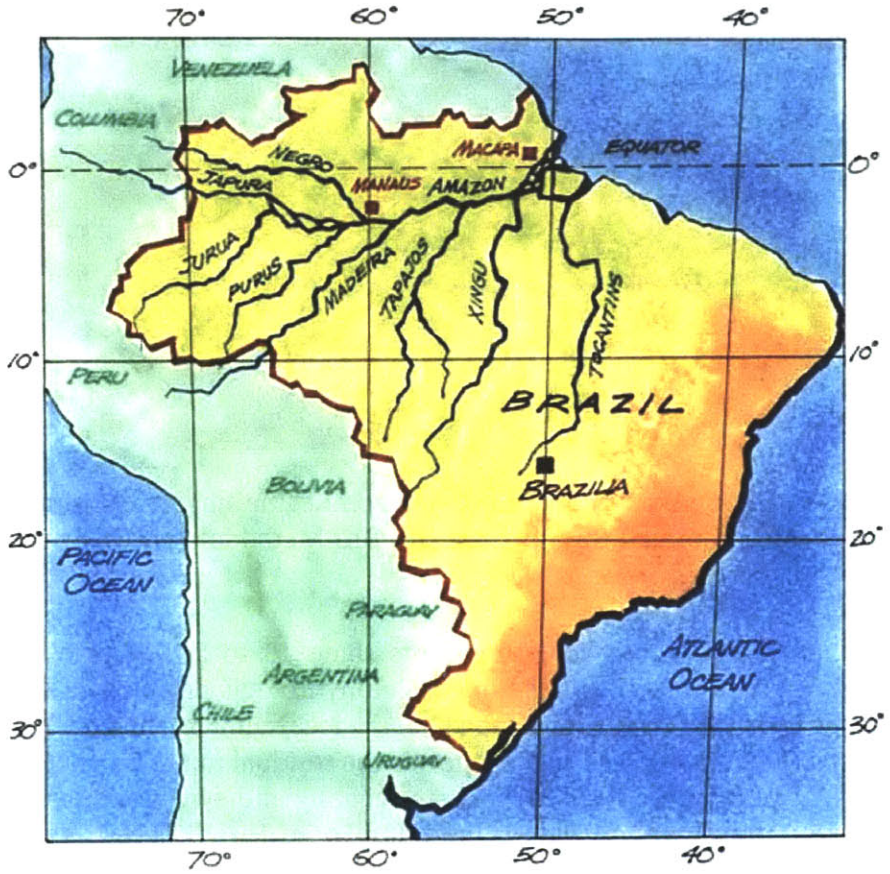

Figure 1-3: The Fluvial Amazon.

As stated above, biomass burning is a popular method to clear forested sites. These burns release large amounts of particles into the atmosphere that act as cloud condensation nuclei (CCN). The aerosols that are released from biomass fires tend to decrease the mean cloud droplet size, increase cloud albedo and thus impact the radiative balance [Kaufman and Fraser, 1997; Kaufman *et al.*, 1998; Ramanathan *et al.*, 2001; Peng *et al.*, 2002; Kaufman *et al.*, 2002; Penner *et al.*, 2004]. This result would indicate a cooling effect, yet aerosols may also indirectly have a heating effect by inhibiting cloud formation itself [Ackerman *et al.*, 2000; Koren *et al.*, 2004]. Biogenic aerosols — organic acids that form through the interaction of UV radiation and hydrocarbons that are emitted by trees — also affect cloud droplet nucleation and hence cloud properties [Kavouras *et al.*, 1998; Facchini *et al.*, 1999;

Ozanne *et al.*, 2003]. Moreover, aerosols may inhibit rainfall [Rosenfeld, 1999; Ramanathan *et al.*, 2001], and have the potential to change global climate by redistributing the vertical heating profile [Andreae *et al.*, 2004]. Eck *et al.* [1998] infers that by modifying the radiative and thermal structure of the atmosphere, biomass smoke may reduce the differential surface heating associated with deforestation, and hence has the potential to suppress the local circulations created by deforestation.

There are many different consequences to tropical deforestation, the interactions between the different processes involved are complex, and a full understanding of the integrated impact of tropical deforestation is not yet upon us. Gaining that understanding is a truly challenging problem that will require open collaboration from scientists of many different disciplines. Yet before such endeavours are undertaken, we must first understand the individual direct, or first-order, impacts of deforestation. This thesis will concentrate on the the effect of the change in the land-surface properties on local climate. The following section will provide a background on these effects, and will motivate the objectives of this thesis.

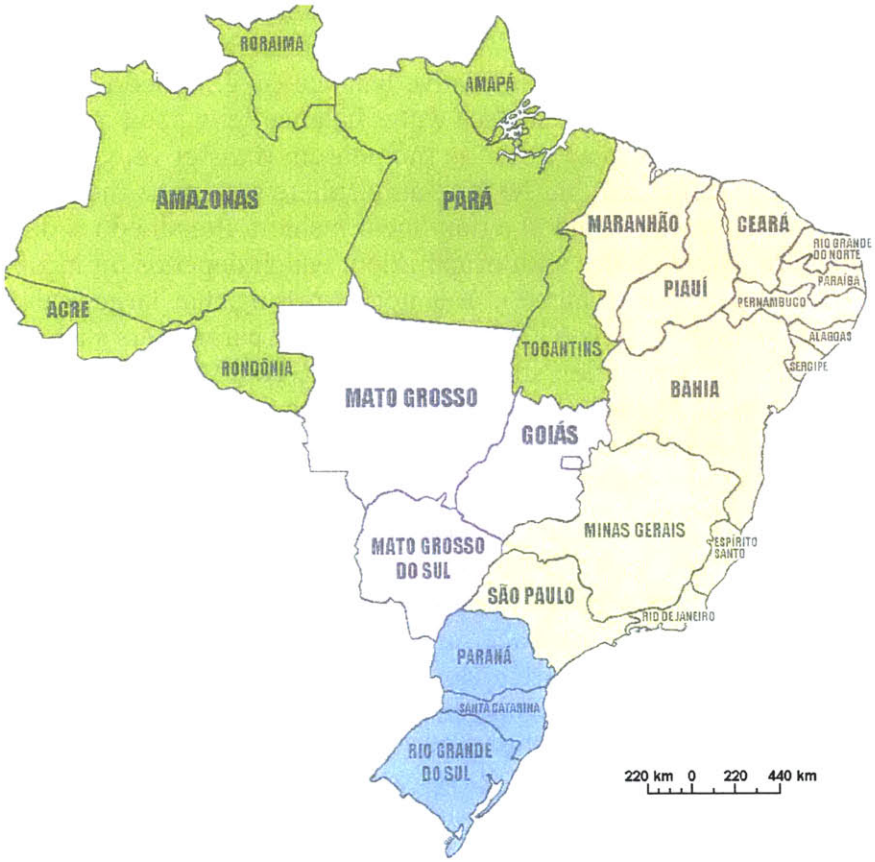

Figure 1-4: Political Map of Brazil.

1.2 The Role of Land Surface Properties in Climate

Charney *et al.* [1975] and Eagleson [1978a,b] are among those who pioneered the notion that the soil-vegetation system plays a fundamental role in atmospheric circulation. Land-surface's impact on atmospheric circulation has since occupied a dominant position in the study of hydrology and the atmospheric sciences. Thus, the ocean-planet assumption that had been standard in climate simulations was replaced, and a number of models representing land-surface hydrological processes were developed, coupled with atmospheric models and evaluated (e. g., Sellers *et al.* [1986], Entekhabi and Eagleson [1989], Xue *et al.* [1991], Dickinson *et al.* [1993], Martin [1993], Liang *et al.* [1994], Chen *et al.* [1996], Chen and Dudhia [2001], etc.). The purpose of this section is to go over the major findings in the field of land-atmosphere interactions.

The characteristics of the land-surface (soil type, vegetation type, topography, etc.) determine the physical properties and associated parameters that govern the exchange of mass and energy between the surface and the overlying atmosphere [Pielke Sr., 2001]. The key properties and variables in the land-atmosphere system are those that modulate the surface radiative balance (e. g., albedo, temperature, emissivity), those that control the surface water balance (e. g., soil moisture, infiltration rate), and those that play a role in momentum transfer (e. g., roughness). There is an inherent complexity in the land-atmosphere system as these properties or variables are often inter-related in a non-linear fashion; the albedo is dependent upon soil moisture, which varies with evaporation, which depends on incoming radiation, which is a function of albedo. It is not surprising that large-scale studies using general circulation models (GCM) have found that parameters such as albedo [Charney *et al.*, 1975], vegetation state [Chase *et al.*, 2000; Kleidon *et al.*, 2000], soil moisture [Yeh *et al.*, 1984], canopy interception capacity [Scott *et al.*, 1995], and root-zone water-holding capacity [Koster and Suarez, 1996; Milly and Dunne, 1994] have a great impact on atmospheric circulation.

The intimate coupling of the land-atmosphere system was discovered early on. Idso *et al.* [1975] showed that near-surface soil moisture and albedo are inversely and linearly related for bare soils and Charney *et al.* [1975] found that an increased Sahara albedo has a negative feedback on regional precipitation; the two results together imply a positive feedback that can lead to sustained drought. Hendersen-Sellers [1978] stated that while "the position and frequency occurrence of clouds is largely determined by the general circulation of the earth's atmosphere and the particular meteorological condition (...) the effect of changing local land surface type upon cloud cover may be of critical importance and could feed back to produce climate change." A non-random organization arises from the coupling of the land-atmosphere. Entekhabi *et al.* [1992] argued that persistence, or memory, in the state of the land-atmosphere is a direct consequence of feedbacks and non-linear interactions between the components of the hydrological cycle in both the land and the atmosphere.

Of particular interest to the hydrological sciences are the energy and water balances at the land-surface. These relations share a common term, which is evapotranspiration. Numerous studies using one-dimensional models of the coupled soil-vegetation-atmosphere system [Pan and Mahrt, 1987; Clark and Arrit, 1995; da Rocha *et al.*, 1996; Dolman *et al.*, 1999] have shown that vegetation affects the partitioning and magnitude of turbulent fluxes at the surface (i. e., latent and sensible heat fluxes). Segal *et al.* [1995] demonstrated the significance of the partitioning, represented by the Bowen ratio (the ratio of sensible to latent heat), on deep convection: a smaller Bowen ratio increases the potential for development of deep convection. Similarly, Clark and Arrit [1995] showed that vegetated surfaces, which tends to have a lower Bowen ratio[1] than bare surfaces, promote convection.

Dramatic changes in the properties of the land-surface could thus modify climate. One such example of dramatic change is deforestation, and one of the most notorious examples of large-scale deforestation is found in the Amazon basin. The initial question posed by the scientific community concerned the impact of the loss of the entire Amazon rainforest — the catastrophe scenario. There is a wide consensus that both evaporation and precipitation would decrease[2] in the Amazon basin if it were stripped of its lush forest [Lettau *et al.*, 1979; Shukla *et al.*, 1990; Salati and Nobre, 1991; Nobre *et al.*, 1991; Gash and Shuttleworth, 1991; Mylne and Rowntree, 1992; Eltahir and Bras, 1993c; Polcher and Laval, 1994; McGuffie *et al.*, 1995; Sud *et al.*, 1996; Xue *et al.*, 1996; Zeng *et al.*, 1996; Zhang *et al.*, 1996; Hahmann and Dickinson, 1997; Lean and Rowntree, 1997, 1999; Zeng, 1998; Werth and Avissar, 2002]. The intense hydrologic activity over the Amazon basin and its tropical location (see Chapter 3) make the Amazon hydrological cycle a key driver of the global climate. Thus, a change in water fluxes caused by complete deforestation would have dramatic implications on global climate [Werth and Avissar, 2002].

Studies have also been undertaken on the impacts of regional-scale deforestation on atmospheric circulation. Eltahir and Bras [1994] used a numerical mesoscale circulation model in conjunction with a land-surface hydrology scheme to study the sensitivity of climate to deforestation at the regional scale ($\sim$250 km.) New parameterizations for rainfall interception and rainfall spatial coverage were developed to aid this study, and are described by Eltahir and Bras [1993a,b]. Results showed a decrease in net surface radiation, evaporation and rainfall, and an increase in surface temperature.

Of course, deforestation represents more than just a simple change in vegetation cover. It is a change in surface roughness, rooting depth, albedo, Leaf-Area

[1]Caution must however be used when making such generalizations around a unique measure such as the Bowen ratio, for it does not comprise a full physical description of the land-atmosphere system. Pre-dawn atmospheric conditions, for example, have been shown to mitigate the development of deep convection regardless of surface Bowen ratio [Wetzel *et al.*, 1996].

[2]Interestingly, there is no consensus on the effects of complete deforestation on the Amazon river flow; runoff is the relatively small term that is the difference between precipitation and evaporation, and an error in the estimates of the change of these fluxes could lead to a change in the sign of the change of river flow [Eltahir and Bras, 1993c].

Index (LAI), etc. The scale of most models, coupled with the need to parametrize most land-surface processes creates much uncertainty. For example, Kleidon and Heinmann [2000] showed that the magnitude of the changes predicted in these models is sensitive to the depth of vegetation roots. Moreover, there is uncertainty that arises from other unrelated model components, such as sea-surface temperature or topography [Meher-Homji, 1991]. Further, the studies reviewed above have assumed idealized and up-scaled patterns of deforestation. While these types of studies are useful to test the sensitivity of the atmosphere to deforestation, the true structure of deforestation plays an important role in the atmosphere's response, and must be included in models [O'Brien, 2000].

1.3 Land-Surface Heterogeneities and Climate

The pattern of deforestation in Amazonia is often likened to a "fish-bone" (Figure 1-1). Deforestation tends to occur along major roadways, and shoot off in dendritic-like structures. The result is a highly heterogeneous land-surface, whose influence on atmospheric circulation cannot be approximated by a lumped area. In this section, a review of the effects of heterogeneous land-surface on climate is presented.

The heterogeneities of the land-surface affect the surface energy and water budgets, and also the fluxes of momentum, heat and vapor between the land and the boundary layer [Giorgi and Avissar, 1997]. In an early study in a semi-arid zone, Anthes [1984] found that vegetated bands 20 to 50 km wide could increase convective precipitation more than uniformly vegetated large areas. Since then, many studies have attempted to understand the effects of landscape heterogeneities of atmospheric circulations, and to study the processes involved in mesoscale circulations induced by surface heterogeneities. The following are some key results:

- The mesoscale fluxes generated by land-surface heating and/or moisture heterogeneities have the potential to enhance shallow convection [Avissar and Liu, 1996; Chen and Avissar, 1994a,?; Hong *et al.*, 1995; Seth and Giorgi, 1996; Wang *et al.*, 2000; Weaver and Avissar, 2001].

- The optimal wavelength of the land-surface forcing is the local Rossby radius of deformation[3] [Dalu and Pielke, 1993; Chen and Avissar, 1994; Lynn *et al.*, 1998].

- The magnitude of the mesoscale heat and momentum fluxes are comparable to or greater than the turbulent heat and momentum fluxes [Anthes, 1984; Ookouchi *et al.*, 1984; Pinty *et al.*, 1989; Dalu and Pielke, 1993; Wang *et al.*, 1998].

[3] $R_0 = (N \times H)/\Omega$; where N is the Brunt-Väisälä frequency, H is the boundary-layer height, $\Omega = (\omega^2 + f^2)^{\frac{1}{2}}$, f is the coriolis force, and ω is the characteristic dissipation frequency

- The intensity of the mesoscale circulation depends on the strength of the land-surface contrast [Ookouchi *et al.*, 1984; Segal *et al.*, 1988]. Avissar and Schmidt [1998] showed that it actually depends non-linearly on the combination of contrast strength and mean heating-rate.

- The land-surface moisture state affects the timing of onset of clouds, their distribution and intensity [Pinty *et al.*, 1989; Chen and Avissar, 1994a; Hong *et al.*, 1995].

- The topology of the contrasting land-surfaces affects the location of lower level mesoscale convergence [Mahfouf *et al.*, 1987; Yan and Anthes, 1988; Hong *et al.*, 1995; Avissar and Liu, 1996; Dalu *et al.*, 1996].

Modelling studies of landscape-driven mesoscale circulations disagree about the sensitivity of these circulations to synoptic wind conditions. Indeed, some have inferred that moderate winds tend to suppress the mesoscale circulations [Chen and Avissar, 1994; Hong *et al.*, 1995; Dalu *et al.*, 1996; Wang *et al.*, 1996; Avissar and Schmidt, 1998], and this sensitivity was also observed in a field study [Doran *et al.*, 1995]. Still, others have found that there is no strong sensitivity to the strength of the background winds [Wang *et al.*, 1998; Weaver and Avissar, 2001; Roy and Avissar, 2002]. These disagreements probably stem from diverging modelling frameworks or parameterizations. The sensitivity to such differences is a direct consequence of the highly non-linear nature of the process under study; Convective Available Potential Energy (CAPE) increases as the regional moisture availability increases, but sensible heating is required to trigger deep convection [Pielke Sr., 2001]. This sensitivity is highlighted by studies such as that by Zhong and Doran [1998] who found no evidence of lanscape-driven mesoscale circulations. Observations of the phenomenon of land-surface heterogeneity induced mesoscale circulations are thus essential for validation.

In an area defined by contrasts between dry steppe and irrigated farm regions, Doran *et al.* [1995] took atmospheric potential temperature soundings on two different days; analysis of the potential temperature profile indicated that a secondary circulation associated with the thermal contrast developed on the day with light wind conditions. In a similar setting, aircraft remote sensing of surface fluxes showed that a moist inland breeze developed over an irrigated area. Downstream of the irrigated area, a convergence zone associated with the inland breeze was found. Its associated vertical transport significantly modified the turbulent fluxes [Mahrt *et al.*, 1994; Sun and Mahrt, 1994].

Using satellite observations of shallow cumulus clouds over the central United States, Carleton *et al.* [2001] studied the difference in GOES albedo and cloud top temperatures for the months of June, July and August from 1991 to 1998 in the U.S. Midwest over three areas characterized by different land-covers (cropland, forest and cropland-forest boundary). Results indicated that there was an association of convective clouds over the area of cropland-forest boundary on days of weak anticyclonicity. Rabin *et al.* [1990] and Rabin and Martin [1996] showed

qualitatively that shallow clouds form preferentially over areas of high Bowen ratio (lighter vegetation) during period of weak atmospheric forcing. These results were corroborated by Cutrim *et al.* [1995] over Rondônia during August 1988, where there was qualitative evidence of enhanced GOES-8 derived shallow cumulus frequency over cleared areas during one particular day. Local measurements of incoming solar radiation during the Anglo-Brazilian Amazonian Climate Observation Study (ABRACOS) also showed a difference in cloud cover over cleared areas in the same region of Brazil [Gash and Nobre, 1997]. Recently, Durieux *et al.* [2003] studied the difference in cloudiness over large areas ($\sim$ 250 km) in the deforested arc of the Amazon. Using data from the International Satellite Cloud Climatology Project (ISCCP, D2 data) they found some evidence of enhanced shallow cloudiness over areas that had extensive deforestation. They were however unable to attribute the enhanced cloudiness to deforestation, citing the geographic differences between their deforested and forested areas.

The work of Negri *et al.* [2004] is the most recent attempt at observing the impact of deforestation on local atmospheric processes. They analysed shallow clouds — derived from GOES-8 using and *ad-hoc* cloud detection algorithm[4] — over 10 days in August 2001 and found a qualitative association (maximum at 14h15 LT). They also studied the pattern of deep convection — determined by looking at GOES-8 pixels with IR temperatures colder than 225 K — over August and September 2000 and 2001. They found a qualitative association here as well, with deep convection occurring apparently more often over deforested areas (maximum for 12h00-19h00 LT). When they aggregate all four months together, they find that there is no significant difference in the mean daily percent cold cloudiness. They do however find that there is a significant[5] (p=*0.05*) difference in the diurnal procession of the cold cloudiness; forested regions have more cold cloudiness in the morning (11h00-15h00 LT), while deforested regions have more cold cloudiness during the afternoon (19h30 LT, 20h30 LT, & 22h00 LT; no significant differences at 20h00, 21h00 and 21h30 LT). They also perform some qualitative analyses of TRMM-TMI rainfall occurrence (defined by instantaneous rain rate $\geqslant$ 0.1 mm/hour at 0.1^o resolution) and find a qualitative association between deforestation and rainfall occurrence. They finish by analysing 14 years of SSM/I rainfall rate data (0.5^o resolution) and also infer a qualitative association for the month of August, although is is weak if at all there.

1.4 Summary

The land-surface exerts influence on climate variability, although many still think that the land-atmosphere coupling is not as strong as the ocean-atmosphere

[4]The visible pixel must be in the top 20% brightest pixels for the scene, and have an IR temperature colder than 300 K. This algorithm is only applied with the *a-priori* knowledge that conditions are "suppressed", or that there are no large-scale convective systems in the scene.

[5]There is no indication in the paper of how the significance is arrived at.

coupling [Dirmeyer, 2001]. The preceding review indicates that the response of the atmosphere to land-surface disturbances (such as tropical deforestation) has been modeled at many scales. Large-scale deforestation certainly modifies the regional climate toward a drier state, and has a potential to affect global climate. Local scale disturbances in the land-surface could give rise to mesoscale circulations, and enhance convection under weak atmospheric forcing. It therefore seems that the modeled response of climate to deforestation is non-linearly related to the scale of the disturbance; small-scale deforestation could enhance the intensity of the hydrological cycle, while large-scale deforestation could dramatically decrease it. The notion that there exists a critical scale is thus introduced.

There is however a dearth of long-term high-resolution observational studies on the atmosphere's response to the present state of deforestation. Hints of mesoscale circulations and enhanced convection have been observed over short time-scales and during selected days over the Amazon basin [Cutrim *et al.*, 1995; Gash and Nobre, 1997], but there are no long-term studies that incorporate detailed climatic and statistical analyses. The studies of Carleton *et al.* [2001] and Durieux *et al.* [2003] attempted climatic analyses of mesoscale effects associated with land-surface contrasts, but comparisons were drawn from areas separated by hundreds of kilometers, and no statistical analyses were presented. The principal objective of this thesis is to assess the climatic impacts of present deforestation in the Amazon basin; to this end, patterns of shallow cumulus clouds and rainfall will be compared to the patterns of deforestation.

The next chapter will provide an account of the physical mechanisms that relate heterogeneities in land-surface properties to local or mesoscale atmospheric circulations. This will be followed by a descriptive chapter on the features of climate in the Amazon basin. Chapter 4 introduces the GOES-8 imager data, the radiometric calibration procedures, and the conversion of the imager data into physical quantities. It includes an overview of satellite-based cloud recognition algorithms, and also the algorithm used to create maps of shallow clouds over the Amazon basin for this study. Chapter 5 presents the domains over which the association between clouds/rainfall and deforestation will be studied. The method used to determine if the shallow clouds/rainfall are associated with the land surface features — based on statistical hypothesis testing and Monte Carlo simulations — is then explained. Chapter 6 presents the results of the analyses on the association of shallow clouds and deforestation, and Chapter 7 presents the results on rainfall and deforestation.

REFERENCES

ACHARD, F., H. D. EVA, H.-J. STIBIG, P. MAYAUX, J. GALLLEGO, T. RICHARDS and J.-P. MALINGREAU. Determination of deforestation rates of the world's humid tropical forests. *Science*, 297(5583):pages 999–1002 [2002].

ACKERMAN, A. S., O. B. TOON, D. E. STEVENS, A. J. HEYMSFIELD, V. RAMANATHAN and E. J. WELTON. Reduction of Tropical Cloudiness by Soot. *Science*, 288:pages 1042–1047 [2000].

ANDREAE, M. O., D. ROSENFELD, P. ARTAXO, A. A. COSTA, G. P. FRANK, K. M. LONGO and M. A. F. SILVA-DIAS. Smoking Rain Clouds over the Amazon. *Science*, 303:pages 1337–1342 [2004].

ANTHES, R. A. Enhancement of Convective Precipitation by Mesoscale Variations in Vegetative Covering in Semiarid Regions. *Journal of Climate and Applied Meteorology*, 23(4):pages 541–554 [1984].

AVISSAR, R. and Y. LIU. Three-dimensional numerical study of shallow convective clouds and precipitation induced by land surface forcing. *Journal of Geophysical Research*, 101(D3):pages 7499–7518 [1996].

AVISSAR, R. and T. SCHMIDT. An evaluation of the scale at which ground-surface heat flux patchiness affects the convective boundary layer using large-eddy simulations. *Journal of the Atmospheric Sciences*, 55(16):pages 2666–2689 [1998].

CARLETON, A. M., J. ADEGOKE, J. ALLARD, D. L. ARNOLD and D. J. TRAVIS. Summer season land cover - convective cloud associations for the Midwest U.S. "Corn Belt". *Geophysical Research Letters*, 28(9):pages 1679–1682 [2001].

CHARNEY, J., P. H. STONE and W. J. QUIRK. Drought in the Sahara: A Biogeophysical Feedback Mechanism. *Science*, 187(4175):pages 434–435 [1975].

CHASE, T. N., R. A. PIELKE SR., T. G. F. KITTEL, R. R. NEMANI and S. W. RUNNING. Simulated impacts of historical land cover changes on global climate in northern winter. *Climate Dynamics*, 16(2-3):pages 93–105 [2000].

CHEN, F. and R. AVISSAR. Impact of land-surface moisture variability on local shallow convective cumulus and precipitation in large-scale models. *Journal of Applied Meteorology*, 33(12):page 1382:1401 [1994a].

—. The impact of land-surface wetness heterogeneity on mesoscale heat fluxes. *Journal of Applied Meteorology*, 33(11):pages 1323–1340 [1994b].

CHEN, F. and J. DUDHIA. Coupling and Advanced Land Surface-Hydrology Model with the Penn State-NCAR MM5 Modeling System. Part I: Model Implementation and Sensitivity. *Monthly Weather Review*, 129(4):pages 569–585 [2001].

CHEN, F., K. MITCHELL, J. SCHAAKE, Y. XUE, H.-L. PAN, V. KOREN, Q. Y. DUAN, M. EK and A. BETTS. Modeling of Land-Surface Evaporation by four Schemes and Comparison with FIFE Observations. *Journal of Geophysical Research*, 101(D3):pages 7251–7268 [1996].

CLARK, C. A. and R. W. ARRIT. Numerical Simulations of the Effect of Soil Moisture and Vegetation Cover on the Development of Deep Convection. *Journal of Applied Meteorology*, 34(9):pages 2029–2045 [1995].

COCHRANE, M. A. Fire Science for Rainforests. *Nature*, 421:pages 913–919 [2003].

CUTRIM, E., D. W. MARTIN and R. RABIN. Enhancement of Cumulus Clouds over Deforested Lands in Amazonia. *Bulletin of the American Meteorological Society*, 76(10):pages 1801–1805 [1995].

DALU, G. A. and R. A. PIELKE. Vertical Heat Fluxes Generated by Mesoscale Atmospheric Flow Induced by Thermal Inhomogeneities in the PBL. *Journal of the Atmospheric Sciences*, 50(6):pages 919–926 [1993]. Notes and Correspondence.

DALU, G. A., R. A. PIELKE, M. BALDI and X. ZENG. Heat and Momentum Fluxes Induced by Thermal Inhomogeneities with and without Large-Scale Flow. *Journal of the Atmospheric Sciences*, 53(22):pages 3286–3302 [1996].

DICKINSON, R. E., A. HENDERSON-SELLERS and P. KENNEDY. Biosphere Atmosphere Transfer Scheme (BATS) Version 1e as Coupled to the NCAR Community Climate Model. STR NCAR/TN-387, Climate and Global Dynamics Division, National Center for Atmospheric Research, Boulder, Colorado [1993]. NCAR Technical Note.

DIRMEYER, P. A. An Evaluation of the Strength of Land-Atmosphere Coupling. *Journal of Hydrometeorology*, 2(4):pages 329–344 [2001].

DOLMAN, A. J., M. A. SILVA DIAS, J.-C. CALVET, M. ASHBY, A. S. TAHARA, C. DELIRE, P. KABAT, G. A. FISH and C. A. NOBRE. Meso-scale effects of tropical deforestation in Amazonia: preparatory LBA modelling studies. *Annales Geophysicae*, 17(8):pages 1095–1110 [1999].

DORAN, J. C., W. J. SHAW and J. M. HUBE. Boundary Layer Characteristics over Areas of Inhomogeneous Surface Fluxes. *Journal of Applied Meteorology*, 34(2):pages 559–571 [1995].

DURIEUX, L., L. A. T. MACHADO and H. LAURENT. The impact of deforestation on cloud cover over the Amazon arc of deforestation. *Remote Sensing of Environment*, 86:pages 132–140 [2003].

EAGLESON, P. S. Climate, Soil, and Vegetation: 1. Introduction to Water Balance Dynamics. *Water Resources Research*, 14(5):pages 705–712 [1978a].

—. Climate, Soil, and Vegetation: 6. Dynamics of the Annual Water Balance. *Water Resources Research*, 14(5):pages 749–764 [1978b].

ECK, T. F., B. N. HOLBEN, I. SLUTSKER and A. SETZER. Measurements of Irradiance Attenuation and Estimation of Aerosol Single Scattering Albedo for Biomass Burning Aerosols in Amazonia. *Journal of Geophysical Research*, 103(D24):pages 31,865–31,878 [1998].

ELTAHIR, E. A. and R. L. BRAS. A Description of Rainfall Interception over Large-areas. *Journal of Climate*, 6(6):pages 1002–1008 [1993a].

—. Estimation of the fractional Coverage of rainfall in Climate Models. *Journal of Climate*, 6(4):pages 639–644 [1993b].

—. On the Response of the Tropical Atmosphere to Large-scale Deforestation. *Quarterly Journal of the Royal Meteorological Society*, 119(512):pages 779–793 [1993c].

—. Sensitivity of Regional Climate to Deforestation in the Amazon Basin. *Advances in Water Resources*, 17(1-2):pages 101–115 [1994].

ENTEKHABI, D. and P. S. EAGLESON. Land Surface Hydrology Parameterization for Atmospheric General Circulation Models Including Subgrid Scale Spatial Variability. *Journal of Climate*, 2(8):pages 816–831 [1989].

ENTEKHABI, D., I. RODRIGUEZ-ITURBE and R. L. BRAS. Variability in Large-Scale Water Balance with Land Surface-Atmosphere Interaction. *Journal of Climate*, 5(8):pages 798–813 [1992].

FACCHINI, M. C., M. MIRCEA, S. FUZZI and R. J. CHARLSON. Cloud Albedo Enhancement by Surface-Active Organic Soluted in Growing Droplets. *Nature*, 401(6750):pages 257–259 [1999].

FARELLA, N., M. LUCOTTE, P. LOUCHOUARN and M. ROULET. Deforestation modifying terrestrial organic transport in thr Rio Tapajós, Brazilian Amazon. *Organic Geochemistry*, 32:pages 1443–1458 [2001].

FEARNSIDE, P. M. Amazonian deforestation and global warming: carbon stocks in vegetation replacing Brazil's Amazon forest. *Forest Ecology and Management*, 80:pages 21–34 [1996].

FERRAZ, G., G. J. RUSSEL, P. C. STOUFFER, R. O. BIERREGAARD JR., S. L. PIMM and T. E. LOVEJOY. Rates of Species Loss from Amazonian Forest Fragments. *Proceedings of the National Academy of Sciences*, 100(24):pages 14,069–14,073 [2003].

GASH, J. H. C. and C. A. NOBRE. Climatic Effects of Amazonian Deforestation: Some Results from ABRACOS. *Bulletin of the American Meteorological Society*, 78(5):pages 823–830 [1997].

GASH, J. H. C. and W. J. SHUTTLEWORTH. Tropical Deforestation: Albedo and the Surface-Energy Balance. *Climatic Change*, 19(1-2):pages 123–133 [1991].

GENTRY, A. H. and J. LOPEZ-PARODI. Deforestation and Increased Flooding of the Upper Amazon. *Science*, 210(4476):pages 1354–1356 [1980].

GIORGI, F. and R. AVISSAR. Representation of heterogeneity effects in earth system modeling: Experience from land surface modeling. *Reviews of Geophysics*, 35(4):pages 413–437 [1997].

HAHMANN, A. N. and R. E. DICKINSON. RCCM2-BATS Model over Tropical South America: Applications to Tropical Deforestation. *Journal of Climate*, 10(8):pages 1944–1964 [1997].

HENDERSEN-SELLERS, A. Surface Type and Its Effect Upon Cloud Cover: A Climatological Investigation. *Journal of Geophysical Research*, 83(C10):pages 5057–5062 [1978].

HONG, X., M. J. LEACH and S. RAMAN. A Sensitivity Study of Convective Cloud Formation by Vegetation Forcing with Different Atmospheric Conditions. *Journal of Applied Meteorology*, 34(9):pages 2008–2028 [1995].

HOUGHTON, R. A., D. L. SKOLE, C. A. NOBRE, J. L. HACKLER, K. T. LAWRENCE and W. H. CHOMENTOWSKI. Annual fluxes of carbon from deforestation and regrowth in the Brazilian Amazon. *Nature*, 403(20):pages 301–304 [2000].

IDSO, S. B., R. D. JACKSON, R. J. REGINATO, B. A. KIMBALL and F. S. NAKAYAMA. The Dependence of Bare Soil Albedo on Soil Water Content. *Journal of Applied Meteorology*, 14(1):pages 109–113 [1975].

INPE. Monitoring of the Brazilian Amazon Forest by Satellite 2001-2002. Tech. rep., São José Dos Campos [2003].

KAUFMAN, Y. J. and R. S. FRASER. The Effect of Smoke Particles on Clouds and Climate Forcing. *Science*, 277:pages 1636–1639 [1997].

KAUFMAN, Y. J., W. J. H. HOBBS, P. V. KIRCHHOFF, P. ARTAXO, L. A. REMER, B. N. HOLBEN, M. D. KING, D. E. WARD, E. M. PRINS, K. M. LONGO, L. F. MATTOS, C. A. NOBRE, J. D. SPINHIRNE, Q. JI, A. M. THOMPSON, J. F. GLEASON, S. A. CHRISTOPHER and S.-C. TSAY. Smoke, Clouds, and Radiation-Brazil (SCAR-B)

Experiment. *Journal of Geophysical Research*, 103(D24):pages 31,783–31,808 [1998].

KAUFMAN, Y. J., D. TANRÉ and O. BOUCHER. A satellite view of aerosols in the climate system. *Nature*, 419:pages 215–223 [2002].

KAVOURAS, I. G., N. MIHALOPOULOS and E. G. STEPHANOU. Formation of Atmospheric Particles from Organic Acids Produced by Forests. *Nature*, 395:pages 683–686 [1998].

KLEIDON, A., K. FRAEDRICH and M. HEIMANN. A green planet versus a desert world: estimating the maximum effect of vegetation on the land surface climate. *Climatic Change*, 44(4):pages 471–493 [2000].

KLEIDON, A. and M. HEINMANN. Assessing the role of deep rooted vegetation in the climate system with model simulations: mechanism, comparison to observations and implications for Amazonian deforestation. *Climate Dynamics*, 16(2-3):pages 183–199 [2000].

KOREN, I., Y. J. KAUFMAN, L. A. REMER and J. V. MARTINS. Measurement of the Effect of Amazon Smoke on Inhibition of Cloud Formation. *Science*, 303:pages 1342–1345 [2004].

KOSTER, R. D. and M. J. SUAREZ. The Influence of Land Surface Moisture Retention on Precipitation Statistics. *Journal of Climate*, 9(10):pages 2551–2567 [1996].

LAURANCE, W. F., S. G. LAURANCE and P. DELAMONICA. Tropical Forest Fragmentation and Greenhouse Gas Emissions. *Forest Ecology and Management*, 110:pages 173–180 [1998].

LEAN, J. and P. R. ROWNTREE. Understanding the Sensitivity of a GCM Simulation of Amazonian Deforestation to the Specification of Vegetation and Soil Characteristics. *Journal of Climate*, 10(6):pages 1216–1235 [1997].

—. Correction Note on "Understanding the Sensitivity of a GCM Simulation of Amazonian Deforestation to the Specification of Vegetation and Soil Characteristics". *Journal of Climate*, 12(5):pages 1549–1551 [1999]. Notes and Correspondence.

LETTAU, H., K. LETTAU and L. C. B. MOLION. Amazonia's Hydrological Cycle and the Role of Atmospheric Recycling in Assessing Deforestation Effects. *Monthly Weather Review*, 107(3):pages 227–238 [1979].

LIANG, X., D. P. LETTENMAIER, E. F. WOOD and S. J. BURGES. A simple hydrologically based model of land surface water and energy fluxes for general circulation models. *Journal of Geophysical Research*, 99(D7):pages 14,415–14,428 [1994].

LYNN, B. H., W.-K. TAO and P. J. WETZEL. A Study of Landscape-Generated Deep Moist Convection. *Monthly Weather Review*, 126(4):pages 928–942 [1998].

MAHFOUF, J.-F., E. RICHARD and P. MASCART. The Influence of Soil and Vegetation on the Development of Mesoscale Circulations. *Journal of Climate and Applied Meteorology*, 26(11):pages 1483–1495 [1987].

MAHRT, L., J. SUN, D. VICKERS, J. I. MACPHEARSON, J. R. PEDERSON and R. L. DESJARDIN. Observations of Fluxes and Inland Breezes over a Heterogeneous Surface. *Journal of the Atmospheric Sciences*, 51(17):pages 2484–2499 [1994].

MARENGO, J. A. Variations and Change in South American Streamflow. *Climatic Change*, 31:pages 99–117 [1995].

MARTIN, P. Vegetation responses and feedbacks to climate: a review of models and processes. *Climate Dynamics*, 8(4):pages 201–210 [1993].

MCGUFFIE, K., A. HENDERSON-SELLERS, H. ZHANG, T. B. DURBRIDGE and A. J. PITMAN. Global Climate Sensitivity to Tropical Deforestation. *Global and Planetary Change*, 10(1-4):pages 97–128 [1995].

MEHER-HOMJI, V. M. Probable Impact of Deforestation on Hydrological Processes. *Climatic Change*, 19(1-2):pages 163–173 [1991].

MILLY, P. C. D. and K. A. DUNNE. Sensitivity of the Global Water Cycle to the Water-Holding Capacity of Land. *Journal of Climate*, 7(4):pages 506–526 [1994].

MORAES, J. F. L., B. VOLKOFF, C. C. CERRI and M. BERNOUX. Soil Properties under Amazon forest and changes due to pasture installation in Rondônia, Brazil. *Geoderma*, 70:pages 63–81 [1996].

MYERS, N. Tropical Forests: Present Status and Future Outlook. *Climatic Change*, 19(1-2):pages 3–32 [1991].

MYLNE, M. F. and P. R. ROWNTREE. Modelling the Effects of Albedo Change Associated with Tropical Deforestation. *Climatic Change*, 21(3):pages 317–343 [1992].

NEGRI, A. J., R. F. ADLER, L. XU and J. SURRAT. The Impact of Amazonian Deforestation on Dry Season Rainfall. *Journal of Climate*, 17(6):pages 1306–1319 [2004].

NOBRE, C. A., P. J. SELLERS and J. SHUKLA. Amazonian Deforestation and Regional Climate Change. *Journal of Climate*, 4(10):pages 957–988 [1991].

NORDIN, C. F. and R. H. MEADE. Deforestation and Increased Flooding of the Upper Amazon (Comments). *Science*, 215(4531):pages 426–427 [1982].

O'BRIEN, K. Upscaling Tropical Deforestation: Implications for Climate Change. *Climatic Change*, 44(3):pages 311–329 [2000].

OOKOUCHI, Y., M. SEGAL, R. C. KESSLER and R. A. PIELKE. Evaluation of Soil Moisture Effects on the Generation and Modification of Mesoscale Circulations. *Monthly Weather Review*, 112(11):pages 2281–2292 [1984].

OZANNE, C. M. P., D. ANHUF, S. L. BOULTER, M. KELLER, R. L. KITCHING, C. KORNER, F. C. MEINZER, A. W. MITCHELL, T. NAKASHIZUKA, P. L. SILVA DIAS, N. E. STROK, S. J. WRIGHT and M. YOSHIMURA. Biodiversity Meets the Atmosphere: A Global View of Forest Canopies. *Science*, 301:pages 183–186 [2003].

PAN, H.-L. and L. MAHRT. Interaction between Soil Hydrology and Boundary-Layer Development. *Boundary-Layer Meteorology*, 38:pages 185–202 [1987].

PENG, Y., U. LOHMANN, R. LEAITCH, C. BANIC and M. COUTURE. The Cloud Albedo-Cloud Droplet Effective Radius Relationship for Clean and Polluted Clouds from RACE and FIRE.ACE. *Journal of Geophysical Research*, 107(D11):page 10.1029/2000JD000,281 [2002].

PENNER, J. E., X. DONG and Y. CHEN. Observational evidence of a change in radiative forcing due to the indirect aerosol effect. *Nature*, 427:pages 231–234 [2004].

PIELKE SR., R. A. Influence of the spatial distribution of vegetation and soils on the prediction of cumulus convective rainfall. *Review of Geophysics*, 39(2):pages 151–177 [2001].

PINTY, J.-P., P. MASCART, E. RICHARD and R. ROSSET. An Investigation of Mesoscale Flows Induced by Vegetation Inhomogeneities Using an Evapotranspiration Model Calibrated Against HAPEX-MOBILHY Data. *Journal of Applied Meteorology*, 28(9):pages 976–992 [1989].

POLCHER, J. and K. LAVAL. A statistical study of the regional impact of deforestation on climate in the LMD GCM. *Climate Dynamics*, 10(4-5):pages 205–219 [1994].

RABIN, R. M. and D. W. MARTIN. Satellite Observations of Shallow Cumulus Coverage over the Central United States: An Exploration of Land Use Impact on Cloud Cover. *Journal of Geophysical Research*, 101(D3):pages 7149–7155 [1996].

RABIN, R. M., S. STADLER, P. J. WETZEL, D. J. STENSRUD and M. GREGORY. Observed Effects of Landscape Variability on Convective Clouds. *Bulletin of the American Meteorological Society*, 71(3):pages 272–280 [1990].

RAMANATHAN, V., P. J. CRUTZEN, J. T. KIEHL and D. ROSENFELD. Aerosols, Climate, and the Hydrological Cycle. *Science*, 294:pages 2119–2124 [2001].

RICHEY, J. E., C. A. NOBRE and C. DESER. Amazon River Discharge and Climate Variability: 1903 to 1985. *Science*, 246(4926):pages 101–103 [1989].

DA ROCHA, H. R., C. A. NOBRE, J. P. BONATTI, I. R. WRIGHT and P. J. SELLERS. A Vegetation-atmosphere Interaction Study for Amazonia Deforestation using Field Data and a 'Single Column' Model. *Quarterly Journal of the Royal Meteorological Society*, 122(531):pages 567–594 [1996]. Part A.

ROSENFELD, D. TRMM Observed First Direct Evidence of Smoke from Forest Fires Inhibiting Rainfall. *Geophysical Research Letters*, 26(20):pages 3105–3108 [1999].

ROY, S. B. and R. AVISSAR. Impact of land use/land cover change on regional hydrometeorology in Amazonia. *Journal of Geophysical Research*, 107(D20) [2002].

SALATI, E. and C. A. NOBRE. Possible Climatic Impacts of Tropical Deforestation. *Climatic Change*, 19(1-2):pages 177–196 [1991].

SALATI, E. and P. B. VOSE. Amazon Basin: A System in Equilibrium. *Science*, 225(4658):pages 129–138 [1984].

SALESKA, S. R., S. D. MILLER, D. M. MATROSS, M. L. GOULDEN, S. C. WOFSY, H. R. DA ROCHA, P. B. DE CAMARGO, P. CRILL, B. C. DAUBE, H. C. DE FREITAS, L. HUTYRA, M. KELLER, V. KIRCHHOFF, M. MENTON, J. W. MUNGER, E. H. PYLE, A. H. RICE and H. SILVA. Carbon in Amazon Forests: Unexpected Seasonal Fluxes and Disturbance-Induced Losses. *Science*, 302:pages 1554–1557 [2003].

SCHEFFER, M., S. CARPENTER, J. A. FOLEY, C. FOLKE and B. WALKER. Catastrophic Shifts in Ecosystems. *Nature*, 413:pages 591–596 [2001].

SCOTT, R., R. D. KOSTER, D. ENTEKHABI and M. J. SUAREZ. Effect of a Canopy Interception Reservoir on Hydrological Persistence in a General Circulation Model. *Journal of Climate*, 8(7):pages 1917–1922 [1995]. Notes and Correspondence.

SEGAL, M., R. W. ARRITT, C. CLARK, R. RABIN and J. BROWN. Scaling Evaluation of the Effect of Surface Characteristics on Potential for Deep Convection over uniform Terrain. *Monthly Weather Review*, 123(2):pages 383–400 [1995].

SEGAL, M., R. AVISSAR, M. C. MCCUMBER and R. A. PIELKE. Evaluation of Vegetation Effects on the Generation and Modification of Mesoscale Circulations. *Journal of the Atmospheric Sciences*, 45(16):pages 2268–2292 [1988].

SELLERS, P. J., Y. MINTZ, Y. C. SUD and A. DALCHER. A Simple Biosphere Model (SIB) for Use with Genral Circulation Models. *Journal of the Atmospheric Sciences*, 43(6):pages 505–531 [1986].

SETH, A. and F. GIORGI. Three-dimensional model study of organized mesoscale circulations induced by vegetation. *Journal of Geophysical Research*, 101(D3):pages 7371–7391 [1996].

SHUKLA, J., C. NOBRE and P. SELLERS. Amazon Deforestation and Climate Change. *Science*, 247(4948):pages 1322–1325 [1990].

SKOLE, D. and C. TUCKER. Tropical Deforestation and habitat Fragmentation in the Amazon: Satellite Data from 1978 to 1988. *Science*, 260(5116):pages 1905–1910 [1993].

STERNBERG, H. O. Aggravation of Floods in the Amazon River as a Consequence of Deforestation? *Geografiska Annaler. Series A, Physical Geography*, 69(1):pages 201–219 [1987].

SUD, Y. C., G. K. WALKER, J.-H. KIM, G. E. LISTON, P. J. SELLERS and W. K.-M. LAU. Biogeophysical Consequences of a Tropical Deforestation Scenario: A GCM Simulation Study. *Journal of Climate*, 9(12):pages 3225–3247 [1996].

SUN, J. and L. MAHRT. Spatial Distribution of Surface Fluxes Estimated from Remotely Sensed Variables. *Journal of Applied Meteorology*, 33(11):pages 1341–1353 [1994].

WANG, J., R. L. BRAS and E. A. B. ELTAHIR. A Stochastic Linear Theory of Mesoscale Circulation Induced by the Thermal Heterogeneity of the Land Surface. *Journal of the Atmospheric Sciences*, 53(22):pages 3349–3366 [1996].

—. The Impact of Observed Deforestation on the Mesoscale Distribution of Rainfall and Clouds in Amazonia. *Journal of Hydrometeorology*, 1(3):pages 267–286 [2000].

WANG, J., E. A. B. ELTAHIR and R. L. BRAS. Numerical Simulations of Nonlinear Mesoscale Circulations Induced by the Thermal Heterogeneities of Land Surface. *Journal of the Atmospheric Sciences*, 55(3):pages 447–464 [1998].

WEAVER, C. P. and R. AVISSAR. Atmospheric Disturbances Caused by Human Modification of the Landscape. *Bulletin of the American Meteorological Society*, 82(2):pages 269–281 [2001].

WERTH, D. and R. AVISSAR. The local and global effects of Amazon deforestation. *Journal of Geophysical Research*, 107(D20) [2002].

WETZEL, P. J., S. ARGENTINI and A. BOONE. Role of land surface in controlling daytime cloud amount: Two case studies in the GCIP-SW area. *Journal of Geophysical Research*, 101(D3):pages 7359–7370 [1996].

XUE, Y., H. G. BASTABLE, P. A. DIRMEYER and P. J. SELLERS. Sensitivity of Simulated Surface Fluxes to Changes in Land Surface Parameterizations - A Study using ABRACOS Data. *Journal of Applied Meteorology*, 35(3):pages 386–400 [1996].

XUE, Y., P. J. SELLERS, J. L. KINTER and J. SHUKLA. A Simplified Biosphere Model for Global Climate Studies. *Journal of Climate*, 4(3):pages 345–364 [1991].

YAN, H. and R. A. ANTHES. The Effect of Variations in Surface Moisture on Mesoscale Circulations. *Monthly Weather Review*, 116(1):pages 192–208 [1988].

YEH, T.-C., R. T. WETHERALD and S. MANABE. The Effect of Soil Moisture on the Short-Term Climate and Hydrology Change - A Numerical Experiment. *Monthly Weather Review*, 112(3):pages 474–490 [1984].

ZENG, N. Understanding Climate Sensitivity to Tropical Deforestation in a Mechanistic Model. *Journal of Climate*, 11(8):pages 1969–1975 [1998].

ZENG, N., R. E. DICKINSON and X. ZENG. Climatic Impact of Amazon Deforestation - A Mechanistic Model Study. *Journal of Climate*, 9(4):pages 859–883 [1996].

ZHANG, H., K. MCGUFFIE and A. HENDERSON-SELLERS. Impacts of Tropical Deforestation. Part II: The Role of Large-Scale Dynamics. *Journal of Climate*, 9(10):pages 2498–2521 [1996].

ZHONG, S. and J. C. DORAN. An Evaluation of the Importance of Surface Flux Variability on GCM-scale Boundary-Layer Characteristics using Realistic Meteorological and Surface Forcing. *Journal of Climate*, 11:pages 2774-2788 [1998].

CHAPTER 2

PHYSICAL INSIGHT AND HYPOTHESES

This chapter briefly presents the physical insight into the phenomenon of land surface heterogeneity driven mesoscale circulations. This chapter does not delve into a thorough treatment of the physical mechanisms that related the land surface to atmospheric circulation, nor does it provide a thorough literature review (the reader is referred to Chapter 1 for a brief literature review, and may wish to consult Pielke Sr. [2001] for a thorough review.) Rather, this chapter is intended as a brief heuristic description of the creation of localized mesoscale circulations that are created by contrasts in land surface properties such as those created by deforestation.

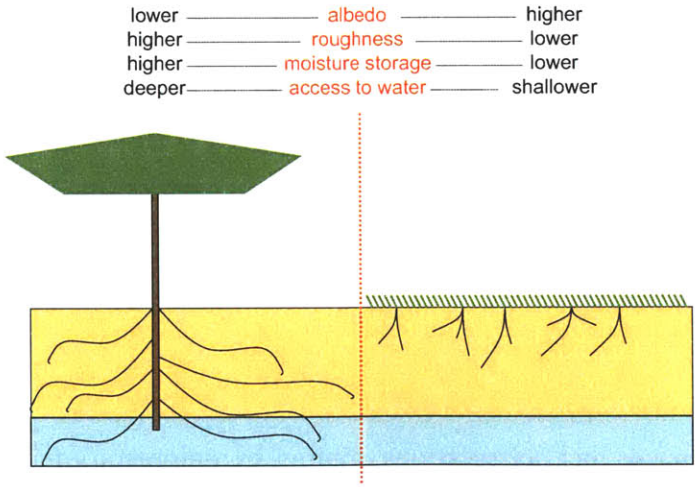

Figure 2-1: Schema of contrasting properties created by deforestation.

Forested and deforested surfaces have different properties with respect to radiation, hydrology and atmospheric forcing. These differences are highlighted in the schematic drawn in Figure 2-1. Forested surfaces have a lower albedo than defor-

ested surfaces. More net radiative energy must thus be absorbed and transformed by forested surfaces. This results in more energy being transfered into the boundary layer above. Energy is transfered from the land surface to the overlying atmosphere through sensible and latent heat fluxes (turbulent heat fluxes) and through longwave radiative energy. The partitioning of the total energy into these fluxes is dependent upon the properties of the surface, as well as the availability of water. Trees, and tropical trees of the Amazon in particular [Kleidon and Heinmann, 2000], have much deeper roots that the vegetation that covers deforested areas. This translates into a greater access to water, and thus a greater water availability. It also results in a lower sensitivity to rainfall inter-storm duration or dry spells. Finally the geometrical differences, particularly in height, between tress and the vegetation that covers deforested areas results in greater roughness over forested areas. Higher roughness results in more intense turbulence and greater energetic exchanges between the surface and the atmosphere. The contrasting properties of forested and deforested areas creates differential interactions between the land surface and the overlying atmosphere.

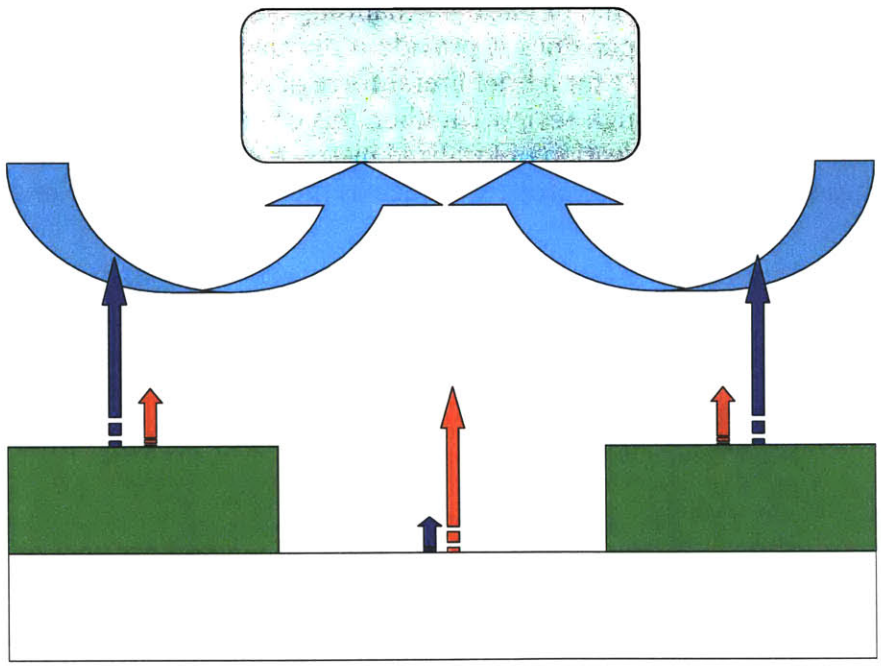

Figure 2-2: Schema of local circulations created by deforestation; the dark blue arrows represent latent heat flux (LH), the red arrows represent sensible heat flux (SH), the large light blue arrows are a representation of the local circulation, and the dark grey mass represent cloud formation. The surface is representative of two strips of forested area that surround a patch of deforestation.

Adjacent patches of forested and deforested areas result in local circulations,

mostly due to the surface heating contrast that arises from the vegetation cover contrast. Such an effect is represented in Figure 2-2. Forested areas, due to their greater moisture availability will have a lower Bowen ratio (ratio of sensible to latent heating) than the adjacent deforested areas. This will result in a near-surface moisture contrast; the higher energy availability (due to the lower albedo) over forested area will result in a contrast of moist static energy. Thus far, we are presented with more energetic and moister boundary-layer over forested areas versus a drier and energetically weaker boundary layer over forested areas. While moist air tends to rise, which would result in cloud formation over forested areas, the moisture and energy gradient leads to a converging circulation centered over the deforested area. Added to this convergence tendency is the pull exerted by the thermal upwelling over deforested areas. This upwelling is a direct result of the bias toward sensible heating over the comparatively water-scarce deforested areas. The thermally driven upward pull over the deforested areas amplifies the convergence tendency and gives rise to a higher convective potential over deforested areas. As a result of this circulation, and upper-level divergence may result in downward flow over the forested areas (in order to conserve mass), and may thus further feed into the original circulation.

The strength and viability of such localized circulations that are borne of land surface contrasts have largely been shown to be dependent upon the scale of the patches as well as the synoptic meteorological conditions. Their existence has been observed and widely documented in the analogous case of the land-sea breeze phenomenon. As has been discussed in Chapter 1, their existence over deforested areas has been studied using models, and has been qualitatively observed. Yet there is no quantitative knowledge concerning their actual existence or persistence in the case of land surface contrasts created by anthropogenic deforestation. This thesis seeks to investigate the impact of Amazonian deforestation on climate by analyzing patterns of clouds and rainfall with respect to the patterns of deforestation.

REFERENCES

KLEIDON, A. and M. HEINMANN. Assessing the role of deep rooted vegetation in the climate system with model simulations: mechanism, comparison to observations and implications for Amazonian deforestation. *Climate Dynamics*, 16(2-3):pages 183–199 [2000].

PIELKE SR., R. A. Influence of the spatial distribution of vegetation and soils on the prediction of cumulus convective rainfall. *Review of Geophysics*, 39(2):pages 151–177 [2001].

CHAPTER 3

CLIMATIC BACKGROUND

Before delving into the study of the effects of deforestation on climate, it is useful to understand the climate of the Amazon basin. This chapter will first provide a brief exposition of climate in the tropics and of the general circulation of the earth's atmosphere. Then, the climate of the Amazon basin will be described, including diurnal variability, seasonal variability, inter-annual variability, decadal variability, and finally long-term variability. This chapter will also cover the climate of Rondônia, a state that is located in the arc of deforestation of the Brazilian Amazon, and will provide the crucial climatological background for the rest of the study.

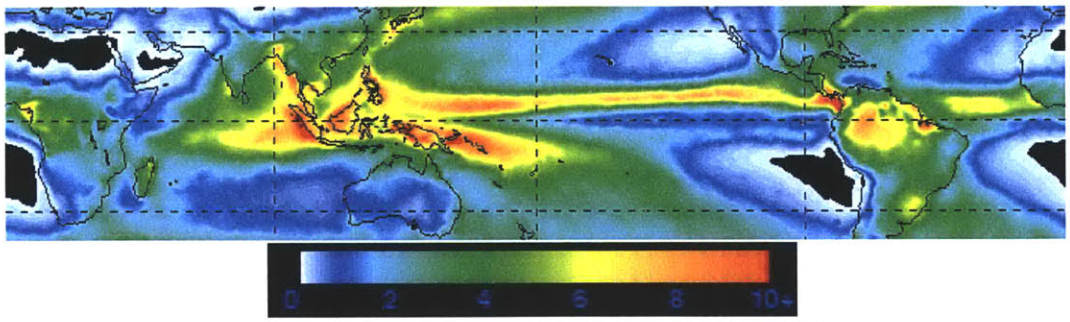

Figure 3-1: TRMM Precipitation Intensity Climatology (1998-2002).

The tropics are often referred to as the "firebox" of the Earth's climate. This colloquial description has its roots on the fact that the tropics — the middle third of the earth, between 30°N and 30°S — receives half of the incoming solar radiation, which is the main driver of climatic circulation. Moreover, the Earth's rotation imparts most of its momentum to the atmosphere in the tropics. This surplus of energy is the reason for which the tropics are at the center of the global climatic circula-

tion. Rising convective towers result from the high energetic input; these convective towers are dramatically clear in Figure 3-1, which is a climatology of precipitation intensity in the latitudinal range covered by the Tropical Rainfall Measuring Mission (TRMM) satellite.

Figures 3-2 & 3-3 highlight the differences between land and sea; lightning is much more frequent over land masses yet rainfall accumulation shows no such preference. Lightning is associated with very intense updrafts and an ice-phase at the cloud top, yet very little is known about the physics of lightning, and the causes for the land-ocean contrast are still under discussion. Williams and Stanfill [2002] cite two possible hypotheses for the contrast: the aerosol hypothesis and the thermal hypothesis. The aerosol hypothesis argues that land-generated aerosols inhibit warm rain and thereby leave more moisture in the atmosphere and creating vigorous deep convection and lightning. The thermal hypothesis argues that the reason for the contrast is the higher proportion of sensible heating over land, which creates deeper more intense thermals. Notwithstanding these uncertainties, it is clear that tropical land masses play an important role in the earth's climate.

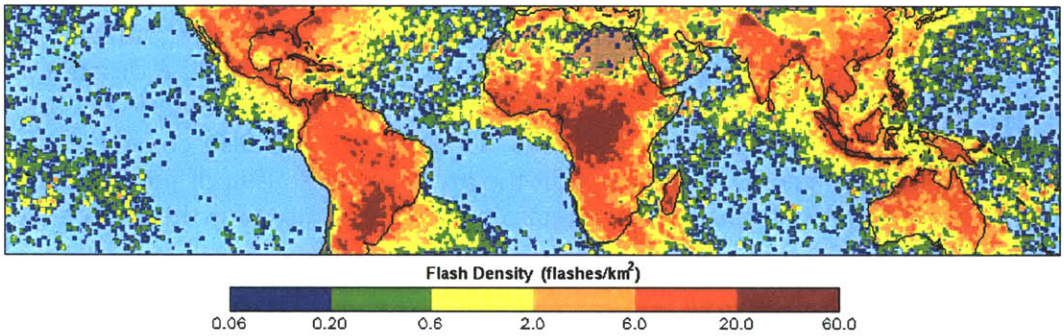

Figure 3-2: Tropical Lightning Climatology (courtesy Earle Williams).

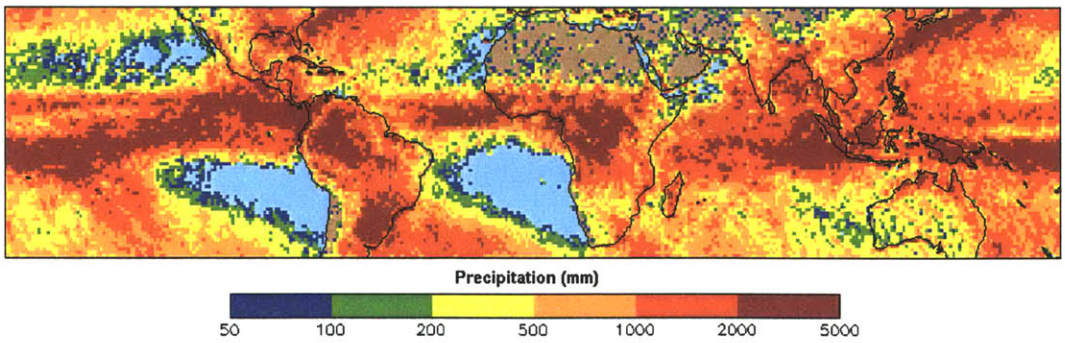

Figure 3-3: Tropical Rainfall Climatology (courtesy Earle Williams).

Indeed, using GCM simulations that contrasts a flat South American continent with no continent at all, Lenters and Cook [1995] demonstrate that continentality

is in effect responsible for a large portion of the structure of January rainfall over South America. They suggest that the generation of a thermal low over the continent is responsible for the observed precipitation structure. Most theoretical work on the Hadley cells and the general circulation have concentrated on the use of axisymmetric models of the atmosphere to derive the role of the meridional heating gradient on driving the atmospheric circulation. However, Cook [2003] finds in a GCM study (all-ocean vs. flat-continents) that the zonal variations (i. e., the land-ocean contrasts) play a fundamental role in the seasonal variations of the Hadley intensity. Through increased surface roughness, the land surface increases the momentum flux into the atmosphere, resulting in a winter hemisphere Hadley cell that has twice the intensity of the all-ocean simulation. For the summer hemisphere, the monsoonal circulations (convergence zones) of the northern (southern) hemispheres result in weaker subtropical highs, which halves the intensity of the Hadley cell. Thus, the meridional temperature gradients are accentuated with the addition of land surfaces due to their lower thermal capacities, and the Hadley intensity varies consequently.

The Amazon basin features prominently in Figures 3-1 & 3-2 & 3-3. Following sections will provide insight into the climate in the Amazon basin at various temporal scales: diurnal, seasonal, inter-annual, decadal and long-term. Particular attention will be given to Rondônia.

3.1 Climate of the Amazon Basin

The climate of rainfall in the Amazon basin varies with distance from the ocean and river. Cutrim *et al.* [2000] infer from raingauge observations that precipitation is most intense at the coast near the mouth of the Amazon, and that the precipitation is more intense inland than near the river. They also observe that the diurnal cycle of rainfall varies with distance from the ocean and river. These variations generated by the ocean-land contrast are corroborated by Minnis and Harrison [1984b] who suggest that there is a "large-scale diurnally modulated circulation feature between Amazon and adjacent ocean (...)".

Daily Variability

Convection in the Amazon basin exhibits clear diurnal variability. As is usual over tropical land masses, the diurnal cycle of cloudiness and precipitation is regular, and intra-day variability is of a scale similar to that of seasonal variability. The diurnal variability is strongly modulated by the surface [Betts and Jakob, 2002]. At sunrise, the surface layer, which is nearly saturated [Betts and Jakob, 2002], is dried off by solar heating and mixing with drier air aloft. Shallow convection is then triggered as the land surface is heated, and shallow clouds are maximum near noon [Minnis and Harrison, 1984b]. The first radar echoes that signify precipita-

tion are observed around 11:00 LST [Betts and Jakob, 2002], and deep convection ensues; higher clouds are maximum later in the afternoon [Minnis and Harrison, 1984b]. The rapidly developing convection saturates the atmosphere and renders it more stable [Machado *et al.*, 2002], thereby shutting deep convection down. The timing of the diurnal cycle is strongly dependent upon the distance from water bodies, whether they are the river or the ocean [Cutrim *et al.*, 2000; Negri *et al.*, 2000]. Through an SSM/I derived 10-year climatology of precipitation, Negri *et al.* [2000] show the strong contrast in the diurnal cycle of precipitation between continental and oceanic events. Inland precipitation rainfall show a maximum intensity at 18h00 LST, while the marine rainfall peaks at 06h00 LST. The climatology also shows associations between rainfall and the topographical and geographical features of the basin. The features of the diurnal cycle of precipitation in the Amazon basin are highlighted in Figure 3-4.

Seasonality

Seasonality in the Amazon basin is described by a wet and dry season, and break periods that separate these seasons. The atmospheric circulation in the Amazon exhibits a monsoonal reversal, which clearly defines wet and dry seasons. This monsoonal circulation is intimately related to the position of the Inter-Tropical Convergence Zone (ITCZ). The ITCZ's latitudinal position varies seasonally, reaching its maximum northern position in August at 10^oN [Nobre *et al.*, 1998] and its maximum southern position in January at 5^oS. When at its maximum northern position, there is large-scale subsidence over the Amazon basin [Nobre *et al.*, 1998], which is the reason for the absence of rain. Rainfall differences between the wet and dry seasons are examined in DeLiberty [2000], who reports that the rainfall peaks in DJF with an average rate of 6.5 mm/day, and the minimum occurs in JJA with about 2 mm/day. Fu *et al.* [1999] discuss the importance of the land surface on the seasonality of convection in the Amazon. The Amazon's seasonality is also influenced/related to other large-scale features of atmospheric/oceanic circulation. For example, the Southern Hemisphere (SH) summer climate of the Amazon basin is strongly modulated by the meridional position of the South-Atlantic Convergence Zone (SACZ) [Rickenbach *et al.*, 2002; Todd *et al.*, 2003].

The seasonal cycle of climate in the Amazon is depicted in Figures 3-5 through 3-9. The mean sea-level pressure maps (Figue 3-5) show the north-south oscillation of low pressure over the central Amazon. The month of July is marked by generalized high pressure over the entire basin, while November sees a large low pressure region pitted against the South-Atlantic and South-Pacific highs. The winds at 200mb (Figure 3-6) show the south-west (January) to north-east (July) oscillation of the center of an upper-level divergence. The 850 mb winds (Figure 3-7) show the transition between the south-easterly (July) to north-easterly winds (January) along the South-American coast. Over the Amazon, the low-level winds are strongly modulated by the physical barrier created by the Andean chain. The seasonal rainfall patterns are shown in Figures 3-8 & 3-9; both show the north-south oscillation of

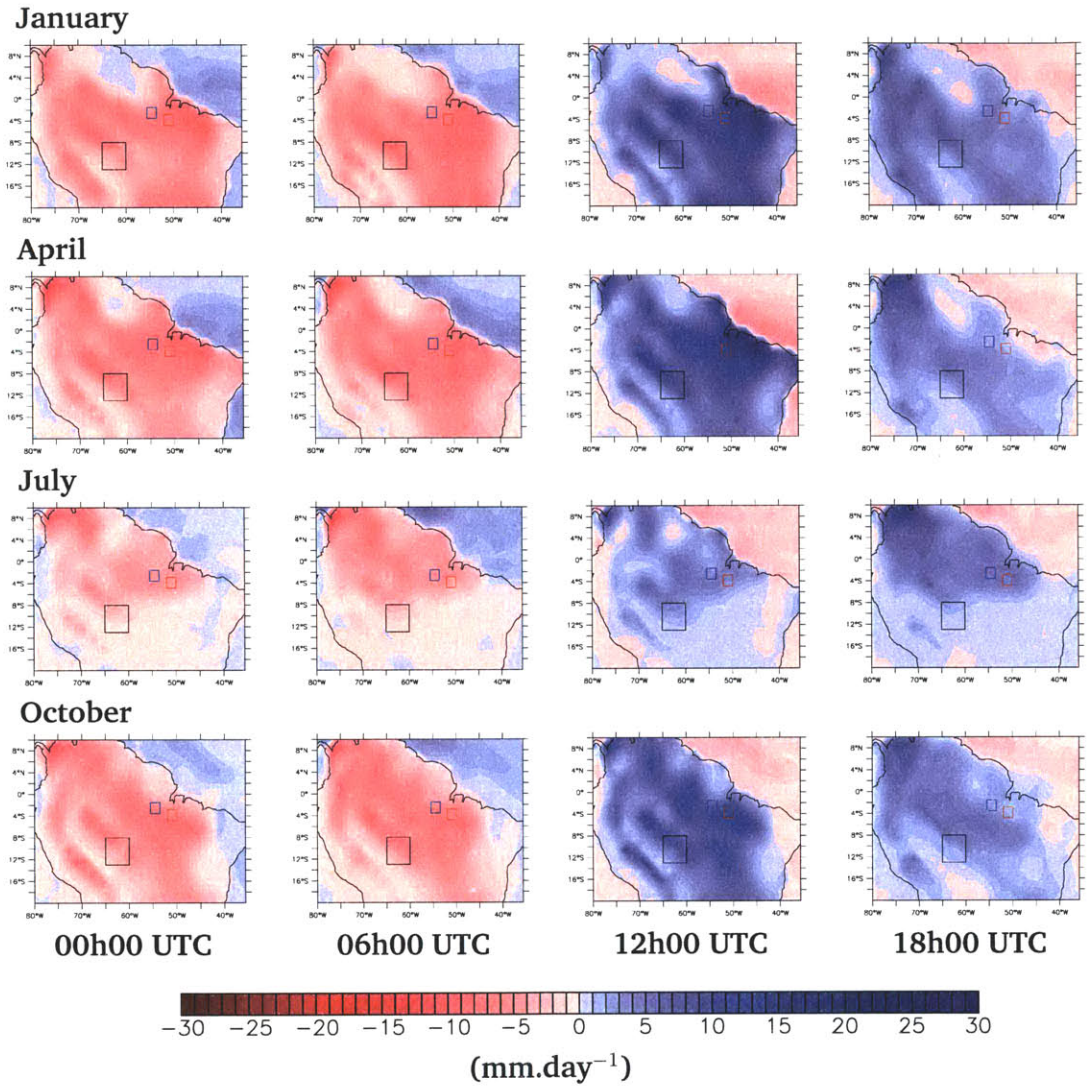

Figure 3-4: Diurnal Precipitation Rate Anomalies (relative to monthly mean) over Amazon Basin (NCEP/NCAR Renanalysis-1).

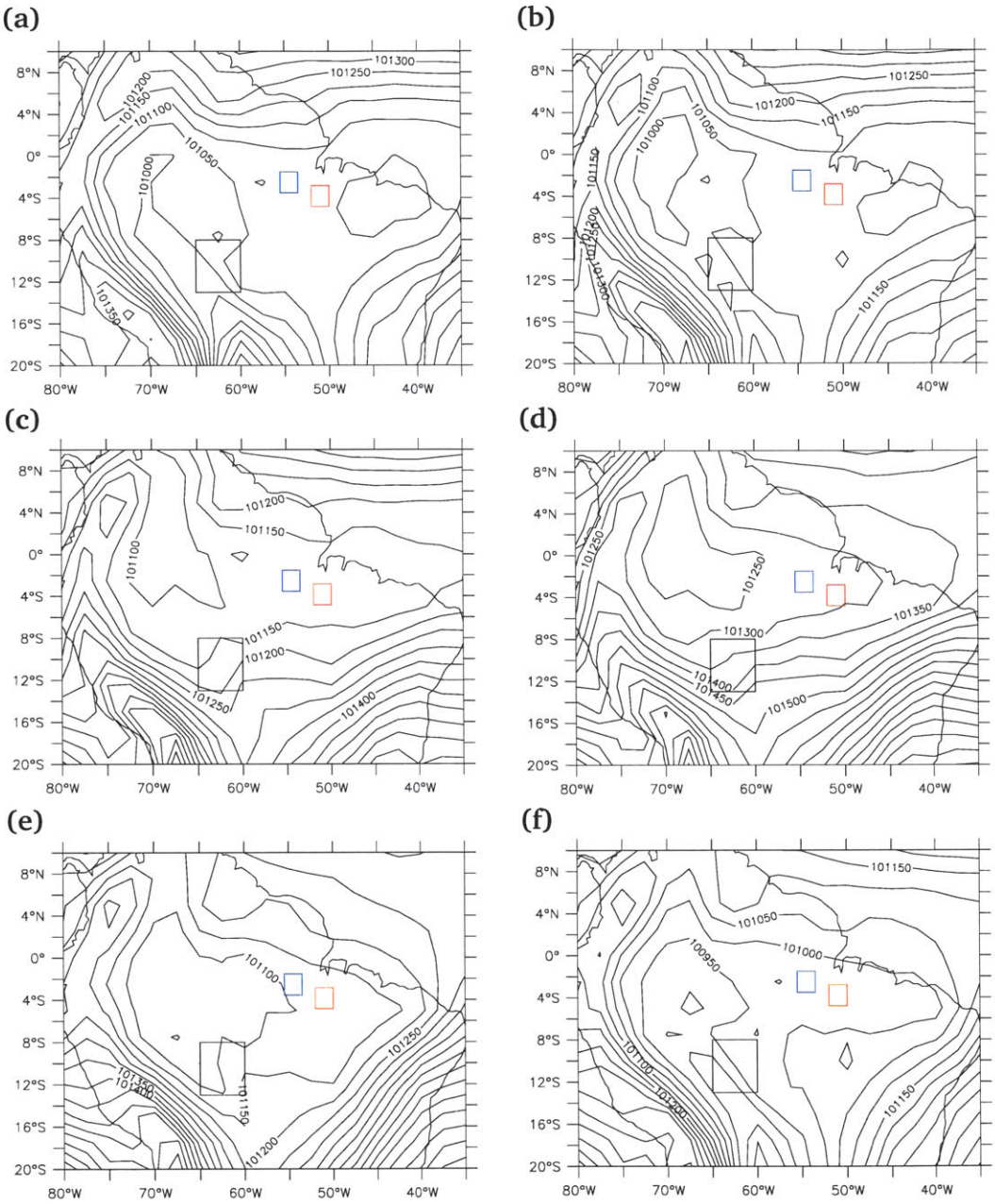

Figure 3-5: Mean Sea-Level Pressure (Pa) over Amazon Basin (NCEP/NCAR Reanalysis-2); **(a)** January; **(b)** March; **(c)** May; **(d)** July; **(e)** September; **(f)** November.

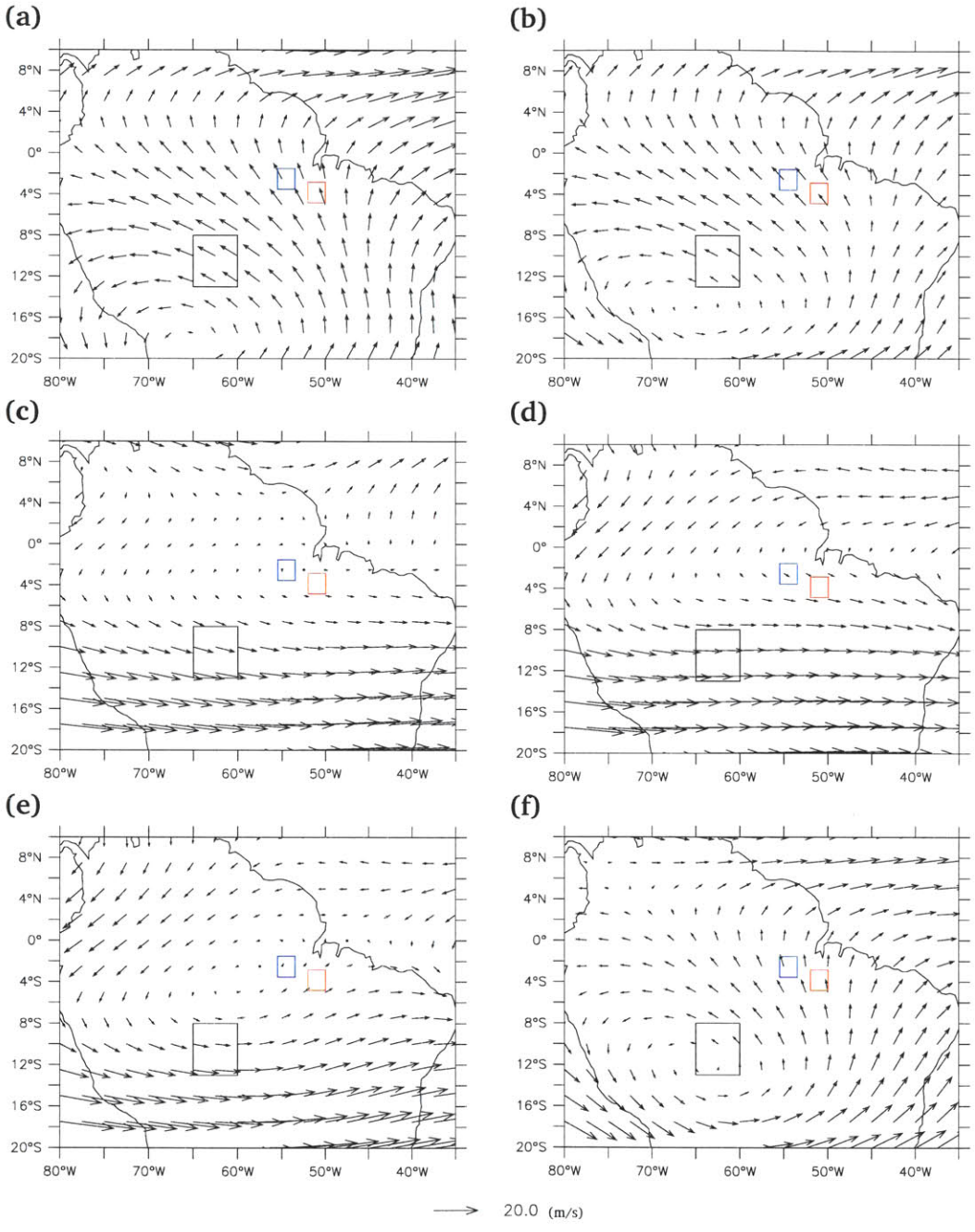

Figure 3-6: Mean 200 mb Winds over Amazon Basin (NCEP/NCAR Reanalysis-2); **(a)** January; **(b)** March; **(c)** May; **(d)** July; **(e)** September; **(f)** November.

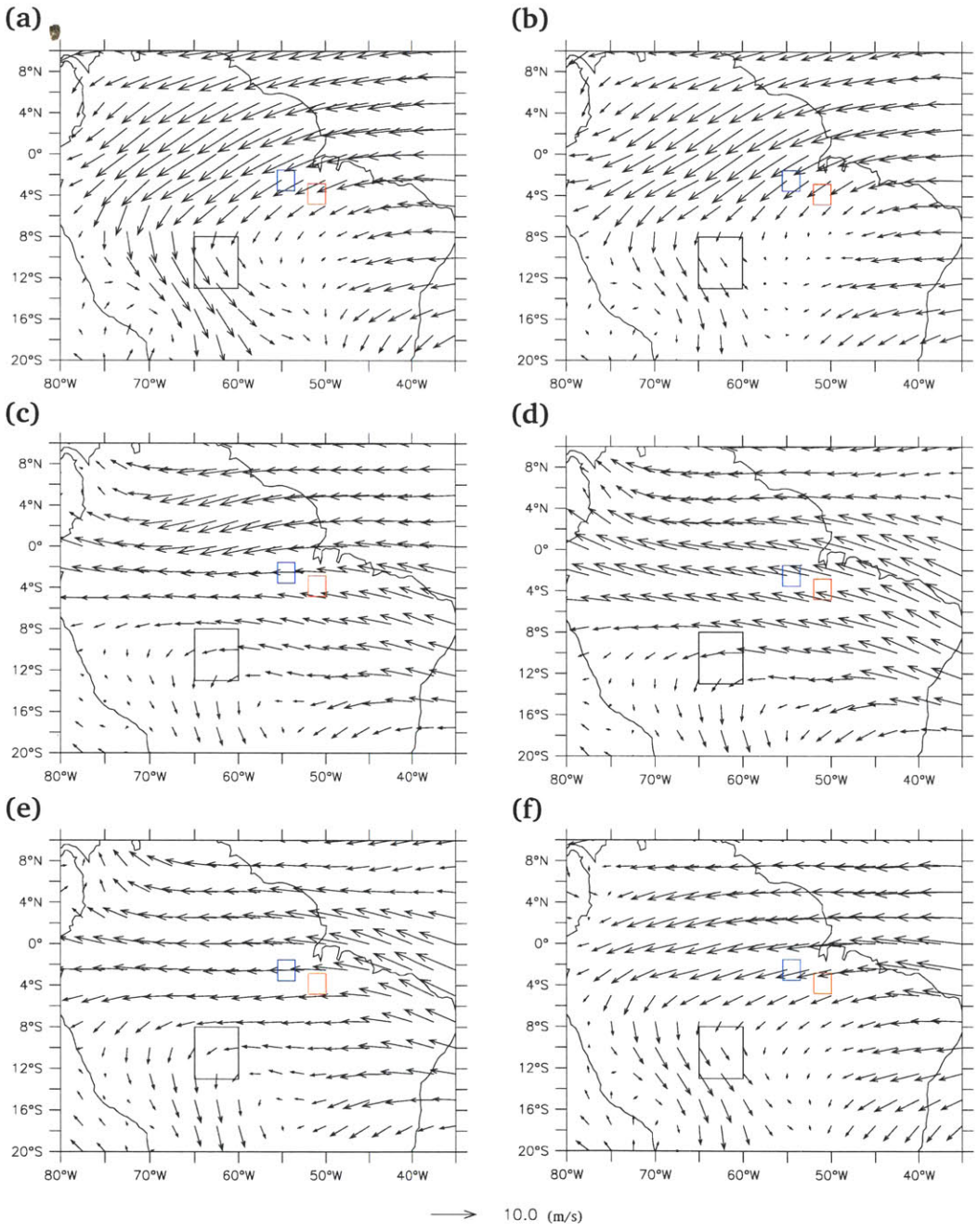

Figure 3-7: Mean 850mb Winds over Amazon Basin (NCEP/NCAR Reanalysis-2); **(a)** January; **(b)** March; **(c)** May; **(d)** July; **(e)** September; **(f)** November.

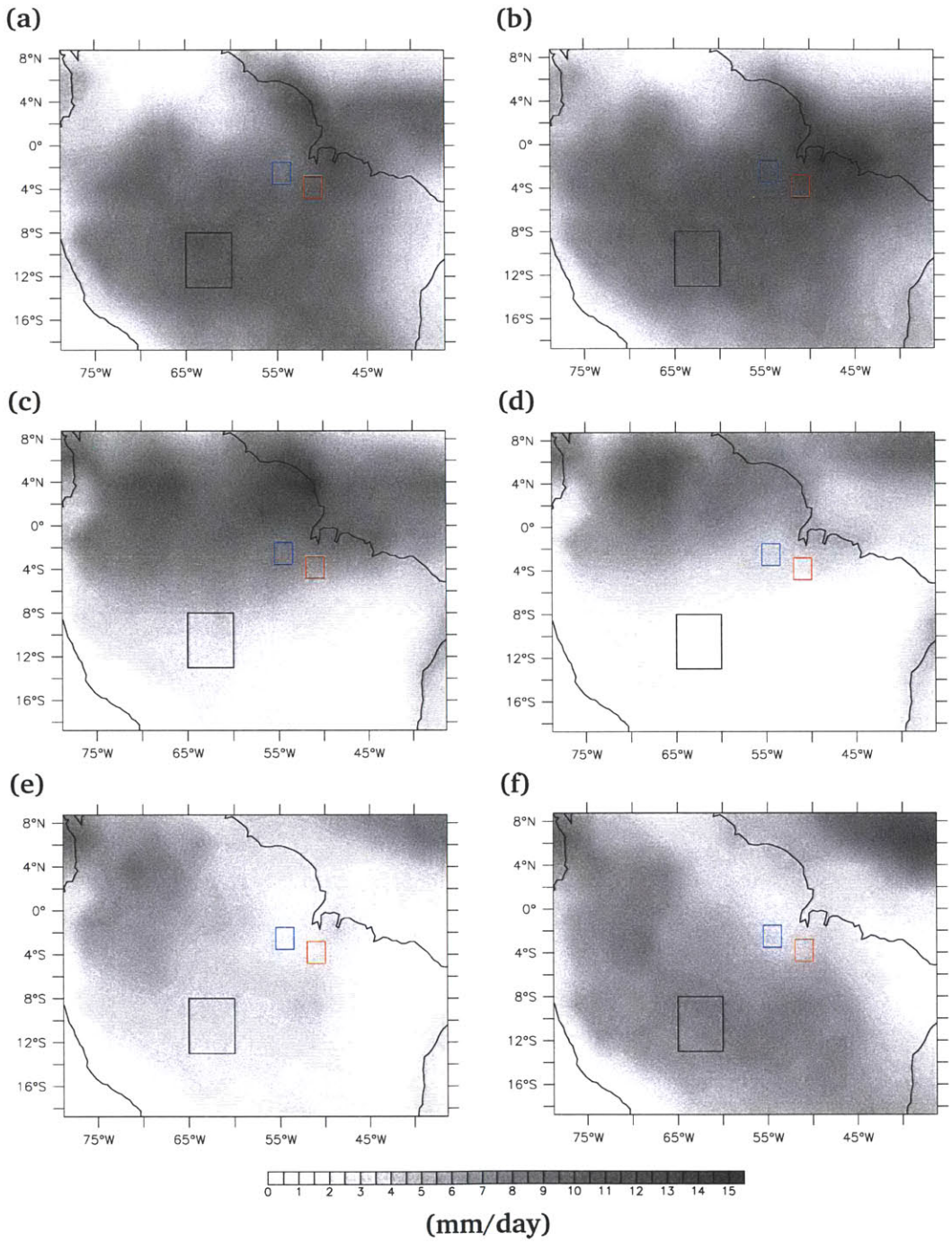

Figure 3-8: Mean Precipitation Rate over Amazon Basin (CMAP STANDARD); **(a)** January; **(b)** March; **(c)** May; **(d)** July; **(e)** September; **(f)** November.

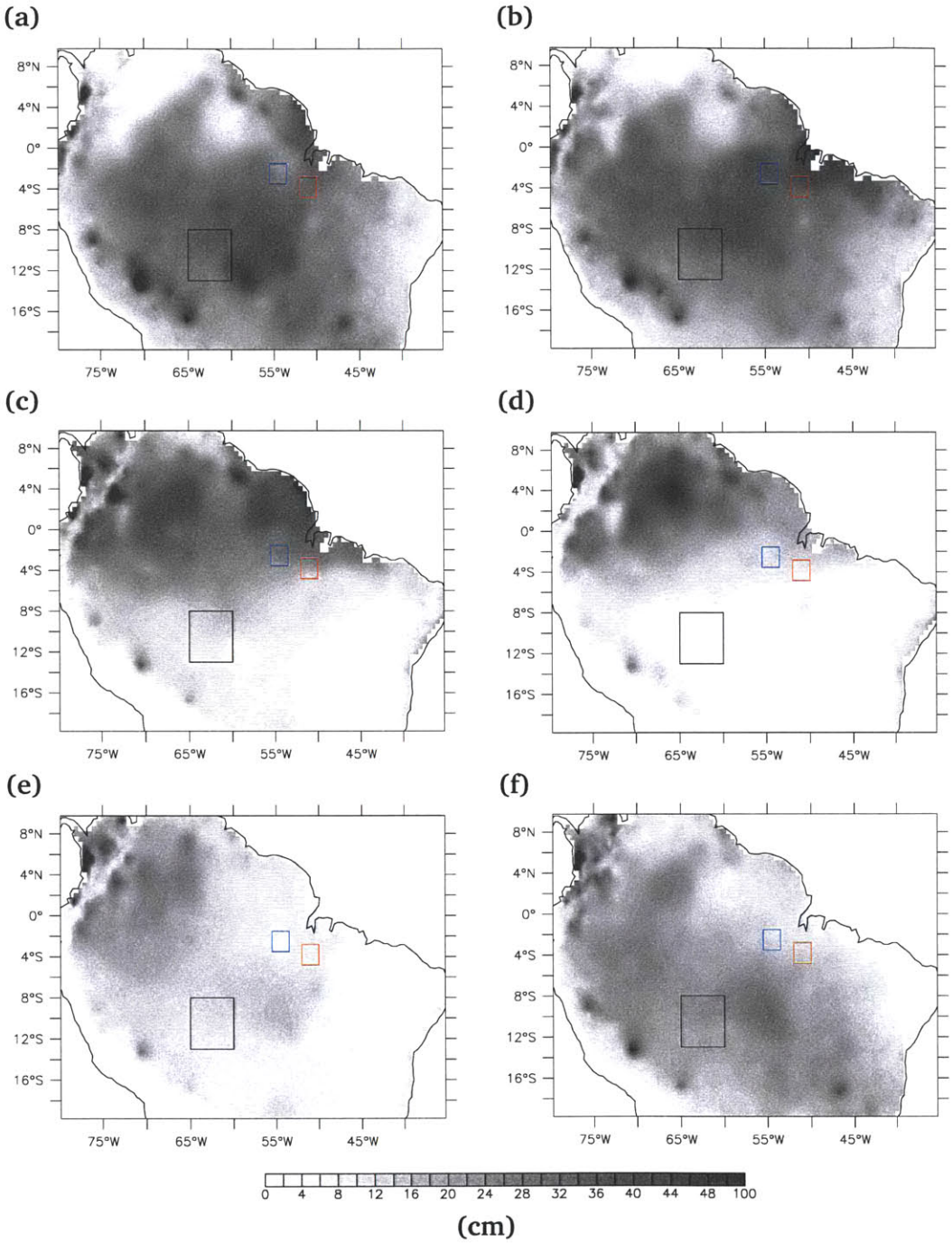

Figure 3-9: Mean Precipitation Accumulation over Amazon Basin (UDELAWARE WILLMOTT); **(a)** January; **(b)** March; **(c)** May; **(d)** July; **(e)** September; **(f)** November.

rainfall. The Willmott gauge-based dataset for precipitation [Legates and Willmott, 1993] also shows clear patterns of orographic rainfall (Figure 3-9).

Inter-Annual Variability

Inter-annual variability of climate in the Amazon basin can be quite significant. Pinker and Laszlo [1992] showed that the interannual variability in downward shortwave radiation can reach 70 $W.m^{-2}$. Most of the inter-annual variability in the prevailing Amazon climate can be attributed to larger-scale atmospheric/oceanic oscillations, such as the El-Niño Southern Oscillation (ENSO) [Nieto Ferreira *et al.*, 2003]. Indeed, ENSO modulates both the position and intensity of the South American Low Level Jet (SALLJ), which during the 1998 El-Niño episode was twice as strong as during the 1999 El-Niña. This lead to six times more large long-lived convective cloud systems during the 1999 La-Niña, and to more precipitation. Williams *et al.* [2003] cite the very strong El-Niño of 1926 as the cause for the "drought of the century" in the western section of the Amazon basin. During that same year, warmer than normal tropical Atlantic sea-surface temperatures contributed to an anomalously wet record for the Nordeste region.

Decadal Variability

The early results of GCM simulations examining the effects of deforestation on climate prompted studies of the trends of rainfall and radiation over the Amazon basin. These studies have mostly used satellite records, which generally start well after deforestation had started making its mark on the Amazonian lanscape in the late 60's. Chu *et al.* [1994] and DeLiberty [2000] both examine monthly series of outgoing longwave radiation (OLR) over the Amazon over 15 years and detect a decreasing trend, which would indicate colder cloud tops and an increase in deep convection over the Amazon basin. DeLiberty [2000] found an increase in rainfall (2.5^o resolution) from January 1979 to December 1995. These results are confirmed by Chen *et al.* [2001], who analyzed OLR, GHCN and NNRP time-series and found that there has been an increasing trend in rainfall over the past 40 years over the Amazon; and also confirmed by Chen *et al.* [2002], who showed that there are signs that the tropical general circulation has intensified over the decade of the 90's. Finally, Wielicki *et al.* [2002] highlight the high degree of decadal variability in the tropical mean radiation budget.

3.2 Climate in Rondônia

The analyses presented in this thesis will be presented for three study domains in the Amazon basin (see next Chapter), but most analyses will concentrate on a study domain in the state of Rondônia. The reasons for the particular interest in

this region of the Amazon basin are that Rondônia is in the arc of deforestation in the Amazon basin, a section that has undergone the most intensive deforestation activities; and also that Rondônia is the site for the Large Biosphere Atmosphere (LBA) experiment, and as such has been studied at length. This section will present the climatic context for the state of Rondônia.

During the rainy season in Rondônia, two distinct circulation regimes are defined: the Easterly regime and the Westerly regime. They are defined by the direction of the layer-averaged 700-850 mb winds [Halverson *et al.*, 2002]. These regimes generally last on the order of a few days to a week, and alternate between each other. The regimes have a significant impact on the type of rainfall observed and the general thermodynamic conditions of the atmosphere. The westerly regime is characterized by an atmosphere that is more oceanic in nature, with weak convection and dominated by stratiform rainfall; it is also termed the "green ocean" regime for its resemblance to oceanic rainfall conditions and low atmospheric aerosol content. The westerly regime is accompanied by mostly cloudy conditions, low CAPE ($1,000 J.kg^{-1}$), high relative humidity ($\sim$90% RH) through 700 mb, and shallow (900 mb) weak shear ($10^{-4}s^{-1}$). The easterly regime, on the other hand, exhibits deeper convection that is highly electrified, and has partly cloudy to sunny skies. It has high CAPE ($1,500 J.kg^{-1}$), a dryer ($\leqslant$80% RH) lower atmosphere, and more intense ($10^{-3}s^{-1}$) deeper (up to 700 mb) shear [Halverson *et al.*, 2002]. The westerly regime is termed the South-Atlantic convergence zone (SACZ) regime by Rickenbach *et al.* [2002], whereas the easterly regime is the non-SACZ regime. Laurent *et al.* [2002] observed that the easterly regime is characterized by mesoscale convective systems (MCS) that are closely related to the mid-level mean flow, whereas the procession of MCS and rain cells during the westerly regime is highly disorganized and points to a strong influence of topographical features. Tokay *et al.* [2002] found that the easterly regime is associated with more intense rain events (6 mm/hr) than the westerly regime (2.6 mm/hr). Precipitation events are more frequent during the westerly regimes, while easterly regime rainfall is characterized by larger rain drops. The drop-size distribution (DSD) might be related to the aerosol content of the atmosphere; higher concentrations of certain types of aerosols inhibit rainfall and result in DSDs that are biased toward bigger drops. Betts *et al.* [2002] observed that the water vapour flux through the cloud base exceeds the surface evaporation during the easterly regime, and that the mean cloud base height is lower during westerly regimes.

Seasonality in Rondônia is characterized by the monsoon. In panels (c) of Figures 3-10 & 3-11, the circulation reversal associated with the monsoon is clearly defined. These figures also distinctly show the seasons of Rondônia. There are however refinements in the definition of seasons in Rondônia due to the intense human activities in the state. These refinements are highlighted by Williams *et al.* [2002], who defines the seasons as follows:

1. Clean Dry Season: May, June & July
2. Polluted Dry Season: End of July through August

3. Polluted Pre-Monsoon: September, October

4. Clean Pre-Monsoon: November, December

5. Wet Season: January — April

The refinements made by Williams *et al.* [2002] concentrate on the effect that biomass burning has on the atmospheric boundary-layer, and highlight the climatic impacts of the method by which most forests are cleared in the Amazon (i. e., through burning).

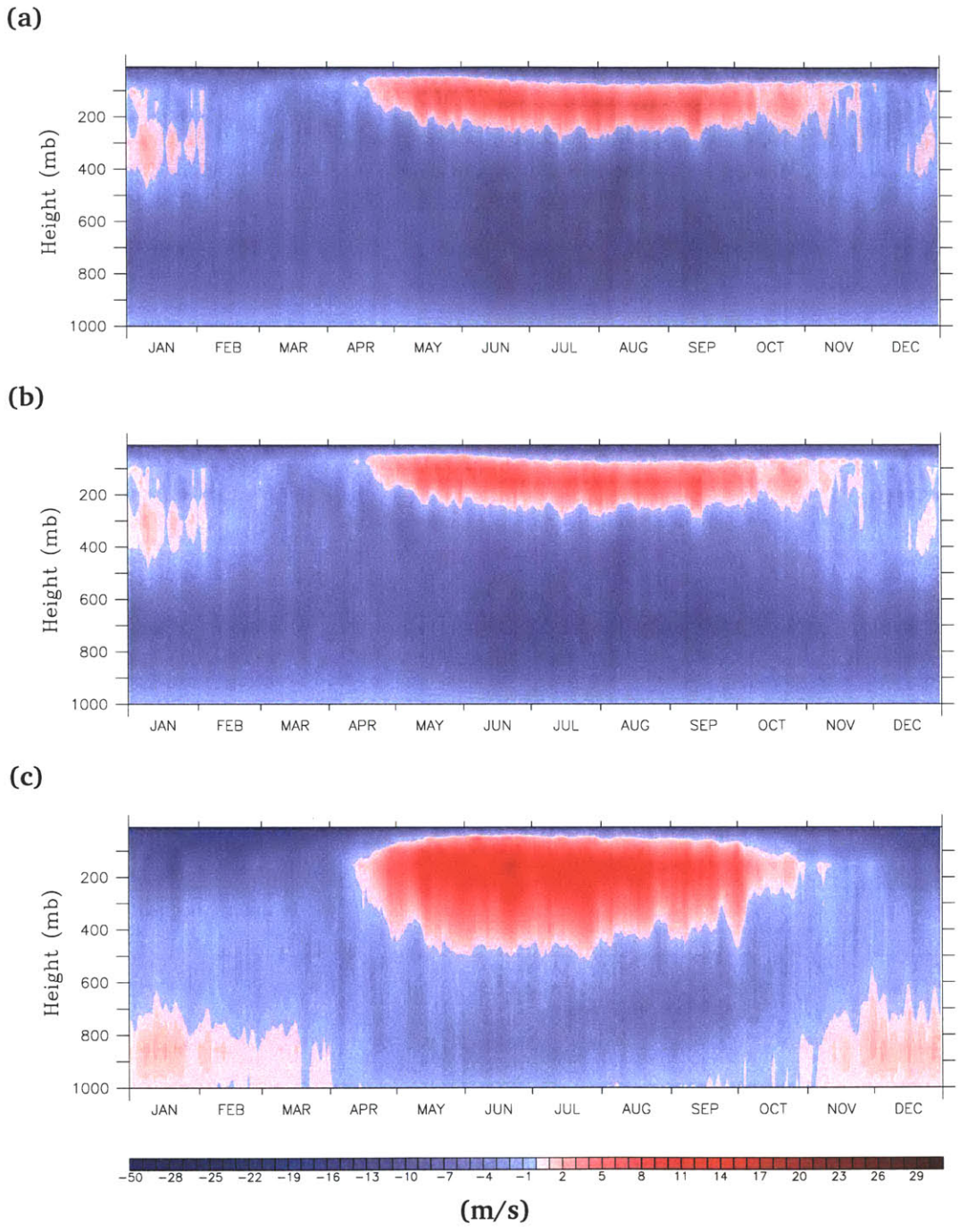

Figure 3-10: Time-Height Climatology of Zonal Winds (NCEP/NCAR Reanalysis-1); **(a)** Marabá-Altamira; **(b)** Tapajós-Santarém; **(c)** Rondônia.

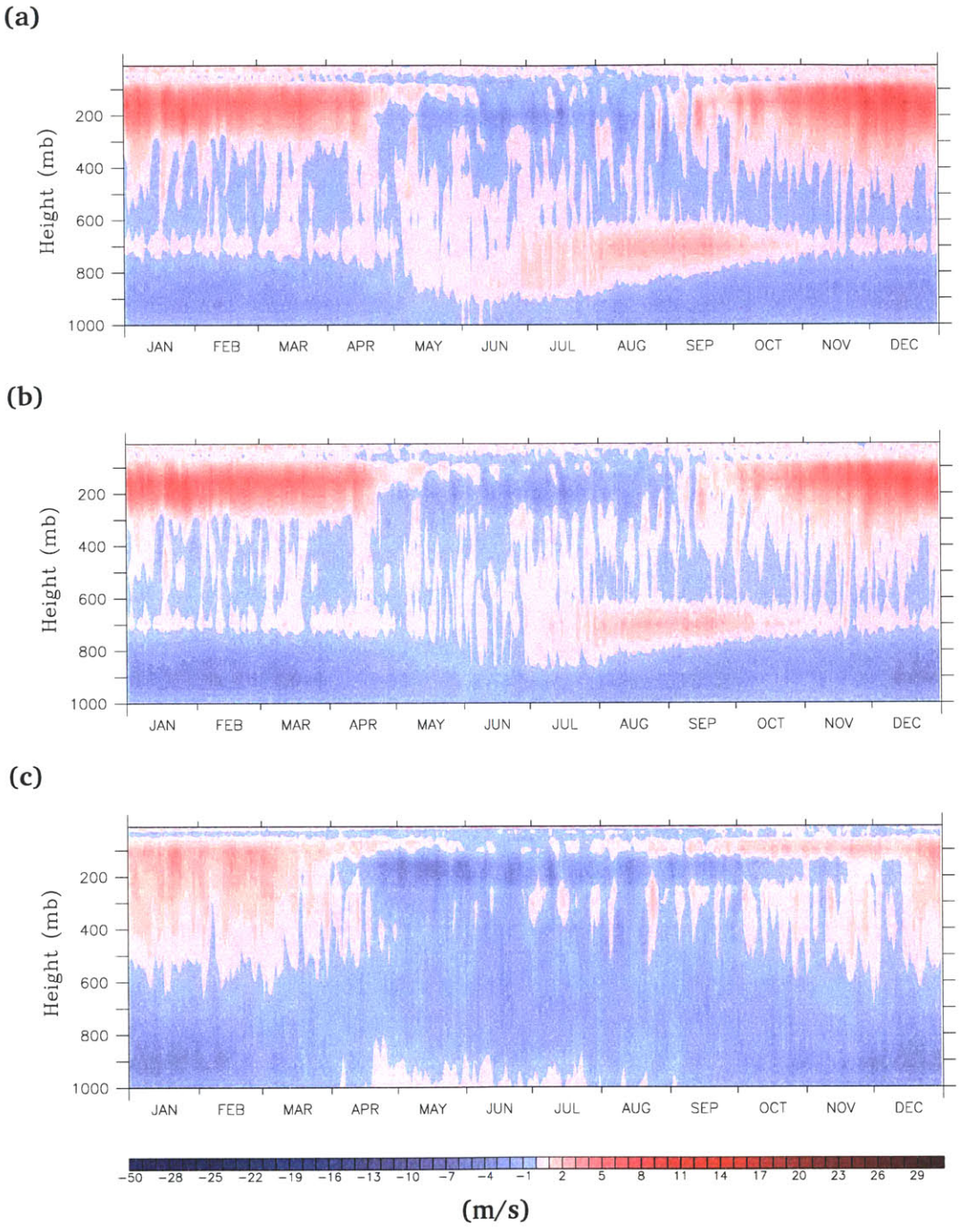

Figure 3-11: Time-Height Climatology of Meridional Winds (NCEP/NCAR Reanalysis-1); **(a)** Marabá-Altamira; **(b)** Tapajós-Santarém; **(c)** Rondônia.

REFERENCES

BETTS, A. K., J. D. FUENTES, M. GARSTANG and J. H. BALL. Surface Diurnal Cycle and Boundary Layer Structure over Rondônia during the Rainy Season. *Journal of Geophysical Research*, 107(D20):page 8065 [2002].

BETTS, A. K. and C. JAKOB. Study of Diurnal Cycle of Convective Precipitation over Amazonia using a Single Column Model. *Journal of Geophysical Research*, 107(D23):page 4732 [2002].

CHEN, J., B. E. CARLSON and A. D. DEL GENIO. Evidence for Strengthening of the Tropical General Circulation in the 1990s. *Science*, 295(5556):pages 838–841 [2002].

CHEN, T.-C., J.-H. YOON, K. J. ST. CROIX and E. S. TAKLE. Suppressing Impacts of the Amazonian Deforestation by the Global Circulation Change. *Bulletin of the American Meteorological Society*, 82(10):pages 2209–2216 [2001].

CHU, P.-S., Z.-P. YU and S. HASTENRATH. Detecting Climate Change Concurrent with Deforestation in the Amazon Basin: Which Way Has it Gone? *Bulletin of the American Meteorological Society*, 75(4):pages 579–583 [1994].

COOK, K. H. Role of Continents in Driving the Hadley Cells. *Journal of the Atmospheric Sciences*, 60(7):pages 957–976 [2003].

CUTRIM, E. M. C., D. W. MARTIN, D. G. BUTZOW, I. M. SILVA and E. YULAEVA. Pilot Analysis of Hourly Rainfall in Central and Easter Amazonia. *Journal of Climate*, 13(7):pages 1326–1334 [2000]. Notes and Correspondence.

DELIBERTY, T. L. A Regional Scale Investigation of Climatological Tropical Convection and Precipitation in the Amazon Basin. *Professional Geographer*, 52(2):pages 258–271 [2000].

FU, R., B. ZHU and R. E. DICKINSON. How Do Atmosphere and Land Surface Influence Seasonal Changes of Convection in the Tropical Amazon. *Journal of Climate*, 12(5):pages 1306–1321 [1999].

HALVERSON, J. B., T. RICKENBACH, B. ROY, H. PIERCE and E. WILLIAMS. Environmental Characteristics of Convective Sytems during TRMM-LBA. *Monthly Weather Review*, 130(6):pages 1493–1509 [2002].

LAURENT, H., L. A. T. MACHADO, C. A. MORALES and L. DURIEUX. Characteristics of the Amazonian Mesoscale Convective Systems Observed from Satellite and Radar during the WETAMC/LBA Experiment. *Journal of Geophysical Research*, 107(D20):page 8054 [2002].

LEGATES, D. R. and C. J. WILLMOTT. A comparison of GCM-simulated and observed mean January and July precipitation. *Global and Planetary Change*, 7(4):pages 345–363 [1993].

LENTERS, J. D. and K. H. COOK. Simulation and Diagnosis of the regional Summertime Precipitation Climatology of South America. *Journal of Climate*, 8(12):pages 2988–3005 [1995].

MACHADO, L. A. T., H. LAURENT and A. A. LIMA. Diurnal March of the Convection Observed during TRMM-WETAMC/LBA. *Journal of Geophysical Research*, 107(D20):page 8064 [2002].

MINNIS, P. and E. F. HARRISON. Diurnal Variability of Regional Cloud and Clear-Sky Radiative Parameters Derived from GOES Data. Part II: November 1978 Cloud Distributions. *Journal of Climate and Applied Meteorology*, 23(7):pages 1012–1031 [1984].

NEGRI, A. J., E. N. ANAGNOSTOU and R. F. ADLER. A 10-yr Climatology of Amazonian Rainfall Derived from Passive Microwave Satellite Observations. *Journal of Applied Meteorology*, 39(1):pages 42–56 [2000].

NIETO FERREIRA, R., T. M. RICKENBACH, D. L. HERDIES and L. M. CARVALHO. Variability of South American Convective Cloud Systems and Tropospheric Circulation during January-March 1998 and 1999. *Monthly Weather Review*, 131(5):pages 961–973 [2003].

NOBRE, C. A., L. F. MATTOS, C. P. DERECSYNSKI, T. A. TARASOVA and I. V. TROSNIKOV. Overview of the Atmospheric Conditions During the Smoke, Clouds, and Radiation-Brazil (SCAR-B) Field Experiment. *Journal of Geophysical Research*, 103(D24):pages 31,809–31,820 [1998].

PINKER, R. T. and I. LASZLO. Interannual Variability of Solar Irradiance over the Amazon Basin Including the 1982-83 El Niño Year. *Journal of Climate*, 5(11):pages 1305–1315 [1992].

RICKENBACH, T. M., R. NIETO FERREIRA, J. B. HALVERSON, D. L. HERDIES and M. A. F. SILVA DIAS. Modulation of Convection in the Southwestern Amazon Basin by Extratropical Stationay Fronts. *Journal of Geophysical Research*, 107(D20) [2002].

TODD, M. C., R. WASHINGTON and T. JAMES. Characteristics of Summertime Daily Rainfall Variability over South America and the South Atlantic Convergence Zone. *Meteorology and Atmospheric Physics*, 83:pages 89–108 [2003].

TOKAY, A., A. KRUGER, W. F. KRAJEWSKI, P. A. KUCERA and A. J. PEREIRA FILHO. Measurements of of Drop Size Distribution in the Southwestern Amazon Basin. *Journal of Geophysical Research,* 107(D20):page 8052 [2002].

WIELICKI, B. A., T. WONG, R. P. ALLAN, A. SLINGO, J. T. KIEHL, B. J. SODEN, C. T. GORDON, A. J. MILLER, S.-K. YANG, D. A. RANDALL, F. ROBERTSON, J. SUSSKIND and H. JACOBOWITZ. Evidence for Large Decadal Variability in the Tropical Mean Radiative Energy Budget. *Science,* 295(5556):pages 841–844 [2002].

WILLIAMS, E., A. DALL' ANTONIA, V. DALL' ANTONIA, J. M. DE ALMEIDA, F. SUAREZ and B. LIEBMANN. The Drought of the Century in the Amazon Basin: An Analysis of the Regional Variation of Rainfall in South America in 1926. *Acta Amazonica,* submitted [2003].

WILLIAMS, E., D. ROSENFELD, N. MADDEN, J. GERLACH, N. GEARS, L. ATKINSON, N. DUNNEMANN, G. FROSTROM, M. ANTONIO, B. BIAZON, R. CAMARGO, H. FRANCA, A. GOMES, M. LIMA, R. MACHADO, S. MANHAES, L. NACHTIGALL, H. PIVA, W. QUINTILIANO, L. MACHADO, P. ARTAXO, G. ROBERTS, N. RENNO, R. BLAKESLEE, J. BAILEY, D. BOCCIPPIO, A. BETTS, D. WOLFF, B. ROY, J. HALVERSON, T. RICKENBACH, J. FUENTES and E. AVELINO. Contrasting Convective Regimes over the Amazon: Implications for Cloud Electrification. *Journal of Geophysical Research,* 107(D20):page 8082 [2002].

WILLIAMS, E. and S. STANFILL. The physical origin of the land-ocean contrast in lightning activity. *Comptes Rendus Physique,* 3(10):pages 1277–1292 [2002].

CHAPTER 4

REMOTE SENSING

The use of remote sensing instruments and their derived data pervades this study. In order to draw useful and correct conclusions from their analysis, it is essential to understand exactly what these space-borne instruments are measuring, and how the radiometric response of an instrument is related to the physical state or variable of interest. Since remote sensing is largely based on the measurement of radiation or backscatter at varying wavelengths and resolutions, this chapter begins with a review of the basics of radiation in the atmosphere, follows-up with targeted reviews of the remote sensing platforms used in this study, and ends with the formulation of algorithms for cloud detection and classification.

4.1 Relevant Elements of Remote Sensing

Atmospheric Radiation: The Basics

The dominant pathway of energy transfer in the earth's atmosphere is electromagnetic radiation [Liou, 2002]. The source of virtually all radiation on earth is the sun, as it is approximately 300,000 times closer to the earth than the next nearest star. Incident solar radiation interacts with the earth's atmospheric constituents and surface as depicted in Figure 4-1. Incident radiation is either transmitted, reflected, scattered or absorbed. The type of interaction depends on the nature of the constituents and the wavelength of the incident radiation.

In radiation studies, the sun and earth are often modelled as blackbodies (i.e. perfect absorbers and emitters) that obey Planck's function, which is expressed by

$$B_{\tilde{\nu}}(T) = \frac{2h\tilde{\nu}^3}{c^2(e^{\frac{h\tilde{\nu}}{KT}} - 1)}, \tag{4.1}$$

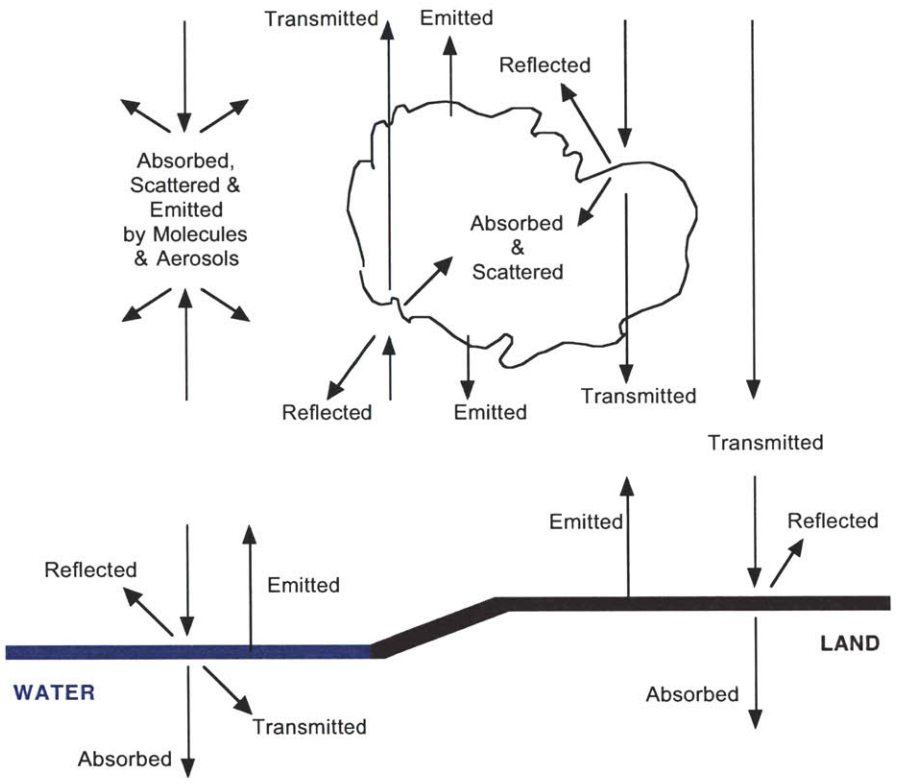

Figure 4-1: Atmospheric Radiation Processes.

or

$$B_\lambda(T) = \frac{2hc^2}{\lambda^5(e^{\frac{hc}{KT\lambda}} - 1)}, \tag{4.2}$$

where K is Boltzmann's constant, c is the velocity of light, T is the absolute temperature, h is Planck's constant, $\tilde{\nu}$ is the frequency, and λ is the corresponding wavelength. Figure 4-2 presents the blackbody intensity curves for the earth and sun assuming blackbody temperatures of 300K and 6000K, respectively. Overlayed on Figure 4-2 are the GOES-8 channel windows.

Any object or matter having a temperature above absolute zero emits radiation due to the random motion and collisions of its molecules. The total amount of radiation emitted by a blackbody can be derived by integrating Planck's function over all wavelengths. The result is Stefan Boltzmann's law, expressed by

$$R = \sigma * T^4, \tag{4.3}$$

where R is the total amount of radiant energy emitted, σ is the Stefan-Boltzmann constant and T is the temperature.

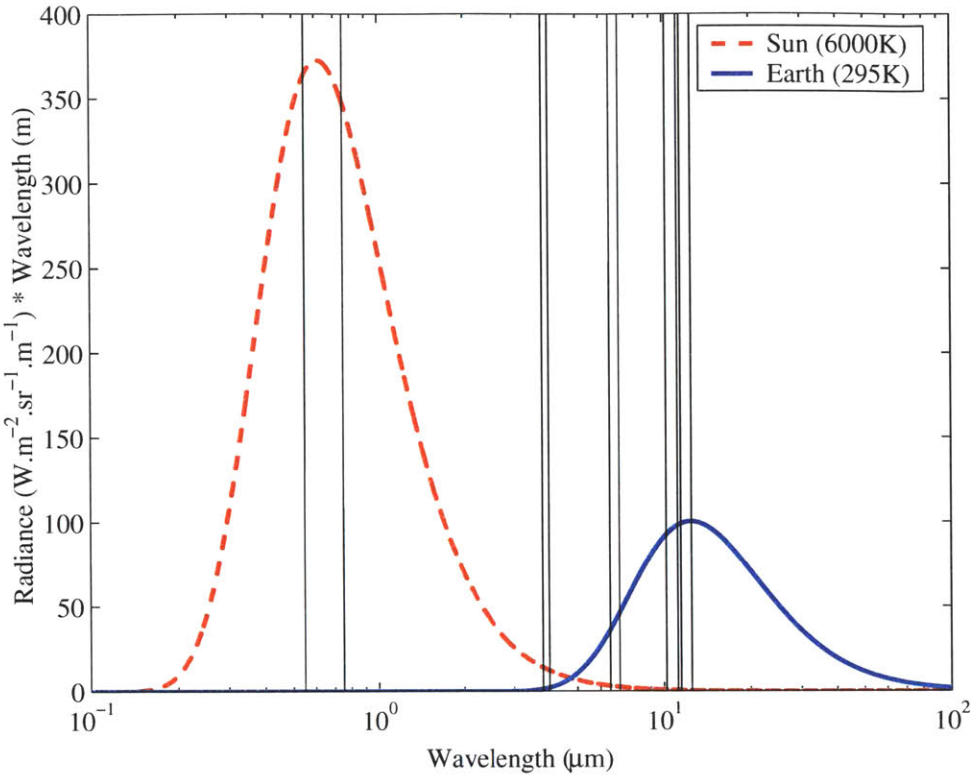

Figure 4-2: Sun and Earth Blackbody Radiance Curves (at Top of Atmosphere) and GOES-8 Channel Spectral Windows (see Table 4.1).

Remote sensing consists of the measurement of radiation intensity emitted by an observed substance at different wavelengths (or corresponding frequencies). The intensity of the radiation emitted at a particular wavelength is then "converted" to the variable of interest by using the knowledge of the substance's radiative properties. It is hence important to understand the physics of radiation for the particular substance studied. For example, Figure 4-3 shows how the earth's atmosphere interacts with radiation at different wavelengths. By measuring the amount of radiation absorption in a certain bandwidth, one may make inferences about the properties of the atmosphere (e. g., its constituents, its state). For an in-depth treatment of the physics of atmospheric radiation, the reader is referred to Liou [2002], while the reader will find a helpful treatise on remote sensing in the work by Elachi [1987].

4.2 GOES-8 Imager Data

GOES-8 is a part of a global network of earth-oriented geostationary satellites that covers the globe. Its primary purpose is to monitor weather patterns. It

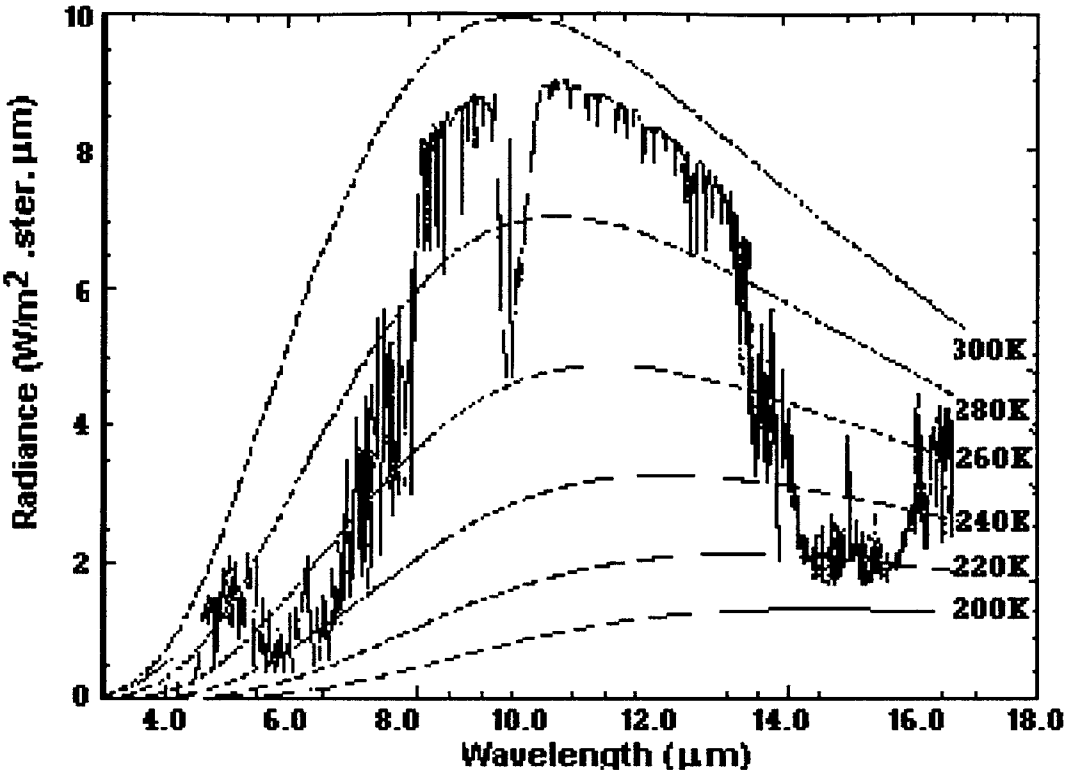

Figure 4-3: Atmospheric Absorption Spectrum and Comparative Blackbody Curves.

achieves this goal by providing high signal-to-noise observations of the earth at high spatial and temporal resolutions. The satellite was launched on 13 April 1994, and is operated by the National Oceanic and Atmospheric Administration (NOAA). It flies at an altitude of 35,790 km over the equator at a longitude of 75° West. There are two earth-sensing instruments on board GOES-8: a five-channel imager and a nineteen-channel sounder. The shallow clouds are derived using data from the imager, the characteristics of which are presented in Table 4.1.

Table 4.1: GOES-8 Imager Characteristics [Space Systems/Loral, 1996].

Channel Number	Wavelength Range (μm)	FOV at Nadir (km)	Number of Detectors in North-South Array	Meteorological Objective
1	0.55 - 0.75	1	8	Clouds
2	3.80 - 4.00	4	2	Clouds (night)
3	6.50 - 7.00	8	1	Water Vapor
4	10.20 - 11.20	4	2	SST & WV
5	11.50 - 12.50	4	2	SST & WV

The imager (see Figure 4-4) operates on 5 channels, each of which utilizes a separate north-south array of linear detectors [Menzel and Purdom, 1994; Weinreb *et al.*, 1997]. For a complete review of the GOES program and the GOES-8 satellite, the reader is referred to Menzel and Purdom [1994] and Space Systems/Loral [1996]. This research is only concerned with the data from three channels of the imager: they are the visible (0.65 μm), the solar-infrared (3.90 μm) and the infrared (10.7 μm) channels. Imager data from GOES-8 is obtained using the Man-computer Interactive Data Access System (McIDAS, Suomi *et al.* [1983]). Images cover the Amazon basin, and are available daily at 14h45 UTC from September 1, 1994 to March 31, 2003. Images of the Amazon at 17h45 and 18h45 UTC are also available from October 1, 2000 to March 31, 2003.

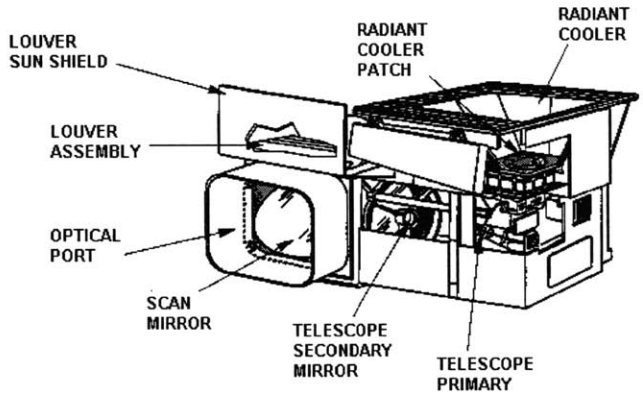

Figure 4-4: GOES-8 Imager.

4.2.1 Calibration of GOES-8 Imager Channels

Satellite-borne radiometers undergo pre-launch calibrations. The objective of the calibrations is to relate the radiometric response of the sensing instruments to physical radiance, which is the radiant flux density per unit solid angle [Kidder and Vonder Haar, 1995]. In the case of the GOES-8 imager, calibration relates the instrument voltage response, stored as a 10-bit count, to the scene radiance. There is a separate calibration for each detector of a specific channel, and image striping — caused by the different response of the detectors in the array — is avoided by normalizing to a reference detector [Menzel and Purdom, 1994; Weinreb *et al.*, 1997]. These pre-launch calibrations are however untested in orbit, and do not account for instrument degradation. In-orbit calibrations are hence extremely important to ensure the consistency of the derived dataset (e. g., when performing long-term

climatic analyses), and to ensure its comparability to datasets derived from other instruments (e. g., comparing reflectivity derived from AVHRR and GOES).

The pre-launch performance of the GOES-8 radiometers was determined by the manufacturer (ITT, Ft. Wayne, Ind.) and the prime contractor (Space Systems - Loral, Palo Alto, Calif.) Examination of in-orbit data revealed that the instruments were not performing as expected. A notable flaw was detected in the scanning mirror, whose emissivity varied according to its East-West position [Weinreb *et al.*, 1997]. Multiple in-orbit calibration methods were developed to improve the quality of GOES-8 imager data. This section provides a review of work done on post-launch GOES-8 imager calibration.

Visible Channel Calibration

There are no on-board calibration reference instruments for the visible channel. The reason for this is that the visible imagery original purpose was purely qualitative in nature. The pre-launch calibration for the visible channel is of the form:

$$I = mX + b \tag{4.4}$$

or

$$I = m\,(X - X_0)\,, \tag{4.5}$$

where the I is the measured scene radiance ($Wm^{-2}sr^{-1}\mu m^{-1}$), X is the instrument output (10-bit count), X_0 denotes a space view or offset count, and m and b are coefficients determined before the launch. Two sets of pre-launch coefficients are reported in Table 4.2; they differ because they are calibration coefficients for different detectors, which are then used as reference for the other detectors in the array.

Table 4.2: Pre-Launch Visible Channel Calibration Coefficients.

	Detector Number	m $Wm^{-2}sr^{-1}\mu m^{-1}count^{-1}$	b $Wm^{-2}sr^{-1}\mu m^{-1}$	X_0 $count$
Weinreb *et al.* [1997]	2	0.5502	-15.955	29
Knapp and Vonder Haar [2000]	6	0.5522	-15.27	27.65

To verify the validity of these coefficients in-orbit, the technique of "vicarious" calibration is used. Rao *et al.* [1999] define vicarious calibration as "the process of relating the radiometric response of an instrument to the radiation sensed by that instrument." In essence, vicarious calibration uses sites of known or constant radiance to calibrate instruments in-orbit. Garand [1988] used such a method to calibrate the visible channel output from the GOES-EAST satellite, GOES-8's predecessor. Analysis of clear-sky images of the White Sands Desert in New Mexico, a

region of known reflectivity, produced the following calibration:

$$I = 0.005393C_8^2 - 2.67, \tag{4.6}$$

where C_8 is the eight-bit digital count.

Ayers *et al.* [1996] used data from Unmanned Aerospace Vehicles (UAV) taken during the 1995 Atmospheric Radiation Measurement (ARM) Program Enhanced Shortwave Experiment field campaign in the Southern Great Plains (SGP) site in northern Oklahoma in 1995 (September 25 to November 1). The ARM/UAV radiance measurement were collocated with those from GOES-8, and the exercise resulted in the following calibration equation:

$$I = 0.606 \times (X - X_0), \tag{4.7}$$

where X_0 is the offset count of 24.65.

Rao *et al.* [1999] chose the Sonora desert in northern Mexico and the Sechura desert in Peru as their radiometrically stable calibration sites. They found a degradation of the visible sensor of 4.5% per year. This result leads to a post-launch calibration of the form [Rao, 2001]:

$$I(DSL) = (0.6556 + 0.0001107 \times DSL) \times (X - X_0), \tag{4.8}$$

where X_0 is 29, and DSL is the number of days since the launch (13 April 1994).

Weinreb *et al.* [1999] also used a vicarious technique to calibrate the sensors on-board GOES-8, but instead of using deserts, they used observations of stars. Averaging observations over 40 stars from 1995 to 1998, they found a rate of decrease in sensor response of about 7.6% ($\pm 0.5\%$) per year. Knapp and Vonder Haar [2000] used clear-sky observations over the southern Pacific, where there is a low optical depth due to aerosols. Based on a radiative transfer model to determine TOA radiance, they found a degradation rate of 5.6% annual decrease, with an initial 7.6% decrease in responsiveness shortly after launch. Finally, Minnis *et al.* [2002a] calibrated the GOES-8 visible sensor to the VIRS[1] instrument onboard the TRMM[2] satellite. The TRMM VIRS is calibrated in-orbit by using space views and sun views through a diffuser plate, and that calibration was shown to be stable. Minnis *et al.* [2002a] found an initial decrease of 16% after launch, and an annual degradation rate of 7.5%, which lead to the following calibration equation:

$$I(DSL) = (0.650 + 0.0001341 \times DSL) \times (X - X_0), \tag{4.9}$$

where the offset X_0 takes a value of 31.

The results of the various calibration studies for the GOES-8 visible imager are summarised in Table 4.3. It is evident that, while the results all show the same

[1]Visible Infrared Scanner

[2]Tropical Rainfall Measuring Mission [Kummerow *et al.*, 1998]

trend, there is great disagreement between these methods. This raises the question of uncertainty in the raw GOES-8 imager data.

Table 4.3: Post Launch Calibration Results.

Authors	Initial Sensor Response Drop (%)	Yearly Sensor Degradation Rate (%)	Offset (X_0) (bit count)
Ayers *et al.* [1996]	10	—	23.65
Bremer *et al.* [1998]	—	7.5	—
Ellrod *et al.* [1998]	9	—	—
Weinreb *et al.* [1999]	—	7.6 ($\pm$0.5)	—
Rao *et al.* [1999]	19	4.5	29
Knapp and Vonder Haar [2000]	7.6	5.6	27.65
Rao [2001]	19	6.1	29
Minnis *et al.* [2002a]	16	7.5	31

The visible channel calibration will follow Minnis *et al.* [2002a]. There are two reasons for which this calibration was chosen: firstly, the calibration exercise of Minnis *et al.* [2002a] is the one that uses the longest time-record of visible imagery, and secondly, it is based on an arguably much more rigorous calibration reference than the other studies (i.e the TRMM VIRS). Indeed, the in-orbit calibration of VIRS has proven to be successful, and most importantly stable in time [Lyu *et al.*, 2000; Barnes *et al.*, 2000]. The final calibration is hence that presented in Equation 4.9.

Infrared Channel Calibration

The imager periodically views space and an onboard warm blackbody of known temperature in order to calibrate the instrument's infrared channels [Menzel and Purdom, 1994; Weinreb *et al.*, 1997]. The pre-launch calibrations for the infrared channels is of the form:

$$I = qX^2 + mX + b, \tag{4.10}$$

where I is the scene radiance, X is the the 10-bit output of the instrument, and q, m and b are coefficients specific to each detector. The value of q, the coefficient of the quadratic term, was determined a-priori in laboratory tests [Weinreb *et al.*, 1997]. Although q can be changed in-orbit, the pre-launch tests did not detect any significant trend of q with the temperature of the optical system, and only a weak correlation between q and the detector temperature [Weinreb *et al.*, 1997]. Hence, q is help constant at its pre-launch value. The slope (m) and intercept (b) coefficients are determined in-orbit using blackbody and space instrument counts as follows:

$$m = \frac{\left[I_{bb} - q\left(X_{bb}^2 - X_{sp}^2\right)\right]}{\left(X_{bb} - X_{sp}\right)} \tag{4.11}$$

$$b = -mX_{sp} - qX_{sp}^2, \tag{4.12}$$

where the bb and sp subscripts refer to the instrument counts taken from blackbody and space views, respectively.

The output of channels 3, 4 and 5 revealed a strong variation with the East-West position of the scanning mirror (see Figure 4-5), corresponding to a perceived difference of 150K between the east and west sides of the scan [Weinreb *et al.*, 1997]. To correct for this geometrical effect, the calibration equation was restated as:

$$[1 - \epsilon(\theta)]\, I + \epsilon(\theta) I_M = qX^2 + mX + b, \tag{4.13}$$

where $\epsilon(\theta)$ is the emissivity of the scan mirror as a function of the scan angle θ. I_M is radiance of the scan mirror, and is determined from the temperature of the mirror, which is monitored by a thermistor. The emissivity of the scan mirror is given by:

$$\epsilon(\theta) = \epsilon(45) + \frac{m\left[X_{sp}(\theta) - X_{sp}(45)\right] + q\left[X_{sp}^2(\theta) - X_{sp}^2(45)\right]}{I_M}, \tag{4.14}$$

where the 45^o emissivity was determined from laboratory measurements. The calibration slope, which must now account for the scanning mirror radiance, is given by:

$$m = \frac{\left[1 - \epsilon(45)\right] I_{bb} - q\left[X_{bb}^2 - X_{sp}^2(45)\right]}{X_{bb} - X_{sp}(45)} \tag{4.15}$$

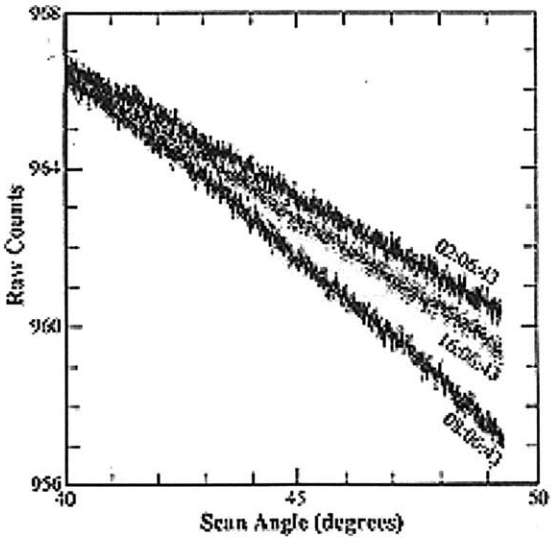

Figure 4-5: Raw output of channel 5 on the GOES-9 imager from an east-west scan of space [Weinreb *et al.*, 1997]

This calibration was implemented operationally and is done in real-time at the

Command and Data Acquisition (CDA) station at Wallops, VA. The emissivity of the scanning mirror is fit to a quadratic (for computational efficiency) as follows:

$$\epsilon(\theta) = a_0 + a_1\theta + a_2\theta^2, \tag{4.16}$$

where the coefficients are fit once every three months to a new emissivity-angle profile [Weinreb *et al.*, 1997]. The radiances are scaled linearly to use the full 10-bit precision of the GOES VARiable (GVAR) data.

Minnis *et al.* [2002b] found no significant trends (e. g., degradation) in the GOES-8 SIR and IR channel calibrations. The infrared imagery data used in this thesis will hence use the operational GOES-8 calibration, which is included in the raw GVAR data.

4.2.2 Obtaining Reflectance and Temperature from Radiance

The visible and infrared channels of the GOES-8 imager provide values of the outgoing radiance in the narrow wavelength windows depicted in Figure 4-2, where it is clear that interpretation of the measured radiometric response is highly channel dependent. The calibrated GOES imager measurements are hence termed narrowband (NB) radiances. The response of the sensors in their respective narrow wavelength windows is not uniform: the spectral response functions are unique to each sensor. These spectral response functions are depicted in Figure 4-6 for the three imager channels of interest. The visible channel radiance is used to infer reflectance, the infrared channel is used as a measure of temperature, and the solar-infrared channel provides information on both temperature and reflectance.

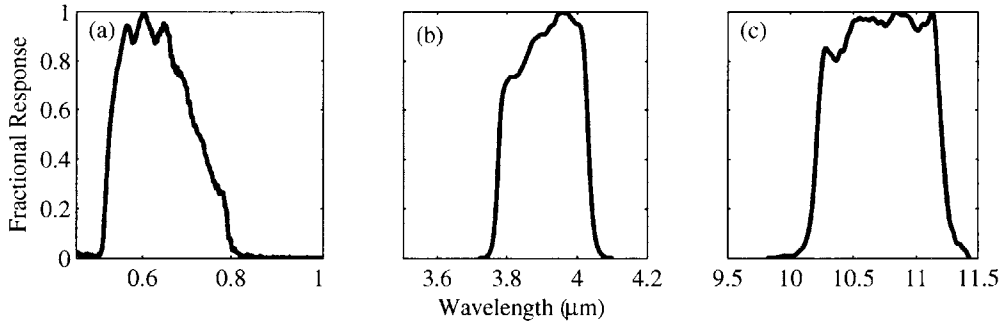

Figure 4-6: Spectral Response Functions for GOES-8; **(a)** Visible; **(b)** Solar-infrared; **(c)** and Infrared Channels.

Visible Channel Reflectance

The radiance measured in the visible channel is reflected solar radiation, with negligible contribution from terrestrial radiation (see Figure 4-2). The most com-

monly used measure to characterize the amount of solar radiation reflected from the earth's surface-atmosphere system is the albedo. The reflectance is often confused with the albedo, but this is misleading. Indeed, the albedo is the ratio of the exiting radiance (or exitance) to the incoming solar radiance (or irrandiance) and is hence a broadband quantity, whereas the reflectance is a narrowband quantity. Albedo is therefore expressed as follows:

$$\alpha = \frac{\int_0^{2\pi} \int_0^{\frac{\pi}{2}} I_r(\theta_r, \phi_r) \cos\theta_r \sin\theta_r d\theta_r d\phi_r}{\int_0^{2\pi} \int_0^{\frac{\pi}{2}} I_i(\theta_i, \phi_i) \cos\theta_i \sin\theta_i d\theta_i d\phi_i} \tag{4.17}$$

To get the value for the narrowband reflectance, the incoming solar radiation in the same band must be calculated. The reflectance is simply the ratio of outgoing (i. e., measured) to incoming. Still, the radiance measured does not account for the system's geometry (see Figure 4-7), which is described by the solar zenith angle (θ_s), the satellite-viewing zenith angle (θ_v), the solar azimuth angle (ϕ_s), and viewing azimuth angles (ϕ_v). This section presents a derivation of reflectance from the measured radiance that follows Kidder and Vonder Haar [1995, chap. 3.6].

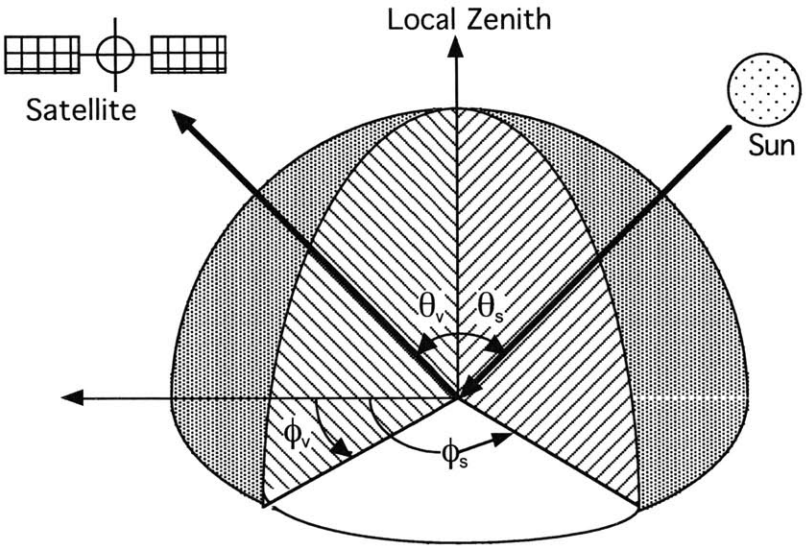

Figure 4-7: Angular relationships for earth radiation measurements (after Minnis and Harrison [1984]). θ_s is the solar zenith angle, θ_v is the satellite-viewing zenith angle, ϕ_s is the solar azimuth angle, and ϕ_v is the viewing azimuth angle.

The reflected radiance can be expressed as follows (Eq. 4.18):

$$I_r(\theta_r, \phi_r) = \int_0^{2\pi} \int_0^{\frac{\pi}{2}} I_i(\theta_i, \phi_i) \gamma_r(\theta_i, \phi_i; \theta_r, \phi_r) \cos\theta_i \sin\theta_i d\theta_i d\phi_i, \tag{4.18}$$

where the subscript $_i$ denotes "incoming" and $_r$ denotes "reflected." The Angular

Distribution Model (ADM), which is also often called a Bi-Directional Reflectance Function (BDRF) due to its dependence on only two directions, $\gamma_r(\theta_i, \phi_i; \theta_r, \phi_r)$ is tantamount to an angular weighting function that describes the relative amount of incoming radiation being reflected in a particular direction. By definition, the reflectance (ρ) is the hemispherically integrated bidirectional reflectance function (Eq. 4.19):

$$\rho = \int_0^{2\pi} \int_0^{\frac{\pi}{2}} \gamma_r(\theta_i, \phi_i; \theta_r, \phi_r) \cos\theta_r \sin\theta_r d\theta_r d\phi_r \tag{4.19}$$

Obtaining an ADM is certainly not a trivial task. Indeed, the ADM is dependent upon the surface type, the radiation wavelength, the amount of cloud in the scene and the cloud type, etc. For this reason, the rest of the derivation will assume that the surface that is remotely sensed is Lambertian (i. e., the reflected radiation from the surface is isotropic, or equal in every direction.) The isotropic assumption allows us to rewrite Eq. 4.19 as:

$$\gamma_r(\theta_i, \phi_i; \theta_r, \phi_r) = \frac{\rho}{\pi}, \tag{4.20}$$

Since the sun can be considered as the only source of incoming radiation at the top of the atmosphere, we may liken the incoming radiation to a delta function such that:

$$I_i(\theta_i, \phi_i) = \begin{cases} I_s & (\forall \quad \theta_i = \theta_s; \quad \phi_i = \phi_s) \\ 0 & (\forall \quad \theta_i \neq \theta_s; \quad \phi_i \neq \phi_s) \end{cases}, \tag{4.21}$$

where I_s is the solar radiance, and θ_s and ϕ_s are the solar zenith and solar azimuth angles, respectively. Moreover, the reflected radiation is measured from the viewing satellite; the reflected radiance is hence the "viewed" radiance I_v with viewing zenith angle θ_v and viewing azimuth angle ϕ_v. This allows us to rewrite Eq. 4.18 into the following equation:

$$I_v(\theta_v, \phi_v) = I_s \Omega_s \cos\theta_s \frac{\rho}{\pi}, \tag{4.22}$$

where Ω_s is the solid angle of the sun onto the remotely sensed scene.

The solar flux density $F_\odot$, where $F_\odot = I_s \Omega_s$, can be expressed as follows:

$$F_\odot = \frac{\int_0^\infty S_\lambda w_\lambda d\lambda}{\int_0^\infty w_\lambda d\lambda} \tag{4.23}$$

where S_λ is the solar flux at a particular wavelength. $F_\odot$ is the average of the wavelength-dependent solar flux weighted by the spectral response of the channel. Since the visible channel's spectral window is spectrally finite, we may write the following approximation:

$$\int_0^{\lambda_{min}} w_\lambda d\lambda + \int_{\lambda_{max}}^\infty w_\lambda d\lambda \approx 0, \tag{4.24}$$

and hence:

$$\int_0^{\infty} w_\lambda d\lambda \approx \int_{\lambda_{min}}^{\lambda_{max}} w_\lambda d\lambda \tag{4.25}$$

For GOES-8, $\{\lambda_{min}; \lambda_{\max}\} = \{0.45\mu m; 1.01\mu m\}$. Coupling this information with the spectral window shape seen in Figure 4-6 results in a TOA solar flux density value of $F_\odot = 1628\ Wm^{-2}$ for a nominal Earth-Sun distance [Knapp and Vonder Haar, 2000]. A correction factor of $(r_0/r)^2$ is applied to this value to correct for the seasonal change in earth sun distance, where r_0 is the mean Earth-Sun distance (1AU), and the instantaneous Earth-Sun distance is r.

We may therefore express the bidirectional reflectance of a scene assumed to be Lambertian as follows:

$$\rho(\theta_v, \phi_v; \theta_s, \phi_s) = \frac{\pi I_v(\theta_v, \phi_v)}{F_\odot (r_0/r)^2 \cos\theta_s} \tag{4.26}$$

Infrared Channel Temperature

The measured infrared radiances of a homogeneous temperature planet would not be homogeneous, but would be dependent on the location of the scene due to limb darkening. Limb darkening is defined as the decrease in brightness of the disk of the observed planet toward its edge, or limb. For the particular case of the Earth, the phenomenon is due to the increase in atmospheric optical depth with distance from nadir. There is no need to take limb darkening into account for viewing zenith angles of less then 30 degrees [Minnis and Harrison, 1984].

The limb darkening function used in Minnis *et al.* [1991] is of the following form:

$$I_{ir}(0^o) = \gamma_{ir} I_{ir}(\theta_v)), \tag{4.27}$$

where:

$$\gamma_{ir} = \begin{cases} 1 & \forall \quad \theta_v \leq 11^o \\ 1.00067 + 0.03247 \ln(\cos(\theta_v)) & \forall \quad \theta_v > 11^o \end{cases}, \tag{4.28}$$

The radiance measured by the infrared channel can be expressed as follows

$$I_{ir} = \frac{\int_0^{\infty} B_\lambda(T) w_\lambda d\lambda}{\int_0^{\infty} w_\lambda d\lambda} \tag{4.29}$$

where $B_\lambda(T)$ is the Planck function, as seen in Equation 4.2 and w_λ is the spectral response function for the infrared channel as seen in panel (c) of Figure 4-6. Again, due to the finite spectral interval in which the channel 4 imager responds, the limits on the integrands in Equation 4.29 may be reduced appropriately.

The infrared radiances, which are stored as scaled 10-bit values in the GVAR data [Weinreb *et al.*, 1997], can be transformed back into radiances using the following

method:

$$I_{ir} = \frac{(X_G - B)}{M}, \tag{4.30}$$

where X_G is the scaled GVAR 10-bit count, and B and M are coefficients, whose values are presented in Table 4.4.

Table 4.4: GOES Imager Scaling Coefficients for GVAR Data [Weinreb *et al.*, 1997].

Channel	M $count/(mW.m^{-2}.sr^{-1}.cm)$	B $count$
2	227.3889	68.2167
3	38.8383	29.1287
4	5.2285	15.6854
5	5.0273	15.3332

As seen in Section 4.2.1, the infrared radiance is obtained through an empirical relationship with the scene count, which is itself linearly related to the instruments voltage response. We may hence invert the relation seen in Equation 4.29 to obtain a measure of the scene's temperature.

$$T_{eff} = \frac{c_2 \nu}{\ln\left[1 + \frac{c_1 \nu^3}{I_{ir}}\right]}, \tag{4.31}$$

where the c_1 and c_2 are two radiation constants (see Equation 4.1) that take the vales $c_1 = 1.191066 \times 10^{-5} mW/(m^2.sr.cm^{-4})$ and $c_2 = 1.438833 K/cm^{-1}$, and ν is the central wave number (one over the wavelength) of the channel. The temperature is termed "effective" due to its dependence on the central wavelength only. Indeed, inverting the relationship presented in Equation 4.29 would be too demanding computationally for operational applications. Hence the central wavelength approximation. The "actual" temperature is retrieved using the following relation [Weinreb *et al.*, 1997]:

$$T = \beta T_{eff} + \alpha, \tag{4.32}$$

where β and α are channel and detector dependent (see Table 4.5.)

Solar-Infrared Channel Temperature and Reflectance

The solar-infrared channel measures a radiance that has contributions from both reflected solar radiation and terrestrial radiation during the daytime (see Figure 4-2), while its sole contribution is upwelling terrestrial radiation during the nightime. Since all of the channel 2 images used in this study are taken during daylight hours, the measured SIR radiance must be separated into a reflected solar component and an infrared component.

Table 4.5: GOES Imager Temperature-Radiance Constants [Weinreb *et al.*, 1997].

Channel	Detector	ν (cm^{-1})	α (K)	β
2	1	2556.71	-0.578526	1.001512
2	2	2558.62	-0.581853	1.001532
3	1	1481.91	-0.593903	1.001418
4	1	934.30	-0.322585	1.001271
4	2	935.38	-0.351889	1.001293
5	1	837.06	-0.422571	1.001170
5	2	837.00	-0.466954	1.001257

The method used to distinguish between the two daytime contributions is to use the temperature derived with the channel 4 (IR) data to infer the channel 2 temperature related radiance using the Planck function. The remaining radiance is attribute to reflection of solar radiation. The method is hence a combination of the methods reviewed in the preceding two sections, and is briefly outlined below.

The channel 2 radiance component attributed to "terrestrial" radiation (I_{T2}) is obtained by convoluting the Planck function with the spectral response function as follows:

$$I_{T2} = \frac{\int_0^\infty B_\lambda(T_4) w_\lambda d\lambda}{\int_0^\infty w_\lambda d\lambda}, \tag{4.33}$$

where T_4 is the temperature derived with the channel 4 data, and w_λ is the spectral response function for channel 2.

The component of channel 2 radiance associated with reflected solar radiation (I_{R2}) is the residual of the measured (I_2) radince minus the terrestrial component (I_{T2}).

$$I_{R2} = I_2 - I_{T2} \tag{4.34}$$

The reflectance in the channel 2 bandwidth is computed similarly to the visible reflectance (again, assuming a Lambertian reflector):

$$\rho(\theta_v, \phi_v; \theta_s, \phi_s) = \frac{\pi I_{R2}(\theta_v, \phi_v)}{F_{\odot_2} (r_0/r)^2 \cos\theta_s}, \tag{4.35}$$

where the solar flux density in the channel 2 window is:

$$F_{\odot_2} = \frac{\int_0^\infty S_\lambda w_\lambda d\lambda}{\int_0^\infty w_\lambda d\lambda} \tag{4.36}$$

where S_λ is the solar flux at a particular wavelength.

4.2.3 Final Calibration and Conversion of GOES-8 Imager Data

The final calculation for the calibration and transformation of the visible count data into reflectance follows (calibration from Minnis *et al.* [2002a]):

$$\rho(\theta_v, \phi_v; \theta_s, \phi_s) = \frac{(0.650 + 0.0001341 \times DSL) \times (X - X_0)}{526.9 \cos(\theta_s)\delta(DOY)}, \tag{4.37}$$

where $\delta(DOY)$ is the normalized Earth-Sun distance, which is a function of the day-of-year (DOY) such that:

$$\begin{aligned} \delta(DOY) &= 1.000110 + 0.034221\cos(\gamma) + 0.001280\sin(\gamma) \\ &+ 0.000719\cos(2\gamma) + 0.000077\sin(2\gamma), \end{aligned} \tag{4.38}$$

with γ

$$\gamma = \frac{2\pi(DOY - 1)}{365} \tag{4.39}$$

This calibration is coded into a McIDAS program (cource code included in Appendix A). Figures 4-8 — 4-10 present the viewing and illuminating geometry for all sampling times over all three domains. The viewing zenith angle is approximately constant throughout, except for an adjustement due to an orbital shift in early 1995 (Figure 4-9). Figures 4-11 — 4-13 show the daily time-series of domain-averaged VIS reflectance, SIR and TIR temperatures at 14h45 UTC. Finally, Figures 4-14 — 4-16 show the monthly-averaged time-series of domain-averaged reflectance and temperatures at all times of day sampled.

4.3 Remote Sensing of Shallow Cumulus Clouds

4.3.1 A Brief overview of Clouds and their Morphology

Cumulus clouds have a wide range of sizes, from 30-m to 10-km, but most have a diameter of $1 \sim 2$km [Wielicki and Welch, 1983]. These clouds are often multi-celled, even for cumuli as small as 1-km in diameter. The within-cloud cells range in size from 250-m to 1-km in diameter. Cumuli are non-uniform reflectors of radiation, due to their morphology [Wielicki and Welch, 1983], and they exhibit large spatial variations in albedo and temperature. The density of cumulus clouds in a given area is also related to the average size of the cumuli, with greater overall densities being associated with larger individual cloud size [Wielicki and Welch, 1983]. In a study of cumulus cloud populations over Florida, Plank [1969] finds that: cloud size was inversely and exponentially related to cloud number density[3]; the characteristic size of clouds varies diurnally; the relation between vertical and horizontal extent of clouds exhibits large variability; a clear mode of cloud size ex-

[3]Neggers *et al.* [2003] arrived at the same conclusion using large-eddy simulations.

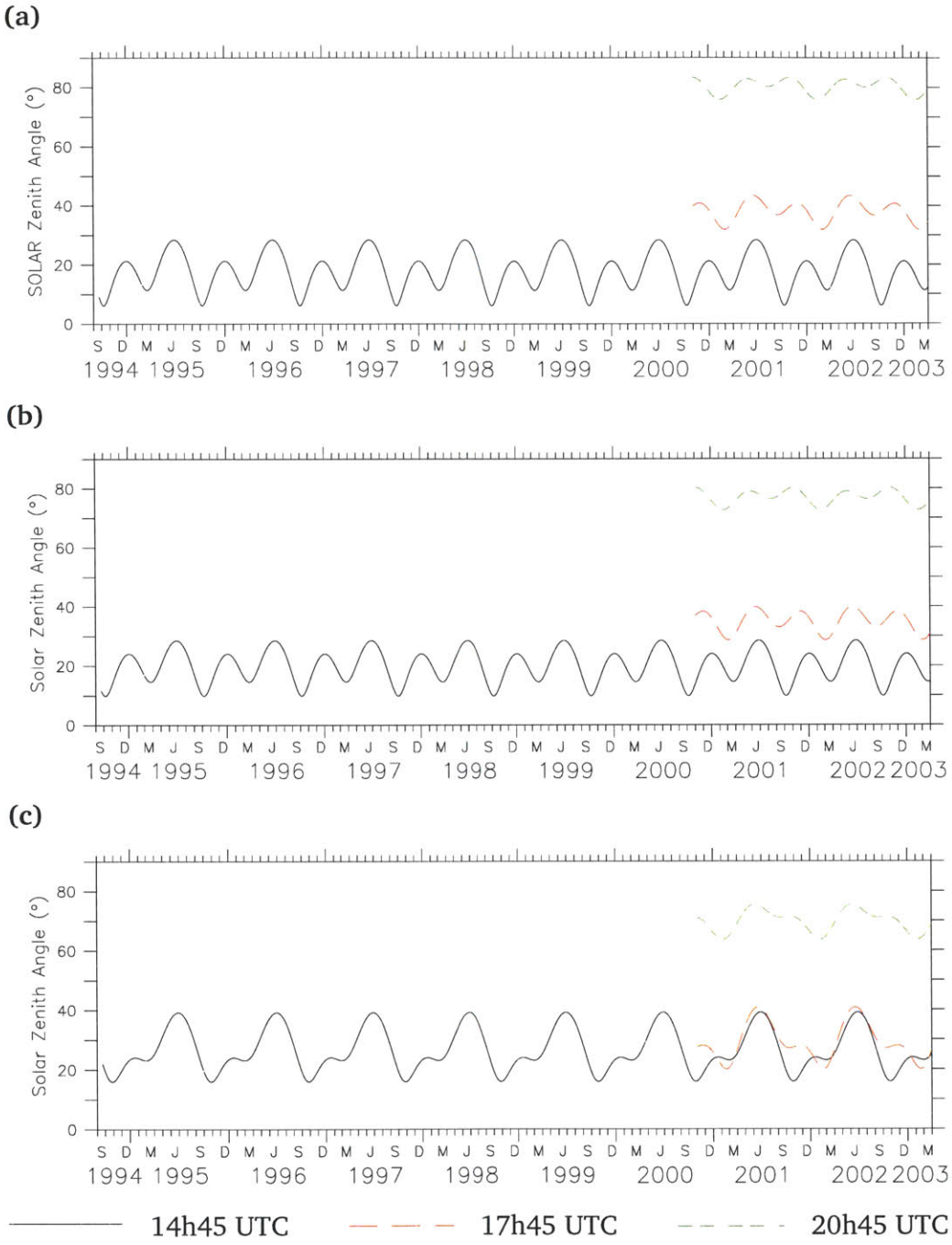

Figure 4-8: Time-Series of Domain Averaged Solar Zenith Angle; **(a)** Marabá-Altamira; **(b)** Tapajós-Santarém; **(c)** Rondônia.

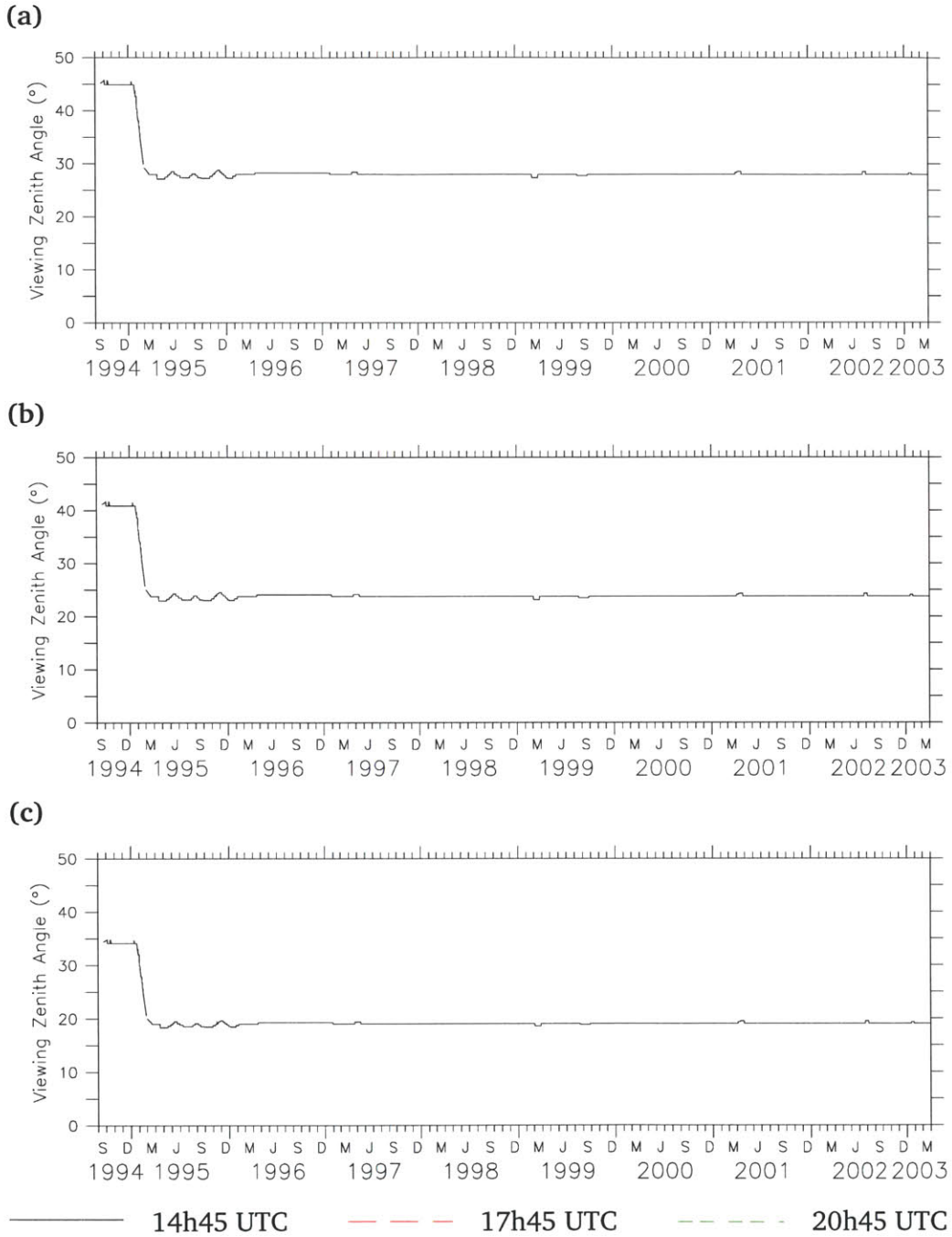

Figure 4-9: Time-Series of Domain Averaged Viewing Zenith Angle; **(a)** Marabá-Altamira; **(b)** Tapajós-Santarém; **(c)** Rondônia.

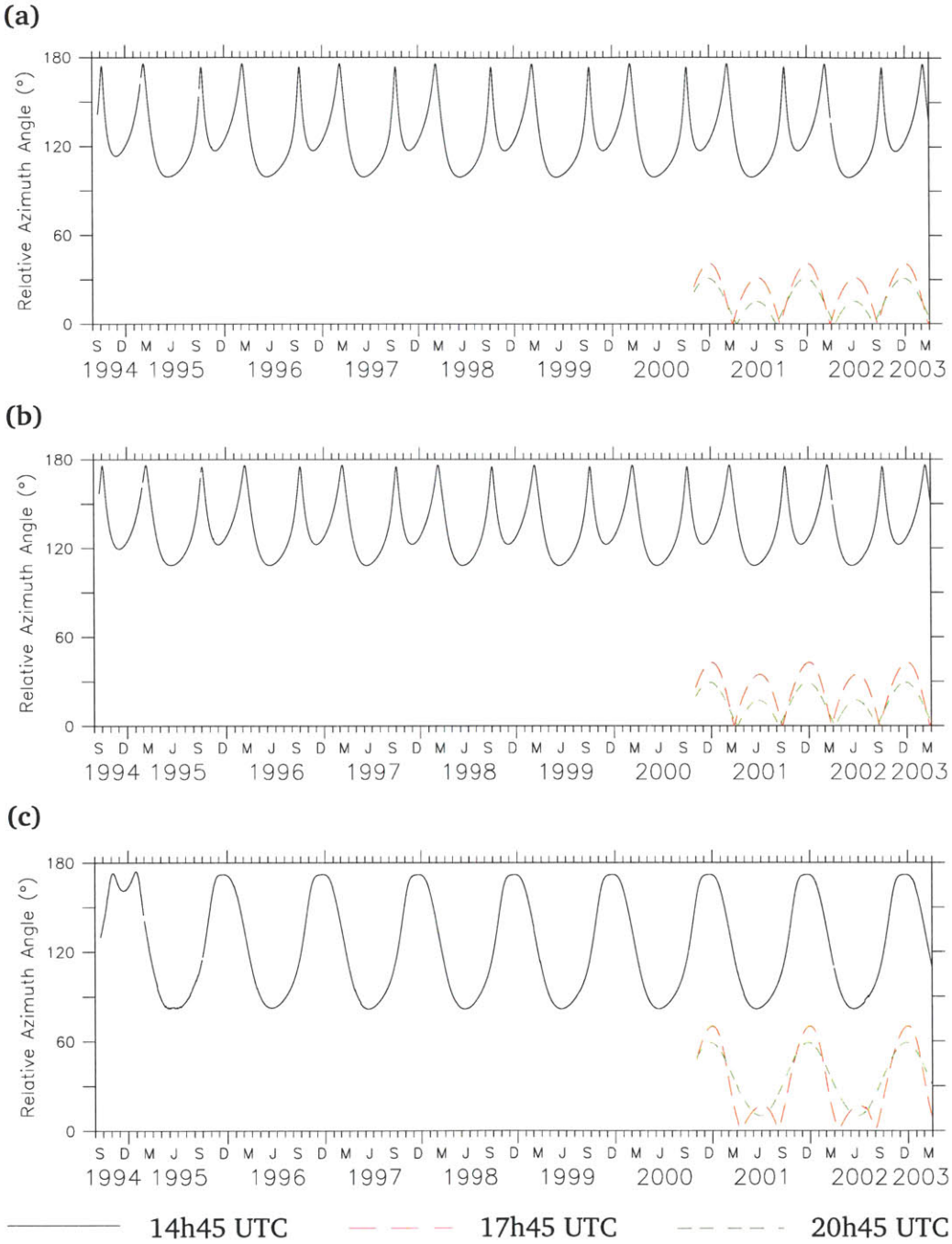

Figure 4-10: Time-Series of Domain Averaged 14h45 UTC Relative Azimuth Angle; **(a)** Marabá-Altamira; **(b)** Tapajós-Santarém; **(c)** Rondônia.

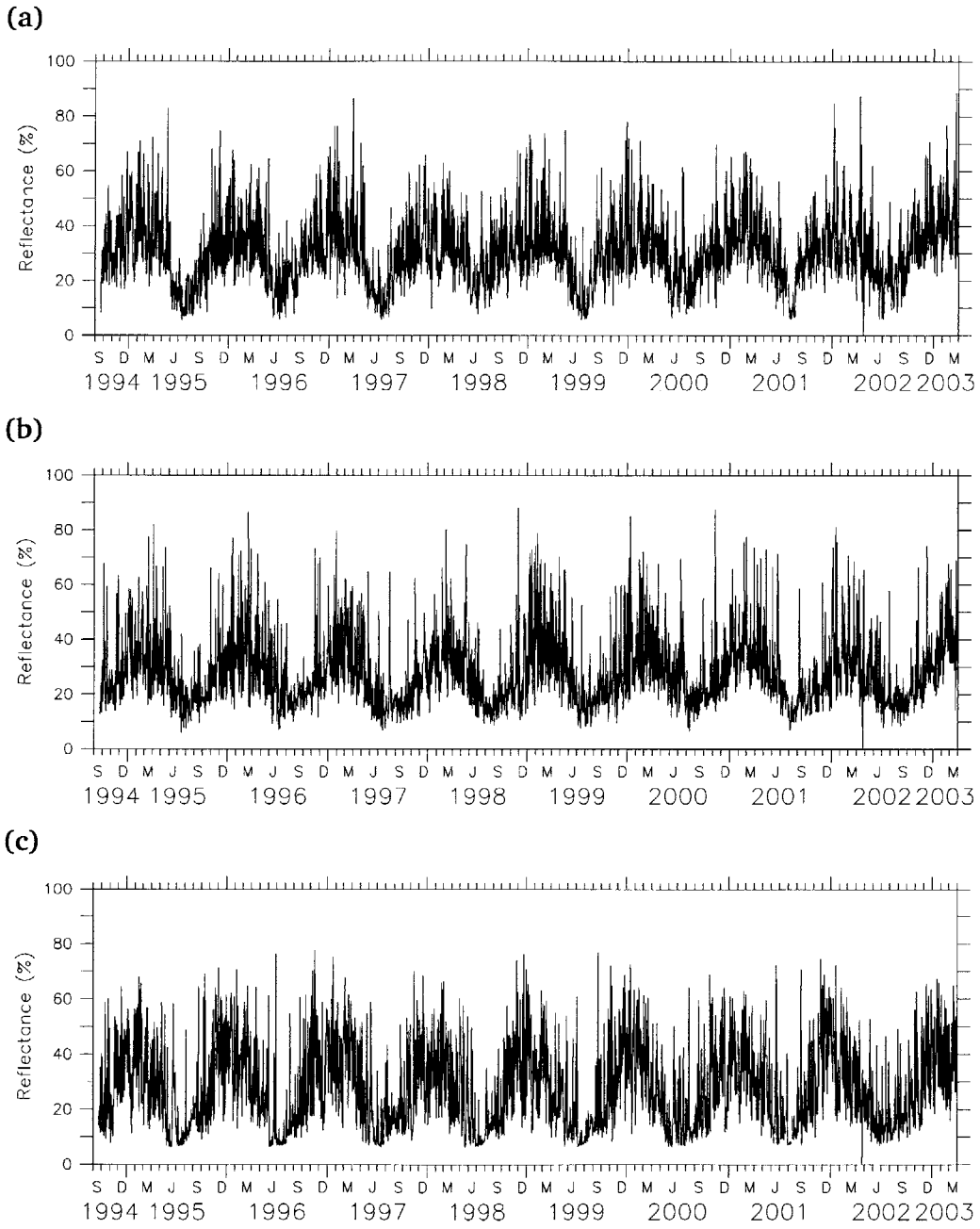

Figure 4-11: Time-Series of Domain Averaged 14h45 UTC Visible Reflectance; **(a)** Marabá-Altamira; **(b)** Tapajós-Santarém; **(c)** Rondônia.

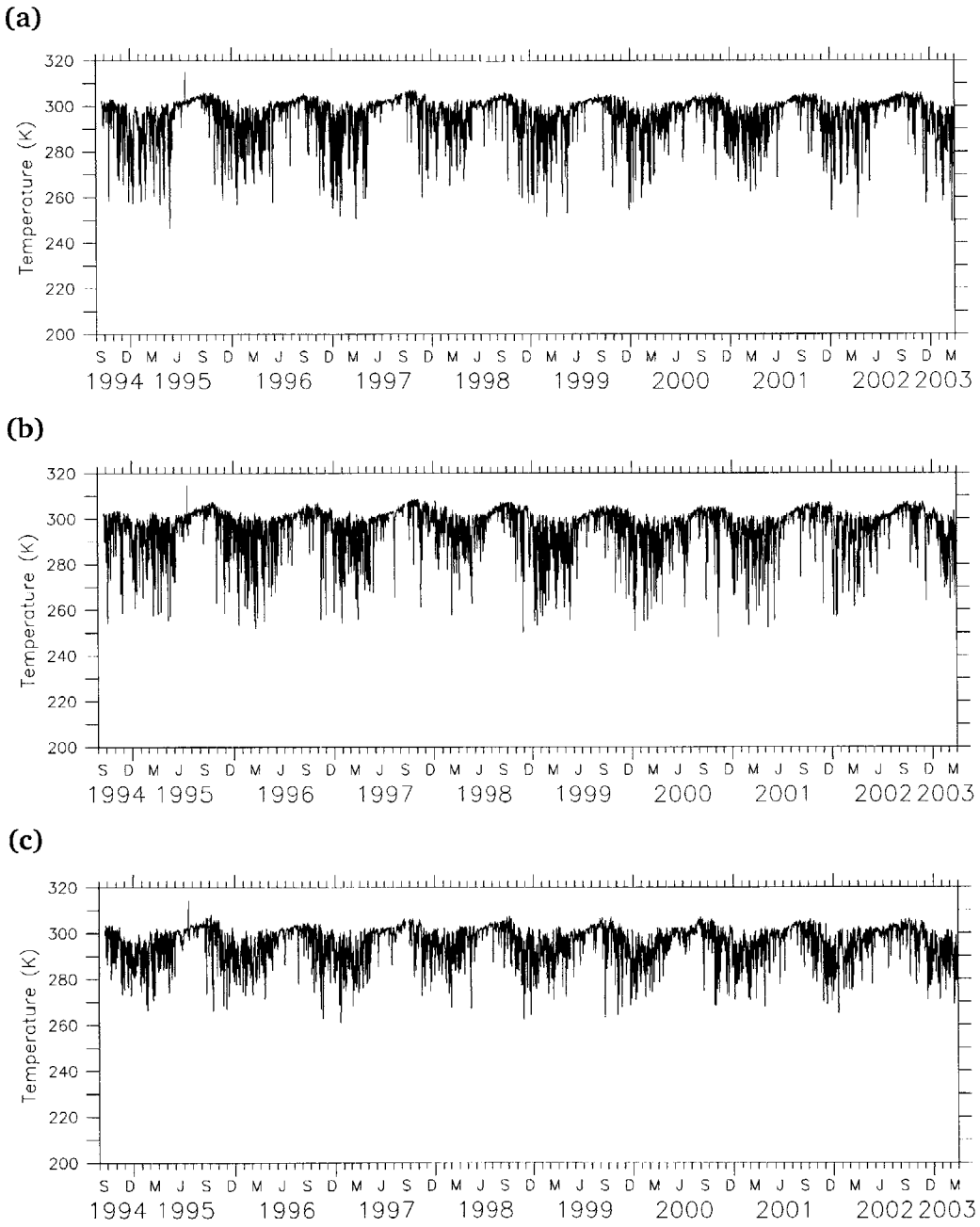

Figure 4-12: Time-Series of Domain Averaged 14h45 UTC Channel 2 Temperature; **(a)** Marabá-Altamira; **(b)** Tapajós-Santarém; **(c)** Rondônia.

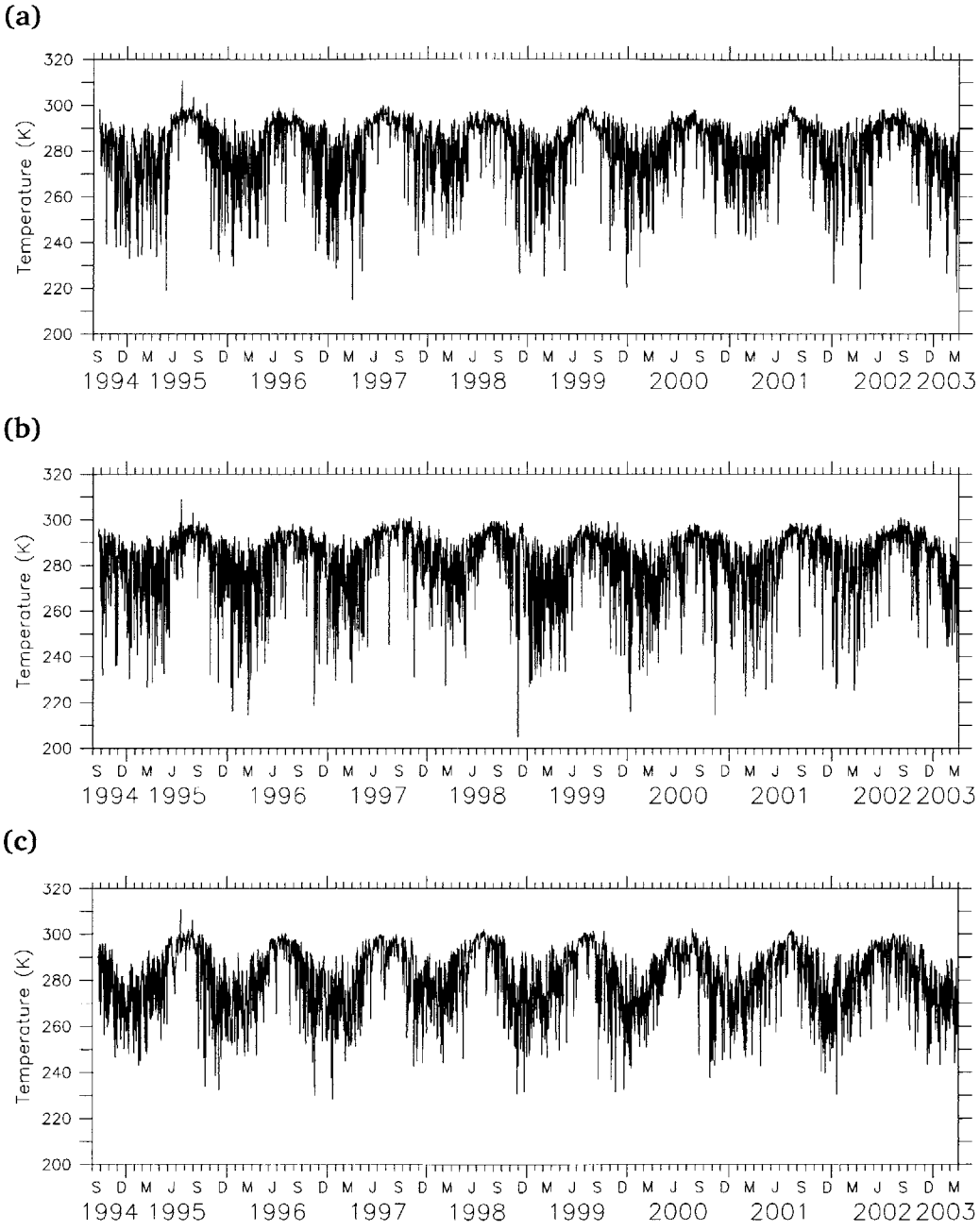

Figure 4-13: Time-Series of Domain Averaged 14h45 UTC Channel 4 Temperature; **(a)** Marabá-Altamira; **(b)** Tapajós-Santarém; **(c)** Rondônia.

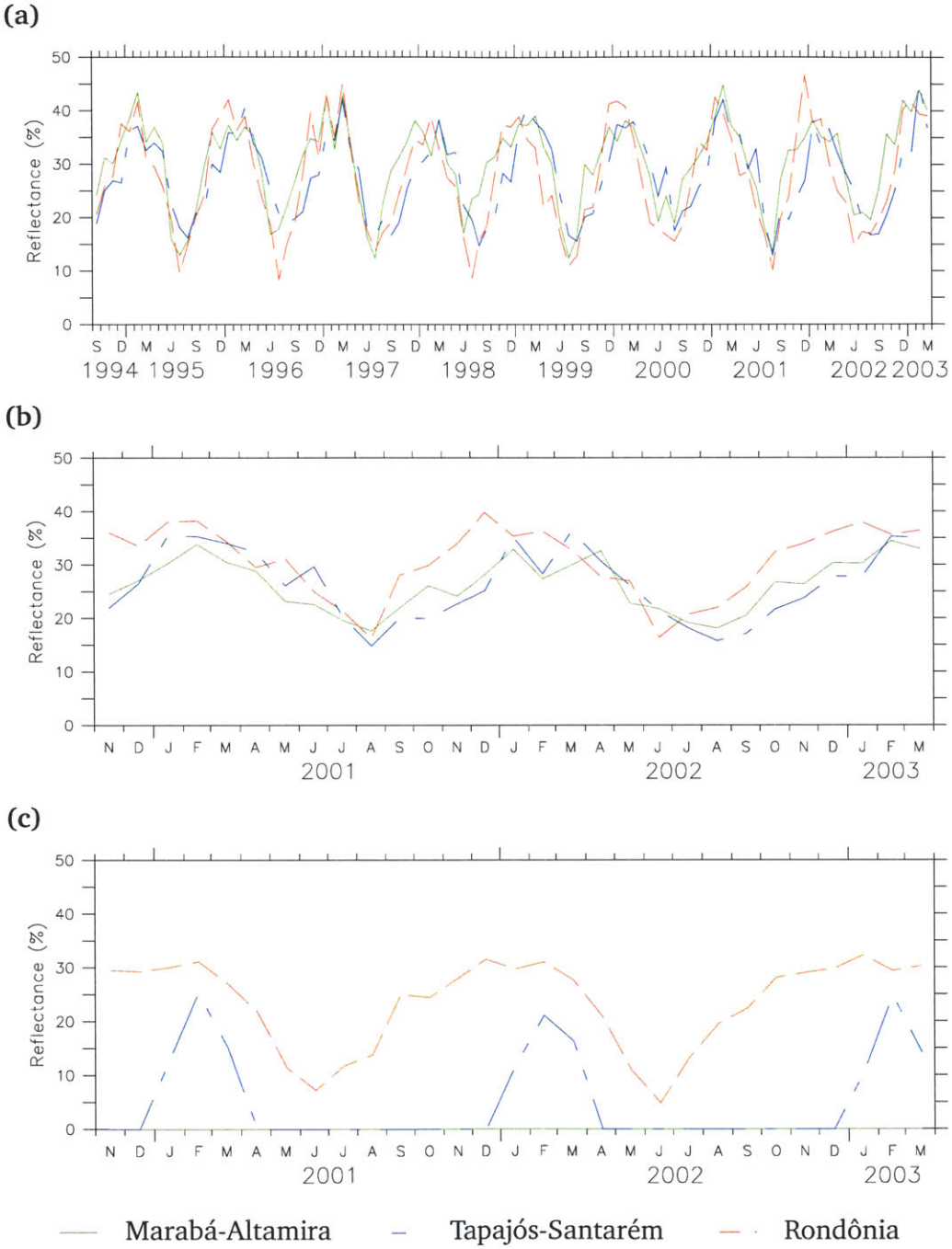

Figure 4-14: Monthly-Averaged Time-Series of Domain-Averaged Visible Reflectance; **(a)** 14h45 UTC; **(b)** 17h45 UTC; **(c)** 20h45 UTC.

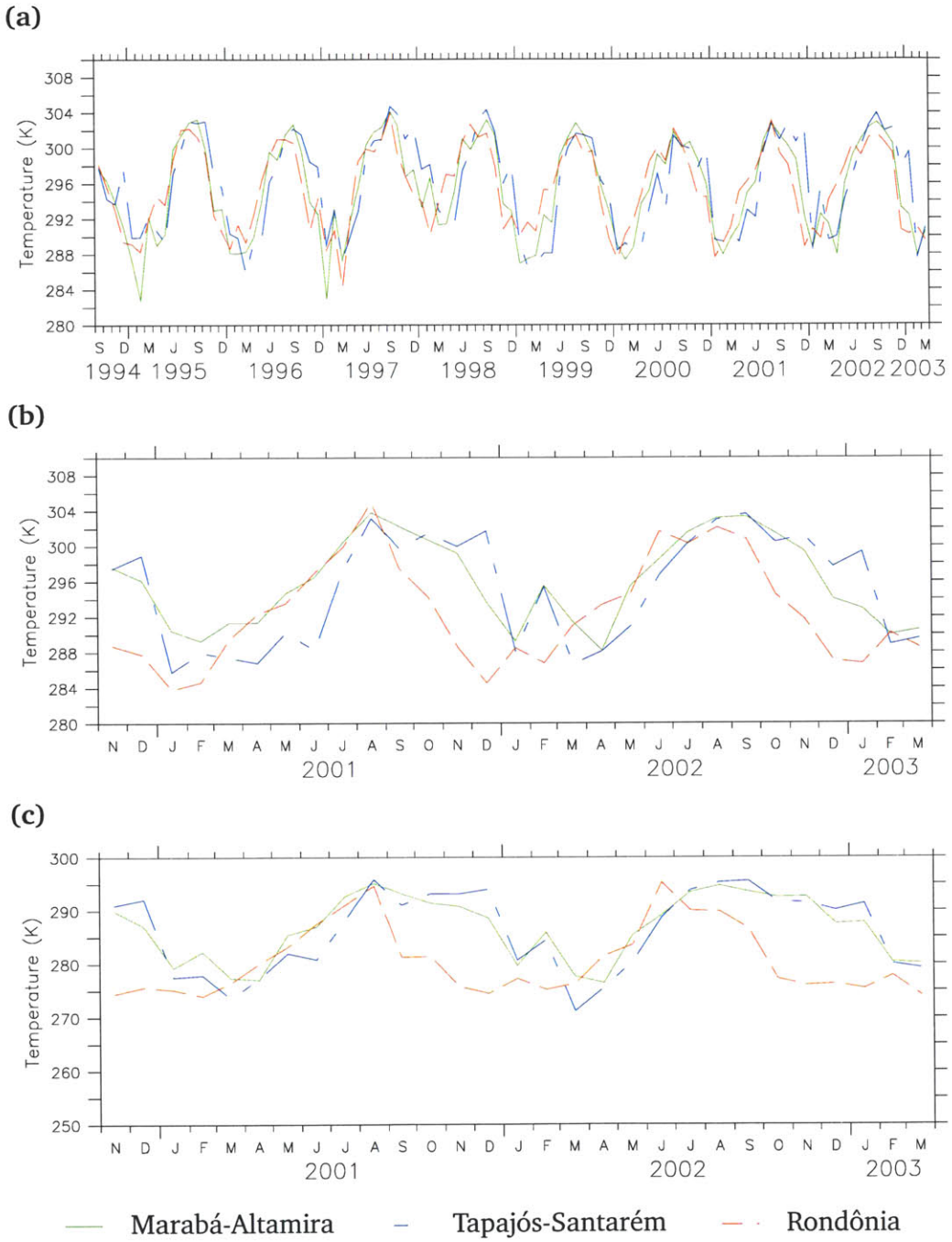

Figure 4-15: Monthly-Averaged Time-Series of Domain-Averaged Channel 2 Temperature; **(a)** 14h45 UTC; **(b)** 17h45 UTC; **(c)** 20h45 UTC.

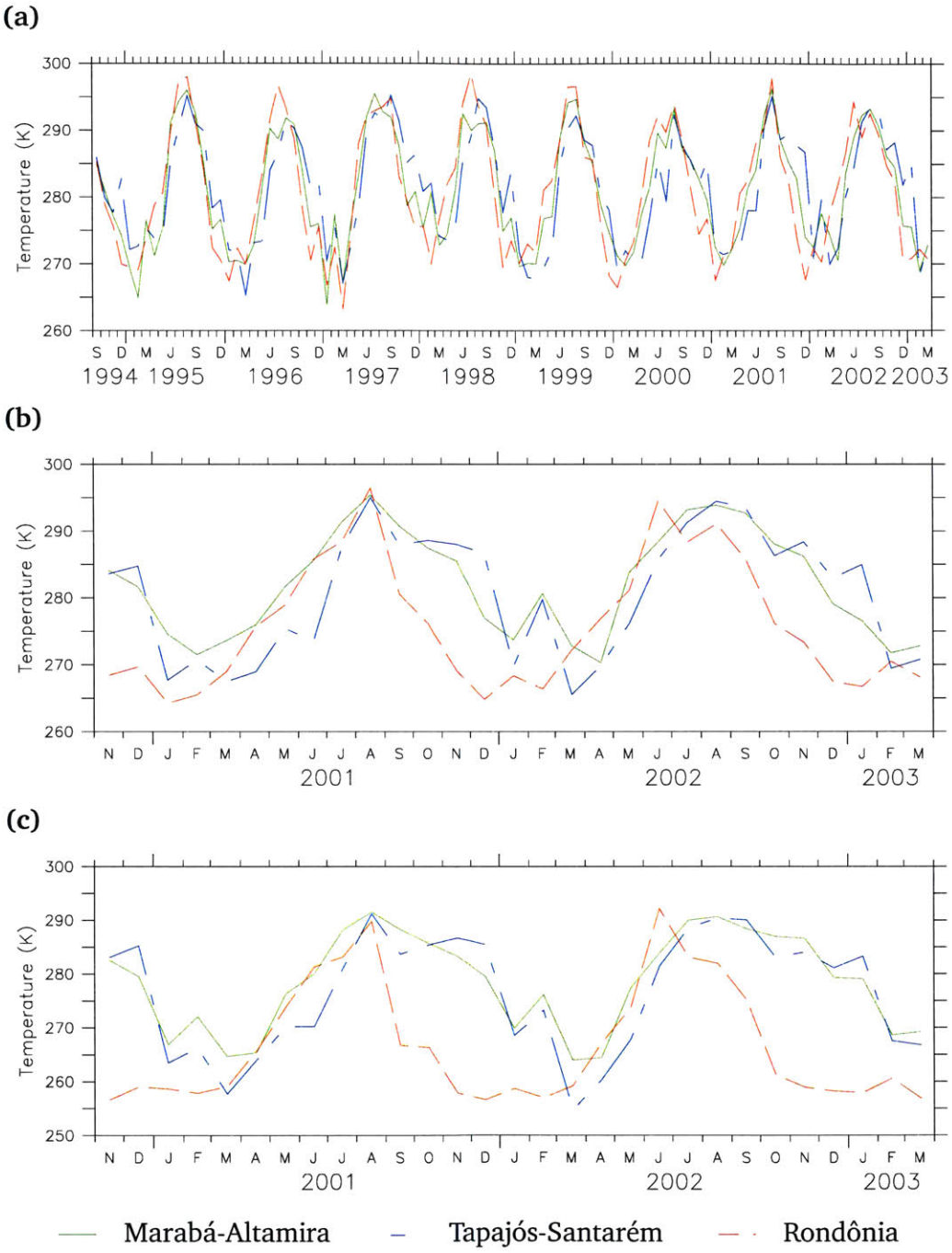

Figure 4-16: Monthly-Averaged Time-Series of Domain-Averaged Channel 4 Temperature; **(a)** 14h45 UTC; **(b)** 17h45 UTC; **(c)** 20h45 UTC.

ists within cloud populations; and clouds that began forming into group structures at mid-morning were important developmental features of cumulus convection.

Shallow cumulus clouds have differing behaviours depending on the nature of the surface over which they evolve. Oceanic clouds generally exhibit a semi-diurnal cycle, whereas clouds over land show a strong diurnal cycle [Liberti *et al.*, 2001]. The nature of the underlying surface may be sometimes more important than the geographic location. For example, Hendersen-Sellers [1978], using ground based observations, found that cloud frequency curves over land are similar irrespective of latitude. In an 8-year climatology using the ISCCP data, Rossow *et al.* [1993] found that clouds occur more often over ocean than land (i. e., the mean cloud amount over ocean is 23% higher than that over land), and that the largest seasonal variations in cloud cover occur in the tropics. The seasonal phase in the tropics (maximum in summer) is opposite to that of the extra-tropics, and the diurnal cycle is characterized by a peak in nighttime clouds over oceans, and daytime clouds over land [Rossow *et al.*, 1993].

Stull [1985] differentiates fair weather cumuli into three subtypes: forced, active and passive. The criteria for the differentiation between these three subtypes lies in the way in which the fair weather cumuli interact with the free atmosphere. Active fair weather cumuli (i. e., cumulus congestus, cumulus mediocris) reach above the level of free convection (LFC) and thereby vent mixed-layer air into the free atmosphere and inhibit mixed-layer (ML) growth. These cumuli are identified by cloud-top turrets that are signs of positive buoyancy. Passive fair weather cumuli are the remnants of active cumuli, whose sole interaction with the mixed-layer is through shading. Forced fair weather cumuli are held entirely within the mixed-layer. Their existence is directly tied to the presence of thermals in the ML, and are usually short-lived although they may develop into active FWC if enough latent heat is fed into them so that they may extend beyond the LFC. The active FWC are particularly important in that they moisten the free atmosphere and develop circulations that are independent of the thermals that originally triggered the clouds.

4.3.2 Cloud Detection and Classification: Background

Clouds are one of the most prominent feature in images of the earth taken from space (see Figure 4-17). While clouds and their properties can be measured from the ground (e. g., Crewel *et al.* [1999]), remote sensing platforms provide an incredible opportunity to observe meteorological patterns over large spatial scales, and — if the record permits — long temporal scales. Because of their high degree of activity (i. e., absorption and scattering of radiation) in the visible and infrared wavelength ranges, clouds are most often studied using satellite-borne instruments that are sensitive in these bands.

The analysis of satellite measured radiances may be used to infer cloud extensive (e. g., horizontal and vertical dimension) and intensive (e. g., liquid water path, albedo) properties. The analysis procedures and results are dependent upon

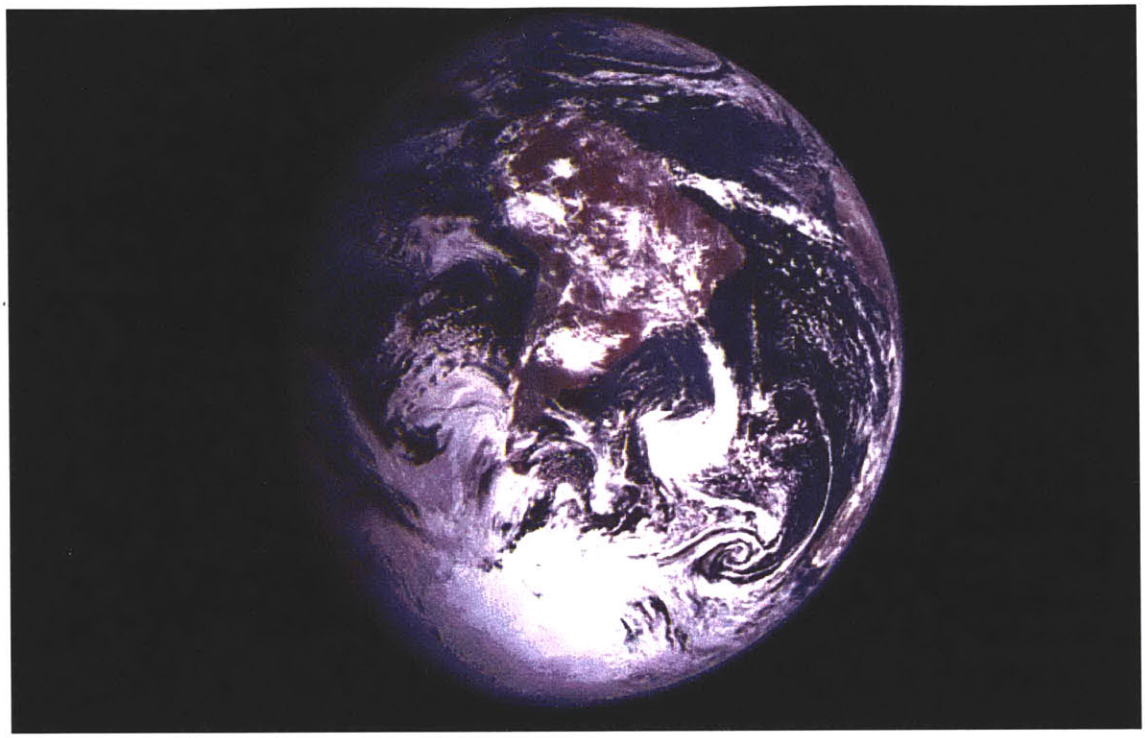

Figure 4-17: Picture of the Earth taken by Solid State Imager (SSI) on Galileo during its first flyby of the Earth in December of 1990 (Created by Dr. Edwin V. Bell, II [NSSDC/Raytheon ITSS]).

the cloud type, the background properties, the viewing and illuminating geometries, the spectral range, the spatial resolution, etc. [Minnis, 1989; Wielicki *et al.*, 1995; Rossow *et al.*, 1985]. Spatial resolution is a particularly important aspect [Shenk and Salomonson, 1972], although some have shown experimentally that it is less important than the theory would suggest [Wielicki and Welch, 1983]. Wielicki and Parker [1992] reports that the optimal resolution for cloud detection and classification is around $1 \sim 2$-km. Higher resolutions are problematic for the detection of optically thin clouds, while lower resolutions are plagued by partially-filled pixels. Using 57 meter resolution LANDSAT imagery degraded to various resolutions, Wielicki and Welch [1983] finds that the optimal scale for cloud detection is about $1/5$ the typical scale of the cloud. So for cumulus clouds that have a typical scale of $1 \sim 2$-km, a sensor resolution of 250 meters is necessary. Wielicki and Welch [1983] found that the $1/4$-km data closely reproduced the results of the $1/16$-km data, whereas the 1-km displayed differences in the range of cloud reflectances and in the sensitivity to the choice of threshold. This said, Wielicki and Welch [1983] affirmed that the 1-km resolution data showed sufficient spatial structure and range of reflectance to be used for cumulus cloud retrieval. Lower resolutions were not found to be appropriate for cumulus retrieval; the 4-km data derived cumulus field bore little resemblance to the full resolution field [Wielicki and Welch, 1983].

There are two general methods to infer cloud cover from satellite imagery: threshold and statistical methods [Rossow *et al.*, 1985]. Threshold methods operate on a pixel-by-pixel basis, whereas statistical methods use the information contained in an area to infer cloud cover. The drawback of threshold methods is their inability to take mesoscale patterns into account [Garand, 1988]. One other problem with threshold methods is caused by partially-filled pixels [Wielicki *et al.*, 1995]. Statistical methods, on the other hand, are unable to characterize the variations in cloudiness within the area on which they are applied. There is widespread agreement that cloud classification algorithms are not universally applicable [Garand, 1988; Wielicki *et al.*, 1995]. Most are targeted for precise cloud types. The great diversity of cloud types is hard to handle with one single algorithm. When targeted, the cloud classification algorithms seem to be robust; comparison studies have found that different cloud algorithms perform roughly equally [Rossow *et al.*, 1993; Berendes *et al.*, 1999].

While both methods approach the problem of cloud classification very differently, they both rely on basic cloud detection, in which clouds are separated from the background surface signal. The cloud detection component of a cloud algorithm is the most fundamental component [Rossow *et al.*, 1985]. This method requires knowledge of the reflectance and temperature of the surface. Such "clear-sky" radiances are critical in deriving accurate cloud classifications [Minnis and Harrison, 1984; Rossow *et al.*, 1985]. This section will present a review of the various methods that have been developed to detect clouds from space, by first introducing "clear-sky" radiance retrieval methods, and then by proposing three algorithms to classify clouds over the Amazon basin.

4.3.3 Clear-Sky Radiance Retrieval

Clear-sky radiance is the term used to describe the radiance detected by the satellite-borne instrument when the atmosphere is free of clouds and relatively clean. Obtaining clear-sky radiances can be problematic in areas of persistent cloudiness. Such areas are listed by Matthews and Rossow [1987], and include the Amazon basin, although this problem may be limited to certain seasons. The most intuitive algorithm to derive clear-sky parameters is the minimum brightness method. This method implies two assumption: **(a)** that the land or water surface is always less reflective and warmer than clouds, and **(b)** that the radiances are monotonic. It is used by Minnis and Harrison [1984] and Rossow *et al.* [1985]. However, by keeping only one value per-pixel, the minimum radiance method is very prone to error. Examples of the sources of the uncertainty are the natural variability of the surface reflectance and temperature, atmospheric noise, the contamination by shadows from broken clouds, navigational uncertainty, radiometric uncertainty, etc. The probability of obtaining an extreme due to the uncertainties also grows with the record length [Matthews and Rossow, 1987]. Averaging across many samples on minimum brightness does not cancel the uncertainty either; Gutman [1988] argues

that the minimum brightness technique leads to an underestimation of the mean clear-sky values due to the interference of cloud shadows and angular variations (although the latter reason is not really applicable to GOES due to regular viewing geometry over the period of minimization).

Matthews and Rossow [1987] obtained clear-sky brightnesses by averaging the reflectances that are associated with the temperatures higher than a certain threshold, and they obtained clear-sky temperatures by averaging over the reflectances smaller than another threshold. In this type of conditional filtering, the visible channel is especially important as a strict test for cloudiness; Matthews and Rossow [1987] showed that the clear-sky visible channel variations associated with aerosols, surface structure, and observation geometry result in small quasi-random variations, whereas clouds exhibit wide variations in that same channel. This said, the variations due to changes in vegetative cover from forest, to grass, to desert, etc. can be inferred from the visible radiance. The conditional filtering methods can be formalized in many different ways. Feijt *et al.* [2000] posited that if mean and median values of the filtered brightnesses are the same, then no cloud contamination is present, and the highest of the mean minus the standard deviation and minimum value was taken as the clear-sky value. The cloud-screening method proposed by Gutman [1988] involves the following steps (implicit in these steps is the angular viewing geometry periodicity of 9-days for the particular orbiting platform studied in that case):

1. Gross screening for clouds by eliminating obviously cloudy pixels:
   (a) Surface temperatures constrained to be greater than the monthly minimum mid-afternoon air temperature;
   (b) Visible reflectance less than 40%;
   (c) Standard deviation of visible reflectances less than 0.5 percentage points greater than monthly minimum;
2. Composite on 9-day cycle: Split each month into 9-day cycles that correspond to the variation in viewing geometry (polar-orbiting platform) and superpose corresponding days of each 9-day period, stratified by ground cover;
3. Average monthly by using the cosine of the solar zenith angle as a weighting function.

International and large-scale projects have put great amounts of effort in devising their cloud detection algorithms. The MODIS cloud mask product is produced using 14 bands of MODIS data and an algorithm that provides a level of confidence that a pixel is cloudy or not [Ackerman *et al.*, 1998]. The clear-sky radiances in the ISCCP cloud algorithm are inferred by examining both the spatial and temporal radiance contrasts [Rossow and Garder, 1993]. Spatial contrast is due to one of four causes: **(1)** a mixture of surface and clouds, **(2)** a change in the cloud properties,

(3) a change in the surface properties, and **(4)** a change in atmospheric properties. Temporal contrast also has four possibles causes: **(1)** variations due to the formation or dissipation of clouds, **(2)** quasi-periodic variations such as the diurnal cycle, **(3)** variations of surface conditions at synoptic or seasonal scales, and **(4)** variations due to changes in atmospheric conditions. The ISCCP algorithm uses the fact that clear-sky conditions have less spatial and temporal variations to determine clear-sky conditions.

Other methods to determine clear-sky radiances include using a limited area numerical weather prediction model to get clear-sky surface temperature values [Feijt *et al.*, 2000]; assuming that the convective cloud brightnesses can be modelled as a beta-distribution, and fitting the measured brightnesses to the distribution to differentiate clouds from land [Koren and Joseph, 2000]. One may also use known values (measured in-situ) to enable cloud detection, however such methods must take atmospheric attenuation into account, as well as the differences in spectral response between the in-situ instrument and the satellite-borne instrument.

There are many sources of uncertainty in clear-sky radiance retrievals. Anisoptropic relations to viewing and illuminating geometries pose great problems. For example, clear-sky surface temperature is strongly dependent upon the viewing geometry[4] [Minnis and Khaiyer, 2000]. Also, the usual assumption of the unique dependence of the clear-sky albedo (or reflectance) on solar zenith angle is flawed [Minnis *et al.*, 1997]; there is a strong dependence of surface state (dew, frost, wind, evaporation, precipitation) which induces a diurnally dependent cycle on top of the solar angle dependence. Another problem is caused by partially-filled pixels (i. e., when a pixel is partly covered by a cloud). A linear combination of cloudy and clear can't be used to solve the partially-filled pixel problem, since the reflected radiance from a broken cloud field can surpass that of an unbroken field [Coakley Jr. and Davies, 1986; McKee and Cox, 1974]. This is due to anisotropic reflectance and more radiation coming out of sides than from the cloud tops. To solve this problem, Minnis *et al.* [1995] used linear combinations weighted by the angular distribution models (ADM[5]) of clear and cloudy sky conditions. Beyond geometrically induced errors, Rayleigh type scattering that occurs in the atmospheric layer above the ground surface contributes to the measured visible radiance with a magnitude that is similar to the magnitude of the reflectance of such "dark" surfaces as water bodies or vegetated land [Matthews and Rossow, 1987]. Such an issue is further complicated with high concentrations of particles that would occur in areas where biomass burning is rife.

[4]This anisotropy is strongly correlated with terrain and surface reflectance anisotropy, and it is hence possible to envisage a simple model to reduce the dependence [Minnis and Khaiyer, 2000].

[5]The ADM describes the dependence of a surface's brightness on the angular viewing and illumination geometry. The ADM's are close to Lambertian when solar zenith angles are low (i. e., close to zero) [Wielicki *et al.*, 1995].

Cloud Detection Algorithm: Clear-Sky Radiances

The cloud detection algorithm used here to determine the clear-sky brightnesses is a conditional histogram method. The brightnesses are first filtered using thresholds of complementary channel brightnesses. Obviously cloudy pixel brightnesses are removed, and the clear-sky values are determined as the histogram peak of the remaining brightnesses. This unidimensional histogram method is applied selectively to each land cover type (i. e., forested or deforested) and is integrated on a monthly time-step. The thresholds used to separate out obviously cloudy conditions are presented in Table 4.6. Examples of the unidimensional histograms derived for a particular month for each channel pair and for each land cover type are presented in Figures 4-18 — 4-20.

Table 4.6: Cross-Channel Thresholds used to determine obviously cloudy conditions.

Channel	Wavelength (μm)	Variable	Lower Threshold	Upper Threshold
1 (VIS)	0.65	Reflectance	20 (%)	N/A
2 (SIR)	3.90	Temperature	N/A	290 (K)
4 (TIR)	10.70	Temperature	N/A	280 (K)

The monthly time-series of clear-sky values are presented in Figures 4-21 — 4-23. The seasonal cycle of visible reflectance shows a minimum in July for all domains and all landcover types, and the amplitude of the seasonal cycle is on the order of 10%. This compares to the observations of Berbet and Costa [2003], who finds a seasonal cycle amplitude of approximately 5%, with the minimum pasture albedo occurring in September and the minimum forest albedo occurring in April. The mean values of the visible reflectances are compared to other observations in Table 4.7. The differences are due to the effects of seasonal variations in illumination and observation geometry (Figures 4-8 — 4-10), and to the specific spectral window of GOES-8 detectors (Figure 4-6) — we are not measuring the hemispherically integrated broadband visible reflectance or albedo.

4.3.4 Statistical Methods for Cloud Classification

Most statistical methods employ a two-dimensional (or bi-spectral) histogram approach, in which the two dimensions are the visible and thermal-infrared radiances. The basic assumption underlying the two-dimensional histogram analysis methods is that the degree of homogeneity of surface types is high enough so that the radiance differences observed over similar surfaces (i. e., vegetation, clouds, bare soil, etc.) under different conditions (e. g., viewing geometry) are

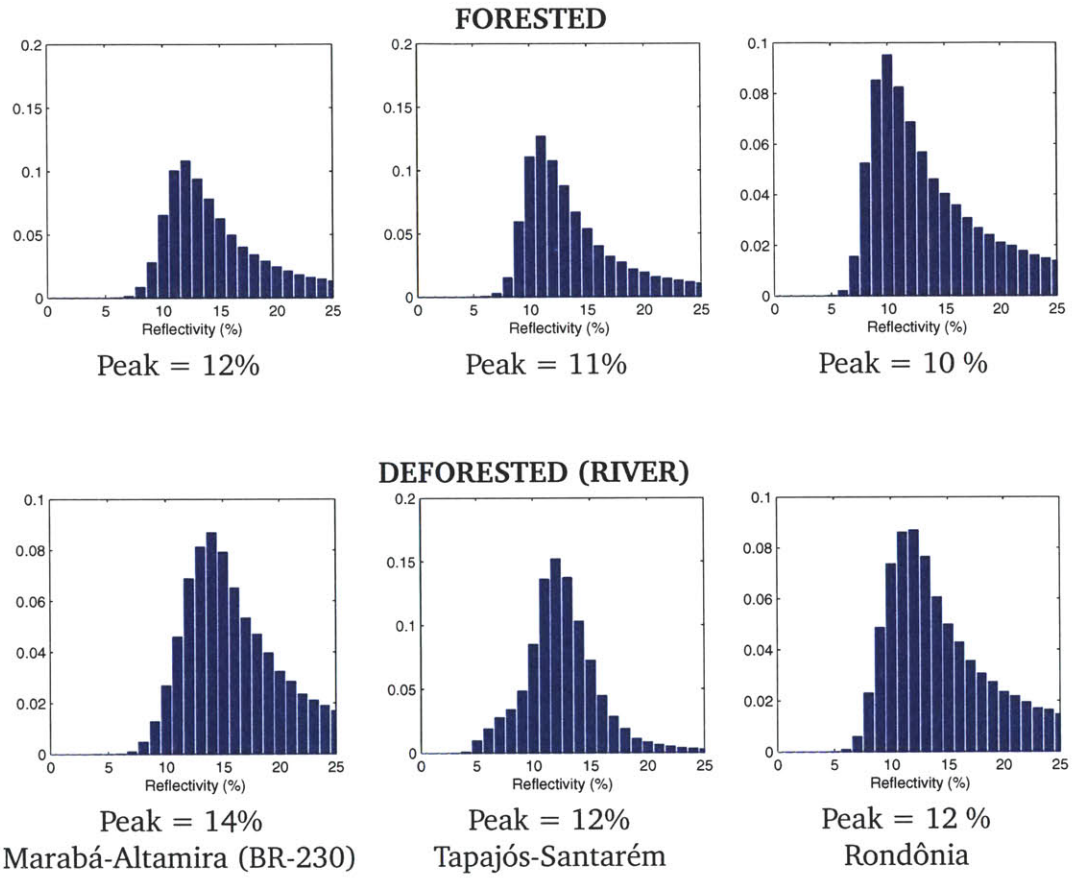

Figure 4-18: TIR Filtered Unidimensional Histogram of Visible Reflectance over each Domain at 17h45 UTC for month of November 2000.

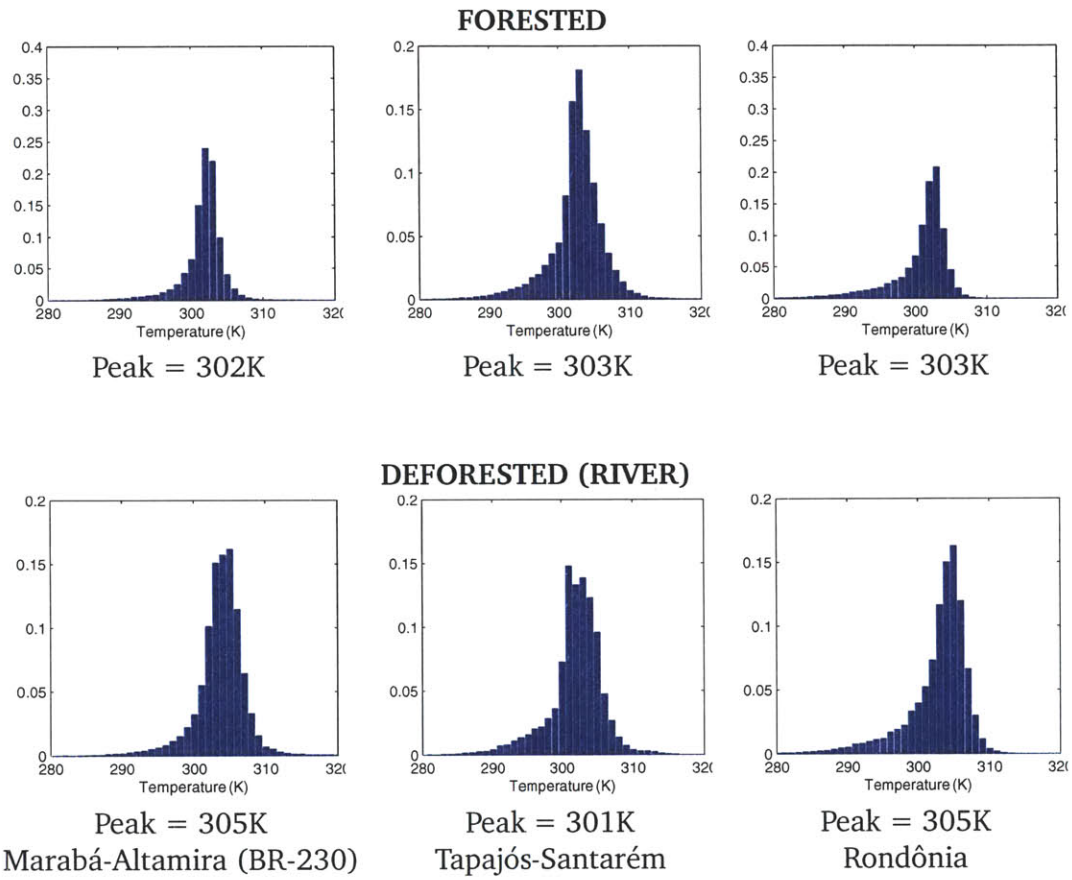

Figure 4-19: VIS Filtered Unidimensional Histogram of Channel 2 Temperature over each Domain at 17h45 UTC for month of November 2000.

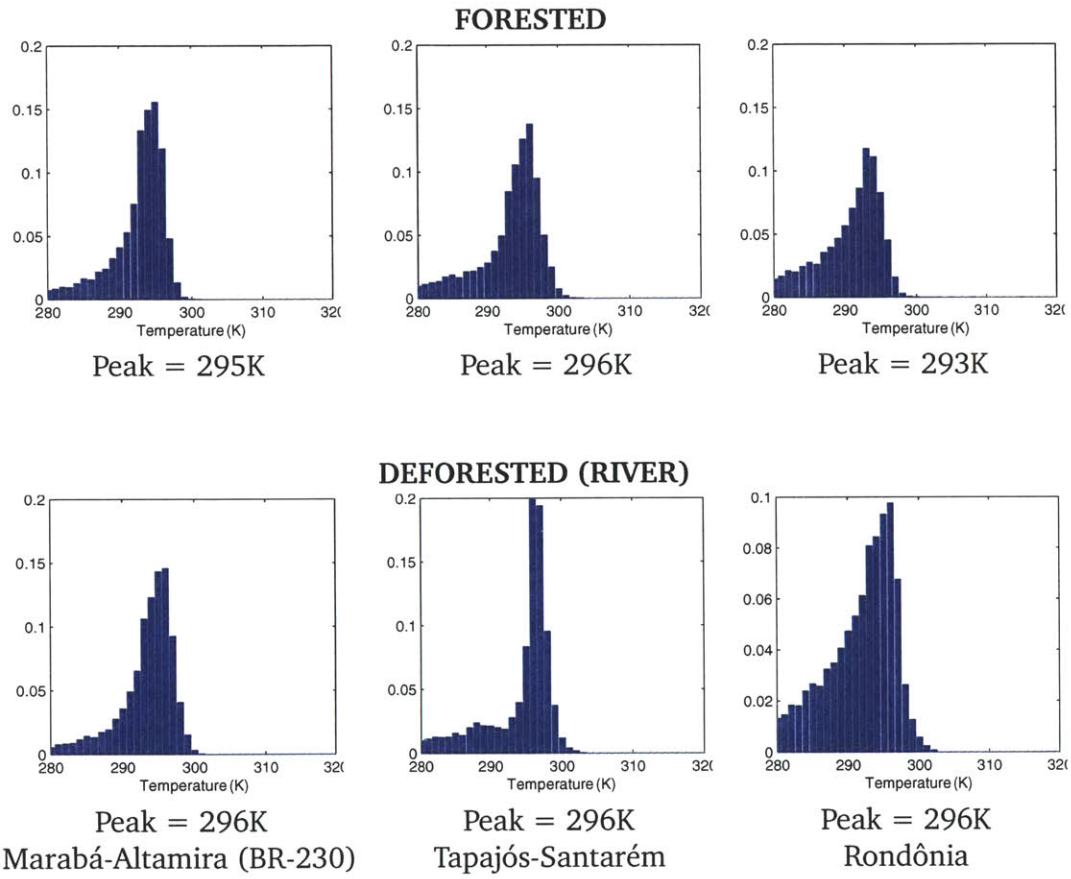

Figure 4-20: VIS Filtered Unidimensional Histogram of Channel 4 Temperature over each Domain at 17h45 UTC for month of November 2000.

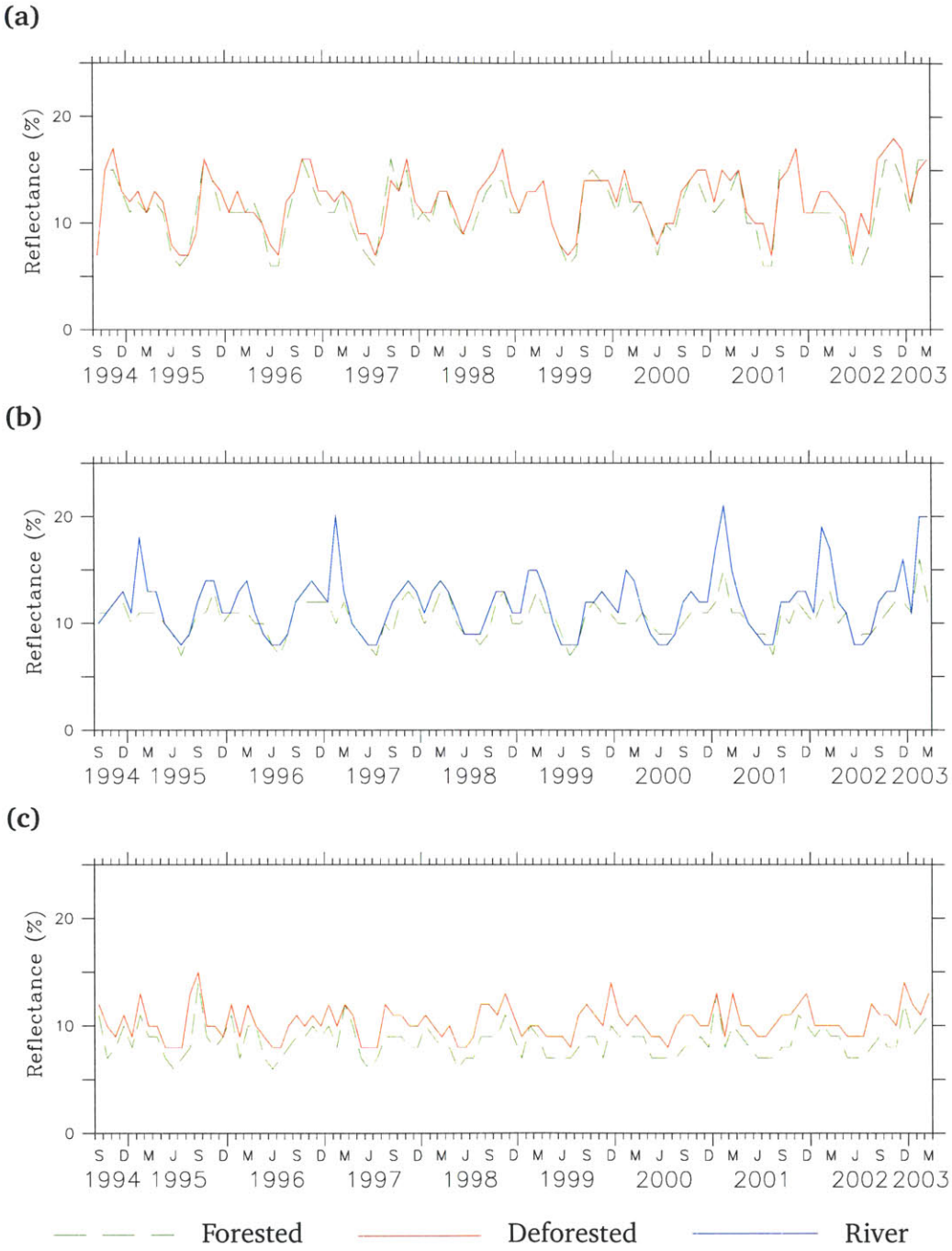

Figure 4-21: Time-Series of Clear-Sky Channel 1 Reflectances; **(a)** Marabá-Altamira; **(b)** Tapajós-Santarém; **(c)** Rondônia.

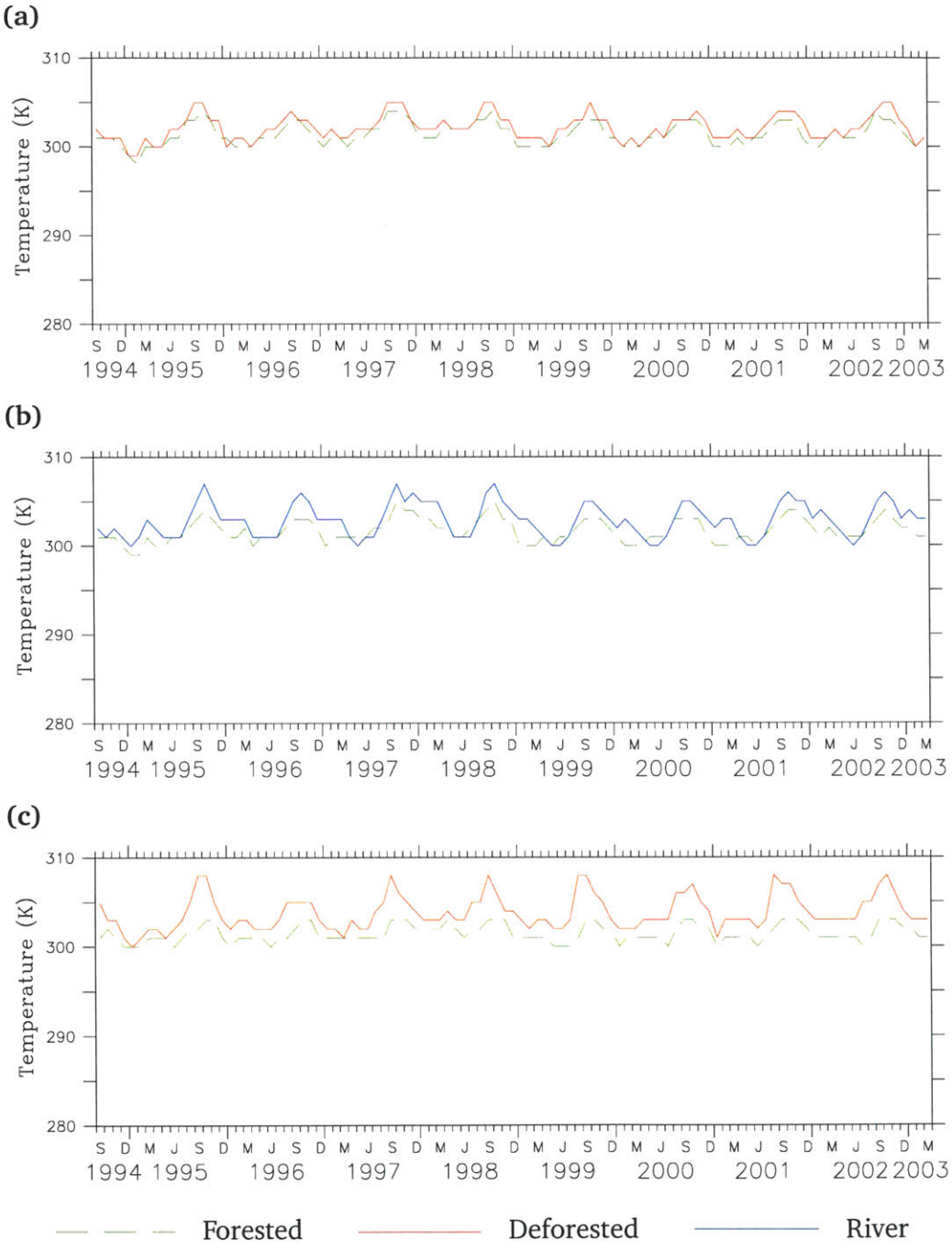

Figure 4-22: Time-Series of Clear-Sky Channel 2 Temperature; **(a)** Marabá-Altamira; **(b)** Tapajós-Santarém; **(c)** Rondônia.

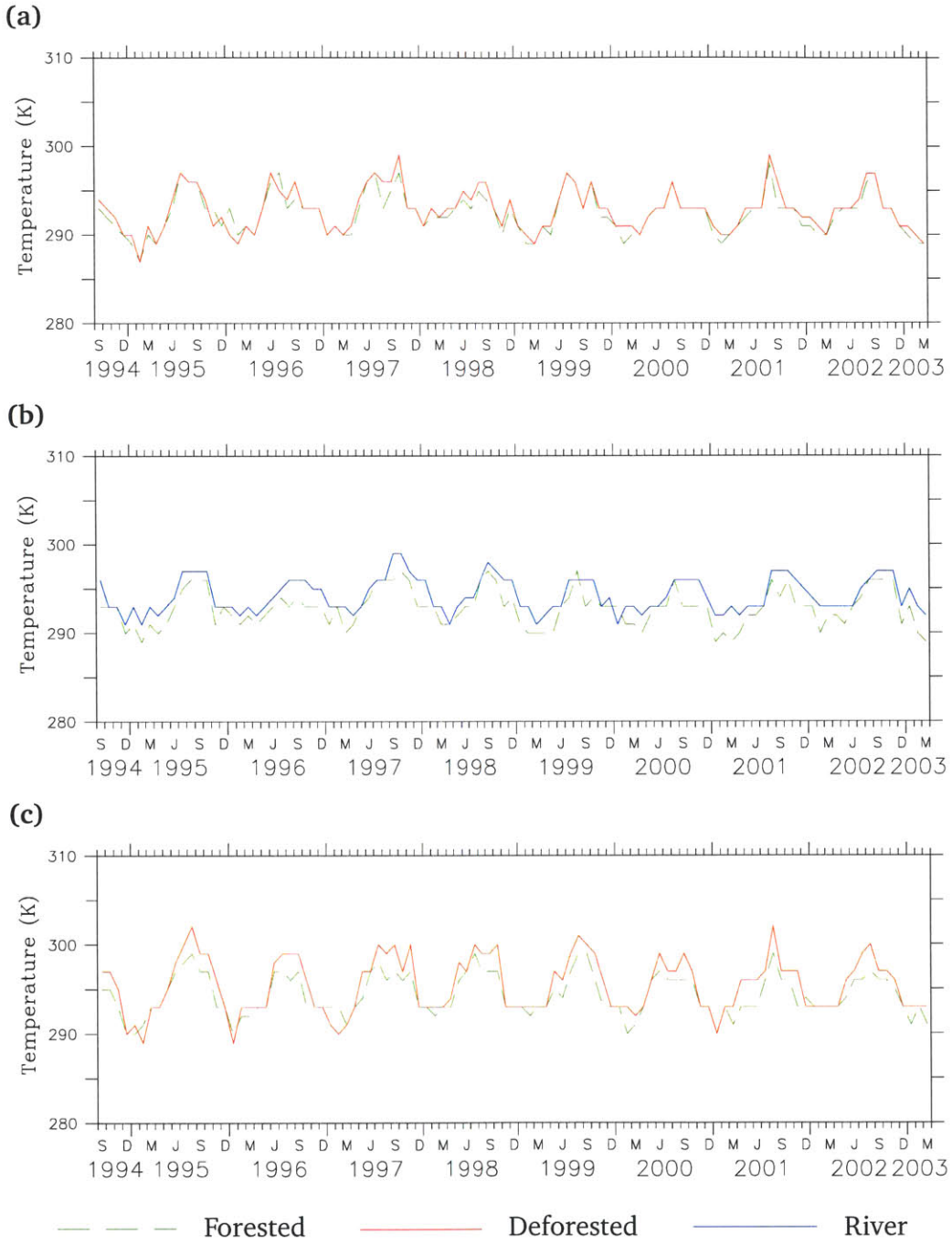

Figure 4-23: Time-Series of Clear-Sky Channel 4 Temperature; **(a)** Marabá-Altamira; **(b)** Tapajós-Santarém; **(c)** Rondônia.

Table 4.7: Comparison of Observed Clear-Sky VIS Reflectance with Other Studies.

Authors	Forest Albedo (%)	Pasture Albedo (%)	Sensor
Matthews and Rossow [1987]	5	9	NOAA-5
Culf *et al.* [1995]	13.4	18	in-situ
Rondônia 14h45 UTC	8.6	10.4	GOES-8
Rondônia 17h45 UTC	10	12.3	GOES-8
Rondônia 20h45 UTC	7.5	8.6	GOES-8

smaller than the radiance differences between different surface types. Different cloud classes may thus be inferred by the various distribution peaks that occur in a bi-dimensional histogram of the radiances measured [Sèze and Desbois, 1987].

The main difference between two-dimensional histogram methods lies in the way in which peak-surrounding regions are separated. The asymmetric Gaussian histogram analysis method used by Simmer *et al.* [1982] relies on the identification of peaks in the one-dimensional histograms and on the assumption that the distribution about these peaks is Gaussian, and that peaks in the visible band have corresponding peaks in the infrared band, and vice-versa. On the other hand, the dynamic cluster analysis (e. g., Desbois *et al.* [1982], Sèze and Desbois [1987], Massons *et al.* [1996], Porcú and Levizzani [1992]) relies on the identification of peaks in the two-dimensional histogram, and on separating classes by associating each brightness pair to its nearest peak (as defined by the Euclidean distance). Yet another method of separating clusters is to use maximum-likelihood by assuming that the distribution of brightnesses about the peaks is log-normal [Li *et al.*, 2003]. Koren and Joseph [2000] used known cloudy images to derive beta-distribution parameters of the brightness of convective clouds. Differentiation between convective and non-convective clouds was achieved by comparing derived beta-distribution with observed scene brightness distributions. This last method could also be used to determine the threshold that separated cloudy from clear pixels (see previous section). Chou *et al.* [1986] employed a statistical method that is based on linear combination of clear and cloudy radiances in the visible and thermal infrared bands. They argued that using a pair of radiance values from a single pixel isn't a good predictor of cloudiness, and that cloudiness must be inferred over a scene that is composed of many pixels. The cloudy radiances were determined from averaging the values for pixels that are certain to be cloudy (i. e., exceeding a threshold value). The clear radiances were obtained using a spatial coherence method that assumed that the background radiances are relatively homogenous. This linear combination method resulted in a unique cloud fraction for a measured radiance, using the following relation:

$$C = \frac{I_{measured} - I_{clear}}{I_{cloudy} - I_{clear}}, \tag{4.40}$$

where C is the cloud fraction, and I are the radiances (visible or thermal infrared).

The drawback of statistical methods is their need for high volumes of data in order to have sufficient samples of each type of "surface" [Rossow *et al.*, 1985]. A second drawback of these methods is that cumuliform and stratiform cloud of same brightness are often confused [6]. Statistical methods are most appropriate at determining the relative coverage of different types of "surfaces" in an image, and not at determining whether a single pixel is occupied by a certain type of cloud. Examples

[6] Diószeghy and Fejes [1995] found that adding a single threshold in the standard deviation of the thermal infrared field solves the problem quite efficiently. The logic behind the use of the standard deviation is that cumuliform clouds exhibit much more irregularity than stratiform clouds.

of bi-dimensional histograms from the GOES-8 sensor are given in Figures 4-24 — 4-27. There is a great deal of variability that depends on time-of-day and location (Figures 4-24 — 4-26), and the time-of-year (Figure 4-27).

4.3.5 Threshold Methods for Cloud Classification

The simplest threshold methods determine that a pixel is cloudy if the measured radiance differs from the clear-sky radiance by at least the prescribed threshold values. This type of methods can be applied to one or many channels. As such, there are visible threshold methods [Arking, 1964], infrared threshold methods [Coakley Jr. and Baldwin, 1984; Coakley Jr., 1987], and bispectral threshold methods [Rossow *et al.*, 1985]. The thresholds can be set arbitrarily, or they can be derived dynamically with models such as NWP. Table 4.8 presents some of the constant thresholds. Some examples of studies that have used threshold methods are Feijt *et al.* [2000], who used a bispectral threshold with NWP derived surface temperatures; Minnis *et al.* [1995] used a layer bispectral threshold method, also used in Minnis and Smith Jr. [1997] in which the thresholds are independent (i. e., either threshold must be met, but not necessarily both).

Table 4.8: Threshold-based Cloud Classification Algorithm Parameters.

Authors	Reflectance Threshold $\Delta\rho$ (%)	Temperature Threshold ΔT (K)	Simultaneous or Independent
Rossow *et al.* [1985]	3	6	I
Minnis *et al.* [1995]	$10.4 + 1.4\ln(\cos(\theta_s))$	5	I

Cloud fraction is sensitive to the choice of thresholds, as was shown by Wielicki and Welch [1983] in LANDSAT derived cumulus cloud field.

4.3.6 Hybrid Methods

Hybrid methods try to reconcile the strengths of threshold and statistical methods. An example of such a cloud classification algorithm is the Hybrid Bispectral Threshold Method (HBTM) of Minnis and Harrison [1984,b,c]. This algorithm is quite involved, and a full description is not relevant. Minnis *et al.* [1992] test the HBTM against surface based observations during the First ISCCP Regional Experiment (FIRE), and find that, while the HBTM underestimated the cloud amount by 5% and results in derived cloud top heights that are on average 53-m lower than the surface observations, the HBTM is successful in its representation of the diurnal variability, height, albedo and thickness of clouds.

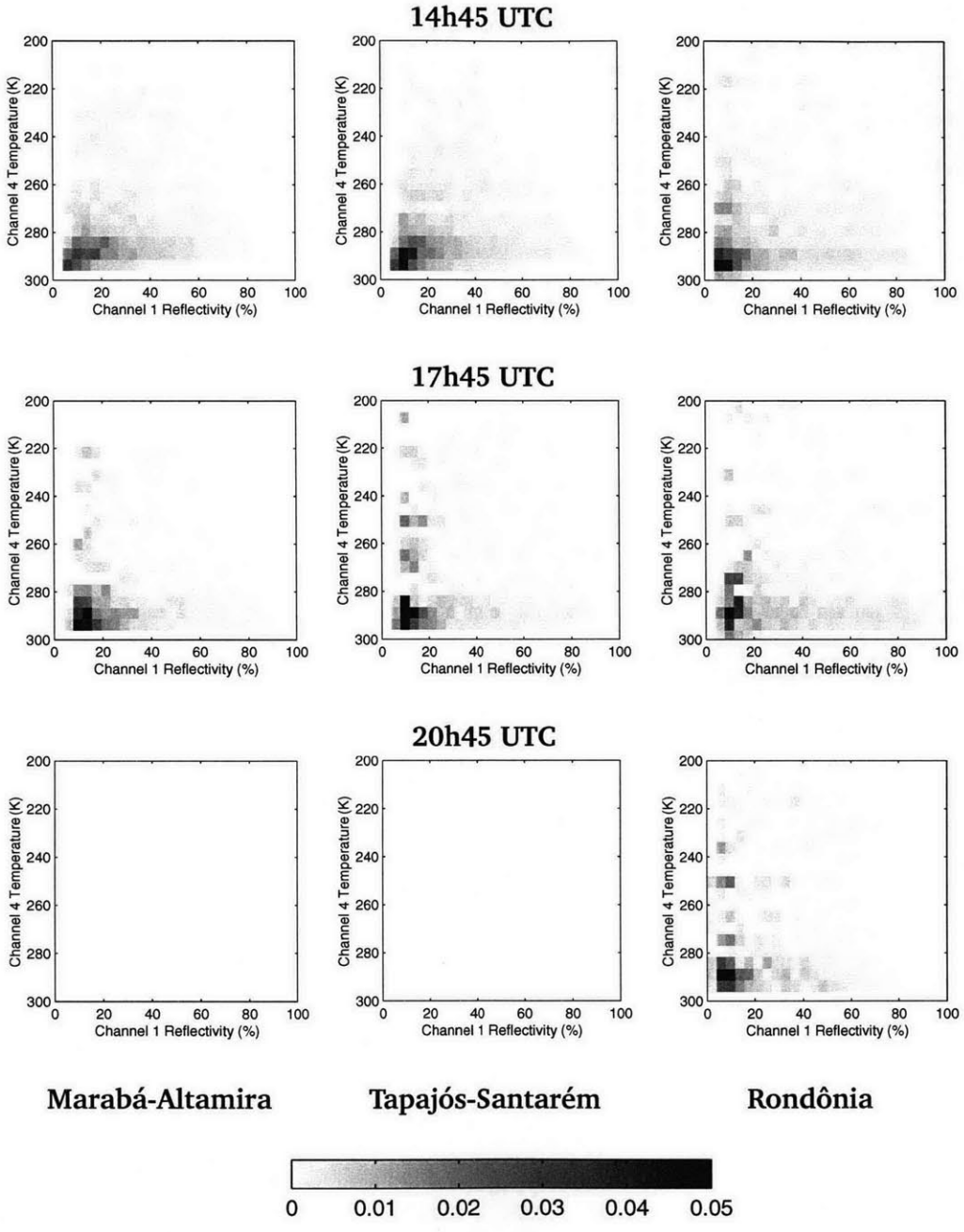

Figure 4-24: VIS-TIR Bi-Dimensional Histograms.

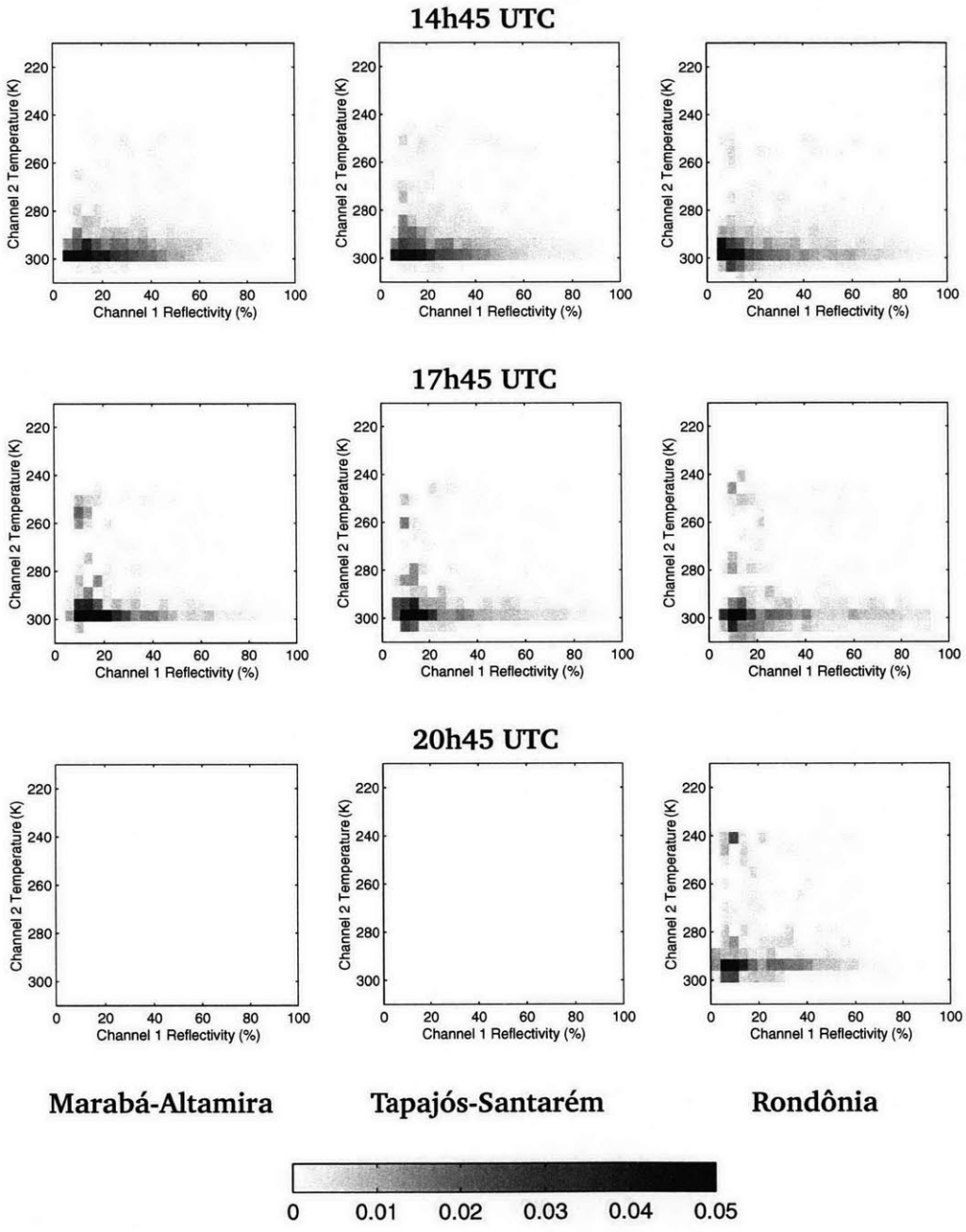

Figure 4-25: VIS-SIR Bi-Dimensional Histograms.

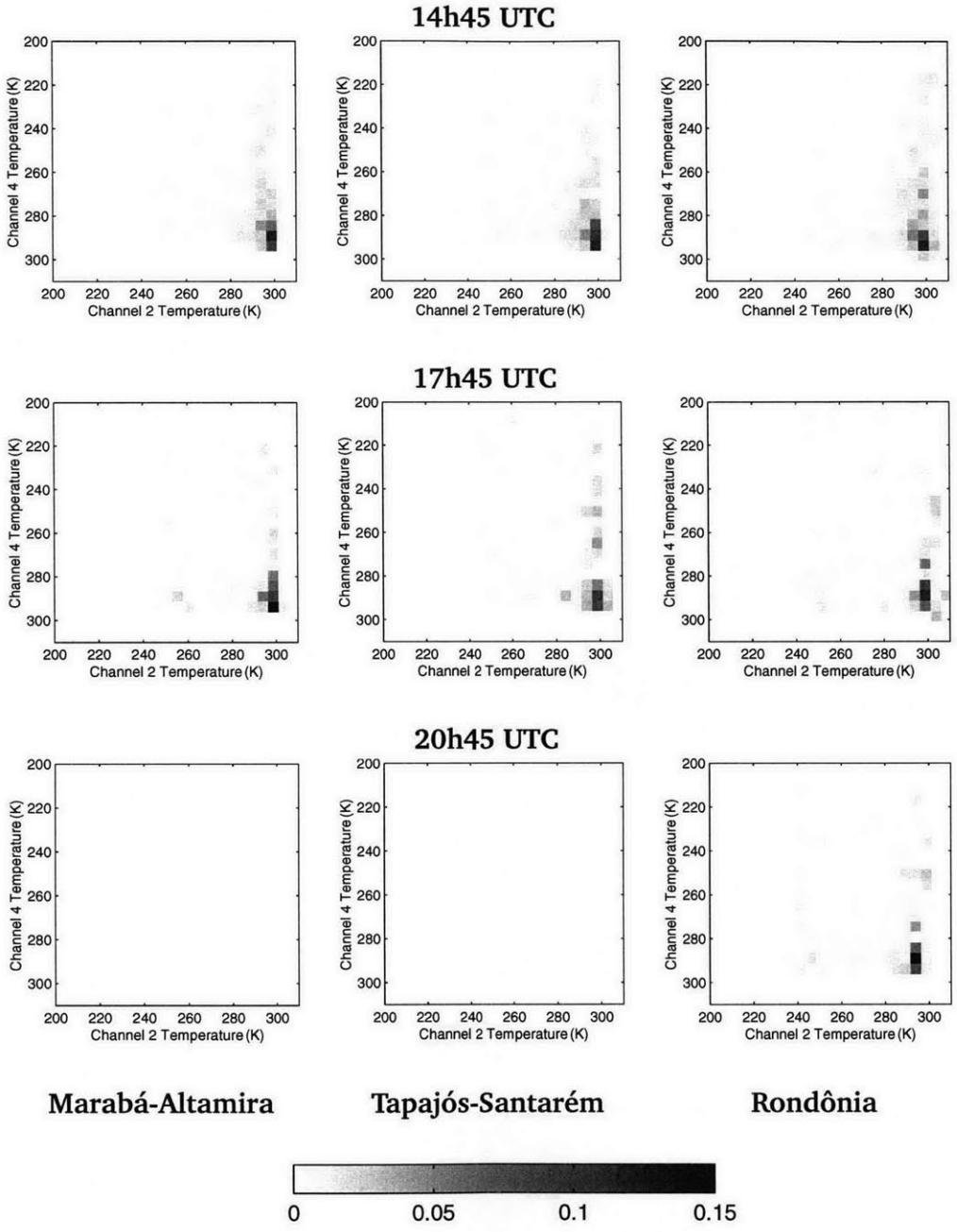

Figure 4-26: SIR-TIR Bi-Dimensional Histograms.

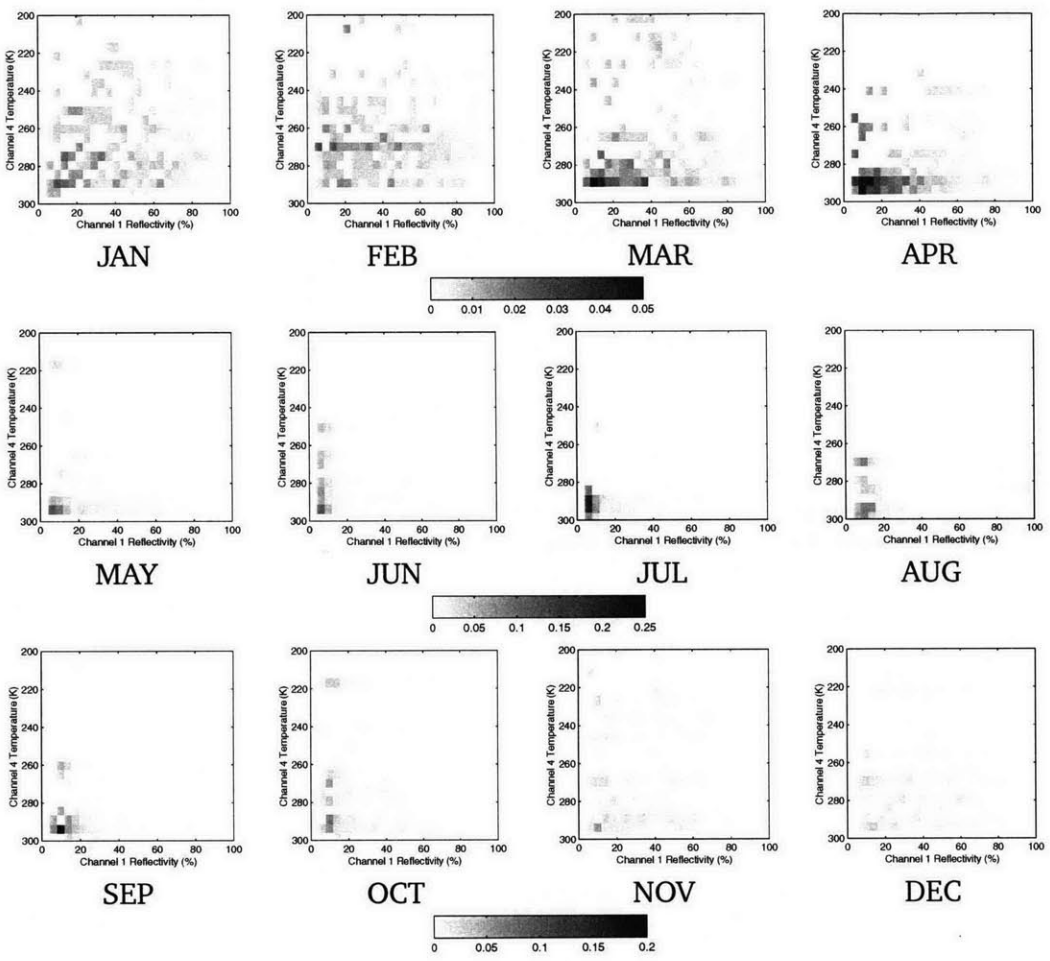

Figure 4-27: VIS-TIR Bi-Dimensional Histogram over Rondônia 14h45 UTC.

4.4 Shallow Cloud Classification Algorithms

In this study, shallow cloud cover is derived using two algorithms. The choice of multiple algorithms is based on a desire to test the robustness of the end results to cloud classification. The first algorithm employed to deduce shallow clouds is based on the findings of Garand [1988], and is similar to the algorithm presented in Rabin *et al.* [1990] and Cutrim *et al.* [1995]. It is a bi-spectral algorithm and it is shown in Table 4.9. It will henceforth be referred to as the CUTRIM algorithm. It is independent of clear-sky brightnesses, as it uses fixed thresholds. A pixel is deemed to be covered by a shallow cloud if it satisfies all the conditions of the algorithm.

Table 4.9: CUTRIM Shallow Cloud Recognition Algorithm.

Criterion	Cloud vs. No Cloud	Shallow vs. Deep	Stratus vs. Cumulus	Proximity to Deep Convection
Parameter	VIS Reflectance (%)	TIR Temperature (K)	VIS Contrast (%)	Distance (pixels)
Threshold	20	280	10	2

The second algorithm, henceforth referred to as ALGORITHM 2, is similar to the first one, but it is dependent upon clear-sky brightness. It also adds a criterion based on the temperature difference between SIR and TIR channels. It is presented in Table 4.10.

Table 4.10: 2nd Cloud Classification Algorithm.

	ALGORITHM 2
VIS Reflectance Threshold $\Delta\rho$ (%)	10
TIR Temperature Threshold ΔT (K)	-12
VIS Reflectance Contrast (%)	10
Proximity to Deep Convection (pixels)	2
SIR-TIR Temperature Difference	25
Simultaneous or **I**ndependent	**S**

Much work on satellite detection of biomass burning has been accomplished (e. g., Prins and Menzel [1992], Kaufman *et al.* [1998], Prins *et al.* [1998]). The difference in temperatures derived from the SIR and TIR channels is normally attributed to the reflected solar radiation component of the SIR channel (see begin-

ning of this chapter), as well as differences in spectrally dependent surface emissivity and water vapor attenuation characterisitcs [Prins and Menzel, 1992]. However, one can exploit the higher sensitivity of the SIR channel to temperature peaks. Indeed, when a part of a pixel is warmer, the relative response (in terms of measured radiance) is greater in the SIR channel than in the IR channel. This is because the "hotter" portion of the pixel contributes more radiance in the shorter wavelengths that in the longer ones. Hence, it is possible to use the temperature difference between the SIR and TIR channels to infer the presence of biomass burning in a pixel. Indeed, biomass burning rarely occupies the full field of view (FOV), which in the case of the GOES-8 infrared imager is 4×4 km pixel. SIR is more sensitive to high-temperature sub-pixel anomalies. The addition of a threshold for the temperature difference between SIR and TIR temperatures is added in **ALGORITHM 2** to prevent the spurious detection of biomass burning as shallow clouds. The albedo of biomass smoke is usually low, and the VIS reflectance threshold will prevent the spurious detection of biomass smoke as shallow cloud.

4.5 Cloud Classification Validation

The International Satellite Cloud Climatology Project (ISCCP) [Rossow *et al.*, 1985] provides a independent estimate of cloud cover through the ISCCP-D2 product. The ISCCP, which was conceived by the World Climate Research Center in 1982, uses data from multiple satellites to study the global distribution, temporal variation and properties of clouds. The D2 product is a monthly average of many ISCCP variables, has a global coverage on a 280-km equal-area grid. Figure 4-28 shows the comparison between the mean monthly ISCCP-D2 low cloud amount and the monthly mean shallow cumulus cloud amounts derived by the CUTRIM and the 2nd Algorithm. The comparisons will be drawn on the three study domains that were selected for this study, which are exposed in Chapter 5.

The comparison yields coherent results for all three domains. The ISCCP values are greater for all three domains, which reflects the fact that the ISCCP "low-cloud" data product includes cumulus, stratus and stratocumulus, and is hence much more comprehensive than the simple shallow isolated cumuli that are retrieved by the two algorithms under study. The seasonal trends are very well reproduced in both the Marabá-Altamira and Tapajós-Santarém domains; for the Rondônia domain, the pre-monsoon peak (SON) that is seen in the ISCCP data is missing from both CUTRIM and 2ND ALGORITHM. This could be a temporal sampling issue; the ISCCP is an average of all times-of-day, while the cloud amount derived from our algorithms is based solely on the 14h45 UTC sample. This discrepancy could also be due to a pre-monsoon peak in stratiform-type clouds in Rondônia. Notwithstanding these minor discrepancies, the comparison between the fractional cover of ISCCP-D2 low-clouds and the fractional cover of shallow clouds derived with the algorithms presented herein yields the expected result.

As a note of interest, there is a difference in the fractional cover of "low" clouds between the Marabá-Altamira, Tapajós-Santarém domains and the Rondônia domain. The average fractional cloud cover is higher over the Marabá-Altamira domain than it is over the Tapajós-Santarém domain; and the fractional cloud cover over the Tapajós-Santarém domain is higher than that over the Rondônia domain. This difference is reflected in both the ISCCP and GOES-8 derived values. This observation is particularly interesting when compared with the variations in rainfall over the Amazon basin that were documented by Cutrim *et al.* [2000]. Cutrim's analysis of raingauge data showed that rainfall was more intense at the coast near the mouth of the Amazon than inland; it also showed that rainfall was more intense inland than near the river. The Marabá-Altamira domain is nearest to the mouth of the Amazon (see Chapter 5 and has the highest fractional cloud cover, which is in intuitive agreement with Cutrim's observations.) Yet, the fractional cloud cover over Rondônia is lower than it is near the river over the Tapajós-Santarém domain, which is in intuitive disagreement with the rainfall intensity observations. This raises interesting questions about low-cloud to rainfall feedbacks, which are unfortunately outside the scope of this thesis.

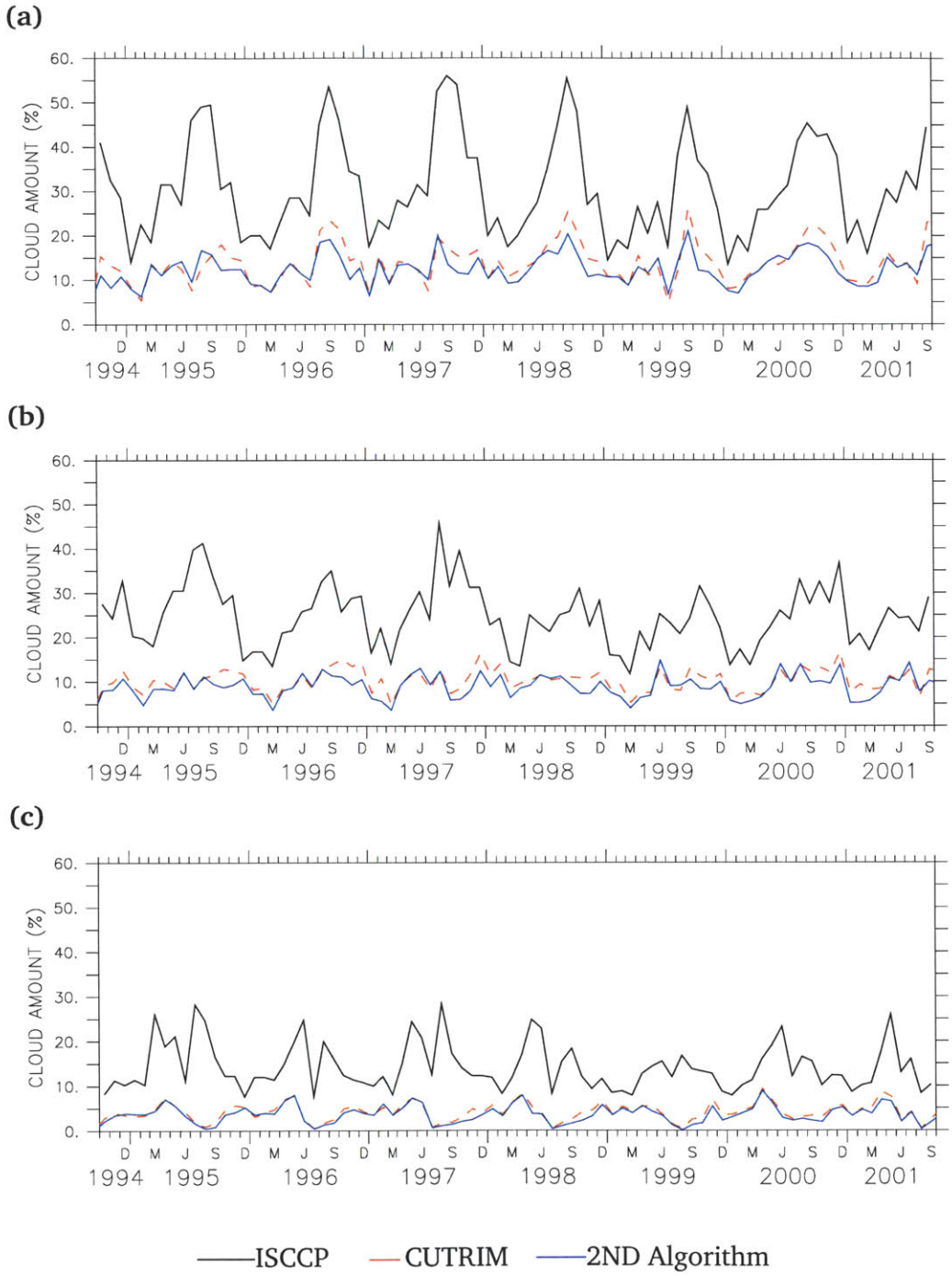

Figure 4-28: Comparison of GOES-8 Shallow Cumulus Cloud Amounts (i. e., cloud fractional cover) with ISCCP-D2 Low Clouds; **(a)** Marabá-Altamira; **(b)** Tapajós-Santarém; **(c)** Rondônia.

4.6 Nepahanalysis: Visual Validation

The distinction between the performance of the two algorithms presented herein, as well as their absolute performance, is assessed in this section by performing visual comparisons under different meteorological scenarios. Such analyses are termed "nepahanlysis", or the synoptic study of clouds. This section will provide graphical examples of the measured GOES-8 radiances in the three channels of interest, as well as the derived shallow cloud fields according to the two different algorithms for shallow cumulus cloud classification.

Examples of Shallow Cloud Contrast

The first meteorological scenario that is tested is the one that is central to this thesis, namely that where shallow cloud contrasts arise. Figures 4-29, 4-30 & 4-31 show examples of clear shallow cloud contrasts that are collocated with forest-cover features for each domain. Both algorithms perform well, and there are no visible aberrations or mis-classifications. The second algorithm seems to be more sensitive and more adept at discerning clouds from land. This is highlighted over the Marabá-Altamira domain (Figure 4-29), where there are noticeably more shallow clouds detected. The infrared images over Rondônia (Figure 4-31) show the clear contrast in surface temperature co-located with deforestation patterns. Shallow clouds are clearly co-located with the inverted v-shaped savannah clearing in the upper-right quadrant of the image. There are also shallow clouds that are clearly associated with the central deforested area. Finally, there is an aberration over the Rondônia domain in the bottom half of the domain caused by striping in the visible imager. Such aberrations are rare and thus not important.

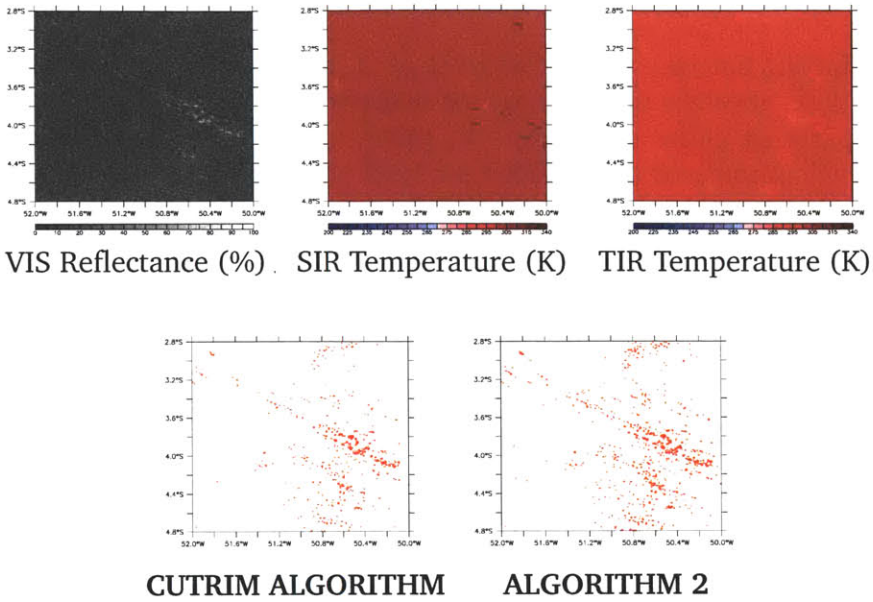

Figure 4-29: GOES-8 Imager Data and Derived Shallow Clouds over the Marabá-Altamira domain on 07/21/1995 at 14h45 UTC.

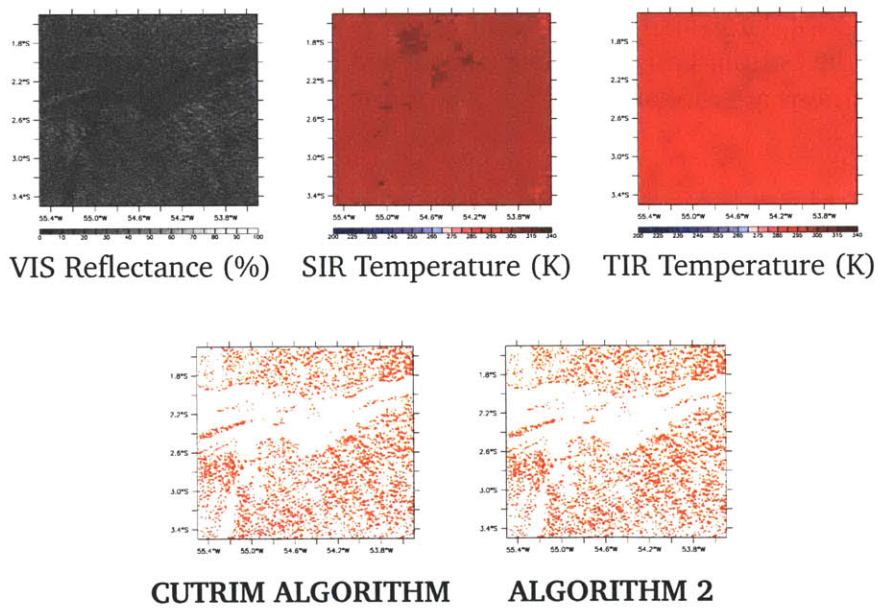

Figure 4-30: GOES-8 Imager Data and Derived Shallow Clouds over the Tapajós-Santarém domain on 09/24/1994 at 14h45 UTC.

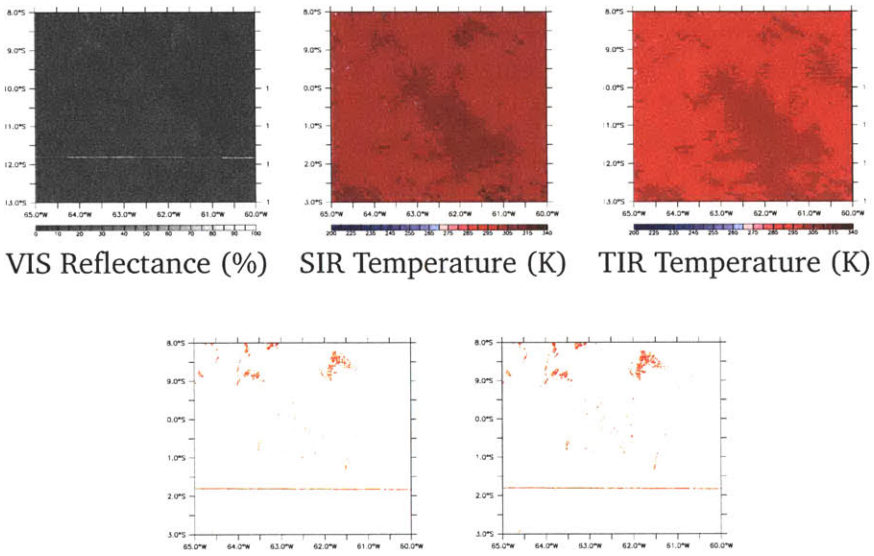

Figure 4-31: GOES-8 Imager Data and Derived Shallow Clouds over the Rondônia domain on 07/29/1995 at 14h45 UTC.

Examples of Mix of Shallow Clouds and Deep Convection

Figures 4-32, 4-33 & 4-34 show examples of how the different algorithms react to a mix of low and high clouds over all three domains. While both perform well and are able to discern between high and low clouds, ALGORITHM 2 proves to be more adept at picking up nuances as is exhibited in Figure 4-32.

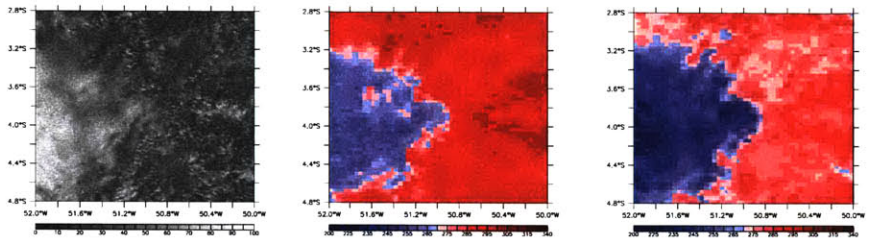

VIS Reflectance (%) SIR Temperature (K) TIR Temperature (K)

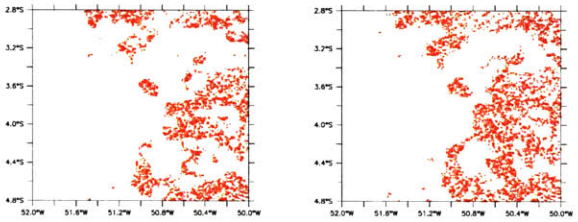

CUTRIM ALGORITHM **ALGORITHM 2**

Figure 4-32: GOES-8 Imager Data and Derived Shallow Clouds over the Marabá-Altamira domain on 02/06/1996 at 14h45 UTC.

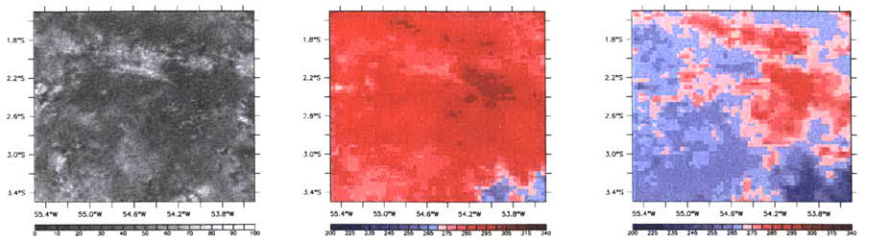

VIS Reflectance (%) SIR Temperature (K) TIR Temperature (K)

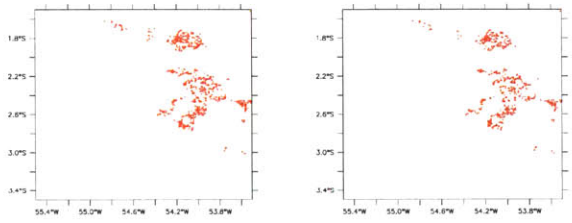

CUTRIM ALGORITHM **ALGORITHM 2**

Figure 4-33: GOES-8 Imager Data and Derived Shallow Clouds over the Tapajós-Santarém domain on 02/06/1996 at 14h45 UTC.

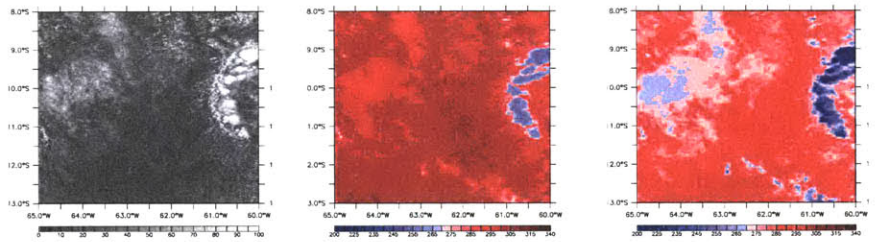

VIS Reflectance (%) SIR Temperature (K) TIR Temperature (K)

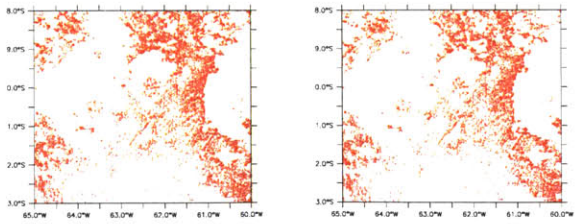

CUTRIM ALGORITHM **ALGORITHM 2**

Figure 4-34: GOES-8 Imager Data and Derived Shallow Clouds over the Rondônia domain on 04/01/1996 at 14h45 UTC.

Examples of Mix of Shallow Clouds and Cirrus

Figures 4-35, 4-36 & 4-37 show examples of how the different algorithms react to a mix of cumuliform and stratiform clouds over all three domains. Again, both algorithms prove to be adept in differentiating stratiform clouds from shallow convective clouds. There are also slight nuances between the CUTRIM algorithm results and ALGORITHM 2, as is noticeable in the upper-right quadrant over the Rondônia domain in Figure 4-37. Such differences are certainly due to the use of clear-sky brightnesses in differentiating between low and high clouds, and are a testament to ALGORITHM 2's refinements.

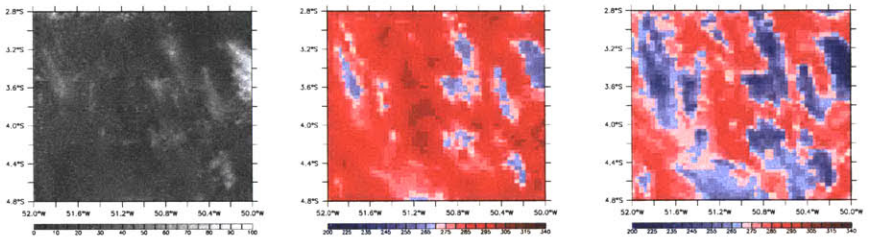

VIS Reflectance (%) SIR Temperature (K) TIR Temperature (K)

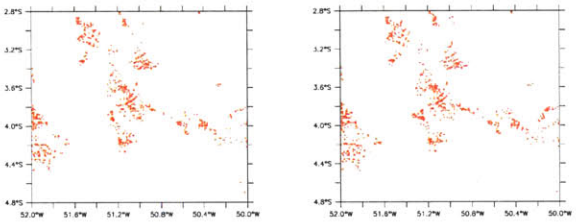

CUTRIM ALGORITHM **ALGORITHM 2**

Figure 4-35: GOES-8 Imager Data and Derived Shallow Clouds over the Marabá-Altamira domain on 01/08/1999 at 14h45 UTC.

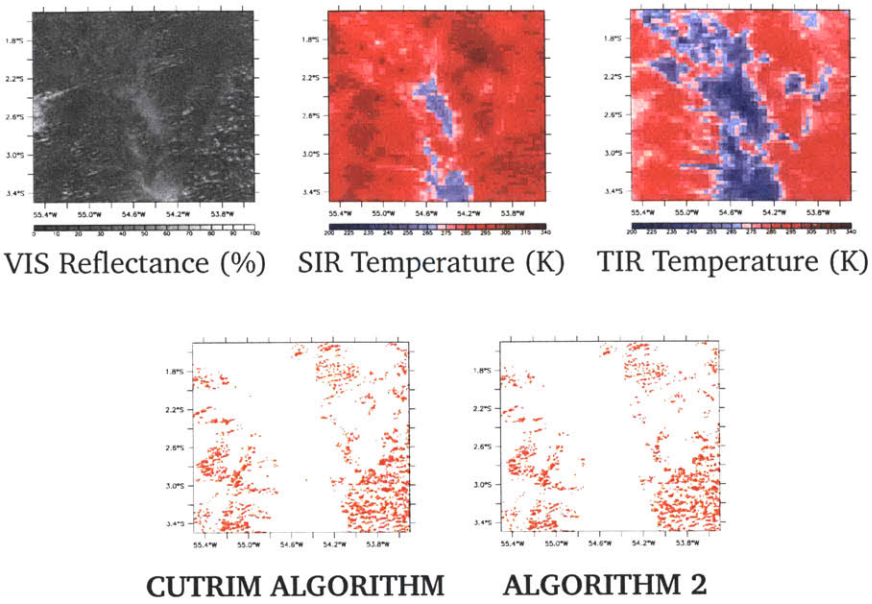

Figure 4-36: GOES-8 Imager Data and Derived Shallow Clouds over the Tapajós-Santarém domain on 01/08/1999 at 14h45 UTC.

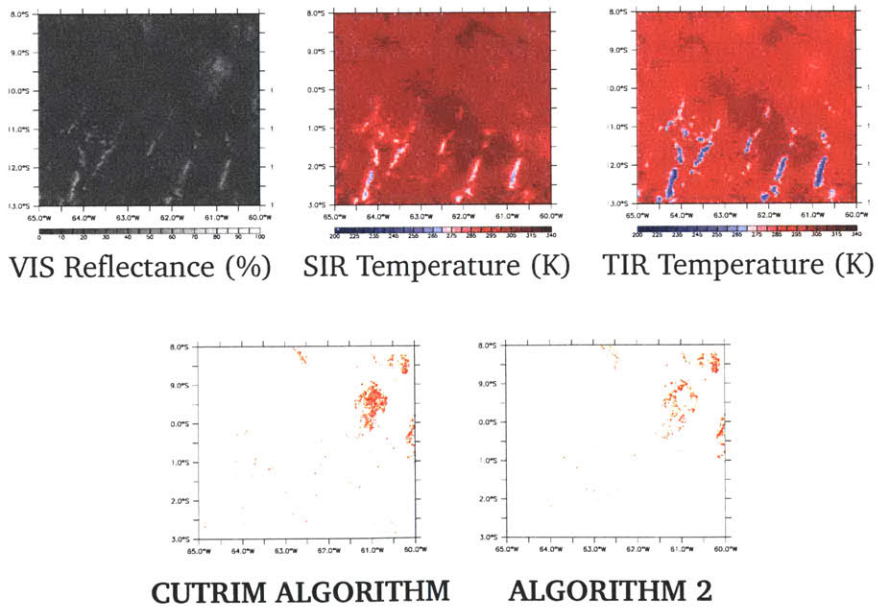

Figure 4-37: GOES-8 Imager Data and Derived Shallow Clouds over the Rondônia domain on 07/17/1997 at 14h45 UTC.

Examples of Specular Reflection and Striping

Figure 4-38 is an example of possible errors in the algorithms due to striping and specular reflection. Image striping (upper half of the TIR image) is rare. Specular reflection (seen in the center of the domain) on the other hand is a much more dangerous problem due to its persistence in terms of spatial location. Here it is clear that ALGORITHM 2 dramatically reduces the aberrations caused by specular reflection. This is a clear indication of the second algorithm's superiority.

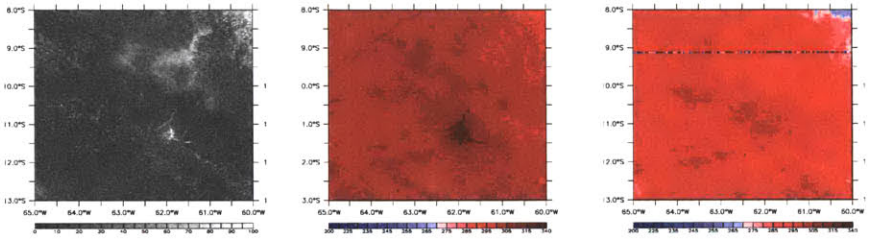

VIS Reflectance (%) SIR Temperature (K) TIR Temperature (K)

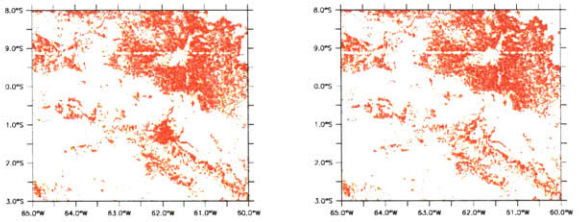

CUTRIM ALGORITHM **ALGORITHM 2**

Figure 4-38: GOES-8 Imager Data and Derived Shallow Clouds over the Rondônia domain on 12/19/2000 at 14h45 UTC.

Example of Deep Convection associated with Landcover

Figure 4-39 shows an example of what seems to be deep convection associated with forest-cover. This is a qualitative observation, and the deep convection street that runs in a diagonal crescent in the center of the domain could also be a reflection of the underlying topographical features (see Chapter 5 for maps of the elevations and slopes of the three domains.)

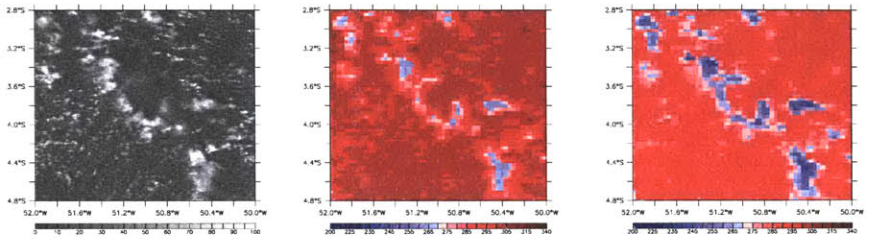

VIS Reflectance (%) SIR Temperature (K) TIR Temperature (K)

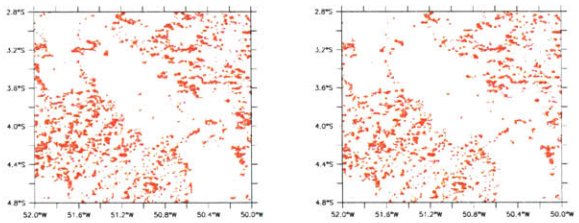

CUTRIM ALGORITHM **ALGORITHM 2**

Figure 4-39: GOES-8 Imager Data and Derived Shallow Clouds over the Marabá-Altamira domain on 12/19/2000 at 17h45 UTC.

4.7 Conclusion

The comparison of the fractional cloud cover derived from the two algorithms presented herein with that of the ISCCP project data, as well as the visual inspection of the cloud fields under various meteorological conditions, have shown that the algorithms for shallow cloud detections perform very well. Further inspection of the differences between the two shallow cloud detection algorithms have shown that the second algorithm is more adept at detecting shallow cumulus clouds through its higher sensitivity resulting from the inherent conditioning on clear-sky radiances. ALGORITHM 2 also proved to be less sensitive to aberrations such as specular reflection, and is thus selected as the definitive algorithm for this study.

REFERENCES

ACKERMAN, S. A., K. I. STRABALA, W. P. MENZEL, C. MOELLER and L. E. GUMLEY. Discriminating Clear Sky from Clouds with MODIS. *Journal of Geophysical Research*, 103(D24):pages 32,141–32,157 [1998].

ARKING, A. Latitudinal Distribution of Cloud Cover from TIROS III Photographs. *Science*, 143(3606):pages 569–572 [1964].

AYERS, J. K., D. R. DOELLING, L. NGUYEN, W. L. SMITH JR. and P. MINNIS. Calibration of GOES Using Satellite and ARESE Aircraft Data. In *Proceedings of the 6th Atmospheric Radiation Measurement Science Team Meeting*. San Antonio, TX [1996].

BARNES, R. A., W. L. BARNES, C.-H. LYU and J. M. GALES. An Overview of the Visible and Infrared Scanner Radiometric Calibration Algorithm. *Journal of Atmospheric and Oceanic Technology*, 17(4):pages 395–405 [2000].

BERBET, M. L. C. and M. H. COSTA. Climate Chnage after Tropical Deforestation: Seasonal Variability of Surface Albedo and Its Effect on Precipitation Change. *Journal of Climate*, 16(12):pages 2099–2104 [2003].

BERENDES, T. A., K. S. KUO, A. M. LOGAR, E. M. CORWIN, R. M. WELCH, B. A. BAUM, A. PRETRE and R. C. WEGER. A Comparison of Paired Histogram, Maximun Likelihood, Class Elimination, and Neural Network Approaches for Daylight Global Cloud Classification using AVHRR Imagery. *Journal of Gephysical Research*, 104(D6):pages 6199–6213 [1999].

BREMER, J. C., J. G. BAUCOM, H. VU, M. P. WEINREB and N. PINKINE. Estimation of Long-Term Throughput Degradation of GOES-8 and -9 Visible Channels by Statistical Analysis of Star Measurements. In BARNES, W. L., ed., *Conference on Earth Observing Systems III* [1998].

CHOU, M.-D., J. CHILDS and P. DORIAN. Cloud Cover Estimation Using Bispectral Satellite Measurements. *Journal of Climate and Applied Meteorology*, 25(9):pages 1280–1292 [1986].

COAKLEY JR., J. A. A Dynamic Threshold Method for Obtaining Cloud Cover from Satellite Imagery Data. *Journal of Geophysical Research*, 92(D4):pages 4917–4932 [1987].

COAKLEY JR., J. A. and D. G. BALDWIN. Towards the Objectie Analysis of Clouds from Satellite Imagery Data. *Journal of Climate and Applied Meteorology*, 23(7):pages 1065–1099 [1984].

COAKLEY JR., J. A. and R. DAVIES. The Effect of Cloud Sides on Reflected Solar Radiation as Deduced from Satellite Observations. *Journal of the Atmopsheric Sciences*, 43(10):pages 1025–1035 [1986].

CREWEL, S., G. HASSE, U. LÖHNERT, H. MEBOLD and C. SIMMER. A Ground Based Multi-Sensor System for the Remote Sensing of Clouds. *Physical and Chemical Earth (B)*, 24(3):pages 207–211 [1999].

CULF, A. D., G. FISCH and M. G. HODNETT. The albedo of Amazonia forest and ranchland. *Journal of Climate*, 8(6):pages 1544–1554 [1995].

CUTRIM, E., D. W. MARTIN and R. RABIN. Enhancement of Cumulus Clouds over Deforested Lands in Amazonia. *Bulletin of the American Meteorological Society*, 76(10):pages 1801–1805 [1995].

CUTRIM, E. M. C., D. W. MARTIN, D. G. BUTZOW, I. M. SILVA and E. YULAEVA. Pilot Analysis of Hourly Rainfall in Central and Eastern Amazonia. *Journal of Climate*, 13(7):pages 1326–1334 [2000]. Notes and Correspondence.

DESBOIS, M., G. SÈZE and G. SZEIWACH. Automatic Classification of Clouds on METEOSAT Imagery: Application to High-Level Clouds. *Journal of Applied Meteorology*, 21(3):pages 401–412 [1982].

DIÓSZEGHY, M. and E. FEJES. Cloud Classification Derived from METEOSAT Data Involving the Standard Deviation Fields of the Brightness Values. *Advances in Space Research*, 16(10):pages 1033–1036 [1995].

ELACHI, C. *Introduction to the Physics and Techniques of Remote Sensing*. Wiley series in remote sensing. Wiley, New York [1987]. A Wiley-Interscience Publication.

ELLROD, G. P., R. V. ACHUTUNI, J. M. DANIELS, E. M. PRINS and J. P. NELSON III. An Assessment of GOES-8 Imager Data Quality. *Bulletin of the American Meteorological Society*, 79(11):pages 2509–2526 [1998].

FEIJT, A., P. DE VALK and S. VAN DER VEEN. Cloud Detection using Meteosat Imagery and Numerical Weather Prediction Model Data. *Journal of Applied Meteorology*, 39(7):pages 1017–1030 [2000].

GARAND, L. Automated Recognition of Oceanic Cloud Patterns. Part I: Methodology and Application to Cloud Climatology. *Journal of Climate*, 1(1):pages 20–39 [1988].

GUTMAN, G. A Simple Method for Estimating Monthly Mean Albedo of Land Surfaces from AVHRR Data. *Journal of Applied Meteorology*, 27(9):pages 973–988 [1988].

HENDERSEN-SELLERS, A. Surface Type and Its Effect Upon Cloud Cover: A Climatological Investigation. *Journal of Geophysical Research*, 83(C10):pages 5057–5062 [1978].

KAUFMAN, Y. J., W. J. H. HOBBS, P. V. KIRCHHOFF, P. ARTAXO, L. A. REMER, B. N. HOLBEN, M. D. KING, D. E. WARD, E. M. PRINS, K. M. LONGO, L. F. MATTOS, C. A. NOBRE, J. D. SPINHIRNE, Q. JI, A. M. THOMPSON, J. F. GLEASON, S. A. CHRISTOPHER and S.-C. TSAY. Smoke, Clouds, and Radiation-Brazil (SCAR-B) Experiment. *Journal of Geophysical Research*, 103(D24):pages 31,783–31,808 [1998].

KIDDER, S. Q. and T. H. VONDER HAAR. *Satellite Meteorology: An Introduction*. Academic Press, Inc., San Diego, CA [1995].

KNAPP, K. R. and T. H. VONDER HAAR. Calibration of the Eighth Geostationary Observational Environmental Satellite (GOES-8) Imager Visible Sensor. *Journal of Atmospheric and Oceanic Technology*, 17(12):pages 1639–1644 [2000].

KOREN, I. and J. H. JOSEPH. The Histogram of the Brightness Distribution of Clouds in High-Resolution Remotely Sensed Images. *Journal of Geophysical Research*, 105(D24):pages 29,369–29,377 [2000].

KUMMEROW, C., W. BARNES, T. KOZU, J. SHIUE and J. SIMPSON. The Tropical Rainfall Measuring Mission (TRMM) Sensor Package. *Journal of Atmospheric and Oceanic Technology*, 15(3):pages 809–817 [1998].

LI, J., W. P. MENZEL, Z. YANG, R. A. FREY and S. A. ACKERMAN. High-Spatial-Resolution Surface and Cloud-Type Classification from MODIS Multispectral Band Measurements. *Journal of Applied Meteorology*, 42(2):pages 204–226 [2003].

LIBERTI, G. L., F. CHÉRUY and M. DESBOIS. Land Effect on the Diurnal Cycle of Clouds over the TOGA COARE Area, as Observed from GMS IR Data. *Monthly Eather Review*, 129(6):pages 1500–1517 [2001].

LIOU, K.-N. *An Introduction to Atmospheric Radiation*, vol. 84 of *International Geophysics Series*. Academic Press, 525 B Street, Suite 1900, San Diego, California 92101, USA, Second ed. [2002].

LYU, C.-H., W. L. BARNES and R. A. BARNES. First Results from the On-Orbit Calibrations of the Visible and Infrared Scanner for the Tropical Rainfall Measuring Mission. *Journal of Atmospheric and Oceanic Technology*, 17(4):pages 385–394 [2000].

MASSONS, J., D. DOMINGO and J. GRAU. Automatic Classification of VIS-IR METEOSAT Images. *Computers and Geosciences*, 22(10):pages 1137–1146 [1996].

MATTHEWS, E. and W. B. ROSSOW. Regional and Seasonal Variations of Surface Reflectance from Satellite Observations at 0.6 μm. *Journal of Climate and Applied Meteorology*, 26(1):pages 170–202 [1987].

McKee, T. B. and S. Cox. Scattering of Visible Radiation from Finite Clouds. *Journal of the Atmospheric Sciences*, 31(10):pages 1885–1892 [1974].

Menzel, W. P. and J. F. W. Purdom. Introducing GOES-I: The First of a New Generation of Geostationary Operational Environmental Satellites. *Bulletin of the American Meteorological Society*, 75(5):pages 757–781 [1994].

Minnis, P. Viewing Zenith Angle Dependence of Cloudiness Determined from Coincident GOES East and GOES West Data. *Journal of Geophysical Research*, 94(D2):pages 2303–2320 [1989].

Minnis, P. and E. F. Harrison. Diurnal Variability of Regional Cloud and Clear-Sky Radiative Parameters Derived from GOES Data. Part I: Analysis Method. *Journal of Climate and Applied Meteorology*, 23(7):pages 993–1011 [1984a].

—. Diurnal Variability of Regional Cloud and Clear-Sky Radiative Parameters Derived from GOES Data. Part II: November 1978 Cloud Distributions. *Journal of Climate and Applied Meteorology*, 23(7):pages 1012–1031 [1984b].

—. Diurnal Variability of Regional Cloud and Clear-Sky Radiative Parameters Derived from GOES Data. Part III: November 1978 Radiative Parameters. *Journal of Climate and Applied Meteorology*, 23(7):pages 1032–1051 [1984c].

Minnis, P., P. W. Heck, D. F. Young, C. W. Fairall and J. B. Snider. Stratocumulus Cloud Properties Derived from Simultaneous Satellite and Island-based Instrumentation during FIRE. *Journal of Applied Meteorology*, 31(4):pages 317–339 [1992].

Minnis, P. and M. M. Khaiyer. Anisotropy of Land Surface Skin Temperature Dervied from Satellite Data. *Journal of Applied Meteorology*, 39(7):pages 1117–1129 [2000].

Minnis, P., S. Mayor, W. L. Smith Jr. and D. F. Young. Asymmetry in the Diurnal Variation of Surface Albedo. *IEEE Transactions on Geoscience and Remote Sensing*, 35(4):pages 879–891 [1997].

Minnis, P., L. Nguyen, D. R. Doelling, D. F. Young, W. F. Miller and D. P. Kratz. Rapid Calibration of Operational and Research Meteorological Satellite Imager. Part I: Evaluation of Research Satellite Visible Channels as References. *Journal of Atmopsheric and Oceanic Technology*, 19(9):pages 1233–1249 [2002a].

—. Rapid Calibration of Operational and Research Meteorological Satellite Imager. Part II: Comparison of Infrared Channels. *Journal of Atmopsheric and Oceanic Technology*, 19(9):pages 1250–1266 [2002b].

Minnis, P. and W. L. Smith Jr. Cloud and Radiative Fields Derived from GOES-8 during SUCCESS and the ARM-UAV Spring 1996 Flight Series. *Geophysical Research Letters*, 25(8):pages 1113–1116 [1997].

MINNIS, P., W. L. SMITH JR., D. P. GARBER, J. K. AYERS and D. R. DOELLING. Cloud Properties Derived from GOES-7 for Spring 1994 ARM Intensive Observing Period Using Version 1.0.0 of ARM Satellite Data Analysis Program. Reference Publication 1366, NASA, Langley Research Center, Hampton, VA 23681-0001 [1995].

MINNIS, P., D. F. YOUNG and E. F. HARRISON. Examination of the Relationship between Outgoing Infrared Window and Total Longwave Fluxes Using Satellite Data. *Journal of Climate*, 4(11):pages 1114–1133 [1991].

NEGGERS, R. A. J., H. J. J. JONKER and A. P. SIEBESMA. Size Statistics of Cumulus Cloud Populations in Large-Eddy Simulations. *Journal of the Atmopsheric Sciences*, 60(9):pages 1060–1074 [2003].

PLANK, V. G. The Size Distribution of Cumulus Clouds in Representative Florida Populations. *Journal of Applied Meteorology*, 8(2):pages 46–67 [1969].

PORCÚ, F. and V. LEVIZZANI. Cloud Classification using METEOSAT VIS-IR Imagery. *International Journal of Remote Sensing*, 13(5):pages 893–909 [1992].

PRINS, E. M., J. M. FELTZ, W. P. MENZEL and D. E. WARD. An Overview of GOES-8 Diurnal Fire and Smoke Results for SCAR-B and 1995 Fire Season in South America. *Journal of Geophysical Research*, 103(D24):pages 31,821–31,835 [1998].

PRINS, E. M. and W. P. MENZEL. Geostationary Satellite Detection of Biomass Burning in South America. *International Journal of Remote Sensing*, 13(15):pages 2783–2799 [1992].

RABIN, R. M., S. STADLER, P. J. WETZEL, D. J. STENSRUD and M. GREGORY. Observed Effects of Landscape Variability on Convective Clouds. *Bulletin of the American Meteorological Society*, 71(3):pages 272–280 [1990].

RAO, C. R. N. *Implementation of the post-launch vicarious calibration of the GOES imager visible channel.* NOAA/NESDIS Office of Research and Applications, Camp Springs, MD 20746 [2001]. NOAA Office of Satellite Operations Website (http://www.oso.noaa.gov/goes/goes-calibration/vicarious-calibration.htm.

RAO, C. R. N., J. CHEN, J. T. SULLIVAN and N. ZHANG. Post-Launch Calibration of Meteorological Satellite Sensors. *Advances in Space Research*, 23(8):pages 1357–1365 [1999].

ROSSOW, W. B. and L. C. GARDER. Cloud Detection Using Satellite Measurements of Infrared and Visible Radiances for ISCCP. *Journal of Climate*, 6(12):pages 2341–2369 [1993].

ROSSOW, W. B., F. MOSHER, E. KINSELLA, A. ARKING, M. DESBOIS, E. HARRISON, P. MINNIS, E. RUPRECHT, G. SÈZE, C. SIMMER and E. SMITH. ISCCP Cloud Algorithm Comparison. *Journal of Climate and Applied Meteorology*, 24(9):pages 877–903 [1985].

ROSSOW, W. B., A. W. WALKER and L. C. GARDER. Comparison of ISCCP and Other Cloud Amounts. *Journal of Climate*, 6(12):pages 2394–2418 [1993].

SÈZE, G. and M. DESBOIS. Cloud Cover Analysis from Satellite imagery using Spatial and Temporal Characteristics of the Data. *Journal of Climate and Applied Meteorology*, 26(2):pages 287–303 [1987].

SHENK, W. E. and V. V. SALOMONSON. A Simulation Study Exploring the Effects of Sensor Spatial Resolution on Estimates of Cloud Cover from Satellites. *Journal of Applied Meteorology*, 11(2):pages 214–220 [1972].

SIMMER, C., E. RASCHKE and E. RUPRECHT. Method for Determination of Cloud Properties from Two-Dimensional Histograms. *Annalen der Meteorologie*, (18):pages 130–132 [1982].

SPACE SYSTEMS/LORAL. *GOES I-M DataBook*. National Aeronautics and Space Administration, Goddard Space Flight Center, Greenbelt, Maryland 20771 [1996]. DRL 101-08, GSFS Specification S-480-21A, Contract NAS5-29500.

STULL, R. B. A Fair-Weather Cumulus Cloud Classification Scheme for Mixed-Layer Studies. *Journal of Climate and Applied Meteorology*, 24(1):pages 49–56 [1985].

SUOMI, V. E., R. FOX, S. S. LIMAYE and W. L. SMITH. McIdas III: A Modern Interactive Data Access and Analysis System. *Journal of Climate and Applied Meteorology*, 22(5):pages 766–778 [1983].

WEINREB, M., M. JAMIESON, N. FULTON, Y. CHEN, J. X. JOHNSON, J. BREMER, C. SMITH and J. BAUCOM. Operational Calibration of Geostationary Operational Environmental Satellite-8 and -9 Imagers and Sounders. *Applied Optics*, 36(27):pages 6895–6904 [1997].

WEINREB, M. P., R. X. JOHNSON, J. G. BAUCOM and J. C. BREMER. GOES 8-10 Calibration Experience. *Advances in Space Research*, 23(8):pages 1367–1375 [1999].

WIELICKI, B. A., R. D. CESS, M. D. KING, D. A. RANDALL and E. F. HARRISSON. Mission to Planet Earth: Role of Clouds and Radiation in Climate. *Bulletin of the American Meteorological Society*, 76(11):pages 2125–2153 [1995].

WIELICKI, B. A. and L. PARKER. On the Determination of Cloud Cover from Satellite Sensors: The Effect of Sensor Spatial Resolution. *Journal of Geophysical Research*, 97(D12):pages 12,799–12,823 [1992].

WIELICKI, B. A. and R. M. WELCH. Cumulus Cloud Properties Derived Using Landsat Data. *Journal of Climate and Applied Meteorology*, 25(3):pages 261–276 [1983].

CHAPTER 5

STUDY DOMAINS & METHODS

The Amazon basin has gone from 998 million hectares of rainforest in 1970 to 913 million hectares in 1994. The major causes of deforestation are logging and settling on the rainforest for agriculture. The latter is most often done by using "slash and burn" techniques, which have prompted many studies on the impact of biomass burning on regional and global climate and atmospheric chemistry. There are specific "hot-spots" of deforestation in the Amazon basin. All of them have a distinct pattern that resembles fish skeletons. Figure 5-1 depicts the areas of the Amazon basin that have undergone extensive deforestation. This chapter will describe the study domains that have been selected for this study, as well as the statistical methods developed to infer associations between deforestation patterns and the patterns of clouds and rainfall.

5.1 Study Domains

Three study areas are selected for this study. The first study-domain is along the BR-230 highway that connects Marabá to Altamira; the area along the BR-230 highway, which runs diagonally from the south-east to the north-west of the domain, shows the typical fish-bone pattern of deforestation. This domain, which will hereafter be referred to as the Marabá-Altamira domain, is approximately 200-km to the side. The second domain, which is also approximately 200-km to the side, is centered around Santarém, where the Tapajós river merges with the Amazon river. The contrast in this domain is one of water versus land, and the domain was selected because the inland sea-breeze effect that such a surface contrast promotes is well documented, which makes the Tapajós-Santarém domain very suitable for method verification. The third domain is approximately 500-km to the side and is centered in the intensely deforested state of Rondônia. Most of this study will concentrate on the Rondônia domain. The three domains are depicted in Figure 5-

1. Figure 5-2 shows synthetic aperture radar (SAR) views of the three domains as seen from the Japanese Earth Resource Satellite (JERS-1).

5.2 Treecover and Topography

The Moderate Resolution Imaging Spectroradiometer (MODIS) Vegetation Continuous Field (VCF) product, which is described in Hansen *et al.* [2003], provides the landcover information for this study. The specific product used in this thesis is the MOD44B product of 2001, which gives relative coverage of trees, bare soil and grasses for each 500-m pixel. The first data processing step is to up-scale the original 500-m pixel data to two different resolutions (i. e., 1-km and 4-km pixels); this is done by simple averaging. The second step is to create a binary state map (deforested and forested), and this is done by selecting arbitrary thresholds in the percent tree cover field of the MOD44B product. The thresholds selected are 50% for the 4-km data; and 30% and 50% for the 1-km data. The resulting deforestation maps are shown in Figure 5-3. The original MOD44B treecover information is mapped in Figure 5-1. This threshold treatment does not apply to the Tapajós-Santarém domain, as the contrast there is one of river versus land. The aggregation scale does, however, change the river map slightly (see Figure 5-3).

The topography data used in this study is from two sources: the United States Geological Survey (USGS) HYDRO1K database, which covers the globe at 1-km resolution and is based on GTOPO30, the global 30-arcsecond elevation dataset; and the digital elevation model (DEM) from the Shuttle Radar Topography Mission (SRTM) [Farr and Kobrick, 2000; Rabus *et al.*, 2003], which has a nominal pixel resolution of 90-m. The HYDRO1K datasets includes values for slope, aspect and topographic-index. SRTM derived slope values are computed as the maximum centered derivative in either direction. The statistical analysis developed for this study relies on binary fields (see Section 5.3). To transform the quasi-continuous fields of elevation, slope and aspect to binary fields, a threshold technique is used. The thresholds are selected based on pixel value distributions (i. e., the 30% highest pixels are ascribed a value of 1 for high, and the 70% lowest are ascribed a value of 0.) The thresholds selected are 30%, 50% and 70%. Topography and slope maps of the study domains are shown in Figure 5-4.

5.3 Statistical Analysis Method

A rigorous statistical test is required to determine whether the patterns of shallow cumuli or rainfall are correlated with the underlying deforestation or topography patterns. The test formulated for this study compares the values of cloud-forest or rain-forest statistics derived from the observed deforestation/topography pattern with the distribution of these same statistics derived from randomized de-

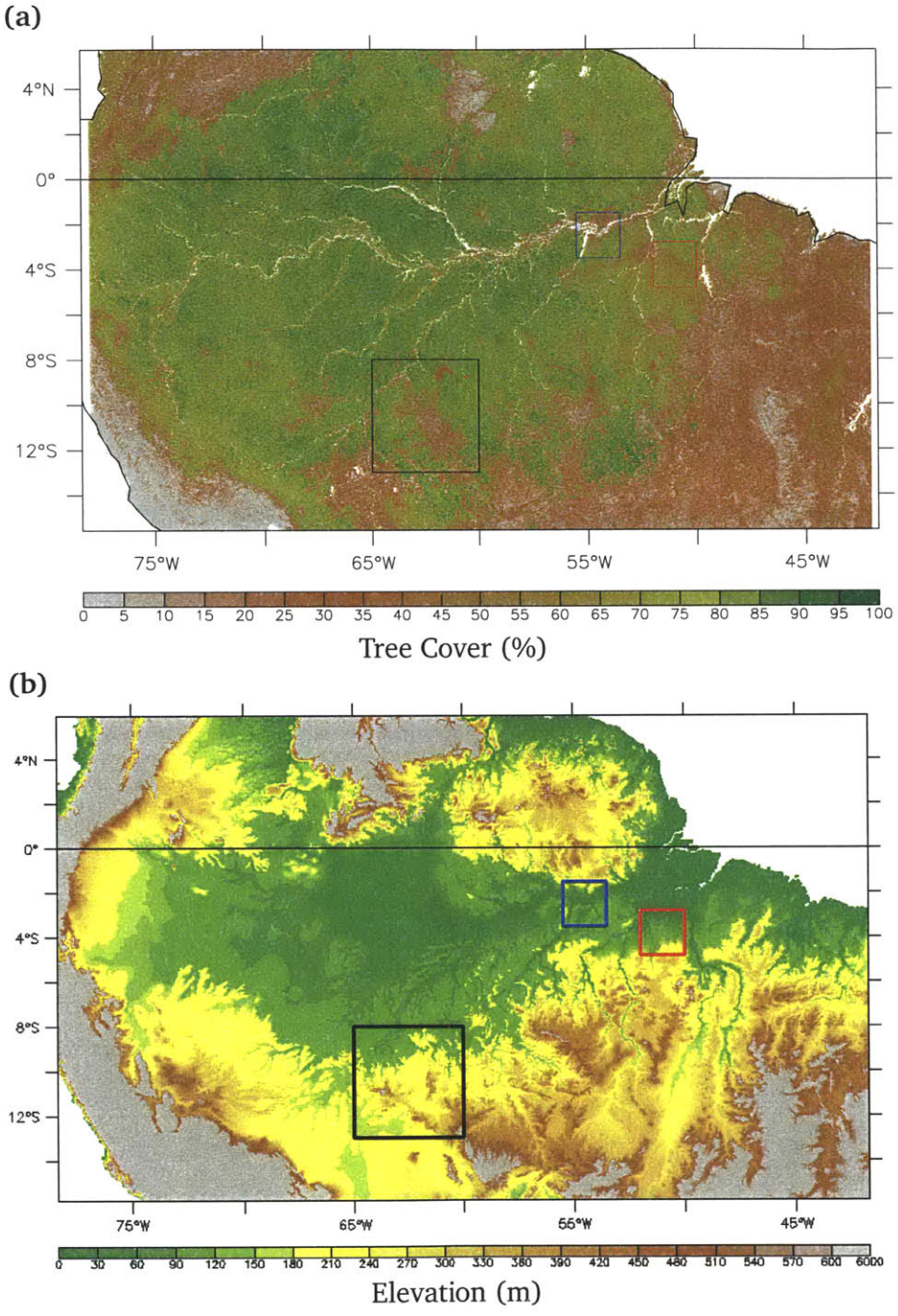

Figure 5-1: The Amazon Basin: **(a)** Deforestation (MOD44B, Hansen *et al.* [2003]) and **(b)** Topography (USGS HYDRO1K). The red box is the Marabá-Altamira domain, the blue box is the Tapajós-Santarém domain, and the large black box is the Rondônia domain.

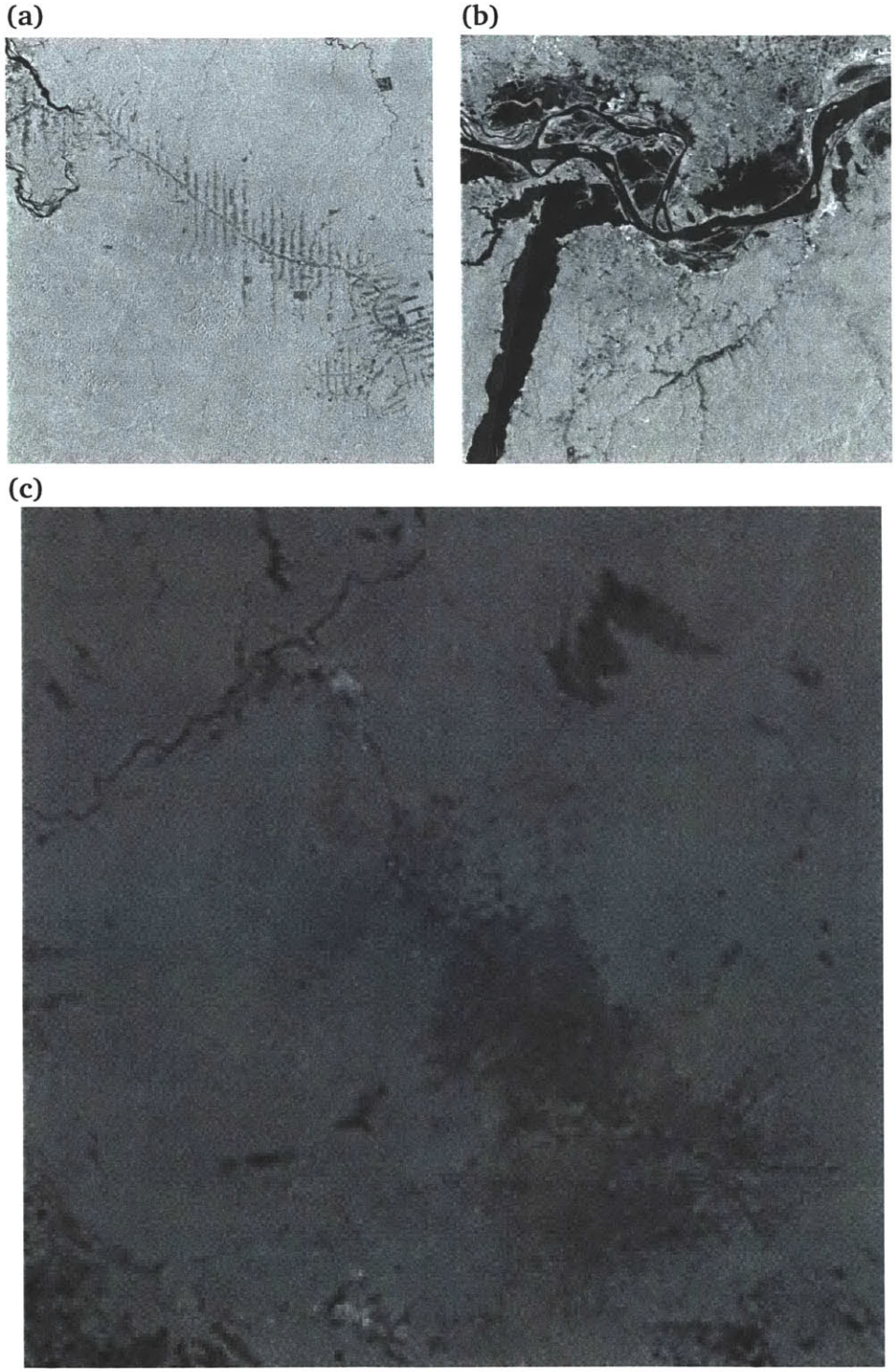

Figure 5-2: Study Domains as seen by the Japanese Earth Resources Satellite (JERS-1). **(a)** Marabá-Altamira (BR-230); **(b)** Tapajós-Santarém; **(c)** Rondônia.

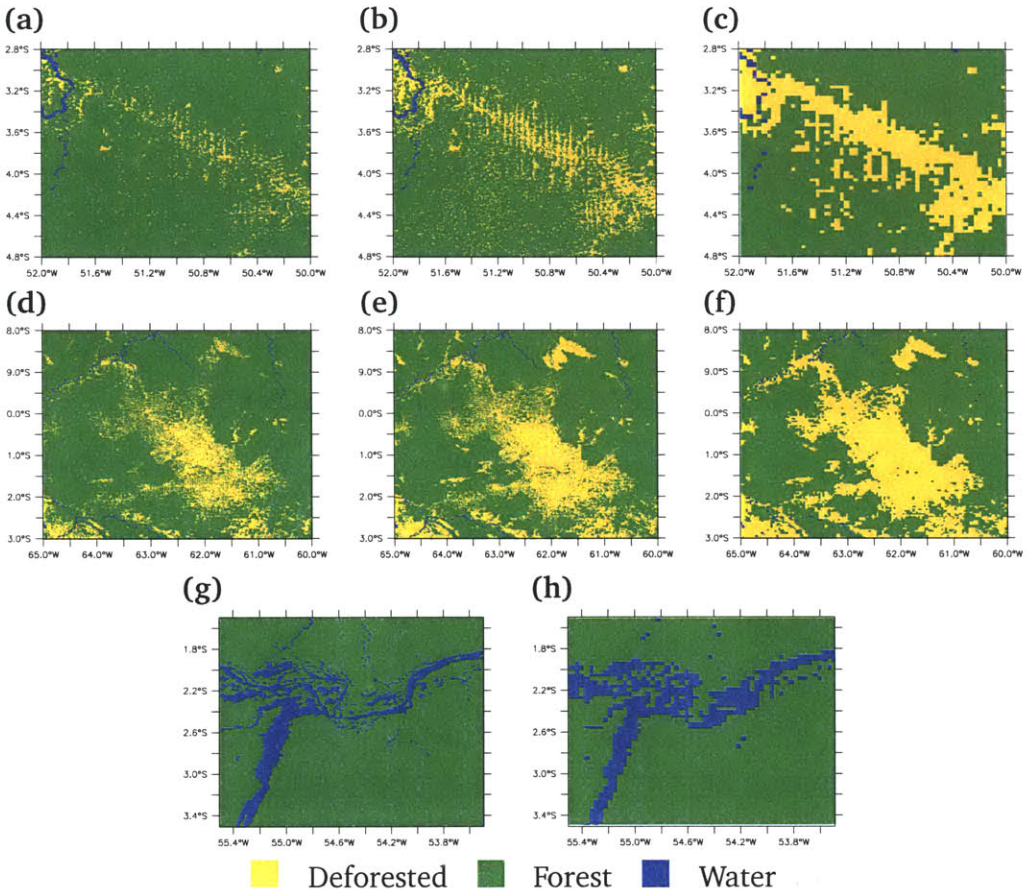

Figure 5-3: Deforestation Maps of Domains: Marabá-Altamira **(a)** 1-km resolution, 30% threshold; **(b)** 1-km resolution, 50% threshold; **(c)** 4-km resolution, 50% threshold. Rondônia **(d)** 1-km resolution, 30% threshold; **(e)** 1-km resolution, 50% threshold; **(f)** 4-km resolution, 50% threshold. Tapajós-Santarém **(g)** 1-km resolution; **(h)** 4-km resolution.

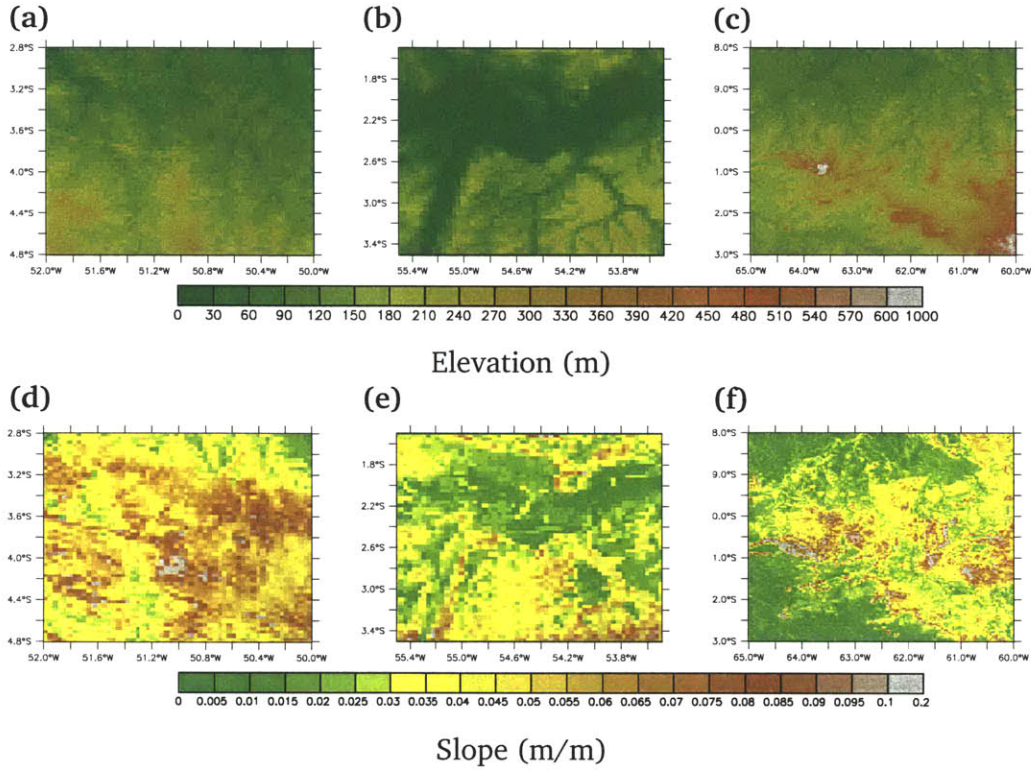

Figure 5-4: Shuttle Topography Radar Mission (SRTM) Slope and Elevation Maps. **(a)** Marabá-Altamira , **(b)** Tapajós-Santarém, and **(c)** Rondônia Elevations; **(d)** Marabá-Altamira, **(e)** Tapajós-Santarém, and **(f)** Rondônia Slopes.

forestation/topography patterns. A full description of the test as it pertains to the relation between shallow clouds and deforestation patterns is outlined below. The tests concerning rainfall or those relating to topography are similar.

5.3.1 Key Statistics for Shallow Clouds and Deforestation

Two statistics that relate shallow cumulus cover to deforestation are examined: the monthly average difference in fractional cloud cover between the deforested and the forested surfaces (hereafter referred to as cloud density difference, CDD); and the count of days in a month when the fractional cloud cover over the deforested surface exceeds that over the forested surfaces (hereafter referred to as the exceedence count, EC). CDD highlights the intensity of a difference in shallow cloud cover, while EC highlights its frequency of occurrence.

The null-hypothesis is that deforestation and shallow cloud patterns are unrelated. Under the null-hypothesis, the expected value of the CDD is zero, and that of the EC is approximately 15 days (or exactly half the number of days in the particular month; see proof below). The null-hypothesis is implicitly true for a completely random landcover, since the random landcover is generated without a-priori knowledge of the cloud pattern. A mathematical treatment of the test follows.

The CDD can be expressed as follows:

$$CDD = \frac{1}{M}\sum_{i=1}^{M}\left(\frac{C_i^{def}}{N^{def}} - \frac{C_i^{for}}{N^{for}}\right), \tag{5.1}$$

where M is the total number of days in the month (or time period studied), C_i^{def} is the number of clouds over deforested pixels on day i, C_i^{for} is the number of clouds over forested pixels on day i, N^{def} is the total number of pixels that are deforested, and N^{for} is the total number of pixels that are forested. The EC can be expressed as follows:

$$e_i = \begin{cases} 1 & \forall \quad \frac{C_i^{def}}{N^{def}} > \frac{C_i^{for}}{N^{for}} \\ 0 & \forall \quad \frac{C_i^{def}}{N^{def}} \leqslant \frac{C_i^{for}}{N^{for}} \end{cases}, \tag{5.2}$$

$$EC_M = \sum_{i=1}^{M} e_i, \tag{5.3}$$

where e_i is the exceedence index defined for day i, and M is the total number of days in the month, or time period studied.

In order to derive the expected values of CDD and EC, let us first define the probability that any given pixel is covered by a cloud on day i as $p_i(c)$. For the random landcover, the null-hypothesis is true and cloudiness has absolutely no correlation with the state of a given pixel's state (whether defined by forest cover or

topography), and we may pose the following equality:

$$p_i(c) = \lim_{N \to \infty} \frac{C_i(N)}{N}, \tag{5.4}$$

where $C_i(N)$ is the total number of cloudy pixels on day i and N is the total number of pixels in the study area. The expected value of CDD can be expressed as follows:

$$E(CDD) = p(c|def) - p(c|for), \tag{5.5}$$

where $p(c|def)$ is the probability that a pixel is cloudy given that it is deforested and $p(c|for)$ is the probability that a pixel is cloudy given that it is forested. The expected value of the cloud density difference can re-written as follows:

$$E(CDD) = \frac{p(c \cap def)}{p(def)} - \frac{p(c \cap for)}{p(for)} \tag{5.6}$$

If the null-hypothesis is true and the clouds are unrelated to the underlying land-cover, then the following holds:

$$p(c \cap def) = p(c) \times p(def), \tag{5.7}$$

and

$$p(c \cap for) = p(c) \times p(for), \tag{5.8}$$

and therefore, it follows that the expected value of CDD is zero:

$$E(CDD) = \frac{p(c) \times p(def)}{p(def)} - \frac{p(c) \times p(for)}{p(for)} = 0. \tag{5.9}$$

The expected value of EC is directly related to the expected value of the exceedence index e_i, which can be compared to the problem of tossing a coin:

$$E(e_i) = \frac{1}{2}, \tag{5.10}$$

and the expected value of EC is thus:

$$E(EC_M) = \sum_{i=1}^{M} E(e_i) = \sum_{i=1}^{M} \frac{1}{2} = \frac{M}{2} \tag{5.11}$$

We thus have two key-statistics, for which we know the expected value when clouds and deforestation patters are mutually random, or independent. We can also theoretically derive the distribution of EC, and hence determine whether the observed EC is significantly different from one that borne of no association between forest cover and shallow clouds. We have, however, no formal knowledge of the spread or distribution of the CDD key-statistic, and must hence rely on other methods to derive this.

Table 5.1: Theoretical 99% Distribution Limits for EC

n (days)	Upper 99% Confidence Bound	Lower 99% Confidence Bound
31	23	8
30	22	8
29	21	8
28	21	7

Theoretical Distribution of EC

Under the null-hypothesis, the theoretical distribution of the EC follows the binomial distribution. EC is a counting random variable — a binomial counting process, in which the counter reading at time i has the following property:

$$e_i = \begin{cases} 1 & \forall \quad \frac{C_i^{def}}{N^{def}} > \frac{C_i^{for}}{N^{for}} \\ 0 & \forall \quad \frac{C_i^{def}}{N^{def}} \leqslant \frac{C_i^{for}}{N^{for}} \end{cases}, \tag{5.12}$$

$$P(e_i = 1) = \frac{1}{2}. \tag{5.13}$$

It follows that the probability that, after n time-periods,

$$P(EC_n = k) = \binom{n}{k} p^k (1-p)^{n-k}, \tag{5.14}$$

where

$$\binom{n}{k} = \frac{n!}{k!(n-k)!}. \tag{5.15}$$

It is thus possible to derive the theoretical 99% confidence limits that will determine whether the observed EC confirms or rejects the null-hypothesis. The known theoretical limits of EC will also enable us to compare the same limits derived from randomized forest cover maps. The 99% limits for months of 28, 29, 30 and 31 days are summarized in Table 5.1.

5.3.2 Randomization Methods: Monte-Carlo Confidence Limits

The test used in this study to determine whether shallow cloud patterns and deforestation patterns are correlated is similar to a Monte-Carlo simulation. A vector of 1,000 randomly generated deforestation patterns is generated; the key-statistics described above are computed for each random deforestation pattern, and the distribution of these key-statistics is generated. The key-statistic derived from the observed deforestation pattern (OKS) is then compared to the distribution of the key-statistic derived from the randomized deforestation patterns (RKS). The null-

hypothesis (i. e., deforestation and shallow cloud patterns are unrelated) is rejected if the OKS lies outside 99% of the mass of the RKS distribution (i. e., if the cloud-forest statistic derived from the observed deforestation pattern lies outside the 99% limits of the distribution of cloud-forest statistics derived from the randomized deforestation patterns). A cloud field that bears no association to the patterns of deforestation would be expected to exceed (be below) the upper (lower) 99% limit 0.5% of the time, making this test extremely strict. When the null hypothesis is rejected, the shallow cloud cover pattern is significantly associated with the underlying deforestation pattern.

The validity of the test outlined above is dependent on the adherence to four strict conditions: comparability; conservation of pixel-state distribution; conservation of scale; and uniqueness of each randomized pattern. The first condition relates to the computation of the key-statistics, while the three other conditions relate to the method by which the randomized deforestation patterns are generated.

The first condition is that the test is meaningful only if the OKS and RKS are actually comparable, in that they must be derived exactly the same way. Both key-statistics are integrated through time (i. e., averaging for the CDD and counting for the EC). The time-integration of the key-statistics derived from the randomized deforestation patterns is performed across the same sample random deforestation pattern, just as the key-statistics derived from the observed deforestation patterns are integrated through time with the same observed deforestation pattern (see Figure 5-5).

The second condition is that the proportion of deforested pixels to forested pixels must be the same in the randomized deforestation patterns than it is in the observed deforestation pattern. So if the observed deforestation pattern is composed of 30% deforested pixels, then each sample random deforestation pattern should comprise 30% deforested pixels as well. This ensures that the randomized patterns are representative of the actual observed patterns; it also ensures that the sampling frequency over each type of state that composes a pattern is homologous.

The third condition is that the spatial scale of the deforestation patterns must be the same in the randomized deforestation maps as it is in the observed deforestation map. In the case where the randomized spatial scale is smaller than the observed spatial scale, the problem of sub-sampling and artificial difference damping occurs. The same occurs when the randomized pattern's spatial scale is much larger that the one observed. Consequently, the rigor of the test is dependent on accurate spatial scale conservation in the randomized patterns. A deviation from accuracy might result in an artificially narrower derived distribution of the key-statistics, making a significant result much more likely. This behaviour is highlighted in Figure 5-6. Two completely random 1-dimensional series are generated; the series are 10,000 numbers long, and each number takes a value of either 1 or 0. Both series have a "scale" of 100 number (i. e., ones and zeroes are clumped together in multiples of 100.) The first series is analogous to the cloud data, and the second, which is restricted to have 30% of zeroes is analogous to forest-cover. The "observed" differ-

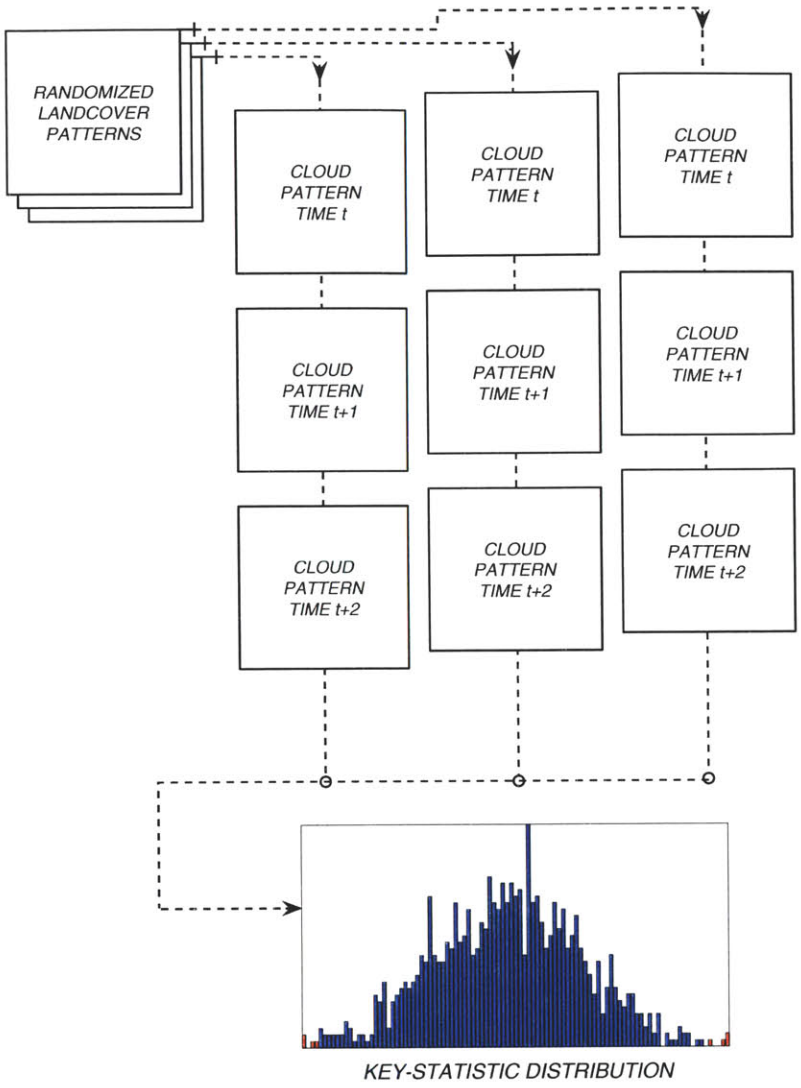

Figure 5-5: Schematic of Time-Integration of Key-Statistics based on Randomized Deforestation Patterns

ence (termed "difference statistic" in Figure 5-6) is taken as the difference between occurrences of ones in the first series collocated with occurrences of zeros in the second and the occurrences of ones in the first series collocated with occurrences of ones in the second. It is analogous to the CDD statistic. This same statistic is computed for series of randomly generated at five different scales: 1 unit, 10 units, 100 units, 1,000 units and 10,000 units. the random series are generated 500 times for each scale, and they each obey the 30% relative occurrence of zeroes. The confidence limits of the derived difference statistics are then generated for each random series. Although the original two series are completely mutually random (i. e., in-

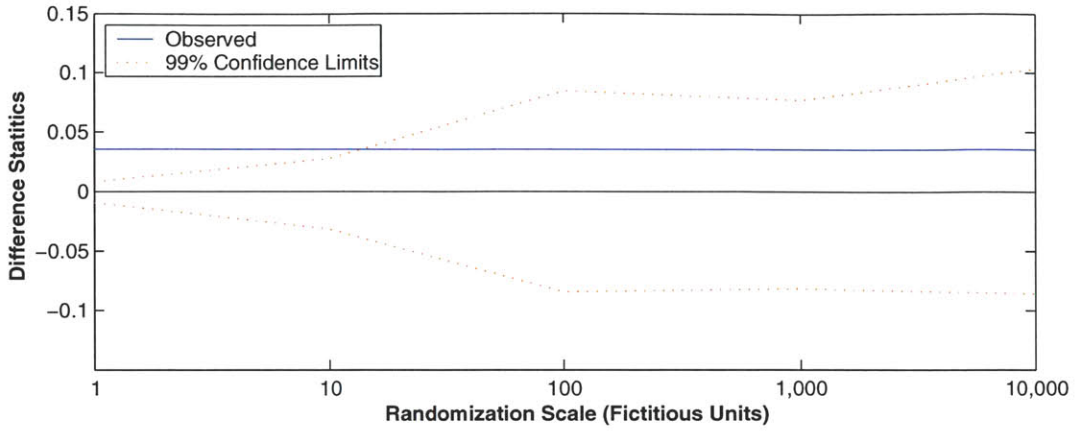

Figure 5-6: Example of Effect of Randomization Scale on Significance; "Observed" difference value based on one random base cover realization at a scale of 100 units.

dependent), the "observed statistic" appears to be "significant" when compared to the confidence bounds generated with random series of smaller scales.

The fourth condition is that each randomly generated deforestation map should be unique, or different from each of the other randomly generated deforestation maps. If repetition occurs in the randomly generated patterns, then the derived distribution of key statistics will be narrowed, and a spurious significant result might be inferred.

Two randomization methods are presented here: the completely spatially random block algorithm (CSR), and the shuffling algorithm (SHF). The CSR algorithm procedes by generating square deforestation blocks of a predetermined scale. The amount of such blocks created for a particular random map is controlled so that the proportion of deforested to forested pixels is conserved from the observed deforestation map. The SHF randomization algorithm divides the observed deforestation pattern into tiles that are in turn randomly rotated, flipped and shuffled. A total of 16 tiles are created for each domain; the tiles are 56-km to the side for the Marabá-Altamira and Tapajós-Santarém domains, and 140-km to the side for the Rondônia domain. The SHF algorithm implicitly conserves the proportion of deforested to forested area. Examples of the CSR randomized deforestation maps at different scales for all three study-domains are represented in Figures 5-7, 5-8 & 5-9. Examples of the SHF randomized deforestation maps are shown in Figure 5-10.

The size of the blocks (or tiles) used in both randomizing algorithms determines whether the scale of the deforested patches is conserved. The validity of the third condition is tested by comparing the two-dimensional power-spectra of the observed deforestation maps to those of the randomized deforestation patterns. The two-dimensional power spectrum of the observed deforestation pattern is compared with that of the randomized patterns (Figures 5-12, 5-13, 5-14, 5-15, 5-16 & 5-17). The CSR algorithm will never perfectly represent the spatial scale of the observed

pattern, since the scale of the randomized pixels is fixed, and hence only multiples of the randomized block-scale may be exhibited. This is clearly shown in the 2-dimensional spectra of CSR randomized patterns (i. e., Figures 5-12, 5-13 & 5-14), which show features that are dependent on the respective block-scales. The SHF algorithm produces 2-dimensional power-spectra that are representative of the observed ones (i. e., Figures 5-15, 5-16 & 5-17). This similarity shows that spatial scales are being conserved with the SHF algorithm.

The validity of the fourth condition can be verified by using combinatorial theory. The problem is one of finding the number of different permutations. For the CSR algorithm, if we define n_1 as the number of pixels of landcover type "1" and n_2 as the number of pixels of landcover type "2", then the number (N) of distinguishable permutations is expressed by Equation 5.16:

$$N = \frac{(n_1 + n_2)!}{n_1! n_2!}. \tag{5.16}$$

The values for n_1 and n_2 are dependent on the block-scale used in the randomization (i. e., 4-km, 12-km, 20-km, 36-km, or 92-km), and the relative proportion of deforested to total pixels, which is dependent on the aggregation scale (i. e., 1-km or 4-km) and the threshold used to determine deforested pixels. The proportions of deforested pixels are summarized in Table 5.2. Table 5.3 presents the values n_1, n_2 and N for the CSR algorithm. The CSR algorithm satisfies the fourth condition in all cases, except for the use of 92-km block scales in the Marabá-Altamira and Tapajós-Santarém domains.

Table 5.2: Aggregation-scale and Threshold Dependent Deforestation Map Parameters

Domain	Aggregation Scale (km)	Threshold (%)	Proportion of Deforested (River) to Forested (Land) Pixels (%)
	1	30	5.7
Marabá-Altamira	1	50	15.9
(49,952 Total Pixels)	4	50	27.0
	1	30	13.0
Tapajós-Santarém	1	50	13.0
(50,176 Total Pixels)	4	50	17.9
	1	30	16.7
Rondônia	1	50	25.3
(316,386 Total Pixels)	4	50	31.2

The number of distinct permutation possible for the SHF algorithm is calculated differently due to the algorithmic procedure. Unlike the CSR algorithm, n_1 and n_2 are not dependent upon the proportion of deforested pixels to total pixels (which

Table 5.3: Distinct Randomized Landcover Possibilities (CSR Algorithm)

Randomization Block Scale (km)		Marabá-Altamira Domain	Tapajós-Santarém Domain	Rondônia Domain
1	n_1	13,487	8,981	98,712
	n_2	34,465	41,195	217,674
	N	$\sim \infty^{\dagger}$	$\sim \infty^{\dagger}$	$\sim \infty^{\dagger}$
4	n_1	843	561	6,169
	n_2	2,279	2,575	13,605
	N	$\sim \infty^{\dagger}$	$\sim \infty^{\dagger}$	$\sim \infty^{\dagger}$
20	n_1	34	40	247
	n_2	91	185	544
	N	4.71×10^{30}	3.74×10^{44}	$\sim \infty^{\dagger}$
36	n_1	10	7	76
	n_2	27	32	168
	N	3.48×10^{8}	1.53×10^{7}	2.95×10^{64}
92	n_1	2	1	12
	n_2	4	5	25
	N	15	6	1.85×10^{9}

† The resulting N is so large, that it is numerically equivalent to infinity

is itself dependent upon aggregation scale and threshold), rather they are simply dependent on the number of tiles. Moreover, since there are the added steps of rotation and flipping, there are added degrees of freedom. There are 16 different tiles for each domain. The total number of different tiles is calculated as follows:

$$N_{tiles} = d_r \times d_f \times 16 = 4 \times 2 \times 16 = 128, \tag{5.17}$$

where d_r is the number of degrees of freedom added due to rotation, and d_f is the number of degrees of freedom added by flipping. The number of distinct randomized patterns is equivalent to the number of permutations of 16 tiles selected from 128 total possible tiles, and may be expressed as follows (Equation 5.18):

$$N = {}^{128}\mathbf{P}_{16} = \frac{128!}{(128-16)!} \simeq 1.95 \times 10^{33}. \tag{5.18}$$

Thus the SHF algorithm satisfies the fourth condition.

The average deforestation state across all randomized deforestation maps is calculated to verify that the mechanics of the algorithm are properly working. These averages are presented for deforestation patterns in Figures 5-20 & 5-21, and for topography and slope maps (using the shuffling algorithm) in Figure 5-22. Under perfect randomized conditions, these average maps should be homogeneous, and

should have the value of the proportion of deforested pixels, or mean elevation or mean slope. This is largely verified for both randomization algorithms and different block-scales.

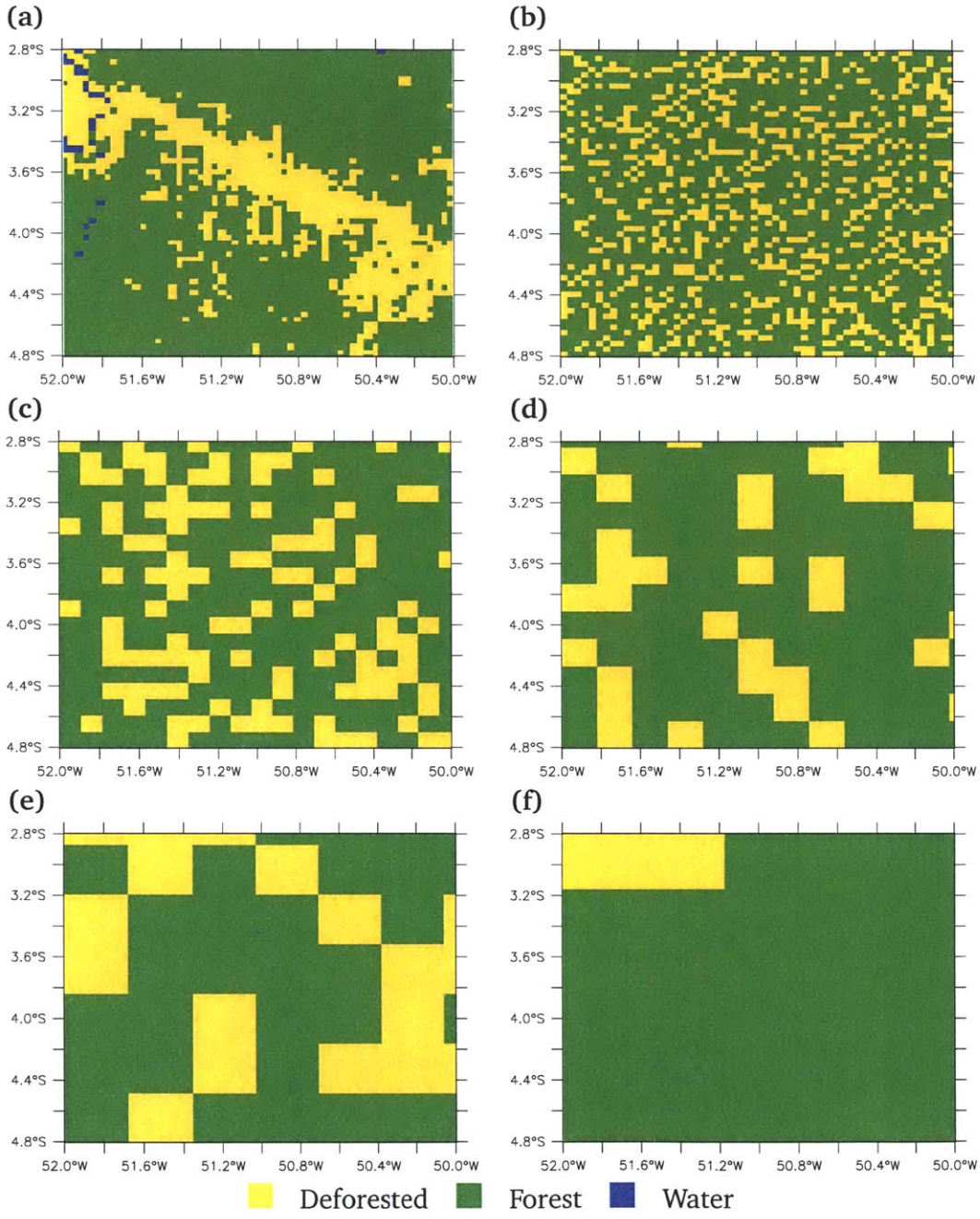

Figure 5-7: Marabá-Altamira Domain Deforestation Patterns: **(a)** Observed (4-km Aggregation Scale, 50% Threshold); CSR Randomized Examples at **(b)** 4-km, **(c)** 12-km, **(d)** 20-km, **(e)** 36-km & **(f)** 92-km Block-Scales.

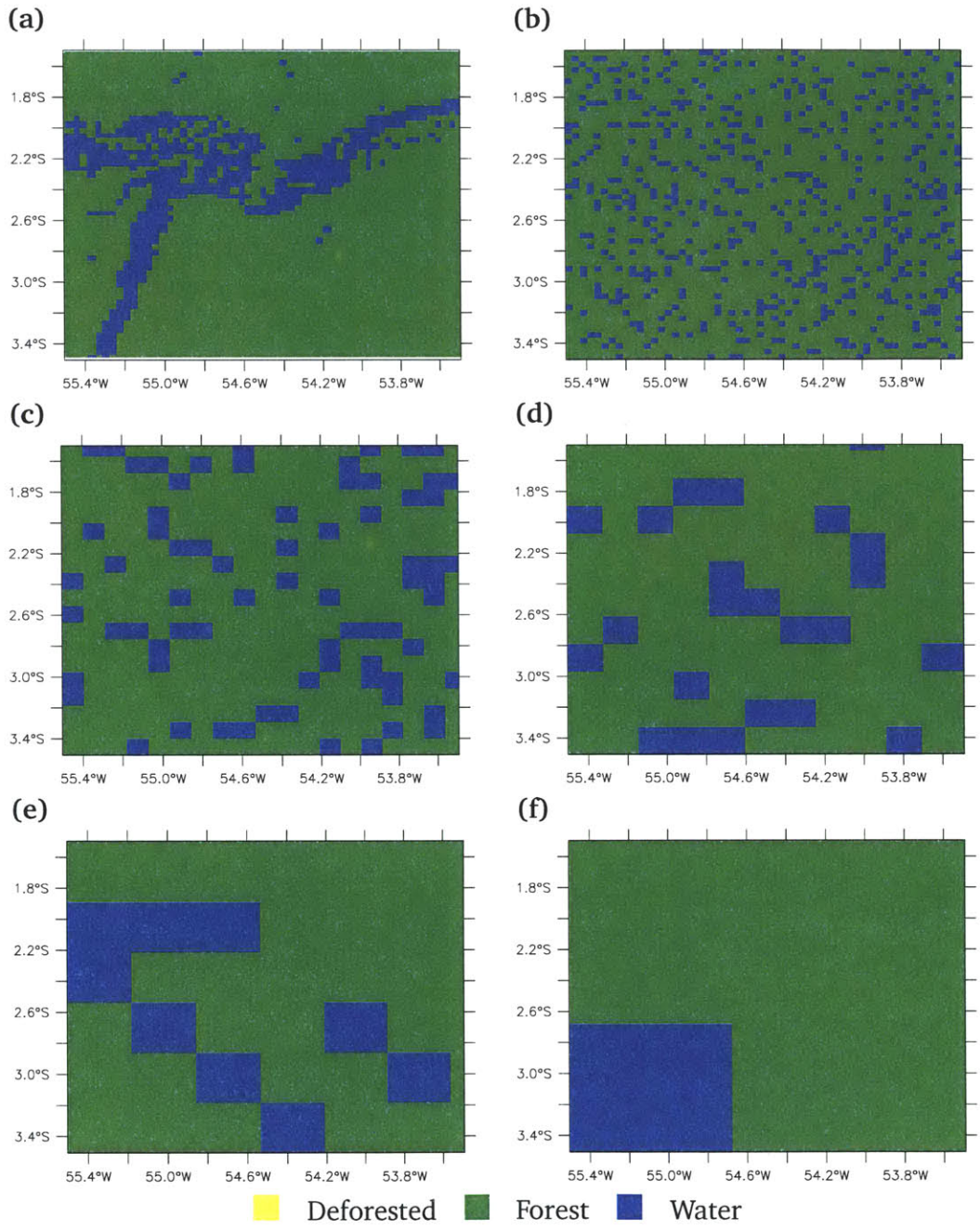

Figure 5-8: Tapajós-Santarém Domain River Patterns: **(a)** Observed (4-km Aggregation Scale); CSR Randomized Examples at **(b)** 4-km, **(c)** 12-km, **(d)** 20-km, **(e)** 36-km & **(f)** 92-km Block-Scales.

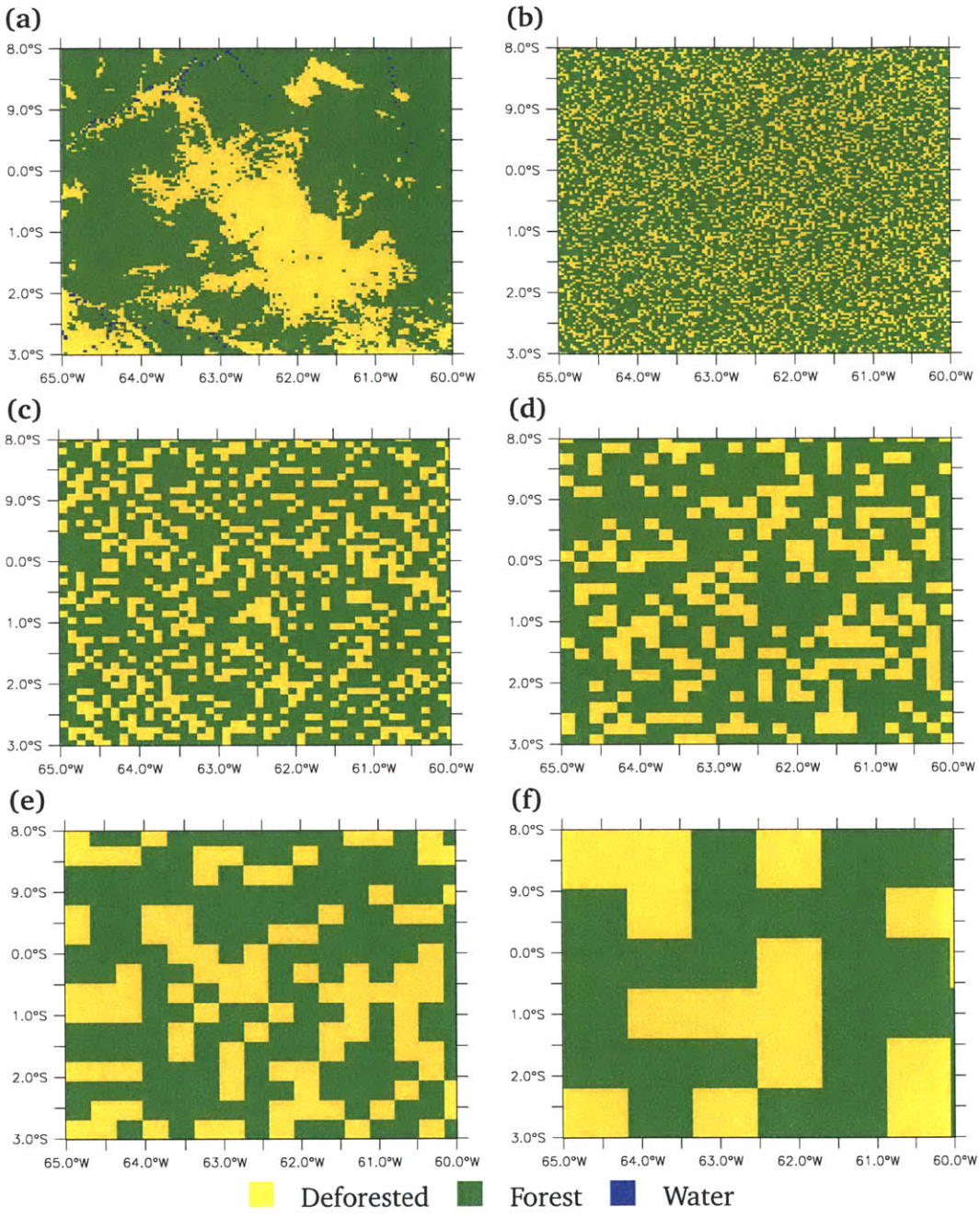

Figure 5-9: Rondônia Domain Deforestation Patterns: **(a)** Observed (4-km Aggregation Scale, 50% Threshold); CSR Randomized Examples at **(b)** 4-km, **(c)** 12-km, **(d)** 20-km, **(e)** 36-km & **(f)** 92-km Block-Scales.

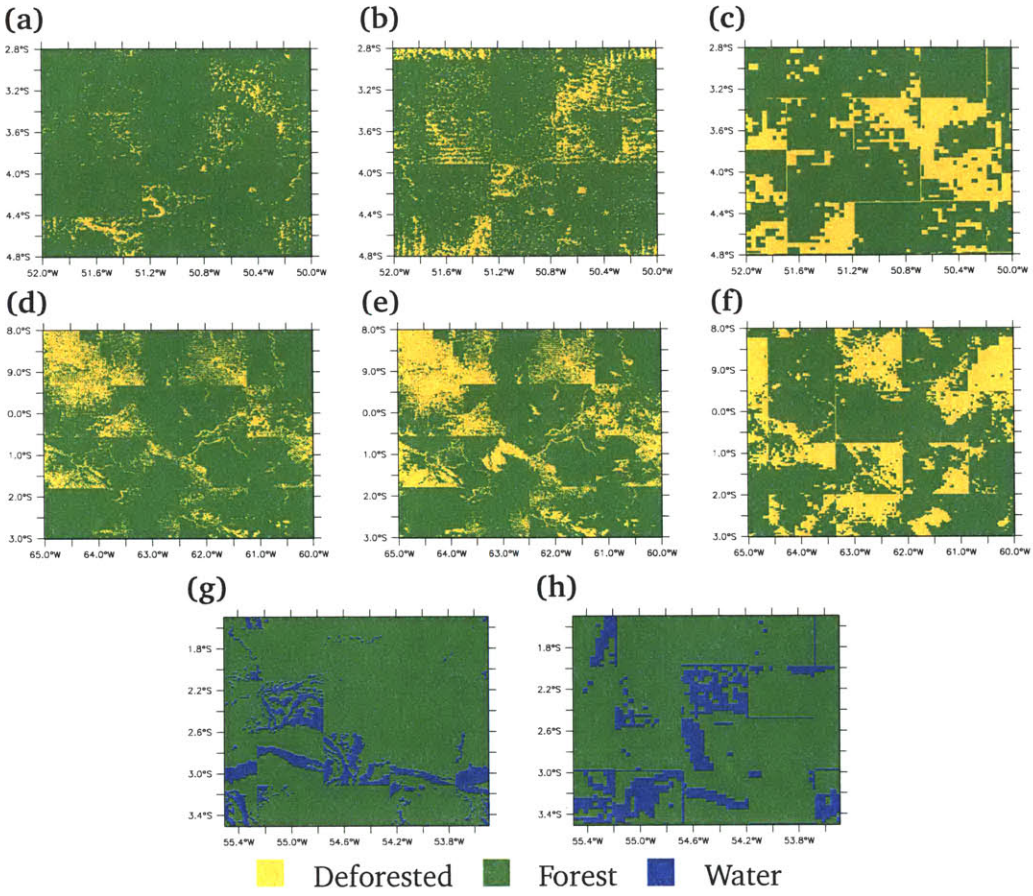

Figure 5-10: Shuffled Deforestation Patterns. Marabá-Altamira Domain: 1-km resolution **(a)** 30% threshold and **(b)** 50% threshold; **(c)** 4-km resolution, 50% threshold. Rondônia Domain: 1-km resolution **(d)** 30% threshold and **(e)** 50% threshold; **(f)** 4-km resolution, 50% threshold. Tapajós-Santarém Domain: **(g)** 1-km resolution; **(h)** 4-km resolution.

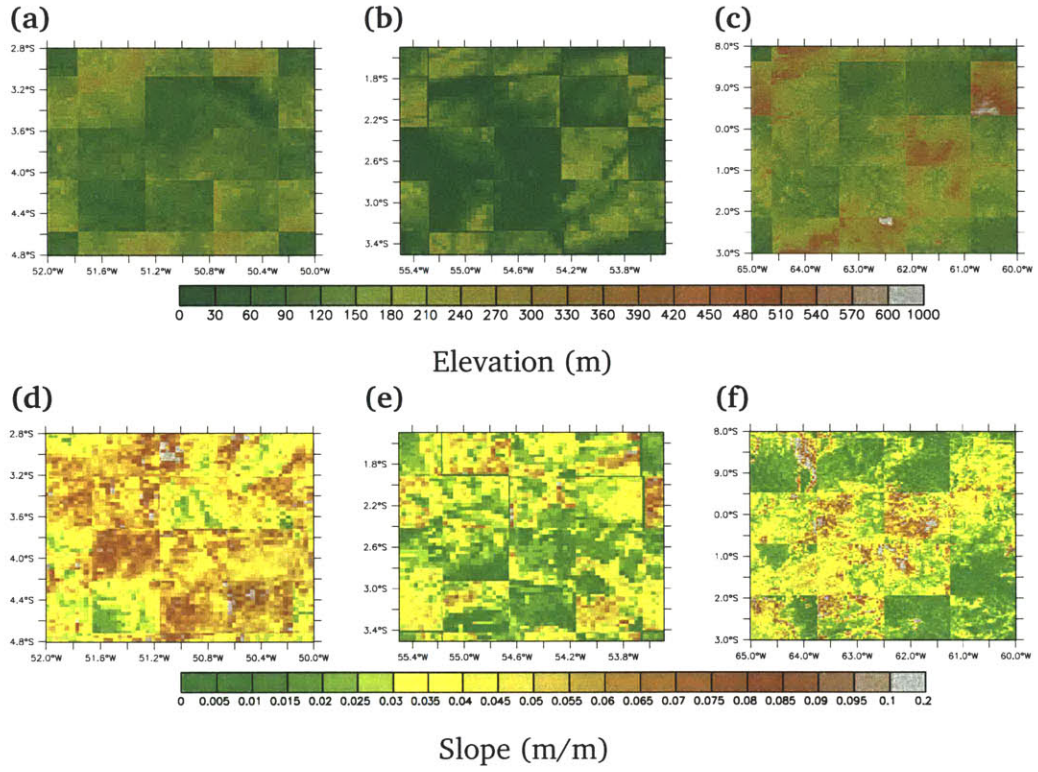

Figure 5-11: Shuffled SRTM Maps of **(a)** Marabá-Altamira Elevation; **(b)** Tapajós-Santarém Elevation; **(c)** Rondônia Elevation; **(d)** Marabá-Altamira Slope; **(e)** Tapajós-Santarém Slope; **(f)** Rondônia Slope.

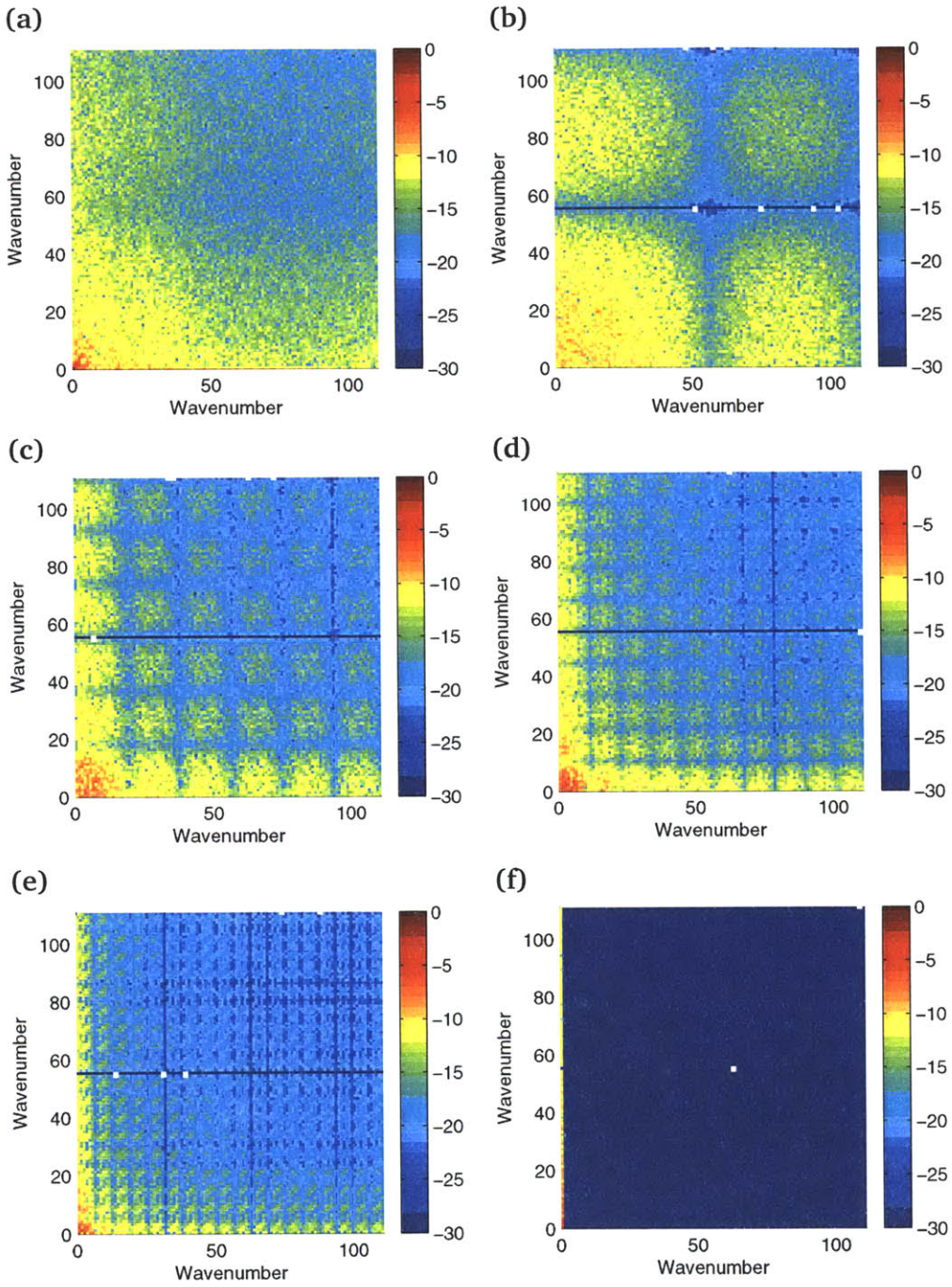

Figure 5-12: Two-Dimensional Normalized Log Power Spectra of Observed and Randomized (CSR Algorithm) Deforestation Patterns for Marabá-Altamira Domain. **(a)** Observed (4-km Aggregation); CSR Randomized at **(b)** 4-km, **(c)** 12-km, **(d)** 20-km, **(e)** 36-km, and **(f)** 92-km Block-Scale.

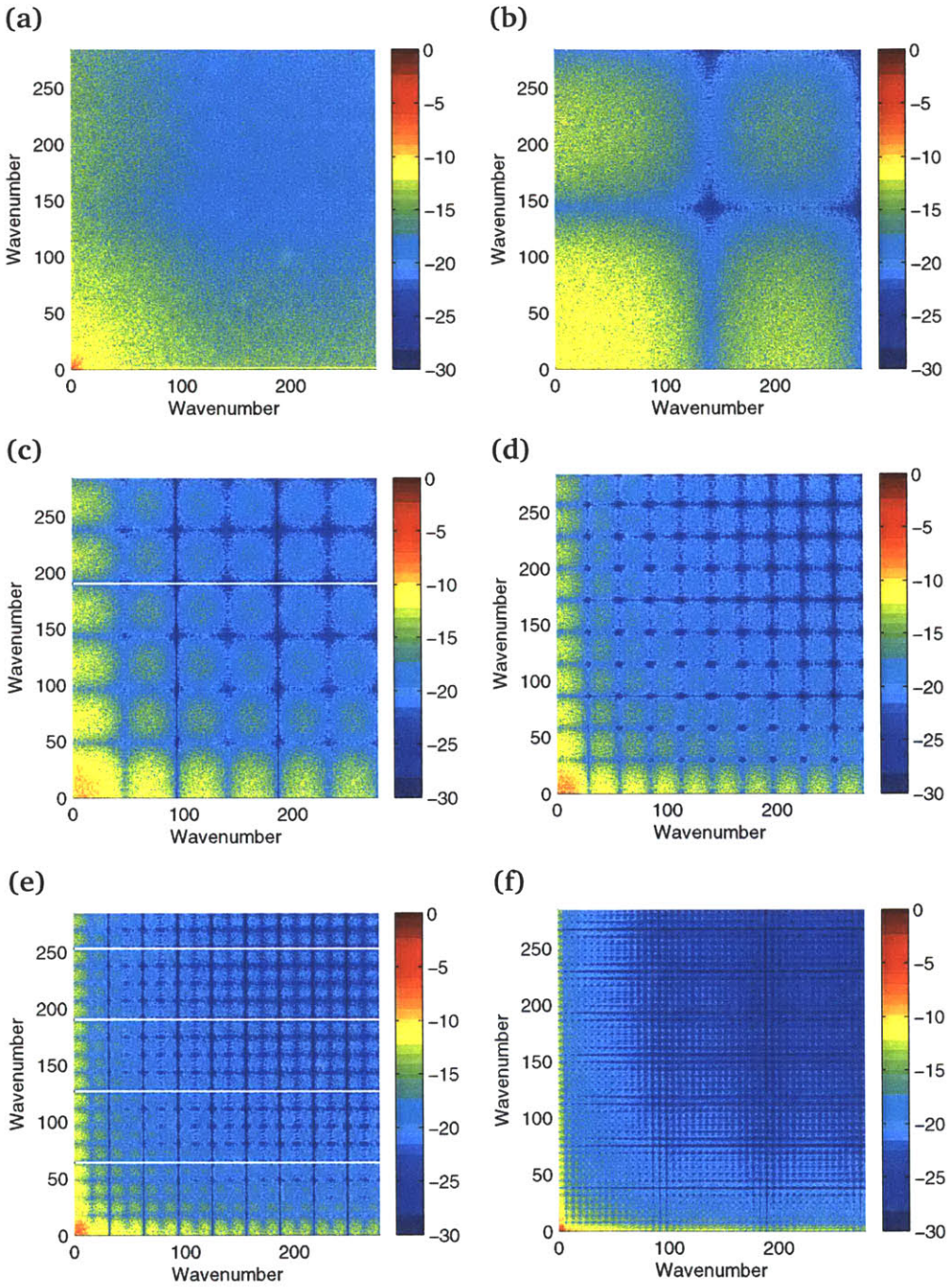

Figure 5-13: Two-Dimensional Normalized Log Power Spectra of Observed and Randomized (CSR Algorithm) Deforestation Patterns for Rondônia Domain. **(a)** Observed (4-km Aggregation); CSR Randomized at **(b)** 4-km, **(c)** 12-km, **(d)** 20-km, **(e)** 36-km, and **(f)** 92-km Block-Scale.

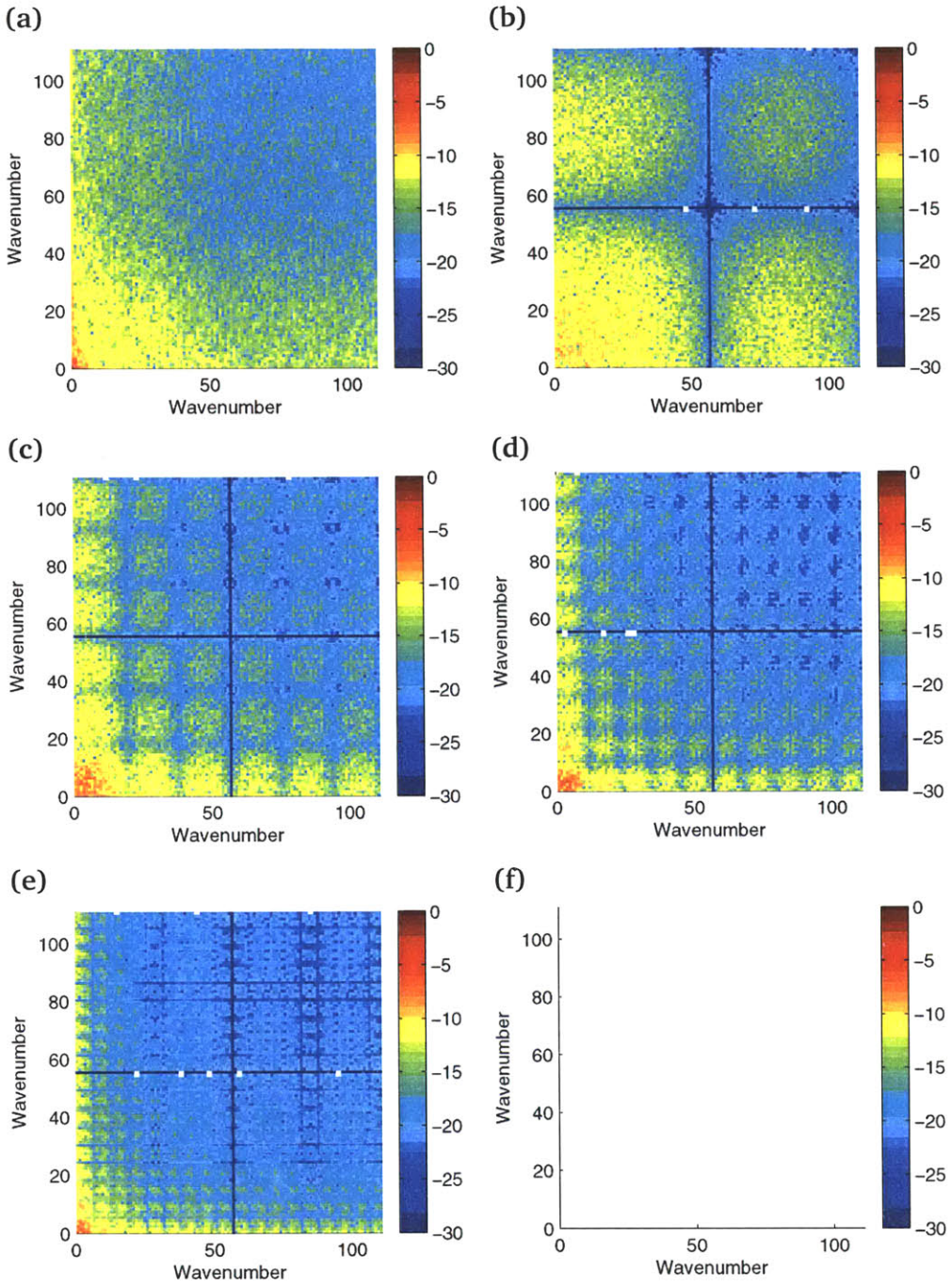

Figure 5-14: Two-Dimensional Normalized Log Power Spectra of Observed and Randomized (CSR Algorithm) Deforestation Patterns for Tapajós-Santarém Domain. **(a)** Observed (4-km Aggregation); CSR Randomized at **(b)** 4-km, **(c)** 12-km, **(d)** 20-km, **(e)** 36-km, and **(f)** 92-km Block-Scale.

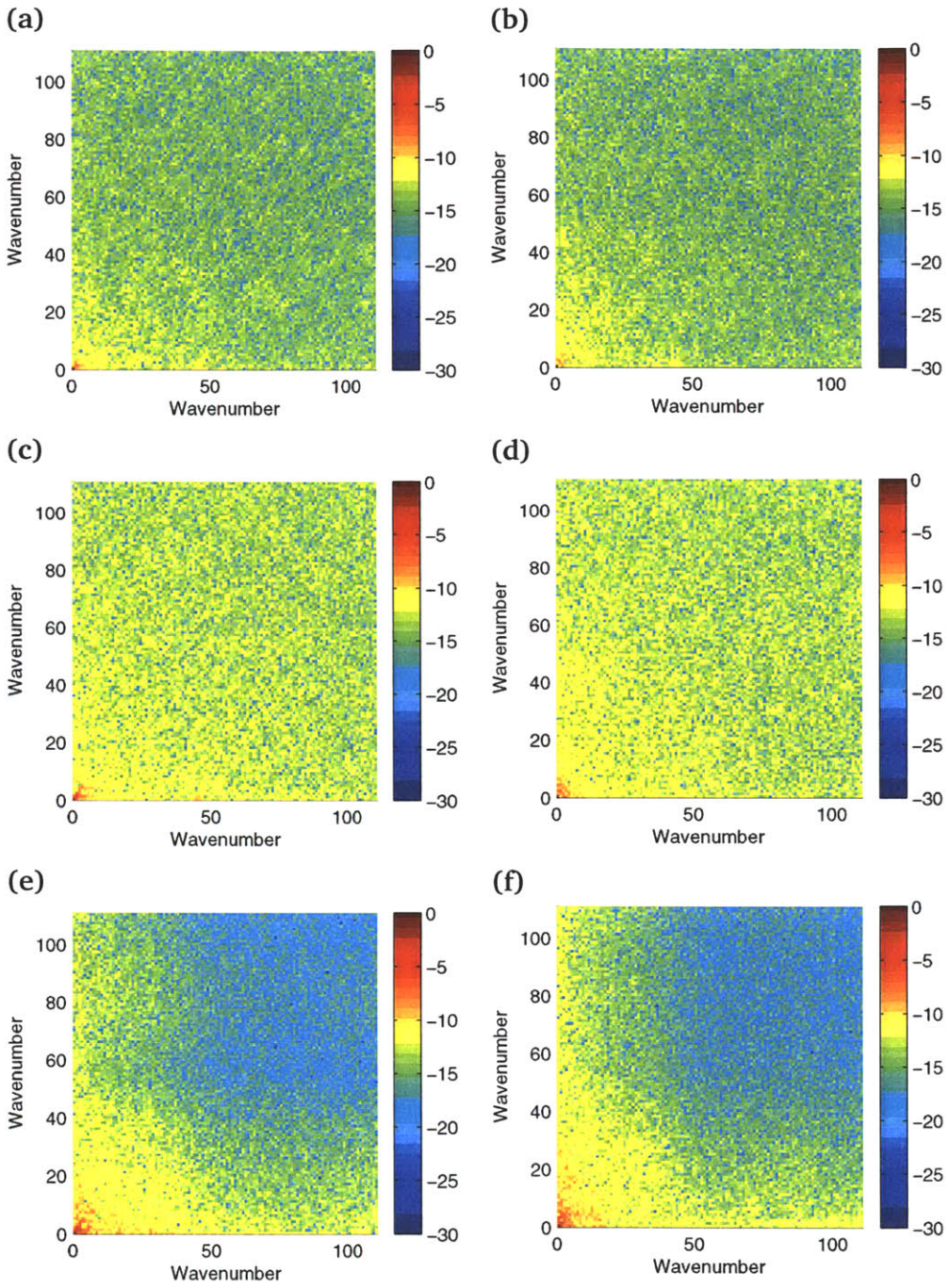

Figure 5-15: Two-Dimensional Normalized Log Power Spectra of Observed and Randomized (SHF Algorithm) Deforestation Patterns for Marabá-Altamira Domain. **(a)** Observed and **(b)** Randomized (1-km Aggregation; 30% Threshold); **(c)** Observed and **(d)** Randomized (1-km Aggregation; 50% Threshold); **(e)** Observed and **(f)** Randomized (4-km Aggregation; 50% Threshold).

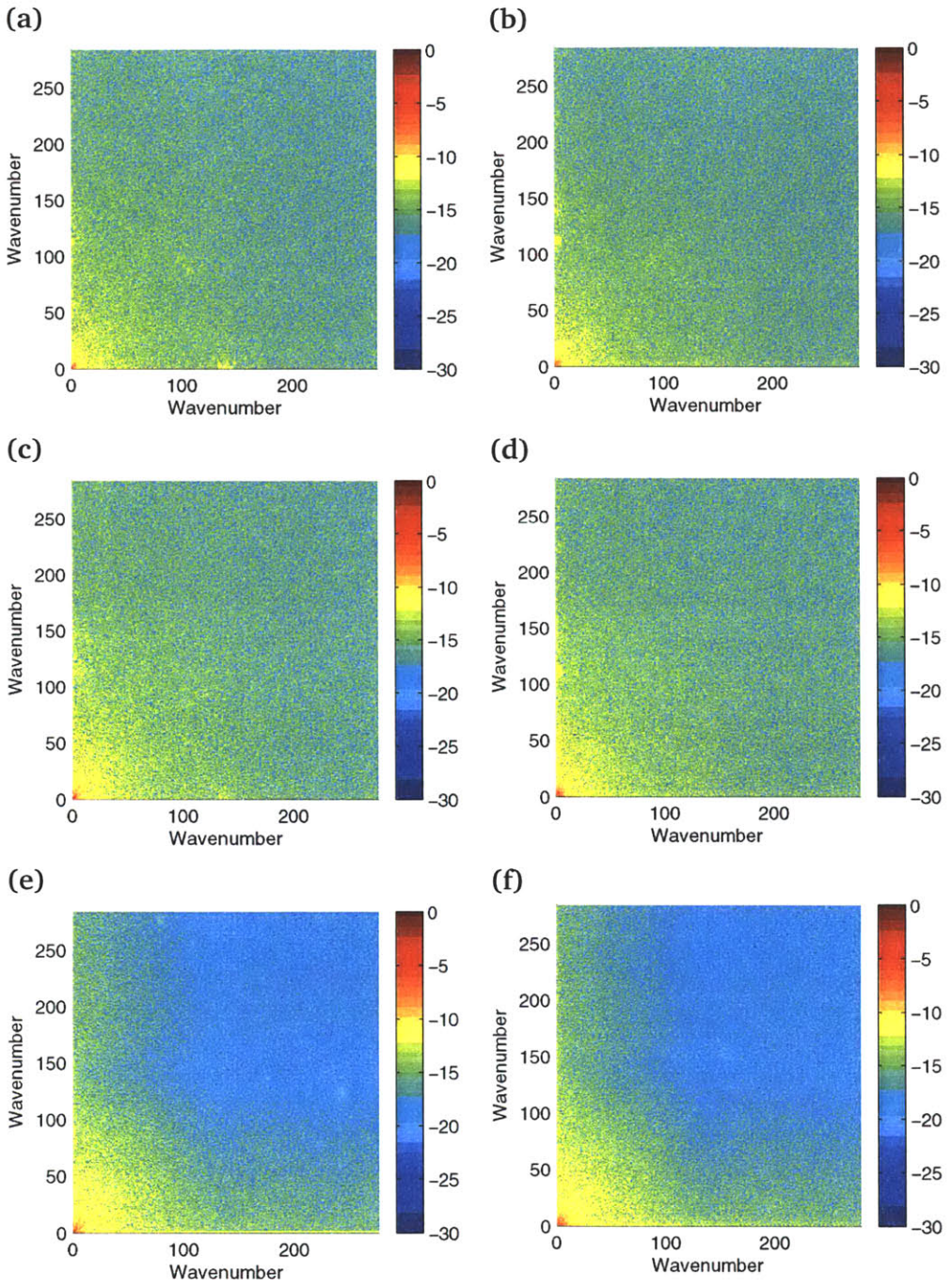

Figure 5-16: Two-Dimensional Normalized Log Power Spectra of Observed and Randomized (SHF Randomization) Deforestation Patterns for Rondônia Domain. **(a)** Observed and **(b)** Randomized (1-km Aggregation; 30% Threshold); **(c)** Observed and **(d)** Randomized (1-km Aggregation; 50% Threshold); **(e)** Observed and **(f)** Randomized (4-km Aggregation; 50% Threshold).

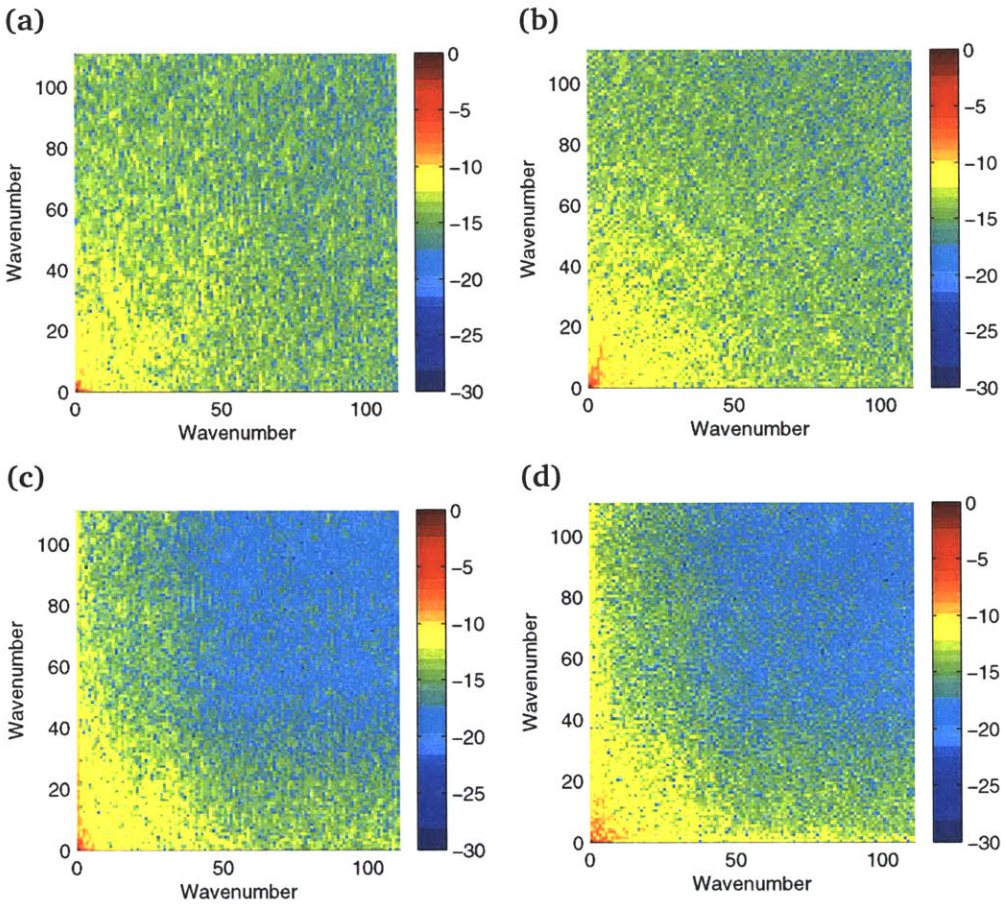

Figure 5-17: Two-Dimensional Normalized Log Power Spectra of Observed and Randomized (SHF Randomization) Deforestation Patterns for Tapajós-Santarém Domain. **(a)** Observed and **(b)** Randomized (1-km Aggregation); **(c)** Observed and **(d)** Randomized (4-km Aggregation).

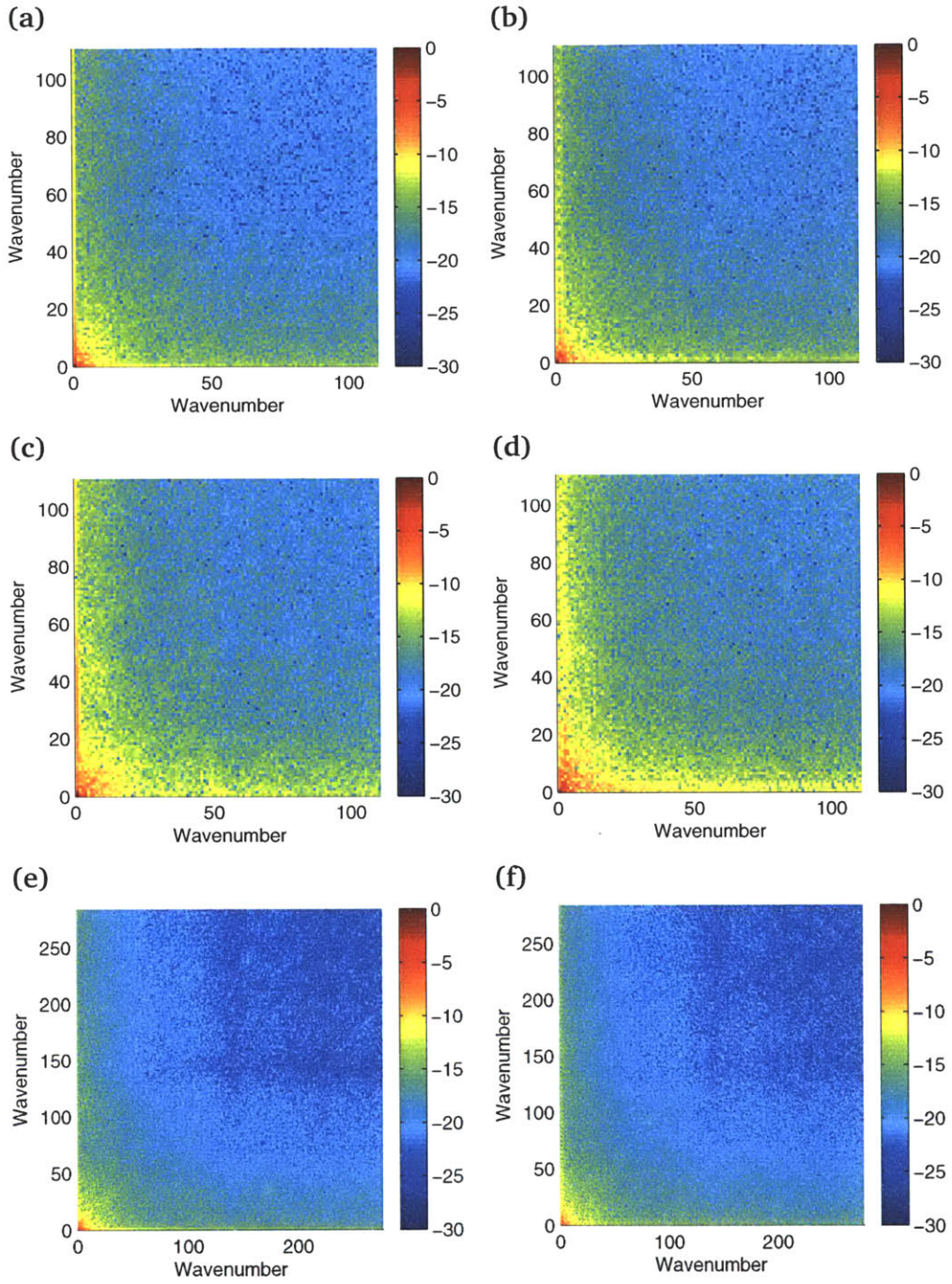

Figure 5-18: Two-Dimensional Normalized Log Power Spectra of Observed and Randomized (SHF Algorithm) Topography for Domains. Marabá-Altamira Domain **(a)** Observed and **(b)** Randomized; Tapajós-Santarém Domain **(c)** Observed and **(d)** Randomized; Rondônia Domain **(e)** Observed and **(f)** Randomized.

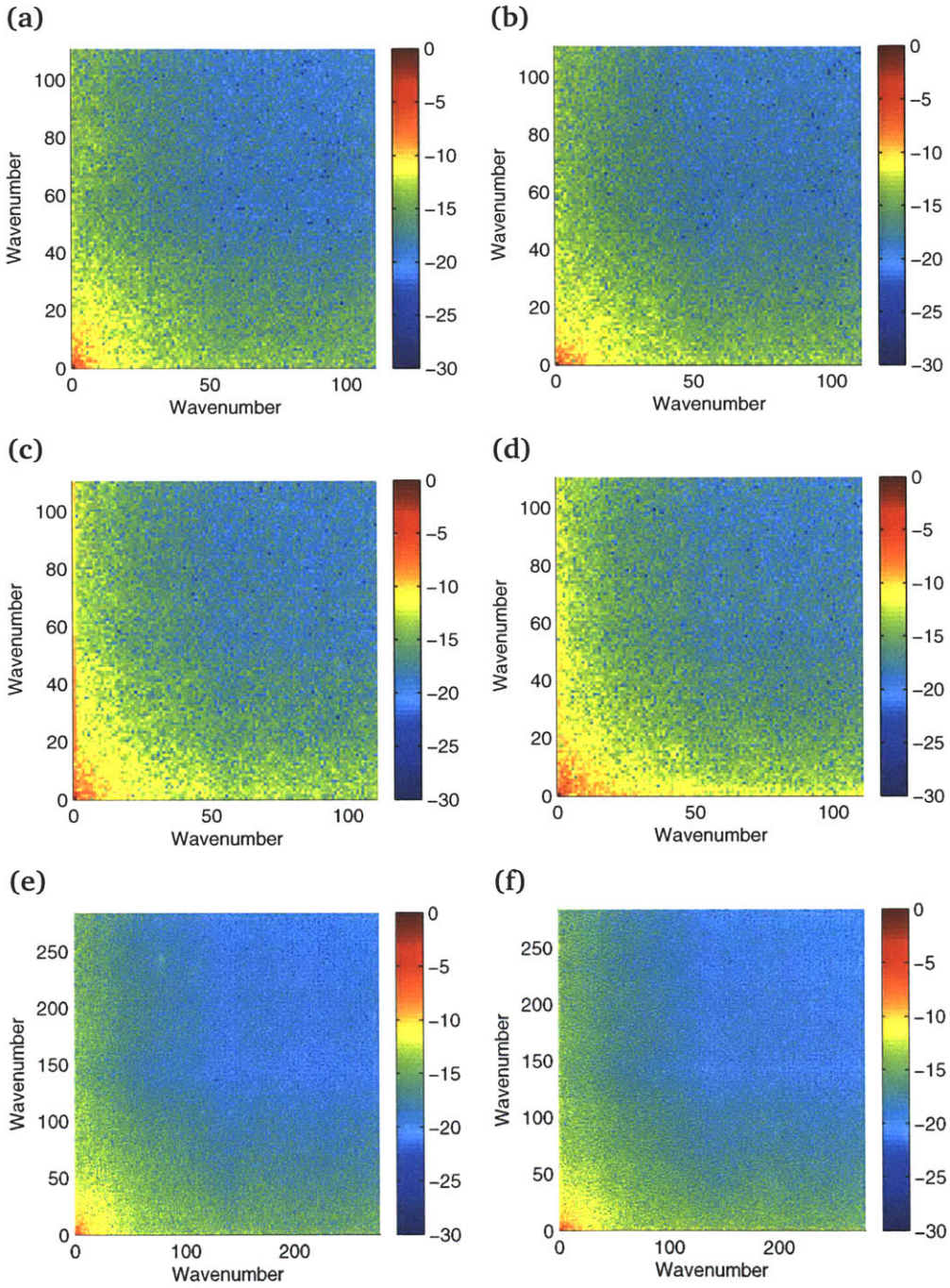

Figure 5-19: Two-Dimensional Normalized Log Power Spectra of Observed and Randomized (SHF Algorithm) Slope for Domains. Marabá-Altamira Domain **(a)** Observed and **(b)** Randomized; Tapajós-Santarém Domain **(c)** Observed and **(d)** Randomized; Rondônia Domain **(e)** Observed and **(f)** Randomized.

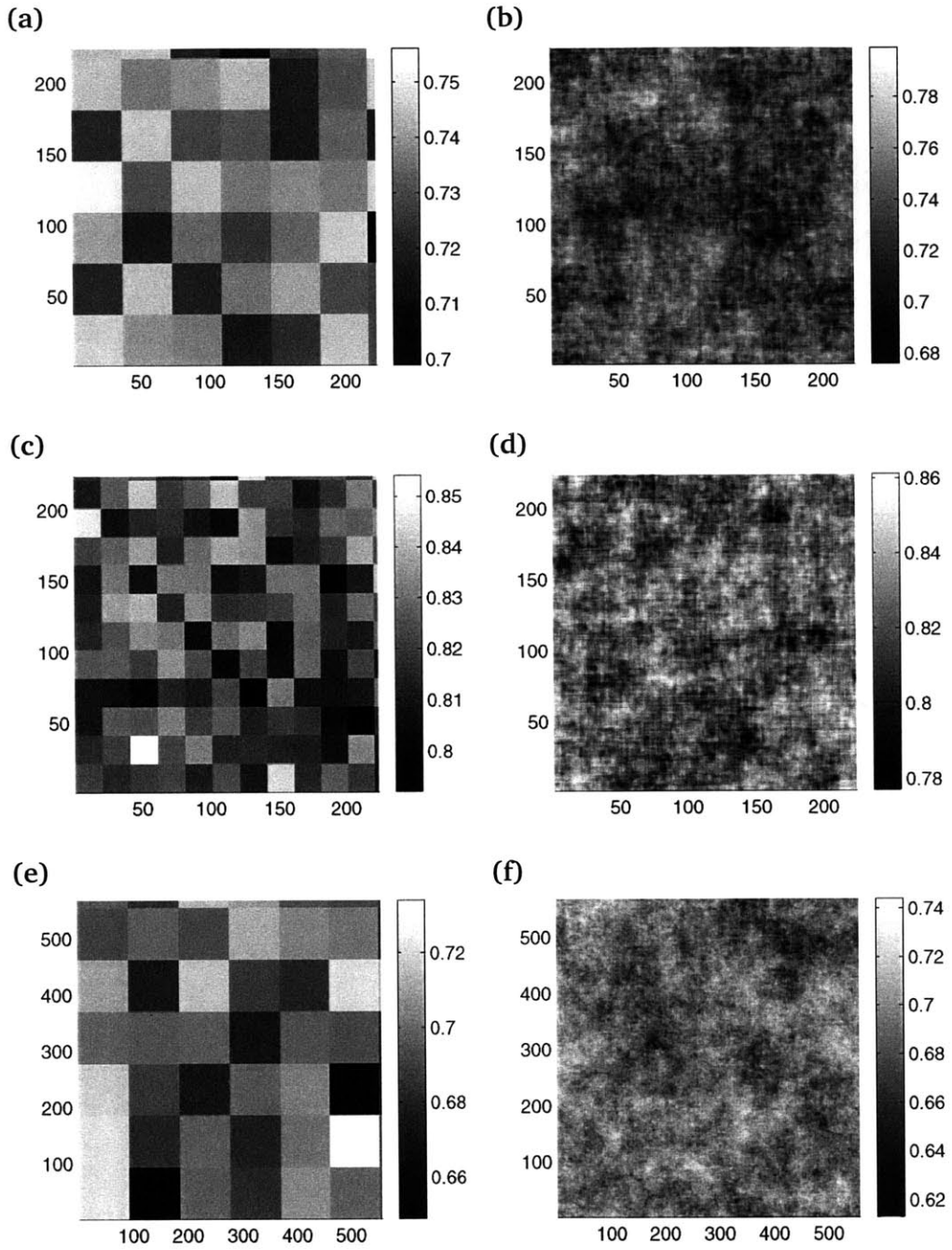

Figure 5-20: Sum of Randomized Deforestation Patterns. Marabá-Altamira Domain **(a)** CSR (36-km Block-Scale) and **(b)** SHF (4-km, 50%); Tapajós-Santarém Domain **(c)** CSR (20-km Block-Scale) and **(d)** SHF (4-km, 50%) ; Rondônia Domain **(e)** CSR (92-km Block-Scale) and **(f)** SHF (4-km, 50%).

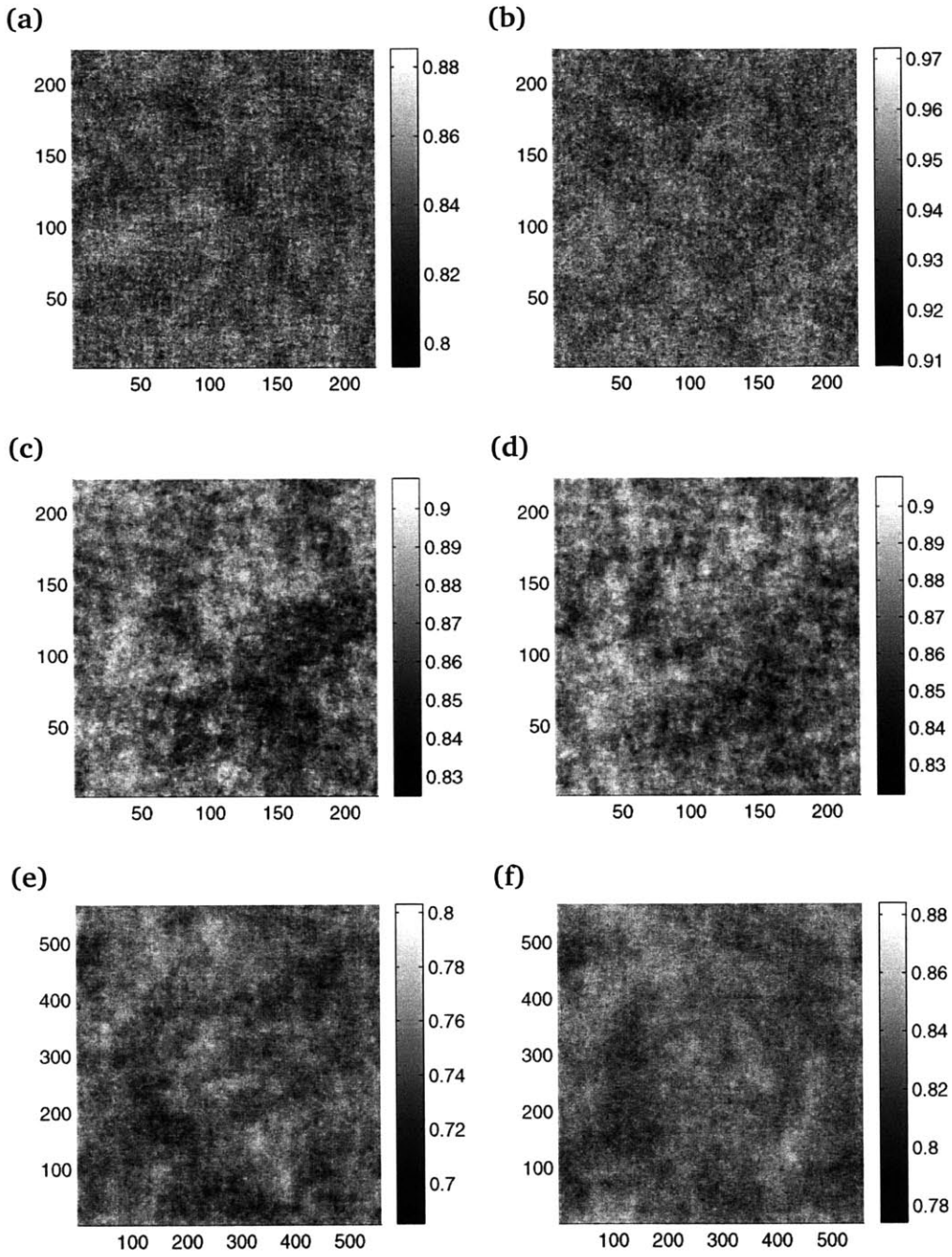

Figure 5-21: Sum of Randomized Deforestation Patterns. Marabá-Altamira Domain **(a)** SHF (1-km, 50%) and **(b)** SHF (1-km, 30%); Tapajós-Santarém Domain **(c)** SHF (1-km, 50%) and **(d)** SHF (1-km, 30%) ; Rondônia Domain **(e)** SHF (1-km, 50%) and **(f)** SHF (1-km, 30%).

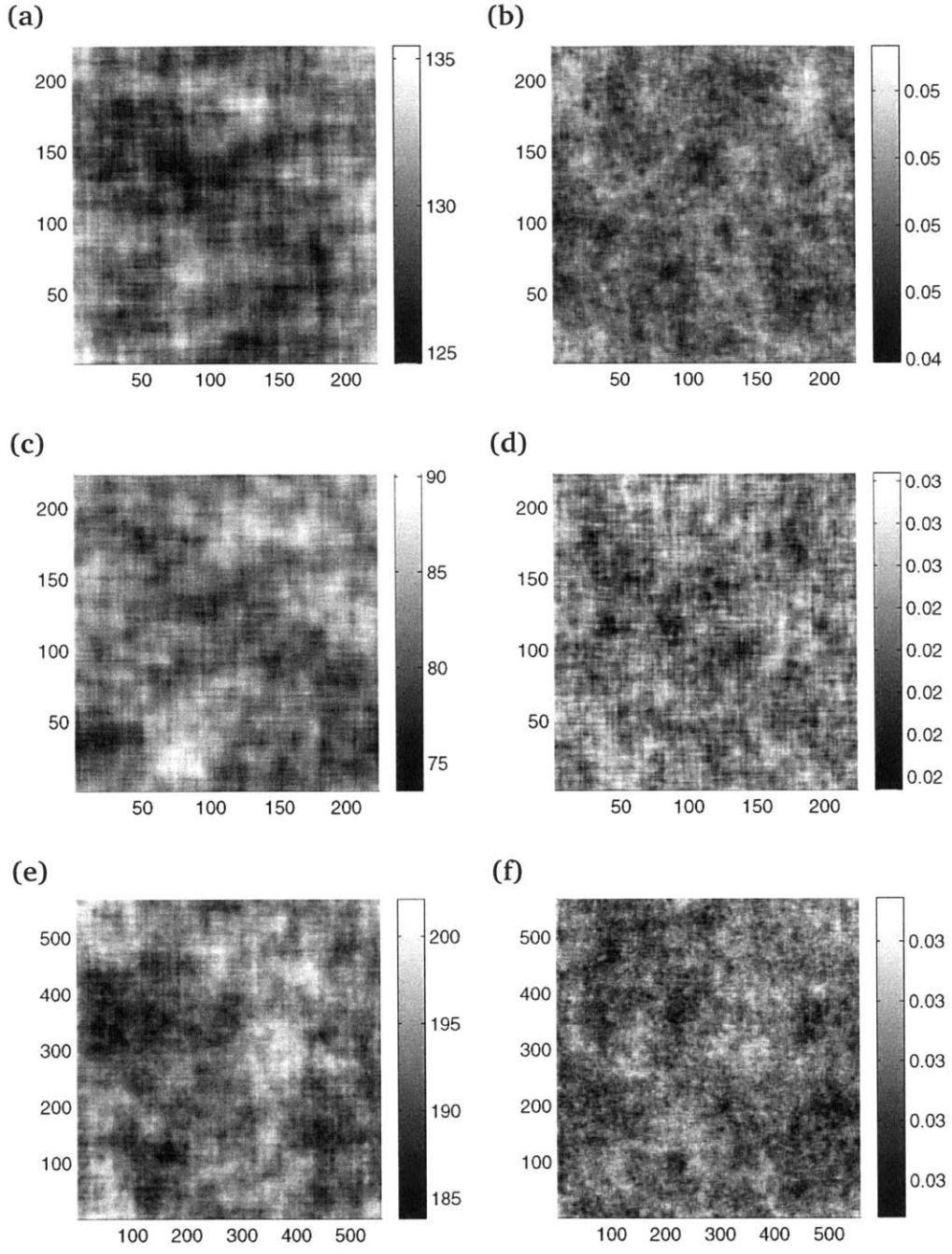

Figure 5-22: Sum of Randomized Elevation and Slope Patterns. Marabá-Altamira Domain **(a)** Elevation and **(b)** Slope; Tapajós-Santarém Domain **(c)** Elevation and **(e)** Slope ; Rondônia Domain **(f)** Elevation and **(h)** Slope.

REFERENCES

FARR, T. G. and M. KOBRICK. Shuttle Radar Topography Mission produces a wealth of data. *American Geophysical Union EOS*, 81:pages 583–585 [2000].

HANSEN, M. C., R. S. DEFRIES, J. R. G. TOWNSHEND, M. CARROLL, C. DIMICELI and R. A. SOHLBERG. Global Percent Tree Cover at a Spatial Resolution of 500 Meters: First Results of the MODIS Vegetation Continuous Field Algorithm. *Earth Interactions*, 7:pages 1–15 [2003].

RABUS, B., M. EINEDER, A. ROTH and R. BARNIER. The Shuttle Radar Topography Mission - A New Class of Digital Elevation Models acquired by Spaceborne Radar. *Photogrammetry Remote Sensing*, 57:pages 241–262 [2003].

CHAPTER 6

SHALLOW CLOUDS & DEFORESTATION

The hypothesis that will be tested in this chapter is that human-driven land surface changes, such as tropical deforestation, tend to create local circulations that result in higher shallow cloud densities over cleared areas[1]. This chapter will also test whether external factors (e. g., synoptic atmospheric circulation conditions) influence the prevalence of any forest-cloud associations.

6.1 Presentation of Results

This short section will introduce the different ways in which the results from the analyses of the cloud-forest statistics are presented, and serves as a guide to the rest of the chapter. The results are presented in three different ways:

1. monthly time-series;
2. monthly climatology;
3. seasonal climatology.

The monthly time-series represents the evolution of a key-statistics along the record length with the associated 99% confidence interval bounds. These confidence limits represent the upper and lower limits of the distribution of the key-statistics derived from the randomized forest-cover patterns. When the 'observed' key-statistic is contained within the 99% confidence limits, then the null-hypothesis is verified and we conclude that there is no clear association (or correlation) between the forest-cover and the shallow cloud cover (see Chapter 5). An example annotated figure of the time-series representation is given in Figure 6-1.

[1]The actual null-hypothesis posed in Chapter 5 is that forest-cover and shallow clouds are unrelated. Rejection of the null-hypothesis is tantamount to acceptance of the hypothesis as stated.

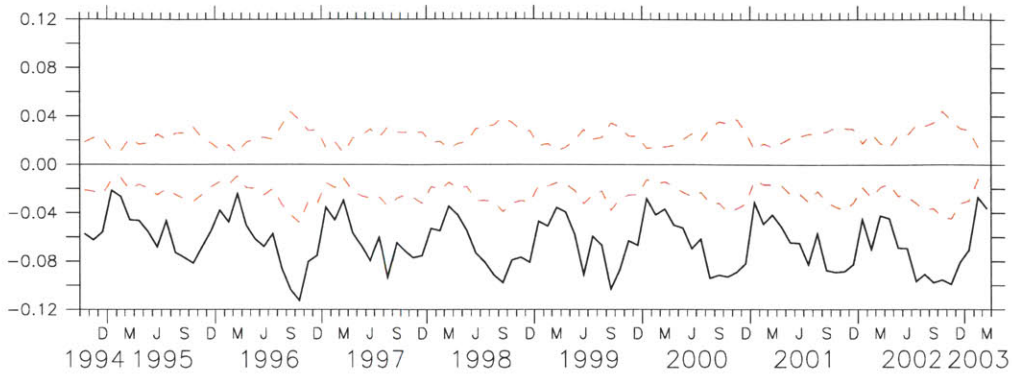

Figure 6-1: Example of CDD Monthly Time-Series.

The monthly climatology representation summarizes the monthly time-series by counting the number of times that the 'observed' statistic lies outside the 99% confidence limits for a particular month of the calendar year. The count is then normalized by the total number of such months, so that we have a monthly frequency of null-hypothesis rejection. Lastly, the "direction" with which the null-hypothesis is rejected is recorded by assigning a negative sign to occurrences where the 'observed' statistic is smaller than the lower confidence limit, and positive numbers to occurrences where the 'observed' statistic is greater than the upper confidence limit. The seasonal climatology is simply an weighted-average (i. e., weighted by the number of months on record) of the monthly climatology. Annotated examples of the monthly and seasonal climatology representations are given in Figure 6-2. To

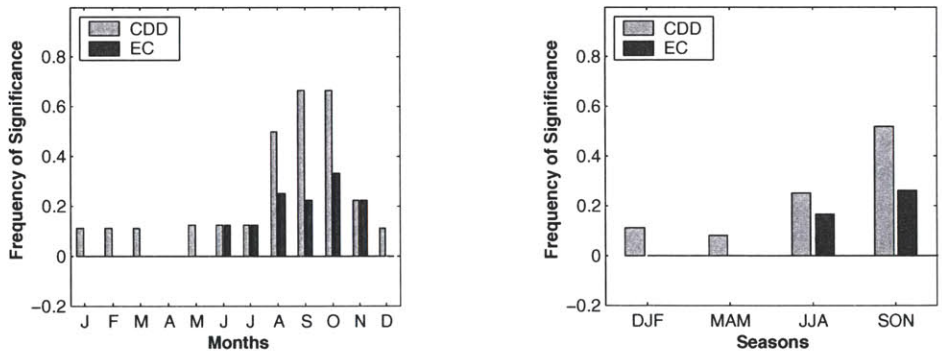

Figure 6-2: Example of Monthly and Seasonal Result Climatologies.

test the sensitivity of the results to external factors, a method of result stratification is used. The daily time series are stratified depending on whether an external factor is met (i. e., differentiating even numbered days from odd numbered days). Two monthly averages for observed and randomized statistics are then generated, and the significance of null-hypothesis rejection frequency can be compared according

to the external factor value.

6.2 Robustness of Results

The aim of this section is to determine the overall robustness of the method used, and hence the validity of the results derived from the method. The first technical aspect of the method under scrutiny is the scale of the blocks or tiles used in the randomization of the forest-cover patterns. This scale is particularly crucial in the CSR randomization algorithm, as it directly dictates the randomly generated scale of the disturbance (i. e., deforestation). The second algorithmic aspect under examination is the actual choice of randomization algorithm (i. e., CSR vs. SHF). The SHF algorithm will conserve the full spectrum of the disturbance scale (up to the scale of the tile used to shuffle the original patterns), and is intuitively the more "intelligent" randomization algorithm. The comparison will be useful to determine the actual sensitivity of the results to such algorithmic differences. After the sensitivity of the results to block-scale and randomization algorithm have been examined, the comparison of EC significance between randomization algorithms and the theoretical binomial distribution will be examined. A good agreement between the results derived from random forest-cover patterns and the theoretical distribution of EC will lend further credence to the methods. Finally, the sensitivity of the results to the choice of resolution and threshold to determine the forest-cover pattern will be examined. Since the actual differentiation between "forested" and "deforested" states is dependent upon the selection of a threshold of percentage forestcover, this last analysis goes beyond the examination of the method's robustness in that it may also highlight the nature of the relation, if any, that exists between forest-cover and shallow cloud patterns (i. e., is there an association between actual deforestation and shallow clouds, or rather between heterogeneous forest-cover and shallow clouds?)

6.2.1 Sensitivity to CSR block-scale

The sensitivity of the 99% CDD confidence limits to the block-scale used in the CSR randomization is shown in Figures 6-3 & 6-4 for all three study domains at 14h45 UTC and 17h45 UTC, respectively. The most prevalent feature in both figures is the highly sensitive nature of the confidence limits to the block-scale; small block-scales result in narrow confidence ranges, and large block-scales result in wider confidence ranges. The 'observed' statistic is thus more likely to be found significantly different from the distribution of randomized statistics when these randomized statistics are derived from small block-scale randomized forest-cover patterns. However, as explained in Chapter 5, the significance may be artificial. The significance is only meaningful when the block-scale used to randomize the forest-cover pattern is chosen such that the randomized pattern conserves the orig-

inal disturbance scale.

As expected, Figures 6-5 & 6-6 show that the block-scale used in randomizing the forest-cover pattern has very little impact on the EC significance. This was discussed in Chapter 5. It is due to the fact that the EC is a binomial counting variable, and the probability of counting an event is theoretically independent of the block-scale. Further discussion about the comparison of theoretically and empirically derived EC confidence limits follows in the next section. In all subsequent sections, CSR results will be derived using the following block-scales: 36-km for the Marabá-Altamira domain, 20-km for the Tapajós-Santarém domain and 92-km for the Rondônia domain. These scales were all chosen to be multiples of 4 because the CSR algorithm is always applied to comparisons with the forest-cover maps that are aggregated to 4-km with a 50% forest-cover threshold; and these scales are all representative of the measured scale of the disturbance on the 4-km, 50% threshold forest-cover maps (c. f., Chapter 5, Section 5.2).

6.2.2 Comparison to Theoretical Exceedence Count (EC)

The monthly EC time-series in Figures 6-5 & 6-6 also show the confidence limits derived theoretically from the binomial distribution[2]. These limits are in general agreement with the CSR derived confidence limits for both the Marabá-Altamira and Rondônia domains. In these two domains, the discrepancies between the empirically generated and theoretically derived confidence limits occur conspicuously during period when the observed EC is outside the 99% confidence bounds (regardless of how they are generated). Moreover, the theoretically derived confidence limits are much narrower than the CSR confidence limits for the Tapajós-Santarém domain at all times; note here that the observed EC for the Tapajós-Santarém domain is almost constantly outside the 99% confidence bounds. Figure 6-7 shows the differences between the theoretical and empirical (SHF algorithm) EC confidence limits for two confidence levels, 99% and 50%. The differences are most pronounced in the Tapajós-Santarém domain, and do not seem to diminish considerably for the lower confidence level. An explanation of these discrepancies is necessary, and is provided here.

Table 6.1: Sensitivity of Theoretical 99% EC Distribution Limits to p

p	Upper 99% Confidence Bound	Lower 99% Confidence Bound
0.9	30	22
0.7	27	14
0.3	16	3
0.1	8	0

[2]The limits are calculated using Equation 5.14 in Chapter 5, and take the actual number of good data days in a month (i. e., there are bad-data days, and their number is subtracted from n.)

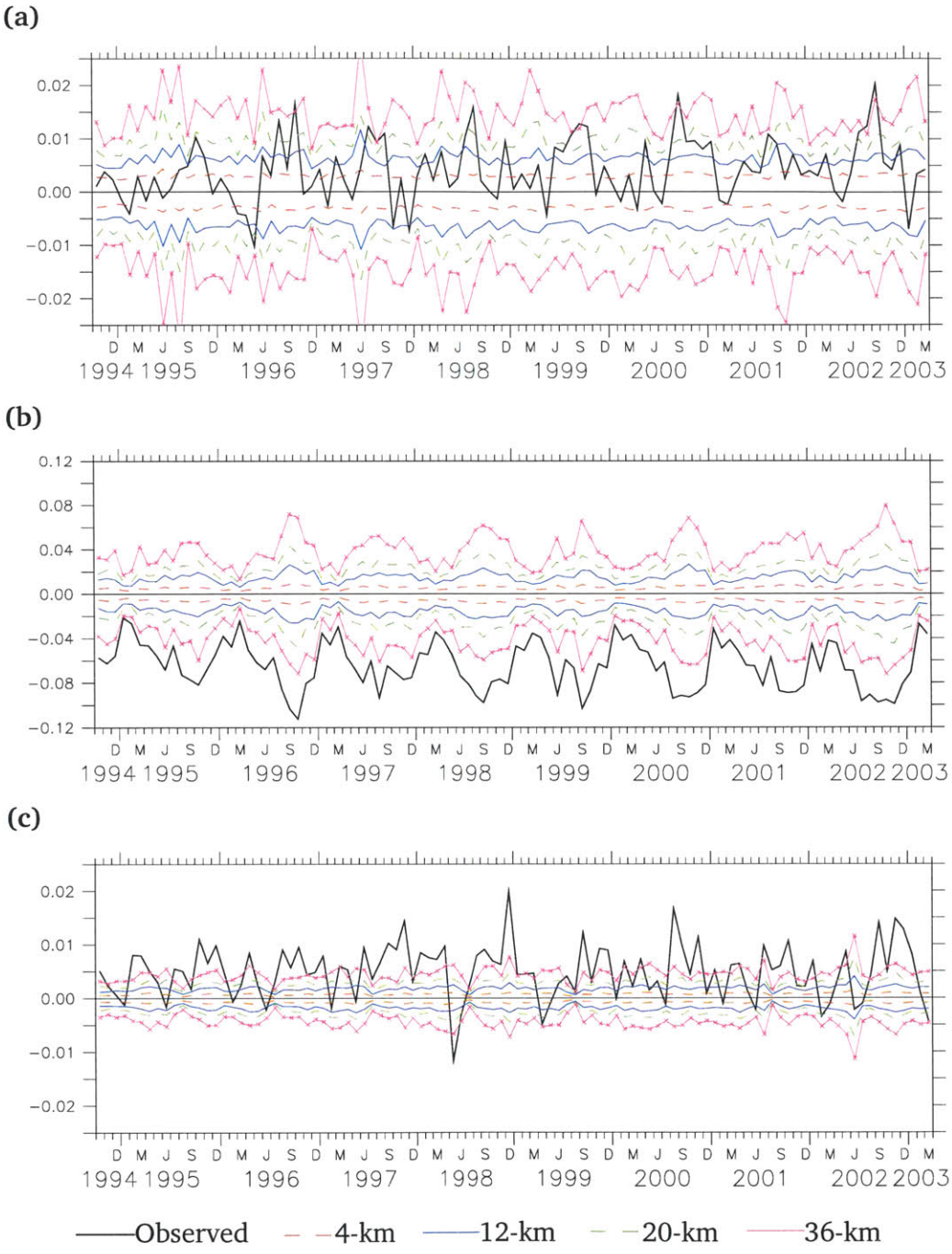

Figure 6-3: CDD Time-Series and CSR Block-Scale Dependent 99% Confidence Limits (14h45 UTC) for **(a)** Marabá-Altamira; **(b)** Tapajós-Santarém; and **(c)** Rondônia Domains.

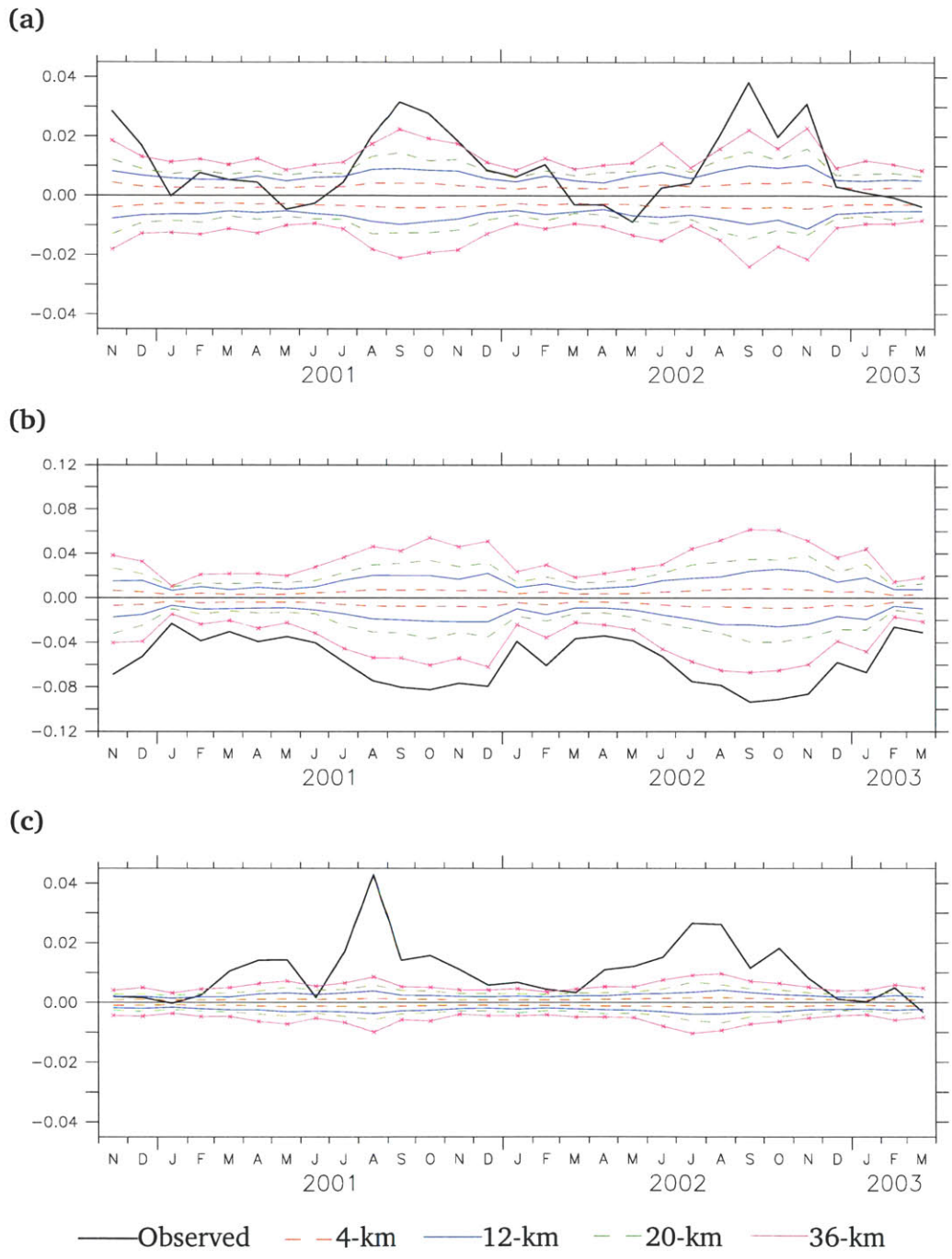

Figure 6-4: CDD Time-Series and CSR Block-Scale Dependent 99% Confidence Limits (17h45 UTC) for **(a)** Marabá-Altamira; **(b)** Tapajós-Santarém; and **(c)** Rondônia Domains.

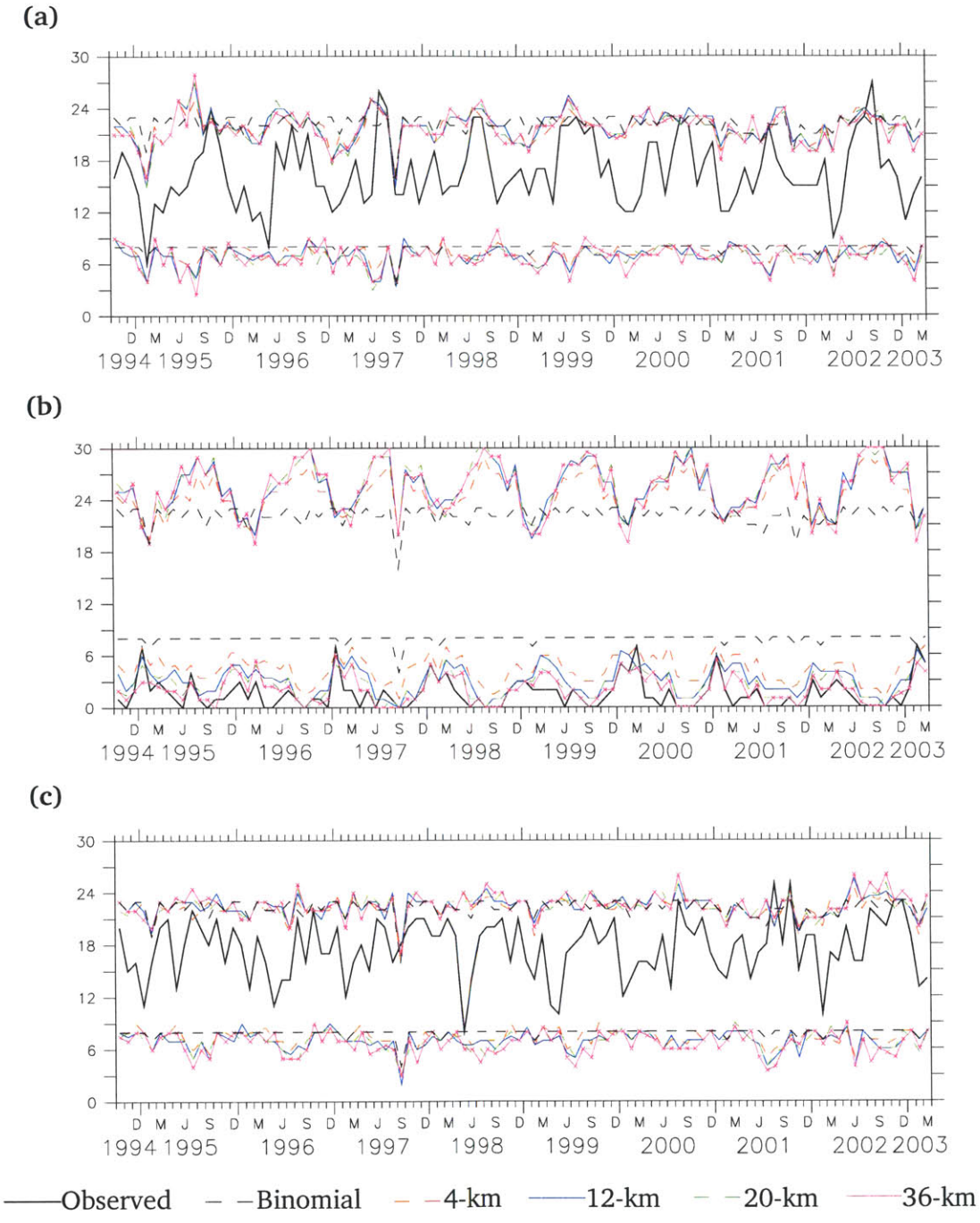

Figure 6-5: EC Time-Series and CSR Block-Scale Dependent 99% Confidence Limits (14h45 UTC) for **(a)** Marabá-Altamira; **(b)** Tapajós-Santarém; and **(c)** Rondônia Domains.

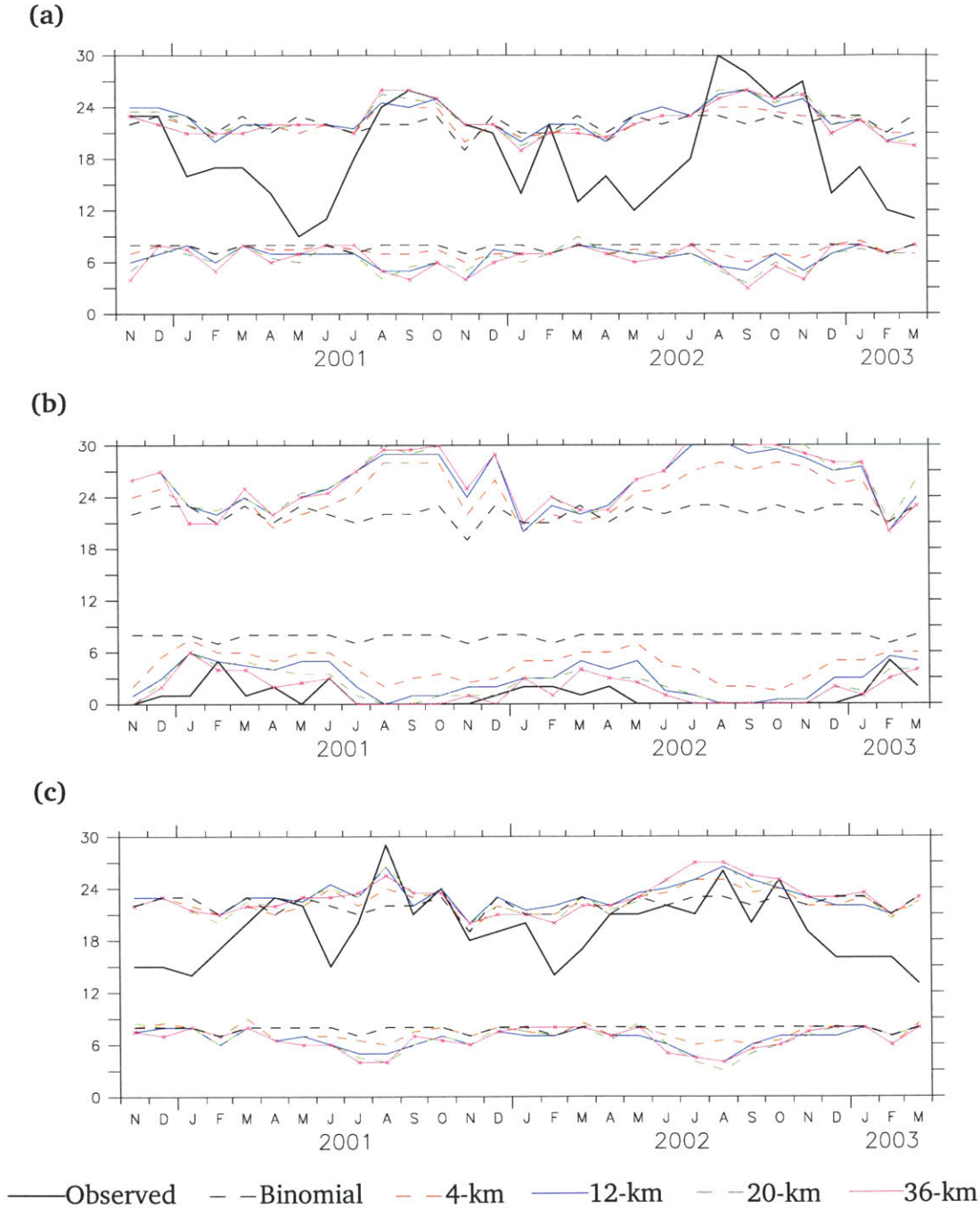

Figure 6-6: EC Time-Series and CSR Block-Scale Dependent 99% Confidence Limits (17h45 UTC) for **(a)** Marabá-Altamira; **(b)** Tapajós-Santarém; and **(c)** Rondônia Domains.

The theoretical confidence limits are derived with the binomial equation (Eq. 5.14) presented in Chapter 5 with the assumption that p, or the probability that the cloud density over deforested areas exceeds the cloud density over forested areas, is exactly 0.5 under the null-hypothesis. Recalling this binomial equation,

$$P(EC_n = k) = \binom{n}{k} p^k (1-p)^{n-k}, \tag{6.1}$$

there are only two parameters that can be responsible for the discrepancy: p and n. It has already been stated that the n used to derive the theoretical limits takes into account the number of bad-data days for each month, and can thus not be held responsible for the discrepancy. The sensitivity of the theoretical limits to p are outlined in Table 6.1 for a fixed n of 30. It is shown that the magnitude of the theoretical limits are highly sensitive to the count probability.

The case of the river-land contrast in the Tapajós-Santarém domain is very useful here to explain the discrepancy. Indeed, the land-water contrast creates a strong local circulation, analogous to the sea-breeze phenomenon[3]. The strength of this circulation is highlighted in Figure 6-8, which shows the monthly sum of detected shallow clouds for a sample month (i. e., November 2000). There is a clear suppression of shallow clouds over the river. The highly organized nature of the shallow cloud patterns may result in what can be described as an effective variability in p. In essence, the highly organized nature of the cloud field engenders a wider distribution of the randomized statistic due to the inevitable occurrence of random deforestation patterns that will be associated with the cloud field. The EC variable is integrated over the number of days in a particular month. The fact that the cloud field exhibits such a tight association with the underlying forest cover will give rise to similar patterns from day to day; a random forest cover field that has either most forest pixels under of not under the clouds will result in an extreme value for the randomized statistic, and thus a wider distribution.

The existence of the imperfect-randomization bias explained above should vanish as the confidence range is narrowed. Indeed, the difference between the theoretical and empirical confidence limits diminishes (Figure 6-7) as the confidence interval narrows because there are less chances of being affected by extreme values. This artefact renders the empirically derived distribution of key-statistics wider, and thus makes the statistical test based on the empirically generated confidence intervals "stricter" in essence. It is arguably fictitiously stricter; nonetheless, it is important to note that, based on the grounds given above, it is improbable that this artefact would result in artificially narrower confidence bounds, and will thus not probably result in spuriously significant results.

The monthly and seasonal climatology representations of the results shown in Figures 6-9, 6-10 & 6-11 compare the frequency of significance of the EC statistic between the CSR, SHF and theoretical (BIN) confidence limits. As stated in Chapter 5, these algorithms are based on the 4-km aggregated forest-cover map using a

[3]The phenomenon here is actually an inland sea-breeze.

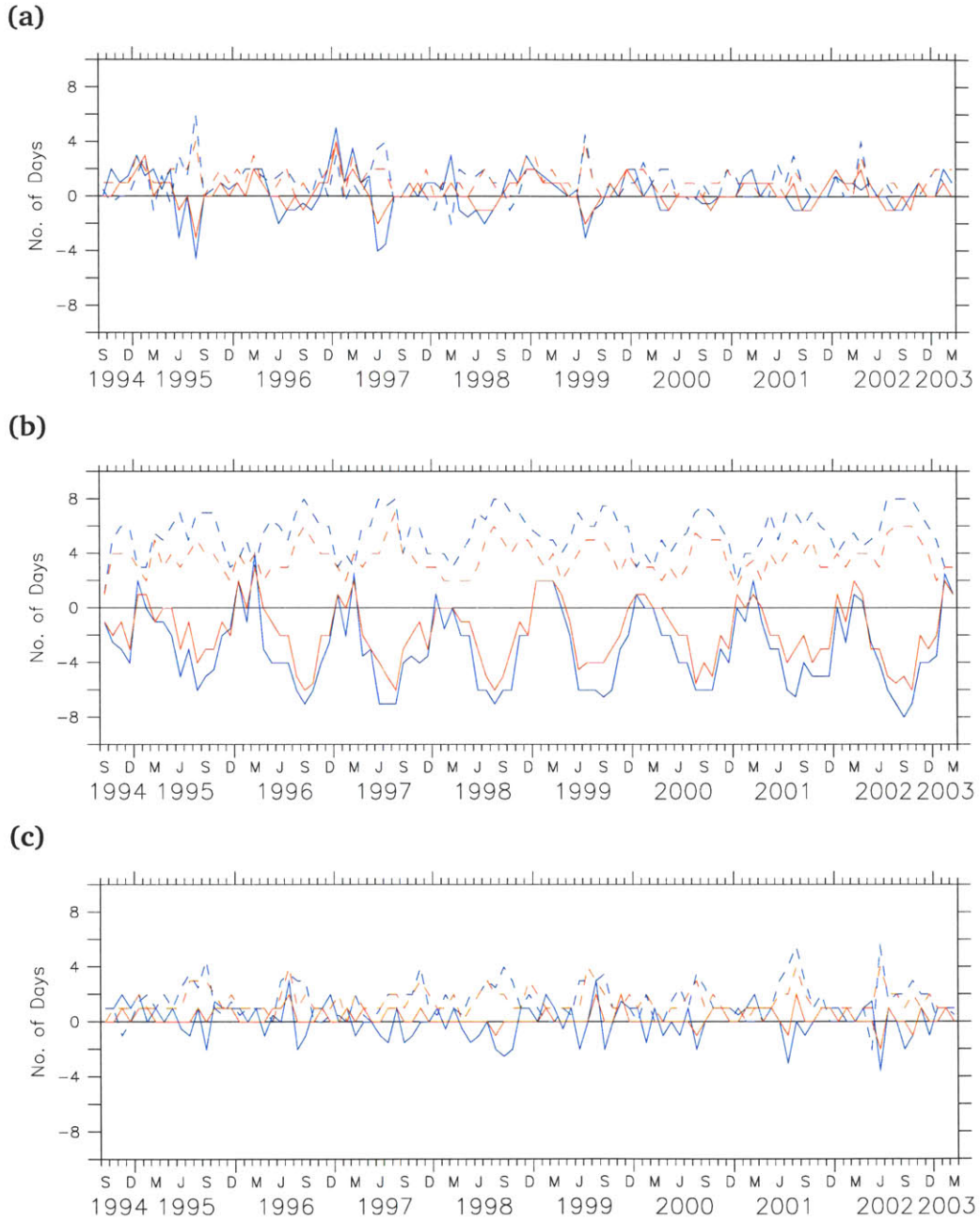

Figure 6-7: Difference between Theoretical and Empirical EC Confidence Limits; Blue (red) line represents difference between 99% (50%) confidence interval; Solid (dashed) line represents difference between upper (lower) limits; **(a)** Marabá-Altamira; **(b)** Tapajós-Santarém; and **(c)** Rondônia Domains.

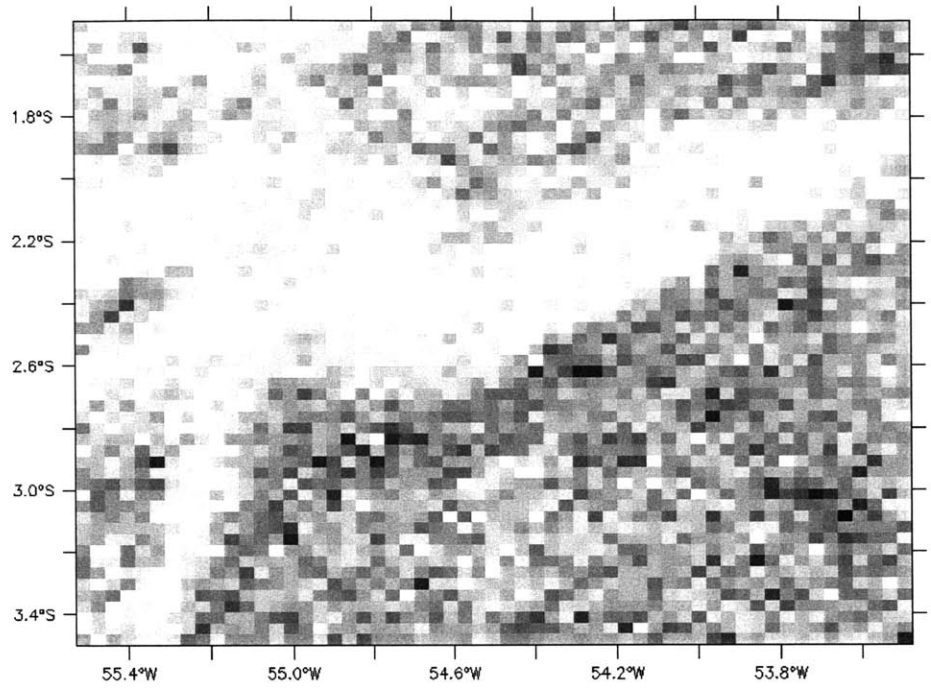

Figure 6-8: Sum of Shallow Cloud Counts over Tapajós-Santarém domain (CUTRIM Algorithm; 14h45 UTC, November 2000).

threshold to differentiate forested from deforested pixels of 50% forest-cover. While the different methods are in general agreement, there are some notable differences. For example, the month of October of Figure 6-9–**(a)** shows that the CSR derived EC significance frequency is greater than the SHF one, which is in turn greater that the BIN (i. e., theoretical) one. The month of November of Figure 6-9–**(e)** shows that the CSR derived EC significance frequency is positive, while those of the SHF and BIN are zero. Otherwise, the theoretically derived frequency of EC significance is always greater than the empirically derived frequencies. In all, there is a good general agreement between the empirical and theoretical methods. This is further supported by the overall agreement in the seasonal aggregation (Figures 6-10 & 6-11–**(b)**).

The reasoning given above can be extended to include possible artefacts in the empirically derived confidence limits for the CDD statistic. The highly organized nature of cloud cover coupled with the possibility that the randomness of some of the 1,000 realizations of forest-cover might coincide with this organization will translate into a higher variability in the empirically generated CDD distribution, and will thus cause wider confidence bounds. It may thus be confidently stated that this type of random bias will not result in spuriously rejecting the null-hypothesis.

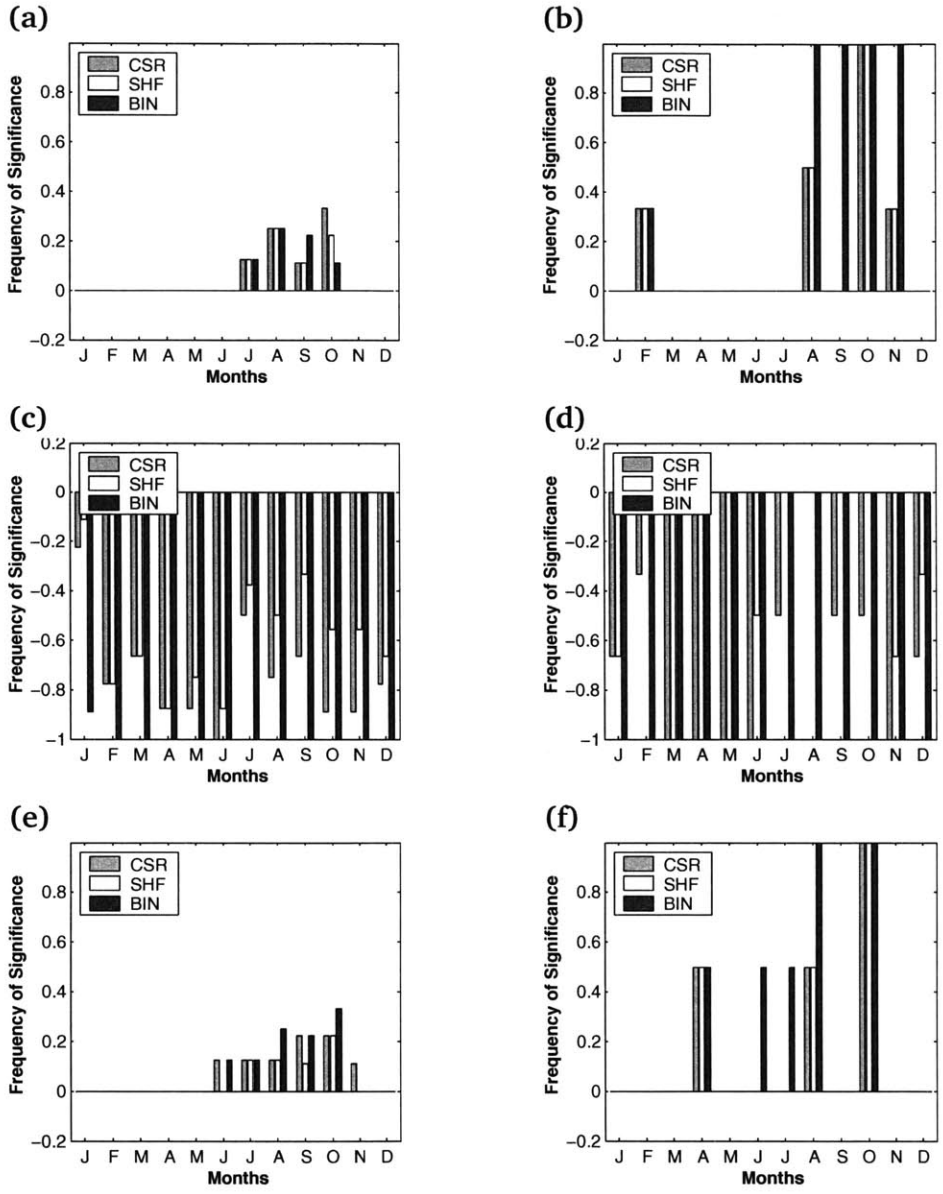

Figure 6-9: Comparison between Theoretical and Derived Monthly EC significance; bars represent normalized number of times that a statistic is significant for a specific month; positive (negative) is for number of times that statistic is greater (smaller) than upper (lower) bound of 99% confidence interval. Frequency of EC significance for Marabá-Altamira at **(a)** 14h45 UTC and **(b)** 17h45 UTC; for Tapajós-Santarém at **(c)** 14h45 UTC and **(d)** 17h45 UTC; for Rondônia at **(e)** 14h45 UTC and **(f)** 17h45 UTC.

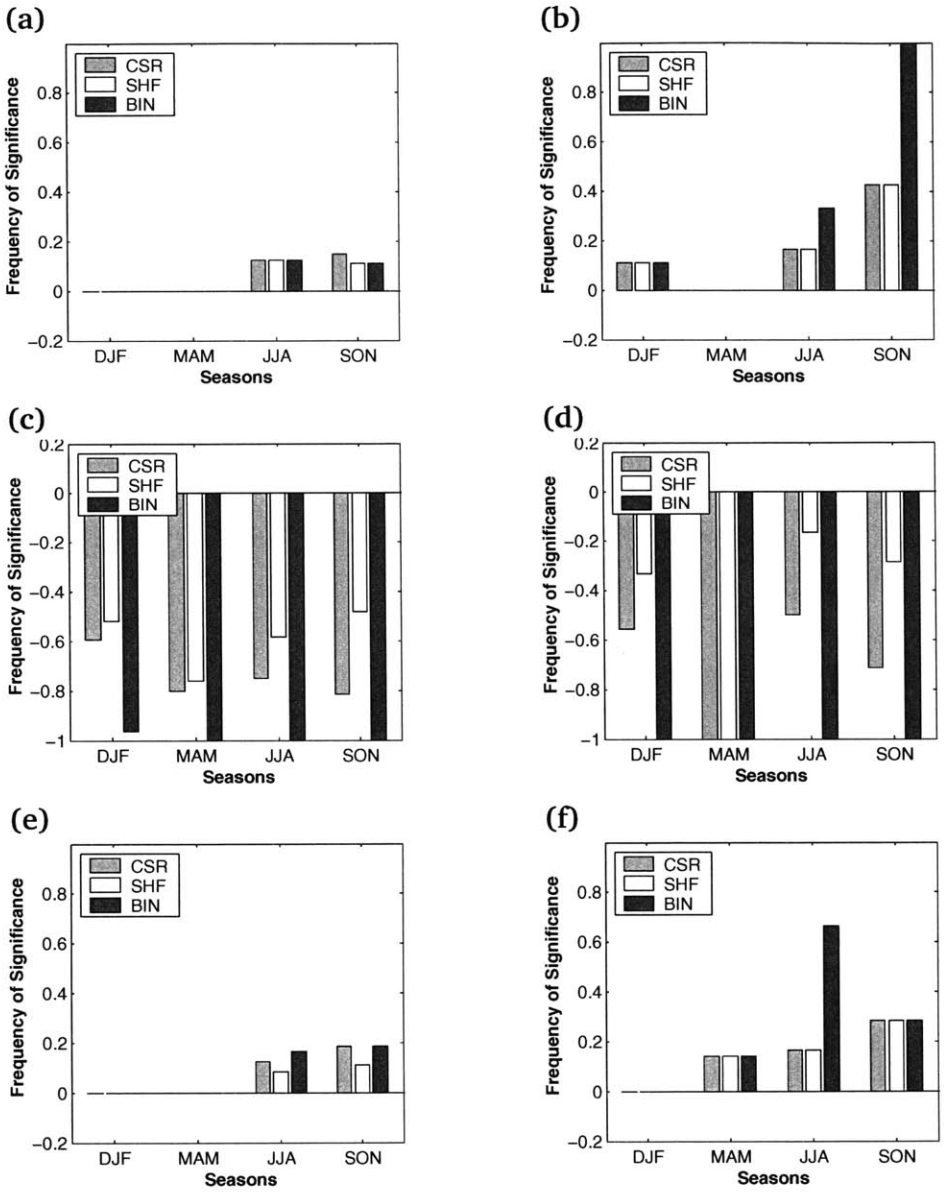

Figure 6-10: Comparison between Theoretical and Derived Seasonal EC significance; bars represent normalized number of times that a statistic is significant for a specific month; positive (negative) is for number of times that statistic is greater (smaller) than upper (lower) bound of 99% confidence interval. Frequency of EC significance for Marabá-Altamira at **(a)** 14h45 UTC and **(b)** 17h45 UTC; for Tapajós-Santarém at **(c)** 14h45 UTC and **(d)** 17h45 UTC; for Rondônia at **(e)** 14h45 UTC and **(f)** 17h45 UTC.

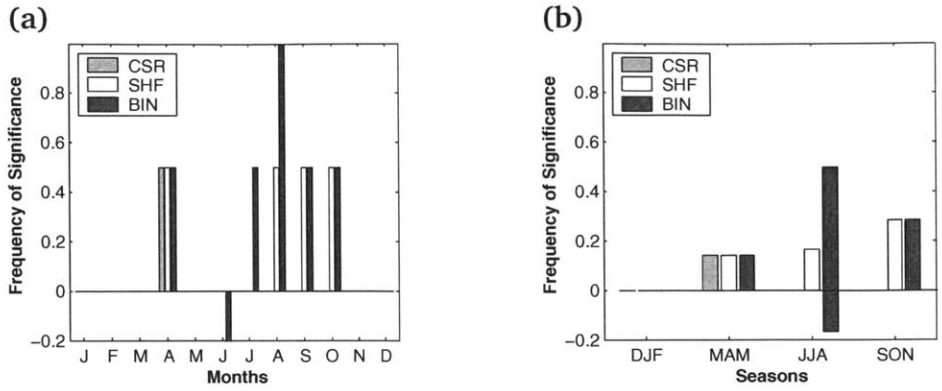

Figure 6-11: Comparison between Theoretical and Derived EC significance for Rondônia at 20h45 UTC; bars represent normalized number of times that a statistic is significant for a specific month; positive (negative) is for number of times that statistic is greater (smaller) than upper (lower) bound of 99% confidence interval. **(a)** Monthly and **(b)** seasonal frequency of EC significance at 20h45 UTC.

6.2.3 Sensitivity to Randomization Algorithm

In light of the general agreement between the empirically generated and theoretically derived EC confidence bounds, it is now appropriate to consider the variations in results caused by the different forest-cover randomization algorithms. Here, the differences between the SHF and CSR algorithms based on the 4-km aggregated, 50% threshold forest-cover maps are examined. The monthly and seasonal comparisons of 14h45 UTC CDD and EC are presented in Figures 6-12 & 6-13. While the CSR algorithm seems to result in less frequency of significance than the SHF algorithm in some cases (i. e., Fig. 6-12–**(a)** & **(e)** and Fig. 6-13–**(a)** & **(e)**), the inverse is also observed in other cases (i. e., Fig. 6-12–**(b)**, **(d)** & **(f)** and Fig. 6-13–**(b)**, **(d)** & **(f)**). These variations highlight one generality: the frequency of CDD significance is higher under the SHF algorithm, while that of EC is higher under the CSR algorithm. This result is intriguing for it emphasizes a regular distinction between the CDD and EC measures, while these statistics should be slightly correlated due to their inter-relatedness.

Recalling the differences between the two statistics, the CDD is a measure of the intensity of the difference while the EC is a measure of the frequency of occurrence of any difference, however slight. These measures are slightly dependent (in the statistical sense); it is however possible to imagine a month during which there are equal occurrences of unit and null counts (i. e., the number of shallow clouds per unit area over deforested pixels being higher and lower than that over forested areas), thus making the EC insignificant. Yet, for the same case, it is possible that the magnitude of the difference is much greater each time the deforested cloud density exceeds the forested cloud density than when the inverse is happening; this

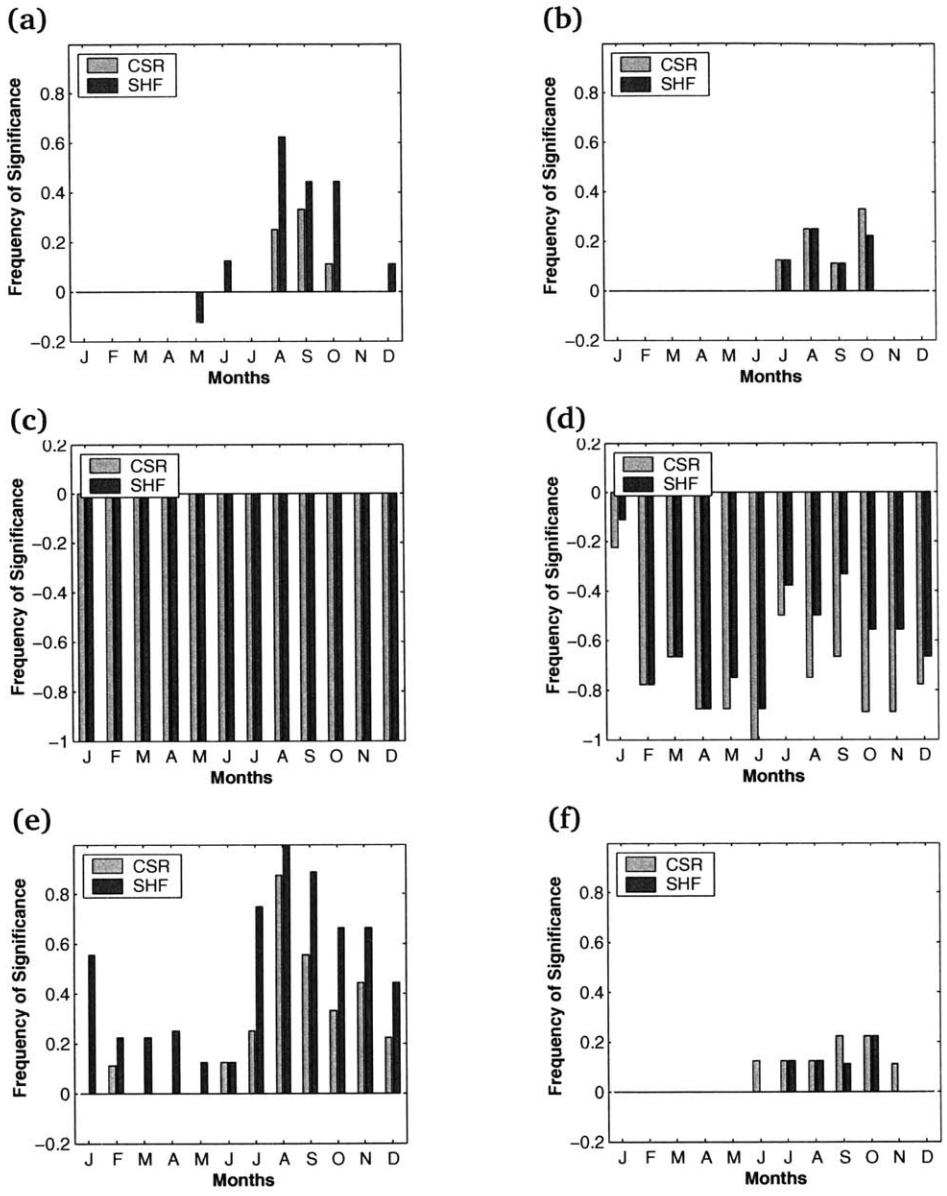

Figure 6-12: Sensitivity of monthly CDD and EC significance to randomization method at 14h45 UTC; bars represent normalized number of times that a statistic is significant for a specific month; positive (negative) is for number of times that statistic is greater (smaller) than upper (lower) bound of 99% confidence interval. Frequency of **(a)** CDD and **(b)** EC significance for Marabá-Altamira; Frequency of **(c)** CDD and **(d)** EC significance for Tapajós-Santarém; Frequency of **(e)** CDD and **(f)** EC significance for Rondônia.

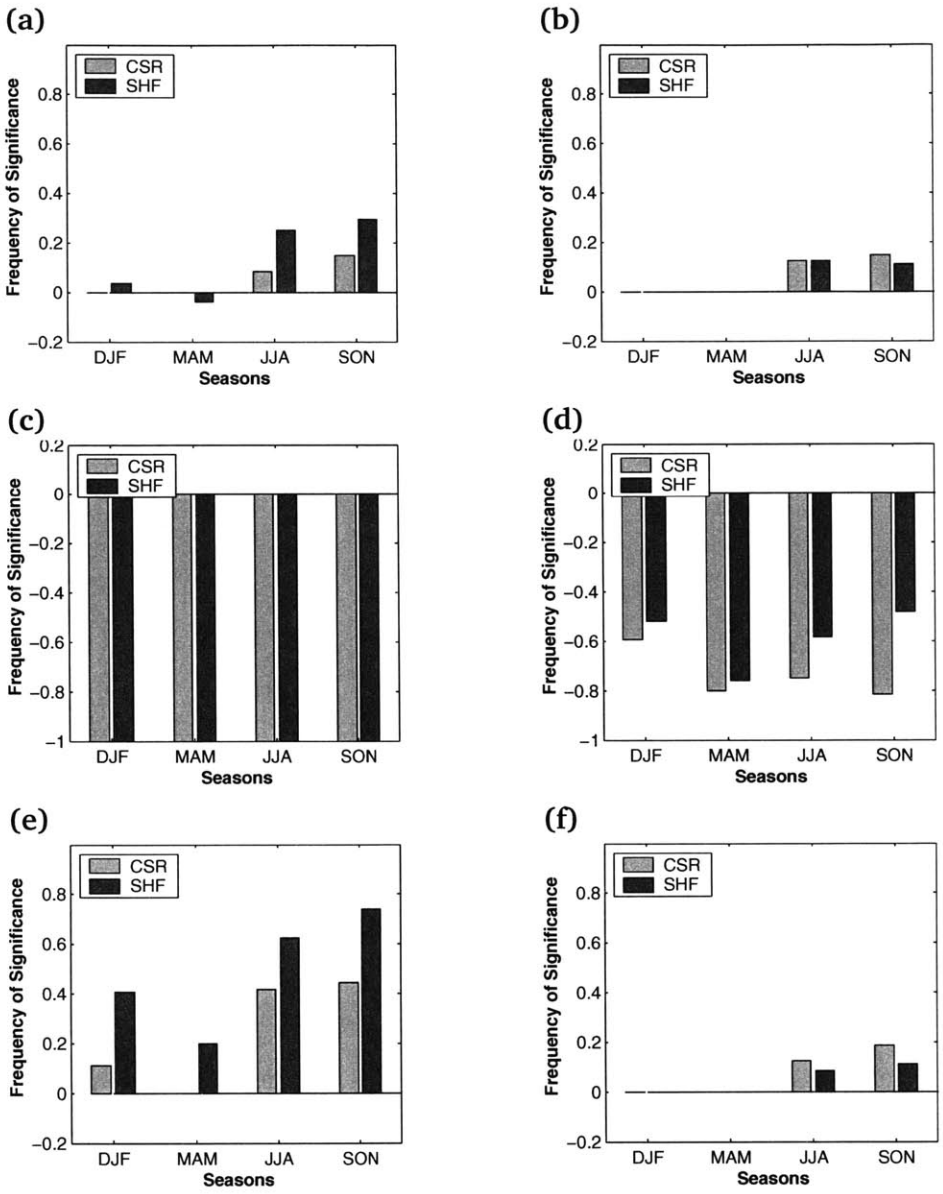

Figure 6-13: Sensitivity of seasonal CDD and EC significance to randomization method at 14h45 UTC; bars represent normalized number of times that a statistic is significant for a specific season; positive (negative) is for number of times that statistic is greater (smaller) than upper (lower) bound of 99% confidence interval. Frequency of **(a)** CDD and **(b)** EC significance for Marabá-Altamira; Frequency of **(c)** CDD and **(d)** EC significance for Tapajós-Santarém; Frequency of **(e)** CDD and **(f)** EC significance for Rondônia.

could result in a significant CDD statistic.

The evidence indicates that the confidence bounds for the EC are narrower for the SHF algorithm than for the CSR algorithm, and the confidence bounds for the CDD are narrower for the CSR algorithm than for the SHF algorithm. The CSR results presented in these figures are based on 36-km block scales for the Marabá-Altamira domain, 20-km block scales for the Tapajós-Santarém domain and 92-km block scales for the Rondônia domain. In Section 6.2.1, the sensitivity of the CDD confidence bounds to block-scale was highlighted for the CSR algorithm. Smaller block scales result is narrower confidence bounds. Yet, the sensitivity of the EC confidence bounds to the block-scale is much more subtle. Thus, it may be inferred that had smaller block scales been chosen to represent the results in Figures 6-12 & 6-13, the trend in CDD and EC significance would have been the same between the CSR and SHF algorithms. This intriguing difference is nothing more than additional evidence that the block-scale is a determining factor for the CSR algorithm. In light of this, and in light of the discussion related to scale in Chapter 5, Section 5.3, it is clear that while both randomization methods seem to produce coherent results, the best algorithm is the SHF since it inherently conserves the original disturbance scale. The SHF algorithm will thus be employed in the final results.

6.2.4 Sensitivity to Forest-cover Resolution & Threshold

The selection of the original binary forest-cover map (i. e., representing forested (land) and deforested (water) states in the three study domains) is not obvious. As discussed in Chapter 5, Section 5.2, three methods were employed to produce the original binary fields. These three methods result in very different deforestation maps (c. f., Figure 5-3). This section will look at the sensitivity of the analysis results to the selection of the original forest-cover map. The monthly and seasonal frequency of significance plots are shown in Figures 6-14 & 6-15; all represent the analysis results for the 14h45 UTC shallow clouds, and all are based on the SHF algorithm. The results are overall consistent across all resolutions and thresholds to determine the forest-cover maps.

The seasonal aggregation in Figure 6-15 shows that for the Marabá-Altamira domain, the CDD is most frequently significant with the TH50 forest-cover (i. e., 1-km resolution, 50% forest-cover threshold), whereas the EC is most frequently significant with the SHF forest-cover (i. e., 4-km resolution, 50% threshold). The exact opposite is true for the Rondônia domain. The sensitivity of the frequency of CDD significance to the forest-cover pattern is particularly interesting. The scale at which the maximum CDD significance frequency occurs is indicative of the scale of the mesoscale circulation that is initiated by the deforested disturbance. It should be noted that the latter statement is only valid under absence of strong advection. Indeed, the method tests for collocated cloud and forest patterns, and any significant advection of shallow convective clouds would render such scaling-related conclusions impossible. It is assumed here that shallow convection borne from the

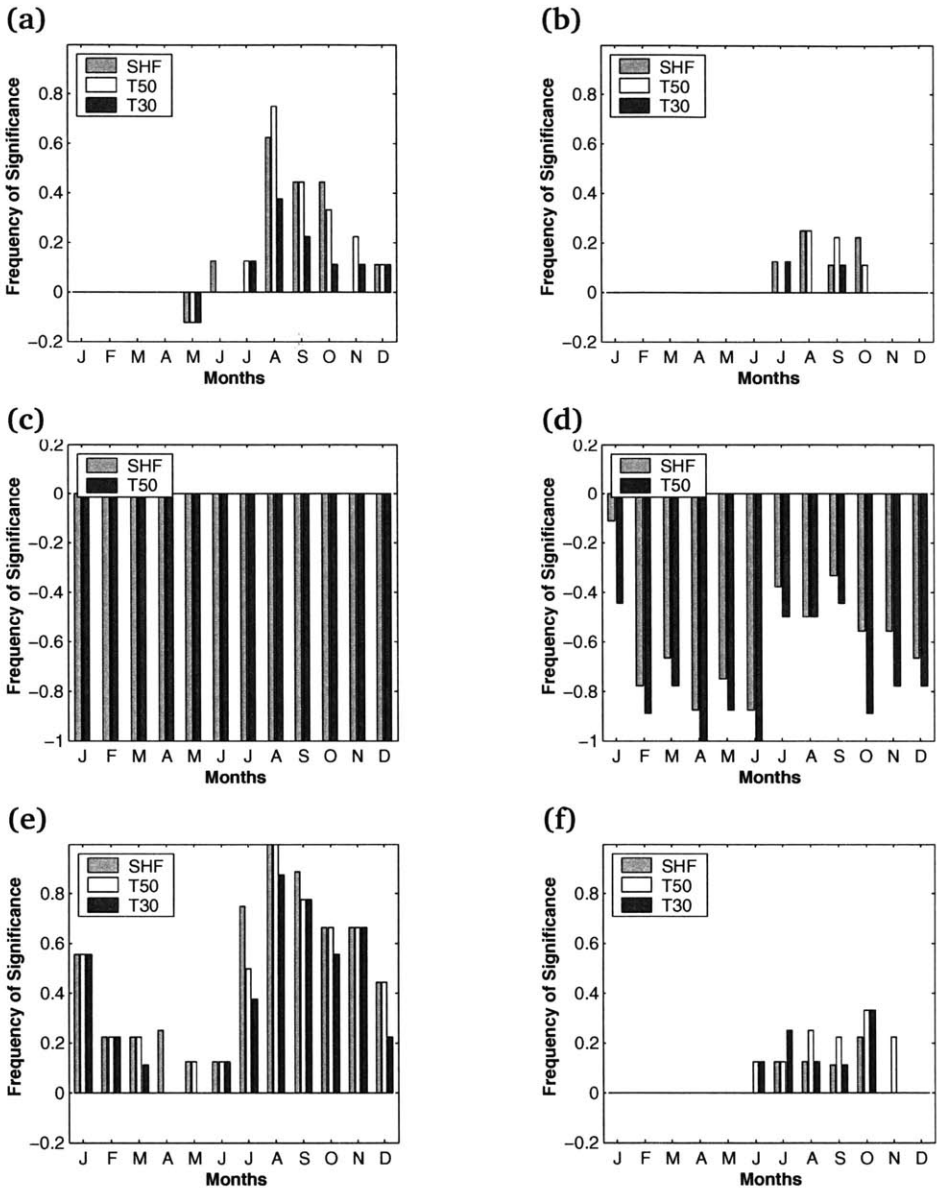

Figure 6-14: Sensitivity of monthly CDD and EC significance to randomization method at 14h45 UTC; bars represent normalized number of times that a statistic is significant for a specific month; positive (negative) is for number of times that statistic is greater (smaller) than upper (lower) bound of 99% confidence interval. Frequency of **(a)** CDD and **(b)** EC significance for Marabá-Altamira; Frequency of **(c)** CDD and **(d)** EC significance for Tapajós-Santarém; Frequency of **(e)** CDD and **(f)** EC significance for Rondônia.

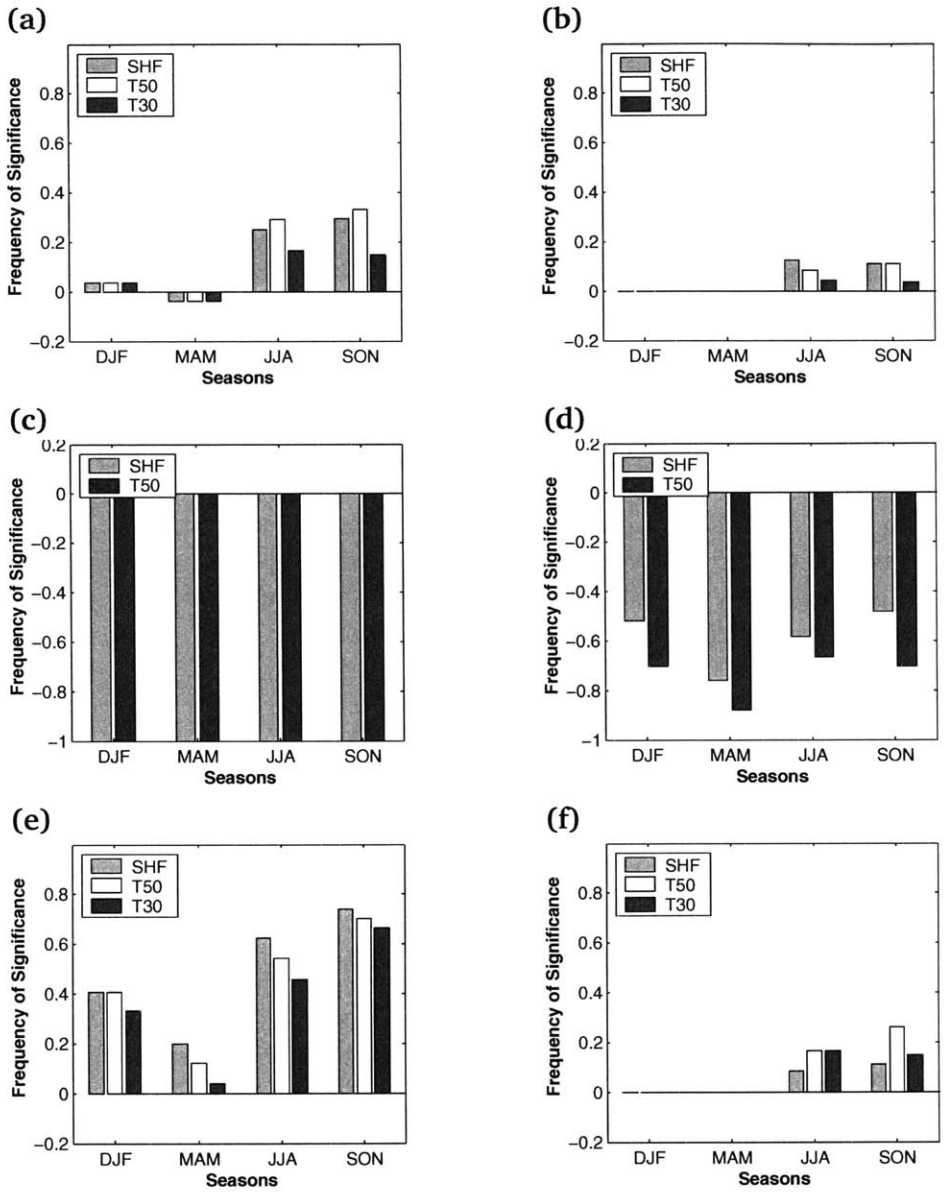

Figure 6-15: Sensitivity of seasonal CDD and EC significance to randomization method at 14h45 UTC; bars represent normalized number of times that a statistic is significant for a specific season; positive (negative) is for number of times that statistic is greater (smaller) than upper (lower) bound of 99% confidence interval. Frequency of **(a)** CDD and **(b)** EC significance for Marabá-Altamira; Frequency of **(c)** CDD and **(d)** EC significance for Tapajós-Santarém; Frequency of **(e)** CDD and **(f)** EC significance for Rondônia.

land-surface heating heterogeneity will invariably be collocated with the low-level convergence zone, and thus be roughly insensitive to advective winds. Since the convection studied here is forced by the land-surface and not by mid- or upper-atmospheric disturbances, it is thought that this assumption is rather safe; the subsidence required for mass-continuity would "kill" any shallow cumuli advected over forested areas.

In comparing the scales of land-surface heterogeneities to the scale of the organized mesoscale circulations that they produced in a numerical weather prediction model (RAMS), Roy *et al.* [2003] found that these organized circulations have a preferred length-scale in the range of 10~20-km regardless of the land-surface heterogeneity scale. In this case, the TH50 deforestation map for the Marabá-Altamira domain exhibits a disturbance scale on the order of 10-km, while the SHF deforestation map for Rondônia exhibits a disturbance scale on the order of 100-km. Thus the results derived from the sensitivity of the CDD significance frequency in this study seem to disagree with Roy *et al.* [2003]. Here, it is found that in the Marabá-Altamira domain, the scale of the resulting change in shallow cumulus clouds is indicative of the "actual" disturbance scale (or the fishbone pattern), while the scale of the change in shallow cumulus cloudiness in the Rondônia domain seems to be dictated by the scale of the heterogeneity of forest-cover.

6.2.5 Sensitivity to Shallow-Cloud Classification Algorithm

Two shallow cloud classification algorithms were introduced in Chapter 4, Section 4.4. The first algorithm (CUTRIM) uses constant thresholds, while the second algorithm is based on the *a-piori* retrieved clear-sky radiances, which are representative of the background radiances. Figures 6-16, 6-17 6-18 & 6-19 show the comparison of the frequency of significance of CDD and EC for both these algorithms at 14h45 & 17h45 UTC based on the TH50 forest-cover with the SHF randomization algorithm. Both algorithms are in good agreement, and neither conspicuously produces more frequency of significance of either CDD or EC. There are months where one algorithm produces a significant result while the other doesn't, but when the results are aggregated seasonally, the only big discrepancy occurs in Rondônia during SON at 17h45 UTC, when the second algorithm produces a significant EC, while the CUTRIM algorithm doesn't. The general robustness of the results with regards to cloud classification algorithm lends credence to both the cloud classification algorithms and the methods. Based on these results, the second cloud classification algorithm is selected for the rest of this study as it is less prone to erroneously classifying the background (land-surface) as cloud, and it's reliance on monthly varying clear-sky brightnesses, renders it more refined.

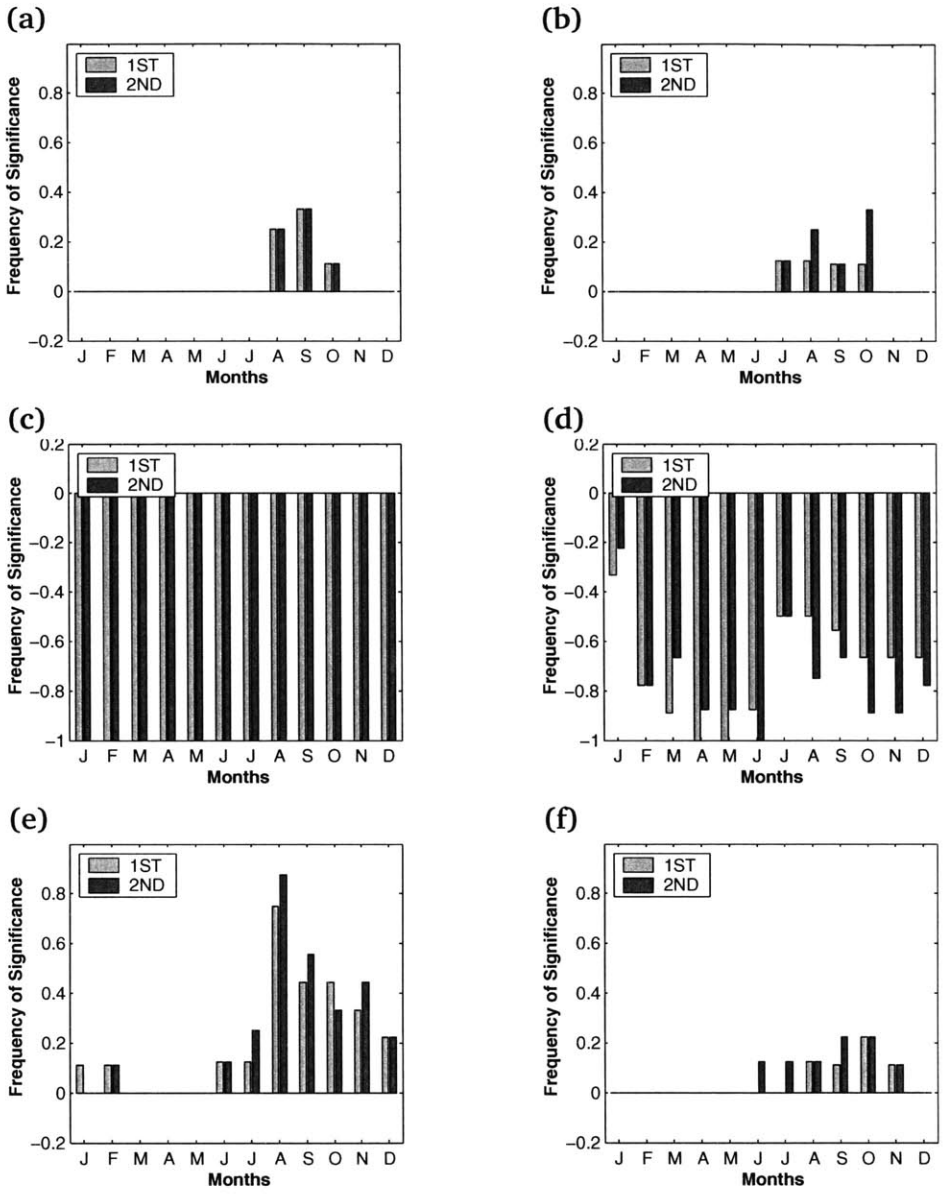

Figure 6-16: Comparison between Shallow Cloud Classification Algorithms of Monthly 14h45 UTC Climatologies of CDD and EC significance; bars represent normalized number of times that a statistic is significant for a specific month; positive (negative) is for number of times that statistic is greater (smaller) than upper (lower) bound of 99% confidence interval. **(a)** Frequency of CDD and **(b)** EC significance for Marabá-Altamira; **(c)** Frequency of CDD and **(d)** EC significance for Tapajós-Santarém; **(e)** Frequency of CDD and **(f)** EC significance for Rondônia.

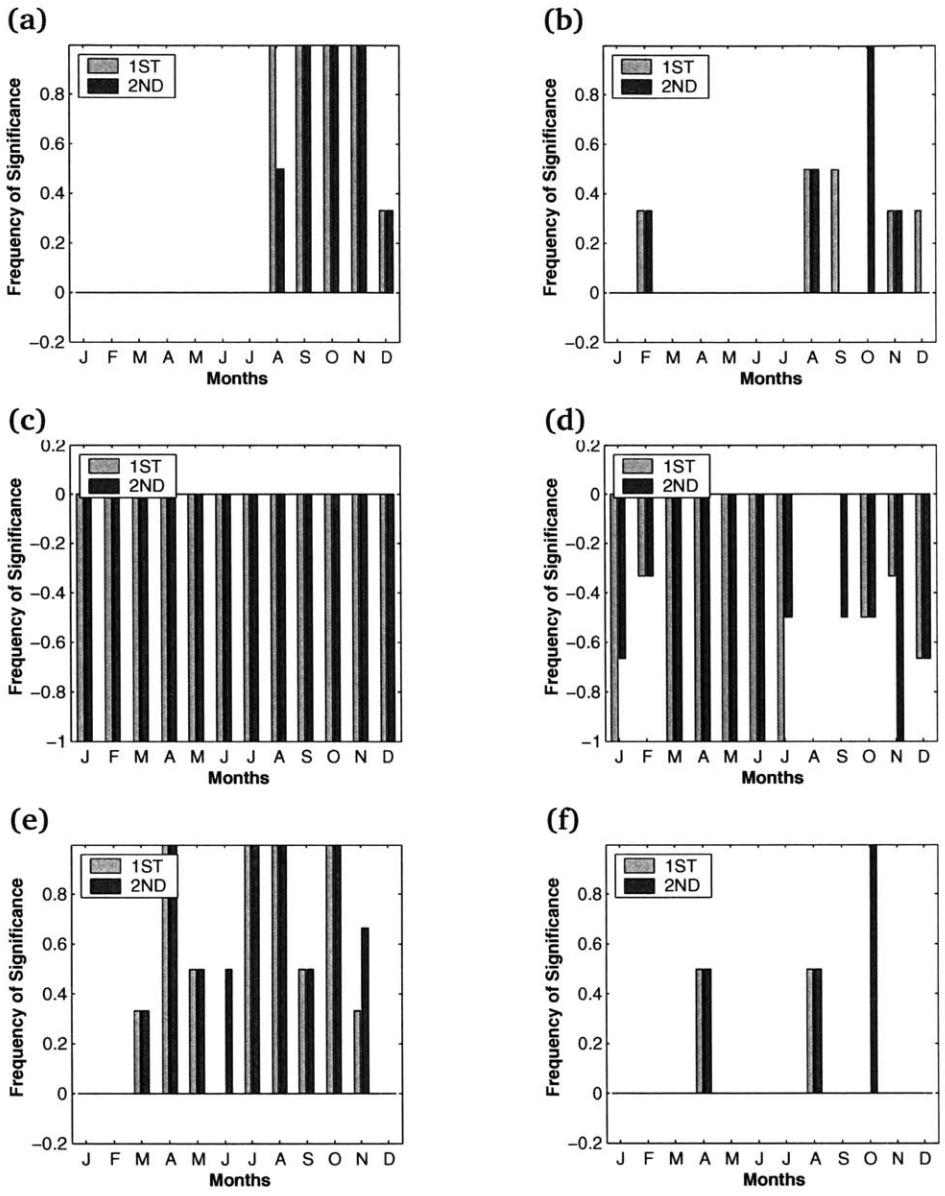

Figure 6-17: Comparison between Shallow Cloud Classification Algorithms of Monthly 17h45 UTC Climatologies of CDD and EC significance; bars represent normalized number of times that a statistic is significant for a specific month; positive (negative) is for number of times that statistic is greater (smaller) than upper (lower) bound of 99% confidence interval. **(a)** Frequency of CDD and **(b)** EC significance for Marabá-Altamira; **(c)** Frequency of CDD and **(d)** EC significance for Tapajós-Santarém; **(e)** Frequency of CDD and **(f)** EC significance for Rondônia.

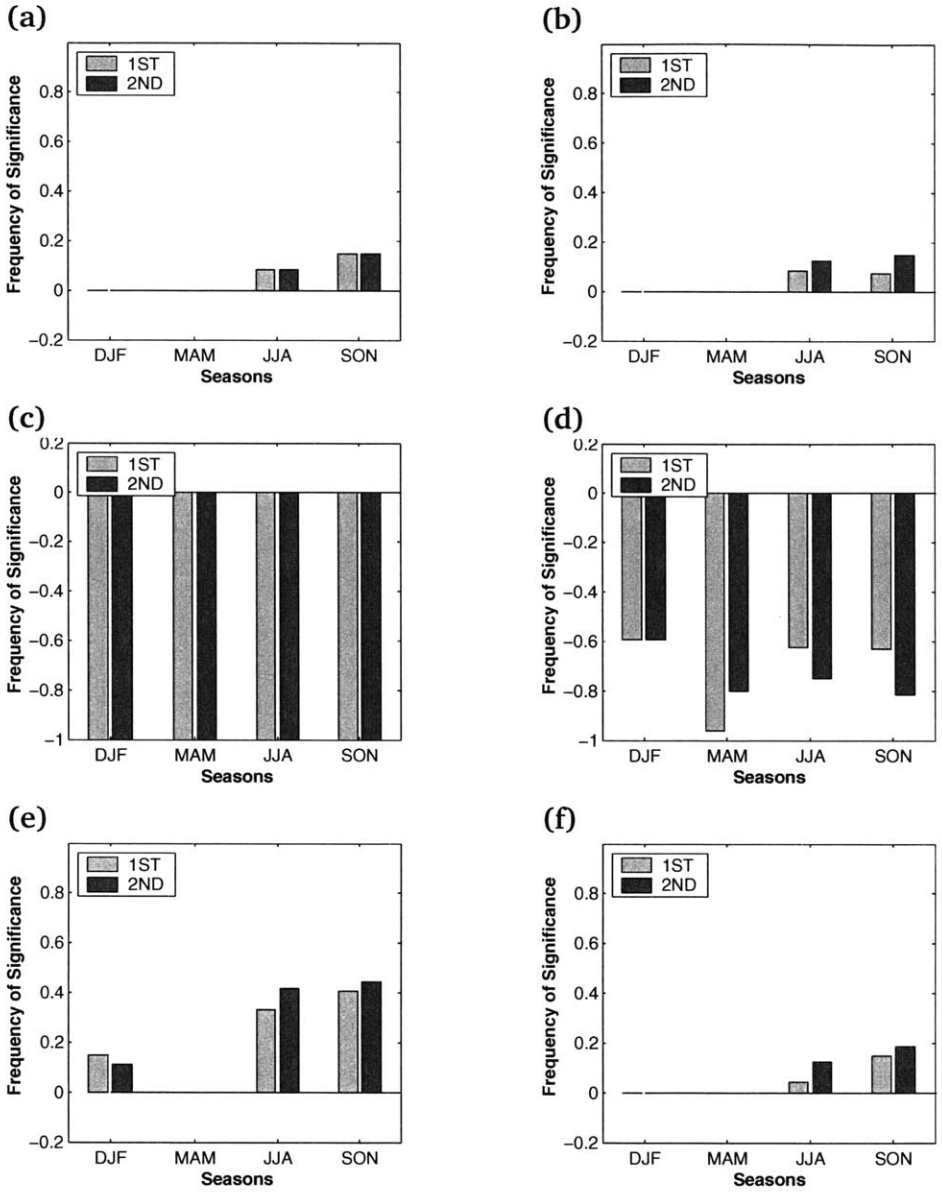

Figure 6-18: Comparison between Shallow Cloud Classification Algorithms of Seasonal 14h45 UTC Climatologies of CDD and EC significance; bars represent normalized number of times that a statistic is significant for a specific month; positive (negative) is for number of times that statistic is greater (smaller) than upper (lower) bound of 99% confidence interval. **(a)** Frequency of CDD and **(b)** EC significance for Marabá-Altamira; **(c)** Frequency of CDD and **(d)** EC significance for Tapajós-Santarém; **(e)** Frequency of CDD and **(f)** EC significance for Rondônia.

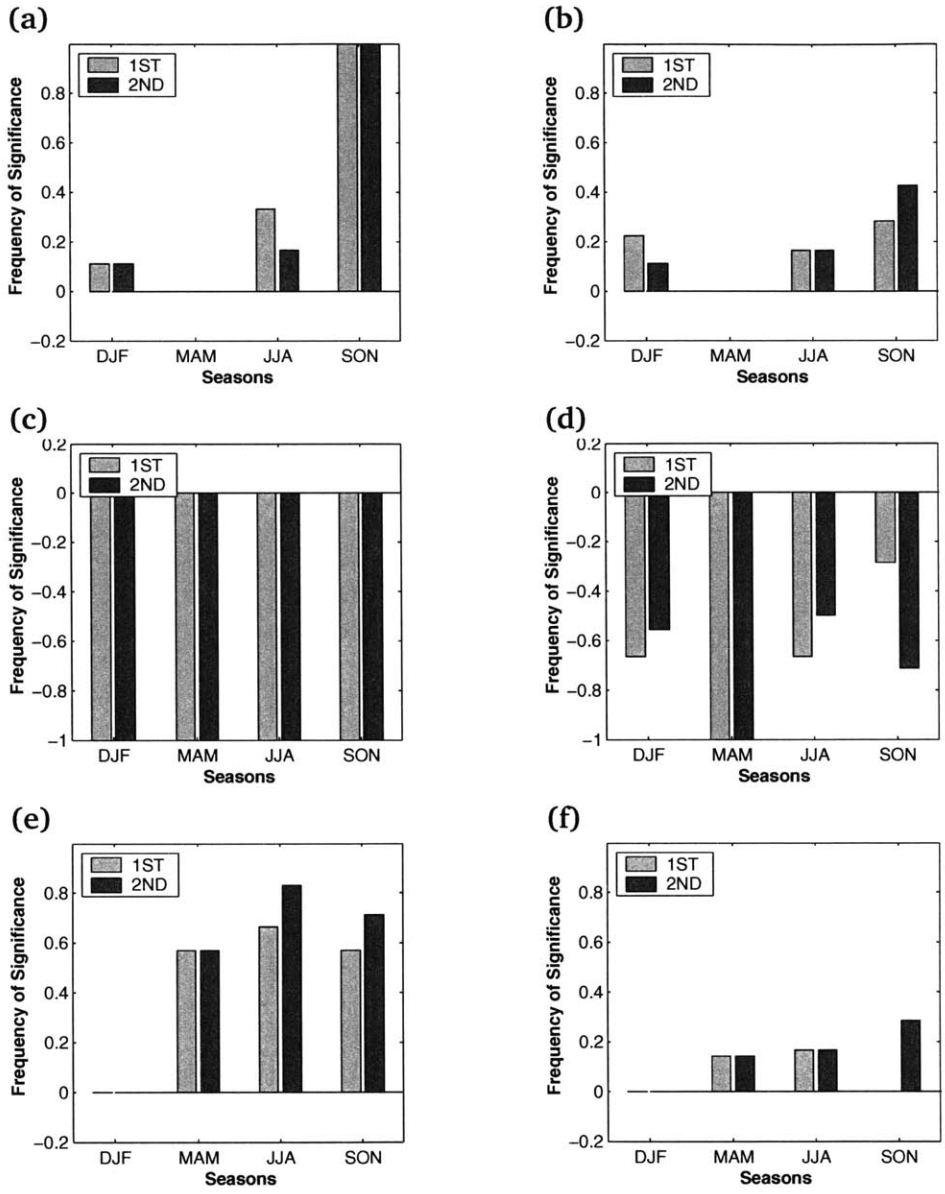

Figure 6-19: Comparison between Shallow Cloud Classification Algorithms of Seasonal 17h45 UTC Climatologies of CDD and EC significance; bars represent normalized number of times that a statistic is significant for a specific month; positive (negative) is for number of times that statistic is greater (smaller) than upper (lower) bound of 99% confidence interval. **(a)** Frequency of CDD and **(b)** EC significance for Marabá-Altamira; **(c)** Frequency of CDD and **(d)** EC significance for Tapajós-Santarém; **(e)** Frequency of CDD and **(f)** EC significance for Rondônia.

6.2.6 Summary: Sensitivity of Results to Algorithmic Mechanics

The block-scale, randomization methods and cloud classification algorithm were analyzed with respect to the sensitivity of the final results that variations within these aspects of the general method employed in this study create. These analyses have shown that block-scale selection in the CSR randomization algorithm is crucial in order to derive appropriate results. It was also seen with the EC significance results derived from the theoretical binomial distribution that the inherent spatial organization of the shallow clouds results in wider confidence bounds from the empirically generated randomized forest-cover patterns. The results showed little sensitivity to the selection of resolution and threshold to derive the binary forest-cover maps, and to the cloud classification algorithm. Most importantly, the null-hypothesis was rejected repeatedly in each case studied in the preceding section, and the results were shown to be robust with respect to algorithmic details (save for CSR block-scale selection).

The rest of the study will be based on the binary forest-cover map created with the 1-km resolution MOD44B data, and using a threshold value of 50%. The SHF randomization algorithm will be used, as it is inherently superior in conserving the scale of the disturbance, and the shallow cumulus cloud maps will be based on the second cloud classification algorithm, as it is much more refined that the CUTRIM algorithm.

6.3 Final Results

The final results are presented in this section, first in a qualitative fashion, second using the simple time-series representation, then moving on to the climatological representations in order to determine whether external factors condition the cloud-forest association. The results will only be presented and analysed for the Rondônia domain to keep things brief. Analogous plots for the other 2 domains are in Appendix A.

6.3.1 Long-Term and Seasonal Fractional Shallow Cloud Cover Maps

The yearly and seasonal fractional cloud cover maps provide a qualitative impression of the shallow cloud contrats over the Rondônia domain. The average fractional shallow cloud cover for the full record of 14h45 UTC observations is shown in Figure 6-20. The underlying forestcover pattern is clearly apparent in the fractional shallow cloud cover map. The central portion of the domain, which is deforested, is associated with increased shallow cloud cover. Within this deforested area, there are signs of elevated shallow cloud fractional cover in the vicinity of topographical features; qualitatively, these topographical features seem to be playing a modulating role, and they does not appear to be a strong association between

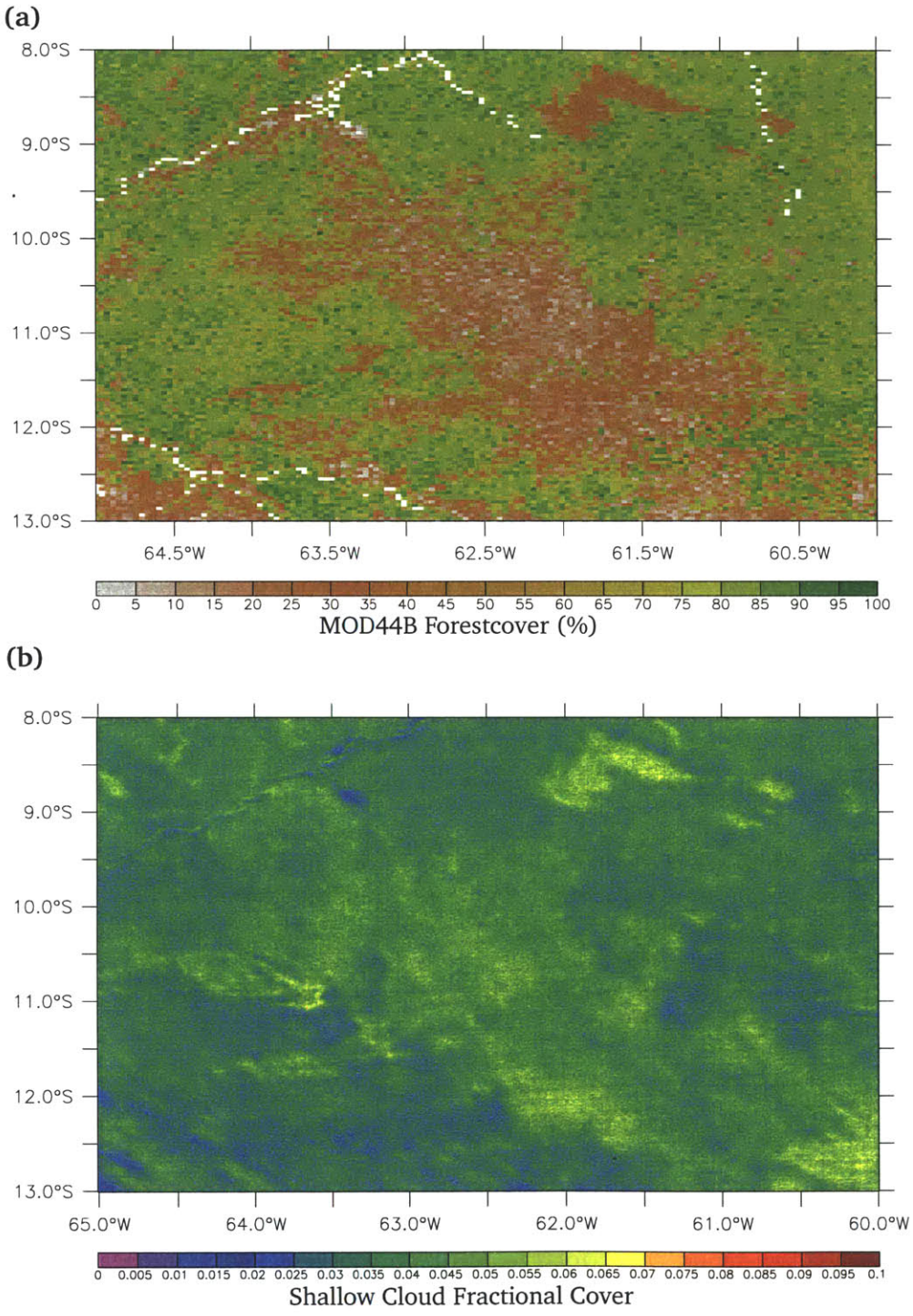

Figure 6-20: Long-Term Mean Shallow Cloud Cover; **(a)** MOD44B Treecover map and **(b)** Average Fractional Cover of 14h45 UTC Shallow Clouds over Rondônia (10/1/1994-3/31/2003)

shallow clouds and topography in general. There are also some other notable features that stand out; the inverted v-shaped savannah area centered around 61.5°W and 8.5°S and the two smaller patches of savannah to the east of it, as well as the sliver of savannah located at 63.6°W and 11°S.

The diurnal evolution of this qualitative association between shallow clouds and deforestation seems to peak at 17h45 UTC, where the shallow clouds are also more concentrated in the central portions of the deforested area, as can be seen in Figure 6-21. Seasonal differences can be observed in Figures 6-22 & 6-23. The most important feature is that the contrast is qualitatively observable in all seasons. It is particularly pronounced in JJA and SON, perhaps because there are less shallow clouds in general. Such inferences are however more readily made using quantitative methods; these follow.

6.3.2 Monthly Time-Series Representation

The monthly-averaged fractional cloud cover time-series are plotted for the forest and deforested pixels in panel (a) of Figure 6-24 along with the percent difference in panel (b) of that same figure. The fractional cloud cover is almost always higher over the deforested areas, and the difference varies between -10% and 80%. There is also a clear seasonality in the difference between fractional shallow cloud cover, as can be observed in panel (c) of Figure 6-24. As expected, the difference is highest during the dry season and into the pre-monsoon. The monthly climatology of percent difference shallow cloud fractional cloud cover is always positive, and is a clear testament to the direct impact that deforestation has on shallow cloud cover.

The monthly time-series of CDD and EC at 14h45 UTC are plotted for the Rondônia domain in Figure 6-25. In addition, another measure is also plotted: the median CDD. The key-statistic of CDD was defined in Section 5.3 as the mean monthly cloud density difference; the median CDD is the median monthly cloud density difference. It is plotted here to verify the robustness of the average CDD results. All three statistics show repeated occurrences of null-hypothesis rejection, and all these occurrences are exceedences. There are thus on average significantly more shallow clouds over deforested areas than over forested areas, and such events occur in significant numbers. Moreover, close examination of panel (a) reveals that the CDD is mostly above zero. There are in fact 86 occurrences of the monthly mean CDD being greater than zero, and only 17 occurrences of it being less than zero. Much like the EC, this can be seen as a binomial counting variable, and if we assume that under no cloud-forest association the probability of this random variable being above zero is $1/2$, this represents a significant signal (using binomial distribution with 1/2 probability) at the $p = 2.8 \times 10^{-12}$ level. Similarly, the EC count is 76 times greater than its theoretical expected value (i. e., half the number of good data days in the month), 22 times smaller and 5 times equal. This is also in itself significant at the $p = 3.9 \times 10^{-8}$ level. Thus, even without relying on the forest-cover randomization method, it can be concluded that there is an over-

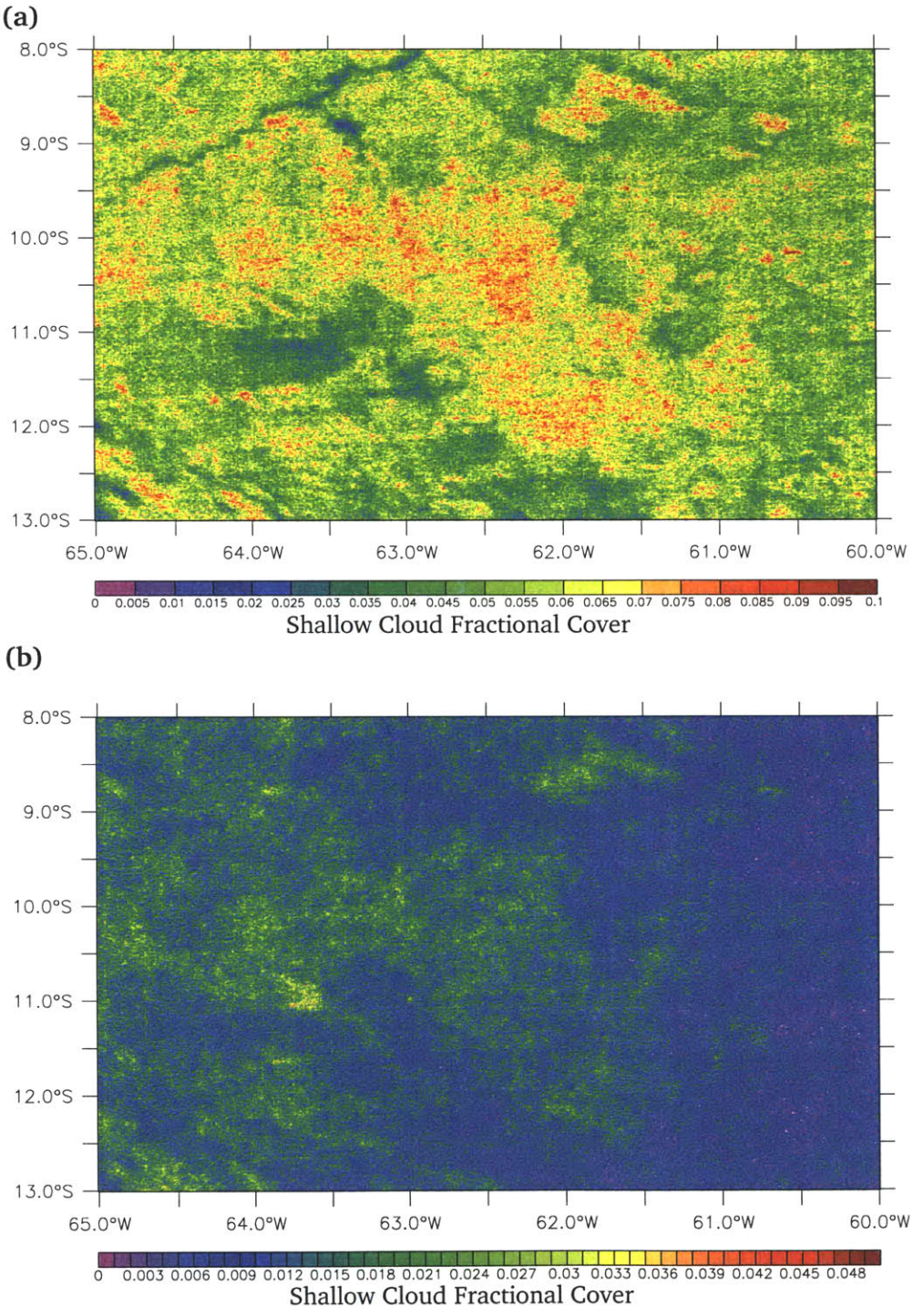

Figure 6-21: Long-Term Mean Shallow Cloud Cover (10/1/1999-3/31/2003); Average Fractional Cover of Shallow Clouds over Rondônia at **(a)** 17h45 UTC and **(b)** 20h45 UTC.

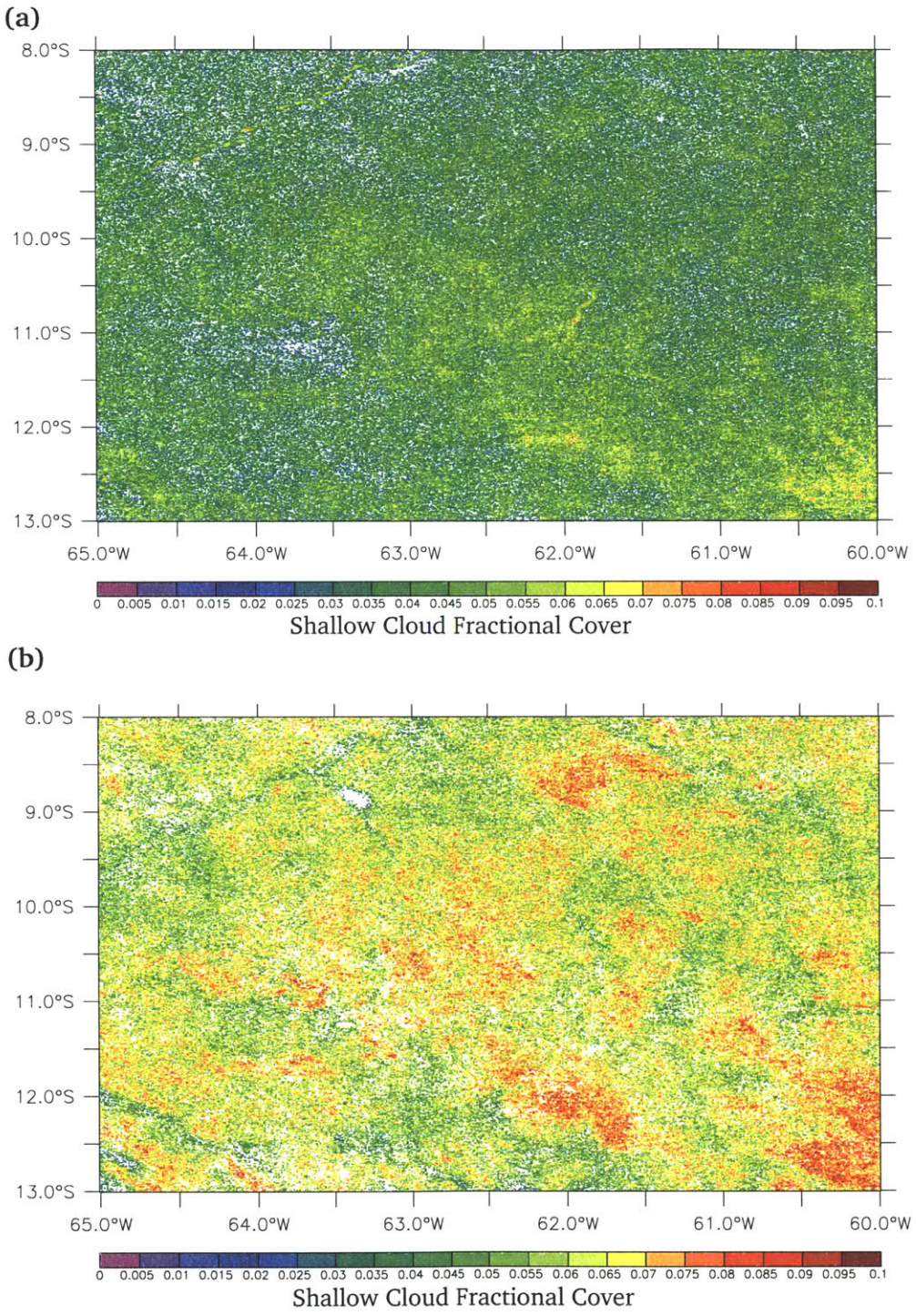

Figure 6-22: Long-Term Seasonal Mean Shallow Cloud Cover (10/1/1994-3/31/2003); Average Fractional Cover of Shallow Clouds over Rondônia at **(a)** DJF and **(b)** MAM.

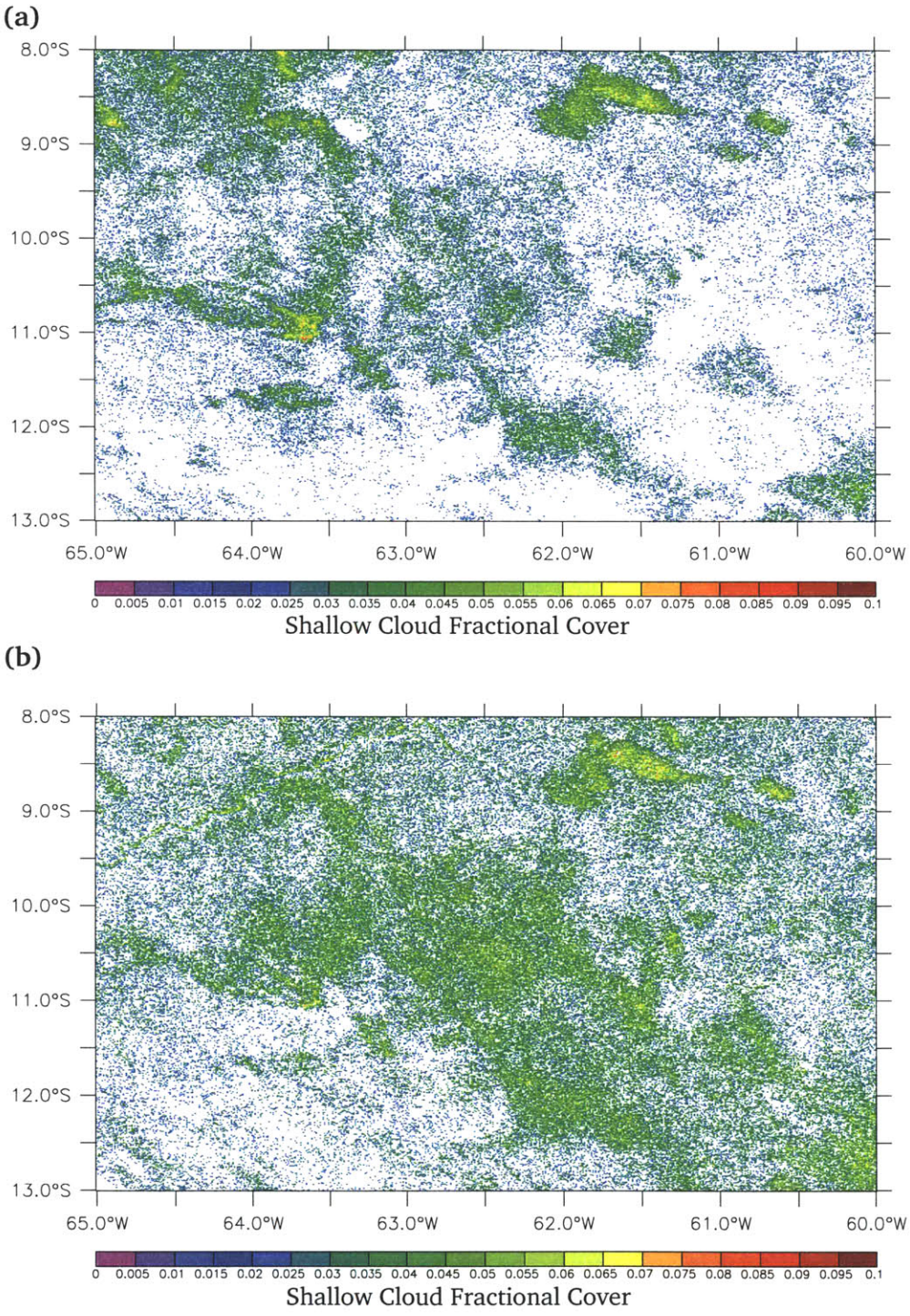

Figure 6-23: Long-Term Seasonal Mean Shallow Cloud Cover (10/1/1994-3/31/2003); Average Fractional Cover of Shallow Clouds over Rondônia at **(a)** JJA and **(b)** SON.

whelmingly significant association between shallow cloud cover and deforestation patterns. This conclusion is also valid for the other observation times, as can be seen in the summary presentation of the binomial analysis of the CDD and EC time-series (Table 6.2). The empirically derived confidence bounds are still useful to study the timing of significant departures. It is however hard to judge exactly when the significant events occur on the monthly time-series plots. The climatological representations are more suited to such analyses.

Table 6.2: Significant Results from the Binomial Analysis of Shallow Cloud Fractional Cover Difference and Exceedence Count v. Forest Cover over Rondônia Domain; The count of positive and negative differences is compared to the binomial distribution to detect significant biases.

Variable	Time	>0 Counts	<0 Counts	Significance
CDD	14h45 UTC	86	17	$p \leqslant 0.0001$
	17h45 UTC	27	2	$p \leqslant 0.0001$
	20h45 UTC	24	5	$p \leqslant 0.0006$
EC	14h45 UTC	76	22	$p \leqslant 0.0001$
	17h45 UTC	22	5	$p \leqslant 0.002$
	20h45 UTC	21	8	$p \leqslant 0.03$

6.3.3 Climatological Representation

The monthly and seasonal climatologies of significance frequency are presented in Figures 6-26 & 6-27. Again, the results clearly show that there is a significant association between forest-cover and shallow clouds. With the exception of one negative frequency (discussed below), there is overwhelming evidence that there is an enhancement of shallow convection over deforested areas. The average and median CDD show good agreement. The greatest difference in the frequency of significance between the average and median CDD occur in March at 17h45 UTC; the median CDD shows a negative frequency while the average CDD shows a positive frequency. This difference can be attributed to the differences in two months, namely March 2001 & 2003, as can be seen in the monthly time-series plots for Rondônia at 17h45 UTC in Figure A-9. In March 2001, the average CDD is greater than the upper 99% confidence limit, while the median CDD is within the 99% confidence range; in March 2003, the average CDD is within the 99% limits, while the median CDD is smaller than the lower limit. This is the only case of contradicting results between the mean and median CDD.

In both monthly and seasonal climatologies (Figures 6-26 & 6-27), the frequency of CDD significance is greater than that of EC significance. This indicates that dur-

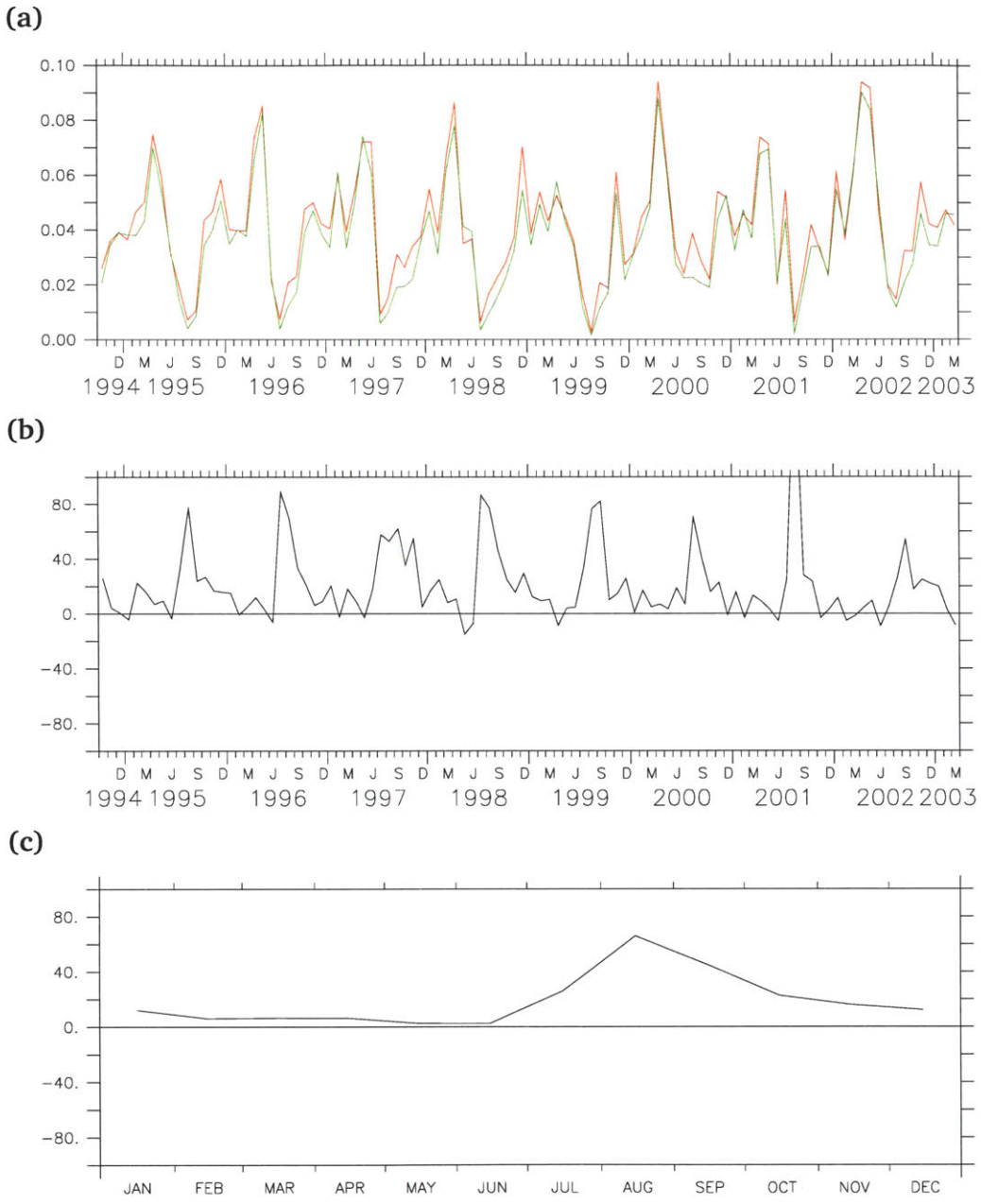

Figure 6-24: Monthly Time-Series of Fractional Shallow Cloud Cover over Forested and Deforested Pixels, and Monthly Difference for Rondônia Domain. **(a)** Monthly time series of 14h45 UTC cloud density over deforested area (red line) and forested area (green line) in Rondônia. **(b)** Monthly time series and **(c)** Monthly climatology of 14h45 UTC percent differences in cloud density over deforested and forested areas in Rondônia.

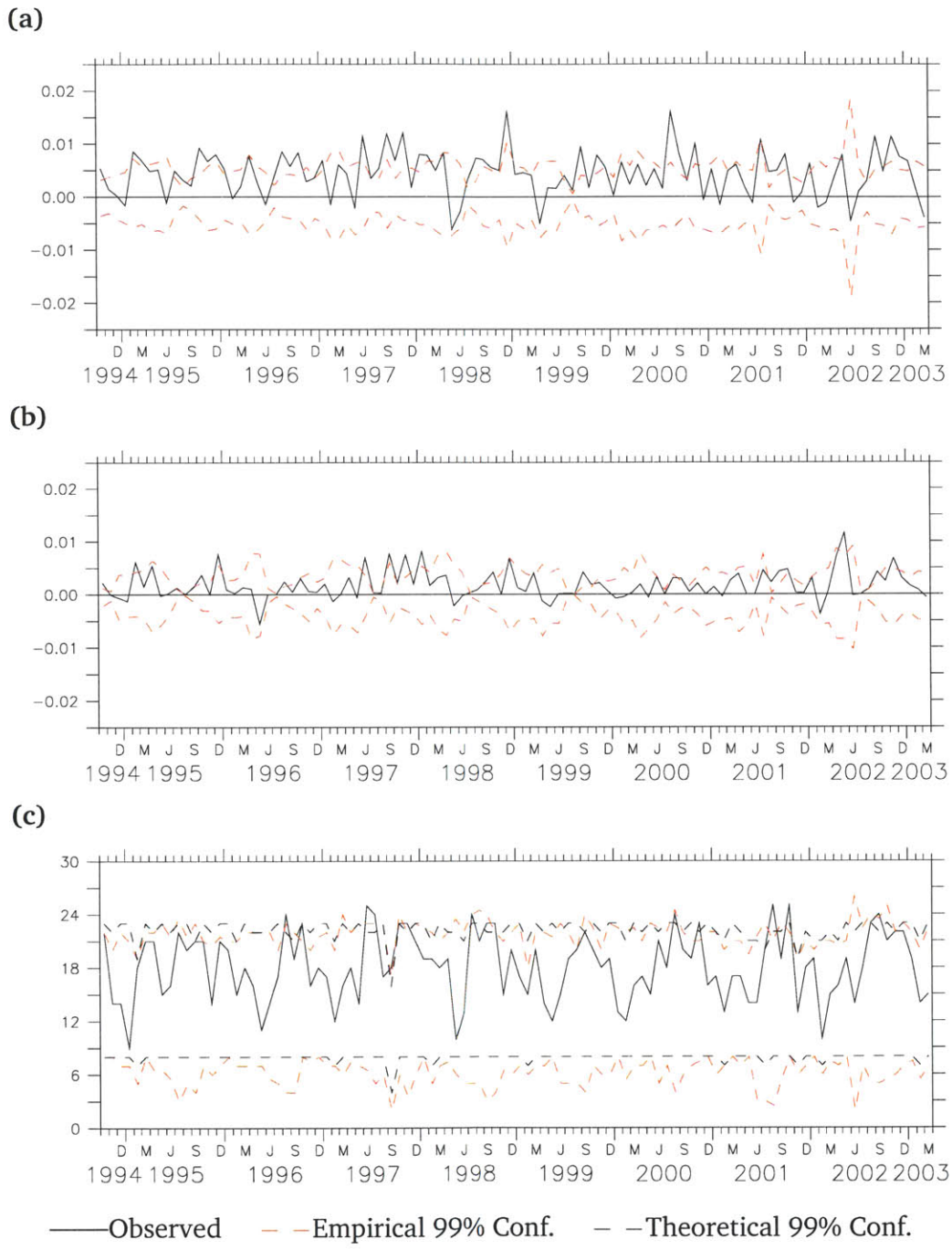

Figure 6-25: Monthly time series of **(a)** CDD, **(b)** median CDD and **(c)** EC at 14h45 UTC over the study domain of Rondônia, along with their respective 99% confidence limits.

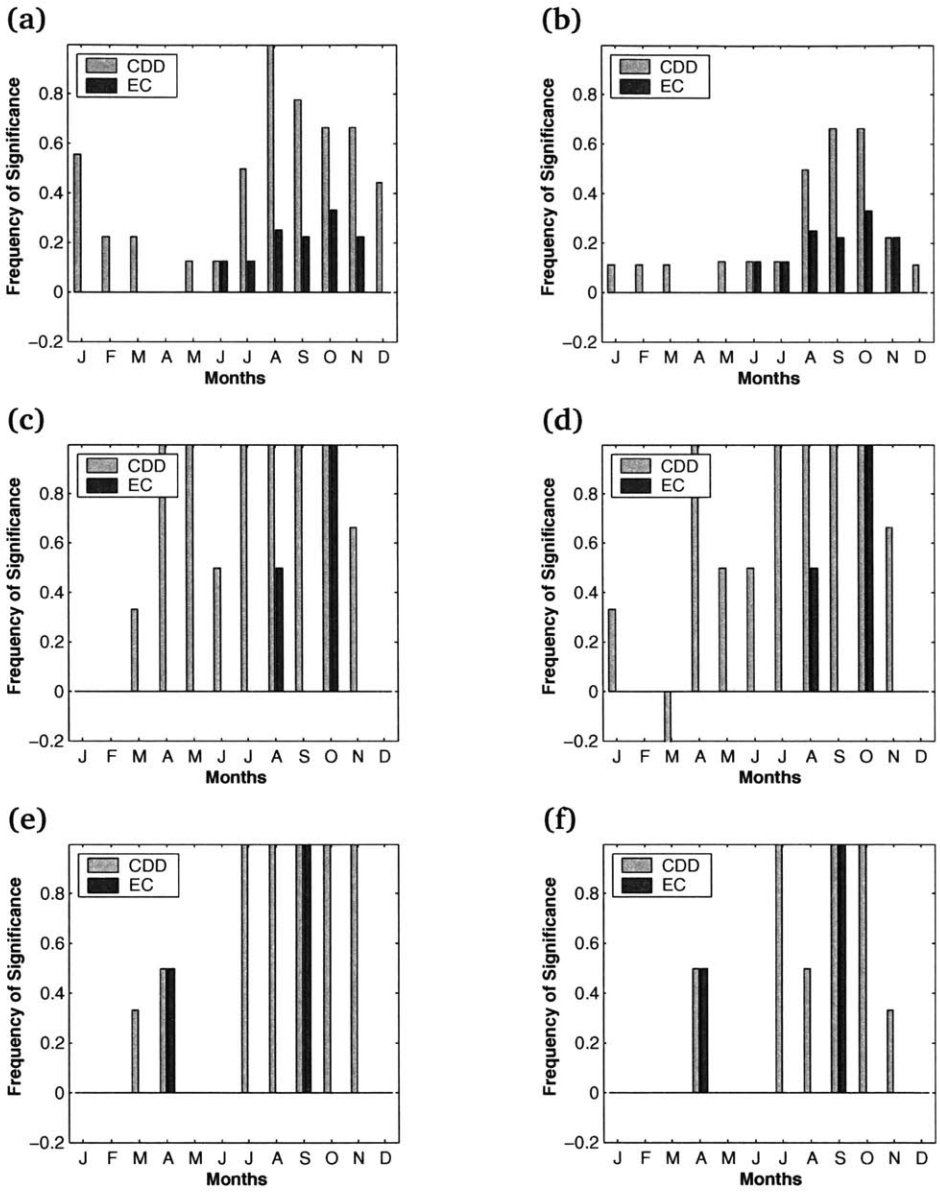

Figure 6-26: Monthly Climatologies of CDD and EC significance for Rondônia; bars represent normalized number of times that a statistic is significant for a specific month; positive (negative) is for number of times that statistic is greater (smaller) than upper (lower) bound of 99% confidence interval. **(a)** Frequency of CDD and EC significance at 14h45 UTC; **(b)** Frequency of Median CDD and EC significance at 14h45 UTC; **(c)** Frequency of CDD and EC significance at 17h45 UTC; **(d)** Frequency of Median CDD and EC significance at 17h45 UTC; **(e)** Frequency of CDD and EC significance at 20h45 UTC; **(f)** Frequency of Median CDD and EC significance at 20h45 UTC.

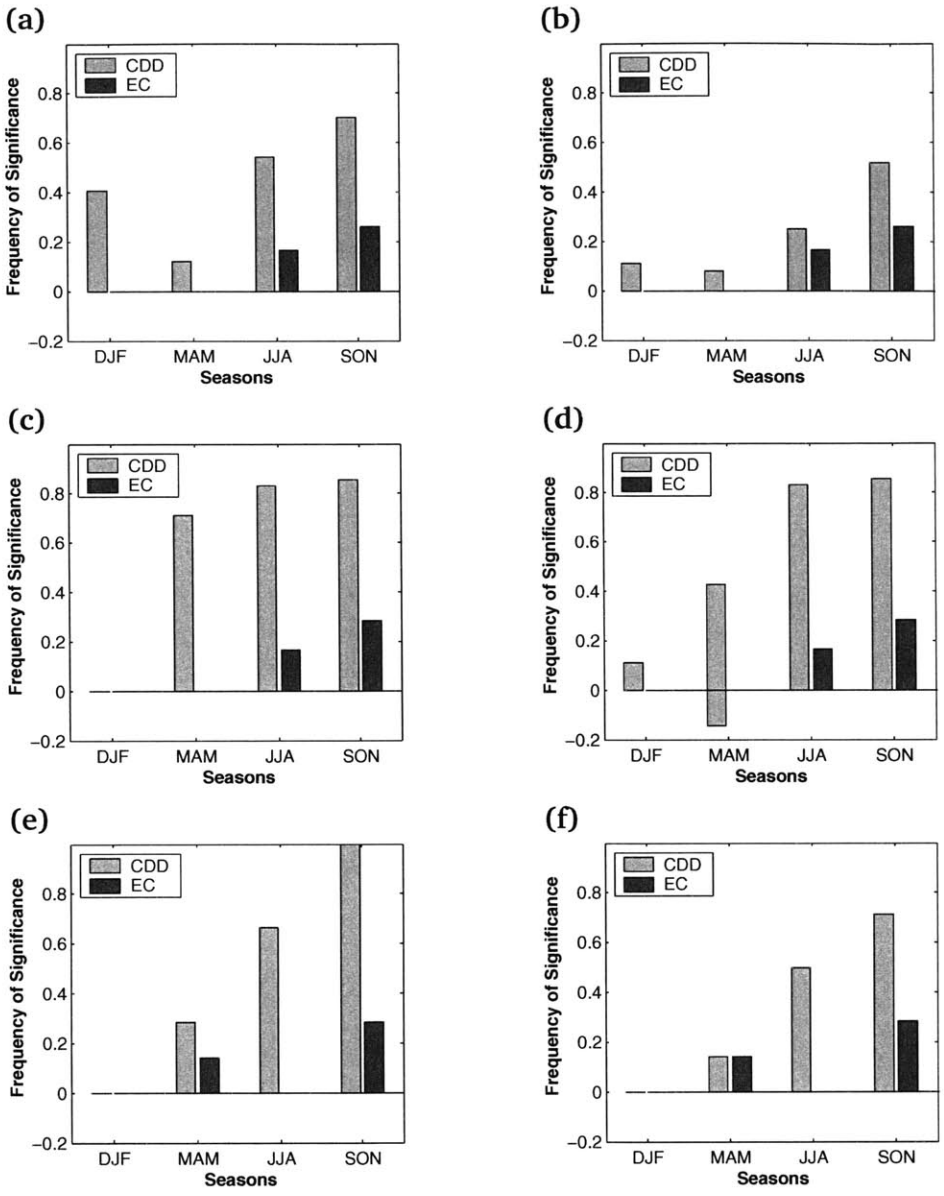

Figure 6-27: Seasonal Climatologies of CDD and EC significance for Rondônia; bars represent normalized number of times that a statistic is significant for a specific month; positive (negative) is for number of times that statistic is greater (smaller) than upper (lower) bound of 99% confidence interval. **(a)** Frequency of CDD and EC significance at 14h45 UTC; **(b)** Frequency of Median CDD and EC significance at 14h45 UTC; **(c)** Frequency of CDD and EC significance at 17h45 UTC; **(d)** Frequency of Median CDD and EC significance at 17h45 UTC; **(e)** Frequency of CDD and EC significance at 20h45 UTC; **(f)** Frequency of Median CDD and EC significance at 20h45 UTC.

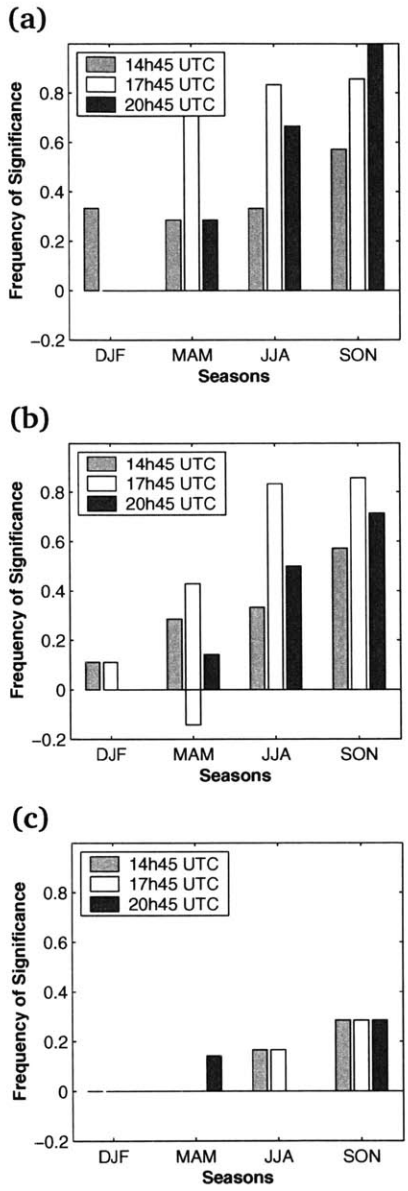

Figure 6-28: Diurnal Cycle of CDD and EC Seasonal Climatology Significance for Rondônia; bars represent normalized number of times that a statistic is significant for a specific month; positive (negative) is for number of times that statistic is greater (smaller) than upper (lower) bound of 99% confidence interval. **(a)** Mean CDD Significance **(b)** Median CDD Significance **(c)** EC Significance.

ing certain months, the magnitude of shallow cloud enhancement is significant on average (or in the median), while the number of times that the enhancement occurs is not significant. Such a nuance signifies that the mesoscale circulations, which create the shallow cloud contrast, do not always occur frequently enough to be significant, but when they do occur the contrast that they generate in shallow cloudiness is stark enough to render the monthly mean difference significant. This may also explain why the phenomenon was so poorly observed in the past.

The seasonal representation in Figure 6-27 shows that the phenomenon is most frequently apparent during the dry season (JJA) and during the pre-monsoon (SON), where there are distinct peaks in the frequency of significance of both CDD and EC. The diurnal evolution of significance is presented in Figure 6-28; the CDD (both average and median) show a consistent diurnal evolution, while the EC does not seem to exhibit any clear pattern. The physical process that created such cloud contrasts was presented in Chapter 1, and the diurnal evolution of CDD significance frequency may be explained under that physical framework. The mesoscale circulations that are created by the heterogeneities of land cover are primarily driven by energetic contrasts. The combination of water availability (which modulates the proportions of latent and sensible heating) as well as the surface albedo (which modulates total available energy) determine the strength (voire présence) of the mesoscale circulations, and hence of the enhancement of localised shallow convection. In all seasons, the onset of such mesoscale circulations occurs at or before 14h45 UTC, which is 10h45 LT[4]. During the monsoon (i. e., DJF), the average CDD is not significant at later times, while the median is significant at 17h45 UTC but not at 20h45 UTC. During other seasons, the significance frequency of CDD peaks at 13h45 LT, except for the pre-monsoon during which the significance frequency of the average CDD peaks at 16h45 LT. Such diurnal processions are consistent with the physical insight; the surface heating contrast is triggered shortly after sunrise and the mesoscale circulations ensue no more than 4 hours later. The circulations intensify as the heating builds up, peaking in the early afternoon, at which point the shallow clouds act as a shut-down mechanism by blocking out the principal energetic driver of short-wave radiation. Thus the seasonal subtleties that deviate from this conjectured diurnal evolution mechanism should be explained by other external factors.

6.3.4 Sensitivity to Synoptic Atmospheric Circulation Strength

The strength of the synoptic atmospheric circulation, as manifested by wind speed and vertical wind shear magnitude, should intuitively suppress, or smear, the local circulations that are created by the land surface heterogeneities. Yet, as reviewed in Chapter 1, there is no consensus in the results of modelling studies regarding the degree to which synoptic circulation characteristics are able to sup-

[4]Local sunrise and sunset times are in the ranges of 05h45 LT~06h30 LT and 18h00 LT~18h45 LT respectively.

press the localised shallow convection. Some have found a suppressing impact from moderate winds [Chen and Avissar, 1994; Hong *et al.*, 1995; Dalu *et al.*, 1996; Wang *et al.*, 1996; Avissar and Schmidt, 1998], while more recent studies have found that the local circulations are not sensitive to the magnitude of background winds [Wang *et al.*, 1998; Weaver and Avissar, 2001; Roy and Avissar, 2002].

Figure 6-29 presents the frequency of average CDD significance stratified by the 700-850 mb layer-averaged NCEP/NCAR re-analysis (NNRP) wind speed and layer wind shear[5]. The wind speed stratification does not show a consistent pattern throughout the day (i. e., from 14h45 UTC to 20h45 UTC.) At 14h45 UTC, all seasons except MAM exhibit the intuitive behavior, with higher CDD significance frequency for low wind speeds. This is however not reflected at 17h45 UTC or 20h45 UTC, where no clear organization can be inferred. There are even occurrences of an inverse circulation, or shallow cloud suppression over deforested areas, during low wind speed days (i. e., MAM at 14h45 UTC and SON at 17h45 UTC). This may indicate that the onset of the localized shallow convective cells is sensitive to the synoptic wind speed, while the procession of the mesoscale circulations isn't. This would indicate that once the circulations have formed and manifested themselves in the form of collocated shallow clouds and deforestation, they are not as sensitive to the synoptic wind speed.

The sensitivity to wind shear is more conspicuous; there is a higher frequency of CDD significance for smaller wind shears at all times. The only exception is during DJF at 20h45 UTC. The effect of wind shear is in agreement with general physical insight into boundary-layer dynamics; high wind shear above or around the top of the boundary-layer is accompanied with a downward momentum flux, which acts to effectively cap the boundary-layer and inhibit convection.

The frequency of CDD significance is also stratified by the 700-850 mb NNRP layer-averaged wind direction, and the results are presented in Figures 6-30 & 6-31. There is a clear pattern in the stratification between northerly and southerly winds at all times (Figure 6-30). The frequency of CDD significance is much higher during northerly wind events, while during some southerly wind events there is a suppression of shallow clouds over deforested areas (DJF, MAM, JJA 14h45 UTC). There is a similar contrast between north-easterly and south-westerly winds (Figure 6-31), but there is one inconsistency during MAM at 14h45 UTC. The stratification between easterly and westerly, and that between north-westerly and south-easterly do not yield a consistent pattern. This is somewhat of a surprising result, since many studies refer to two contrasting synoptic regimes in Rondônia as the westerly and easterly regimes (c. f., Chapter 3).

[5]The particular 700-850mb layer was chosen as it has been used previously to describe synoptic conditions in Rondônia [Halverson *et al.*, 2002]. Similar analyses were performed for the 850-925mb layer (results not shown) and the results were similar.

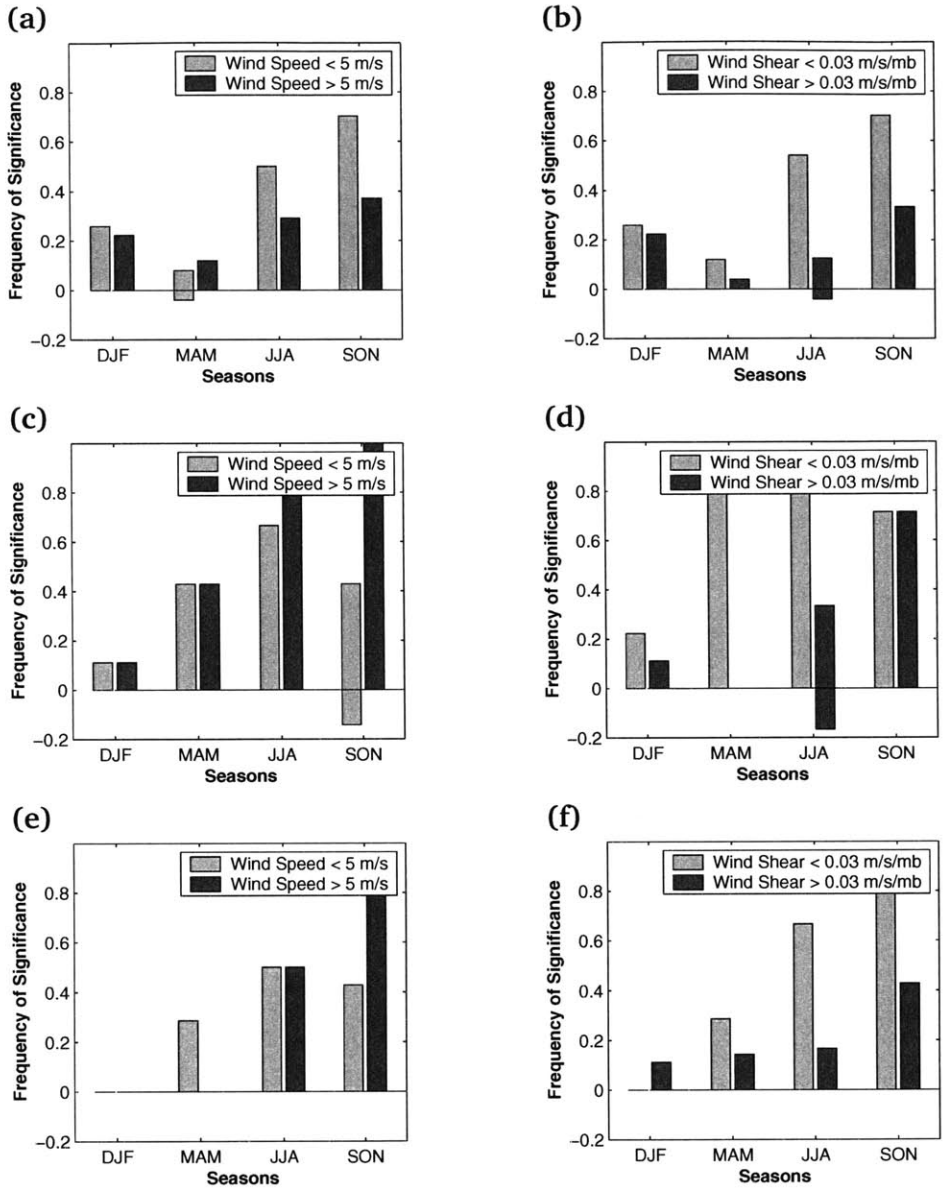

Figure 6-29: Seasonal Climatologies of CDD and EC Significance for Rondônia Stratified by 700-850 mb NCEP/NCAR Reanalysis Wind Speed and Shear; bars represent normalized number of times that a statistic is significant for a specific month; positive (negative) is for number of times that statistic is greater (smaller) than upper (lower) bound of 99% confidence interval. **(a)** Frequency of CDD significance at 14h45 UTC stratified by 700-850 mb layer-averaged wind speed; **(b)** Frequency of CDD significance at 14h45 UTC stratified by wind shear; **(c)** Frequency of CDD significance at 17h45 UTC stratified by layer-averaged wind speed; **(d)** Frequency of CDD significance at 17h45 UTC stratified by wind shear; **(e)** Frequency of CDD significance at 20h45 UTC stratified by layer-averaged wind speed; **(f)** Frequency of CDD significance at 20h45 UTC stratified by wind shear.

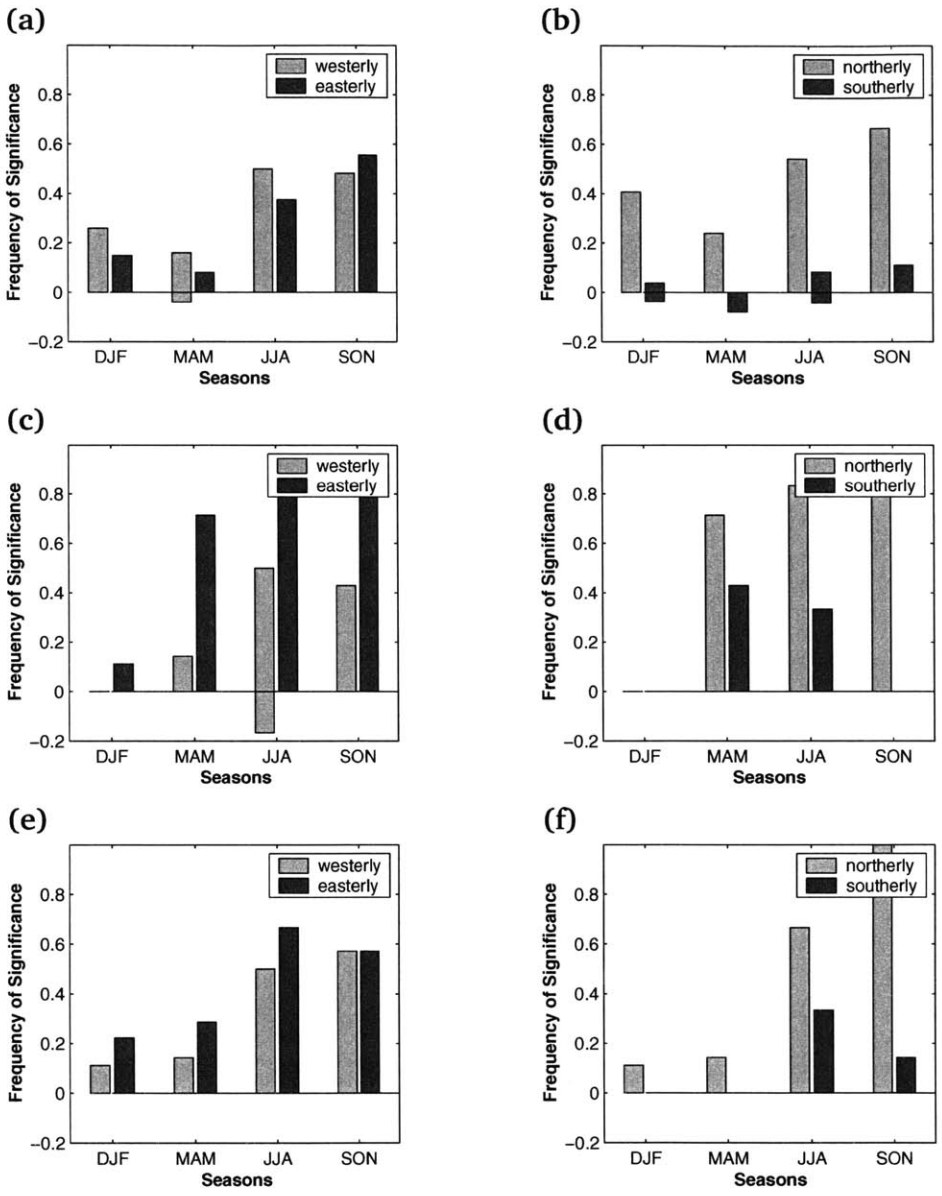

Figure 6-30: Climatologies of CDD Significance for Rondônia Stratified by Cardinal Wind Direction; positive (negative) is for number of times that CDD is greater (smaller) than upper (lower) bound of 99% confidence interval. Frequency of CDD significance at 14h45 UTC **(a)** & **(b)**; 17h45 UTC **(c)** & **(d)**; 20h45 UTC **(e)** & **(f)** stratified by 700-850 mb layer-averaged NCEP/NCAR reanalysis wind direction (summarized seasonally).

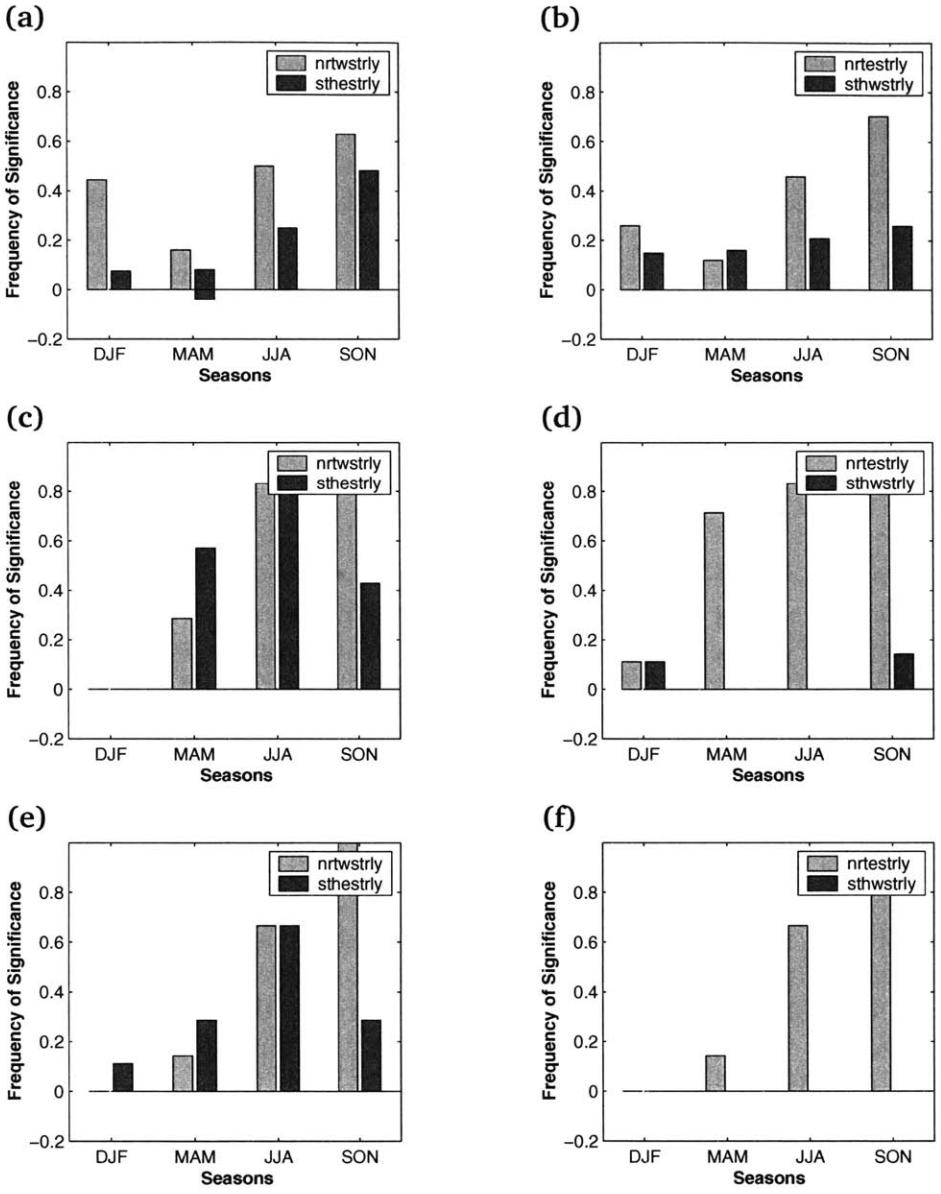

Figure 6-31: Climatologies of CDD Significance for Rondônia Stratified by off-Cardinal Wind Direction; positive (negative) is for number of times that CDD is greater (smaller) than upper (lower) bound of 99% confidence interval. Frequency of CDD significance at 14h45 UTC **(a)** & **(b)**; 17h45 UTC **(c)** & **(d)**; 20h45 UTC **(e)** & **(f)** stratified by 700-850 mb layer-averaged NCEP/NCAR reanalysis wind direction (summarized seasonally).

Table 6.3: Description of ANA Raingauges

Raingauge Name	ID	Coordinates	Temporal Coverage
Mineração Jacunda	#9620001	9.18**S**; 62.95**W**	01/01/1999—08/31/2002
Ariquemes	#9630000	9.93**S**; 63.06**W**	01/01/1999—07/31/2003
San Antonia (BR-364)	#9630001	9.26**S**; 63.16**W**	01/01/1999—08/31/2002
Fazenda Rio Branco	#9630004	9.89**S**; 62.99**W**	01/01/1999—07/31/2003
Setor Cachoeirinha	#9630006	9.89**S**; 62.99**W**	3/18/1999—11/30/1999 05/21/2000—06/30/2000 12/01/2000—06/19/2001 10/19/2001—11/31/2001

6.3.5 Sensitivity to Antecedent Precipitation

The contrast in land-surface heating that is created by heterogeneities in the vegetation cover should intuitively be suppressed by large-scale wetness. After a raining event, the difference between the energetic allocation to sensible and latent heating between forested and deforested areas should narrow down, and the local circulations that are promoted by the land-surface heating contrast should be suppressed. The latter hypothesis can be tested by looking at the frequency of the CDD significance with respect to the time-lag since the last precipitation event. This is precisely what is presented in Figures 6-33 & 6-34. The precipitation data used for Figure 6-33 is raingauge data that was generously supplied by the Agência Nacional de Águas of Brazil. The daily accumulations are available from January 1, 1999 to July 31, 2003 for the five raingauges described in Table 6.3. The precipitation data used for Figure 6-34 is from the Global Precipitation Climatology Project (GPCP) [Huffman *et al.*, 2001; Adler *et al.*, 2003]. The product used in this study is the 1DD (one degree day) estimate from GPCP version 2 [Huffman *et al.*, 2001], which is available from October 1996 to December 2003.

A point-to-point comparison of ANA and GPCP rainfall data is shown in Figure 6-32. The daily data show a fair level of discrepancies (Figure 6-32–panel (a)). The raingauge accumulations exhibit more pronounced variance than the satellite estimates. There are, in particular, multiple occasions of zero gauge readings associated with non-zero rate estimates. It is impossible to determine which data source gives the best estimate of daily rainfall; the gauge readings are hindered by their lack of spatial knowledge, while the satellite estimates suffer from irregular visitations. The monthly averaged values show much closer agreement (Figure 6-32–panel (b)), which reinforces the possibility that the disagreement between daily values is a sampling problem, and not a data quality problem.

The CDD statistic is compiled depending on the daily rainfall accumulation (ANA gauge data) or average daily rainfall rate (GPCP satellite data). Arbitrary thresh-

olds are selected to differentiate "rainy" days from "dry" days. These thresholds are 0.1mm, 0.5mm, 1mm and 2mm. The frequency of CDD significance is then plotted according to the number of days since the last "rain" event. If the hypothesis is that large-scale wetness suppresses the surface heating contrast that initiates the local circulations that result in the localised shallow convection, then it is expected that the frequency of significance will monotonically increase as the time since the last raining event increases. Right after a raining event, the surface should be uniformly wet, and the frequency of significance should be null. As the number of days since the last wetting event increases, the surface heating contrast should augment; tropical trees have much deeper roots and thus greater access to water whilst the pasture vegetation has shallow roots and relies much more of near-surface soil moisture which should be depleted quickly through evaporative losses.

The results plotted in Figures 6-33 & 6-34 however do not show a clear trend as expected. Moreover, there is extensive disagreement between the results derived from ANA gauge data and those derived with GPCP satellite estimates. It is only during the dry season months of JJA that the results show a monotonically increasing trend, and only when stratified with the ANA gauge data (Figure 6-33). The results based on the GPCP data (Figure 6-34) show a trend that is contrary to the one expected for all seasons except the dry season (JJA). It could be inferred from the ANA–based results that the surface wetness significantly modulated the local surface heating contrast only during the dry periods. Such a conclusion would indeed make sense, as the evaporative losses may occur more rapidly during the dry season. However the disagreement between ANA and GPCP derived results renders a definitive conclusion impossible.

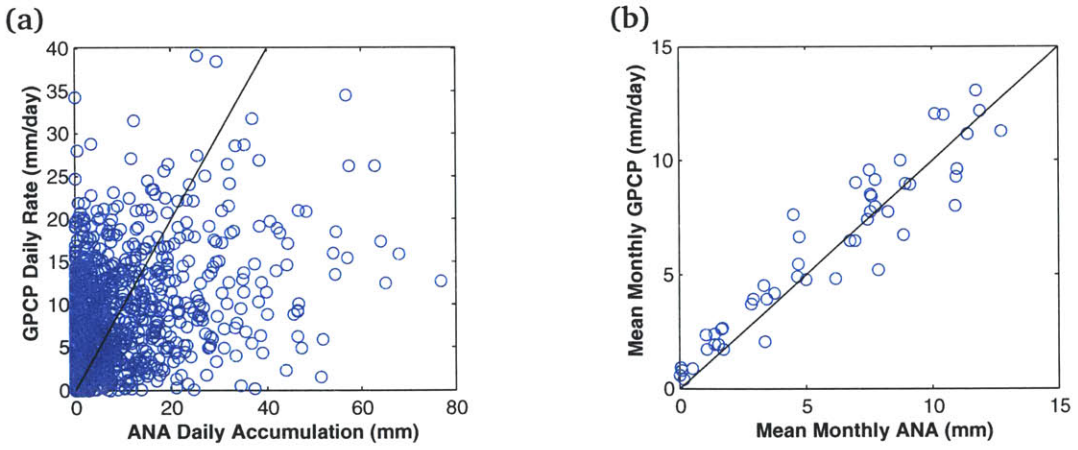

Figure 6-32: Comparison of ANA and GPCP Precipitation Estimates; **(a)** Comparison of Daily Data; **(b)** Comparison of Monthly Averaged Data.

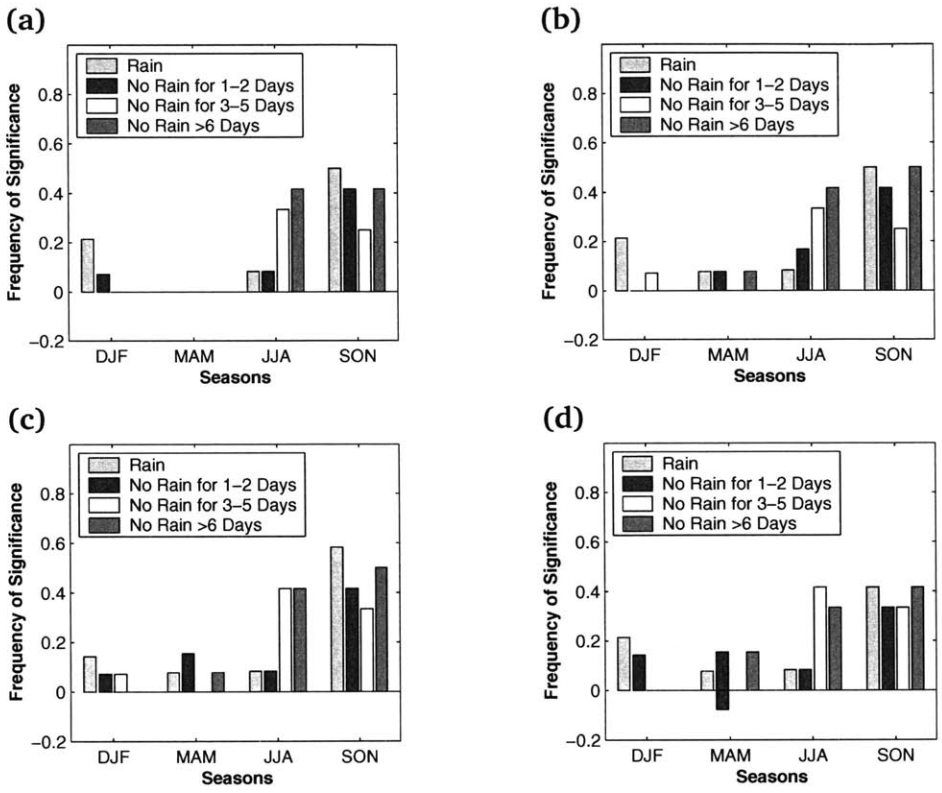

Figure 6-33: Climatologies of CDD significance for Rondônia Stratified by ANA Antecedent Precipitation Accumulation; bars represent relative number of times that CDD is significant for a specific month; positive (negative) is for number of times that CDD is greater (smaller) than upper (lower) bound of 99% confidence interval. Frequency of CDD significance at 14h45 UTC stratified by antecedent daily rainfall accumulation. Threshold to determine rain is **(a)** 0.1 mm; **(b)** 0.5 mm; **(c)** 1.0 mm; **(d)** 2.0 mm.

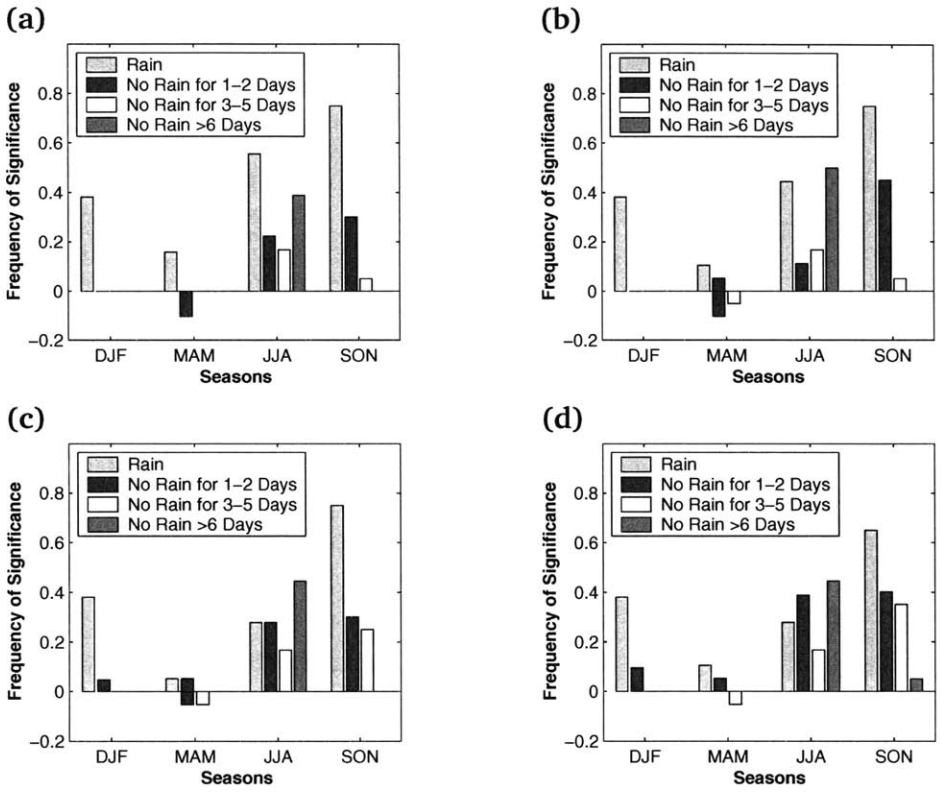

Figure 6-34: Climatologies of CDD significance for Rondônia Stratified by GPCP Satellite Antecedent Precipitation Rate Estimates; bars represent relative number of times that CDD is significant for a specific month; positive (negative) is for number of times that CDD is greater (smaller) than upper (lower) bound of 99% confidence interval. Frequency of CDD significance at 14h45 UTC stratified by antecedent rainfall rate estimates. Threshold to determine rain is **(a)** 0.1 mm/day; **(b)** 0.5 mm/day; **(c)** 1.0 mm/day; **(d)** 2.0 mm/day.

6.3.6 Shallow Clouds and Topography

The horizontal flow of a fluid over terrain that exhibits topographical relief creates vertical motion, which can result in the formation or enhancement of clouds and precipitation [Houze, Jr., 1993] in a process known as orography. Until now, the relation between topography and cloudiness has been ignored in favor of looking for relations between cloudiness and forest-cover. Yet the Rondônia domain is characterized by moderate topography (c. f., Figure 6-35); the elevations range from 40m to 1,080m. It is probable that orographic clouds and precipitation are a prominent feature in Rondônia. In this section, the role of topographical features will be examined with respect to shallow cloud patterns.

To test the role of topographical features on determining the location of the areas of shallow convection, the key-statistics of CDD and EC are compiled using elevation and slope. Instead of computing CDD as the average difference in cloud density between deforested and forested pixels, we compute CDD as the average difference in cloud fractional cover between high and low elevations, or between steep and gradual slopes. The separation between "high" and "low", "steep" and "gradual" is determined by using arbitrary thresholds. The arbitrary thresholds are set using the distribution of pixel elevations and slopes; the 30% highest (steepest) pixels are compared to the 70% lowest (most gradual) pixels, the 50% highest (steepest) pixels are compared to the 50% lowest (most gradual) pixels, and the 70% highest (steepest) pixels are compared to the 30% lowest (most gradual) pixels. The resulting monthly time-series of these analyses are presented in Appendix A, while the climatological results are plotted here in Figure 6-37.

There is a clearly significant associative relationship between both elevation and shallow cloudiness, and slope and cloudiness. Yet, in comparing these results to those presented in Figure 6-27, it becomes apparent that the relation between average or median CDD with elevation is much weaker than that between the same statistics and forest-cover, and the seasonal cycles are opposed. Moreover, the contrast between the frequency of EC significance related to elevation and that related to forest-cover is even starker. The distinction between slope and forest-cover is not as clear. The frequency of significance for CDD related to slope peaks in SON, which is synchronized with the peak of CDD related to forest-cover. the difference in magnitudes is not as pronounced. There is however, a very pronounced difference between the EC related to slope and that related to forest-cover. The latter exhibits a larger frequency of significance (the frequency of significance of EC related to slope is nearly null.)

Table 6.4 summarizes the monthly time-series results with respect to the significance of the entire series (i. e., the distribution of the observed key statistics with respect to their expected values under the null hypothesis.) From the results presented in Table 6.4, it appears that shallow clouds are significantly biased towards higher ground, or regions of steeper slopes. The comparison between the distribution of elevation and slopes depending on the forest-cover is presented in Figure 6-36. The distributions are roughly similar, although there does seem to be

a slight bias for deforestation in lower elevations or more gradual slopes. Thus the shallow cloud preference over deforested areas is in contradiction with the shallow cloud preference for higher ground and steeper slopes. The results therefore appear to be distinct. This type of observation, coupled with the analysis above, may indicate that while topographical features do play a role in determining the location of shallow convection, it is a role that is statistically independent of the role that the land cover disturbance plays in initiating the secondary circulations that result in the enhanced cloud cover of deforested areas.

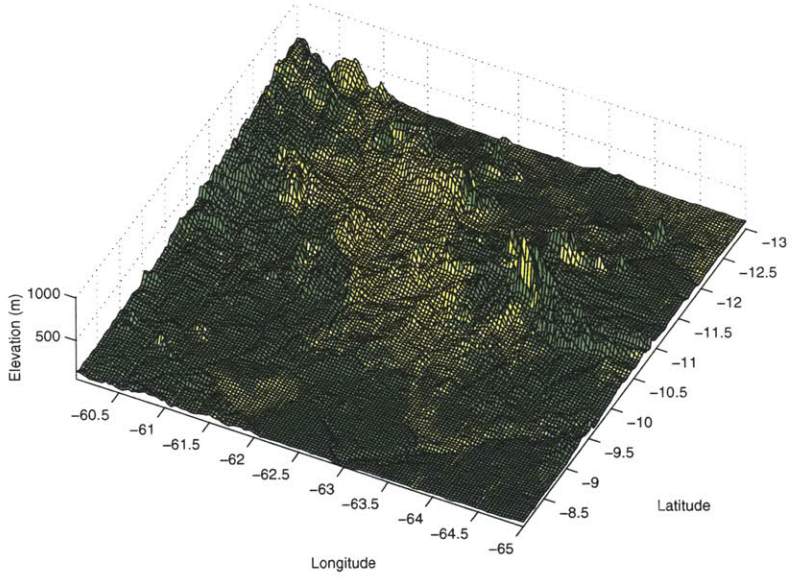

Figure 6-35: Rondônia Topograhy & Land-cover; SRTM Digital Elevation Model overlayed with 4-km resolution, 50% threshold forest-cover.

Table 6.4: Summary of Analyses with respect to Elevation and Slope

Statistic Description	Clouds over...	Significance Level
DEM CDD 30: Cloud Density Difference between 30% highest and 70% lowest pixels.	N/A	**N/A**
DEM CDD 50: Cloud Density Difference between 50% highest and 50% lowest pixels.	highest	**$p=0.001$**
DEM CDD 70: Cloud Density Difference between 70% highest and 30% lowest pixels.	highest	**$p\leqslant 0.0001$**
SLP CDD 30: Cloud Density Difference between 30% steepest and 70% most gradual pixels.	steepest	**$p\leqslant 0.0001$**
SLP CDD 50: Cloud Density Difference between 50% steepest and 50% most gradual pixels.	steepest	**$p\leqslant 0.0001$**
SLP CDD 70: Cloud Density Difference between 70% steepest and 30% most gradual pixels.	steepest	**$p\leqslant 0.0001$**
DEM EC 30: Exceedence Count of 30% highest over 70% lowest pixels.	deforested	**$p=0.001$**
DEM EC 50: Exceedence Count of 50% highest over 50% lowest pixels.	N/A	**N/A**
DEM EC 70: Exceedence Count of 70% highest over 30% lowest pixels.	N/A	**N/A**
SLP EC 30: Exceedence Count of 30% steepest over 70% most gradual pixels.	steepest	**$p=0.001$**
SLP EC 50: Exceedence Count of 50% steepest over 50% most gradual pixels.	steepest	**$p=0.0001$**
SLP EC 70: Exceedence Count of 70% steepest over 30% most gradual pixels.	steepest	**$p\leqslant 0.0001$**

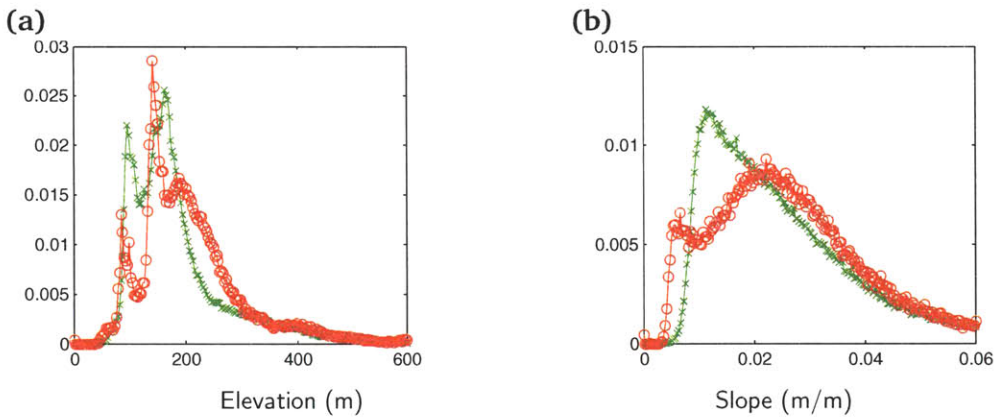

Figure 6-36: Probability density functions of SRTM elevations **(a)** and slope **(b)** for forested (green line) and deforested (red line) pixels

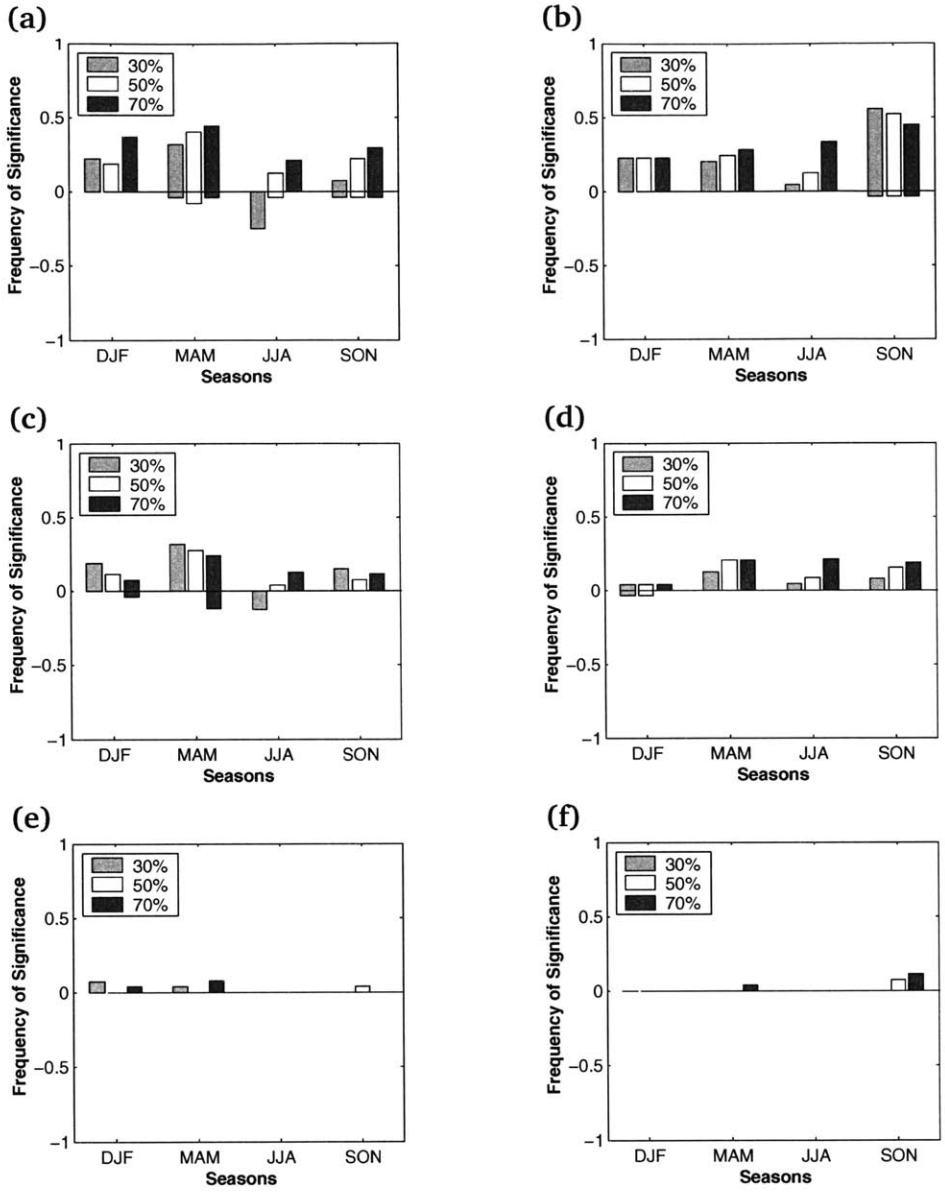

Figure 6-37: Climatologies of 14h45 UTC CDD and EC significance for Rondônia Stratified by Elevation and Slope; bars represent relative number of times that CDD is significant for a specific month; positive (negative) is for number of times that CDD is greater (smaller) than upper (lower) bound of 99% confidence interval. Key to legend: **30%** signifies the difference between the 30% highest (steepest) pixels and the 70% lowest (most gradual) pixels; **50%** signifies the difference between the 50% highest (steepest) pixels and the 50% lowest (most gradual) pixels; **70%** signifies the difference between the 70% highest (steepest) pixels and the 30% lowest (most gradual) pixels. Frequency of Significance for **(a)** Elevation Average CDD; **(b)** Slope Average CDD; **(c)** Elevation Median CDD; **(d)** Slope Median CDD; **(e)** Elevation EC; **(f)** Slope EC.

6.4 Disturbance Scale Analysis

In order to assess the influence of the scale of the land cover disturbance on shallow cloud enhancement, the contrast in cloudiness is examined here over two sub-areas in the domain: the inverted v-shaped savannah area, as well as an area that exhibits the typical fishbone pattern of deforestation. Both domains are exactly the same size, measuring 1.3° to the side. The forest cover and topography of these sub-domains are depicted in Figures 6-38 & 6-39. The scale of the land cover inhomogeneity is different in both domains, with the savannah domain having a quasi-continuous savannah in the center of the domain with a typical scale of approximately 50 km, while the fishbone domain has features that exhibit much smaller scale heterogeneities. Moreover, the surface properties of the savannah clearing and deforested areas are different; the savannah is naturally occurring, while the fishbone deforestation pattern is most probably under agricultural use.

The analysis comparing the monthly CDD time-series in both these sub-domains to a binomial variable, which is given in Table 6.5, reveals that both clearings promote shallow cumulus convection. The scale of the land-cover "disturbance" in both cases is thus equally able to create the conditions under which the differential surface forcing creates localized convective activity.

Table 6.5: Significant Results from the Binomial Analysis of Shallow Cloud Fractional Cover Difference v. Forest Cover over Savannah and Fishbone Domains; The count of positive and negative differences is compared to the binomial distribution to detect significant biases.

Domain	Time	>0 Counts	<0 Counts	Significance
Savannah	14h45 UTC	94	9	$p \leqslant 0.0001$
	17h45 UTC	28	1	$p \leqslant 0.0001$
	20h45 UTC	29	0	$p \leqslant 0.0001$
Fishbone	14h45 UTC	89	14	$p \leqslant 0.0001$
	17h45 UTC	28	1	$p \leqslant 0.0001$
	20h45 UTC	27	2	$p \leqslant 0.0001$

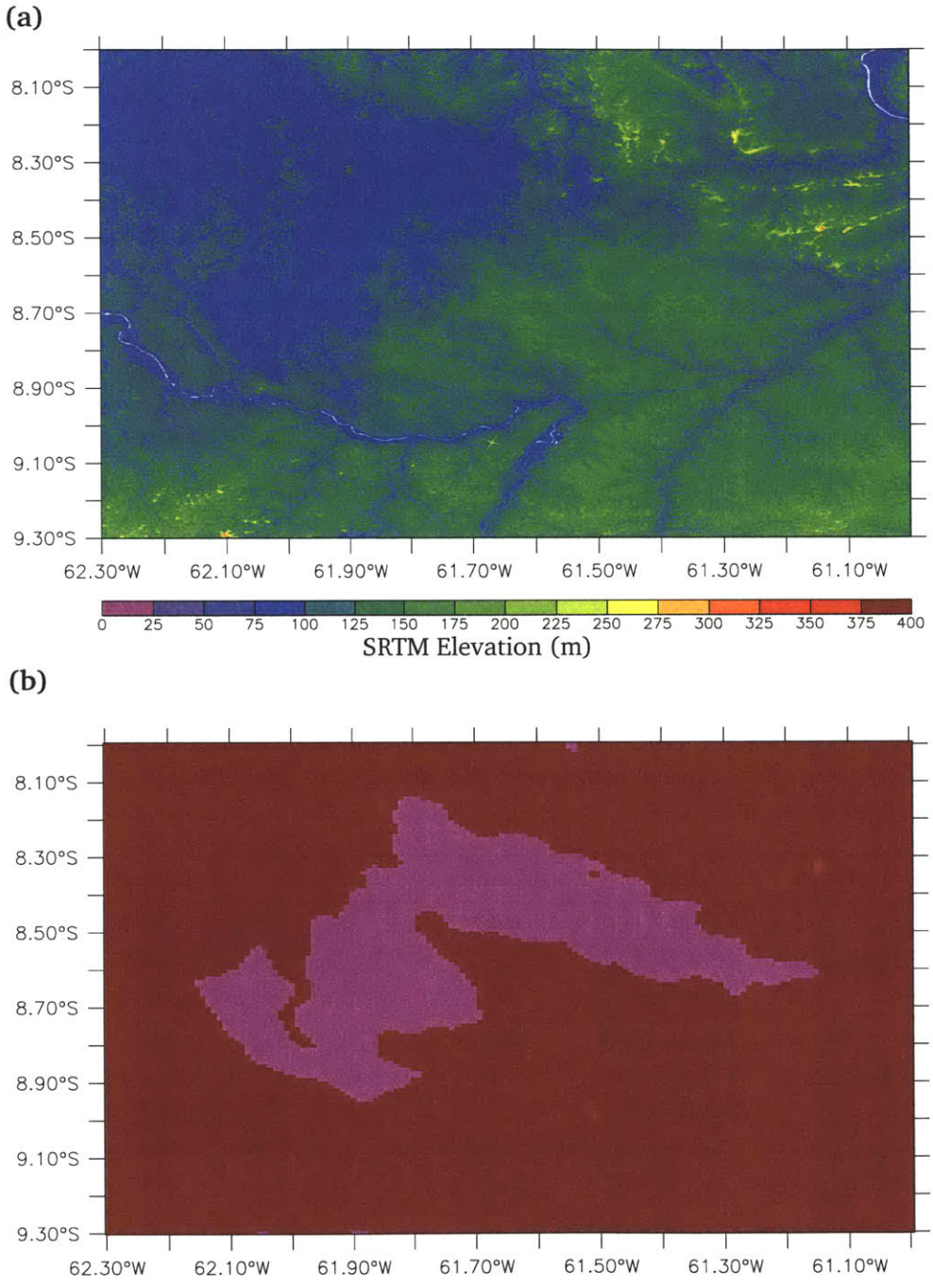

Figure 6-38: Savannah domain; **(a)** SRTM Elevation map and **(b)** Forest Cover (1 km resolution, 50% threshold).

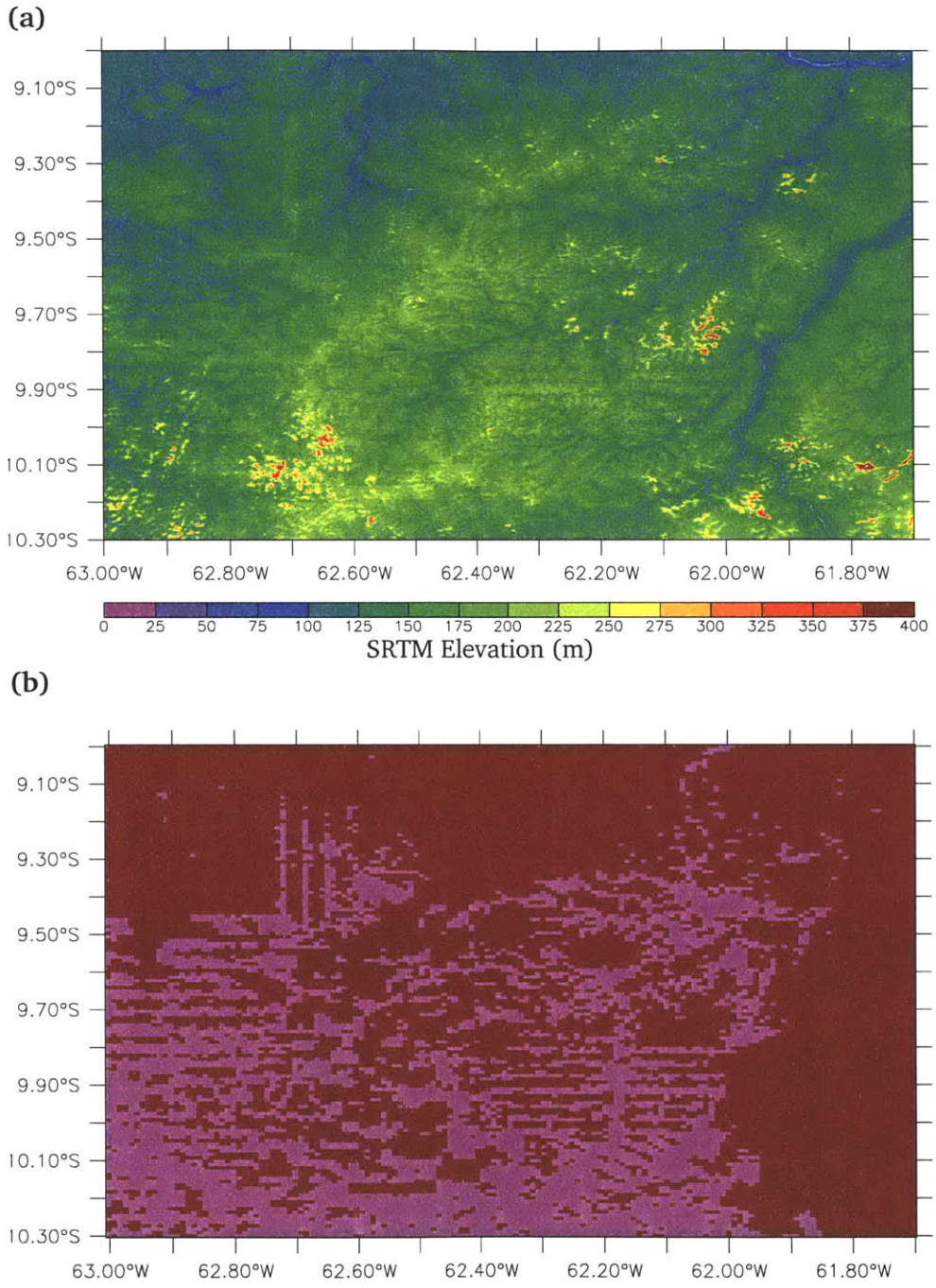

Figure 6-39: Fishbone domain; **(a)** SRTM Elevation map and **(b)** Forest Cover (1 km resolution, 50% threshold).

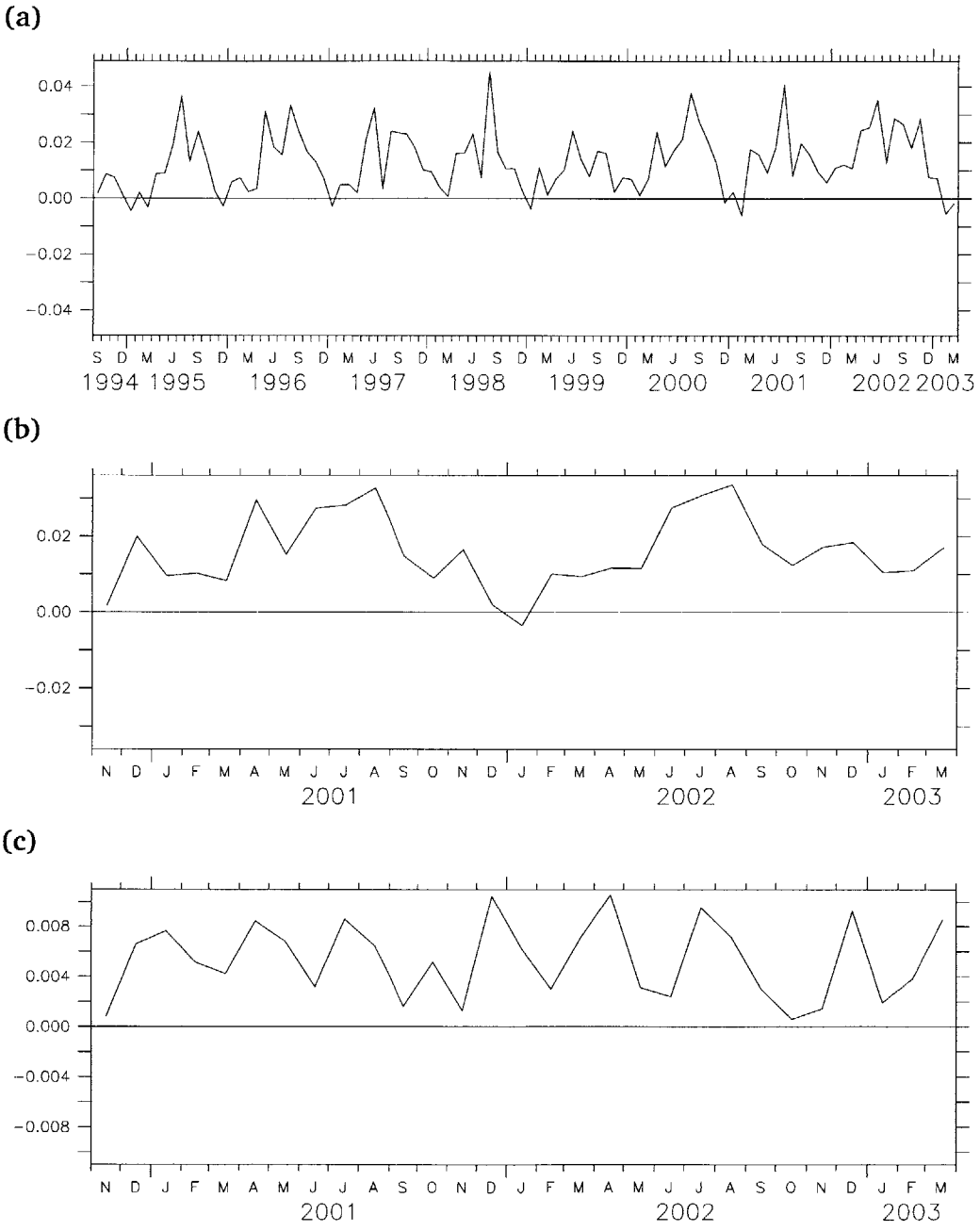

Figure 6-40: Monthly Time-Series of Fractional Shallow Cloud Cover Differences between Deforested and Forested Pixels over the Savannah Domain at **(a)** 14h45 UTC, **(b)** 17h45 UTC and **(c)** 20h45 UTC.

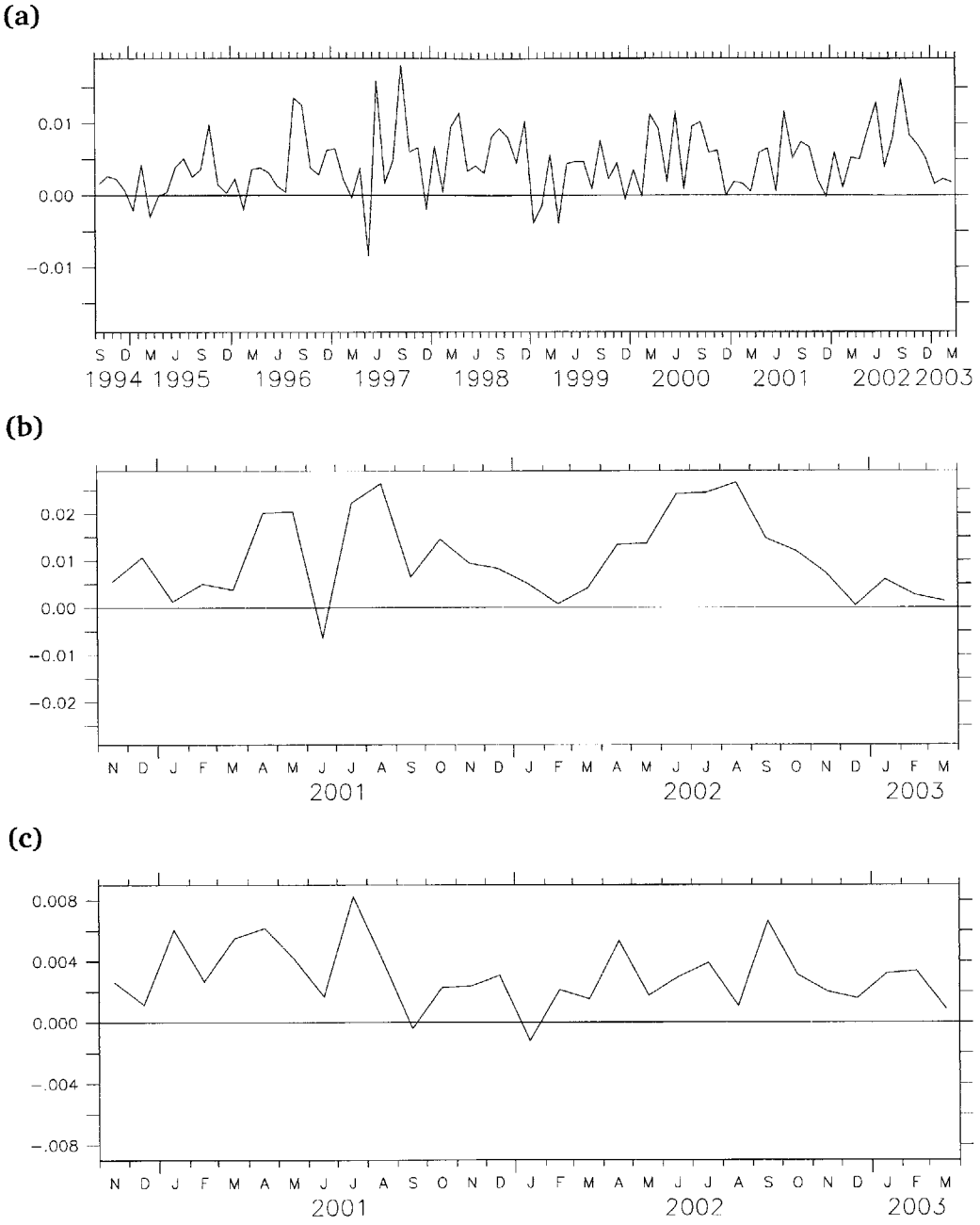

Figure 6-41: Monthly Time-Series of Fractional Shallow Cloud Cover Differences between Deforested and Forested Pixels over the Fishbone Domain at **(a)** 14h45 UTC, **(b)** 17h45 UTC and **(c)** 20h45 UTC.

6.5 Summary & Conclusions

Patterns of remotely-sensed shallow cumulus clouds over the Amazon basin were compared to the underlying patterns of deforestation. The statistical analysis of this comparison, which was shown to be robust with respect to algorithmic variations, revealed that there are significantly more shallow cumulus clouds over deforested regions, and that the occurrence of such local enhancements of shallow convective clouds is also significant. By comparing the results to external factors, it was found that only the onset of the localized shallow cloud enhancement is sensitive to synoptic wind speed, while it is always sensitive (i. e., liable to be suppressed) to synoptic wind shear magnitude. The direction of the synoptic circulation was also found to be a determining factor, as southerly winds strongly suppressed the deforestation-induced shallow cloud contrast. The sensitivity of the shallow cloud enhancement to previous surface wetting events was only exhibited during the dry season (JJA) using the gauge-based data. During other seasons, the influence of antecedent precipitation was found to be inconclusive. Finally, the results were tested by comparing shallow clouds and topography (i. e., elevation and slope). While there was a clear association between the topography and shallow clouds, it was inferred that this relationship was not clouding the cumulus-forest results, as the timing of the topography-cloud associations are different, and the distribution of elevation and slope are similar over forested and deforested regions.

REFERENCES

ADLER, R. F., J. SUSSKIND, G. J. HUFFMAN, D. BOLVIN, E. NELKIN, A. CHANG, R. FERRARO, A. GRUBER, P.-P. XIE, J. JANOWIAK, B. RUDOLF, U. SCHNEIDER, S. CURTIS and P. ARKIN. The Version-2 Global Precipitation Climatology Project (GPCP) Monthly Precipitation Analysis (1979-Present). *Journal of Hydrometeorology*, 4(6):pages 1147–1167 [2003].

AVISSAR, R. and T. SCHMIDT. An evaluation of the scale at which ground-surface heat flux patchiness affects the convective boundary layer using large-eddy simulations. *Journal of the Atmospheric Sciences*, 55(16):pages 2666–2689 [1998].

CHEN, F. and R. AVISSAR. The impact of land-surface wetness heterogeneity on mesoscale heat fluxes. *Journal of Applied Meteorology*, 33(11):pages 1323–1340 [1994].

DALU, G. A., R. A. PIELKE, M. BALDI and X. ZENG. Heat and Momentum Fluxes Induced by Thermal Inhomogeneities with and without Large-Scale Flow. *Journal of the Atmospheric Sciences*, 53(22):pages 3286–3302 [1996].

HALVERSON, J. B., T. RICKENBACH, B. ROY, H. PIERCE and E. WILLIAMS. Environmental Characteristics of Convective Sytems during TRMM-LBA. *Monthly Weather Review*, 130(6):pages 1493–1509 [2002].

HONG, X., M. J. LEACH and S. RAMAN. A Sensitivity Study of Convective Cloud Formation by Vegetation Forcing with Different Atmospheric Conditions. *Journal of Applied Meteorology*, 34(9):pages 2008–2028 [1995].

HOUZE, JR., R. A. *Cloud Dynamics*, vol. 53 of *International Geophysics Series*. Academic Press [1993].

HUFFMAN, G. J., R. F. ADLER, M. M. MORRISSEY, D. T. BOLVIN, S. CURTIS, R. JOYCE, B. MCGAVOCK and J. SUSSKIND. Global Precipitation at One-Degree Daily Resolution from Multisatellite Observations. *Journal of Hydrometeorology*, 2(1):pages 36–50 [2001].

ROY, S. B. and R. AVISSAR. Impact of land use/land cover change on regional hydrometeorology in Amazonia. *Journal of Geophysical Research*, 107(D20) [2002].

ROY, S. B., C. P. WEAVER, D. S. NOLAN and R. AVISSAR. A preferred scale for landscape forced mesoscale circulations? *Journal of Geophysical Research*, 108(D22):pages 8854–8864 [2003].

WANG, J., R. L. BRAS and E. A. B. ELTAHIR. A Stochastic Linear Theory of Mesoscale Circulation Induced by the Thermal Heterogeneity of the Land Surface. *Journal of the Atmospheric Sciences*, 53(22):pages 3349–3366 [1996].

WANG, J., E. A. B. ELTAHIR and R. L. BRAS. Numerical Simulations of Nonlinear Mesoscale Circulations Induced by the Thermal Heterogeneities of Land Surface. *Journal of the Atmospheric Sciences*, 55(3):pages 447–464 [1998].

WEAVER, C. P. and R. AVISSAR. Atmospheric Disturbances Caused by Human Modification of the Landscape. *Bulletin of the American Meteorological Society*, 82(2):pages 269–281 [2001].

CHAPTER 7

RAINFALL & TROPICAL DEFORESTATION

The clear association between shallow cumulus clouds and deforestation that has been demonstrated in Chapter 6 prompts us to investigate the impact of deforestation on rainfall. Rainfall records in the Amazon basin are available from multiple sources, and they have varied temporal and spatial extents and resolutions. There are many plausible hypotheses regarding the relation between forest cover and rainfall. The following hypotheses are formulated, and are thought to be the most reasonable:

1. warm rain (i. e., rain from clouds that do not have a solid/ice phase) is related to deforestation in the same way that the shallow clouds are;

2. convective rainfall is enhanced over deforested regions;

3. rainfall is related to deforestation indirectly through the shallow cloud enahancement; the shallow clouds promote an increase in subsequent rainfall by increasing the moisture content of the atmosphere.

Some of these hypotheses are contradictory; one would not expect to see enhanced warm rain over deforested regions if the shallow cloud enhancement promoted subsequent rainfall. Indeed, a warm rain — deforestation association would be indicative of a raining-out of the moisture contained in the shallow clouds, whereas a cloud moistening hypothesis would have to be accompanied by an initial suppression of rainfall.

The chapter will first briefly expose the rainfall datasets used, and an examination of the relation between rainfall and deforestation will be undertaken. Rainfall statistics will also be examined in relation to topography. Due to the nature of the data available, targeted tests that could provide direct verification of the hypotheses postulated above are not formulated in this chapter. Instead, a comprehensive method will be used; all available data will be examined with respect to forest cover

and topography in order to detect any significant associations. It is thought that this approach is better suited to the multitude of data available. Moreover, such an approach has the advantage of possibly revealing unforeseen results. A description of the datasets follows.

7.1 The Tropical Rainfall Measuring Mission

The Tropical Rainfall Measuring Mission (TRMM) is a joint mission between the National Aeronautics and Space Agency (NASA) of the United States and the National Space Development Agency (NASDA) of Japan. The TRMM satellite consists of three primary rainfall instruments: the passive microwave radiometer (TMI), the precipitation radar (PR) and the visible/infrared scanner (VIRS); the instrument characterisitcs are summarized in Table 7.1. TRMM's main objective is to measure the three-dimensional distribution of rainfall in the tropics. TRMM was flying in a low-earth orbit (LEO) at 350 km altitude until operational constraints required a boost to an altitude of 405 km in August 2002. It's orbit is circular and has a 35^o inclination angle. It was successfully launched in November 1997, and has been actively collecting data since December 1997.

Table 7.1: TRMM Instrument Characteristics

	Visible Infrared Scanner	TRMM Microwave Imager	Precipitation Radar
Frequency or Wavelength	0.63, 1.6, 3.75, 10.8, 12 μm	10.65, 19.35, 37.0, 85.5 GHz dual polarization, 21.3 GHz vertical polarization	13.8 GHz horizontal polarization
Scanning Mode	Cross track	Conical	Cross track
Ground Resolution	2.1 km	Ranges from 5 km at 85.5 GHz to 45 km at 10.65 GHz	4.3 km at nadir
Swath Width	720 km	760 km	215 km

The data of interest in this paper are provided by the Precipitation Radar (PR), which is the first rain radar in space. The precipitation radar is the only instrument on-board TRMM that is capable of supplying rainfall estimates at a resolution high enough to perform the statistical tests in this chapter[1]. Kummerow *et al.* [1998] state that its key goals are to provide the three-dimensional structure of rainfall, to obtain quantitative rainfall measurements over land and ocean, and to improve

[1]As of the writing of this thesis, the version 6 TRMM data products, which contain a TMI product at 0.5^o resolution, have not been released.

the overall precipitation retrieval accuracy by combined use of the active PR and passive TMI and VIRS. The PR operates at a frequency of 13.8 GHz, has a swath width of 215 km, a ranging resolution of 250 m at nadir, and a horizontal resolution of 4.3 km at nadir.

The TRMM data is supplied in HDF format. HDF was developed by the National Center for Supercomputing Applications (NCSA) as a platform independent self-describing data format for large datasets. The data products studied in this section are the TRMM-2A23 and TRMM-3A25 rainfall products. These products are supplied by the Tropical Rainfall Measuring Mission Science data and Information System (TSDIS). The TRMM-HDF files were accessed and read with MATLAB using the HDF functions in the *iofun* toolbox. The two TRMM data products that are studied here are presented in the following sub-sections, immediately after a description of the scanning geometry of TRMM precipitation radar, and a description of relevant terminology concerning the TRMM-PR.

The scanning geometry of the TRMM Precipitation Radar is schematically drawn in Figure 7-1. The PR scans right to left, and each scan contains 49 rays. The preboost swath width was 215 km, which was covered by a 34^o angular sector. In each ray, the PR records samples at each 125 m, starting from a fixed distance from the satellite. The PR samples approximately 30 km along each ray.

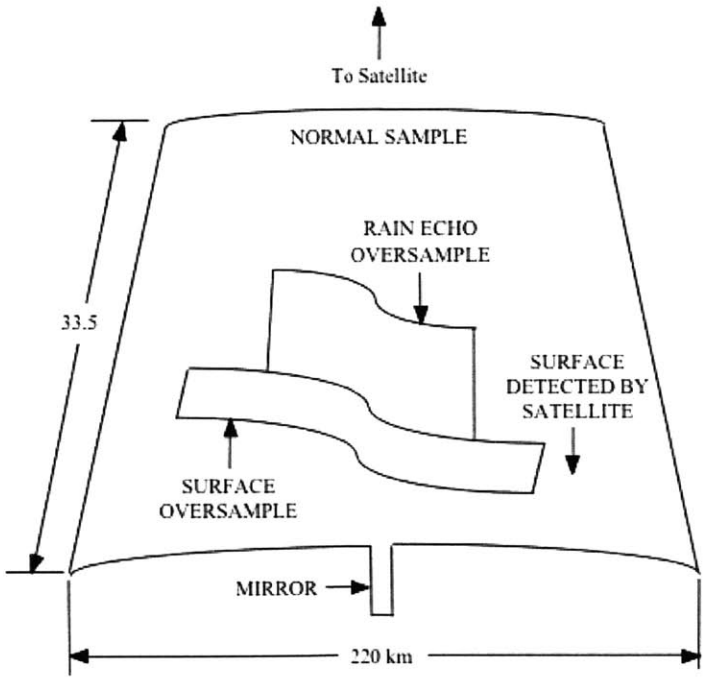

Figure 7-1: TRMM-PR Scanning Geometry (from TSDIS File Specifications for TRMM Products, Volume 3, available at http://gcdc.gsfc.nasa.gov/iso/home.html)

When rainfall is detected, it is qualified as stratiform, convective or other. The

output power measured by the PR is first converted to the "Z-factor", or radar reflectivity factor, by applying the radar equation. If the maximum Z-factor with respect to range is detected at the expected freezing level, and if this maximum is prominent, then a bright band is deemed detected and the rainfall is qualified as being stratiform. The height of the bright band is also recorded. If there is no bright band detection, the rainfall is deemed convective if the Z-factor surpasses a certain threshold along the range. Otherwise, the rainfall is termed "other". Warm rain is detected when the storm height (determined by the greatest altitude at which rainfall is detected) is below the expected freezing level. Warm rain can be convective or other, but not stratiform.

7.1.1 TRMM-2A23

The TRMM-2A23 data product provides a qualitative description of the precipitation radar retrievals. The data product is supplied by TSDIS in a swath structure. The 2A23 swaths were initially subset over the Rondônia domain by Dr. Erich F. Stocker at NASA Goddard. These subsetted swaths were then encoded with land cover and topographical features from 4-km resolution maps of Rondônia, using nearest central coordinates. The TRMM-2A23 data product provides rain/no-rain flags, and conditionally on presence of rain determines other parameters as presented in Table 7.2[2]. The parameters were re-interpreted as per Table 7.3 in order to simplify and rationalize the analysis.

There are two types of rainfall parameters analyzed in the TRMM-2A23 dataset; the difference in rainfall occurrence counts (stratified by type) between deforested and forested areas, and the difference in magnitude of three PR retrievals: storm height, bright band height and bright band intensity. The difference in rainfall occurrence counts are computed by taking the difference between deforested and forested areas of the count of the number of occurrences of a certain type of rain over a month, normalized by the total number of pixels of the particular land cover type (i. e., forested or deforested). The validity of such statistics is based on the assumption that the satellite instrument visits both land cover types an even number of times and that the visitation time-of-day values are evenly distributed over the two land cover types. The difference in PR retrival magnitudes are computed by averaging the values of storm height, bright band height and bright band intensity over deforested and forested areas on a monthly time-scale, and taking their difference. The averages are conditional, in that they are averages of non-zero PR retrievals.

[2]The occurrence of multiple similar descriptions for different parameter values serves to differentiate between the different methods used to identify the rain types. These are of no interest to the present study.

Table 7.2: Description TRMM-2A23 Parameters

Parameter Name	Value	Description
Rain Flag	0	no rain
	10	rain possible
	11	rain possible (echo > threshold #1 in clutter region)
	12	rain possible (echo > threshold #2 in clutter region)
	20	rain certain
Rain Type Flag	10	stratiform certain (BB exists)
	11	stratiform certain (BB exists)
	12	probably stratiform
	13	maybe stratiform (BB detection certain)
	14	maybe stratiform (BB hardly expected)
	15	maybe stratiform; shallow isolated warm rain
	20	convective certain (no BB)
	21	convective certain
	22	convective certain
	23	probably convective (BB exists)
	24	maybe convective
	25	maybe convective (BB detection not so confident)
	26	maybe convective; shallow isolated warm rain
	27	maybe convective; shallow isolated warm rain
	28	maybe convective; shallow isolated warm rain
	29	maybe convective; shallow isolated warm rain
	30	others
	31	others; shallow isolated warm rain
Warm Rain Flag	0	warm rain not detected
	1	maybe warm rain
	2	warm rain detected
Height of Bright Band	>0	bright band height (meters above sea level)
Bright Band Intensity	>0	maximum bright band intensity; 0—100 dBZ
Height of Storm	>0	height of storm top (meters above sea level)

Table 7.3: Rationalized TRMM-2A23 Parameters for Analysis

Description	Parameter	Value
Rain Certain	rain flag	20
Rain Possible	rain flag	$\geqslant$10
Stratiform Rain	rain type	$\geqslant$10 & $\leqslant$15
Convective Rain	rain type	$\geqslant$20 & $\leqslant$29
Shallow Isolated Rain	rain type	15; 26; 27; 28; 29; 31
Warm Rain Certain	warm rain	2
Warm Rain Possible	warm rain	1; 2
Height of Bright Band	height of bright band	height in meters
Bright Band Intensity	bright band intensity	intensity in dBZ
Storm Height	storm height	height in meters

7.1.2 TRMM-3A25

The TRMM-3A25 Scientific Datasets (SDS) that are analyzed in this study are described below in Tables 7.4 & 7.5. For purposes of simplicity, the conditional intensities will be referred to simply as mean rainfall intensities for the rest of the report. The TRMM Science Data and Information System computes monthly statistics of the PR measurements both at low (5^o) and high (0.5^o) horizontal resolutions for the 3A25 product. In this study, only the high horizontal resolution Scientific Data Sets (SDS) are analyzed, since the biggest study domain (i. e., Rondônia) is exactly 5^o to the side.

The analysis of the TRMM-3A25 dataset with respect to forest cover and topography are undertaken at a resolution of 0.5^o, on a grid that coincides with the TRMM-3A25 grid. Figure 7-2 shows the forest, elevation and slope fields on that particular grid. The randomization used for these base covers follows the CSR algorithm, with a randomization block scale of 100-km. All of the TRMM-3A25 variables given in Tables 7.4 & 7.5 are analyzed by taking their monthly mean difference between different forest cover states or topographical ranges.

7.2 Analysis of Rainfall and Deforestation Patterns

This section will provide a product-by-product analysis of the rainfall association with deforestation. Since there are many variables under study, only those variables that yielded a significant result will be presented in this chapter. The full results are presented in Appendix B. The rainfall products TRMM-2A23, TRMM-3A25 are analyzed using the landcover and topography randomization method explained in Chapter 5. The TRMM-2A23 uses the shuffling algorithm for a forest cover based

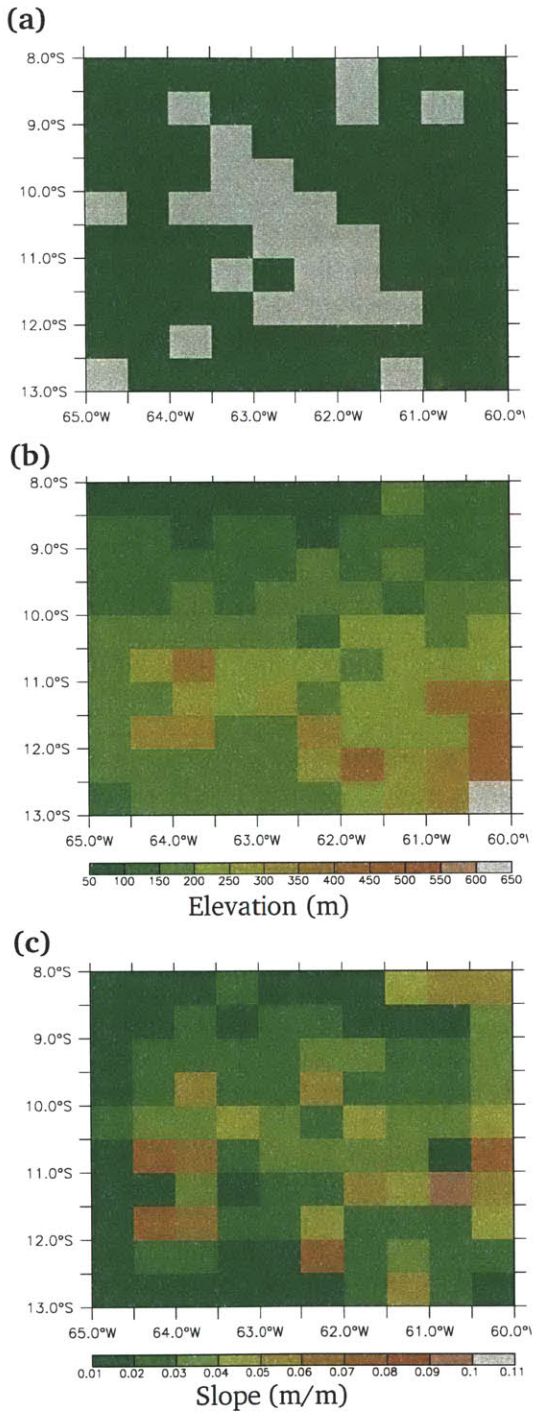

Figure 7-2: Maps of **(a)** forest cover, **(b)** elevation and **(c)** slope for the Rondônia domain on the TRMM-3A25 grid.

Table 7.4: Description of 3-D TRMM-3A25 Scientific Datasets

Name	Description
Mean Rain Rate	Mean of non-zero rain-rates over $0.5^o \times 0.5^o$ boxes for one month. The rain rates are determined in 2A-25 and evaluated at fixed heights of 2 km, 4 km, 6 km, and path average. It ranges from 0 to 3,000 mm/h.
Rain Rate Dev.	Standard deviation of non-zero rain-rates.
Mean Conv. Rain Rate	Mean of non-zero rain-rates for convective rain.
Conv. Rain Rate Dev.	Std. deviation of non-zero rain-rates for convective rain.
Mean Strat. Rain Rate	Mean of non-zero rain-rates for stratiform rain.
Strat. Rain Rate Dev	Std. Deviation of non-zero rain-rates for stratiform rain.
Mean Zm (Zt)	Mean Zm (Zt) gives the monthly means of the measured (corrected) reflectivity at the fixed height levels of 2 km, 4 km, 6 km, and path average. Zm ranges from -20 to 80 dBZ; Zt ranges from 0.1 to 80 dBZ.
Mean Conv. Zm (Zt)	Monthly mean measured (corrected) reflectivity of convective rain.
Mean Strat. Zm (Zt)	Monthly mean measured (corrected) reflectivity of stratiform rain.
Rain Pixel Number	Monthly number of non-zero rain-rate pixels for path-averaged rainfall and rainfall at the fixed height of 2 km, 4 km, and 6 km over $0.5^o \times 0.5^o$ boxes. The range is 0 to 2,000,000.
Conv. Rain Pixel Number	Monthly number of non-zero rain-rate pixels for convective rain.
Strat. Rain Pixel Number	Monthly number of non-zero rain-rate pixels for stratiform rain.

Table 7.5: Description of 2-D TRMM-3A25 Scientific Datasets

Name	Description
Mean Storm Height	Monthly mean of storm height, unconditioned and conditioned for stratiform and convective rain over $0.5^o \times 0.5^o$. It has units of meters and ranges from 0 to 20,000.
BB Height Mean	Monthly mean of bright band height.
Mean Surf. Rain	Mean of non-zero near-surface rain rate.
Surf. Rain Dev.	Std. deviation of non-zero near-surface rain rate.
Mean BB Zmax	Mean of maximum reflectivity in bright band at horizontal resolution of $0.5^o \times 0.5^o$. It ranges from 0 to 100 dBZ.
BB Zmax Dev.	Std. deviation of maximum bright band height.
Storm Height Dev.	Std. deviation of storm height, unconditioned and conditioned for stratiform and convective rain.
BB Height Dev.	Std. deviation of bright band height.
Mean Surf. Rain All	Mean of non-zero near-surface rain rate using rain certain and rain possible.
Surf. Rain All Dev.	Std. deviation of non-zero near-surface rain rate using rain certain and rain possible.
Total Pixel Number	Number of total pixel visitations over $0.5^o \times 0.5^o$ boxes for one month. The range is 0 to 2,000,000.
BB Pixel Number	Number of bright band pixel counts over $0.5^o \times 0.5^o$ for one month.
Warm Rain Pixel	Warm rain pixel counts.
Surf. Rain Pixels	Near-surface rain counts at a horizontal resolution of $0.5^o \times 0.5^o$. It ranges from 0 to 2,000,000,000.
Surf Rain All Pixels	Near-surface rain counts using rain certain and rain possible.

at 4-km resolution, and the TRMM-3A25 uses the CSR algorithm. The base forest cover and topography maps for the TRMM-3A25 observed statistics have a 0.5^o (i. e., approximately 50-km) resolution; the CSR randomization uses 100 km blocks to create the base maps that determine the randomized statistics.

7.2.1 TRMM-2A23 Results

The analysis of TRMM-2A23 rainfall fields with respect to deforestation points to an increase of rainfall occurrence over deforested areas. The monthly time-series of rainfall occurrence differences between the two land cover types are analyzed as binomial counting variables, under the assumption that fields that bear no associative relation to deforestation have a probability of one-half of being either above or below zero. The full results from this binomial analysis are presented in Appendix B (Table B.1). "Rain certain", "rain possible", "rain stratiform" and "rain convective" counts are significantly higher over deforested areas[3]; Table 7.6 shows that the level of significance associated with the rainfall occurrence difference is quite high. The counts of "rain isolated" and "warm rain possible" show no significant association with deforestation, and neither do the differences in storm height, bright band intensity or bright band height. The time-series of the occurrence count differences for the variables that show a significant signal are plotted in Figures 7-3 & 7-4. These figures also show the 99% confidence bounds that were derived using the randomized land cover analysis. Table B.2 summarizes the behavior of the TRMM-2A23 variables with respect to the confidence bounds. Of all the variables, only "rain certain" and "rain stratiform" exhibit repeated confidence bound exceedences (Table 7.7). The "rain certain" confidence bound exceedences occur in February, March, April, July, and September (once each); the time-series also dips twice below the lower confidence bound in June and October. "Rain stratiform" exceeds the upper 99% confidence bound five times as well (February, March, April, August and September), while it dips below the lower 99% confidence bound once in October.

The time-of-day at which the rainfall occurrences are recorded is also analyzed in order to assess whether there is a significant difference in the timing of rainfall event as a result of the deforestation. The analysis proceeds by examining the timing difference of rainfall events between deforested and forested areas. The results are then treated as realization of a binomial variable (i. e., under the null hypothesis that deforestation does not affect the timing of rainfall, it is expected that rainfall will occur earlier over deforested areas as many times as it occurs earlier over forested areas.) The results are also inspected with the land cover randomization method. The time-series of the timing differences for certain variables are presented in Figure 7-5. The results are summarized in Tables B.3 & B.4, respectively. There is no persistent difference in the timing of any rainfall type, as can be seen in Table B.3. There are, however, some occurrences of organization on particular months. Indeed, the "rain certain", "rain possible", "rain convective" and "rain

[3]The definition of the different 2A23 rainfall counts are given in Table 7.3.

Table 7.6: Significant Results from the Binomial Analysis of TRMM-2A23 Event Counts v. Forest Cover; The count of positive and negative normalized event count differences is compared to the binomial distribution to detect significant biases.

Difference Statistic	>0 Counts	<0 Counts	Significance
Rain Certain	59	17	$p \leqslant 0.0001$
Rain Possible	72	4	$p \leqslant 0.0001$
Rain Convective	54	22	$p \leqslant 0.0005$
Rain Stratiform	59	17	$p \leqslant 0.0001$

Table 7.7: Significant Results from the Randomization Analysis of TRMM-2A23 Event Counts v. Forest Cover; The count of times that the normalized event count difference is greater than the upper 99% confidence bound, and the count of the number of times that the difference is less than the lower 99% confidence bound are summarized.

Difference Statistic	$>\uparrow$99% Limit	$<\downarrow$99% Limit
Rain Certain	5	2
Rain Stratiform	5	1

Table 7.8: Significant Results from TRMM-2A23 Event Timing v. Forest Cover Randomization Analysis; The count of times that the mean event occurrence time difference is greater than the upper 99% confidence bound, and the count of the number of times that the difference is less than the lower 99% confidence bound are summarized.

Difference Statistic	$>\uparrow$99% Limit	$<\downarrow$99% Limit
Rain Certain	0	4
Rain Possible	1	3
Rain Convective	0	2
Rain Stratiform	1	3

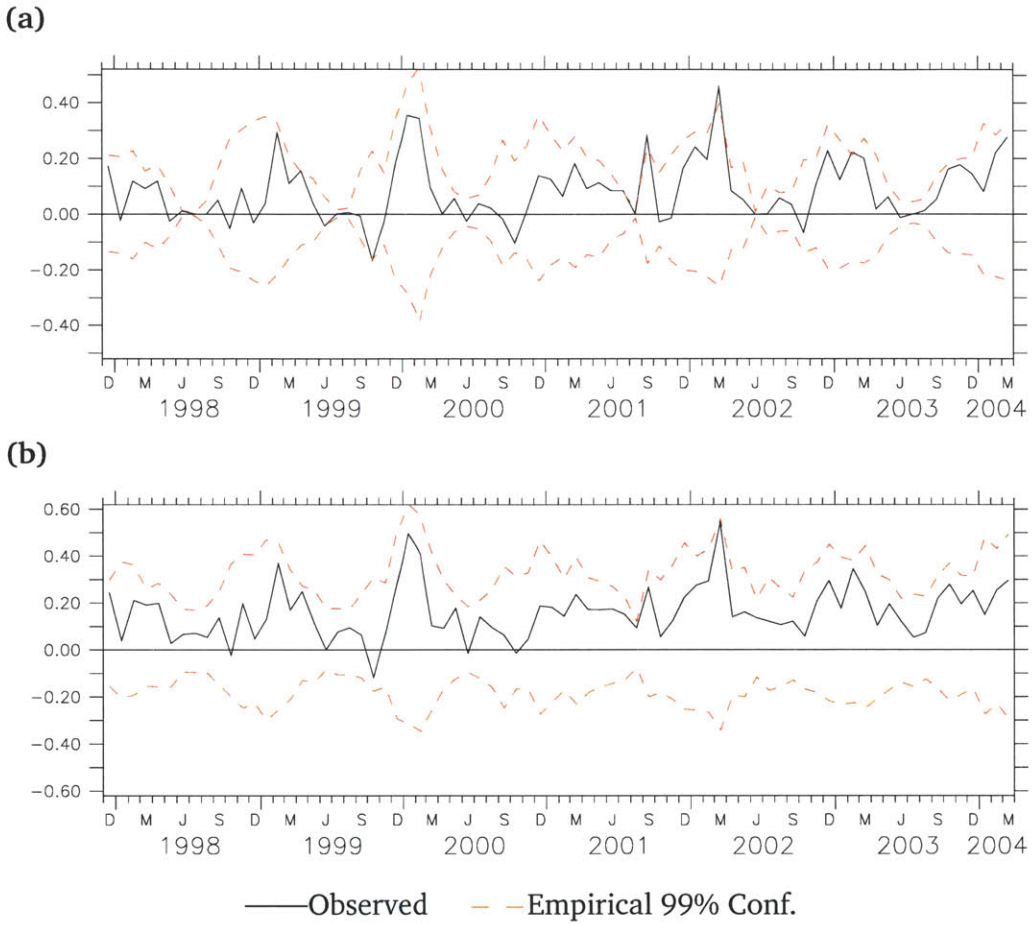

Figure 7-3: Monthly time series of TRMM-2A23 **(a)** "rain certain" and **(b)** "rain possible" count differences (normalized count over deforested pixels minus normalized count over forested areas) over the study domain of Rondônia, along with their respective 99% confidence limits.

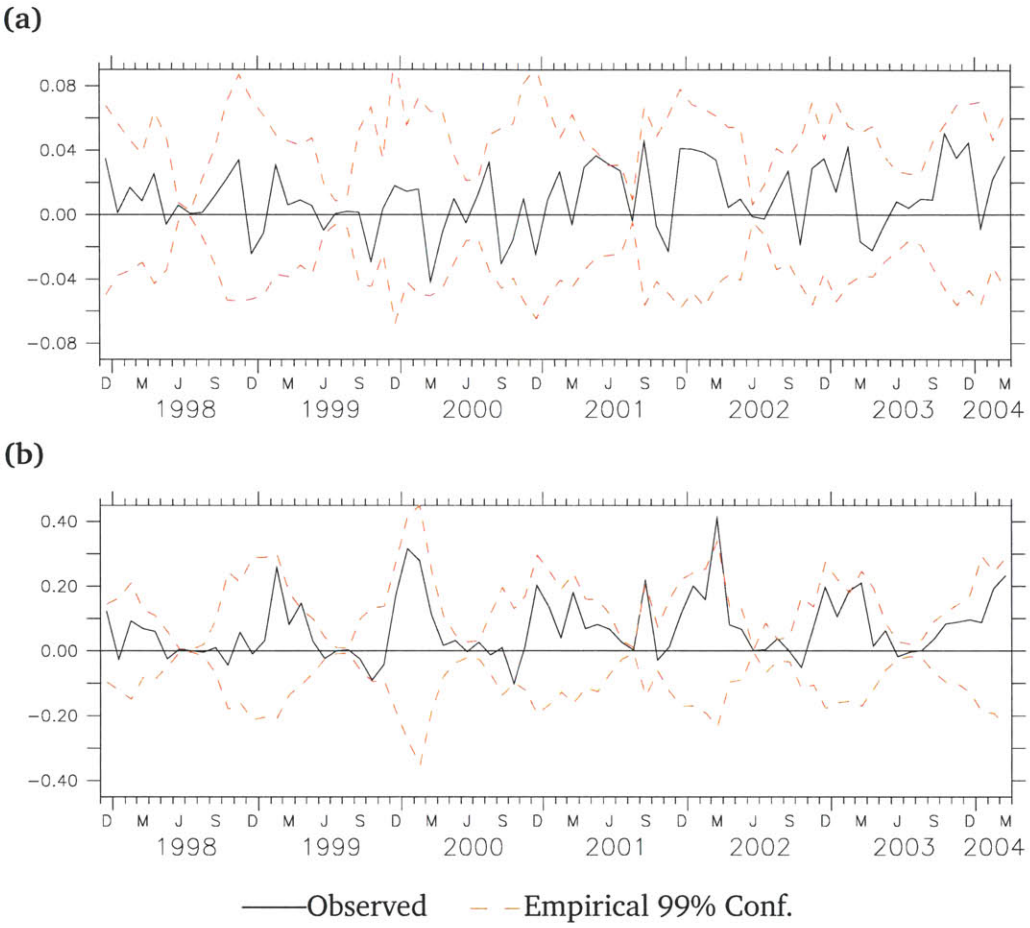

Figure 7-4: Monthly time series of TRMM-2A23 **(a)** "rain convective" and **(b)** "rain stratiform" count differences (normalized count over deforested pixels minus normalized count over forested areas) over the study domain of Rondônia, along with their respective 99% confidence limits.

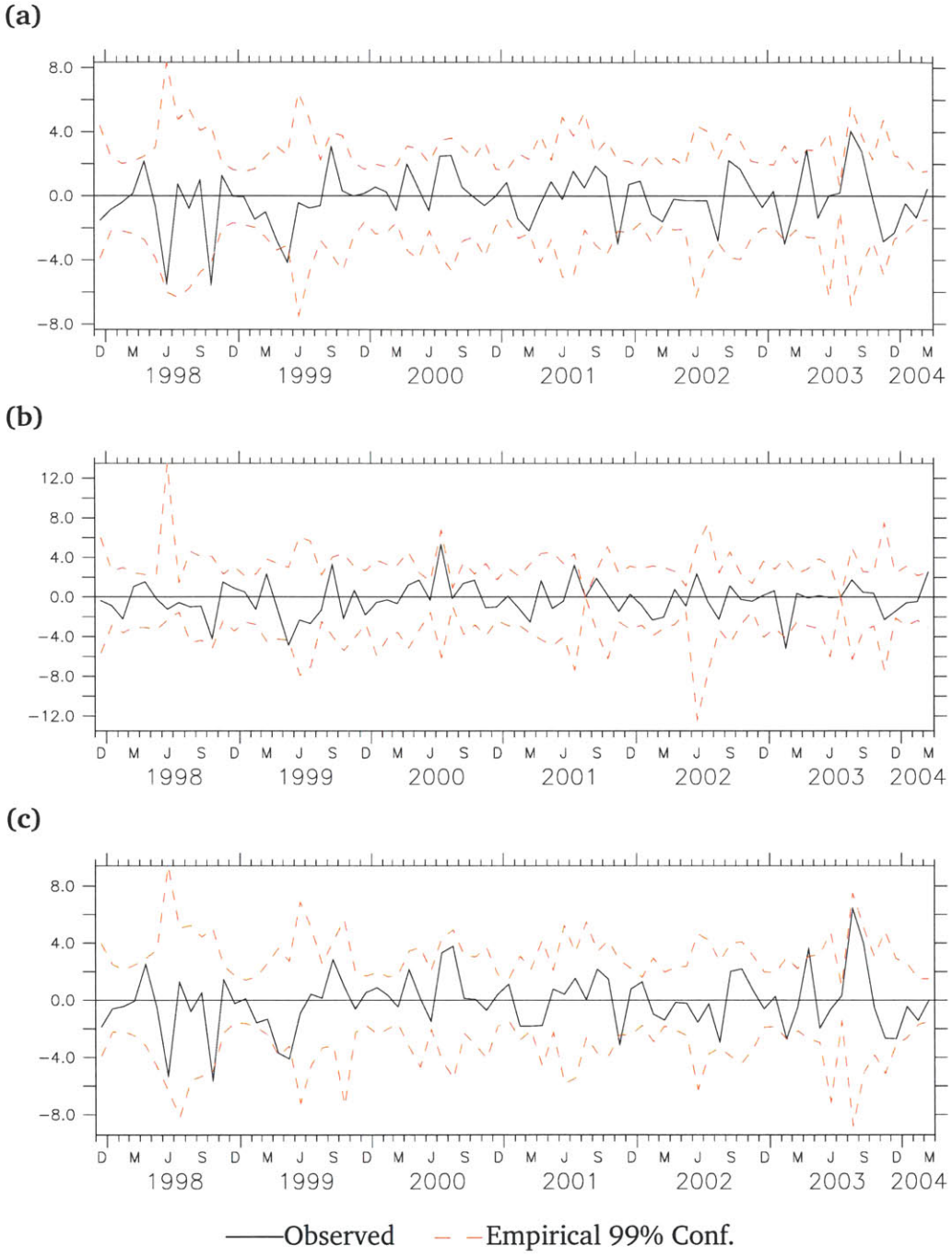

Figure 7-5: Monthly time series of TRMM-2A23 **(a)** "rain certain", **(b)** "rain convective" and **(c)** "rain stratiform" occurrence time differences over the study domain of Rondônia, along with their respective 99% confidence limits.

stratiform" all dip below the lower 99% confidence bound more than once[4], indicating that there are months during which the rainfall over deforested areas occurs significantly earlier than over the forested areas (Table 7.8). These occurrences are recorded four times for "rain certain" (February, May, October, November), three times for "rain possible" (October, November, December), twice for "rain convective" (February, May), and three times for "rain stratiform" (May, October, November). These results indicate an episodic influence of forest cover on rainfall timing, not a persistent shift.

7.2.2 TRMM-3A25 Results

The analysis of the TRMM-3A25 data products yields much more subtle results than those found with the TRMM-2A23 product. None of the variables show significance with respect to the 99% confidence bounds derived using randomized forest cover fields (see Tables B.14 , B.18 & B.19). There are, however, some significant results in the binomial analysis. The analysis of 2-D variables (Table 7.9) shows that the mean bright band height is higher over deforested areas ($p \leqslant 0.05$), whereas there are more warm rain pixels counts over the forested areas ($p \leqslant 0.1$). The analysis of the 2-D variables also shows that there is no sampling bias between forested and deforested areas, as the "total pixel count" variable is not significantly different than a binomial random variable, nor does it show a significant association with deforestation from the randomization analysis (Table 7.10).

There are also significant tendencies in the height-dependent TRMM-3A25 variables (Table 7.11). The most significant results ($p \leqslant 0.07$) are that there is a higher variability in the rate of stratiform rainfall over forested areas, and the measured convective rainfall reflectivity is higher over deforested areas at the 6 km level. The next most significant results ($p \leqslant 0.11$) are that the mean rate of stratiform rainfall is higher over forested areas, the count of convective rain pixels is higher over forested areas at the 6 km level, and the corrected convective rainfall reflectivity is higher over deforested areas. Finally, with weaker confidence ($p \leqslant 0.14$), the standard deviation of rainfall rates is higher over deforested pixels; there are more convective rain pixels counts over forested areas at the 2 km and 4 km levels, and on a path-averaged basis; and the measured reflectivity of rainfall events is higher over deforested areas at the 6 km level.

[4]A random variable with respect to forest cover is expected to be reach outside the 99% confidence bounds once every hundred months. Here we have a record of 76 months, thus it is expected to lie outside the confidence bounds 0.76 months, which we round to 1. Thus, we regard one outlier as insignificant.

7.3 Analysis of Rainfall and Topography Patterns

The analysis of rainfall with respect to topography (elevation and slope) is done using the same methods explained in Chapter 6. The elevation and slope fields are transformed into binary fields using thresholds that are determined by the distribution of elevation and slope within the Rondônia domain. For example, the difference in rainfall counts is calculated between the 30% highest pixels and the 70% lowest.

7.3.1 TRMM-2A23 Results

There is an overwhelming association of rainfall counts and elevation, as can be noticed in Table 7.12. There is a general bias of rainfall counts of all types over higher terrain. These results are however marred by the total pixel count, which is determined at a lower resolution (i. e., 50 km instead of 4 km) in the TRMM-3A25 product, that can be seen in Table 7.19. Indeed, there appears to be a very significant bias in terms of sampling over higher altitudes. The results associating rainfall counts with elevation must thus be discounted. For the same reason, the departures from the 99% confidence bounds derived with the randomization method, which are summarized in Table B.7, must also be discounted.

The differences in bright band height and bright band intensity, both of which exhibit significant biases with respect to elevation (Table 7.12), are not be be discounted for they are not affected by the bias in total pixel counts, since they are not count variables. The bright band height is significantly higher over lower elevations, and the bright band is less intense over lower elevations. No similar trend is detected in the departures from the 99% confidence bounds (Table B.7).

Fortunately, there is no significant bias in sampling stratified by slope (Table 7.21). Thus the overwhelmingly significant association of rain counts with slope are not sampling artefacts (Table 7.13). Rain counts are much higher over steeper slopes, although there is no clear association of isolated or warm rain counts with slope, nor do the bright band height, storm height or bright band intensity show any significant biases with respect to slopes. The departures from the randomization-based 99% confidence interval (Table 7.14) are coherent with the results from the binomial analysis. Moreover, there appears to be some evidence of episodic associations between slope and storm and bright band heights. Mean monthly storm heights are sometimes significantly higher over steep slope pixels, while mean monthly bright band heights are sometimes significantly higher over gradual slope pixels.

The time associated with the rainfall events is also studied with respect to elevation and slope. Rain certain and convective rain occurrences occur both significantly earlier on the 30% lowest elevations (Table 7.15). There is a weaker significant association of isolated and warm rain occurrences with slope. Both types of rain occur later on the 50% steepest pixels (Table 7.16). The randomization analysis yields

repeated outliers from the 99% confidence bounds. The general trend from the randomization analysis shows that rain certain, rain possible, rain convective and rain stratiform occur earlier over lower elevations (Table 7.17), while the relation with slope does not show any strong trend (Table B.12).

Table 7.9: Significant Results from the Binomial Analysis of 2-D TRMM-3A25 Conditional Statistics v. Forest Cover; The count of positive and negative conditional statistic differences is compared to the binomial distribution to detect significant biases.

Difference Statistic	>0 Counts	<0 Counts	Significance
Bright Band Height Mean	46	27	$p \leqslant 0.05$
Warm Rain Pixel Counts	28	43	$p \leqslant 0.1$
Total Pixel Counts	42	34	—

Table 7.10: Significant Results from the Randomization Analysis of 2-D TRMM-3A25 Conditional Statistics v. Forest Cover; The count of times that the conditional statistic difference is greater than the upper 99% confidence bound, and the count of the number of times that the difference is less than the lower 99% confidence bound are summarized.

Difference Statistic	$>\uparrow$99% Limit	$<\downarrow$99% Limit
Total Pixel Counts	0	0

Table 7.11: Significant Results from the Binomial Analysis of 3-D TRMM-3A25 Conditional Statistics v. Forest Cover (Part a); The count of positive and negative conditional statistic differences is compared to the binomial distribution to detect significant biases.

Difference Statistic	Level	>0 Counts	<0 Counts	Significance
Rain Std. Dev.	Avg.	37	39	—
	2 km	36	40	—
	4 km	39	37	—
	6 km	45	31	$p \leqslant 0.14$
Strat. Rain Mean	Avg.	35	41	—
	2 km	36	40	—
	4 km	36	40	—
	6 km	30	45	$p \leqslant 0.11$
Strat. Rain Std. Dev.	Avg.	33	43	—
	2 km	35	41	—
	4 km	34	42	—
	6 km	29	46	$p \leqslant 0.07$
Conv. Rain Pixels	Avg.	31	45	$p \leqslant 0.14$
	2 km	31	45	$p \leqslant 0.14$
	4 km	31	45	$p \leqslant 0.14$
	6 km	30	45	$p \leqslant 0.11$
Measured Reflectivity (Zm)	Avg.	44	32	—
	2 km	40	36	—
	4 km	43	33	—
	6 km	45	31	$p \leqslant 0.14$
Convective Zm	Avg.	42	34	—
	2 km	34	42	—
	4 km	40	36	—
	6 km	46	29	$p \leqslant 0.07$
Convective Zt	Avg.	44	32	—
	2 km	37	39	—
	4 km	39	37	—
	6 km	45	30	$p \leqslant 0.11$

Table 7.12: Significant Results from the Binomial Analysis of TRMM-2A23 Event Counts v. Elevation; The count of positive and negative normalized event count differences is compared to the binomial distribution to detect significant biases. The ranges are the percentile cutoffs used to create a binary ("high" v. "low") field from the original DEM (e. g., a range of "30" specifies the difference of the statistic between the 30% highest pixels and the 70% lowest.)

Difference Statistic	Range	>0 Counts	<0 Counts	Significance
Rain Certain	30	49	27	$p \leqslant 0.02$
	50	61	15	$p \leqslant 0.0001$
	70	58	18	$p \leqslant 0.0001$
Rain Possible	30	68	8	$p \leqslant 0.0001$
	50	70	6	$p \leqslant 0.0001$
	70	69	7	$p \leqslant 0.0001$
Rain Convective	30	44	32	—
	50	44	32	—
	70	56	20	$p \leqslant 0.0001$
Rain Stratiform	30	51	25	$p \leqslant 0.004$
	50	59	17	$p \leqslant 0.0001$
	70	61	15	$p \leqslant 0.0001$
Rain Isolated	30	37	37	—
	50	38	31	—
	70	49	26	$p \leqslant 0.02$
Warm Possible	30	37	37	—
	50	38	31	—
	70	49	26	$p \leqslant 0.02$
Bright Band Height	30	22	47	$p \leqslant 0.004$
	50	30	39	—
	70	29	39	—
Bright Band Intensity	30	36	33	—
	50	39	30	—
	70	42	26	$p \leqslant 0.07$

Table 7.13: Significant Results from the Binomial Analysis of TRMM-2A23 Event Counts v. Slope; The count of positive and negative normalized event count differences is compared to the binomial distribution to detect significant biases. The ranges are the percentile cutoffs used to create a binary ("steep" v. "gradual") field from the original DEM (e. g., a range of "30" specifies the difference of the statistic between the 30% steepest pixels and the 70% most gradual.)

Difference Statistic	Range	>0 Counts	<0 Counts	Significance
Rain Certain	30	54	22	$p \leqslant 0.0005$
	50	52	24	$p \leqslant 0.002$
	70	56	20	$p \leqslant 0.0001$
Rain Possible	30	65	11	$p \leqslant 0.0001$
	50	72	4	$p \leqslant 0.0001$
	70	73	3	$p \leqslant 0.0001$
Rain Convective	30	49	27	$p \leqslant 0.02$
	50	52	24	$p \leqslant 0.002$
	70	57	19	$p \leqslant 0.0001$
Rain Stratiform	30	48	28	$p \leqslant 0.03$
	50	53	23	$p \leqslant 0.001$
	70	53	23	$p \leqslant 0.001$

Table 7.14: Significant Results from the Randomization Analysis of TRMM-2A23 Event Counts v. Slope; The count of times that the normalized event count difference is greater than the upper 99% confidence bound, and the count of the number of times that the difference is less than the lower 99% confidence bound are summarized. The ranges are the percentile cutoffs used to create a binary ("steep" v. "gradual") field from the original DEM (e. g., a range of "30" specifies the difference of the statistic between the 30% steepest pixels and the 70% most gradual.)

Difference Statistic	Range	$>\uparrow$99% Limit	$<\downarrow$99% Limit
Rain Certain	30	4	1
	50	4	2
	70	6	1
Rain Possible	30	0	0
	50	2	0
	70	11	0
Rain Convective	30	2	0
	50	3	1
	70	4	1
Rain Stratiform	30	3	1
	50	3	0
	70	4	0
Storm Height	30	0	0
	50	2	0
	70	3	1
Bright Band Heigth	30	1	0
	50	1	3
	70	2	4
Bright Band Intensity	30	0	0
	50	0	0
	70	2	0

Table 7.15: Significant Results from the Binomial Analysis of TRMM-2A23 Event Timing v. Elevation; The count of positive and negative mean event occurrence time differences is compared to the binomial distribution to detect significant biases. The ranges are the percentile cutoffs used to create a binary ("high" v. "low") field from the original DEM (e. g., a range of "30" specifies the difference of the statistic between the 30% highest pixels and the 70% lowest.)

Difference Statistic	Range	>0 Counts	<0 Counts	Significance
Rain Certain	30	38	38	—
	50	35	41	—
	70	30	46	$p \leqslant 0.09$
Rain Convective	30	37	38	—
	50	32	43	—
	70	25	50	$p \leqslant 0.006$

Table 7.16: Significant Results from the Binomial Analysis of TRMM-2A23 Event Timing v. Slope; The count of positive and negative mean event occurrence time differences is compared to the binomial distribution to detect significant biases. The ranges are the percentile cutoffs used to create a binary ("steep" v. "gradual") field from the original DEM (e. g., a range of "30" specifies the difference of the statistic between the 30% steepest pixels and the 70% most gradual.)

Difference Statistic	Range	>0 Counts	<0 Counts	Significance
Rain Isolated	30	32	37	—
	50	28	42	$p \leqslant 0.12$
	70	31	37	—
Warm Possible	30	32	37	—
	50	28	42	$p \leqslant 0.12$
	70	31	37	—

Table 7.17: Significant Results from the Randomization Analysis of TRMM-2A23 Event Timing v. Elevation; The count of times that the normalized occurrence time difference is greater than the upper 99% confidence bound, and the count of the number of times that the difference is less than the lower 99% confidence bound are summarized. The ranges are the percentile cutoffs used to create a binary ("high" v. "low") field from the original DEM (e. g., a range of "30" specifies the difference of the statistic between the 30% highest pixels and the 70% lowest.)

Difference Statistic	Range	$>\uparrow$99% Limit	$<\downarrow$99% Limit
Rain Certain	30	5	4
	50	3	11
	70	2	10
Rain Possible	30	5	3
	50	5	7
	70	2	10
Rain Convective	30	1	3
	50	1	6
	70	1	4
Rain Stratiform	30	3	6
	50	3	9
	70	2	11
Rain Isolated	30	0	0
	50	0	0
	70	2	0
Warm Possible	30	0	0
	50	0	0
	70	2	0

7.3.2 TRMM-3A25 Results

The analysis of TRMM-3A25 rainfall statistics with respect to elevation and slope also yields significant results. Table 7.18 shows that surface rain intensity is significantly higher over the 50% highest pixels; the mean bright band height is significantly lower over the 30% highest pixels; the variability in mean bright band height is higher over the 70% highest pixels; the variability of storm height is weakly higher over the 50% highest pixels and the variability of stratiform storm heights is higher over the 70% lowest pixels.

As mentioned in the analysis of TRMM-2A23 data with respect to elevation, there is a significant bias of sampling toward higher elevations, as is shown by the total pixel count in Table 7.19. Yet Table 7.19 shows also that — despite the sampling artefact — surface rain counts, surface rain all counts, bright band pixel counts and warm rain pixel counts are all significantly biased toward lower elevations. This trend is also reflected in the departures from the 99% confidence bounds that are summarized in Table 7.20.

With respect to slope, TRMM-3A25 statistics also show some significant trends, as is seen in Table 7.21. The surface rain and surface all rain mean intensities are significantly lower over the 30% most gradual pixels, while their variability is higher over the 30% steepest pixels. The mean bright band height is significantly lower over the 30% steepest pixels, while the mean convective storm height is significantly higher over the 30% steepest pixels. There are also significantly less warm rain counts over the 30% steepest pixels. The randomization analysis does not yield interesting patterns of departures from the 99% confidence bounds (Tables B.30, B.31 & B.32).

The height dependent statistics from TRMM-3A25, when analyzed against elevation, yield the following results: the mean rain rate and its standard deviation are higher over elevated pixels (Table 7.22); the standard deviation of path averaged and 6 km level convective rain rates is higher over higher elevations, and stratiform rainfall rates at the 6 km level are higher over higher elevations (Tables 7.23 & 7.24); the mean stratiform rain rate is higher over lower elevations (Table 7.24); there are more rainfall and stratiform rainfall occurrences over lower elevations (Tables 7.25 & 7.26); there are more convective rain pixel counts over higher elevations (Table 7.26), but this result must again be discounted due to the sampling bias; the measured and corrected reflectivities are higher over lower pixels at the 4 km level (Table 7.27); and the path averaged measured and corrected stratiform reflectivities are higher over lower pixels (Table 7.28). The randomization analyses of height-dependent TRMM-3A25 statistics shows a coherent pattern of departures from the 99% confidence bounds for the count of rain pixels and stratiform rain pixels that concurs with the binomial analyses of these statistics (Table 7.29). The same is observed for the measured and corrected reflectivities (Table 7.30).

The mean rain rate and its standard deviation are both higher over steeper areas

(Table 7.31); the mean convective rain rate shows the same preference for steeper slopes at the 4 km and 6 km levels, while its standard deviation only shows a very week significance at 4 km (Table 7.32); The stratiform rain rate is higher (weak significance) over more gradual slopes at the 4 km level, and the standard deviation of the stratiform rain rate is also higher over more gradual slopes at the 4 km level (Table 7.33); there are more convective rain pixels over steep slopes (Table 7.34); the measured and corrected reflectivities are higher over steeper slopes at the 2 km and 6 km levels (Table 7.35); and the measured and corrected convective reflectivities are higher over steeper slopes (Table 7.36). The randomization analyses yield coherent results for the mean convective rain rate (Table 7.37); and for the measured and corrected convective rainfall reflectivites (Table 7.38).

Table 7.18: Significant Results from the Binomial Analysis of 2-D TRMM-3A25 Conditional Statistics v. Elevation (Part a); The count of positive and negative conditional statistic differences is compared to the binomial distribution to detect significant biases. The ranges are the percentile cutoffs used to create a binary ("high" v. "low") field from the original DEM (e. g., a range of "30" specifies the difference of the statistic between the 30% highest pixels and the 70% lowest.)

Difference Statistic	Range	>0	<0	Significance
Surface Rain Mean Intensity	30	42	34	—
	50	46	30	$p \leqslant 0.09$
	70	39	37	—
Surface Rain All Mean Intensity	30	42	34	—
	50	46	30	$p \leqslant 0.09$
	70	39	37	—
Bright Band Height Mean	30	29	44	$p \leqslant 0.11$
	50	32	40	—
	70	31	41	—
Bright Band Height Std. Dev.	30	40	33	—
	50	40	32	—
	70	44	28	$p \leqslant 0.08$
Storm Height Std. Dev.	30	39	37	—
	50	45	31	$p \leqslant 0.15$
	70	39	37	—
Strat. Storm Height Std. Dev.	30	31	45	$p \leqslant 0.15$
	50	38	38	—
	70	34	42	—

Table 7.19: Significant Results from the Binomial Analysis of 2-D TRMM-3A25 Conditional Statistics v. Elevation (Part b); The count of positive and negative conditional statistic differences is compared to the binomial distribution to detect significant biases. The ranges are the percentile cutoffs used to create a binary ("high" v. "low") field from the original DEM (e. g., a range of "30" specifies the difference of the statistic between the 30% highest pixels and the 70% lowest.)

Difference Statistic	Range	>0	<0	Significance
Surface Rain Pixel Counts	30	28	48	$p \leqslant 0.03$
	50	26	50	$p \leqslant 0.008$
	70	29	47	$p \leqslant 0.06$
Surface Rain All Pixel Counts	30	28	48	$p \leqslant 0.03$
	50	26	50	$p \leqslant 0.008$
	70	29	47	$p \leqslant 0.06$
Bright Band Pixel Counts	30	23	53	$p \leqslant 0.0008$
	50	31	45	$p \leqslant 0.15$
	70	32	44	—
Warm Rain Pixel Counts	30	24	50	$p \leqslant 0.004$
	50	26	45	$p \leqslant 0.04$
	70	25	49	$p \leqslant 0.004$
Total Pixel Counts	30	48	28	$p \leqslant 0.03$
	50	55	21	$p \leqslant 0.0002$
	70	59	17	$p \leqslant 0.0001$

Table 7.20: Significant Results from the Randomization Analysis of 2-D TRMM-3A25 Conditional Statistics v. Elevation; The count of times that the conditional statistic difference is greater than the upper 99% confidence bound, and the count of the number of times that the difference is less than the lower 99% confidence bound are summarized. The ranges are the percentile cutoffs used to create a binary ("high" v. "low") field from the original DEM (e. g., a range of "30" specifies the difference of the statistic between the 30% highest pixels and the 70% lowest.)

Difference Statistic	Range	$>\uparrow$99% Limit	$<\downarrow$99% Limit
Surface Rain Pixel Counts	30	0	2
	50	0	4
	70	1	6
Surface Rain All Pixel Counts	30	0	2
	50	0	4
	70	1	6
Bright Band Pixel Counts	30	0	2
	50	0	4
	70	1	2
Warm Rain Pixel Counts	30	1	1
	50	0	1
	70	0	0
Total Pixel Counts	30	0	0
	50	0	1
	70	2	1

Table 7.21: Significant Results from the Binomial Analysis of 2-D TRMM-3A25 Conditional Statistics v. Slope; The count of positive and negative conditional statistic differences is compared to the binomial distribution to detect significant biases. The ranges are the percentile cutoffs used to create a binary ("steep" v. "gradual") field from the original DEM (e. g., a range of "30" specifies the difference of the statistic between the 30% steepest pixels and the 70% most gradual.)

Difference Statistic	Range	>0	<0	Significance
Surface Rain Mean Intensity	30	45	31	—
	50	37	39	—
	70	47	29	$p \leqslant 0.06$
Surface Rain Std. Dev.	30	50	26	$p \leqslant 0.008$
	50	44	32	—
	70	45	31	—
Surface Rain All Mean Intensity	30	45	31	—
	50	37	39	—
	70	47	29	$p \leqslant 0.06$
Surface Rain All Std. Dev.	30	50	26	$p \leqslant 0.008$
	50	44	32	—
	70	45	31	—
Bright Band Height Mean	30	29	44	$p \leqslant 0.11$
	50	30	44	—
	70	31	43	—
Convective Storm Height Mean	30	46	30	$p \leqslant 0.09$
	50	43	33	—
	70	41	34	—
Warm Rain Pixel Counts	30	29	45	$p \leqslant 0.09$
	50	28	41	—
	70	35	39	—
Total Pixel Counts	30	41	35	—
	50	43	33	—
	70	44	32	—

Table 7.22: Significant Results from the Binomial Analysis of 3-D TRMM-3A25 Conditional Statistics v. Elevation (Part a); The count of positive and negative conditional statistic differences is compared to the binomial distribution to detect significant biases. The ranges are the percentile cutoffs used to create a binary ("high" v. "low") field from the original DEM (e. g., a range of "30" specifies the difference of the statistic between the 30% highest pixels and the 70% lowest.)

Difference Statistic	Level	Range	>0 Counts	<0 Counts	Significance
Rain Mean	Avg.	30	41	35	—
		50	45	31	$p \leqslant 0.14$
		70	37	39	—
	2 km	30	44	32	—
		50	46	30	$p \leqslant 0.09$
		70	38	38	—
	4 km	30	37	39	—
		50	36	40	—
		70	36	40	—
	6 km	30	47	29	$p \leqslant 0.06$
		50	45	31	$p \leqslant 0.14$
		70	43	33	—
Rain Std. Dev.	Avg.	30	46	30	$p \leqslant 0.09$
		50	44	32	—
		70	40	36	—
	2 km	30	48	28	$p \leqslant 0.03$
		50	40	36	—
		70	41	35	—
	4 km	30	45	31	$p \leqslant 0.14$
		50	42	34	—
		70	39	37	—
	6 km	30	51	25	$p \leqslant 0.004$
		50	47	29	$p \leqslant 0.06$
		70	41	35	—

Table 7.23: Significant Results from the Binomial Analysis of 3-D TRMM-3A25 Conditional Statistics v. Elevation (Part b); The count of positive and negative conditional statistic differences is compared to the binomial distribution to detect significant biases. The ranges are the percentile cutoffs used to create a binary ("high" v. "low") field from the original DEM (e. g., a range of "30" specifies the difference of the statistic between the 30% highest pixels and the 70% lowest.)

Difference Statistic	Level	Range	>0 Counts	<0 Counts	Significance
Conv. Rain Std. Dev.	Avg.	30	46	30	$p \leqslant 0.09$
		50	43	32	—
		70	37	38	—
	2 km	30	43	33	—
		50	42	33	
		70	39	36	—
	4 km	30	44	32	—
		50	44	31	—
		70	33	42	—
	6 km	30	46	29	$p \leqslant 0.07$
		50	43	31	—
		70	38	36	—

Table 7.24: Significant Results from the Binomial Analysis of 3-D TRMM-3A25 Conditional Statistics v. Elevation (Part c); The count of positive and negative conditional statistic differences is compared to the binomial distribution to detect significant biases. The ranges are the percentile cutoffs used to create a binary ("high" v. "low") field from the original DEM (e. g., a range of "30" specifies the difference of the statistic between the 30% highest pixels and the 70% lowest.)

Difference Statistic	Level	Range	>0 Counts	<0 Counts	Significance
Strat. Rain Mean	Avg.	30	31	45	$p \leqslant 0.14$
		50	31	45	$p \leqslant 0.14$
		70	38	38	—
	2 km	30	32	44	—
		50	36	40	—
		70	37	39	—
	4 km	30	30	46	$p \leqslant 0.09$
		50	32	44	—
		70	36	40	—
	6 km	30	31	45	$p \leqslant 0.14$
		50	32	44	—
		70	41	34	—
Strat. Rain Std. Dev.	Avg.	30	36	40	—
		50	34	42	—
		70	34	42	—
	2 km	30	36	40	—
		50	36	40	—
		70	32	44	—
	4 km	30	35	41	—
		50	33	43	—
		70	33	43	—
	6 km	30	44	32	—
		50	49	27	$p \leqslant 0.02$
		70	38	37	—

Table 7.25: Significant Results from the Binomial Analysis of 3-D TRMM-3A25 Conditional Statistics v. Elevation (Part d); The count of positive and negative conditional statistic differences is compared to the binomial distribution to detect significant biases. The ranges are the percentile cutoffs used to create a binary ("high" v. "low") field from the original DEM (e. g., a range of "30" specifies the difference of the statistic between the 30% highest pixels and the 70% lowest.)

Difference Statistic	Level	Range	>0 Counts	<0 Counts	Significance
Rain Pixels	Avg.	30	30	46	$p \leqslant 0.09$
		50	29	47	$p \leqslant 0.06$
		70	28	47	$p \leqslant 0.04$
	2 km	30	25	51	$p \leqslant 0.004$
		50	28	48	$p \leqslant 0.03$
		70	28	48	$p \leqslant 0.03$
	4 km	30	30	46	$p \leqslant 0.09$
		50	30	46	$p \leqslant 0.09$
		70	28	48	$p \leqslant 0.03$
	6 km	30	28	48	$p \leqslant 0.03$
		50	30	46	$p \leqslant 0.09$
		70	30	46	$p \leqslant 0.09$

Table 7.26: Significant Results from the Binomial Analysis of 3-D TRMM-3A25 Conditional Statistics v. Elevation (Part e); The count of positive and negative conditional statistic differences is compared to the binomial distribution to detect significant biases. The ranges are the percentile cutoffs used to create a binary ("high" v. "low") field from the original DEM (e. g., a range of "30" specifies the difference of the statistic between the 30% highest pixels and the 70% lowest.)

Difference Statistic	Level	Range	>0 Counts	<0 Counts	Significance
Conv. Rain Pixels	Avg.	30	45	31	$p \leqslant 0.14$
		50	42	34	—
		70	37	39	—
	2 km	30	45	31	$p \leqslant 0.14$
		50	40	36	—
		70	37	39	—
	4 km	30	45	31	$p \leqslant 0.14$
		50	42	34	—
		70	38	38	—
	6 km	30	42	34	—
		50	41	34	—
		70	39	37	—
Strat. Rain Pixels	Avg.	30	26	50	$p \leqslant 0.008$
		50	25	51	$p \leqslant 0.004$
		70	29	47	$p \leqslant 0.06$
	2 km	30	27	49	$p \leqslant 0.02$
		50	26	50	$p \leqslant 0.008$
		70	29	47	$p \leqslant 0.06$
	4 km	30	27	49	$p \leqslant 0.02$
		50	28	48	$p \leqslant 0.03$
		70	28	48	$p \leqslant 0.03$
	6 km	30	25	51	$p \leqslant 0.004$
		50	29	46	$p \leqslant 0.07$
		70	29	47	$p \leqslant 0.06$

Table 7.27: Significant Results from the Binomial Analysis of 3-D TRMM-3A25 Conditional Statistics v. Elevation (Part f); The count of positive and negative conditional statistic differences is compared to the binomial distribution to detect significant biases. The ranges are the percentile cutoffs used to create a binary ("high" v. "low") field from the original DEM (e. g., a range of "30" specifies the difference of the statistic between the 30% highest pixels and the 70% lowest.)

Difference Statistic	Level	Range	>0 Counts	<0 Counts	Significance
Measured Reflectivity (Zm)	Avg.	30	36	40	—
		50	37	39	—
		70	37	39	—
	2 km	30	40	36	—
		50	35	41	—
		70	39	37	—
	4 km	30	27	49	$p \leqslant 0.02$
		50	30	46	$p \leqslant 0.09$
		70	34	42	—
	6 km	30	36	40	—
		50	38	38	—
		70	39	37	—
Corrected Reflectivity (Zt)	Avg.	30	36	40	—
		50	38	38	—
		70	37	39	—
	2 km	30	42	34	—
		50	37	39	—
		70	40	36	—
	4 km	30	28	48	$p \leqslant 0.03$
		50	30	46	$p \leqslant 0.09$
		70	33	43	—
	6 km	30	34	42	—
		50	40	36	—
		70	38	38	—

Table 7.28: Significant Results from the Binomial Analysis of 3-D TRMM-3A25 Conditional Statistics v. Elevation (Part g); The count of positive and negative conditional statistic differences is compared to the binomial distribution to detect significant biases. The ranges are the percentile cutoffs used to create a binary ("high" v. "low") field from the original DEM (e. g., a range of "30" specifies the difference of the statistic between the 30% highest pixels and the 70% lowest.)

Difference Statistic	Level	Range	>0 Counts	<0 Counts	Significance
Stratiform Zm	Avg.	30	28	48	$p \leqslant 0.03$
		50	30	46	$p \leqslant 0.09$
		70	37	39	—
	2 km	30	36	40	—
		50	40	36	—
		70	39	37	—
	4 km	30	31	45	$p \leqslant 0.14$
		50	33	43	—
		70	35	41	—
	6 km	30	32	44	—
		50	36	40	—
		70	42	33	—
Stratiform Zt	Avg.	30	28	48	$p \leqslant 0.03$
		50	30	46	$p \leqslant 0.09$
		70	36	40	—
	2 km	30	37	39	—
		50	40	36	—
		70	41	35	—
	4 km	30	32	44	—
		50	33	43	—
		70	35	41	—
	6 km	30	32	44	—
		50	34	42	—
		70	39	36	—

Table 7.29: Significant Results from the Randomization Analysis of 3-D TRMM-3A25 Conditional Statistics v. Elevation (Part a); The count of times that the conditional statistic difference is greater than the upper 99% confidence bound, and the count of the number of times that the difference is less than the lower 99% confidence bound are summarized. The ranges are the percentile cutoffs used to create a binary ("high" v. "low") field from the original DEM (e. g., a range of "30" specifies the difference of the statistic between the 30% highest pixels and the 70% lowest.)

Difference Statistic	Level	Range	>↑99% Limit	<↓99% Limit
Rain Pixels	Avg.	30	0	2
		50	0	4
		70	0	4
	2 km	30	0	2
		50	0	3
		70	0	6
	4 km	30	0	2
		50	0	3
		70	0	6
	6 km	30	0	0
		50	1	3
		70	0	4
Strat. Rain Pixels	Avg.	30	0	2
		50	0	4
		70	0	7
	2 km	30	0	2
		50	0	4
		70	0	6
	4 km	30	0	2
		50	0	5
		70	0	6
	6 km	30	0	3
		50	0	5
		70	1	3

Table 7.30: Significant Results from the Randomization Analysis of 3-D TRMM-3A25 Conditional Statistics v. Elevation (Part b); The count of times that the conditional statistic difference is greater than the upper 99% confidence bound, and the count of the number of times that the difference is less than the lower 99% confidence bound are summarized. The ranges are the percentile cutoffs used to create a binary ("high" v. "low") field from the original DEM (e. g., a range of "30" specifies the difference of the statistic between the 30% highest pixels and the 70% lowest.)

Difference Statistic	Level	Range	$>\uparrow$99% Limit	$<\downarrow$99% Limit
Measured Reflectivity (Zm)	Avg.	30	1	0
		50	1	2
		70	1	4
	2 km	30	2	0
		50	1	3
		70	0	1
	4 km	30	1	0
		50	1	2
		70	1	6
	6 km	30	3	0
		50	2	1
		70	1	1
Corrected Reflectivity (Zt)	Avg.	30	1	0
		50	1	2
		70	1	4
	2 km	30	2	0
		50	1	3
		70	1	0
	4 km	30	1	0
		50	1	2
		70	1	6
	6 km	30	1	0
		50	1	1
		70	1	1

Table 7.31: Significant Results from the Binomial Analysis of 3-D TRMM-3A25 Conditional Statistics v. Slope (Part a); The count of positive and negative conditional statistic differences is compared to the binomial distribution to detect significant biases. The ranges are the percentile cutoffs used to create a binary ("steep" v. "gradual") field from the original DEM (e. g., a range of "30" specifies the difference of the statistic between the 30% steepest pixels and the 70% most gradual.)

Difference Statistic	Level	Range	>0 Counts	<0 Counts	Significance
Rain Mean	Avg.	30	46	30	$p \leqslant 0.09$
		50	38	38	—
		70	42	34	—
	2 km	30	47	29	$p \leqslant 0.06$
		50	38	38	—
		70	45	31	$p \leqslant 0.14$
	4 km	30	47	29	$p \leqslant 0.06$
		50	40	36	—
		70	43	33	—
	6 km	30	47	29	$p \leqslant 0.06$
		50	44	32	—
		70	42	34	—
Rain Std. Dev.	Avg.	30	48	28	$p \leqslant 0.03$
		50	44	32	—
		70	45	31	$p \leqslant 0.14$
	2 km	30	49	27	$p \leqslant 0.02$
		50	43	33	—
		70	47	29	$p \leqslant 0.06$
	4 km	30	48	28	$p \leqslant 0.03$
		50	44	32	—
		70	46	30	$p \leqslant 0.09$
	6 km	30	48	28	$p \leqslant 0.03$
		50	44	32	—
		70	45	31	$p \leqslant 0.14$

Table 7.32: Significant Results from the Binomial Analysis of 3-D TRMM-3A25 Conditional Statistics v. Slope (Part b); The count of positive and negative conditional statistic differences is compared to the binomial distribution to detect significant biases. The ranges are the percentile cutoffs used to create a binary ("steep" v. "gradual") field from the original DEM (e. g., a range of "30" specifies the difference of the statistic between the 30% steepest pixels and the 70% most gradual.)

Difference Statistic	Level	Range	>0 Counts	<0 Counts	Significance
Conv. Rain Mean	Avg.	30	44	32	—
		50	38	38	—
		70	40	35	—
	2 km	30	44	32	—
		50	41	35	—
		70	44	31	—
	4 km	30	45	31	$p \leqslant 0.14$
		50	46	30	$p \leqslant 0.09$
		70	42	33	—
	6 km	30	42	34	—
		50	45	30	$p \leqslant 0.11$
		70	42	32	—
Conv. Rain Std. Dev.	Avg.	30	41	35	—
		50	43	33	—
		70	37	38	—
	2 km	30	44	32	—
		50	36	40	—
		70	44	31	—
	4 km	30	45	31	$p \leqslant 0.14$
		50	44	32	—
		70	44	31	—
	6 km	30	40	36	—
		50	38	37	—
		70	41	33	—

Table 7.33: Significant Results from the Binomial Analysis of 3-D TRMM-3A25 Conditional Statistics v. Slope (Part c); The count of positive and negative conditional statistic differences is compared to the binomial distribution to detect significant biases. The ranges are the percentile cutoffs used to create a binary ("steep" v. "gradual") field from the original DEM (e. g., a range of "30" specifies the difference of the statistic between the 30% steepest pixels and the 70% most gradual.)

Difference Statistic	Level	Range	>0 Counts	<0 Counts	Significance
Strat. Rain Mean	Avg.	30	32	44	—
		50	35	41	—
		70	35	41	—
	2 km	30	32	44	—
		50	34	42	—
		70	36	40	—
	4 km	30	31	45	$p \leqslant 0.14$
		50	33	43	—
		70	32	44	—
	6 km	30	42	34	—
		50	39	37	—
		70	38	38	—
Strat. Rain Std. Dev.	Avg.	30	38	38	—
		50	36	40	—
		70	37	39	—
	2 km	30	33	43	—
		50	39	37	—
		70	34	42	—
	4 km	30	37	39	—
		50	30	46	$p \leqslant 0.09$
		70	31	45	$p \leqslant 0.14$
	6 km	30	44	32	—
		50	44	32	—
		70	39	37	—

Table 7.34: Significant Results from the Binomial Analysis of 3-D TRMM-3A25 Conditional Statistics v. Slope (Part d); The count of positive and negative conditional statistic differences is compared to the binomial distribution to detect significant biases. The ranges are the percentile cutoffs used to create a binary ("steep" v. "gradual") field from the original DEM (e. g., a range of "30" specifies the difference of the statistic between the 30% steepest pixels and the 70% most gradual.)

Difference Statistic	Level	Range	>0 Counts	<0 Counts	Significance
Conv. Rain Pixels	Avg.	30	44	32	—
		50	45	31	$p \leqslant 0.14$
		70	48	28	$p \leqslant 0.03$
	2 km	30	44	31	—
		50	45	31	$p \leqslant 0.14$
		70	47	29	$p \leqslant 0.06$
	4 km	30	45	31	$p \leqslant 0.14$
		50	46	30	$p \leqslant 0.09$
		70	45	31	$p \leqslant 0.14$
	6 km	30	46	30	$p \leqslant 0.09$
		50	50	26	$p \leqslant 0.008$
		70	42	34	—

Table 7.35: Significant Results from the Binomial Analysis of 3-D TRMM-3A25 Conditional Statistics v. Slope (Part e); The count of positive and negative conditional statistic differences is compared to the binomial distribution to detect significant biases. The ranges are the percentile cutoffs used to create a binary ("steep" v. "gradual") field from the original DEM (e. g., a range of "30" specifies the difference of the statistic between the 30% steepest pixels and the 70% most gradual.)

Difference Statistic	Level	Range	>0 Counts	<0 Counts	Significance
Measured Reflectivity (Zm)	Avg.	30	43	33	—
		50	40	36	—
		70	40	36	—
	2 km	30	45	31	$p \leqslant 0.14$
		50	43	33	—
		70	38	38	—
	4 km	30	38	38	—
		50	42	34	—
		70	38	38	—
	6 km	30	46	30	$p \leqslant 0.09$
		50	38	38	—
		70	40	36	—
Corrected Reflectivity (Zt)	Avg.	30	43	33	—
		50	42	34	—
		70	40	36	—
	2 km	30	46	30	$p \leqslant 0.09$
		50	43	33	—
		70	40	36	—
	4 km	30	38	38	—
		50	43	33	—
		70	38	38	—
	6 km	30	45	31	$p \leqslant 0.14$
		50	37	39	—
		70	40	36	—

Table 7.36: Significant Results from the Binomial Analysis of 3-D TRMM-3A25 Conditional Statistics v. Slope (Part f); The count of positive and negative conditional statistic differences is compared to the binomial distribution to detect significant biases. The ranges are the percentile cutoffs used to create a binary ("steep" v. "gradual") field from the original DEM (e. g., a range of "30" specifies the difference of the statistic between the 30% steepest pixels and the 70% most gradual.)

Difference Statistic	Level	Range	>0 Counts	<0 Counts	Significance
Convective Zm	Avg.	30	46	30	$p \leqslant 0.09$
		50	40	36	—
		70	36	39	—
	2 km	30	43	33	—
		50	40	36	—
		70	38	37	—
	4 km	30	43	33	—
		50	47	29	$p \leqslant 0.06$
		70	45	30	$p \leqslant 0.11$
	6 km	30	40	36	—
		50	44	31	—
		70	47	27	$p \leqslant 0.03$
Convective Zt	Avg.	30	45	31	$p \leqslant 0.14$
		50	41	35	—
		70	40	35	—
	2 km	30	45	31	$p \leqslant 0.14$
		50	43	33	—
		70	40	35	—
	4 km	30	43	33	—
		50	47	29	$p \leqslant 0.06$
		70	45	30	$p \leqslant 0.11$
	6 km	30	42	34	—
		50	46	29	$p \leqslant 0.07$
		70	47	27	$p \leqslant 0.03$

Table 7.37: Significant Results from the Randomization Analysis of 3-D TRMM-3A25 Conditional Statistics v. Slope (Part a); The count of times that the conditional statistic difference is greater than the upper 99% confidence bound, and the count of the number of times that the difference is less than the lower 99% confidence bound are summarized. The ranges are the percentile cutoffs used to create a binary ("steep" v. "gradual") field from the original DEM (e. g., a range of "30" specifies the difference of the statistic between the 30% steepest pixels and the 70% most gradual.)

Difference Statistic	Level	Range	$>\uparrow$99% Limit	$<\downarrow$99% Limit
Conv. Rain Mean	Avg.	30	2	0
		50	4	0
		70	1	0
	2 km	30	1	0
		50	2	0
		70	0	0
	4 km	30	1	0
		50	3	0
		70	0	0
	6 km	30	1	0
		50	2	0
		70	1	0

Table 7.38: Significant Results from the Randomization Analysis of 3-D TRMM-3A25 Conditional Statistics v. Slope (Part b); The count of times that the conditional statistic difference is greater than the upper 99% confidence bound, and the count of the number of times that the difference is less than the lower 99% confidence bound are summarized. The ranges are the percentile cutoffs used to create a binary ("steep" v. "gradual") field from the original DEM (e. g., a range of "30" specifies the difference of the statistic between the 30% steepest pixels and the 70% most gradual.)

Difference Statistic	Level	Range	>↑99% Limit	<↓99% Limit
Convective Zm	Avg.	30	2	0
		50	4	1
		70	2	0
	2 km	30	1	0
		50	3	0
		70	0	0
	4 km	30	2	0
		50	3	1
		70	0	0
	6 km	30	2	0
		50	2	1
		70	0	0
Convective Zt	Avg.	30	2	0
		50	4	1
		70	2	0
	2 km	30	2	0
		50	3	0
		70	0	0
	4 km	30	2	0
		50	3	0
		70	0	0
	6 km	30	2	0
		50	2	0
		70	0	0

7.4 Discussion

7.4.1 Rainfall & Deforestation

The analyses of rainfall's association with forest cover has so far yielded interesting, yet somewhat inconsistent results. Indeed, while the analysis of warm rain pixel counts from the TRMM-3A25 product showed that there were persistently more warm rain events over forested areas (which proves one of the initial hypotheses wrong), the same analysis using the TRMM-2A23 product did not yield a significant result. Similarly, the difference in bright band height from TRMM-

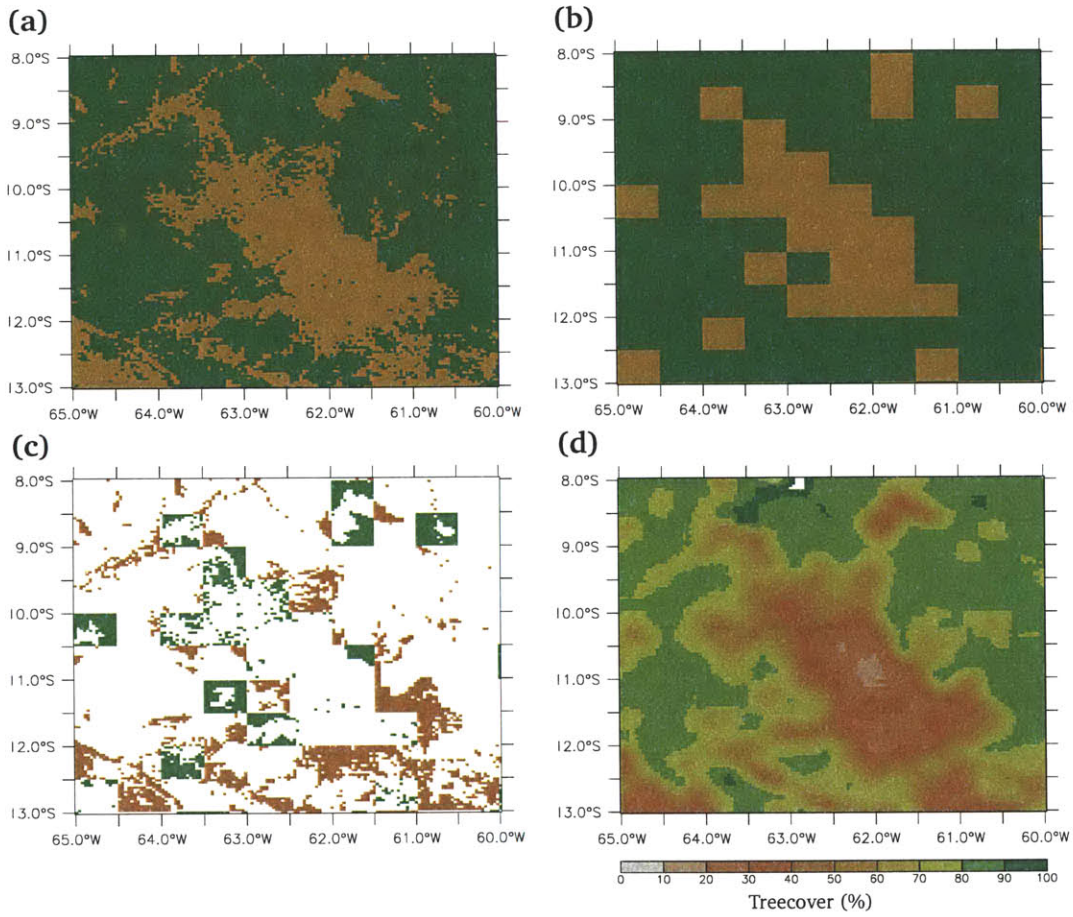

Figure 7-6: Deforestation Maps of Domains: **(a)** 4-km resolution, 50% threshold; **(b)** 50-km resolution, 50% threshold; **(c)** Difference between high & low resolution (white areas are unchanged; green areas are comparatively deforested in low resolution; brown areas are comparatively forested in low resolution); **(d)** Smoothed (30 km boxcar smoother) and regridded (4 km grid) 500 m resolution MOD44B Treecover Estimates.

2A23 was not significant, while that same difference from the TRMM-3A25 product showed that the mean monthly bright band was significantly biased higher over deforested areas. While these inconsistencies do not strictly constitute contradictions, they are peculiar. The TRMM-3A25 product algorithm is partly based on the TRMM-2A23 product, thus both products are tightly related. They only differ in spatial and temporal resolution, and the analyses differ in the base forest cover map used (due to the resolution differences).

Other inconsistencies also exist between height-dependent TRMM-3A25 results and the TRMM-2A23 results. The count of convective rain events is biased toward forested pixels according to the TRMM-3A25 results (with a weak level of significance ~85%), yet they are biased toward deforested pixels in the TRMM-2A23 analysis (with a very high level of significance ~99.9995%). The count of stratiform rain pixels shows no significant bias according to the TRMM-3A25 product, whereas it is significantly biased toward deforested areas according to the TRMM-2A23 data product. Similarly, the count of rain pixels according to TRMM-3A25 isn't significantly biased with respect to forest cover, whereas both rain certain and rain possible counts are biased according to the TRMM-2A23 product. The TRMM-2A23 results concerning theses rain event counts are very significant, and are based on a higher resolution dataset.

There are, however, significant results relating forest cover to rainfall that aren't inconsistent between data products due to the absence of corresponding variables. The TRMM-3A25 mean monthly stratiform rain rate and its standard deviation are both biased toward forested pixels, while the standard deviation of rainfall rates, the measured reflectivities at 6 km, and the measured and corrected convective rainfall reflectivities at 6 km are biased toward deforested areas. The inconsistencies highlighted above can only be explained by the difference in the spatial

Table 7.39: Results from the Binomial Analysis of TRMM-2A23 Event Counts v. Low Resolution Forest Cover; The count of positive and negative normalized event count differences is compared to the binomial distribution to detect significant biases.

Difference Statistic	>0 Counts	<0 Counts	Significance
Rain Certain	23	**53**	$p \leqslant 0.0008$
Rain Possible	1	**75**	$p \leqslant 0.0001$
Rain Convective	24	**52**	$p \leqslant 0.002$
Rain Stratiform	24	**52**	$p \leqslant 0.002$
Rain Isolated	28	**47**	$p \leqslant 0.04$
Warm Possible	28	**47**	$p \leqslant 0.04$
Storm Height	36	40	—
Bright Band Height	36	34	—
Bright Band Intensity	39	31	—

resolution of the data product, or the representation of the underlying forest cover map.

The TRMM-2A23 products are analyzed against the lower resolution forest cover map, which was used in the TRMM-3A25 analysis, to determine whether is is the delineation between forested and deforested areas that is causing the inconsistencies. Table 7.39 shows these results, which are a dramatic reversal of the results that were reported using the high resolution forest cover. The high and low resolution forest covers are exhibited side-by-side in Figure 7-6, along with the difference field. This reversal in the results could indicate that the marginal area, or transition zone between forested and deforested areas, is the actual beneficiary of increased rainfall. The marginal area between the forest and deforested may be a hotbed for convective triggering. Indeed, the TRMM-2A23 results over the high resolution forest cover field showed that there were significant biases for rain certain, rain possible, rain convective and rain stratiform over deforested areas. The analysis using the low resolution forest cover revealed significant biases for rain certain, rain possible, rain stratiform, rain convective, warm rain and isolated rain over forested areas. The only plausible explanation for such a dramatic sensitivity to the representation of forest cover is that the transition zone is the area where rainfall occurrence is enhanced.

Such transition zones between forested and deforested regions are created and plotted in Figure 7-7. The transition zones are created by spatially smoothing the original 500 m resolution MOD44B treecover estimates with a 30 km boxcar smoother. The smoothed treecover field is then regridded onto a 4 km resolution grid by averging. The outcome of this smoothing and regridding is presented in panel (d) of Figure 7-6. Three marginal zones are delineated; the first cover the 30%—60% treecover range in the smoothed forest cover map; the second covers the 40%—70% range; and the third transition zone covers the 50%—80% range. The results of the analyses that compare the TRMM-2A23 rainfall statistics to the transition zones are presented in Tables 7.40, 7.41 & 7.42. The transition of significant rainfall association from the **MARGIN 30—60** (significantly less rain on transition zone) through **MARGIN 40—70** (near neutral association) to **MARGIN 50—80** (overwhelming association between rainfall events and transition zone) is extraordinary, and this is due in no small part to the unexpected nature of this result.

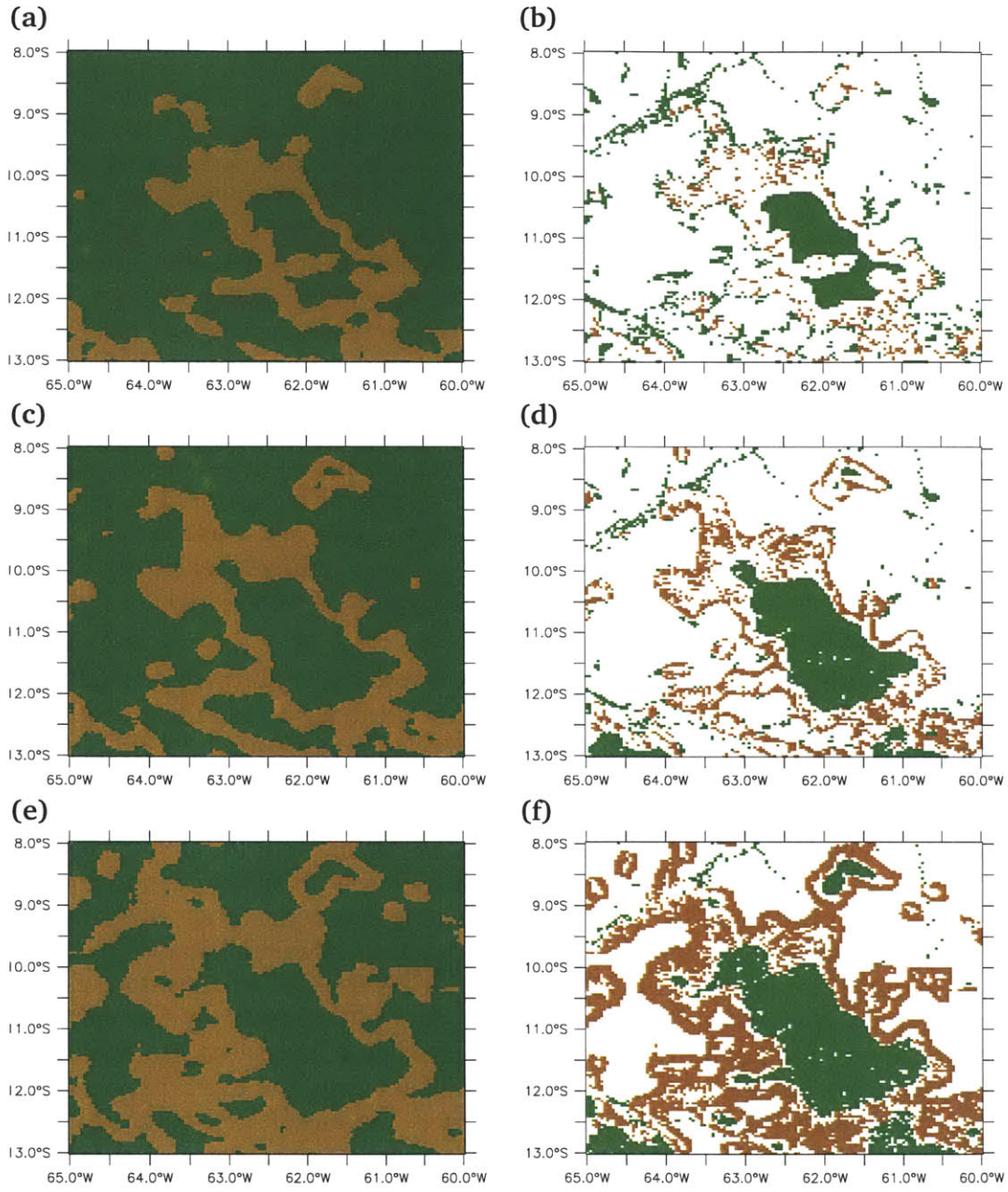

Figure 7-7: Deforestation Transition Maps of Domains: **(a)** Transition zone, 4-km resolution, 30%—60% threshold (**MARGIN 30—60**); **(c)** Transition zone, 4-km resolution, 40%—70% threshold (**MARGIN 40—70**); **(e)** Transition zone, 4-km resolution, 50%—80% threshold (**MARGIN 50—80**); **(b)** Difference between high resolution & MARGIN 30—60 transition zone; **(d)** Difference between high resolution & MARGIN 40—70 transition zone; **(f)** Difference between high resolution & MARGIN 50—80 transition zone. White areas are unchanged; green areas are comparatively forested in transition zone; brown areas are comparatively deforested in transition zone.

Table 7.40: Results from the Binomial Analysis of TRMM-2A23 Event Counts v. Transition between Forested & Deforested **(MARGIN 30—60)**; The count of positive and negative normalized event count differences is compared to the binomial distribution to detect significant biases.

Difference Statistic	>0 Counts	<0 Counts	Significance
Rain Certain	10	**66**	$p \leqslant 0.0001$
Rain Possible	0	**76**	$p \leqslant 0.0001$
Rain Convective	15	**61**	$p \leqslant 0.0001$
Rain Stratiform	10	**66**	$p \leqslant 0.0001$
Rain Isolated	18	**57**	$p \leqslant 0.0001$
Warm Possible	18	**57**	$p \leqslant 0.0001$
Storm Height	43	33	—
Bright Band Height	**45**	24	$p \leqslant 0.02$
Bright Band Intensity	32	37	—

Table 7.41: Results from the Binomial Analysis of TRMM-2A23 Event Counts v. Transition between Forested & Deforested **(MARGIN 40—70)**; The count of positive and negative normalized event count differences is compared to the binomial distribution to detect significant biases.

Difference Statistic	>0 Counts	<0 Counts	Significance
Rain Certain	40	36	—
Rain Possible	16	**60**	$p \leqslant 0.0001$
Rain Convective	37	39	—
Rain Stratiform	40	36	—
Rain Isolated	28	**47**	$p \leqslant 0.04$
Warm Possible	28	**47**	$p \leqslant 0.04$
Storm Height	39	37	—
Bright Band Height	42	29	—
Bright Band Intensity	40	31	—

Table 7.42: Results from the Binomial Analysis of TRMM-2A23 Event Counts v. Transition between Forested & Deforested **(MARGIN 50—80)**; The count of positive and negative normalized event count differences is compared to the binomial distribution to detect significant biases.

Difference Statistic	>0 Counts	<0 Counts	Significance
Rain Certain	**76**	0	$p \leqslant 0.0001$
Rain Possible	**76**	0	$p \leqslant 0.0001$
Rain Convective	**75**	1	$p \leqslant 0.0001$
Rain Stratiform	**76**	0	$p \leqslant 0.0001$
Rain Isolated	**57**	18	$p \leqslant 0.0001$
Warm Possible	**57**	18	$p \leqslant 0.0001$
Storm Height	**45**	31	$p \leqslant 0.14$
Bright Band Height	36	34	—
Bright Band Intensity	38	32	—

The analysis of TRMM-2A23 rainfall occurrence counts with respect to different representation of the transition zone between forested and deforested regions has revealed that there are significantly more rainfall occurrences over the transition between forested and deforested areas, depending on how the transition zone is defined. In order to understand these results, analyses of the TRMM-2A23 rainfall statistics in relation to intensively deforested areas are carried out. Forest cover maps are created using lower thresholds to differentiate between forested and deforested pixels (i. e., 40% and 30%). These new maps are presented in Figure 7-8. The results of the analyses (shown in Tables 7.43 & 7.44) indicate that there are significantly less rainfall occurrences of all types over these intensively deforested areas.

There is thus a very high association between rainfall and deforestation. The results presented heretofore show that rainfall occurrences are significantly suppressed over intensely deforested areas, and they are significantly enhanced over the transitions zones. As in the analysis of shallow clouds, the role of topography in these results must be examined. The results of rainfall and topography were shown in the previous section; they are summarized and discussed in the following subsection.

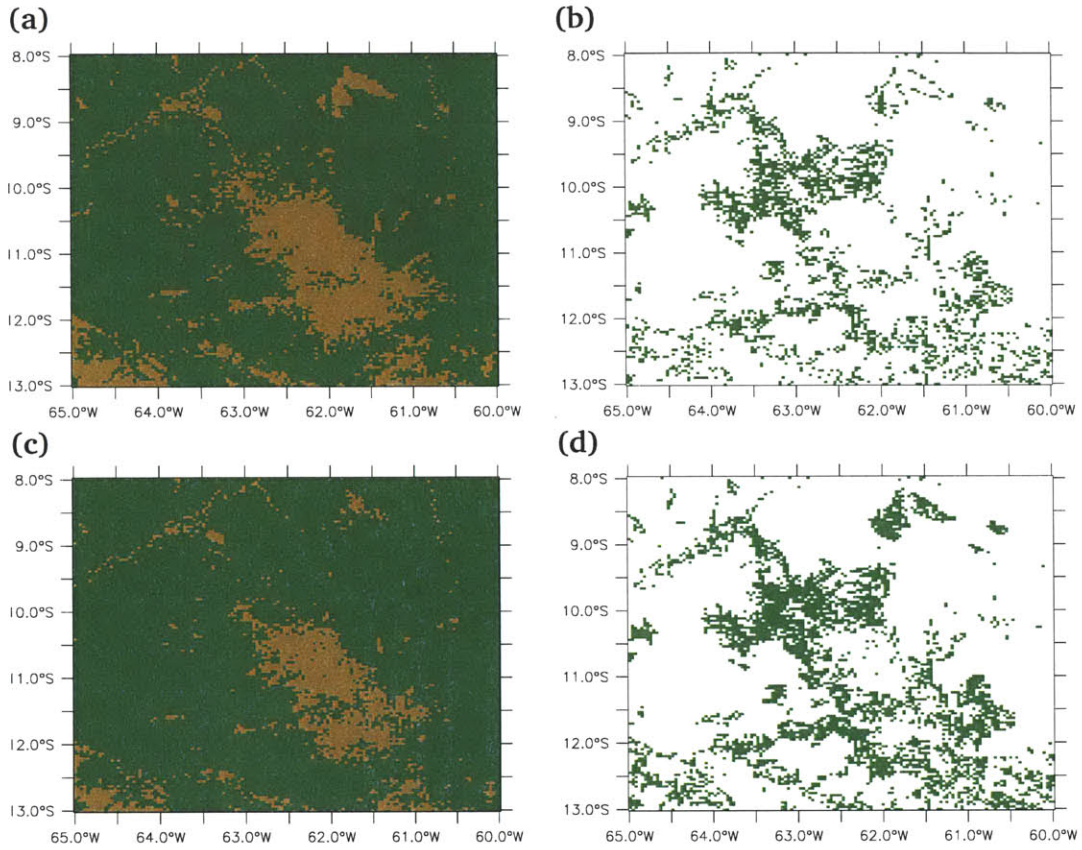

Figure 7-8: Deforestation Maps of Domains: **(a)** 4-km resolution, 40% threshold; **(c)** 4-km resolution, 30% threshold; ; **(b)** Difference between 50%-threshold & 40%-threshold deforestation maps (white areas are unchanged; green areas are comparatively forested in 40%-threshold map; brown areas are comparatively deforested in 40%-threshold map); **(d)** Difference between 50%-threshold & 30%-threshold deforestation maps (white areas are unchanged; green areas are comparatively forested in 30%-threshold map; brown areas are comparatively deforested in 30%-threshold map).

Table 7.43: Results from the Binomial Analysis of TRMM-2A23 Event Counts v. Deforestation **(40% Threshold)**; The count of positive and negative normalized event count differences is compared to the binomial distribution to detect significant biases.

Difference Statistic	>0 Counts	<0 Counts	Significance
Rain Certain	0	**76**	$p \leqslant 0.0001$
Rain Possible	0	**76**	$p \leqslant 0.0001$
Rain Convective	2	**74**	$p \leqslant 0.0001$
Rain Stratiform	0	**76**	$p \leqslant 0.0001$
Rain Isolated	15	**60**	$p \leqslant 0.0001$
Warm Possible	15	**60**	$p \leqslant 0.0001$
Storm Height	32	44	—
Bright Band Height	40	29	—
Bright Band Intensity	34	35	—

Table 7.44: Results from the Binomial Analysis of TRMM-2A23 Event Counts v. Deforestation **(30% Threshold)**; The count of positive and negative normalized event count differences is compared to the binomial distribution to detect significant biases.

Difference Statistic	>0 Counts	<0 Counts	Significance
Rain Certain	0	**76**	$p \leqslant 0.0001$
Rain Possible	0	**76**	$p \leqslant 0.0001$
Rain Convective	0	**76**	$p \leqslant 0.0001$
Rain Stratiform	0	**76**	$p \leqslant 0.0001$
Rain Isolated	7	**68**	$p \leqslant 0.0001$
Warm Possible	7	**68**	$p \leqslant 0.0001$
Storm Height	32	44	—
Bright Band Height	**42**	26	$p \leqslant 0.07$
Bright Band Intensity	30	38	—

7.4.2 Rainfall & Topography

In relation to topographical features, the analyses of rainfall have shown that:

1. TRMM-2A23 rainfall occurrence counts are biased toward higher terrain for all types of rainfall, as are TRMM-3A25 convective rainfall occurrence counts; while TRMM-3A25 rainfall and stratiform rainfall occurrence counts are biased toward lower elevations, as are TRMM-3A25 surface rainfall and warm rainfall occurrence counts;

2. TRMM-2A23 and TRMM-3A25 bright band height is biased toward lower elevations;

3. TRMM-2A23 bright band intensity is negatively biased toward lower elevations;

4. TRMM-3A25 surface rain intensity and mean rain rates are biased toward higher elevations;

5. TRMM-3A25 path-averaged stratiform reflectivites and 4 km level reflectivities are biased toward lower elevations.

6. TRMM-3A25 bright band pixels counts are biased toward lower elevations;

7. TRMM-2A23 rainfall occurrence counts are biased toward steeper slopes, (except for warm and isolated rainfall events), as are TRMM-3A25 convective rainfall counts;

8. TRMM-3A25 surface rain intensity, 6 km convective rain rate and reflectivity, mean rain rate and the standard deviation of the mean rain rate are biased toward steeper slopes, as are the measured and corrected reflectivitiees at the 2 and 6 km levels;

9. TRMM-3A25 4 km level stratiform rain rate and its standard deviation are biased toward more gradual slopes;

10. TRMM-3A25 bright band height biased toward more gradual slopes;

There are again some discrepancies between the TRMM-2A23 and TRMM-3A25 results. These discrepancies are again probably due to the spatial resolution differences in the elevation and slope fields used for TRMM-2A23 and TRMM-3A25. Seeing that the TRMM-2A23 analyses were carried out with a higher resolution representation of topography, these results will be accepted as being more representative.

From the analysis of TRMM-2A23 and topography, the following are found: *(i)* rainfall occurrence counts of all types are biased toward higher elevations; *(ii)* bright band intensities are lower over the lowest elevations; *(iii)* bright band heights

are lower over the highest elevations; and *(iv)* rainfall occurrences for rain certain, rain possible, rain convective and rain stratiform are higher over steeper slope. The distributions of elevation and slope with respect to base cover are plotted in Figure 7-10 for the three margin base covers. From the analysis of TRMM-2A23 and marginal areas (MARGIN 50—80), it was found that: *(i)* rainfall occurrences for all types of rainfall are higher over the marginal area; and *(ii)* bright band heights are higher over non marginal areas. For the MARGIN 50—80 base cover, the distributions of slope and elevation over marginal versus non-marginal areas are very similar (Figure 7-10 (e) & (f)). It can thus be argued that topographically-related rainfall associations are not exclusively responsible for the observed behavior of rainfall over marginal areas[5]. Thus, although the role of topography cannot be neglected in the spatial organization of rainfall occurrences, it is safe to conclude that the effect of deforestation is distinct enough not be be overwhelmed by orographical processes.

7.5 Summary & Conclusion

The association between rainfall and deforestation was examined quantitatively in this chapter using data from the Tropical Rainfall Measuring Mission (TRMM). It was found that rainfall occurrences are significantly increased over the transition zone between forested and deforested regions. It was also found that the same rainfall occurrences are significantly suppressed over intensely deforested areas. These results were examined in relation to topographical influences, and although orography certainly plays an important role in modulating the spatial distribution of rainfall, the effect of the land cover disturbance is "real", and not a contrived by-product of topography. the results found in this chapter are — to the author's knowledge — new discoveries about the impacts of deforestation on rainfall, which have not even been inferred from previous modeling exercises.

[5]By the same token, it can be said that the associations that were found between rainfall and the two other marginal base covers are not a result of orography.

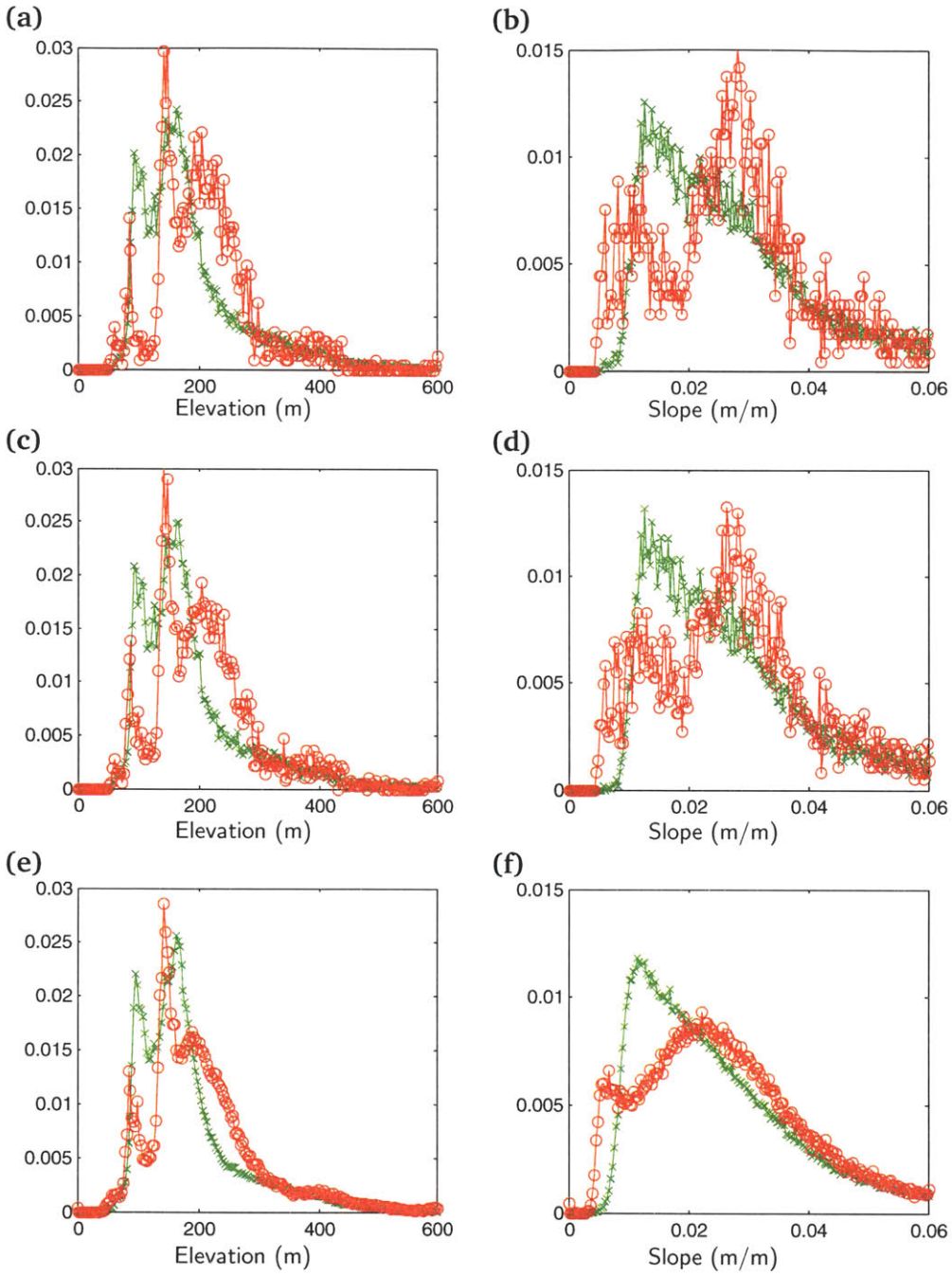

Figure 7-9: Elevation and Slope Distribution v. Deforestation over Rondônia: **(a)** 30% Threshold v. Elevation & **(b)** Slope; **(c)** 40% Threshold v. Elevation & **(d)** Slope; **(e)** 50% Threshold v. Elevation & **(f)** Slope. Deforested areas are represented with the red line, while non forested areas are in green. Elevation is from the Shuttle Radar Topography Mission (SRTM). Slopes are derived from elevation field.

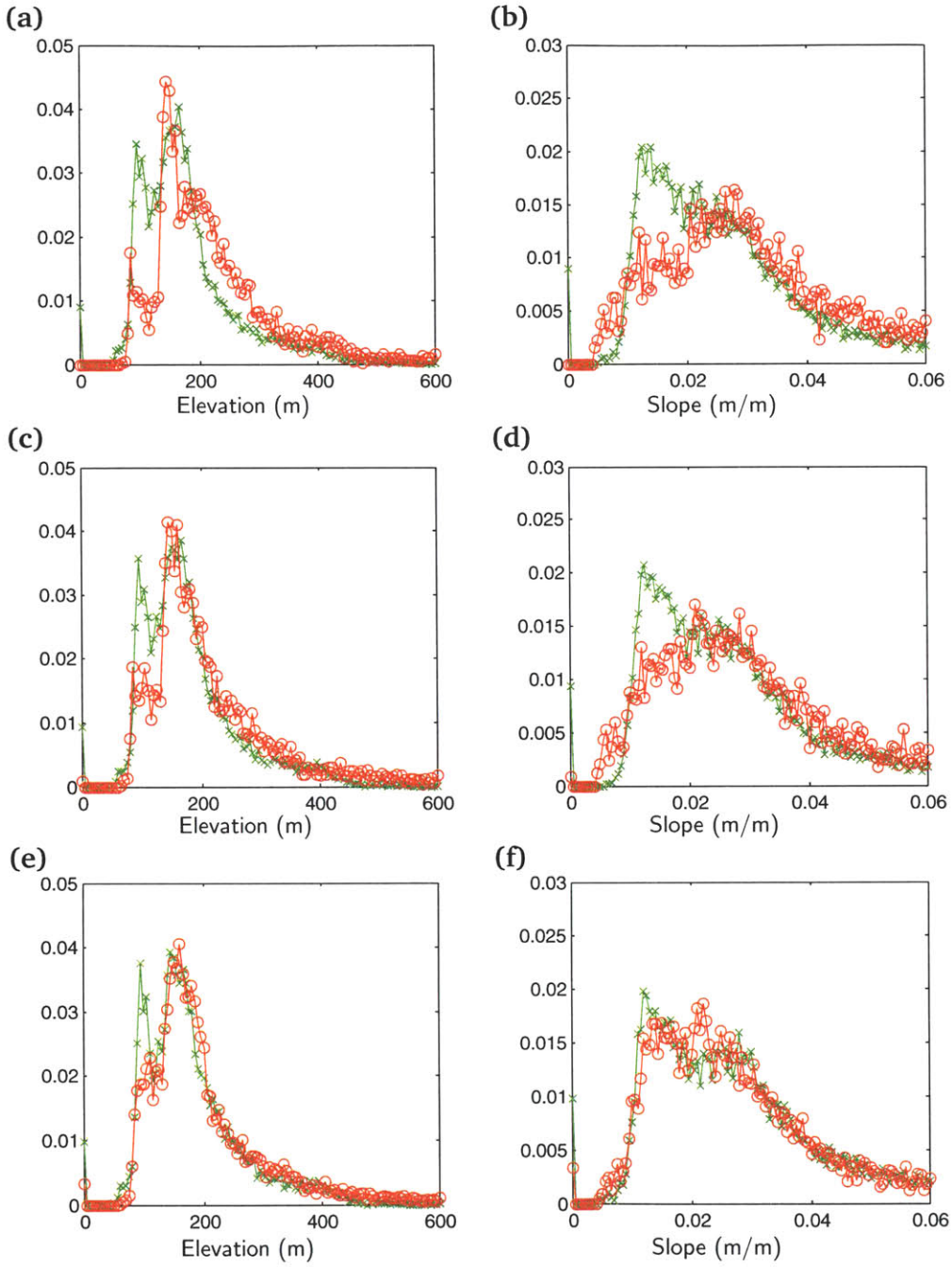

Figure 7-10: Elevation and Slope Distribution v. Marginal Areas over Rondônia: **(a)** MARGIN 30—60 Elevation & **(b)** Slope; **(c)** MARGIN 40—70 Elevation & **(d)** Slope; **(e)** MARGIN 50—80 Elevation & **(f)** Slope. Marginal areas are represented with the red line, while non marginal areas are in green. Elevation is from the Shuttle Radar Topography Mission (SRTM). Slopes are derived from elevation field.

REFERENCES

KUMMEROW, C., W. BARNES, T. KOZU, J. SHIUE and J. SIMPSON. The Tropical Rainfall Measuring Mission (TRMM) Sensor Package. *Journal of Atmospheric and Oceanic Technology*, 15(3):pages 809–817 [1998].

CHAPTER 8

COLD CLOUDS & DEFORESTATION

The availability of the GOES-8 dataset that was used for the examination of shallow cumulus clouds, coupled with a desire to corroborate the TRMM rainfall results presented in Chapter 7, behoove an analysis of high clouds, whose tops fall below a certain threshold in temperature. The record of GOES-8 imager data over the Amazon basin that was used for the analyses in Chapter 6 is used here to derive cold clouds. These clouds are not necessarily raining clouds (e. g., cirrus), but Negri *et al.* [2004] found evidence of a relation between high clouds and deforestation. In this chapter, cold cloud maps are produced over the Rondônia domain, and they are subsequently analyzed in the same fashion that the shallow clouds were analyzed in Chapter 6.

8.1 Cold Cloud Detection

The cold clouds are derived here using a single reflectivity threshold and three separate temperature thresholds. The algorithm is given in Table 8.1. The cold cloud fields are analyzed in exactly the same manner as the shallow cumulus clouds were analyzed in Chapter 6. The cold cloud fields are compared to forest cover patterns using the SHF algorithm with the same base forest cover and randomized realizations of forest cover that were use in the shallow cloud analysis.

8.2 Analysis of Cold Clouds and Deforestation

A qualitative assessment of the maps of average fractional cold cloud cover over the Rondônia domain shown in Figures 8-1, 8-2, 8-3 & 8-4 indicates that cold clouds have a predominant association with topographical features, which are depicted in Figure 8-1(a). The cold cloud features at other times of day bear less resemblance

Table 8.1: Cold Cloud Classification Algorithm.

	Cloud-275	Cloud-255	Cloud-235
VIS Reflectance Threshold (%)	70	70	70
TIR Temperature Threshold (K)	275	255	235
Simultaneous or Independent	S	S	S

to surface features, as is seen in Figure 8-2. The mean fractional 17h45 UTC cold cloud cover exhibits a clear signature of the ridge that runs north-west to south-east in the lower half of the domain. The cold cloud features are not exactly co-located with that ridge, as they are slightly to the south and west. This feature is repeated in the seasonal maps of cold cloud fractional cover (Figures 8-3 & 8-4). There is, however, another remarkable feature in the cold cloud maps that seems to correspond to the inverted v-shape savannah region centered about 61.5°W and 8.5°S. This feature seems to be persistent as it shows up during all seasons (Figures 8-3 & 8-4). This observation gives credence to the observations of Negri *et al.* [2004], who found that there was an increase in fractional cold cloud occurrence over the same area. Negri *et al.* [2004]'s dataset was based on an IR threshold of 225 K covering August and September of 2000 and 2001[1]. Negri hypothesized that this increase in convective activity was due to the surface heating contrast created by the savannah. Interestingly, Negri *et al.* [2004] did not observe this type of surface driven convective activity contrast in other months of the year. They thus concluded that this type of phenomenon was easily "overwhelmed by the transport of synoptic-scale moisture into the domain". Some of the qualitative observations herein are thus at odds with the results of Negri *et al.* [2004], and prompt further quantitative investigations.

The quantitative analysis of the cold cloud cover relies on the same type of statistics that were used in the analysis of shallow clouds. The monthly mean difference in cold cloud fractional cover between deforested and forest areas is calculated (CDD), as is the count of days in a month when the fractional cold cloud cover over deforested areas is greater than that over forested areas (EC). The monthly time-series of 255 K cold cloud CDD and EC are plotted in Figures 8-5 & 8-6 along with their 99% confidence intervals, which were generated using the shuffled forest cover maps. As in the shallow cloud analysis, the relative frequency of departures from the 99% confidence intervals is calculated for each month, and rationalized as a seasonal climatology in Figure 8-7. The frequency of departures from he 99% confidence bounds do not show many consistent features across the 3 cold cloud fields (that differ by the temperature threshold), nor do they exhibit consistent features across the 3 times of day. The only two consistent features are the significantly higher cold cloud fractional cover over deforested areas at 17h45 UTC during the monsoon (DJF), and the significantly lower cold cloud fractional cover over defor-

[1]Negri *et al.* [2004] state that their results are similar using a threshold of 255 K.

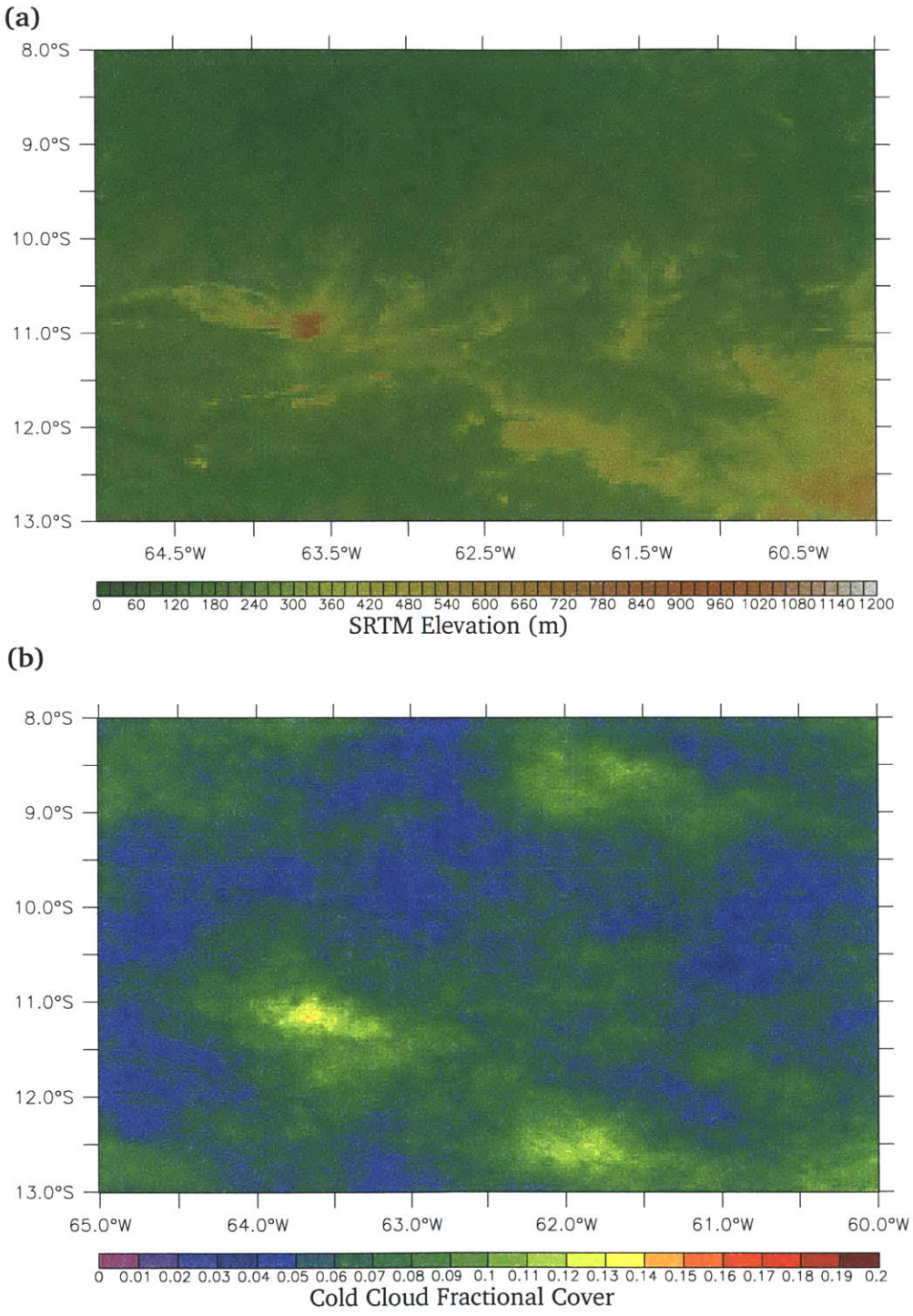

Figure 8-1: Long-Term Mean Cold Cloud Cover; **(a)** SRTM Elevation map and **(b)** Average Fractional Cover of 17h45 UTC Cold Clouds (colder than 235 K) over Rondônia.

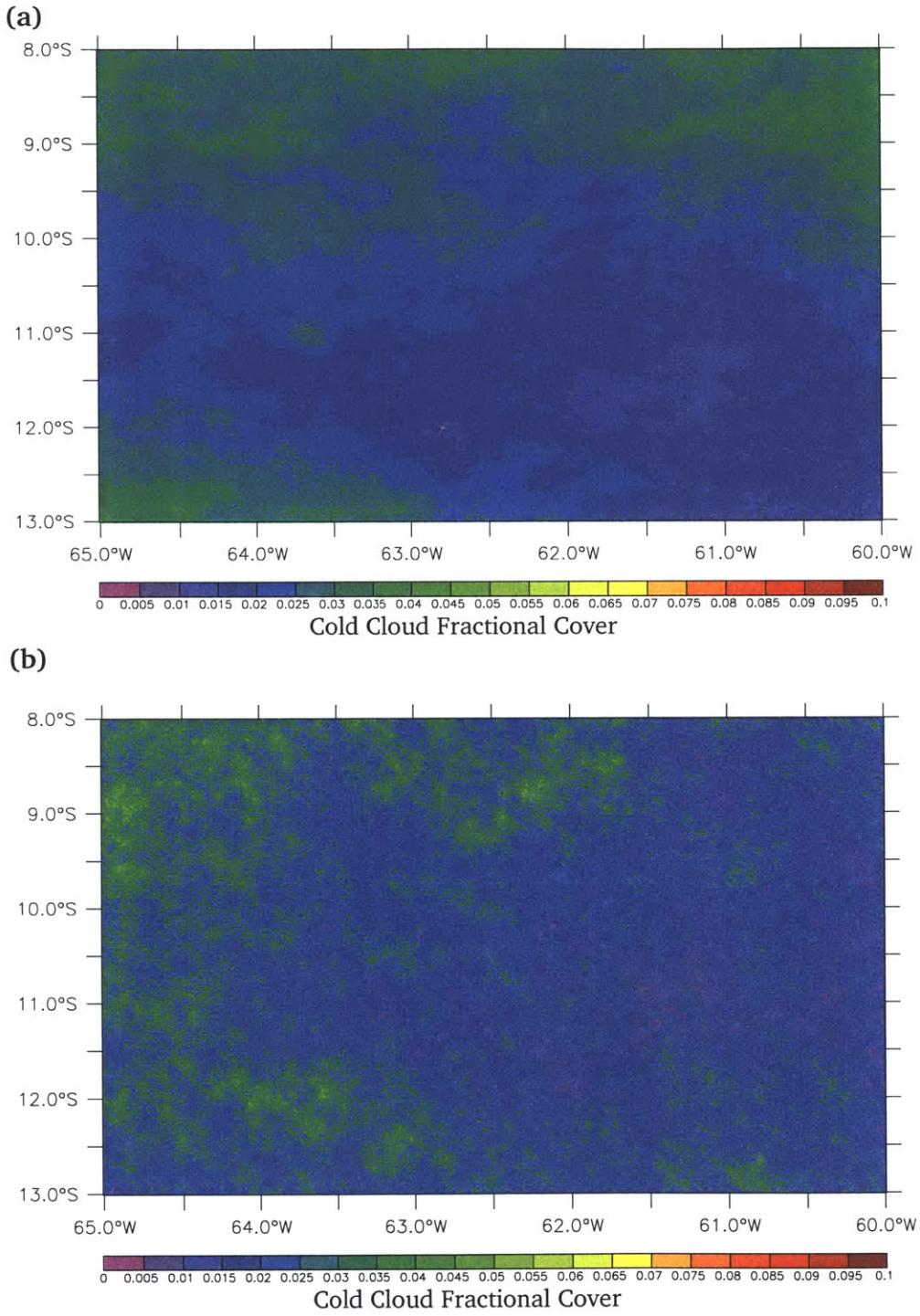

Figure 8-2: Long-Term Mean Cold Cloud Cover;Average Fractional Cover of **(a)** 14h45 UTC and **(b)** 20h45 UTC Cold Clouds (colder than 235 K) over Rondônia.

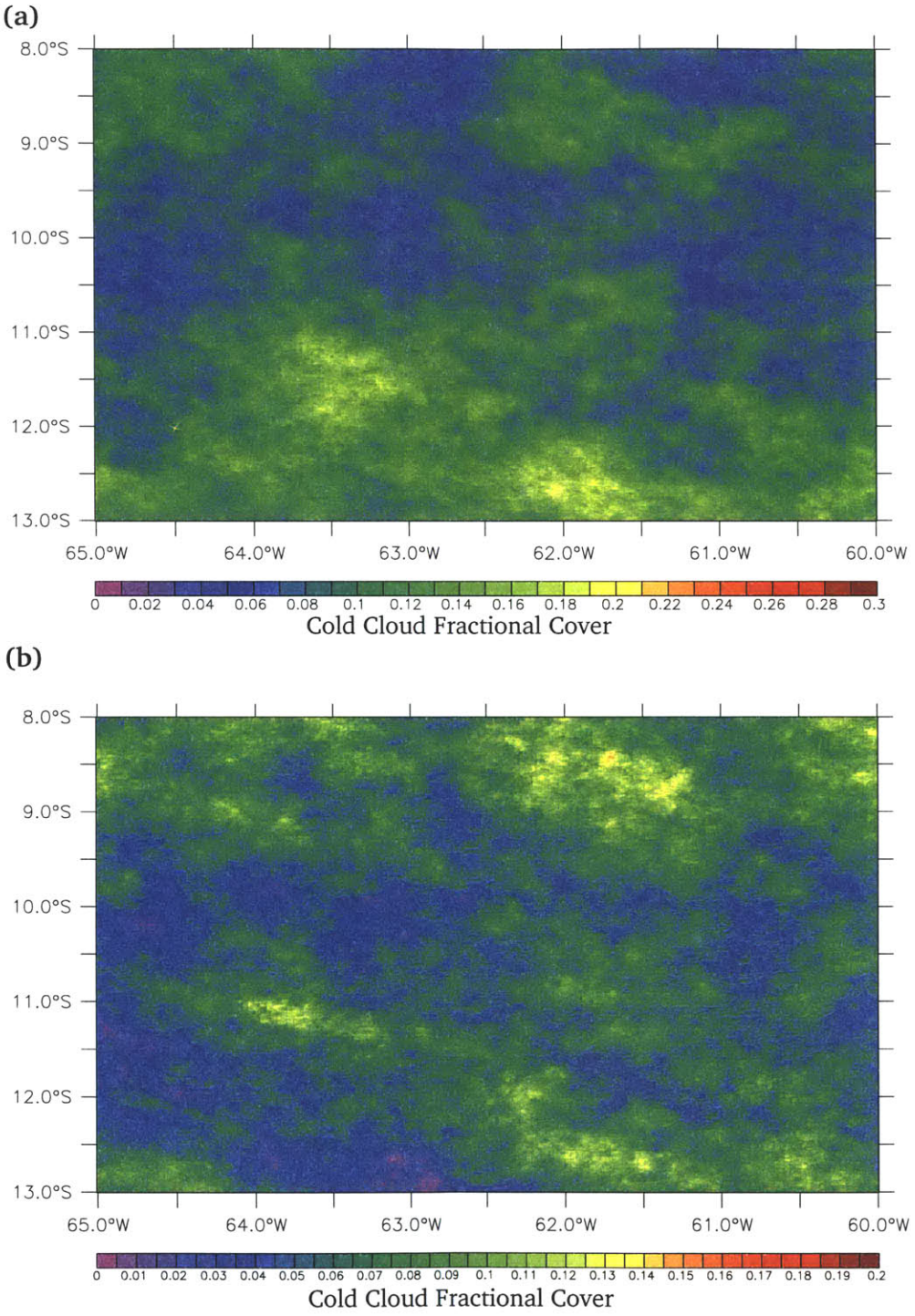

Figure 8-3: Long-Term Seasonal Mean Cold Cloud Cover (12/1/2000-3/31/2003); Average Fractional Cover of Cold Clouds over Rondônia at **(a)** DJF and **(b)** MAM.

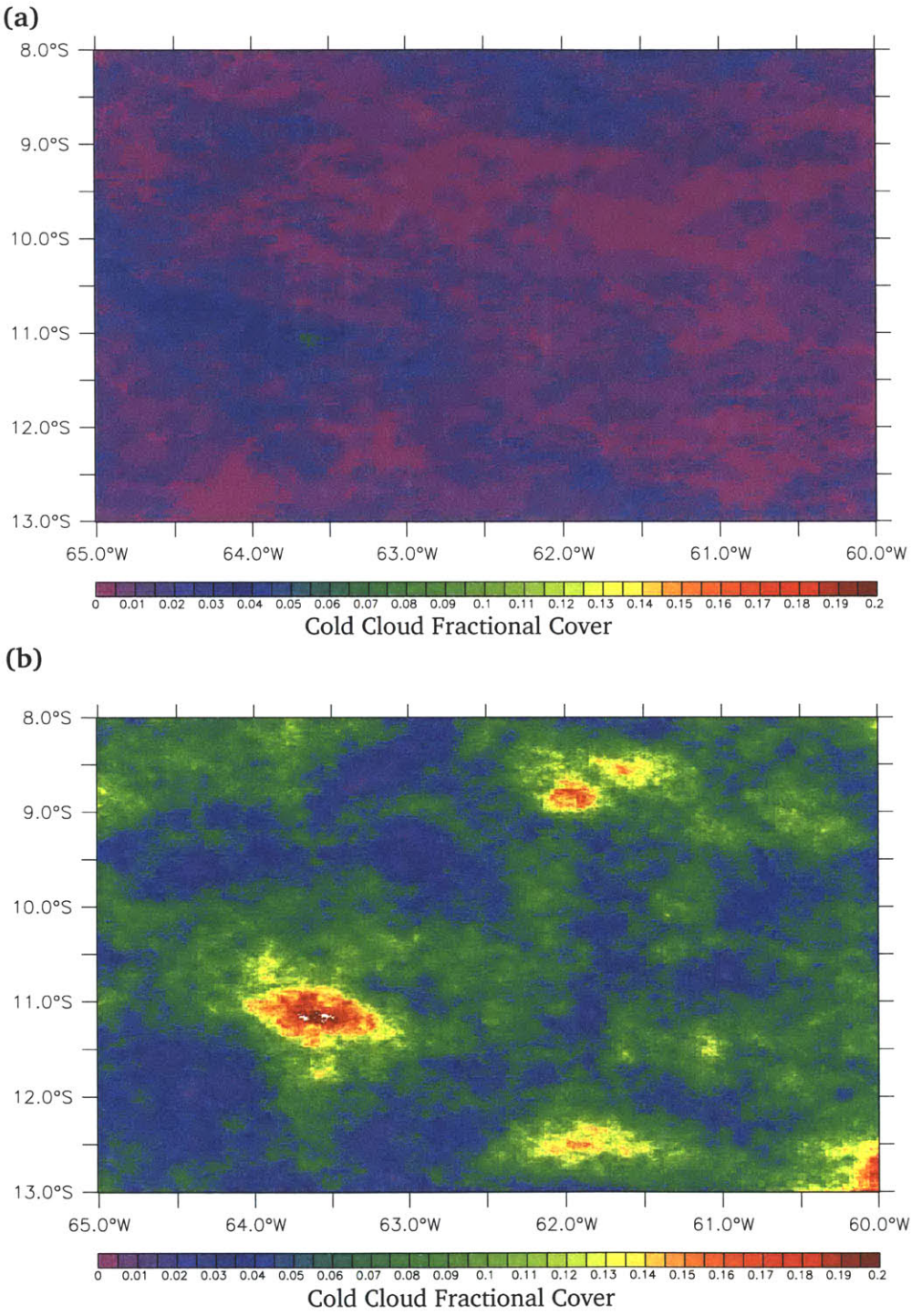

Figure 8-4: Long-Term Seasonal Mean Cold Cloud Cover (12/1/2000-3/31/2003); Average Fractional Cover of Cold Clouds over Rondônia at **(a)** JJA and **(b)** SON.

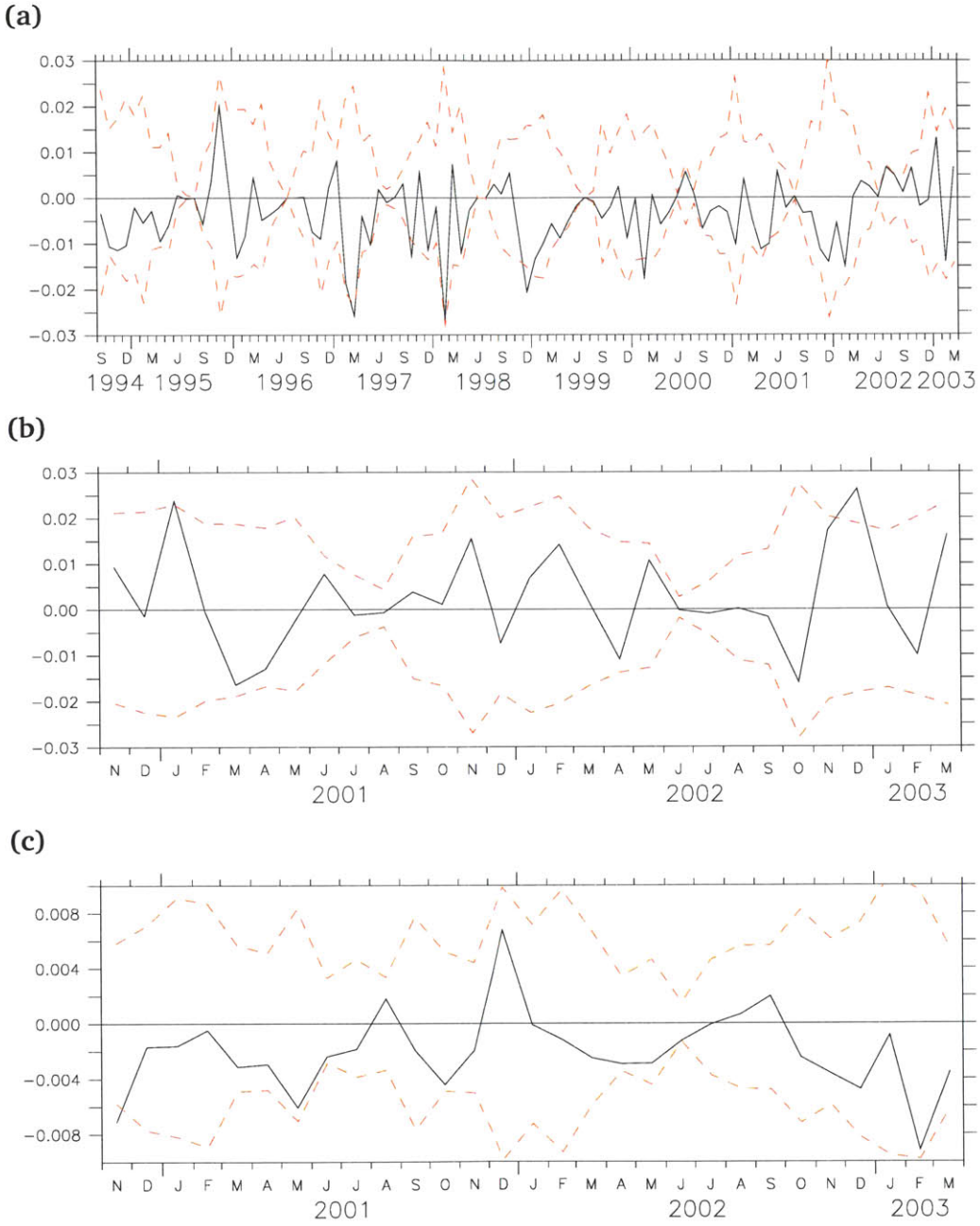

Figure 8-5: Monthly Time-Series of Fractional 255 K Cold Cloud Cover Differences between Deforested and Forested Pixels over the Rondônia Domain at **(a)** 14h45 UTC, **(b)** 17h45 UTC and **(c)** 20h45 UTC.

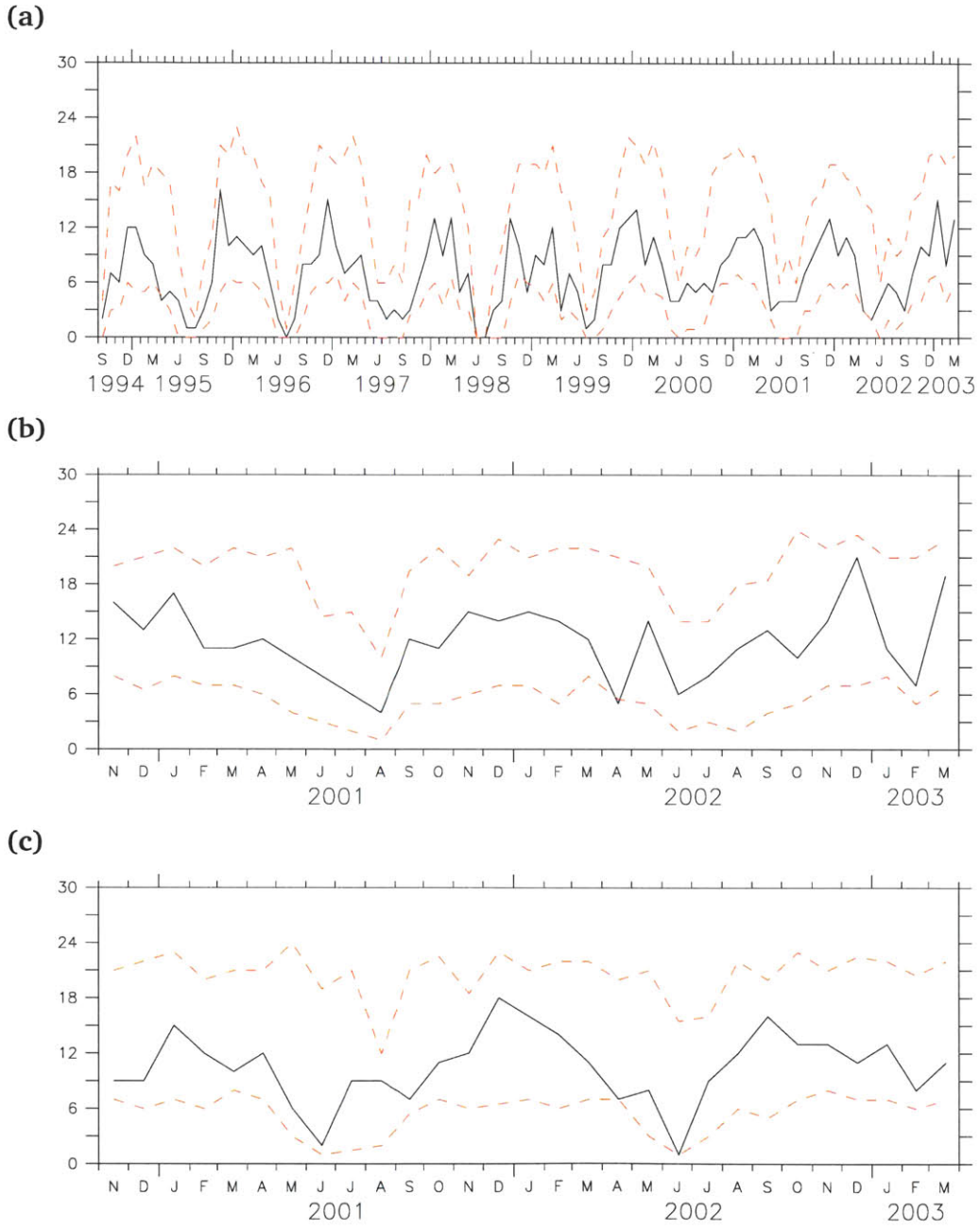

Figure 8-6: Monthly Time-Series of Fractional 255 K Cold Cloud Exceedence Counts over the Rondônia Domain at **(a)** 14h45 UTC, **(b)** 17h45 UTC and **(c)** 20h45 UTC.

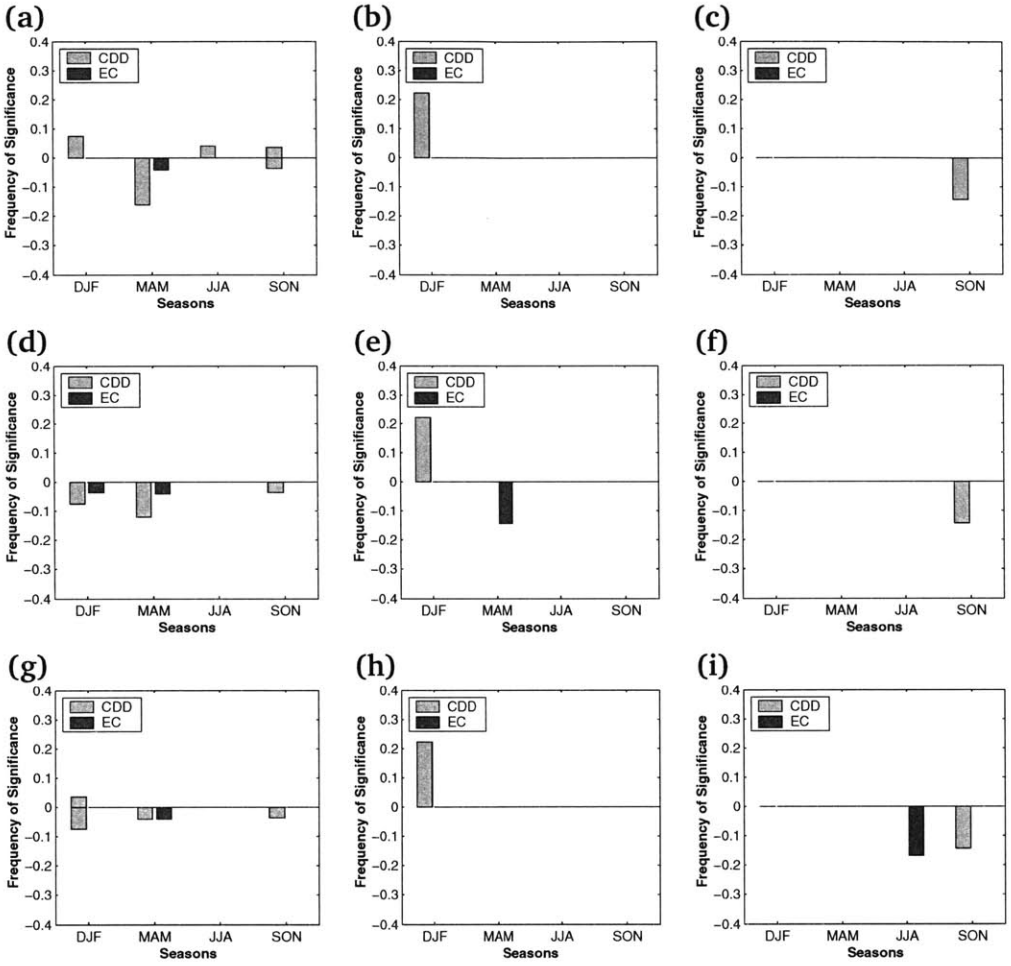

Figure 8-7: Seasonal Climatologies of Cold Cloud CDD and EC significance for Rondônia; bars represent normalized number of times that a statistic is significant for a specific month; positive (negative) is for number of times that statistic is greater (smaller) than upper (lower) bound of 99% confidence interval. Frequency of 275 K Cold Clouds CDD and EC significance at **(a)** 14h45 UTC, **(b)** 17h45 UTC, and **(c)** 20h45 UTC; Frequency of 255 K Cold Clouds CDD and EC significance at **(d)** 14h45 UTC, **(e)** 17h45 UTC, and **(f)** 20h45 UTC; Frequency of 235 K Cold Clouds CDD and EC significance at **(g)** 14h45 UTC, **(h)** 17h45 UTC, and **(i)** 20h45 UTC.

Table 8.2: Significant Results from the Binomial Analysis of Cold Cloud Fractional Cover Difference v. Forest Cover; The count of positive and negative differences is compared to the binomial distribution to detect significant biases.

Variable	Time	>0 Counts	<0 Counts	Significance
Cold Cloud (275 K)	14h45 UTC	41	62	$p \leqslant 0.05$
	17h45 UTC	17	12	—
	20h45 UTC	5	24	$p \leqslant 0.0006$
Cold Cloud (255 K)	14h45 UTC	35	66	$p \leqslant 0.003$
	17h45 UTC	15	14	—
	20h45 UTC	4	25	$p \leqslant 0.0002$
Cold Cloud (235 K)	14h45 UTC	31	68	$p \leqslant 0.0003$
	17h45 UTC	13	16	—
	20h45 UTC	4	25	$p \leqslant 0.0002$

Table 8.3: Significant Results from the Binomial Analysis of Cold Cloud Fractional Cover Exceedence Counts v. Forest Cover; The count of EC counts greater and smaller than half the number of days is compared to the binomial distribution to detect significant biases.

Variable	Time	$> d_{\frac{1}{2}}$ Counts	$< d_{\frac{1}{2}}$ Counts	Significance
Cold Cloud (275 K)	14h45 UTC	14	84	$p \leqslant 0.0001$
	17h45 UTC	11	18	—
	20h45 UTC	6	23	$p \leqslant 0.003$
Cold Cloud (255 K)	14h45 UTC	10	85	$p \leqslant 0.0001$
	17h45 UTC	8	20	$p \leqslant 0.04$
	20h45 UTC	4	24	$p \leqslant 0.0002$
Cold Cloud (235 K)	14h45 UTC	15	79	$p \leqslant 0.0001$
	17h45 UTC	7	20	$p \leqslant 0.02$
	20h45 UTC	3	25	$p \leqslant 0.0001$

ested areas at 20h45 UTC during the pre-monsoon (SON).

There are however some consistent features in the cold clouds when they are examined as a binomial variable. The CDD and EC time-series are analyzed under the hypothesis that if cold clouds and deforestation are unrelated, the distribution of positive and negative CDDs (EC greater or smaller than half the number of days in month) distribution should mimic that of a binomial variable. The results of that analysis are presented in Tables 8.2 & 8.3. This analysis reveals that there are significantly more cold clouds over forested pixels at 14h45 UTC and 20h45 UTC. The distribution of EC also show some significance at 17h45 UTC for the 255 K and 235 K clouds, but the level of significance is lower, and these results are not reflected in the CDD distribution. The role of topography in these results must be questioned though. It was seen in Chapter 6 that deforested areas are slightly biased toward lower elevations and more gradual slopes.

8.3 Cold Clouds & Topography

The qualitative evaluation of the cold cloud fields (Figures 8-1, 8-2, 8-3 & 8-4) revealed that cold clouds were associated with two prominent features in the Rondônia domain: the ridge that runs from north-west to south-east in the bottom half of the domain, and the inverted v-shaped savannah clearing in the nort-eastern quadrant of the domain. Both these associations were more prominent at 17h45 UTC (13h45 LT). In the previous section, it was found that there were apparent associations between deforestation and cold clouds at 14h45 UTC and 20h45 UTC, when cold clouds dominated over forested areas. This section will employ the same analysis tools to explore the association between topography and cold cloud fields.

The seasonal climatology of departures from the empirically derived 99% confidence bounds is represented in Figure 8-8 for elevations and Figure 8-9 for slopes. With respect to elevation, there are consistent results at 14h45 UTC and 20h45 UTC when cold clouds are significantly more prevalent over lower elevations. This is reflected for all elevation thresholds in the CDD analysis, and only for the 30% highest v. 70% lowest in the EC analysis. The results at 17h45 UTC are consistent with the qualitative analysis of the cold cloud cover over the domain made in the previous section. The CDD analysis at 17h45 UTC shows that there are consistently more clouds over the 30% highest pixels. It should also be noted that during the post-monsoon and dry seasons (i. e., MAM and JJA), there are more clouds over the 30% lowest pixels at 17h45 UTC, and that no consistent trend is detected at all for the EC analysis at 17h45 UTC. There is thus a strong diurnal modulation of cold clouds with respect to topography. The analysis with respect to slopes reveals much the same trends, although the diurnal reversal of association is not as clear. In all, cold clouds seem to be more prevalent over more gradual slopes.

The binomial analyses of the time series of cold cloud CDD and EC over eleva-

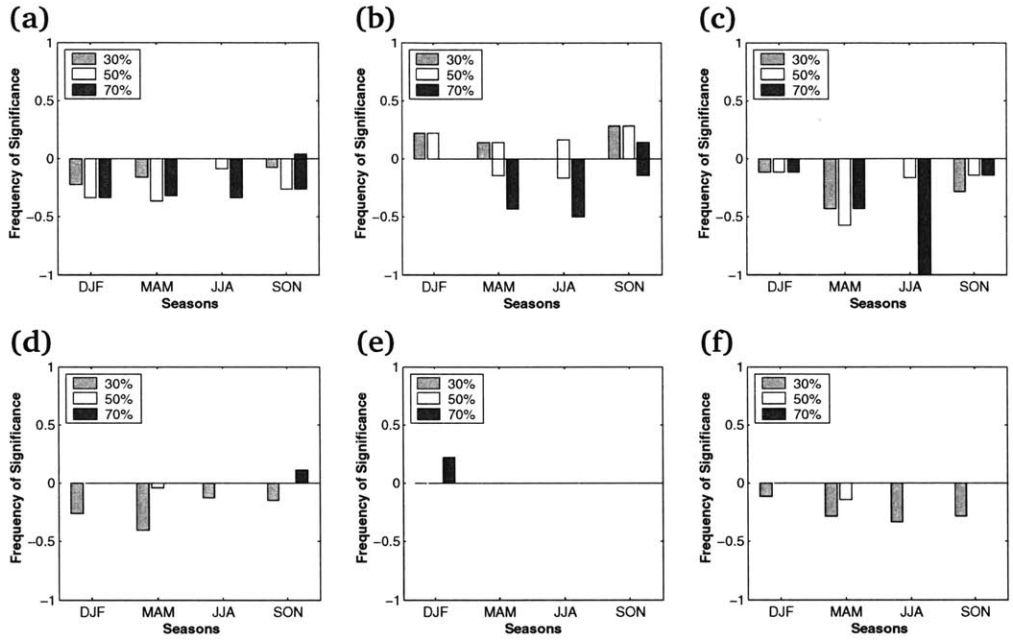

Figure 8-8: Seasonal Climatologies of Cold Cloud CDD and EC significance for Rondônia Elevations; bars represent normalized number of times that a statistic is significant for a specific month; positive (negative) is for number of times that statistic is greater (smaller) than upper (lower) bound of 99% confidence interval. Frequency of 235 K Cold Clouds CDD significance at **(a)** 14h45 UTC, **(b)** 17h45 UTC, and **(c)** 20h45 UTC; Frequency of 235 K Cold Clouds EC significance at **(d)** 14h45 UTC, **(e)** 17h45 UTC, and **(f)** 20h45 UTC. Key to legend: **30%** signifies the difference between the 30% highest pixels and the 70% lowest pixels; **50%** signifies the difference between the 50% highest pixels and the 50% lowest pixels; **70%** signifies the difference between the 70% highest pixels and the 30% lowest pixels.

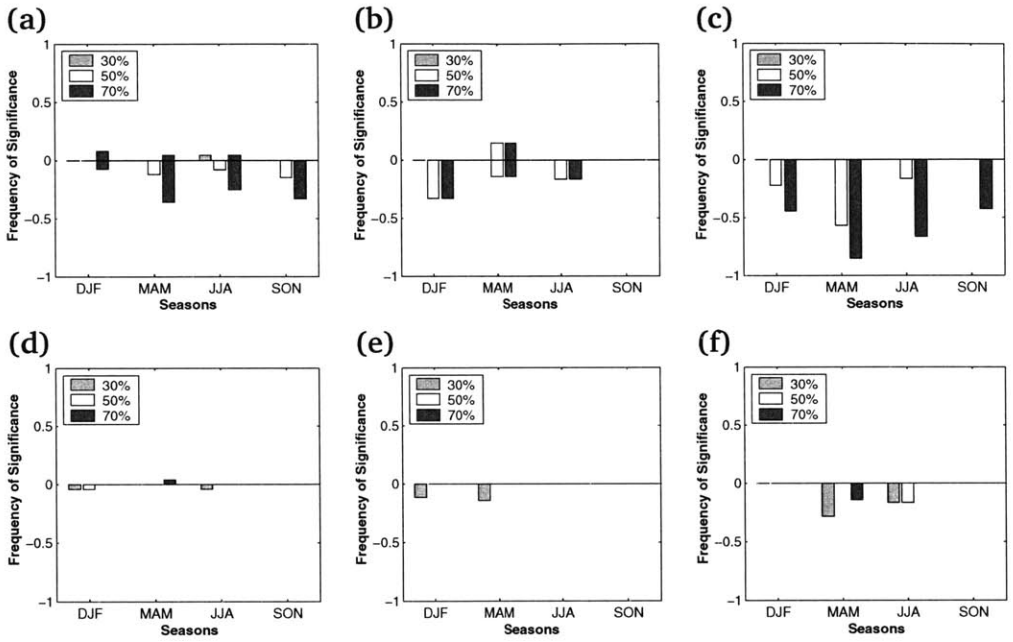

Figure 8-9: Seasonal Climatologies of Cold Cloud CDD and EC significance for Rondônia Slopes; bars represent normalized number of times that a statistic is significant for a specific month; positive (negative) is for number of times that statistic is greater (smaller) than upper (lower) bound of 99% confidence interval. Frequency of 235 K Cold Clouds CDD significance at **(a)** 14h45 UTC, **(b)** 17h45 UTC, and **(c)** 20h45 UTC; Frequency of 235 K Cold Clouds EC significance at **(d)** 14h45 UTC, **(e)** 17h45 UTC, and **(f)** 20h45 UTC. Key to legend: **30%** signifies the difference between the 30% steepest pixels and the 70% most gradual pixels; **50%** signifies the difference between the 50% steepest pixels and the 50% most gradual pixels; **70%** signifies the difference between the 70% steepest pixels and the 30% most pixels.

Table 8.4: Significant Results from the Binomial Analysis of Cold Cloud Fractional Cover Difference v. Elevation; The count of positive and negative differences is compared to the binomial distribution to detect significant biases. The ranges are the percentile cutoffs used to create a binary ("high" v. "low") field from the original DEM (e. g., a range of "30" specifies the difference of the statistic between the 30% highest pixels and the 70% lowest.)

Variable	Time	Range	>0 Counts	<0 Counts	Significance
		30	28	75	$p \leqslant 0.0001$
	14h45 UTC	50	29	74	$p \leqslant 0.0001$
		70	34	69	$p \leqslant 0.0008$
		30	20	9	$p \leqslant 0.07$
Cold Cloud (275 K)	17h45 UTC	50	22	7	$p \leqslant 0.009$
		70	17	12	—
		30	6	23	$p \leqslant 0.003$
	20h45 UTC	50	4	25	$p \leqslant 0.0002$
		70	4	25	$p \leqslant 0.0002$
		30	21	80	$p \leqslant 0.0001$
	14h45 UTC	50	19	82	$p \leqslant 0.0001$
		70	30	71	$p \leqslant 0.0001$
		30	20	9	$p \leqslant 0.07$
Cold Cloud (255 K)	17h45 UTC	50	19	10	$p \leqslant 0.14$
		70	17	12	—
		30	6	23	$p \leqslant 0.003$
	20h45 UTC	50	5	24	$p \leqslant 0.0006$
		70	4	25	$p \leqslant 0.0002$
		30	14	84	$p \leqslant 0.0001$
	14h45 UTC	50	18	81	$p \leqslant 0.0001$
		70	26	73	$p \leqslant 0.0001$
		30	18	11	—
Cold Cloud (235 K)	17h45 UTC	50	19	10	$p \leqslant 0.14$
		70	15	14	—
		30	4	25	$p \leqslant 0.0002$
	20h45 UTC	50	5	24	$p \leqslant 0.0006$
		70	4	25	$p \leqslant 0.0002$

Table 8.5: Significant Results from the Binomial Analysis of Cold Cloud Fractional Cover Exceedences v. Elevation; The count of positive and negative differences is compared to the binomial distribution to detect significant biases. The ranges are the percentile cutoffs used to create a binary ("high" v. "low") field from the original DEM (e. g., a range of "30" specifies the difference of the statistic between the 30% highest pixels and the 70% lowest.)

Variable	Time	Range	>0 Counts	<0 Counts	Significance
Cold Cloud (275 K)	14h45 UTC	30	11	89	$p \leqslant 0.0001$
		50	21	73	$p \leqslant 0.0001$
		70	57	43	—
	17h45 UTC	30	17	10	—
		50	16	12	—
		70	15	11	—
	20h45 UTC	30	4	25	$p \leqslant 0.0002$
		50	2	26	$p \leqslant 0.0001$
		70	7	22	$p \leqslant 0.009$
Cold Cloud (255 K)	14h45 UTC	30	7	93	$p \leqslant 0.0001$
		50	15	80	$p \leqslant 0.0001$
		70	43	43	—
	17h45 UTC	30	16	11	—
		50	15	12	—
		70	13	15	—
	20h45 UTC	30	4	23	$p \leqslant 0.0004$
		50	3	24	$p \leqslant 0.0001$
		70	5	22	$p \leqslant 0.002$
Cold Cloud (235 K)	14h45 UTC	30	5	91	$p \leqslant 0.0001$
		50	16	81	$p \leqslant 0.0001$
		70	44	45	—
	17h45 UTC	30	15	12	—
		50	14	12	—
		70	14	13	—
	20h45 UTC	30	3	26	$p \leqslant 0.0001$
		50	5	23	$p \leqslant 0.001$
		70	5	21	$p \leqslant 0.003$

Table 8.6: Significant Results from the Binomial Analysis of Cold Cloud Fractional Cover Difference v. Slope; The count of positive and negative differences is compared to the binomial distribution to detect significant biases. The ranges are the percentile cutoffs used to create a binary ("steep" v. "gradual") field from the original DEM (e. g., a range of "30" specifies the difference of the statistic between the 30% steepest pixels and the 70% most gradual.)

Variable	Time	Range	>0 Counts	<0 Counts	Significance
Cold Cloud (275 K)	14h45 UTC	30	37	66	$p \leqslant 0.006$
		50	36	67	$p \leqslant 0.003$
		70	35	68	$p \leqslant 0.002$
	17h45 UTC	30	13	16	—
		50	12	17	—
		70	11	18	—
	20h45 UTC	30	1	28	$p \leqslant 0.0001$
		50	2	27	$p \leqslant 0.0001$
		70	2	27	$p \leqslant 0.0001$
Cold Cloud (255 K)	14h45 UTC	30	33	68	$p \leqslant 0.0007$
		50	26	75	$p \leqslant 0.0001$
		70	34	67	$p \leqslant 0.002$
	17h45 UTC	30	13	16	—
		50	13	16	—
		70	13	16	—
	20h45 UTC	30	0	29	$p \leqslant 0.0001$
		50	0	29	$p \leqslant 0.0001$
		70	2	27	$p \leqslant 0.0001$
Cold Cloud (235 K)	14h45 UTC	30	32	67	$p \leqslant 0.0006$
		50	30	69	$p \leqslant 0.0002$
		70	28	71	$p \leqslant 0.0001$
	17h45 UTC	30	13	16	—
		50	12	17	—
		70	13	16	—
	20h45 UTC	30	0	29	$p \leqslant 0.0001$
		50	0	29	$p \leqslant 0.0001$
		70	1	28	$p \leqslant 0.0001$

Table 8.7: Significant Results from the Binomial Analysis of Cold Cloud Fractional Cover Exceedences v. Slope; The count of positive and negative differences is compared to the binomial distribution to detect significant biases. The ranges are the percentile cutoffs used to create a binary ("steep" v. "gradual") field from the original DEM (e. g., a range of "30" specifies the difference of the statistic between the 30% steepest pixels and the 70% most gradual.)

Variable	Time	Range	>0 Counts	<0 Counts	Significance
Cold Cloud (275 K)	14h45 UTC	30	31	64	$p \leqslant 0.001$
		50	35	58	$p \leqslant 0.03$
		70	42	51	—
	17h45 UTC	30	7	21	$p \leqslant 0.02$
		50	10	18	—
		70	15	13	—
	20h45 UTC	30	1	27	$p \leqslant 0.0001$
		50	3	25	$p \leqslant 0.0001$
		70	4	21	$p \leqslant 0.001$
Cold Cloud (255 K)	14h45 UTC	30	28	62	$p \leqslant 0.0005$
		50	39	49	—
		70	58	33	$p \leqslant 0.02$
	17h45 UTC	30	9	19	$p \leqslant 0.09$
		50	9	17	—
		70	14	13	—
	20h45 UTC	30	1	28	$p \leqslant 0.0001$
		50	2	25	$p \leqslant 0.0001$
		70	2	24	$p \leqslant 0.0001$
Cold Cloud (235 K)	14h45 UTC	30	27	64	$p \leqslant 0.0002$
		50	41	49	—
		70	57	35	$p \leqslant 0.03$
	17h45 UTC	30	9	19	$p \leqslant 0.09$
		50	9	17	—
		70	17	11	—
	20h45 UTC	30	1	28	$p \leqslant 0.0001$
		50	0	27	$p \leqslant 0.0001$
		70	3	25	$p \leqslant 0.0001$

tions are summarized in Tables 8.4 & 8.5. The results from these binomial analyses are consistent with the randomization analyses. There is a significant bias for cold clouds over low elevations at 14h45 UTC and 20h45 UTC; this is reflected in both the CDD and EC binomial analysis. Moreover, there is a significant bias for cold clouds over higher elevations at 17h45 UTC, although is is only observed in the CDD analysis and it does not hold true for all combinations of elevation thresholds and maximum cloud top temperatures. The binomial analyses of the CDD and EC time-series with respect to slopes are summarized in Tables 8.6 & 8.7. These are again consistent with the randomization analyses. They show the preference of cold clouds for gradual slopes at 14h45 UTC and 20h45 UTC. There is also a bias in the EC at 17h45 UTC between the 30% steepest and 70% most gradual slopes; there is a bias of cold clouds toward more gradual slopes.

The analysis of cold cloud and topography thus shows that cold clouds are significantly associated with lower elevations and more gradual slopes at 14h45 UTC and 20h45 UTC, while there is a significant association of cold clouds with higher elevations but still more gradual slopes at 17h45 UTC. There is thus a diurnal reversal in the association of cold clouds with elevation, while there is merely a diurnal weakening of the association between cold clouds and slopes. Yet the effect of land cover changes is still not clear. As such, an analysis on sub domains similar to that carried out in Chapter 6 is given in the following section, and is expected to highlight the feature of cold clouds that was qualitatively observed over the inverted v-shaped savannah.

8.4 Scale Analysis

As in the analysis of shallow clouds, the contrast in cloudiness is examined here over two sub-areas in the domain: the inverted v-shaped savannah areas, as well as an area that exhibits the typical fishbone pattern of deforestation. Both domains are exactly the same size, measuring 1.3^o to the side. The forest cover and topography of these sub-domains are depicted in Figures 6-38 & 6-39. Figures 8-10 & 8-11 show the monthly time-series of CDD for 255 K cold clouds at all three times of day for the savannah and fishbone domains respectively. Cursory examination of these figures indicates that there seems to be more cold clouds over the savannah, while the difference between deforested and forested areas isn't clearly significant.

The binomial analysis of these time series for both domains are presented in Tables 8.8 & 8.9 for the savannah and fishbone domains respectively. For the savannah domain, these analyses reveal that there are more cold clouds over the savannah clearing at 17h45 UTC for all temperature thresholds. This is in contrast with the fact that forested areas have more cold cloud cover at 14h45 UTC (for 275 K and 235 K clouds), while there are more 275 K clouds only over the savannah clearing at 20h45 UTC. The deforested domain analysis shows that there are more cold clouds over the forested pixels at 20h45 UTC for all cloud top temperature thresh-

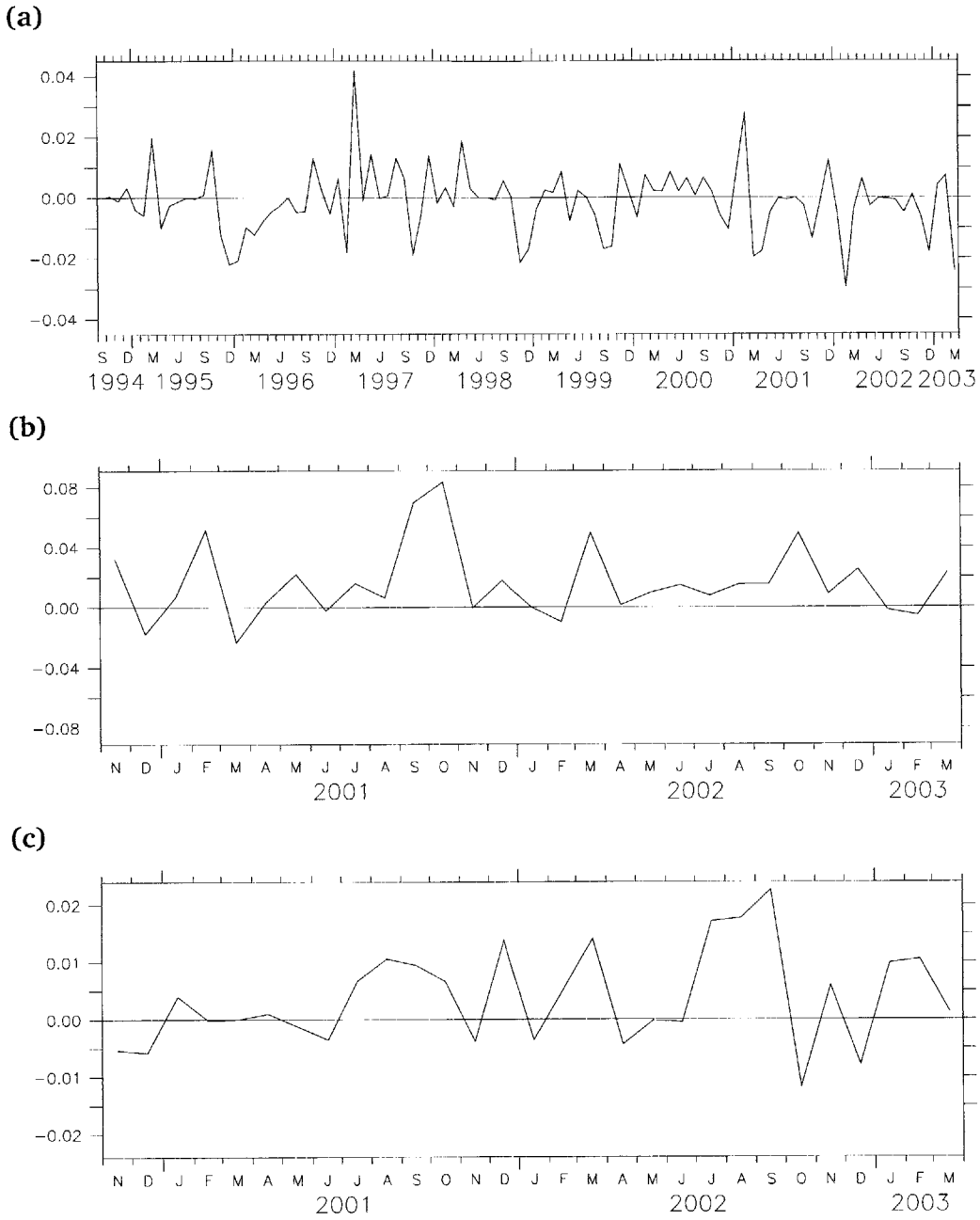

Figure 8-10: Monthly Time-Series of Fractional 255 K Cold Cloud Cover Differences between Deforested and Forested Pixels over the Savannah Domain at **(a)** 14h45 UTC, **(b)** 17h45 UTC and **(c)** 20h45 UTC.

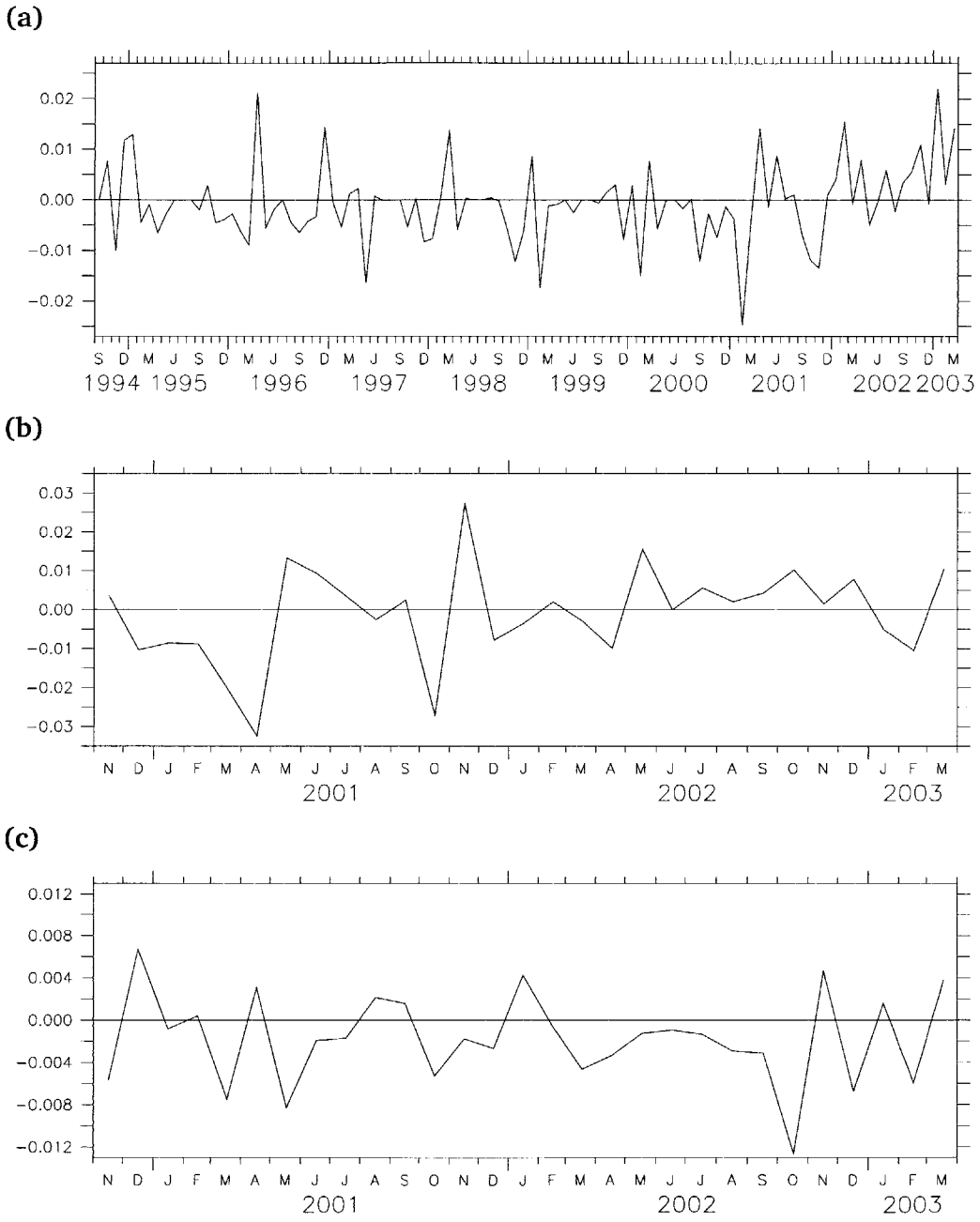

Figure 8-11: Monthly Time-Series of Fractional 255 K Cold Cloud Cover Differences between Deforested and Forested Pixels over the Fishbone Domain at **(a)** 14h45 UTC, **(b)** 17h45 UTC and **(c)** 20h45 UTC.

olds, and there are more 255 K clouds over forested areas at 14h45 UTC. Comparing the results from the savannah and fishbone domains may indicate that the clearing does promote deep convection around mid-day, but only the savannah sub domain exhibits a strong enough surface contrast to actually promote significant convective development. The fishbone domain sees a decrease in the preference of cold clouds for forested pixels around mid-day, but the surface contrast may not be strong enough to actually promote deep convection reliably over the cleared areas.

8.5 Discussion & Conclusions

The initial qualitative assessment of cold clouds seemed to indicate that cold clouds were associated with both elevation (the ridge in the south-western quadrant of the domain) and land cover (the inverted v-shaped savannah clearing in the north-eastern quadrant of the domain). The quantitative analysis of the cold cloud fields confirmed that around mid-day (17h45 UTC), cold clouds show a strong association with higher elevation and the savannah clearing. The correspondence of cold clouds with the savannah clearing is consistent with Negri *et al.* [2004]'s results, although it also contradicts the same study. Indeed, Negri *et al.* [2004]'s conclusions were that this enhancement of cold clouds over the savannah clearing only occurred under weak synoptic circulation and only during the pre-monsoon. Here, it is shown that the cold cloud enhancement occurs throughout the year, thus leading to a persistent bias of cold cloudiness around mid-day.

The quantitative analysis also revealed that the cold cloud fields were significantly associated with forested areas at 14h45 UTC and 20h45 UTC. This result, in conjunction with the result that shows that there are more cold clouds over lower elevations at these same times, proves very interesting. Indeed, as stated in Chapter 6, the distribution of elevations and slopes are roughly similar for both forested and deforested pixels, although there is a slight bias toward lower elevations and more gradual slopes in the case of deforested pixels. Thus, the results concerning cold clouds and forest cover and those relating cold clouds with topography are at odds with each other. It would thus seems that both elevation and land cover have influences on the location of cold clouds. The same logic applies to the results that show more cold clouds over high elevation at 17h45 UTC, while showing more cold clouds over deforestation at the same time of day. These results together decisively affirm the initial qualitative observations that cold cloud fields are influenced both by topography and forest cover. This result also fits very well within the context of the shallow clouds and rainfall results presented in the preceeding chapters. The inter-relatedness of these three sets of results still remains conjectural though, and behooves some further investigation.

Table 8.8: Significant Results from the Binomial Analysis of Cold Cloud Fractional Cover Difference v. Forest Cover over Savannah Domain; The count of positive and negative differences is compared to the binomial distribution to detect significant biases.

Variable	Time	>0 Counts	<0 Counts	Significance
Cold Cloud (275 K)	14h45 UTC	43	60	$p \leqslant 0.12$
	17h45 UTC	25	4	$p \leqslant 0.0002$
	20h45 UTC	19	10	$p \leqslant 0.14$
Cold Cloud (255 K)	14h45 UTC	41	55	—
	17h45 UTC	21	8	$p \leqslant 0.03$
	20h45 UTC	17	12	—
Cold Cloud (235 K)	14h45 UTC	36	54	$p \leqslant 0.08$
	17h45 UTC	22	7	$p \leqslant 0.009$
	20h45 UTC	18	11	—

Table 8.9: Significant Results from the Binomial Analysis of Cold Cloud Fractional Cover Difference v. Forest Cover over Fishbone Domain; The count of positive and negative differences is compared to the binomial distribution to detect significant biases.

Variable	Time	>0 Counts	<0 Counts	Significance
Cold Cloud (275 K)	14h45 UTC	42	57	—
	17h45 UTC	16	14	—
	20h45 UTC	10	19	$p \leqslant 0.14$
Cold Cloud (255 K)	14h45 UTC	37	56	$p \leqslant 0.07$
	17h45 UTC	15	14	—
	20h45 UTC	9	20	$p \leqslant 0.07$
Cold Cloud (235 K)	14h45 UTC	37	48	—
	17h45 UTC	15	13	—
	20h45 UTC	9	20	$p \leqslant 0.07$

REFERENCES

NEGRI, A. J., R. F. ADLER, L. XU and J. SURRAT. The Impact of Amazonian Deforestation on Dry Season Rainfall. *Journal of Climate*, 17(6):pages 1306–1319 [2004].

CHAPTER 9

STUDY OF LONG TERM RAINFALL RECORD

Deforestation in the Amazon basin has proceeded rapidly during the past 50 years. Figures 9-1 & 9-2 provide snapshots of the Amazon basin's forested state throughout the past 30 years. There has been a dramatic change in the surface cover during these past decades, especially in the southern areas of the Amazon. Such a dramatic change in the land cover properties has prompted research into long term trends of climatic variables that could be related to deforestation. The hydrologic importance of the Amazon river (20% of global runoff [Salati and Vose, 1984]) may transform small relative changes into significant alterations in flood peaks or river flows. Some have posited that river flows should be impacted, as the contributing catchments' response to rainfall is intimately related to the surface properties. Also, runoff represents the integrated hydrologic response of a basin, and is thus an interesting measure of change. Yet, studies on Amazon river flows have been either detected increasing trends [Gentry and Lopez-Parodi, 1980] that have subsequently been overshadowed by uncertainties in the measure [Nordin and Meade, 1982]; or they have been unable to detect changes that could be related to deforestation (Sternberg [1987], Richey *et al.* [1989], Marengo [1995]). Others have concentrated on long term trends in outgoing longwave radiation (OLR). These studies have detected increasing trends in trends in OLR (Chu *et al.* [1994],DeLiberty [2000],Chen *et al.* [2002]), which indicate that the convective activity over the Amazon has increased over the past few decades. In this chapter, a long record of monthly raingauge accumulations at Porto Velho (Rondônia) is studied in order to verify the latter findings, and perhaps to understand how the results from the TRMM analysis can be set into a context of long term change.

(a)

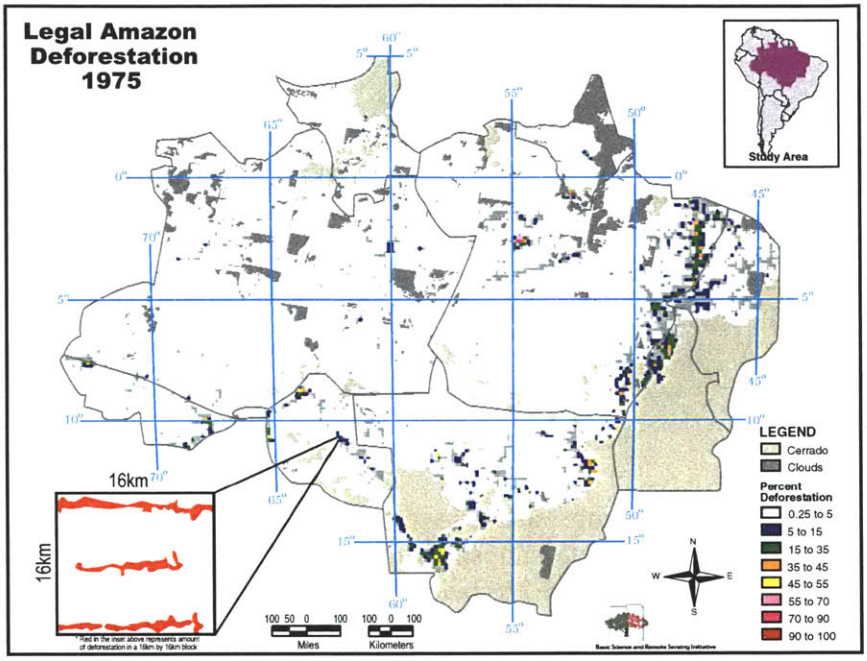

(b)

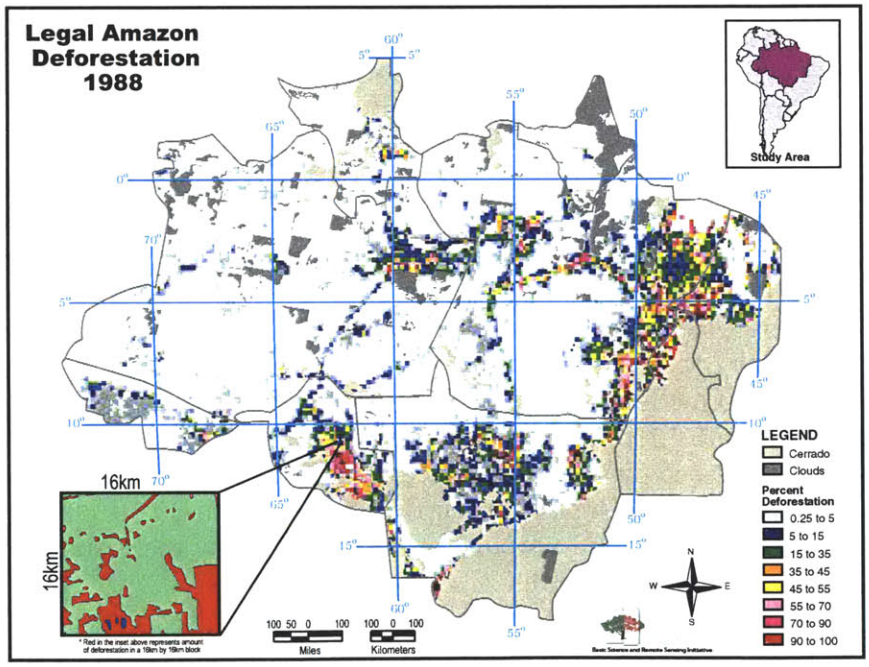

Figure 9-1: TRFIC Deforestation Maps (http://bsrsi.msu.edu/trfic) for **(a)** 1975 and **(b)** 1988.

(a)

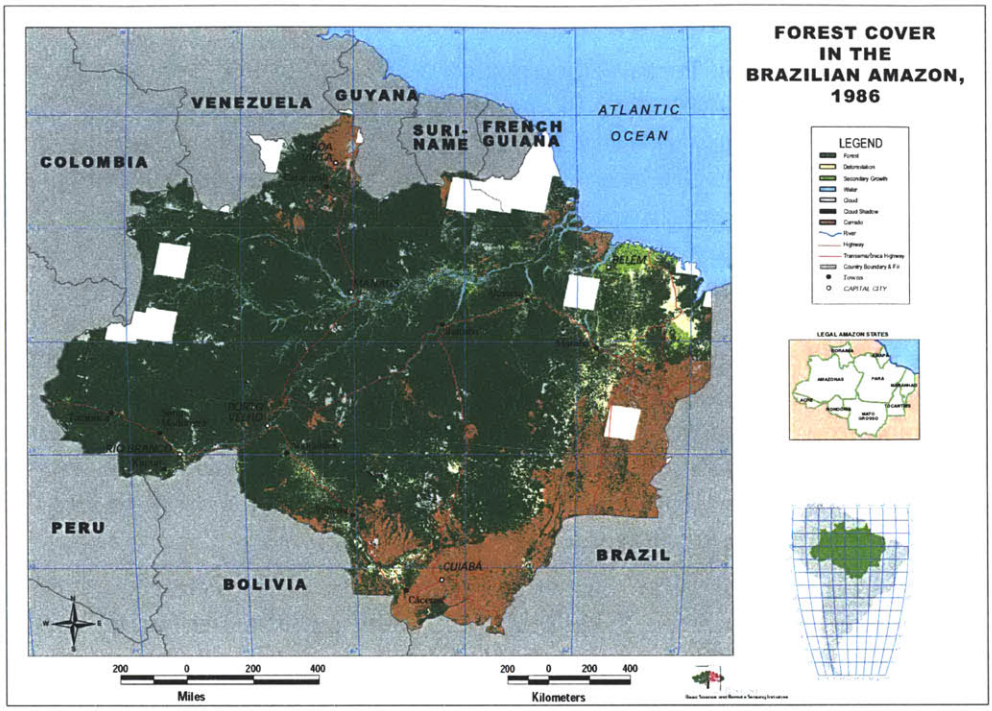

(b)

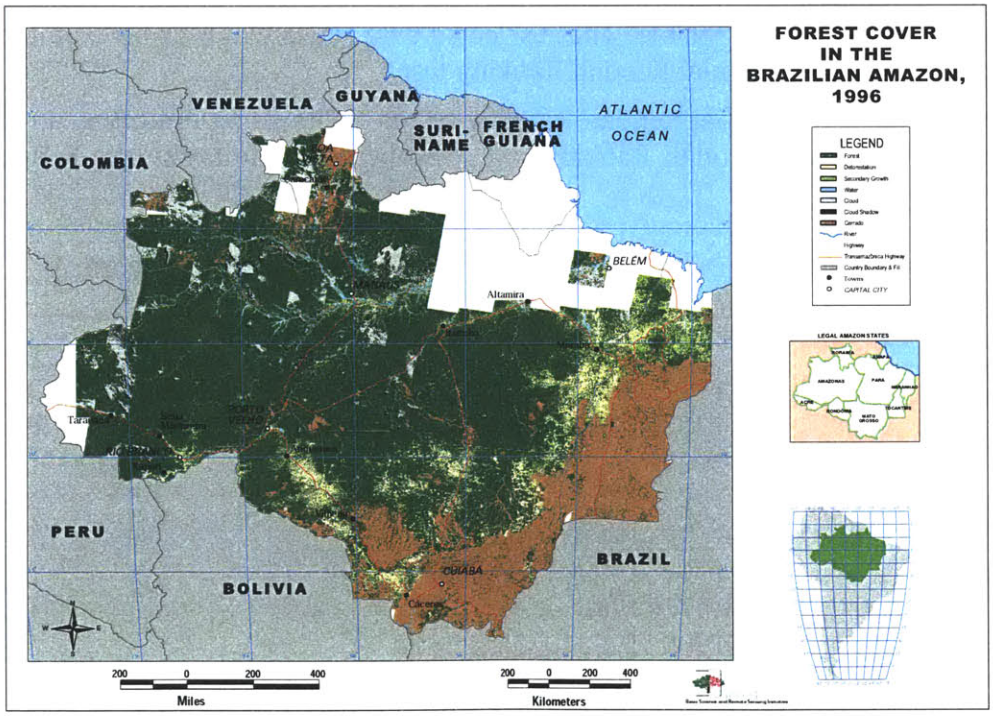

Figure 9-2: TRFIC Deforestation Maps (http://bsrsi.msu.edu/trfic) for **(a)** 1986 and **(b)** 1996.

9.1 Precipitation Record at Porto Velho: Data and Analysis

The raingauge record at Porto Velho (station #30382825000), which is located on the Solimões (or Madeira) river in the north of Rondônia, is from the Global Historical Climatology Network (GHCN) (Eischeid *et al.* [1991], Easterling *et al.* [1996], Vose *et al.* [1992]). GHCN comprises surface monthly measurements of surface temperature, surface pressure, sea level pressure and precipitation from a collection of 20,000 stations around the world. The record at Porto Velho was selected as it is the only long term record available in the Amazon basin; it's monthly record goes as far back as 1928. The raw data time series of monthly precipitation accumulations is plotted in panel (a) of Figure 9-3, while the gap-filled record (using climatological values to fill in missing data months) is presented in panel (b). The monthly climatology of monthly precipitation accumulations is plotted in panel (c), and shows the dramatic difference in rainfall accumulations between the wet and dry seasons (i. e., from over 300 mm per month during the wet season, to less than 50 mm per month during the dry season).

Most gaps in the Porto Velho raingauge record occur in the latter third of the record. Moreover, as is attested to in Table 9.1, some months are particularly affected by missing data. The four months that have the least amount of missing data are March, April, July and August. The time-series of rainfall accumulations for these months are plotted in panels (b) & (c) of Figure 9-4, along with the total annual accumulation in panel (a) (from the gap-filled record). Trends from these time-series are not clearly visible. These selected data series will thus be examined using an Extended Sequential Kendall Ranking test.

The Extended Sequential Kendall Ranking test is, as its name indicates, an extension to the normal Kendall Ranking test. It proceeds as follows: the Kendall

Table 9.1: Missing Data Months from Porto Velho Raingauge Record.

Month	Missing Years
January	1937; 1938; 1956; 1981; 1988; 1992; 1993; 1994; 1995; 1999; 2003
February	1929; 1981; 1988; 1992; 1993; 1994; 1995; 1997; 1998; 1999; 2003
March	1988; 1997; 2001
April	1971; 1988; 1997; 2001
May	1988; 1993; 1997; 1998; 2002
June	1929; 1971; 1982; 1993; 1994; 1995; 1999
July	1929; 1953; 1971; 1982
August	1971; 1982; 1989; 1993
September	1982; 1987; 1992; 1993; 1995; 1997
October	1970; 1981; 1982; 1983; 1987; 1992; 1993; 1995
November	1982; 1987; 1992; 1993; 1994; 1995
December	1957; 1982; 1987; 1992; 1993; 1994; 1995

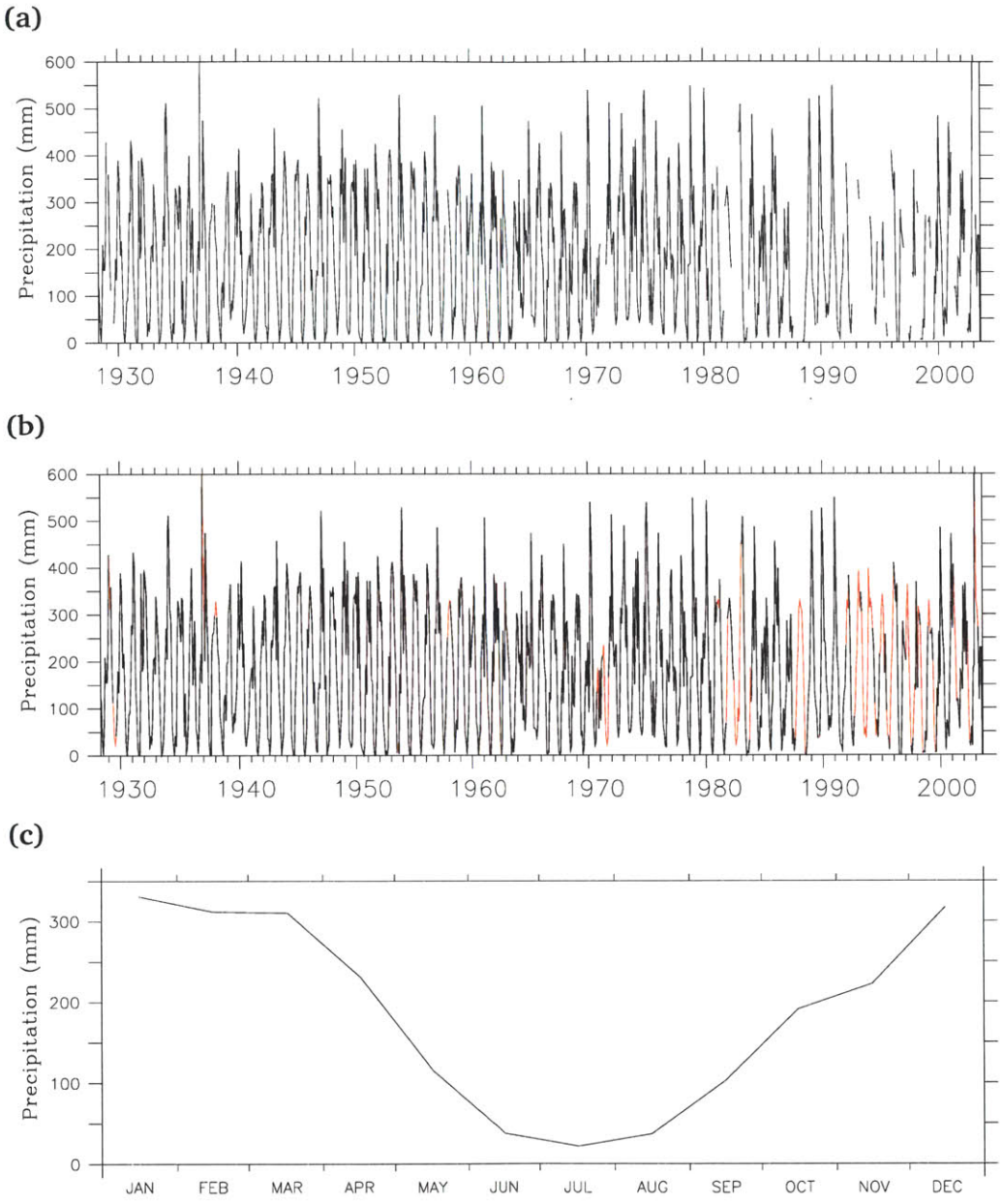

Figure 9-3: Monthly Raingauge Accumulations at Porto Velho; **(a)** Raw Record, **(b)** Merged Record and **(c)** Seasonal Cycle.

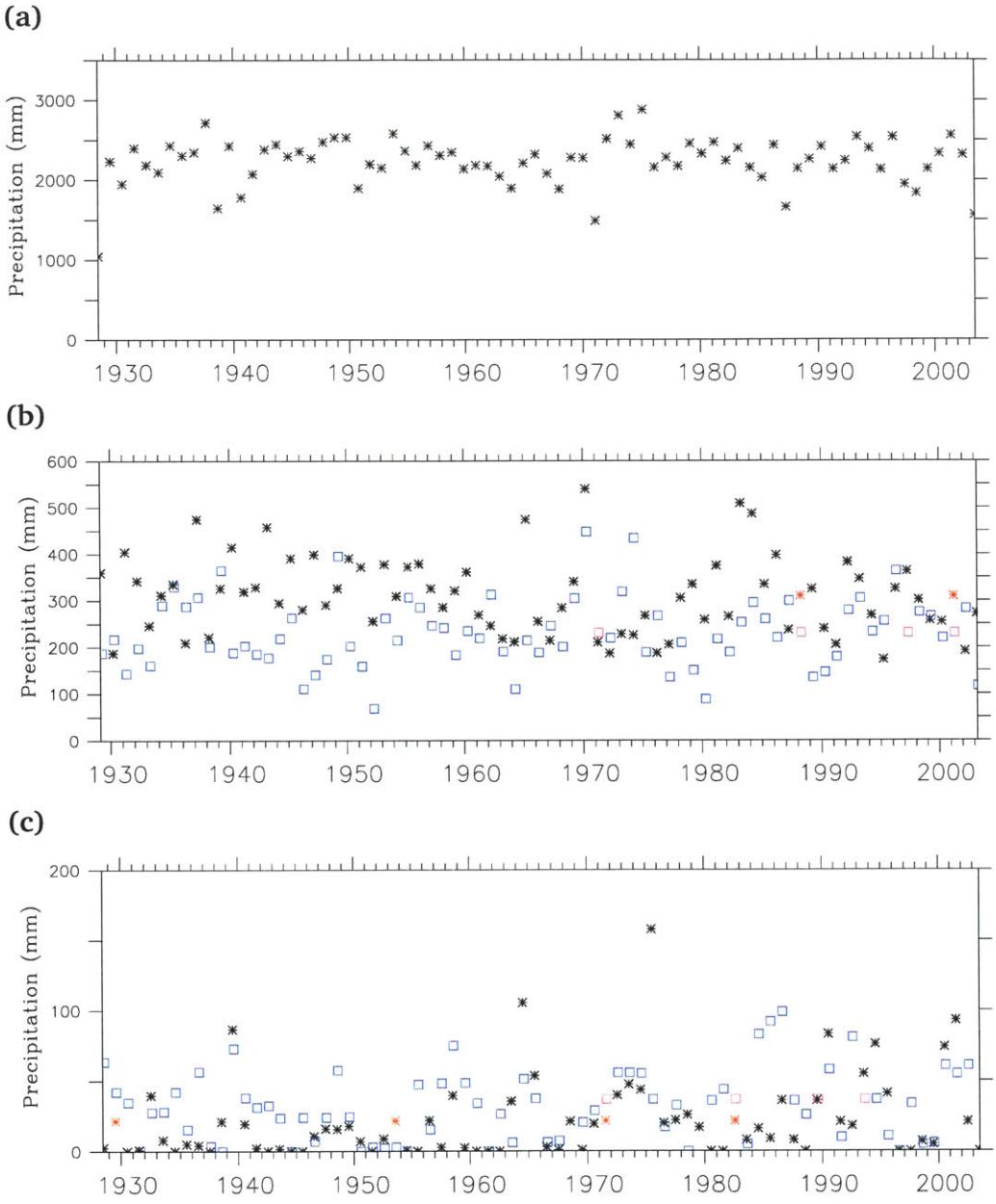

Figure 9-4: Rainfall Accumulations at Porto Velho; **(a)** Annual accumulations from gap-filled record, **(b)** March (stars) and April (boxes) accumulations **(c)** July (stars) and August (boxes) accumulations. red stars and pink boxes denote missing data months that have been filled with climatological values.

ranking test is applied sequentially to each point on record, starting from the beginning of the record, and ending some pre-determined length before the end. It is a forward looking test only, since records that are located before the starting point are dropped from the analysis with each sequential increment. The result of the test is a significance level associated with an increasing or decreasing trend. As in the original Kendall test, the significance level takes the number of data points into account, which makes an inter-year comparison possible. The results from the Extended Sequential Kendall Ranking test are plotted in Figure 9-5.

The Extended Sequential Kendall Ranking test detects a significant decreasing trend in the rainfall accumulations for the month of March that is detectable for records starting in the years 1930 to 1945, and again from 1978 to 1983. The trends detected for the months of July and August are increasing for records starting with years 1930 to 1950. The significance of the increasing trend is weaker for July than it is for August. These results indicate that rainfall accumulations have decreased significantly at the end of the wet season, while they have significantly increased at the end of the dry season.

9.2 Discussion & Conclusion

Even though the GHCN project has rigorous quality control procedure, the results from the above analysis must be understood in the context that they are derived from one raingauge, and as such represent trends in rainfall at one point. The results do not, and should not be generalized to describe areal rainfall totals in Rondônia. Historically, Porto Velho was founded around 1907 and officially named Porto Velho in October 1914. It was originally a way point along the railway that connected the rubber plantations of Bolivia to the Atlantic for trade with Europe and the United States (the railway was completed in 1912.) The population of Porto Velho now stands at 300,000 inhabitants, with most of the growth occurring around the end of the seventies and during the eighties when the Brazilian government decided to open lands to agriculture. The rainfall trends could thus be attributable to nothing more than urbanization. Due to the absence of corroborating evidence from other raingauges, a conjectural treatment of the significant trends in rainfall accumulations follows.

In the context of the results found in previous chapters, it could be stipulated that the increase in late dry season rainfall is a direct consequence of deforestation. Indeed, shallow clouds were greatly enhanced over deforested regions, especially toward the end of the dry season and during the pre-monsoon. If the significant increase in marginal area rainfall occurrence detected in Chapter 7 is assumed to be related to the shallow cloud enhancement, then it is plausible to stipulate that the increase in rainfall accumulation detected for the month of August in the Porto Velho raingauge record is directly related to deforestation. This hypothesis would gain in credibility if similar increasing trends were found for the months of Septem-

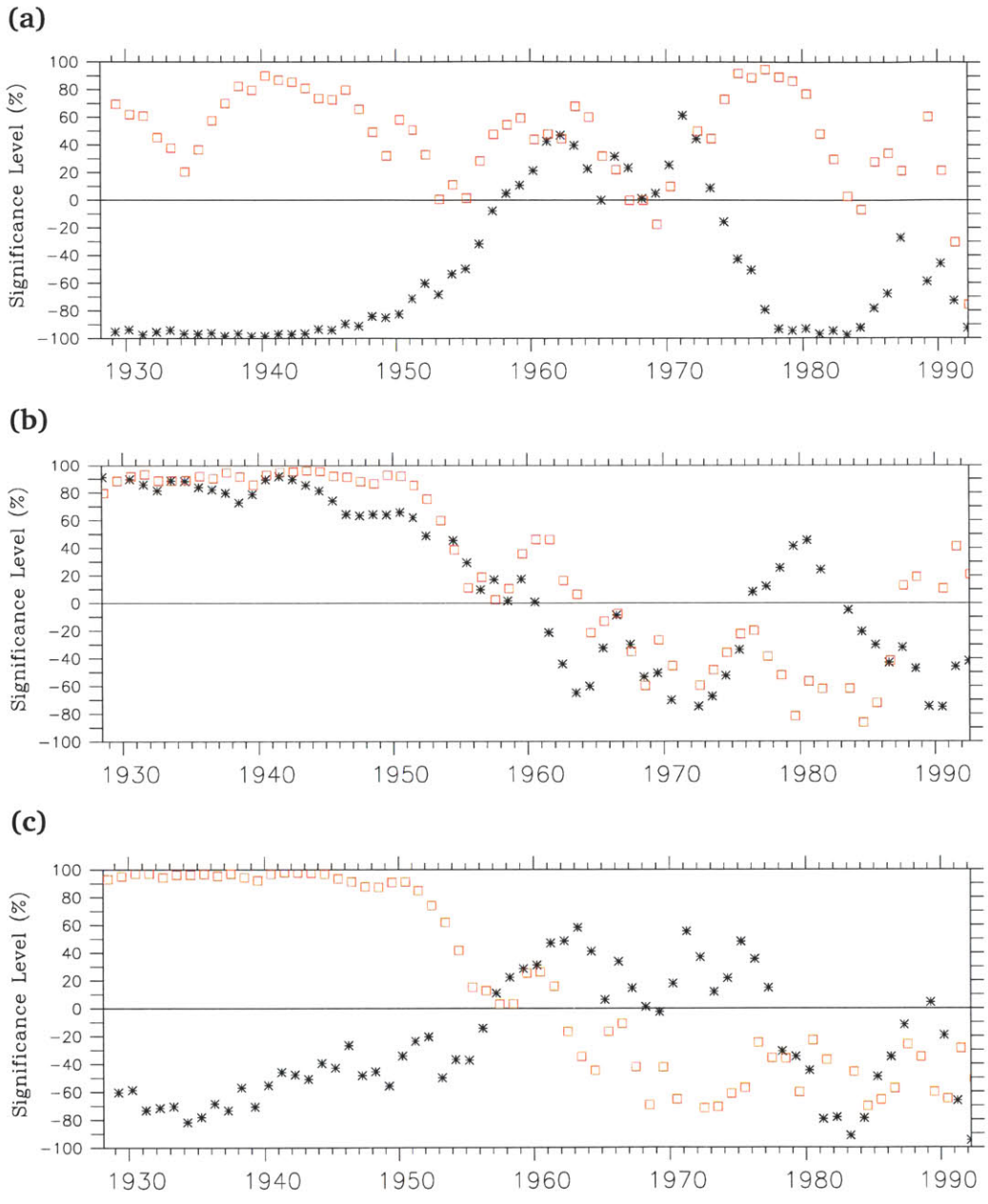

Figure 9-5: Extended Sequential Kendall Ranking Test (ESKRT) for Porto Velho; **(a)** ESKRT for March (stars) and April (boxes); **(b)** ESKRT for July (stars) and August (boxes); **(c)** ESKRT for March & April (stars) and July & August (boxes). Positive significance levels denote the level of significance of an increasing trend, while negative significance levels denote the level of significance for decreasing trends.

ber, October and November. The decreasing trend in March rainfall is harder to relate to deforestation. It certainly does no sit well with the increasing OLR trends found by Chu *et al.* [1994], DeLiberty [2000] and Chen *et al.* [2002]. Both results taken together (decrease in late wet season rainfall and increase in late dry season rainfall) could be a sign of a shift in seasonality, and perhaps a symptom of a larger-scale long term variation.

REFERENCES

CHEN, J., B. E. CARLSON and A. D. DEL GENIO. Evidence for Strengthening of the Tropical General Circulation in the 1990s. *Science*, 295(5556):pages 838–841 [2002].

CHU, P.-S., Z.-P. YU and S. HASTENRATH. Detecting Climate Change Concurrent with Deforestation in the Amazon Basin: Which Way Has it Gone? *Bulletin of the American Meteorological Society*, 75(4):pages 579–583 [1994].

DELIBERTY, T. L. A Regional Scale Investigation of Climatological Tropical Convection and Precipitation in the Amazon Basin. *Professional Geographer*, 52(2):pages 258–271 [2000].

EASTERLING, D. R., T. C. PETERSON and T. R. KARL. On the development and use of homogenized climate data sets. *Journal of Climate*, 9(6):pages 1429–1434 [1996].

EISCHEID, J. K., H. F. DIAZ, R. S. BRADLEY and P. D. JONES. A comprehensive precipitation dataset for global land areas. Tech. Rep. DOE/ER-6901T-H1, Carbon Dioxide Research Division, U.S. Department of Energy, Washington, D.C. [1991].

GENTRY, A. H. and J. LOPEZ-PARODI. Deforestation and Increased Flooding of the Upper Amazon. *Science*, 210(4476):pages 1354–1356 [1980].

MARENGO, J. A. Variations and Change in South American Streamflow. *Climatic Change*, 31:pages 99–117 [1995].

NORDIN, C. F. and R. H. MEADE. Deforestation and Increased Flooding of the Upper Amazon (Comments). *Science*, 215(4531):pages 426–427 [1982].

RICHEY, J. E., C. A. NOBRE and C. DESER. Amazon River Discharge and Climate Variability: 1903 to 1985. *Science*, 246(4926):pages 101–103 [1989].

SALATI, E. and P. B. VOSE. Amazon Basin: A System in Equilibrium. *Science*, 225(4658):pages 129–138 [1984].

STERNBERG, H. O. Aggravation of Floods in the Amazon River as a Consequence of Deforestation? *Geografiska Annaler. Series A, Physical Geography*, 69(1):pages 201–219 [1987].

VOSE, R. S., R. L. SCMOYER, P. M. STEURER, T. C. PETERSON, R. HEIM, T. R. KARL and J. EISCHEID. The Global Historical Climatology Network: long-term monthly temperature, precipitation, sea level pressure, and station pressure data. Tech. Rep. ORNL/CDIAC-53, NDP-041, Carbon Dioxide Information Analysis Center, Oak Ridge National Laboratory, Oak Ridge, Tenessee [1992].

CHAPTER 10

CONCLUSIONS

The earth's climate exhibits variability at many temporal (diurnal, seasonal, inter-annual, decadal, etc.) and spatial scales (local, regional, continental, global). The interest of the scientific community has been to describe this climatic variability, and to determine the part of climatic variability that arises as a result of anthropogenic activity. One of the key science objectives posed in Entekhabi *et al.* [1999] is to determine methods to differentiate human-induced effects on the hydrological cycle from those resulting from natural climate variability. This thesis' objective was to quantitatively assess the impacts of current deforestation on the hydrological climate of the Amazon basin, which is certainly one of the most notorious examples of anthropogenic modification of the natural environment.

In order to achieve that objective, this thesis has examined the spatial patterns of shallow cumulus clouds, cold clouds and rainfall in relation to the patterns of observed deforestation over the Amazon basin. In summarizing the results about shallow clouds, it was concluded that deforestation has induced significant shifts in such climatological patterns. Shallow cumulus clouds are significantly enhanced over deforested areas at all times of day. The result was also tested against synoptic atmospheric conditions, and while the enhancement shows some sensitivity to winds (magnitude, direction and shear) and antecedent precipitation, the enhancement was robust enough to appear under most circumstances. An analysis of the shallow clouds over smaller sub-domains revealed that the shallow cloud enhancement was robust with regards to the range of disturbance scales observed in the Amazon. It was found that there are more cold clouds over forested areas at 14h45 UTC and 20h45 UTC. Upon examination of the patterns of cold clouds over a patch of savannah in northern Rondônia, it was found that cold clouds form preferentially over the savannah clearing at 17h45 UTC (13h45 LT). In general, the patterns of cold clouds were found to be more strongly associated with topographical features. Finally, the results on rainfall patterns, records from the Precipitation Radar on board the TRMM satellite revealed that there was a significant

increase in rainfall occurrences over the transition zone that separates deforested from forested areas. It was also shown that there were significantly less rainfall events over intensely deforested areas. The spatial patterns of rainfall occurrences were also shown to be modulated by topographical features, although these modulations were shown to be separate from those originating from the land surface contrasts. An analysis of a long-term record of monthly precipitation accumulations at Porto Velho (Rondônia, Brazil) pointed to a significant decrease in rainfall occurrences during the late monsoon season since 1945, and to a significant increase in rainfall accumulation at the end of the dry season (August) over the same time period. No definitive conclusions about the role of deforestation in these trends were drawn. There is however a conspicuous synchrony between the long term changes in rainfall accumulations and deforestation in the Amazon basin.

The enhancement of shallow clouds has potentially important ramifications. Indeed, due to their high variability, extent (at any time, about two-thirds of the earth is covered by clouds) and pronounced optical characteristics, clouds plays a dominant role in the earth's radiation balance and hence in global climate [Minnis and Harrison, 1984; Rossow *et al.*, 1989; Rossow and Garder, 1993]. Rossow and Garder [1993] add that the exchange of radiation (solar and terrestrial) at the top of the atmosphere, which is critically modulated by clouds, "establish[es] the fundamental constraint on climate." Clouds are all the more important due to their active role in the transport and exchange of water. Moreover, the clouds studied in this thesis occur in the tropics — a latitudinal band that exports moisture and energy poleward — and are thus all the more significant on the global system. Thus, beyond the simple change in shallow cloud patterns that was reported in this thesis, the shallow and cold cloud results may be related to large-scale changes in the equatorial radiation and moisture budgets that have recently been observed (e. g., Chen *et al.* [2002], Wielicki *et al.* [2002]). Further study of the implications of the observed shifts in the patterns of shallow and cold clouds is necessary in order to fully understand their impact of the local and regional radiation balance.

Understanding how the climatic shifts in regional cloud cover affect the global climate is certainly an interesting future avenue of research, albeit non-trivial. Indeed, the predominant uncertainty in accurately describing the earth's climate lies in cloud-radiative feedbacks [Rossow *et al.*, 1989]. The complexity of the nature of interactions of clouds with radiation is at the root of this uncertainty. Some of the properties that are responsible for this complexity are enumerated by Rossow *et al.* [1989] as: *(i)* cloud microphysical properties (e. g., particle size, shape, orientation, phase and number diversity); *(ii)* cloud macrophysical properties (e. g., cloud cover, optical thickness, cloud top temperature, morphology and geometrical extent); *(iii)* cloud context (i. e., surface albedo, atmospheric temperature profile, aerosol size distribution and concentration); and *(iv)* variability (e. g., temporal and spatial variability, geometry relative to solar irradiance). The state-of-the-art knowledge is still not sufficient to tackle these problems. While comparing the data showing spuriously high absorption of solar radiation by clouds with models, Cess *et al.* [1995] highlighted the shortcomings in the knowledge of the scientific com-

munity in the affairs of cloud radiative transfer processes. Their emphasis was on the role of particles in absorption properties, and in the heterogeneous nature of the spatial distribution of particles in the atmosphere. Nonetheless, many studies have attempted and been able to describe the integrated effect of cloud-radiative interactions. For example, Wang *et al.* [2002] examined the impact of clouds on outgoing longwave radiation (OLR) in the tropics between 1985 and 1998 using satellite-derived cloud vertical distributions and radiation parameters. They found a drying in the upper troposphere as indicated by a decrease in cloud frequency at that level. Coinciding with this was an increase in cloud frequency in the lower troposphere, and they hypothesized that the change arose from an increase in the intensity of the large-scale circulation. It remains to be seen whether the long-term changes in cloudiness that were observed in this thesis are capable of promoting large-scale changes in the Earth's radiative budget and thus it's climate.

The results presented in this thesis show that current Amazonian deforestation gives rise to significant and persistent mesoscale circulations, which are known to enhance the transport of moisture from the land into the boundary-layer (e. g., Anthes [1984]). The interaction of these mesoscale circulations with the rain-suppressing aerosols from biomass burning [Koren *et al.*, 2004] during the dry season (JJA) poses another interesting problem. While the particles released by the burning of forest stands tends to suppress rainfall, the results presented herein indicate that the surface thermal inhomogeneities created by the change in land surface properties act to enhance rainfall occurrences. There is a caveat, in that a clear suppression of rainfall occurrences were found to occur over intensely deforested areas. Hence, if biomass burning is practised more frequently in areas of intense deforestation, rather than in the transition zones that separate forested from deforested areas, then the suppressed rainfall could be a product of the aerosols and not a result of atmospheric subsidence. The complexities of the system under study render definitive conclusions impossible until the interactions between the various components of the system are further understood. Indeed, there is still a profound lack of knowledge regarding even the simple unidirectional impact of aerosols on climate; their potential importance is however not missed, and hypotheses are not lacking. Andreae *et al.* [2004] argued the potential global implications of biomass burning smoke through their effect on clouds and rainfall; it could be that the enhancement of shallow clouds found here actually serves to moisten the atmospheric boundary-layer and further invigorate the the convective towers of the Amazon. It could conversely be hypothesized that the increase in precipitation occurrences reported in this thesis may potentially cancel the effect of biomass burning aerosols on the deep convective towers that are characteristics of the tropical South-American continent.

Finally, the impacts of the local changes in cloud cover and rainfall occurrence may direct the brunt of their weight on the local ecosystem dynamics. There is an intimate relationship between the make-up of ecosystems and the climate in which they thrive. Notwithstanding the direct alteration of the ecosystems by the mere act of deforestation, shifts in available radiation and precipitation may lead to changes

in the ecosystems' intensive properties (e. g., relative proportion of species), and may even lead to dramatic changes in the ecosystems' extensive properties (e. g., total biomass, localized species extinction). Such changes have already been reported by Laurance *et al.* [1998, 2004], who report the gradual change in the composition of Amazon forest stands toward early-successional and fire-adapted tree species, and who suggest there are edge effects that decrease the above-ground biomass in tree stands that neighbor deforested patches. It is unknown whether these observed changes are direct impacts of the changes in cloudiness and rainfall, or whether these changes are stable or a symptom of a wider ecosystem transition.

The full implications of deforestation in the Amazon require a systems-based approach that includes biological and physical processes across a wide range of spatial and temporal scales. The results reported in this thesis will certainly aid in such an endeavor, although they represent a small aspect of this very complex and intriguing system. Nonetheless, the results presented in this thesis bear important news: climate in the Amazon has already been subjected to a persistent shift that is caused by deforestation. These results refute the hitherto conventional wisdom about the effects of present Amazonian deforestation; they are a clear indication of the tremendous sensitivity of the hydrological climate to human disturbances.

REFERENCES

ANDREAE, M. O., D. ROSENFELD, P. ARTAXO, A. A. COSTA, G. P. FRANK, K. M. LONGO and M. A. F. SILVA-DIAS. Smoking Rain Clouds over the Amazon. *Science*, 303:pages 1337–1342 [2004].

ANTHES, R. A. Enhancement of Convective Precipitation by Mesoscale Variations in Vegetative Covering in Semiarid Regions. *Journal of Climate and Applied Meteorology*, 23(4):pages 541–554 [1984].

CESS, R. D., M. H. ZHANG, P. MINNIS, L. CORSETTI, E. G. DUTTON, B. W. FORGAN, D. P. GARBER, W. L. GATES, J. J. HACK, E. F. HARRISON, X. JING, J. T. KIEHL, C. N. LONG, J.-J. MORCRETTE, G. L. POTTER, V. RAMANATHAN, B. SUBASILAR, C. H. WHITLOCK, D. F. YOUNG and Y. ZHOU. Absorption of Solar Radiation by Clouds: Observations verus Models. *Science*, 267(5197):pages 496–499 [1995].

CHEN, J., B. E. CARLSON and A. D. DEL GENIO. Evidence for Strengthening of the Tropical General Circulation in the 1990s. *Science*, 295(5556):pages 838–841 [2002].

ENTEKHABI, D., G. R. ASRAR, A. K. BETTS, K. J. BEVEN, R. L. BRAS, C. J. DUFFY, T. DUNNE, R. D. KOSTER, D. P. LETTENMAIER, D. B. MCLAUGHLIN, W. J. SHUTTLEWORTH, M. T. VAN GENUCHTEN, M.-Y. WEI and E. F. WOOD. An Agenda for Land Surface Hydrology Research and a Call for the Second International Hydrological Decade. *Bulletin of the American Meteorological Society*, 80(10):pages 2043–2058 [1999].

KOREN, I., Y. J. KAUFMAN, L. A. REMER and J. V. MARTINS. Measurement of the Effect of Amazon Smoke on Inhibition of Cloud Formation. *Science*, 303:pages 1342–1345 [2004].

LAURANCE, W. F., S. G. LAURANCE and P. DELAMONICA. Tropical Forest Fragmentation and Greenhouse Gas Emissions. *Forest Ecology and Management*, 110:pages 173–180 [1998].

LAURANCE, W. F., A. A. OLIVEIRA, S. G. LAURANCE, R. CONDIT, H. E. M. NASCIMENTO, A. C. SANCHEZ-THORIN, T. E. LOVEJOY, A. ANDRADE, S. D'ANGELO, J. E. RIBEIRO and C. W. DICK. Pervasive alteration of tree communities in the undisturbed Amazonian forests. *Nature*, 428:pages 171–175 [2004].

MINNIS, P. and E. F. HARRISON. Diurnal Variability of Regional Cloud and Clear-Sky Radiative Parameters Derived from GOES Data. Part I: Analysis Method. *Journal of Climate and Applied Meteorology*, 23(7):pages 993–1011 [1984].

ROSSOW, W. B. and L. C. GARDER. Cloud Detection Using Satellite Measurements of Infrared and Visible Radiances for ISCCP. *Journal of Climate*, 6(12):pages 2341–2369 [1993].

ROSSOW, W. B., L. C. GARDER and A. A. LACIS. Global, Seasonal Cloud Variations from Satellite Radiance MEasurements. Part I: Sensitivity of Analysis. *Journal of Climate*, 2(5):pages 419–458 [1989].

WANG, P.-H., P. MINNIS, B. A. WIELICKI, T. WONG and L. B. VANN. Satellite Observations of Long-Term Chagnes in Tropical Cloud and Outgoing Longwave Radiation from 1985 to 1998. *Geophysical Research Letters*, 29(10):page 10.1029/2001GL014,264 [2002].

WIELICKI, B. A., T. WONG, R. P. ALLAN, A. SLINGO, J. T. KIEHL, B. J. SODEN, C. T. GORDON, A. J. MILLER, S.-K. YANG, D. A. RANDALL, F. ROBERTSON, J. SUSSKIND and H. JACOBOWITZ. Evidence for Large Decadal Variability in the Tropical Mean Radiative Energy Budget. *Science*, 295(5556):pages 841–844 [2002].

APPENDIX A

SUPPLEMENTARY CLOUD RESULTS

A.1 Long-Term Shallow Cloud Climatology Maps

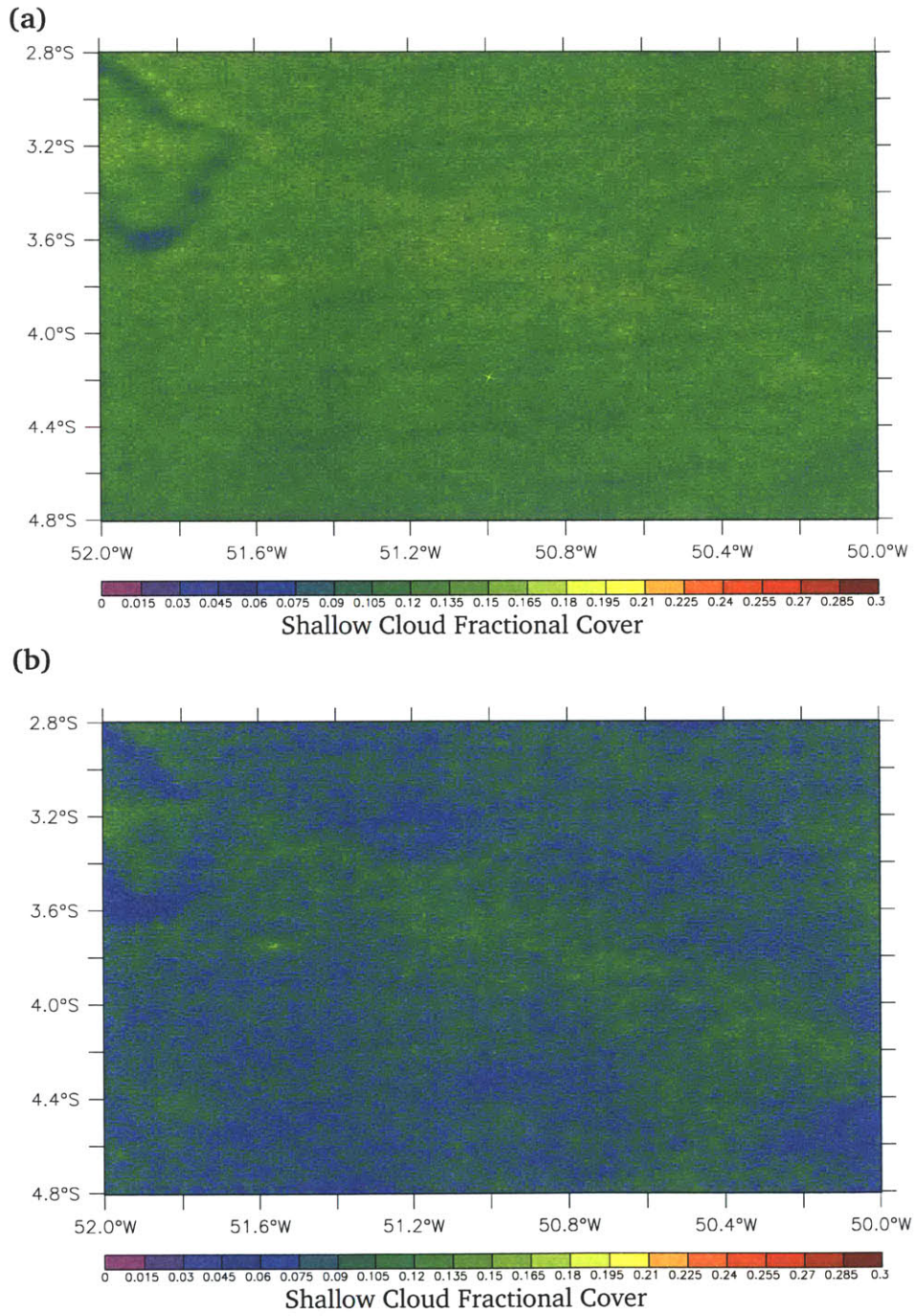

Figure A-1: Long-Term Mean Shallow Cloud Cover; Average Fractional Cover of Shallow Clouds over Marabá-Altamira at **(a)** 14h45 UTC and **(b)** 17h45 UTC.

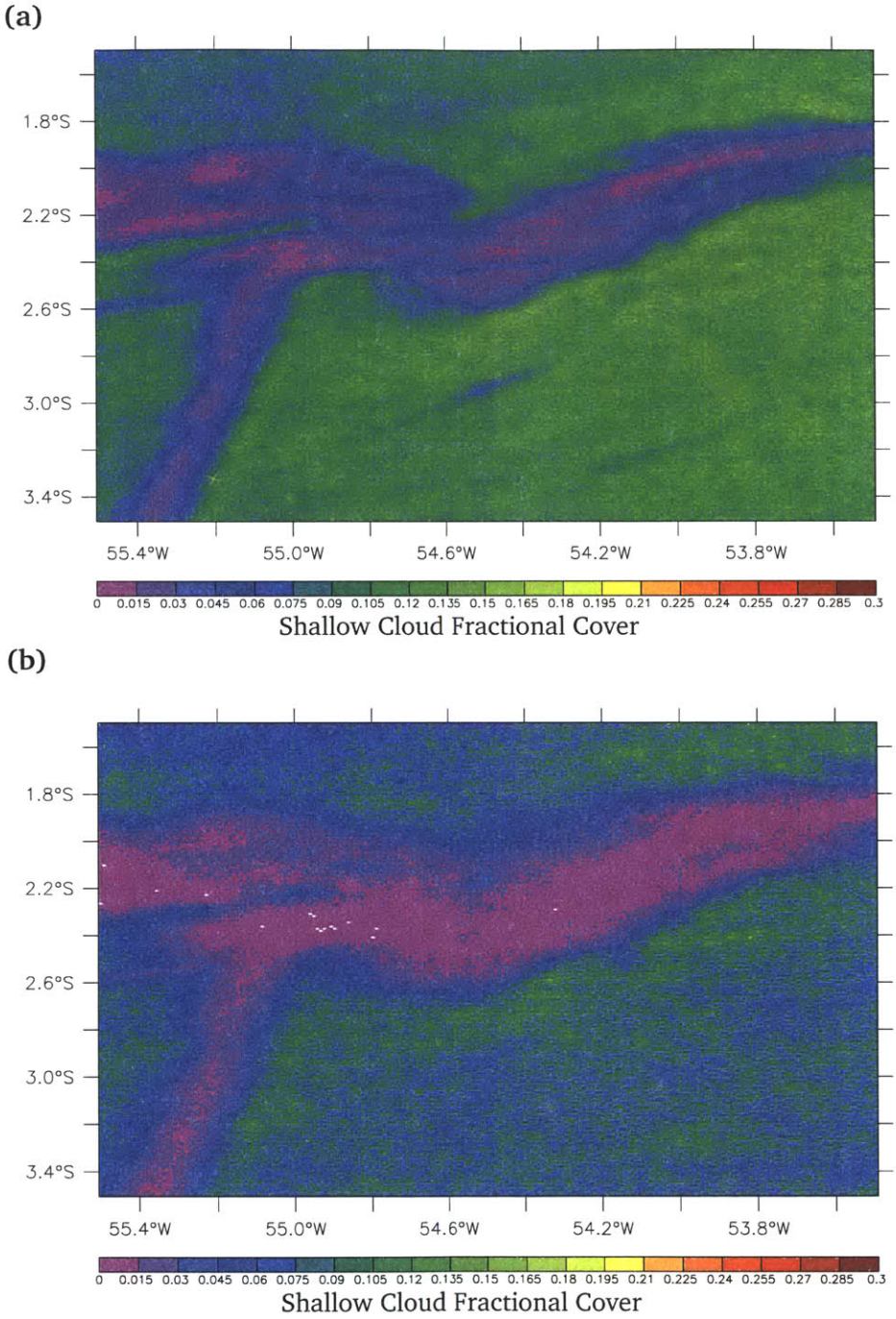

Figure A-2: Long-Term Mean Shallow Cloud Cover; Average Fractional Cover of Shallow Clouds over Tapajós-Santarém at **(a)** 14h45 UTC and **(b)** 17h45 UTC.

A.2 Seasonal Shallow Cloud Climatology Maps

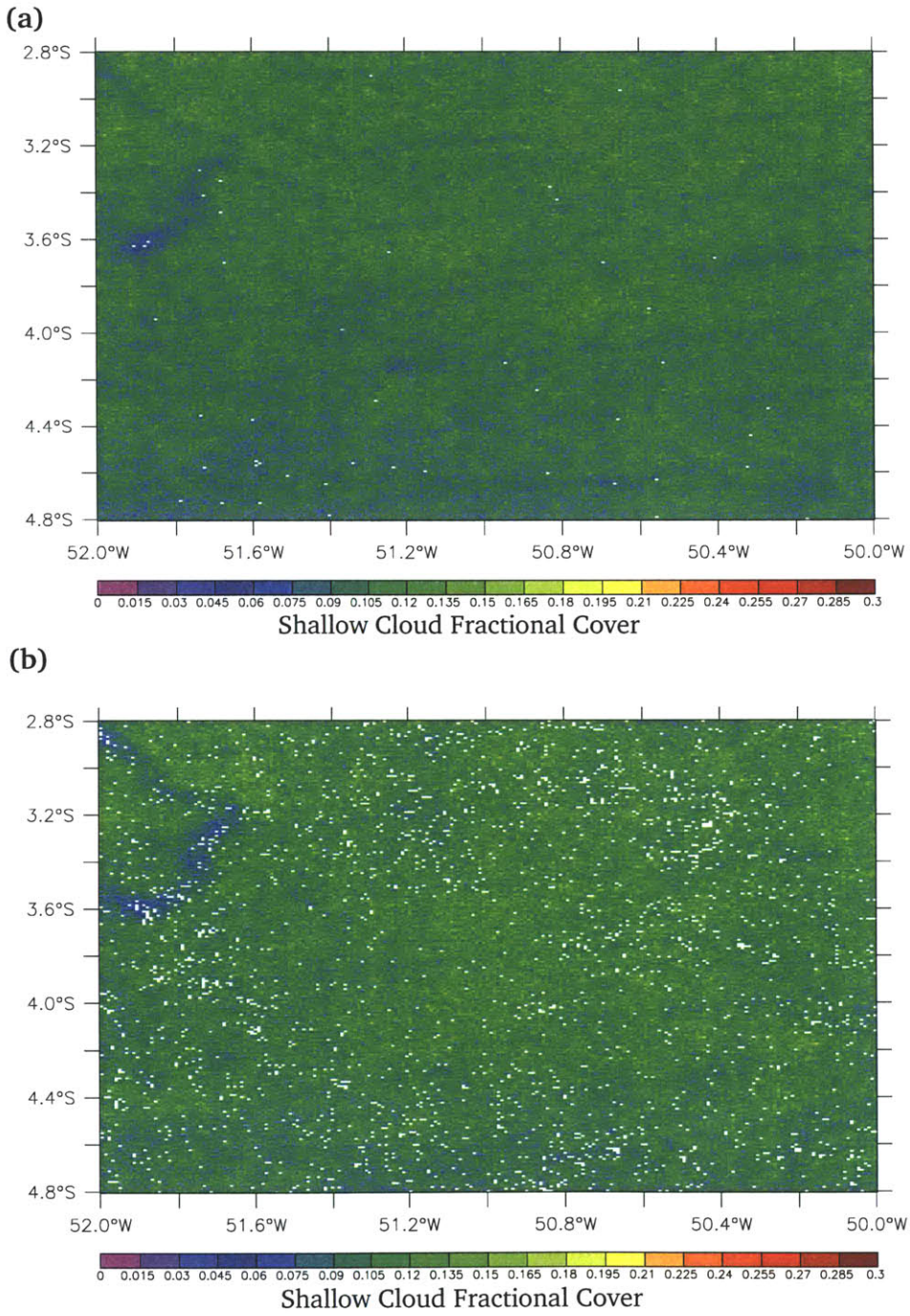

Figure A-3: Seasonal Mean Shallow Cloud Cover; Average Fractional Cover of Shallow Clouds over Marabá-Altamira at 14h45 UTC during **(a)** DJF and **(b)** MAM.

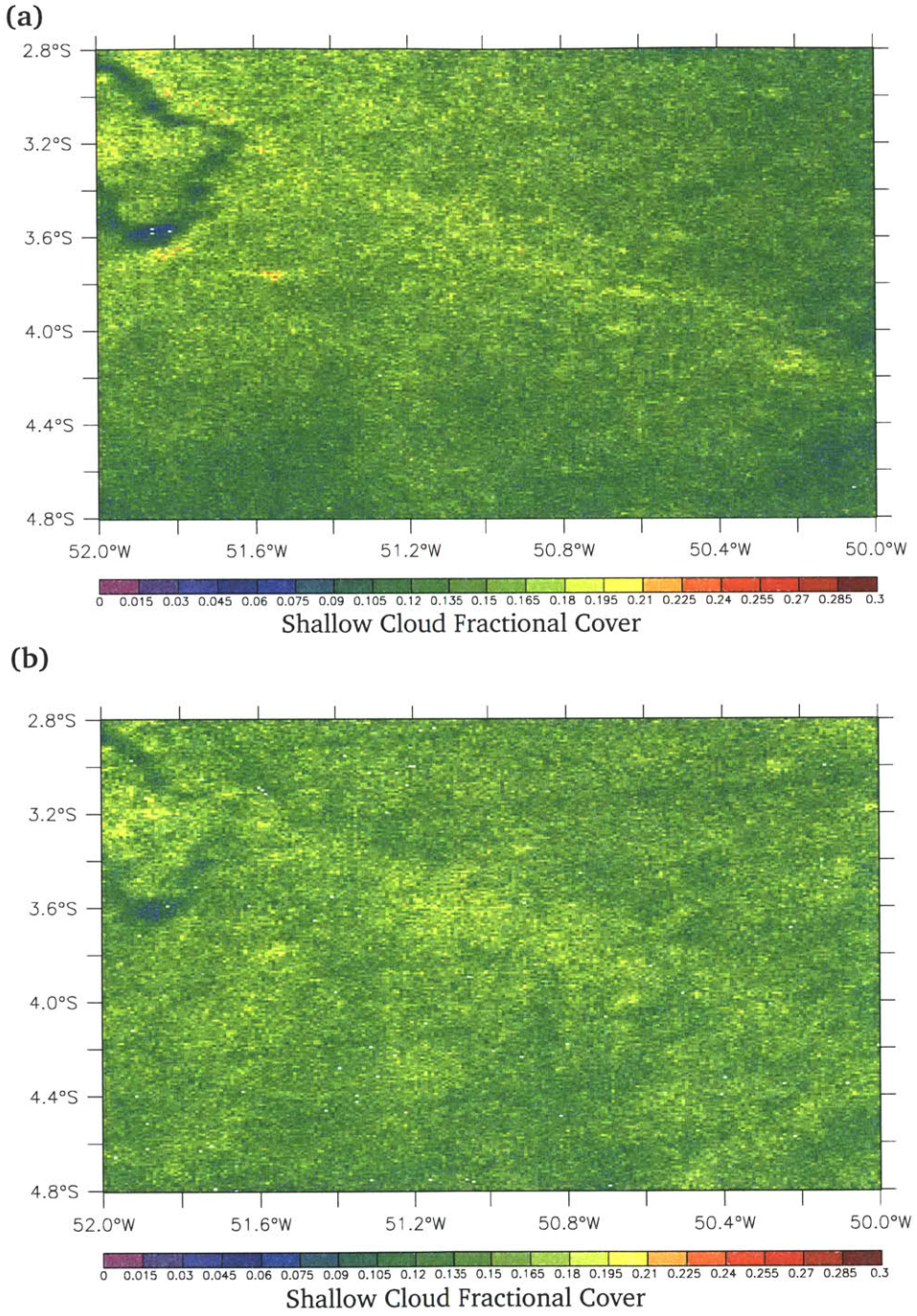

Figure A-4: Seasonal Mean Shallow Cloud Cover; Average Fractional Cover of Shallow Clouds over Marabá-Altamira at 14h45 UTC during **(a)** JJA and **(b)** SON.

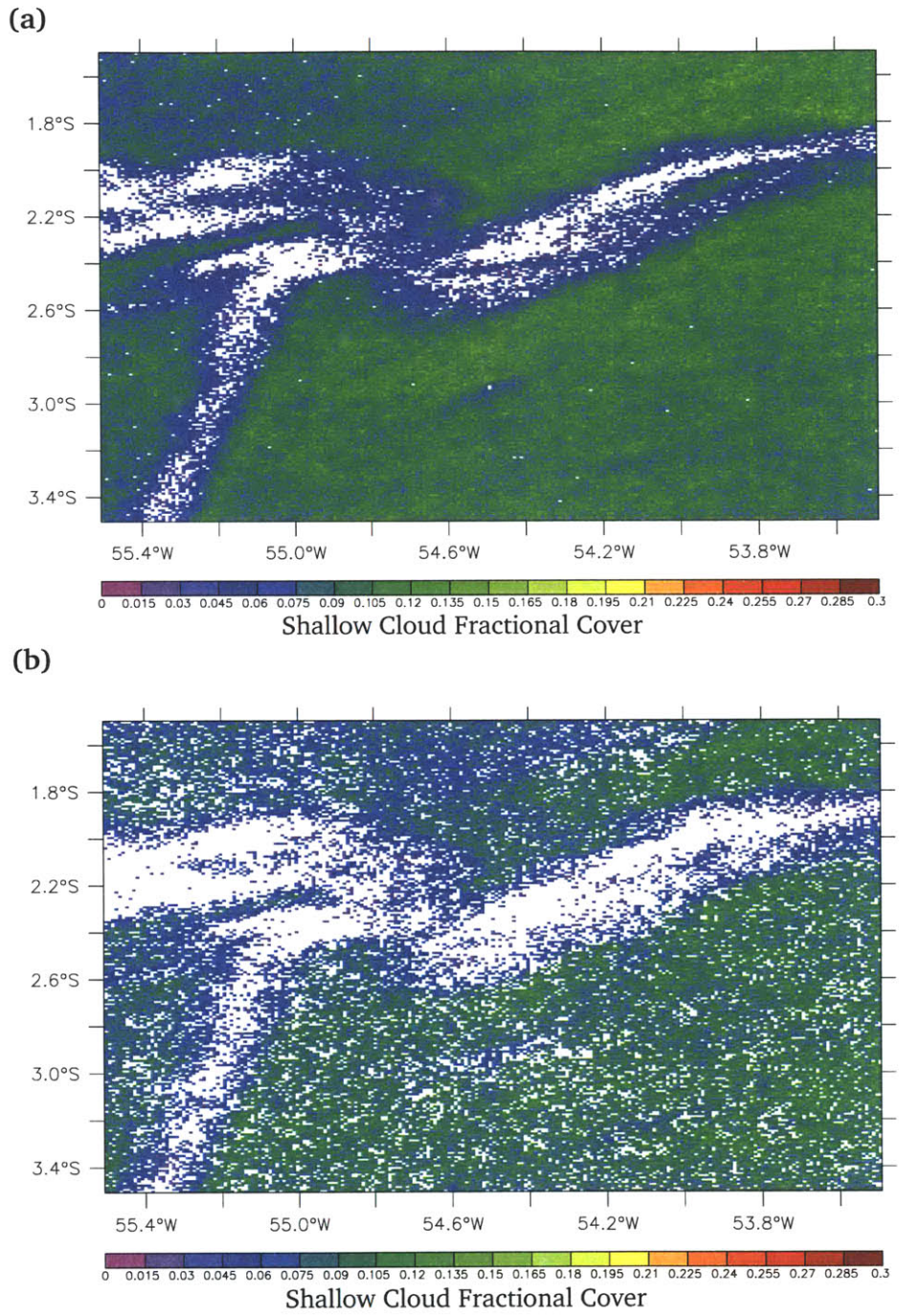

Figure A-5: Seasonal Mean Shallow Cloud Cover; Average Fractional Cover of Shallow Clouds over Tapajós-Santarém at 14h45 UTC during **(a)** DJF and **(b)** MAM.

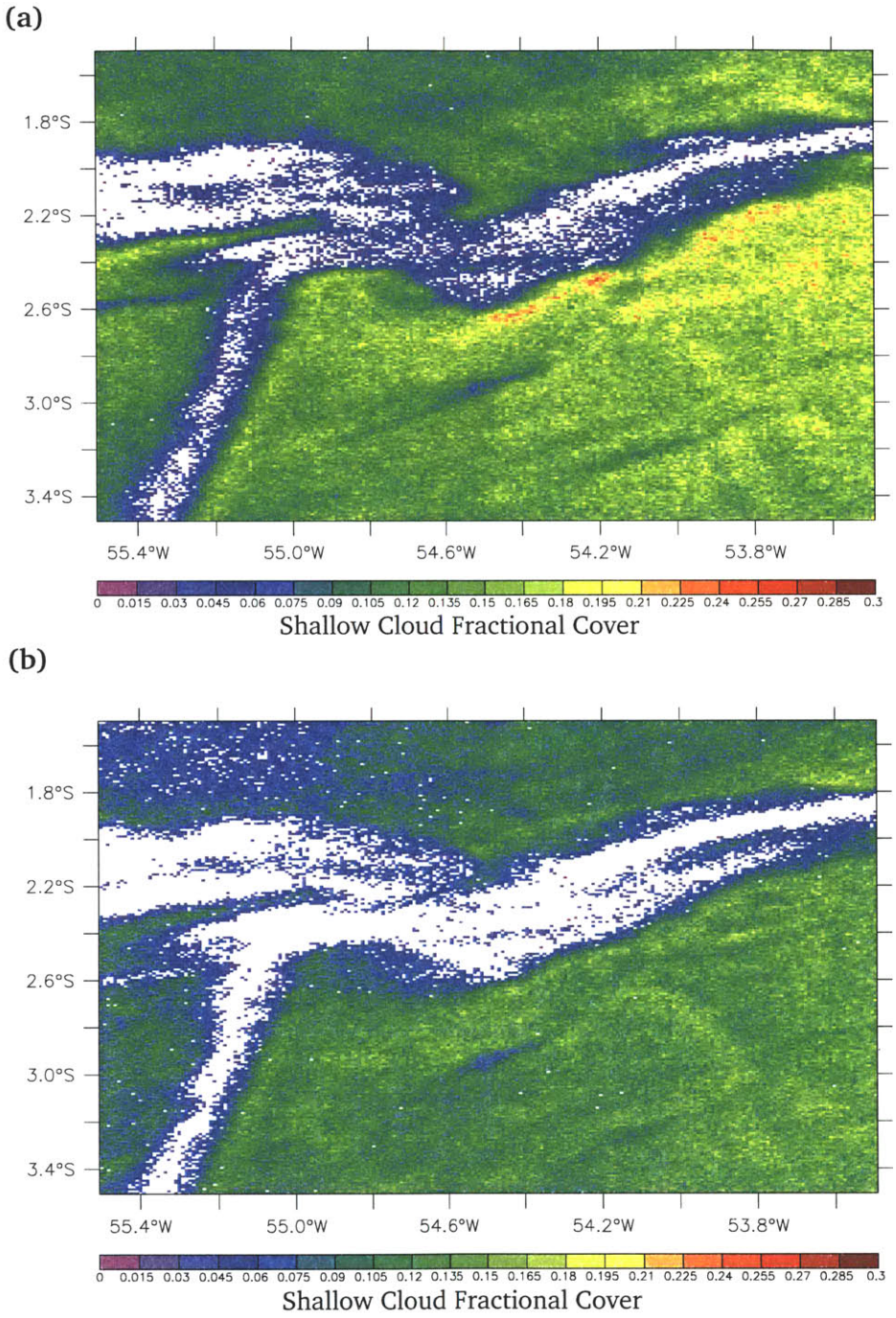

Figure A-6: Seasonal Mean Shallow Cloud Cover; Average Fractional Cover of Shallow Clouds over Tapajós-Santarém at 14h45 UTC during **(a)** JJA and **(b)** SON.

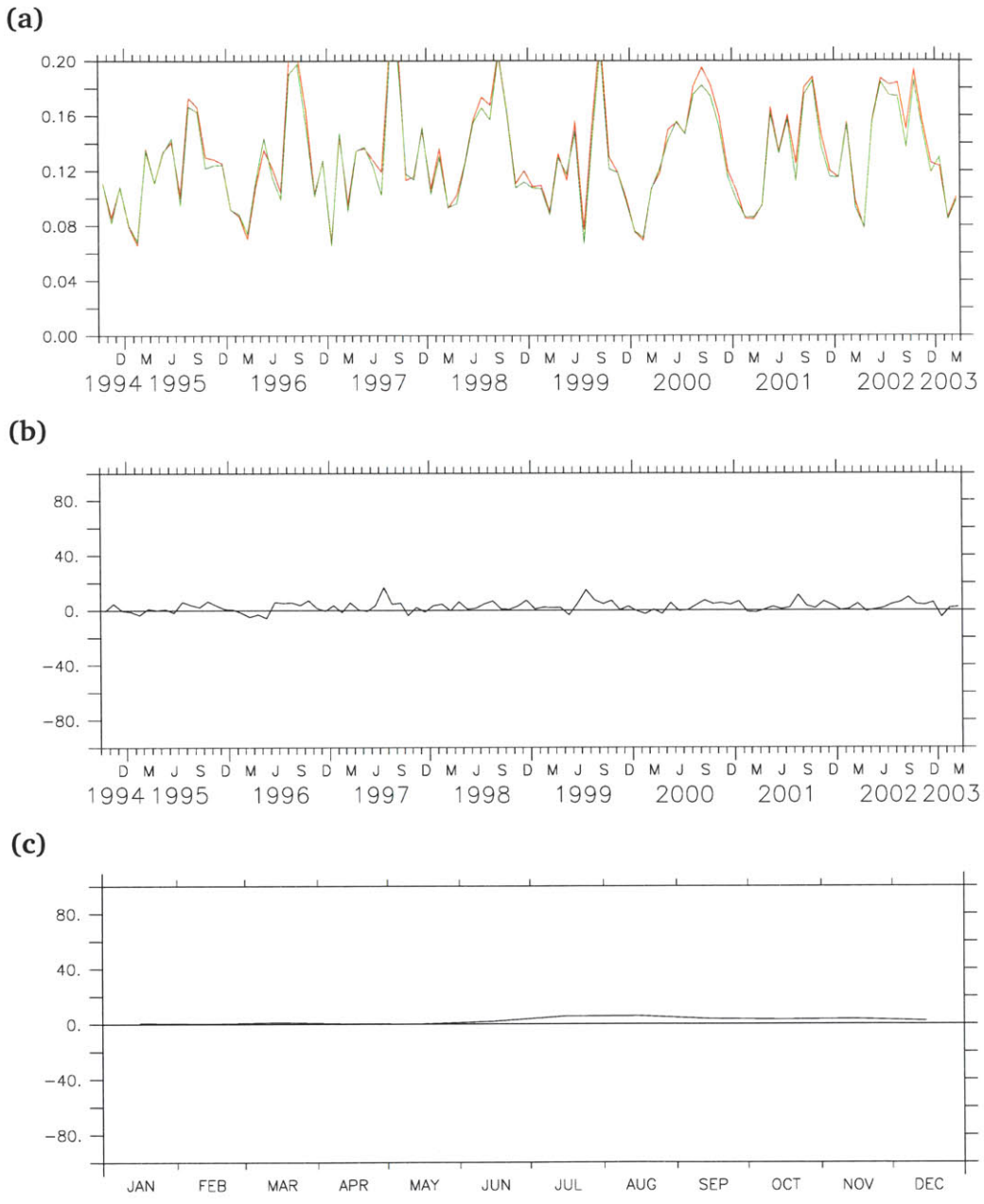

Figure A-7: Monthly Time-Series of Fractional Shallow Cloud Cover over Forested and Deforested Pixels, and Monthly Difference for Marabá -Altamira Domain. **(a)** Monthly time series of 14h45 UTC cloud density over deforested area (red line) and forested area (green line) in Marabá-Altamira. **(b)** Monthly time series and **(c)** Monthly climatology of 14h45 UTC percent differences in cloud density over deforested and forested areas in Marabá-Altamira.

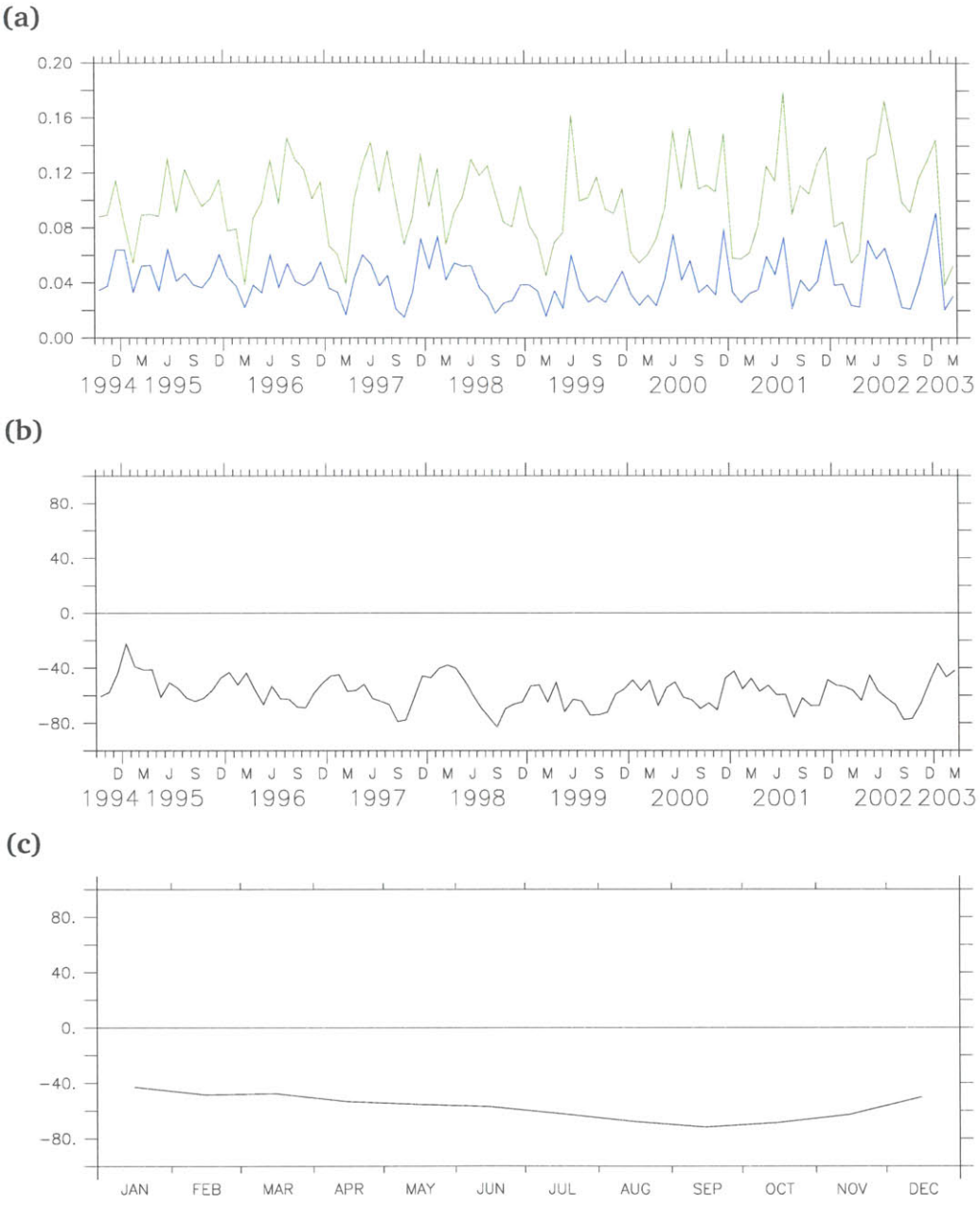

Figure A-8: Monthly Time-Series of Fractional Shallow Cloud Cover over Forested and Deforested Pixels, and Monthly Difference for Tapajós-Santarém Domain. **(a)** Monthly time series of 14h45 UTC cloud density over deforested area (red line) and forested area (green line) in Tapajós-Santarém. **(b)** Monthly time series and **(c)** Monthly climatology of 14h45 UTC percent differences in cloud density over deforested and forested areas in Tapajós-Santarém.

A.3 Monthly Time-Series

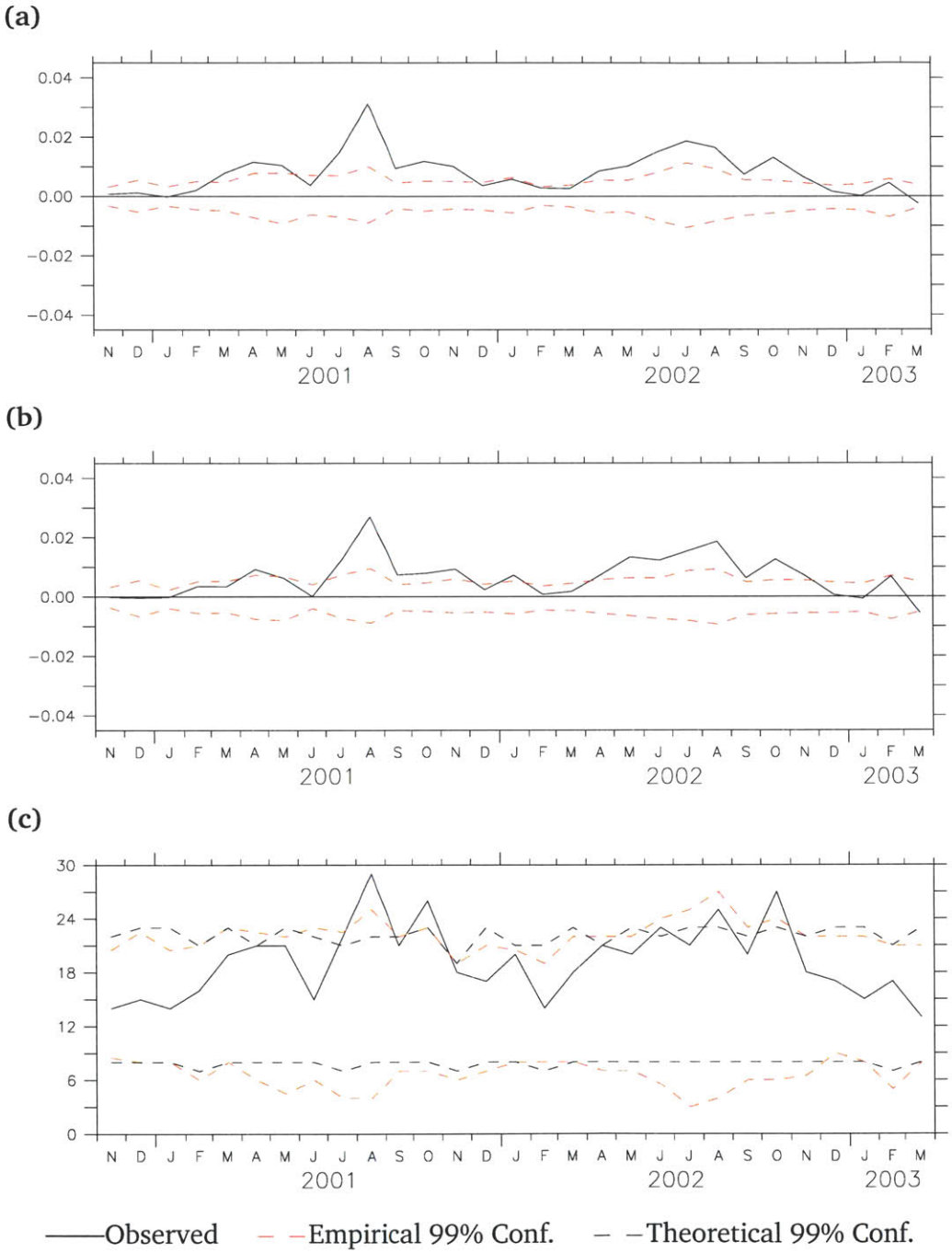

Figure A-9: Monthly time series of **(a)** CDD, **(b)** median CDD and **(c)** EC at 17h45 UTC over the study domain of Rondônia, along with their respective 99% confidence limits.

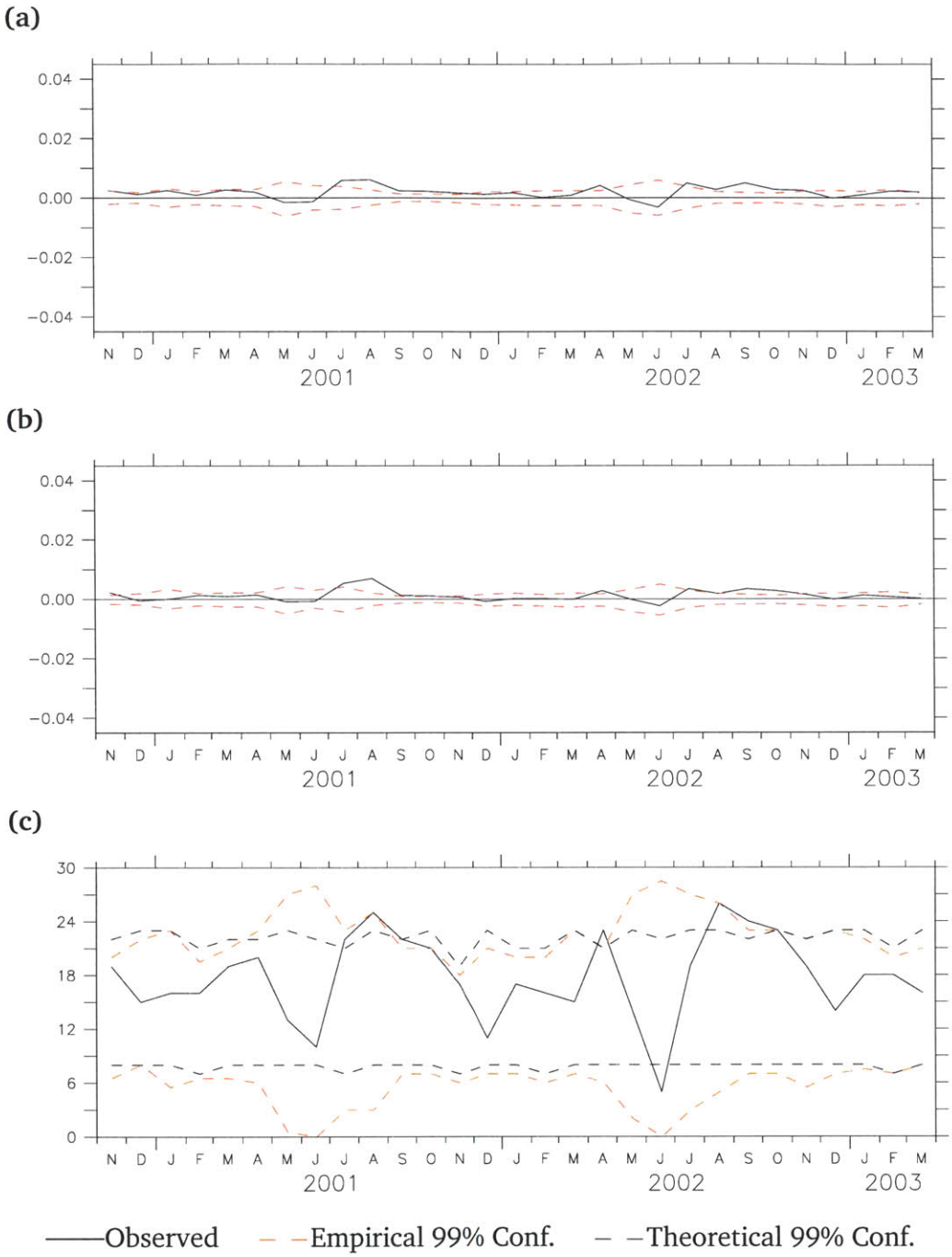

Figure A-10: Monthly time series of **(a)** CDD, **(b)** median CDD and **(c)** EC at 20h45 UTC over the study domain of Rondônia, along with their respective 99% confidence limits.

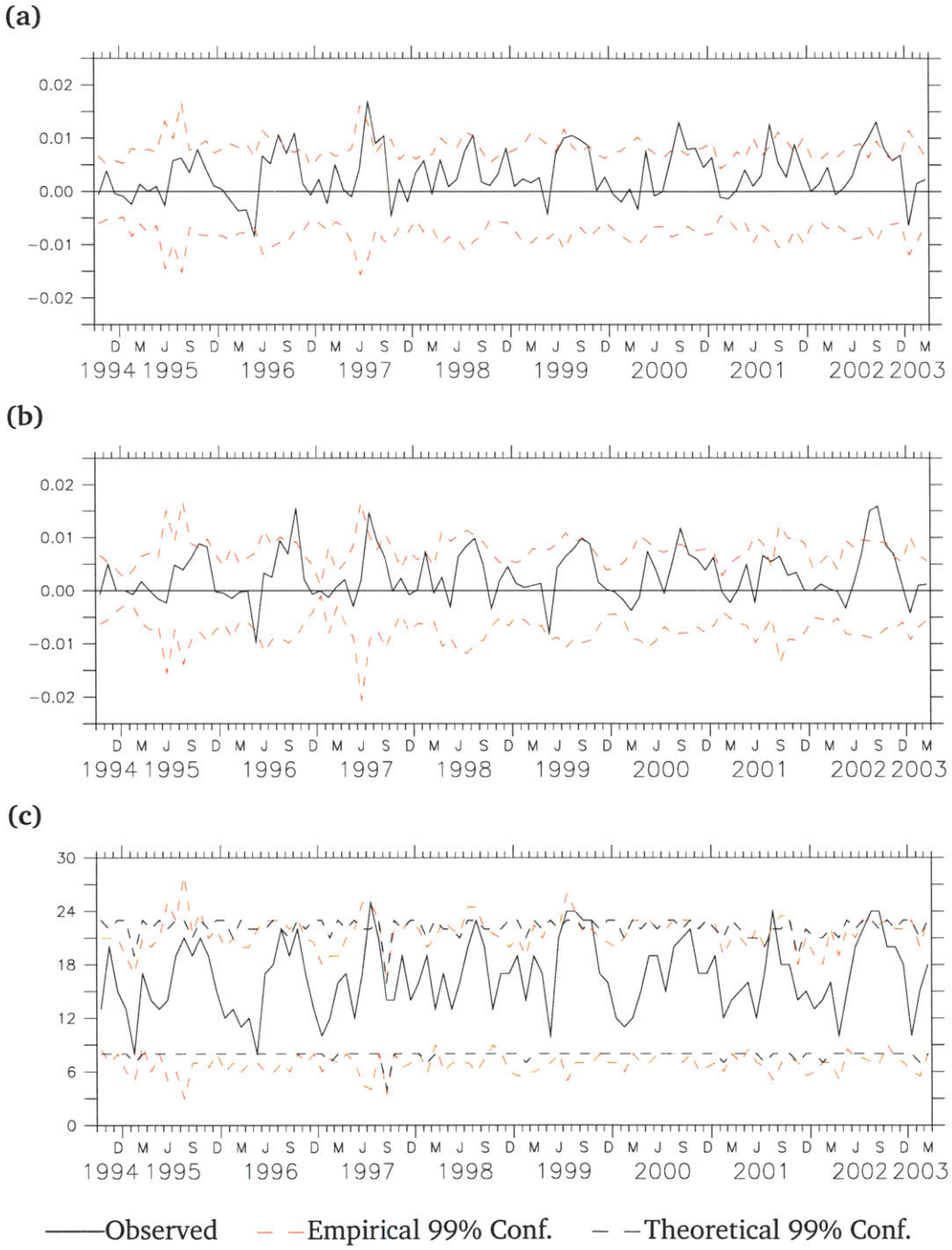

Figure A-11: Monthly time series of **(a)** CDD, **(b)** median CDD and **(c)** EC at 14h45 UTC over the study domain of Marabá-Altamira, along with their respective 99% confidence limits.

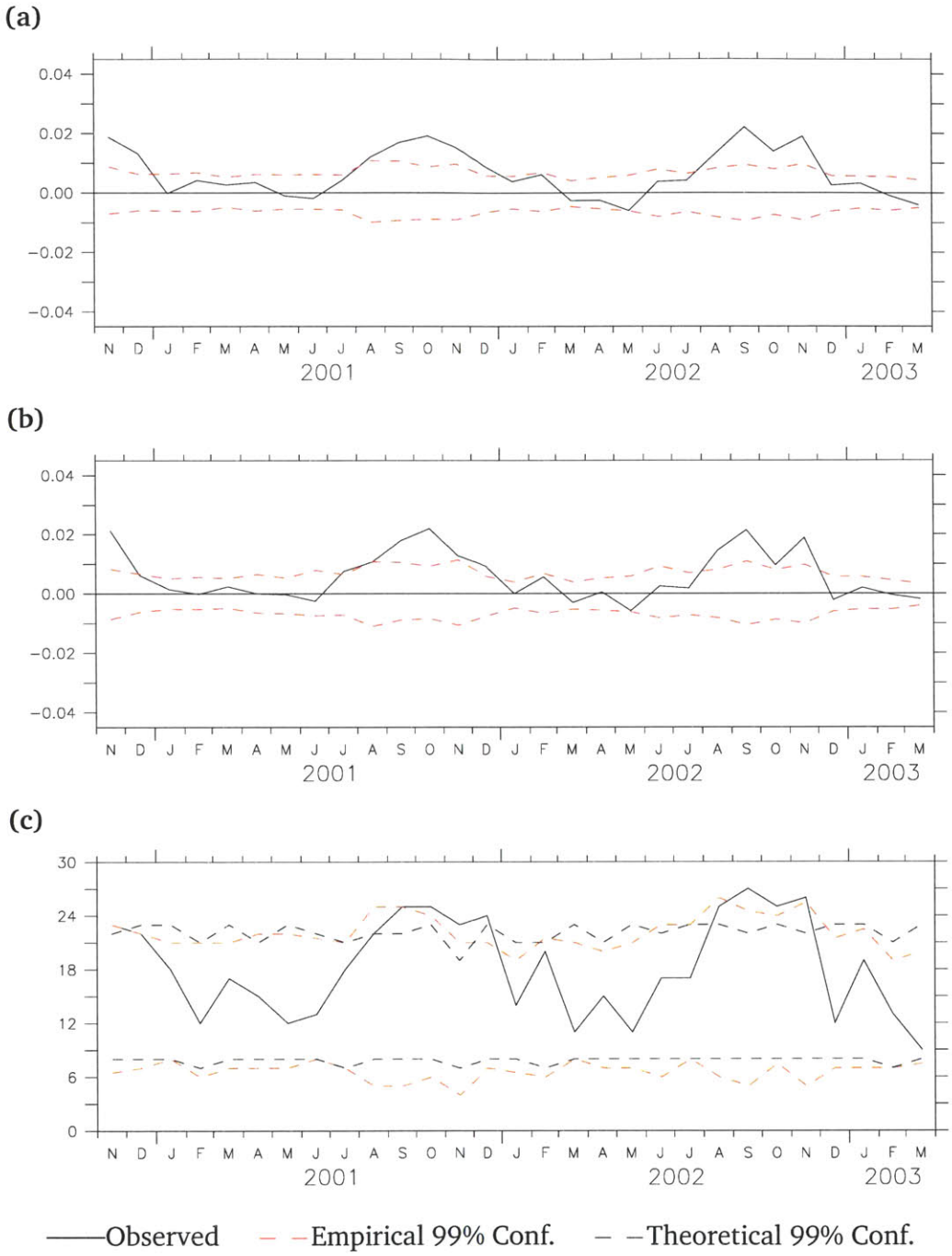

Figure A-12: Monthly time series of **(a)** CDD, **(b)** median CDD and **(c)** EC at 17h45 UTC over the study domain of Marabá-Altamira, along with their respective 99% confidence limits.

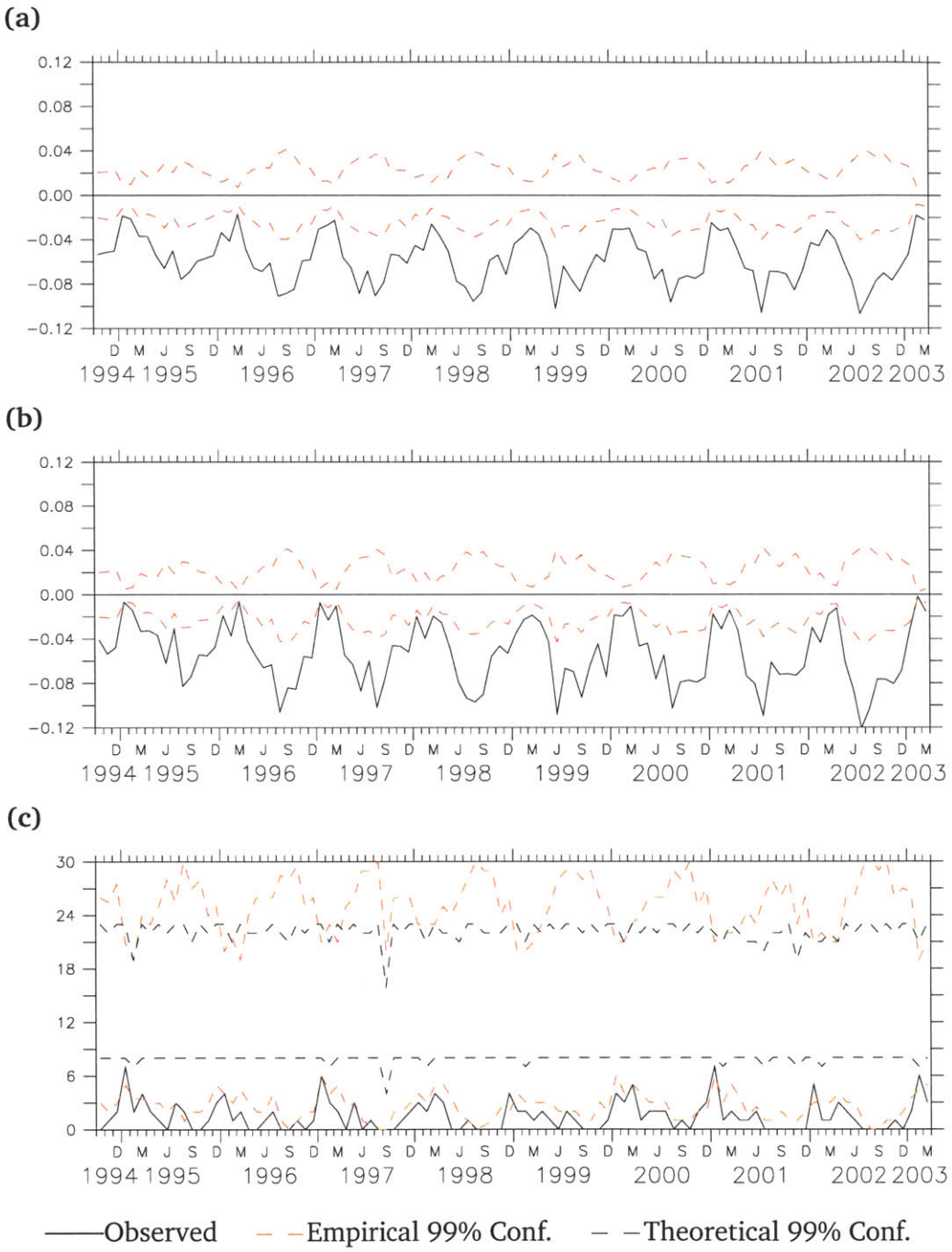

Figure A-13: Monthly time series of **(a)** CDD, **(b)** median CDD and **(c)** EC at 14h45 UTC over the study domain of Tapajós-Santarém, along with their respective 99% confidence limits.

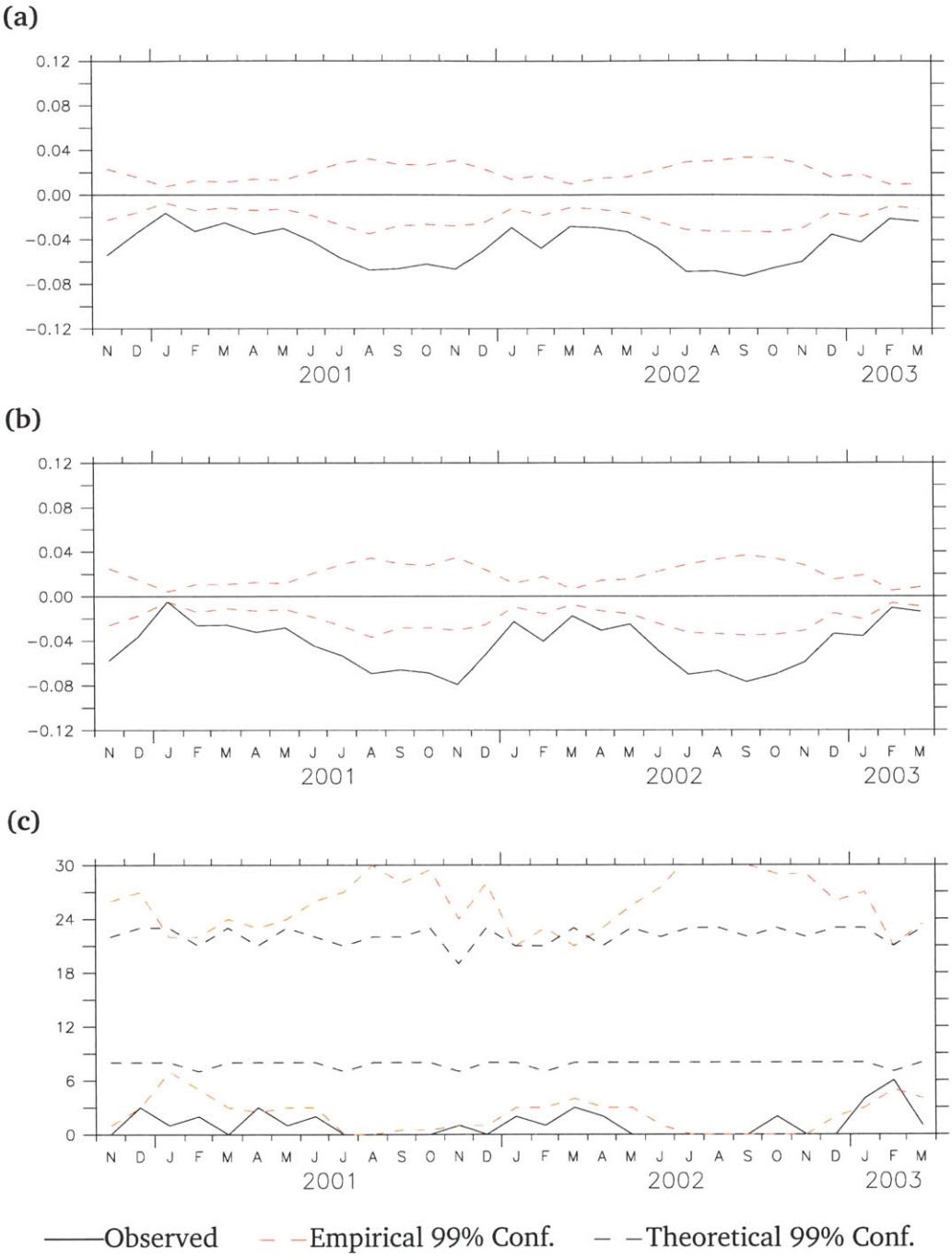

Figure A-14: Monthly time series of **(a)** CDD, **(b)** median CDD and **(c)** EC at 17h45 UTC over the study domain of Tapajós-Santarém, along with their respective 99% confidence limits.

A.4 Monthly Climatologies

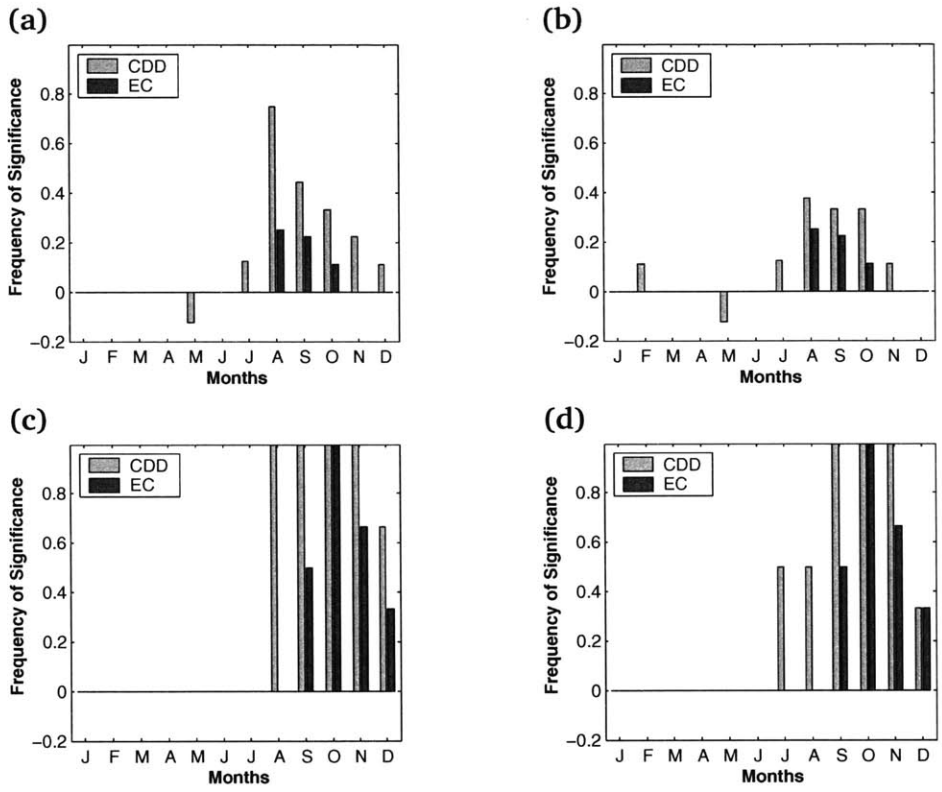

Figure A-15: Monthly Climatologies of CDD and EC significance for Marabá-Altamira; bars represent normalized number of times that a statistic is significant for a specific month; positive (negative) is for number of times that statistic is greater (smaller) than upper (lower) bound of 99% confidence interval. **(a)** Frequency of CDD and EC significance at 14h45 UTC; **(b)** Frequency of Median CDD and EC significance at 14h45 UTC; **(c)** Frequency of CDD and EC significance at 17h45 UTC; **(d)** Frequency of Median CDD and EC significance at 17h45 UTC.

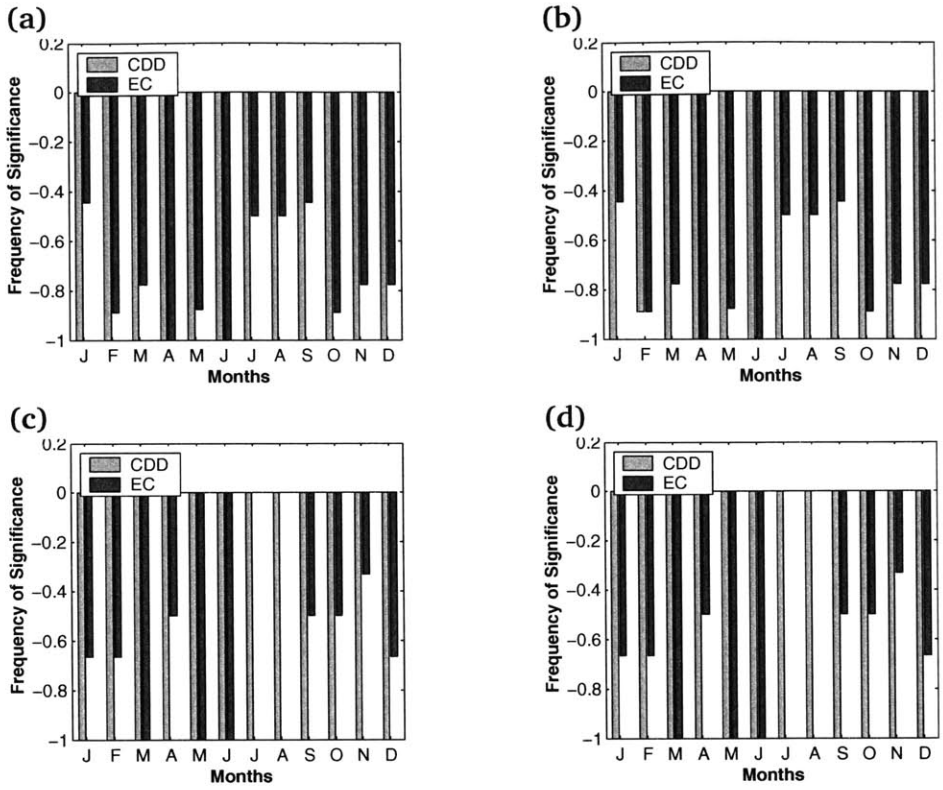

Figure A-16: Monthly Climatologies of CDD and EC significance for Tapajós-Santarém; bars represent normalized number of times that a statistic is significant for a specific month; positive (negative) is for number of times that statistic is greater (smaller) than upper (lower) bound of 99% confidence interval. **(a)** Frequency of CDD and EC significance at 14h45 UTC; **(b)** Frequency of Median CDD and EC significance at 14h45 UTC; **(c)** Frequency of CDD and EC significance at 17h45 UTC; **(d)** Frequency of Median CDD and EC significance at 17h45 UTC.

A.5 Seasonal Climatologies

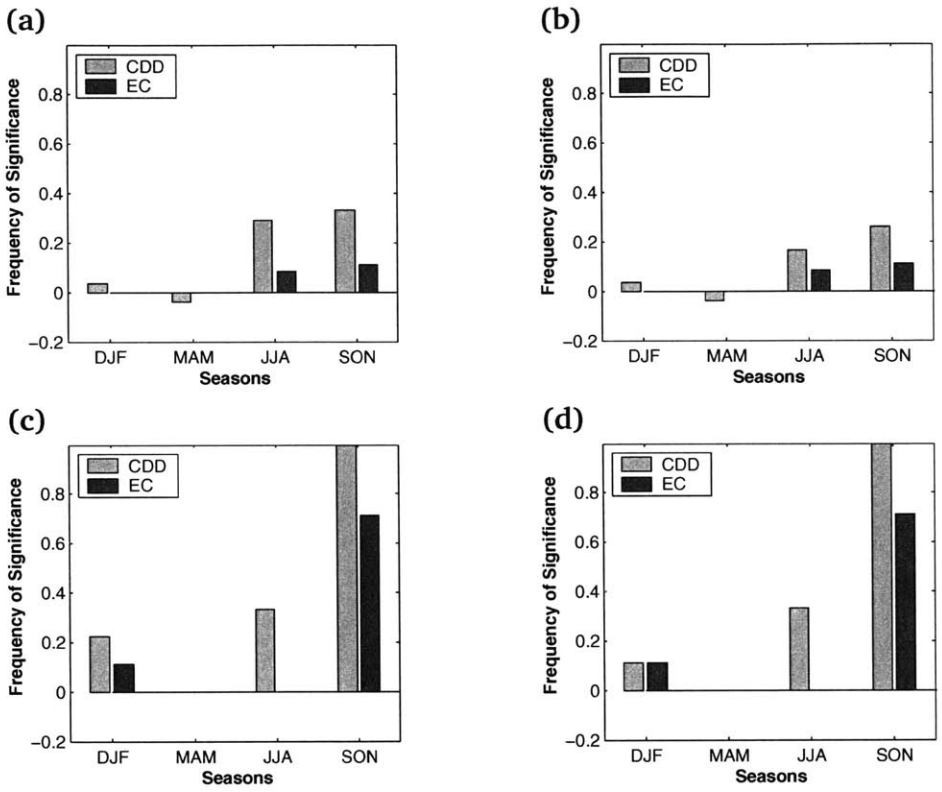

Figure A-17: Seasonal Climatologies of CDD and EC significance for Marabá-Altamira; bars represent normalized number of times that a statistic is significant for a specific month; positive (negative) is for number of times that statistic is greater (smaller) than upper (lower) bound of 99% confidence interval. **(a)** Frequency of CDD and EC significance at 14h45 UTC; **(b)** Frequency of Median CDD and EC significance at 14h45 UTC; **(c)** Frequency of CDD and EC significance at 17h45 UTC; **(d)** Frequency of Median CDD and EC significance at 17h45 UTC.

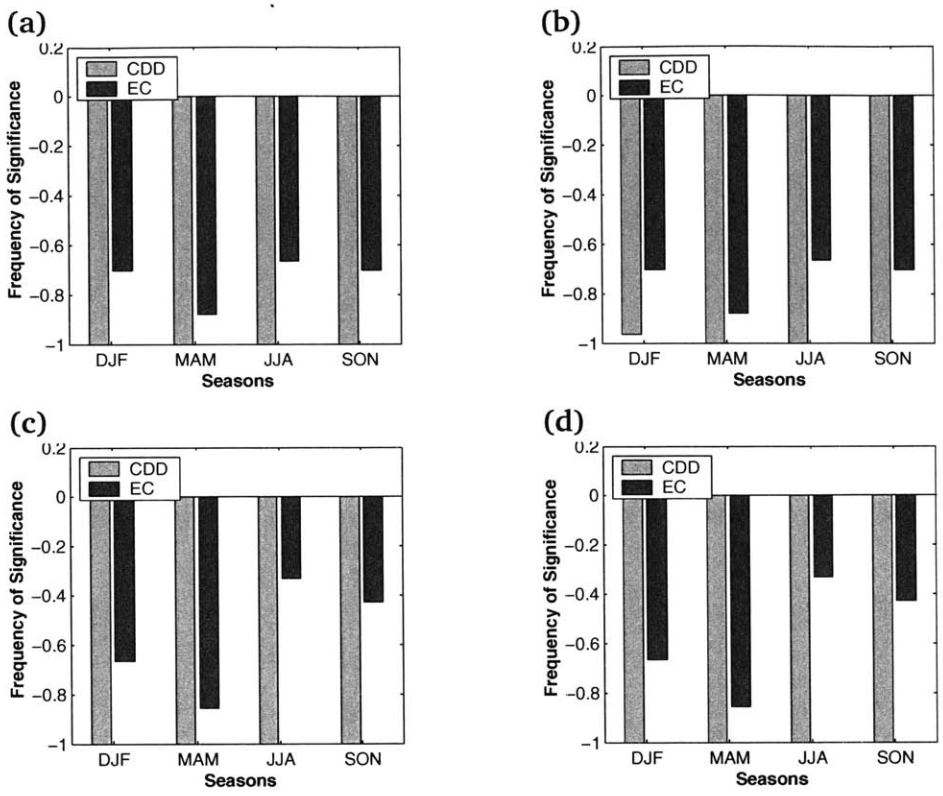

Figure A-18: Seasonal Climatologies of CDD and EC significance for Tapajós-Santarém; bars represent normalized number of times that a statistic is significant for a specific month; positive (negative) is for number of times that statistic is greater (smaller) than upper (lower) bound of 99% confidence interval. **(a)** Frequency of CDD and EC significance at 14h45 UTC; **(b)** Frequency of Median CDD and EC significance at 14h45 UTC; **(c)** Frequency of CDD and EC significance at 17h45 UTC; **(d)** Frequency of Median CDD and EC significance at 17h45 UTC.

A.6 Clouds and Elevation

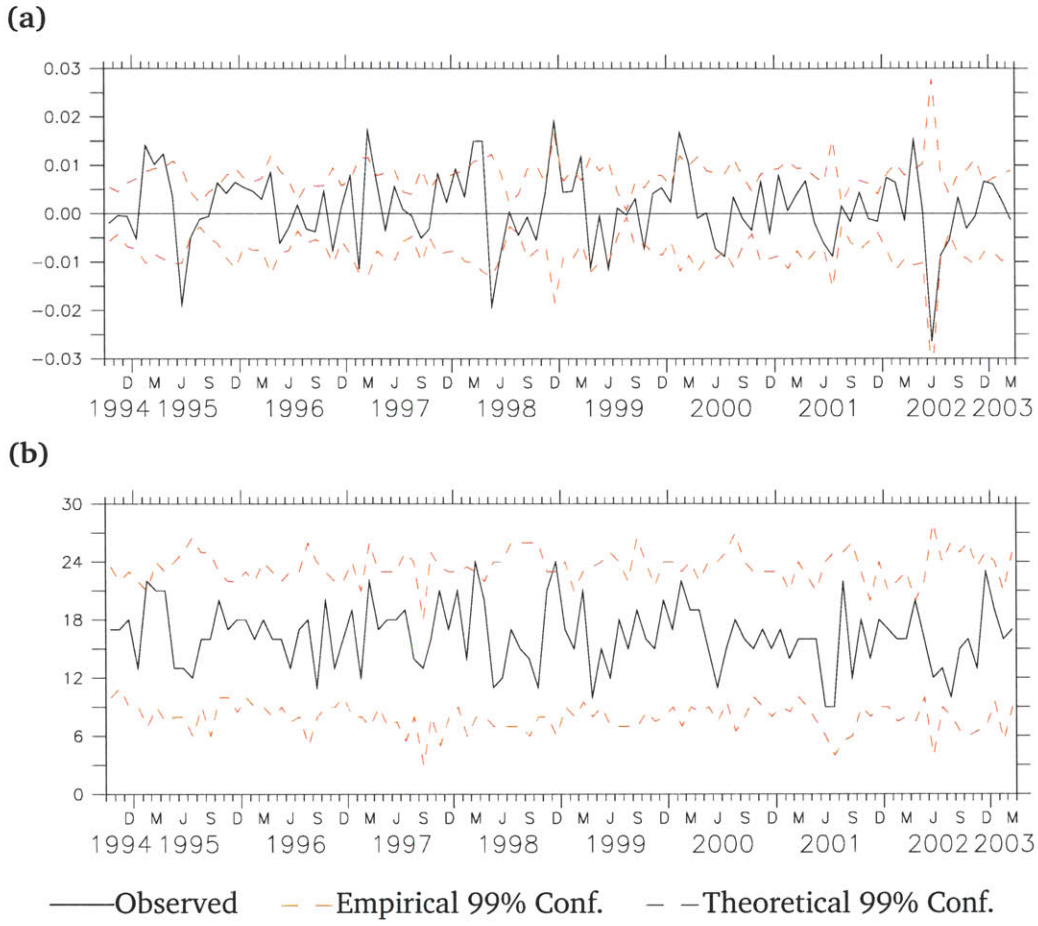

Figure A-19: Monthly time series of **(a)** CDD, and **(b)** EC relative to 30% highest pixels at 14h45 UTC over the study domain of Rondônia, along with their respective 99% confidence limits.

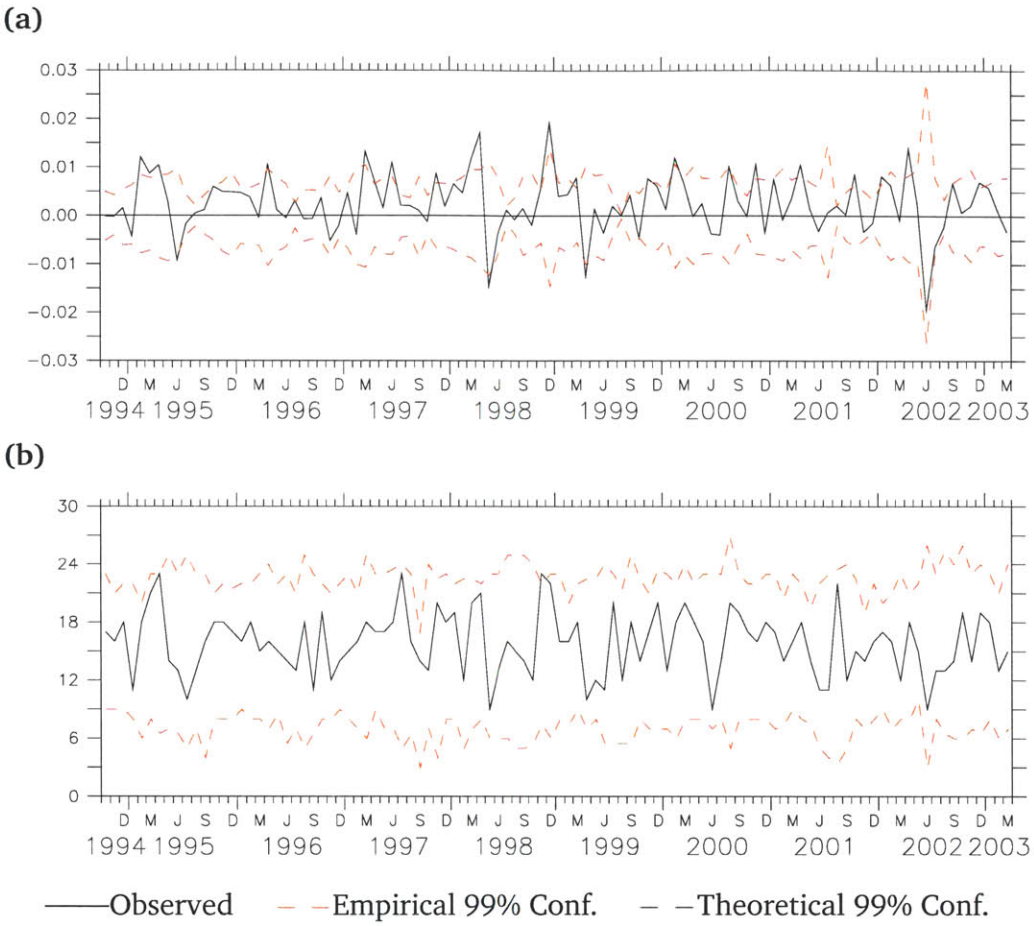

Figure A-20: Monthly time series of **(a)** CDD, and **(b)** EC relative to 50% highest pixels at 14h45 UTC over the study domain of Rondônia, along with their respective 99% confidence limits.

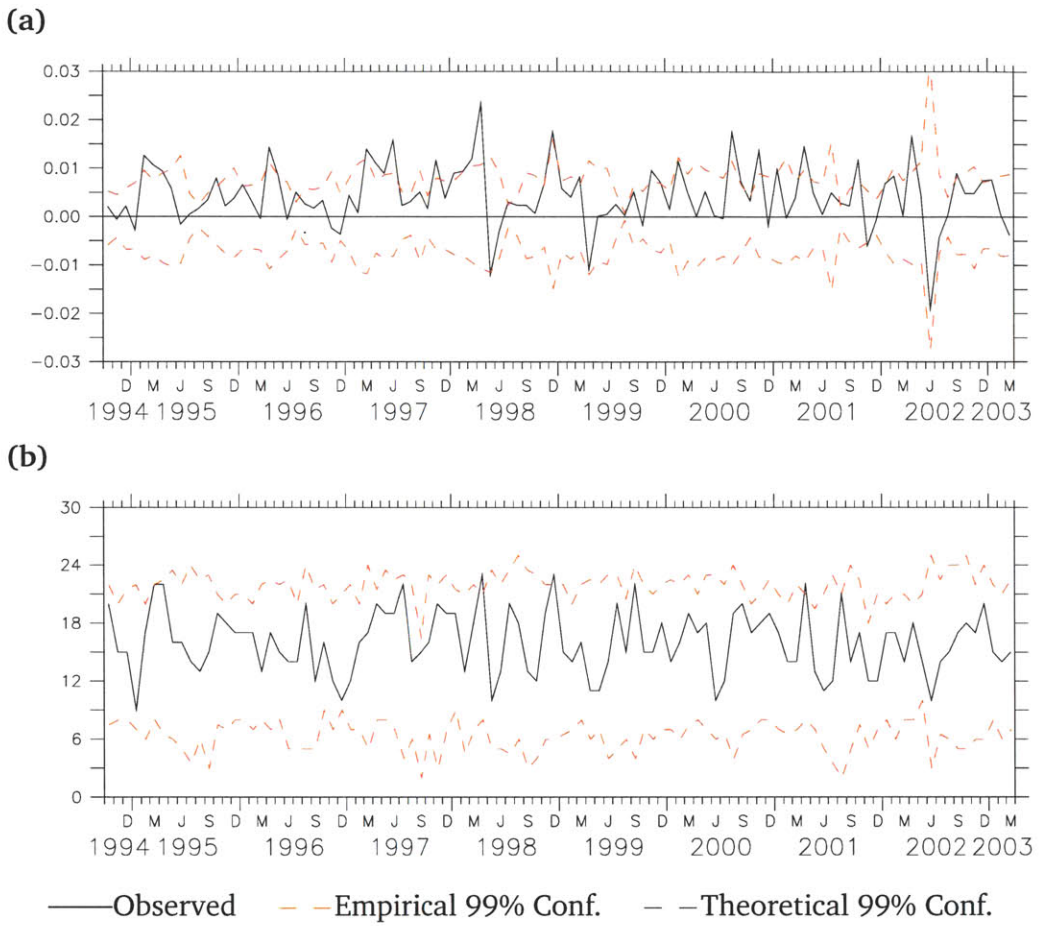

Figure A-21: Monthly time series of **(a)** CDD, and **(b)** EC relative to 70% highest pixels at 14h45 UTC over the study domain of Rondônia, along with their respective 99% confidence limits.

A.7 Clouds and Slope

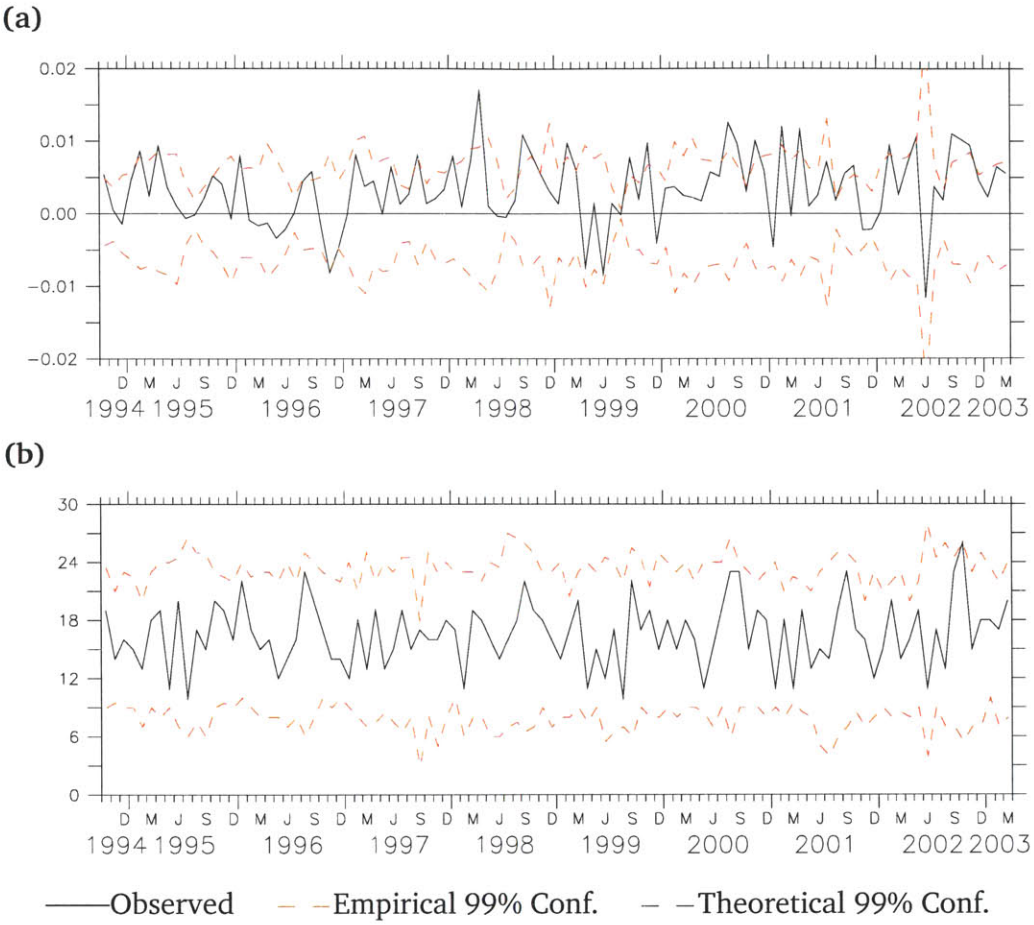

Figure A-22: Monthly time series of **(a)** CDD, and **(b)** EC relative to 30% steepest pixels at 14h45 UTC over the study domain of Rondônia, along with their respective 99% confidence limits.

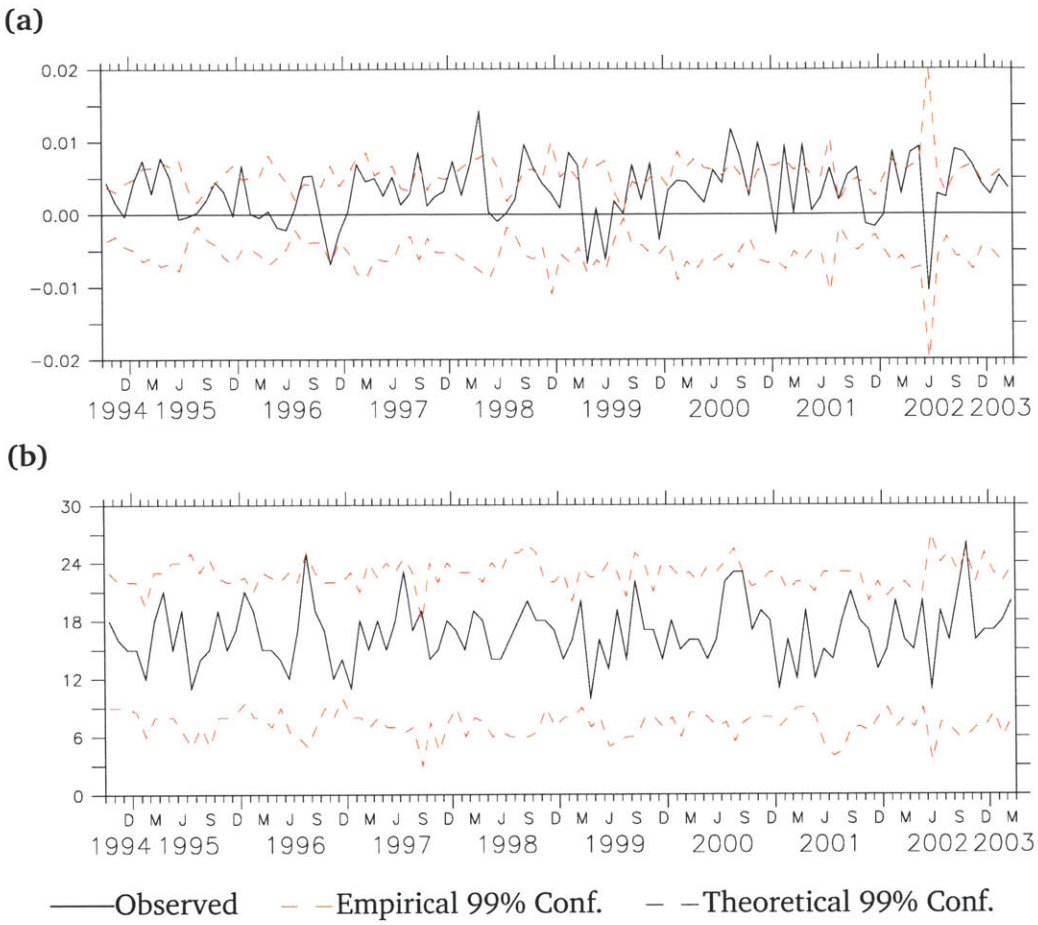

Figure A-23: Monthly time series of **(a)** CDD, and **(b)** EC relative to 50% steepest pixels at 14h45 UTC over the study domain of Rondônia, along with their respective 99% confidence limits.

Figure A-24: Monthly time series of **(a)** CDD, and **(b)** EC relative to 70% steepest pixels at 14h45 UTC over the study domain of Rondônia, along with their respective 99% confidence limits.

APPENDIX B

SUPPLEMENTARY RAINFALL RESULTS

B.1 2A23 Results

Table B.1: Results from the Binomial Analysis of TRMM-2A23 Event Counts v. Forest Cover; The count of positive and negative normalized event count differences is compared to the binomial distribution to detect significant biases.

Difference Statistic	>0 Counts	<0 Counts	Significance
Rain Certain	59	17	$p \leqslant 0.0001$
Rain Possible	72	4	$p \leqslant 0.0001$
Rain Convective	54	22	$p \leqslant 0.0005$
Rain Stratiform	59	17	$p \leqslant 0.0001$
Rain Isolated	36	39	—
Warm Possible	36	39	—
Storm Height	33	43	—
Bright Band Height	41	30	—
Bright Band Intensity	32	39	—

Table B.2: Results from the Randomization Analysis of TRMM-2A23 Event Counts v. Forest Cover; The count of times that the normalized event count difference is greater than the upper 99% confidence bound, and the count of the number of times that the difference is less than the lower 99% confidence bound are summarized.

Difference Statistic	$>\uparrow$99% Limit	$<\downarrow$99% Limit
Rain Certain	5	2
Rain Possible	0	0
Rain Convective	1	0
Rain Stratiform	5	1
Rain Isolated	0	0
Warm Possible	0	0
Storm Height	0	1
Bright Band Heigth	1	0
Bright Band Intensity	0	1

Table B.3: Results from the Binomial Analysis of TRMM-2A23 Event Timing v. Forest Cover; The count of positive and negative mean event occurrence time differences is compared to the binomial distribution to detect significant biases.

Difference Statistic	>0 Counts	<0 Counts	Significance
Rain Certain	33	43	—
Rain Possible	36	40	—
Rain Convective	31	41	—
Rain Stratiform	37	39	—
Rain Isolated	35	37	—
Warm Possible	35	37	—

Table B.4: Results from TRMM-2A23 Event Timing v. Forest Cover Randomization Analysis; The count of times that the mean event occurrence time difference is greater than the upper 99% confidence bound, and the count of the number of times that the difference is less than the lower 99% confidence bound are summarized.

Difference Statistic	$>\uparrow$99% Limit	$<\downarrow$99% Limit
Rain Certain	0	4
Rain Possible	1	3
Rain Convective	0	2
Rain Stratiform	1	3
Rain Isolated	0	0
Warm Possible	0	0

Table B.5: Results from the Binomial Analysis of TRMM-2A23 Event Counts v. Elevation; The count of positive and negative normalized event count differences is compared to the binomial distribution to detect significant biases. The ranges are the percentile cutoffs used to create a binary ("high" v. "low") field from the original DEM (e. g., a range of "30" specifies the difference of the statistic between the 30% highest pixels and the 70% lowest.)

Difference Statistic	Range	>0 Counts	<0 Counts	Significance
Rain Certain	30	49	27	$p \leqslant 0.02$
	50	61	15	$p \leqslant 0.0001$
	70	58	18	$\leqslant 0.0001$
Rain Possible	30	68	8	$p \leqslant 0.0001$
	50	70	6	$p \leqslant 0.0001$
	70	69	7	$p \leqslant 0.0001$
Rain Convective	30	44	32	—
	50	44	32	—
	70	56	20	$p \leqslant 0.0001$
Rain Stratiform	30	51	25	$p \leqslant 0.004$
	50	59	17	$p \leqslant 0.0001$
	70	61	15	$p \leqslant 0.0001$
Rain Isolated	30	37	37	—
	50	38	31	—
	70	49	26	$p \leqslant 0.02$
Warm Possible	30	37	37	—
	50	38	31	—
	70	49	26	$p \leqslant 0.02$
Storm Height	30	34	42	—
	50	36	40	—
	70	41	35	—
Bright Band Height	30	22	47	$p \leqslant 0.004$
	50	30	39	—
	70	29	39	—
Bright Band Intensity	30	36	33	—
	50	39	30	—
	70	42	26	$p \leqslant 0.07$

Table B.6: Results from the Binomial Analysis of TRMM-2A23 Event Counts v. Slope; The count of positive and negative normalized event count differences is compared to the binomial distribution to detect significant biases. The ranges are the percentile cutoffs used to create a binary ("steep" v. "gradual") field from the original DEM (e. g., a range of "30" specifies the difference of the statistic between the 30% steepest pixels and the 70% most gradual.)

Difference Statistic	Range	>0 Counts	<0 Counts	Significance
Rain Certain	30	54	22	$p \leqslant 0.0005$
	50	52	24	$p \leqslant 0.002$
	70	56	20	$p \leqslant 0.0001$
Rain Possible	30	65	11	$p \leqslant 0.0001$
	50	72	4	$p \leqslant 0.0001$
	70	73	3	$p \leqslant 0.0001$
Rain Convective	30	49	27	$p \leqslant 0.02$
	50	52	24	$p \leqslant 0.002$
	70	57	19	$p \leqslant 0.0001$
Rain Stratiform	30	48	28	$p \leqslant 0.03$
	50	53	23	$p \leqslant 0.001$
	70	53	23	$p \leqslant 0.001$
Rain Isolated	30	32	43	—
	50	41	30	—
	70	42	33	—
Warm Possible	30	32	43	—
	50	41	30	—
	70	42	33	—
Storm Height	30	35	41	—
	50	40	36	—
	70	41	35	—
Bright Band Height	30	37	33	—
	50	33	38	—
	70	38	32	—
Bright Band Intensity	30	37	33	—
	50	40	31	—
	70	37	33	—

Table B.7: Results from the Randomization Analysis of TRMM-2A23 Event Counts v. Elevation; The count of times that the normalized event count difference is greater than the upper 99% confidence bound, and the count of the number of times that the difference is less than the lower 99% confidence bound are summarized. The ranges are the percentile cutoffs used to create a binary ("high" v. "low") field from the original DEM (e. g., a range of "30" specifies the difference of the statistic between the 30% highest pixels and the 70% lowest.)

Difference Statistic	Range	$>\uparrow$99% Limit	$<\downarrow$99% Limit
Rain Certain	30	8	2
	50	14	1
	70	9	3
Rain Possible	30	3	0
	50	7	0
	70	3	0
Rain Convective	30	4	0
	50	5	0
	70	6	0
Rain Stratiform	30	9	1
	50	16	1
	70	12	2
Rain Isolated	30	0	0
	50	0	0
	70	1	2
Warm Possible	30	0	0
	50	0	0
	70	1	2
Storm Height	30	0	0
	50	2	2
	70	4	2
Bright Band Heigth	30	2	3
	50	5	5
	70	4	6
Bright Band Intensity	30	0	0
	50	3	1
	70	3	3

Table B.8: Results from the Randomization Analysis of TRMM-2A23 Event Counts v. Slope; The count of times that the normalized event count difference is greater than the upper 99% confidence bound, and the count of the number of times that the difference is less than the lower 99% confidence bound are summarized. The ranges are the percentile cutoffs used to create a binary ("steep" v. "gradual") field from the original DEM (e. g., a range of "30" specifies the difference of the statistic between the 30% steepest pixels and the 70% most gradual.)

Difference Statistic	Range	$>\uparrow$99% Limit	$<\downarrow$99% Limit
Rain Certain	30	4	1
	50	4	2
	70	6	1
Rain Possible	30	0	0
	50	2	0
	70	11	0
Rain Convective	30	2	0
	50	3	1
	70	4	1
Rain Stratiform	30	3	1
	50	3	0
	70	4	0
Rain Isolated	30	0	0
	50	0	0
	70	0	1
Warm Possible	30	0	0
	50	0	0
	70	0	1
Storm Height	30	0	0
	50	2	0
	70	3	1
Bright Band Heigth	30	1	0
	50	1	3
	70	2	4
Bright Band Intensity	30	0	0
	50	0	0
	70	2	0

Table B.9: Results from the Binomial Analysis of TRMM-2A23 Event Timing v. Elevation; The count of positive and negative mean event occurrence time differences is compared to the binomial distribution to detect significant biases. The ranges are the percentile cutoffs used to create a binary ("high" v. "low") field from the original DEM (e. g., a range of "30" specifies the difference of the statistic between the 30% highest pixels and the 70% lowest.)

Difference Statistic	Range	>0 Counts	<0 Counts	Significance
Rain Certain	30	38	38	—
	50	35	41	—
	70	30	46	$p \leqslant 0.09$
Rain Possible	30	35	41	—
	50	39	37	—
	70	38	38	—
Rain Convective	30	37	38	—
	50	32	43	—
	70	25	50	$p \leqslant 0.006$
Rain Stratiform	30	37	39	—
	50	38	38	—
	70	34	42	—
Rain Isolated	30	31	35	—
	50	31	41	—
	70	28	39	—
Warm Possible	30	31	35	—
	50	31	41	—
	70	28	39	—

Table B.10: Results from the Binomial Analysis of TRMM-2A23 Event Timing v. Slope; The count of positive and negative mean event occurrence time differences is compared to the binomial distribution to detect significant biases. The ranges are the percentile cutoffs used to create a binary ("steep" v. "gradual") field from the original DEM (e. g., a range of "30" specifies the difference of the statistic between the 30% steepest pixels and the 70% most gradual.)

Difference Statistic	Range	>0 Counts	<0 Counts	Significance
Rain Certain	30	37	39	—
	50	37	39	—
	70	37	39	—
Rain Possible	30	37	39	—
	50	35	41	—
	70	37	39	—
Rain Convective	30	35	40	—
	50	34	41	—
	70	34	40	—
Rain Stratiform	30	40	36	—
	50	37	39	—
	70	35	41	—
Rain Isolated	30	32	37	—
	50	28	42	$p \leqslant 0.12$
	70	31	37	—
Warm Possible	30	32	37	—
	50	28	42	$p \leqslant 0.12$
	70	31	37	—

Table B.11: Results from the Randomization Analysis of TRMM-2A23 Event Timing v. Elevation; The count of times that the normalized occurrence time difference is greater than the upper 99% confidence bound, and the count of the number of times that the difference is less than the lower 99% confidence bound are summarized. The ranges are the percentile cutoffs used to create a binary ("high" v. "low") field from the original DEM (e. g., a range of "30" specifies the difference of the statistic between the 30% highest pixels and the 70% lowest.)

Difference Statistic	Range	$>\uparrow$99% Limit	$<\downarrow$99% Limit
Rain Certain	30	5	4
	50	3	11
	70	2	10
Rain Possible	30	5	3
	50	5	7
	70	2	10
Rain Convective	30	1	3
	50	1	6
	70	1	4
Rain Stratiform	30	3	6
	50	3	9
	70	2	11
Rain Isolated	30	0	0
	50	0	0
	70	2	0
Warm Possible	30	0	0
	50	0	0
	70	2	0

Table B.12: Results from the Randomization Analysis of TRMM-2A23 Event Timing v. Slope; The count of times that the normalized occurrence time difference is greater than the upper 99% confidence bound, and the count of the number of times that the difference is less than the lower 99% confidence bound are summarized. The ranges are the percentile cutoffs used to create a binary ("steep" v. "gradual") field from the original DEM (e. g., a range of "30" specifies the difference of the statistic between the 30% steepest pixels and the 70% most gradual.)

Difference Statistic	Range	$>\uparrow$99% Limit	$<\downarrow$99% Limit
Rain Certain	30	2	2
	50	3	4
	70	4	4
Rain Possible	30	2	2
	50	2	2
	70	2	2
Rain Convective	30	4	3
	50	5	2
	70	3	2
Rain Stratiform	30	2	1
	50	1	3
	70	4	4
Rain Isolated	30	0	0
	50	2	0
	70	1	0
Warm Possible	30	0	0
	50	2	0
	70	1	0

B.2 TRMM-3A25 Results

Table B.13: Results from the Binomial Analysis of 2-D TRMM-3A25 Conditional Statistics v. Forest Cover; The count of positive and negative conditional statistic differences is compared to the binomial distribution to detect significant biases.

Difference Statistic	>0 Counts	<0 Counts	Significance
Surface Rain Mean Intensity	41	35	—
Surface Rain Std. Dev.	36	40	—
Surface Rain All Mean Intensity	41	35	—
Surface Rain All Std. Dev.	36	40	—
Bright Band Height Mean	46	27	$p \leqslant 0.05$
Bright Band Height Std. Dev.	33	40	—
Bright Band Zmax Mean	31	42	—
Bright Band Zmax Std. Dev.	37	36	—
Storm Height Mean	37	39	—
Stratiform Storm Height Mean	43	33	—
Convective Storm Height Mean	42	34	—
Storm Height Std. Dev.	32	44	—
Strat. Storm Height Std. Dev.	40	36	—
Conv. Storm Height Std. Dev.	35	41	—
Surface Rain Pixel Counts	40	36	—
Surface Rain All Pixel Counts	40	36	—
Bright Band Pixel Counts	35	40	—
Warm Rain Pixel Counts	28	43	$p \leqslant 0.1$
Total Pixel Counts	42	34	—

Table B.14: Results from the Randomization Analysis of 2-D TRMM-3A25 Conditional Statistics v. Forest Cover; The count of times that the conditional statistic difference is greater than the upper 99% confidence bound, and the count of the number of times that the difference is less than the lower 99% confidence bound are summarized.

Difference Statistic	$>\uparrow$99% Limit	$<\downarrow$99% Limit
Surface Rain Mean Intensity	0	0
Surface Rain Std. Dev.	0	0
Surface Rain All Mean Intensity	0	0
Surface Rain All Std. Dev.	0	0
Bright Band Height Mean	0	0
Bright Band Height Std. Dev.	0	0
Bright Band Zmax Mean	0	0
Bright Band Zmax Std. Dev.	0	0
Storm Height Mean	0	0
Stratiform Storm Height Mean	0	0
Convective Storm Height Mean	0	1
Storm Height Std. Dev.	1	0
Strat. Storm Height Std. Dev.	0	0
Conv. Storm Height Std. Dev.	1	1
Surface Rain Pixel Counts	0	0
Surface Rain All Pixel Counts	0	0
Bright Band Pixel Counts	0	0
Warm Rain Pixel Counts	0	0
Total Pixel Counts	0	0

Table B.15: Results from the Binomial Analysis of 3-D TRMM-3A25 Conditional Statistics v. Forest Cover (Part a); The count of positive and negative conditional statistic differences is compared to the binomial distribution to detect significant biases.

Difference Statistic	Level	>0 Counts	<0 Counts	Significance
Rain Mean	Avg.	40	36	—
	2 km	35	41	—
	4 km	39	37	—
	6 km	43	33	—
Rain Std. Dev.	Avg.	37	39	—
	2 km	36	40	—
	4 km	39	37	—
	6 km	45	31	$p \leqslant 0.14$
Conv. Rain Mean	Avg.	40	36	—
	2 km	38	38	—
	4 km	41	35	—
	6 km	43	32	—
Conv. Rain Std. Dev.	Avg.	38	38	—
	2 km	40	36	—
	4 km	42	34	—
	6 km	44	31	—
Strat. Rain Mean	Avg.	35	41	—
	2 km	36	40	—
	4 km	36	40	—
	6 km	30	45	$p \leqslant 0.11$
Strat. Rain Std. Dev.	Avg.	33	43	—
	2 km	35	41	—
	4 km	34	42	—
	6 km	29	46	$p \leqslant 0.07$

Table B.16: Results from the Binomial Analysis of 3-D TRMM-3A25 Conditional Statistics v. Forest Cover (Part b); The count of positive and negative conditional statistic differences is compared to the binomial distribution to detect significant biases.

Difference Statistic	Level	>0 Counts	<0 Counts	Significance
Rain Pixels	Avg.	37	39	—
	2 km	38	38	—
	4 km	38	38	—
	6 km	37	39	—
Conv. Rain Pixels	Avg.	31	45	$p \leqslant 0.14$
	2 km	31	45	$p \leqslant 0.14$
	4 km	31	45	$p \leqslant 0.14$
	6 km	30	45	$p \leqslant 0.11$
Strat. Rain Pixels	Avg.	36	40	—
	2 km	36	40	—
	4 km	36	39	—
	6 km	40	36	—

Table B.17: Results from the Binomial Analysis of 3-D TRMM-3A25 Conditional Statistics v. Forest Cover (Part c); The count of positive and negative conditional statistic differences is compared to the binomial distribution to detect significant biases.

Difference Statistic	Level	>0 Counts	<0 Counts	Significance
Measured Reflectivity (Zm)	Avg.	44	32	—
	2 km	40	36	—
	4 km	43	33	—
	6 km	45	31	$p \leqslant 0.14$
Stratiform Zm	Avg.	39	37	—
	2 km	41	35	—
	4 km	42	34	—
	6 km	33	42	—
Convective Zm	Avg.	42	34	—
	2 km	34	42	—
	4 km	40	36	—
	6 km	46	29	$p \leqslant 0.07$
Corrected Reflectivity (Zt)	Avg.	44	32	—
	2 km	40	36	—
	4 km	41	35	—
	6 km	44	32	—
Stratiform Zt	Avg.	40	36	—
	2 km	42	34	—
	4 km	40	36	—
	6 km	31	44	—
Convective Zt	Avg.	44	32	—
	2 km	37	39	—
	4 km	39	37	—
	6 km	45	30	$p \leqslant 0.11$

Table B.18: Results from the Randomization Analysis of 3-D TRMM-3A25 Conditional Statistics v. Forest Cover (Part a); The count of times that the conditional statistic difference is greater than the upper 99% confidence bound, and the count of the number of times that the difference is less than the lower 99% confidence bound are summarized.

Difference Statistic	Level	$>\uparrow$99% Limit	$<\downarrow$99% Limit
Rain Mean	Avg.	0	0
	2 km	0	0
	4 km	0	0
	6 km	0	0
Rain Std. Dev.	Avg.	0	0
	2 km	0	0
	4 km	0	0
	6 km	0	0
Conv. Rain Mean	Avg.	0	1
	2 km	1	1
	4 km	0	0
	6 km	1	1
Conv. Rain Std. Dev.	Avg.	1	1
	2 km	1	0
	4 km	0	1
	6 km	1	0
Strat. Rain Mean	Avg.	0	0
	2 km	0	0
	4 km	0	0
	6 km	0	1
Strat. Rain Std. Dev.	Avg.	0	0
	2 km	0	0
	4 km	0	0
	6 km	0	0

Table B.19: Results from the Randomization Analysis of 3-D TRMM-3A25 Conditional Statistics v. Forest Cover (Part b); The count of times that the conditional statistic difference is greater than the upper 99% confidence bound, and the count of the number of times that the difference is less than the lower 99% confidence bound are summarized.

Difference Statistic	Level	$>\uparrow$99% Limit	$<\downarrow$99% Limit
Rain Pixels	Avg.	0	0
	2 km	0	0
	4 km	0	0
	6 km	0	0
Conv. Rain Pixels	Avg.	0	0
	2 km	0	0
	4 km	0	0
	6 km	0	0
Strat. Rain Pixels	Avg.	0	0
	2 km	0	0
	4 km	0	0
	6 km	0	0

Table B.20: Results from the Randomization Analysis of 3-D TRMM-3A25 Conditional Statistics v. Forest Cover (Part c); The count of times that the conditional statistic difference is greater than the upper 99% confidence bound, and the count of the number of times that the difference is less than the lower 99% confidence bound are summarized.

Difference Statistic	Level	>↑99% Limit	<↓99% Limit
Measured Reflectivity (Zm)	Avg.	0	0
	2 km	0	0
	4 km	0	0
	6 km	0	0
Stratiform Zm	Avg.	0	0
	2 km	0	0
	4 km	0	1
	6 km	0	0
Convective Zm	Avg.	0	1
	2 km	0	0
	4 km	0	0
	6 km	1	0
Corrected Reflectivity (Zt)	Avg.	0	0
	2 km	0	0
	4 km	0	0
	6 km	0	0
Stratiform Zt	Avg.	0	0
	2 km	0	0
	4 km	0	0
	6 km	0	0
Convective Zt	Avg.	0	1
	2 km	0	1
	4 km	0	0
	6 km	1	0

Table B.21: Results from the Binomial Analysis of 2-D TRMM-3A25 Conditional Statistics v. Elevation (Part a); The count of positive and negative conditional statistic differences is compared to the binomial distribution to detect significant biases. The ranges are the percentile cutoffs used to create a binary ("high" v. "low") field from the original DEM (e. g., a range of "30" specifies the difference of the statistic between the 30% highest pixels and the 70% lowest.)

Difference Statistic	Range	>0	<0	Significance
Surface Rain Mean Intensity	30	42	34	—
	50	46	30	$p \leqslant 0.09$
	70	39	37	—
Surface Rain Std. Dev.	30	44	32	—
	50	43	33	—
	70	40	36	—
Surface Rain All Mean Intensity	30	42	34	—
	50	46	30	$p \leqslant 0.09$
	70	39	37	—
Surface Rain All Std. Dev.	30	44	32	—
	50	43	33	—
	70	40	36	—

Table B.22: Results from the Binomial Analysis of 2-D TRMM-3A25 Conditional Statistics v. Elevation (Part b); The count of positive and negative conditional statistic differences is compared to the binomial distribution to detect significant biases. The ranges are the percentile cutoffs used to create a binary ("high" v. "low") field from the original DEM (e. g., a range of "30" specifies the difference of the statistic between the 30% highest pixels and the 70% lowest.)

Difference Statistic	Range	>0	<0	Significance
Bright Band Height Mean	30	29	44	$p \leqslant 0.11$
	50	32	40	—
	70	31	41	—
Bright Band Height Std. Dev.	30	40	33	—
	50	40	32	—
	70	44	28	$p \leqslant 0.08$
Bright Band Zmax Mean	30	30	43	—
	50	32	40	—
	70	35	37	—
Bright Band Zmax Std. Dev.	30	31	42	—
	50	34	38	—
	70	33	39	—
Storm Height Mean	30	37	39	—
	50	38	38	—
	70	42	34	—
Stratiform Storm Height Mean	30	32	44	—
	50	38	38	—
	70	40	36	—
Convective Storm Height Mean	30	40	36	—
	50	41	34	—
	70	42	33	—
Storm Height Std. Dev.	30	39	37	—
	50	45	31	—
	70	39	37	—
Strat. Storm Height Std. Dev.	30	31	45	—
	50	38	38	—
	70	34	42	—
Conv. Storm Height Std. Dev.	30	43	33	—
	50	38	37	—
	70	37	38	—

Table B.23: Results from the Binomial Analysis of 2-D TRMM-3A25 Conditional Statistics v. Elevation (Part c); The count of positive and negative conditional statistic differences is compared to the binomial distribution to detect significant biases. The ranges are the percentile cutoffs used to create a binary ("high" v. "low") field from the original DEM (e. g., a range of "30" specifies the difference of the statistic between the 30% highest pixels and the 70% lowest.)

Difference Statistic	Range	>0	<0	Significance
Surface Rain Pixel Counts	30	28	48	$p \leqslant 0.03$
	50	26	50	$p \leqslant 0.008$
	70	29	47	$p \leqslant 0.06$
Surface Rain All Pixel Counts	30	28	48	$p \leqslant 0.03$
	50	26	50	$p \leqslant 0.008$
	70	29	47	$p \leqslant 0.06$
Bright Band Pixel Counts	30	23	53	$p \leqslant 0.0008$
	50	31	45	—
	70	32	44	—
Warm Rain Pixel Counts	30	24	50	$p \leqslant 0.004$
	50	26	45	$p \leqslant 0.04$
	70	25	49	$p \leqslant 0.004$
Total Pixel Counts	30	48	28	$p \leqslant 0.03$
	50	55	21	$p \leqslant 0.0002$
	70	59	17	$p \leqslant 0.0001$

Table B.24: Results from the Randomization Analysis of 2-D TRMM-3A25 Conditional Statistics v. Elevation (Part a); The count of times that the conditional statistic difference is greater than the upper 99% confidence bound, and the count of the number of times that the difference is less than the lower 99% confidence bound are summarized. The ranges are the percentile cutoffs used to create a binary ("high" v. "low") field from the original DEM (e. g., a range of "30" specifies the difference of the statistic between the 30% highest pixels and the 70% lowest.)

Difference Statistic	Range	$>\uparrow$99% Limit	$<\downarrow$99% Limit
	30	3	1
Surface Rain Mean Intensity	50	2	2
	70	3	1
	30	3	0
Surface Rain Std. Dev.	50	3	2
	70	3	1
	30	4	1
Surface Rain All Mean Intensity	50	2	2
	70	3	1
	30	3	0
Surface Rain All Std. Dev.	50	3	2
	70	3	1

Table B.25: Results from the Randomization Analysis of 2-D TRMM-3A25 Conditional Statistics v. Elevation (Part b); The count of times that the conditional statistic difference is greater than the upper 99% confidence bound, and the count of the number of times that the difference is less than the lower 99% confidence bound are summarized. The ranges are the percentile cutoffs used to create a binary ("high" v. "low") field from the original DEM (e. g., a range of "30" specifies the difference of the statistic between the 30% highest pixels and the 70% lowest.)

Difference Statistic	Range	$>\uparrow$99% Limit	$<\downarrow$99% Limit
	30	0	0
Bright Band Height Mean	50	0	2
	70	0	1
	30	1	1
Bright Band Height Std. Dev.	50	1	0
	70	0	0
	30	1	2
Bright Band Zmax Mean	50	0	1
	70	0	1
	30	0	2
Bright Band Zmax Std. Dev.	50	0	0
	70	0	4
	30	1	0
Storm Height Mean	50	1	0
	70	0	2
	30	1	0
Stratiform Storm Height Mean	50	0	1
	70	1	1
	30	3	0
Convective Storm Height Mean	50	2	0
	70	0	2
	30	3	0
Storm Height Std. Dev.	50	2	0
	70	1	0
	30	2	0
Strat. Storm Height Std. Dev.	50	1	0
	70	0	0
	30	1	0
Conv. Storm Height Std. Dev.	50	1	1
	70	1	1

Table B.26: Results from the Randomization Analysis of 2-D TRMM-3A25 Conditional Statistics v. Elevation (Part c); The count of times that the conditional statistic difference is greater than the upper 99% confidence bound, and the count of the number of times that the difference is less than the lower 99% confidence bound are summarized. The ranges are the percentile cutoffs used to create a binary ("high" v. "low") field from the original DEM (e. g., a range of "30" specifies the difference of the statistic between the 30% highest pixels and the 70% lowest.)

Difference Statistic	Range	$>\uparrow$99% Limit	$<\downarrow$99% Limit
	30	0	2
Surface Rain Pixel Counts	50	0	4
	70	1	6
	30	0	2
Surface Rain All Pixel Counts	50	0	4
	70	1	6
	30	0	2
Bright Band Pixel Counts	50	0	4
	70	1	2
	30	1	1
Warm Rain Pixel Counts	50	0	1
	70	0	0
	30	0	0
Total Pixel Counts	50	0	1
	70	2	1

Table B.27: Results from the Binomial Analysis of 2-D TRMM-3A25 Conditional Statistics v. Slope (Part a); The count of positive and negative conditional statistic differences is compared to the binomial distribution to detect significant biases. The ranges are the percentile cutoffs used to create a binary ("steep" v. "gradual") field from the original DEM (e. g., a range of "30" specifies the difference of the statistic between the 30% steepest pixels and the 70% most gradual.)

Difference Statistic	Range	>0	<0	Significance
Surface Rain Mean Intensity	30	45	31	—
	50	37	39	—
	70	47	29	$p \leqslant 0.06$
Surface Rain Std. Dev.	30	50	26	$p \leqslant 0.008$
	50	44	32	—
	70	45	31	—
Surface Rain All Mean Intensity	30	45	31	—
	50	37	39	—
	70	47	29	$p \leqslant 0.06$
Surface Rain All Std. Dev.	30	50	26	$p \leqslant 0.008$
	50	44	32	—
	70	45	31	—

Table B.28: Results from the Binomial Analysis of 2-D TRMM-3A25 Conditional Statistics v. Slope (Part b); The count of positive and negative conditional statistic differences is compared to the binomial distribution to detect significant biases. The ranges are the percentile cutoffs used to create a binary ("steep" v. "gradual") field from the original DEM (e. g., a range of "30" specifies the difference of the statistic between the 30% steepest pixels and the 70% most gradual.)

Difference Statistic	Range	>0	<0	Significance
Bright Band Height Mean	30	29	44	$p \leqslant 0.11$
	50	30	44	—
	70	31	43	—
Bright Band Height Std. Dev.	30	41	32	—
	50	41	33	—
	70	37	37	—
Bright Band Zmax Mean	30	34	39	—
	50	37	37	—
	70	35	39	—
Bright Band Zmax Std. Dev.	30	39	34	—
	50	41	33	—
	70	41	33	—
Storm Height Mean	30	35	41	—
	50	37	39	—
	70	40	36	—
Stratiform Storm Height Mean	30	36	40	—
	50	41	35	—
	70	45	31	—
Convective Storm Height Mean	30	46	30	$p \leqslant 0.09$
	50	43	33	—
	70	41	34	—
Storm Height Std. Dev.	30	40	36	—
	50	36	40	—
	70	39	37	—
Strat. Storm Height Std. Dev.	30	41	35	—
	50	33	43	—
	70	35	41	—
Conv. Storm Height Std. Dev.	30	34	42	—
	50	41	35	—
	70	41	34	—

Table B.29: Results from the Binomial Analysis of 2-D TRMM-3A25 Conditional Statistics v. Slope (Part c); The count of positive and negative conditional statistic differences is compared to the binomial distribution to detect significant biases. The ranges are the percentile cutoffs used to create a binary ("steep" v. "gradual") field from the original DEM (e. g., a range of "30" specifies the difference of the statistic between the 30% steepest pixels and the 70% most gradual.)

Difference Statistic	Range	>0	<0	Significance
Surface Rain Pixel Counts	30	41	35	—
	50	44	32	—
	70	41	35	—
Surface Rain All Pixel Counts	30	41	35	—
	50	44	32	—
	70	41	35	—
Bright Band Pixel Counts	30	36	40	—
	50	36	40	—
	70	39	37	—
Warm Rain Pixel Counts	30	29	45	$p \leqslant 0.09$
	50	28	41	—
	70	35	39	—
Total Pixel Counts	30	41	35	—
	50	43	33	—
	70	44	32	—

Table B.30: Results from the Randomization Analysis of 2-D TRMM-3A25 Conditional Statistics v. Slope (Part a); The count of times that the conditional statistic difference is greater than the upper 99% confidence bound, and the count of the number of times that the difference is less than the lower 99% confidence bound are summarized. The ranges are the percentile cutoffs used to create a binary ("steep" v. "gradual") field from the original DEM (e. g., a range of "30" specifies the difference of the statistic between the 30% steepest pixels and the 70% most gradual.)

Difference Statistic	Range	$>\uparrow$99% Limit	$<\downarrow$99% Limit
Surface Rain Mean Intensity	30	0	0
	50	2	0
	70	0	0
Surface Rain Std. Dev.	30	0	0
	50	1	0
	70	0	0
Surface Rain All Mean Intensity	30	0	0
	50	2	0
	70	0	0
Surface Rain All Std. Dev.	30	0	0
	50	1	0
	70	0	0

Table B.31: Results from the Randomization Analysis of 2-D TRMM-3A25 Conditional Statistics v. Slope (Part b); The count of times that the conditional statistic difference is greater than the upper 99% confidence bound, and the count of the number of times that the difference is less than the lower 99% confidence bound are summarized. The ranges are the percentile cutoffs used to create a binary ("steep" v. "gradual") field from the original DEM (e. g., a range of "30" specifies the difference of the statistic between the 30% steepest pixels and the 70% most gradual.)

Difference Statistic	Range	$>\uparrow$99% Limit	$<\downarrow$99% Limit
Bright Band Height Mean	30	0	0
	50	0	0
	70	1	1
Bright Band Height Std. Dev.	30	1	0
	50	0	0
	70	0	0
Bright Band Zmax Mean	30	1	0
	50	1	0
	70	1	0
Bright Band Zmax Std. Dev.	30	0	1
	50	0	0
	70	0	0
Storm Height Mean	30	0	0
	50	2	1
	70	0	0
Stratiform Storm Height Mean	30	0	0
	50	1	0
	70	0	0
Convective Storm Height Mean	30	1	1
	50	4	0
	70	0	0
Storm Height Std. Dev.	30	0	0
	50	1	0
	70	1	2
Strat. Storm Height Std. Dev.	30	1	0
	50	1	2
	70	0	0
Conv. Storm Height Std. Dev.	30	1	0
	50	0	0
	70	0	0

Table B.32: Results from the Randomization Analysis of 2-D TRMM-3A25 Conditional Statistics v. Slope (Part c); The count of times that the conditional statistic difference is greater than the upper 99% confidence bound, and the count of the number of times that the difference is less than the lower 99% confidence bound are summarized. The ranges are the percentile cutoffs used to create a binary ("steep" v. "gradual") field from the original DEM (e. g., a range of "30" specifies the difference of the statistic between the 30% steepest pixels and the 70% most gradual.)

Difference Statistic	Range	$>\uparrow$99% Limit	$<\downarrow$99% Limit
Surface Rain Pixel Counts	30	0	0
	50	0	0
	70	0	0
Surface Rain All Pixel Counts	30	0	0
	50	0	0
	70	0	0
Bright Band Pixel Counts	30	0	0
	50	0	0
	70	0	0
Warm Rain Pixel Counts	30	0	0
	50	1	0
	70	1	0
Total Pixel Counts	30	0	0
	50	0	0
	70	0	0

Table B.33: Results from the Binomial Analysis of 3-D TRMM-3A25 Conditional Statistics v. Elevation (Part a); The count of positive and negative conditional statistic differences is compared to the binomial distribution to detect significant biases. The ranges are the percentile cutoffs used to create a binary ("high" v. "low") field from the original DEM (e. g., a range of "30" specifies the difference of the statistic between the 30% highest pixels and the 70% lowest.)

Difference Statistic	Level	Range	>0 Counts	<0 Counts	Significance
Rain Mean	Avg.	30	41	35	—
		50	45	31	$p \leqslant 0.14$
		70	37	39	—
	2 km	30	44	32	—
		50	46	30	$p \leqslant 0.09$
		70	38	38	—
	4 km	30	37	39	—
		50	36	40	—
		70	36	40	—
	6 km	30	47	29	$p \leqslant 0.06$
		50	45	31	$p \leqslant 0.14$
		70	43	33	—
Rain Std. Dev.	Avg.	30	46	30	$p \leqslant 0.09$
		50	44	32	—
		70	40	36	—
	2 km	30	48	28	$p \leqslant 0.03$
		50	40	36	—
		70	41	35	—
	4 km	30	45	31	$p \leqslant 0.14$
		50	42	34	—
		70	39	37	—
	6 km	30	51	25	$p \leqslant 0.004$
		50	47	29	$p \leqslant 0.06$
		70	41	35	—

Table B.34: Results from the Binomial Analysis of 3-D TRMM-3A25 Conditional Statistics v. Elevation (Part b); The count of positive and negative conditional statistic differences is compared to the binomial distribution to detect significant biases. The ranges are the percentile cutoffs used to create a binary ("high" v. "low") field from the original DEM (e. g., a range of "30" specifies the difference of the statistic between the 30% highest pixels and the 70% lowest.)

Difference Statistic	Level	Range	>0 Counts	<0 Counts	Significance
Conv. Rain Mean	Avg.	30	38	38	—
		50	42	33	—
		70	38	37	—
	2 km	30	40	36	—
		50	42	33	—
		70	38	37	—
	4 km	30	37	39	—
		50	40	35	—
		70	38	37	—
	6 km	30	42	33	—
		50	42	32	—
		70	38	36	—
Conv. Rain Std. Dev.	Avg.	30	46	30	$p \leqslant 0.09$
		50	43	32	—
		70	37	38	—
	2 km	30	43	33	—
		50	42	33	
		70	39	36	—
	4 km	30	44	32	—
		50	44	31	—
		70	33	42	—
	6 km	30	46	29	$p \leqslant 0.07$
		50	43	31	—
		70	38	36	—

Table B.35: Results from the Binomial Analysis of 3-D TRMM-3A25 Conditional Statistics v. Elevation (Part c); The count of positive and negative conditional statistic differences is compared to the binomial distribution to detect significant biases. The ranges are the percentile cutoffs used to create a binary ("high" v. "low") field from the original DEM (e. g., a range of "30" specifies the difference of the statistic between the 30% highest pixels and the 70% lowest.)

Difference Statistic	Level	Range	>0 Counts	<0 Counts	Significance
Strat. Rain Mean	Avg.	30	31	45	$p \leqslant 0.14$
		50	31	45	$p \leqslant 0.14$
		70	38	38	—
	2 km	30	32	44	—
		50	36	40	—
		70	37	39	—
	4 km	30	30	46	$p \leqslant 0.09$
		50	32	44	—
		70	36	40	—
	6 km	30	31	45	$p \leqslant 0.14$
		50	32	44	—
		70	41	34	—
Strat. Rain Std. Dev.	Avg.	30	36	40	—
		50	34	42	—
		70	34	42	—
	2 km	30	36	40	—
		50	36	40	—
		70	32	44	—
	4 km	30	35	41	—
		50	33	43	—
		70	33	43	—
	6 km	30	44	32	—
		50	49	27	$p \leqslant 0.02$
		70	38	37	—

Table B.36: Results from the Binomial Analysis of 3-D TRMM-3A25 Conditional Statistics v. Elevation (Part d); The count of positive and negative conditional statistic differences is compared to the binomial distribution to detect significant biases. The ranges are the percentile cutoffs used to create a binary ("high" v. "low") field from the original DEM (e. g., a range of "30" specifies the difference of the statistic between the 30% highest pixels and the 70% lowest.)

Difference Statistic	Level	Range	>0 Counts	<0 Counts	Significance
Rain Pixels	Avg.	30	30	46	$p \leqslant 0.09$
		50	29	47	$p \leqslant 0.06$
		70	28	47	$p \leqslant 0.04$
	2 km	30	25	51	$p \leqslant 0.004$
		50	28	48	$p \leqslant 0.03$
		70	28	48	$p \leqslant 0.03$
	4 km	30	30	46	$p \leqslant 0.09$
		50	30	46	$p \leqslant 0.09$
		70	28	48	$p \leqslant 0.03$
	6 km	30	28	48	$p \leqslant 0.03$
		50	30	46	$p \leqslant 0.09$
		70	30	46	$p \leqslant 0.09$

Table B.37: Results from the Binomial Analysis of 3-D TRMM-3A25 Conditional Statistics v. Elevation (Part e); The count of positive and negative conditional statistic differences is compared to the binomial distribution to detect significant biases. The ranges are the percentile cutoffs used to create a binary ("high" v. "low") field from the original DEM (e. g., a range of "30" specifies the difference of the statistic between the 30% highest pixels and the 70% lowest.)

Difference Statistic	Level	Range	>0 Counts	<0 Counts	Significance
Conv. Rain Pixels	Avg.	30	45	31	$p \leqslant 0.14$
		50	42	34	—
		70	37	39	—
	2 km	30	45	31	$p \leqslant 0.14$
		50	40	36	—
		70	37	39	—
	4 km	30	45	31	$p \leqslant 0.14$
		50	42	34	—
		70	38	38	—
	6 km	30	42	34	—
		50	41	34	—
		70	39	37	—
Strat. Rain Pixels	Avg.	30	26	50	$p \leqslant 0.008$
		50	25	51	$p \leqslant 0.004$
		70	29	47	$p \leqslant 0.06$
	2 km	30	27	49	$p \leqslant 0.02$
		50	26	50	$p \leqslant 0.008$
		70	29	47	$p \leqslant 0.06$
	4 km	30	27	49	$p \leqslant 0.02$
		50	28	48	$p \leqslant 0.03$
		70	28	48	$p \leqslant 0.03$
	6 km	30	25	51	$p \leqslant 0.004$
		50	29	46	$p \leqslant 0.07$
		70	29	47	$p \leqslant 0.06$

Table B.38: Results from the Binomial Analysis of 3-D TRMM-3A25 Conditional Statistics v. Elevation (Part f); The count of positive and negative conditional statistic differences is compared to the binomial distribution to detect significant biases. The ranges are the percentile cutoffs used to create a binary ("high" v. "low") field from the original DEM (e. g., a range of "30" specifies the difference of the statistic between the 30% highest pixels and the 70% lowest.)

Difference Statistic	Level	Range	>0 Counts	<0 Counts	Significance
Measured Reflectivity (Zm)	Avg.	30	36	40	—
		50	37	39	—
		70	37	39	—
	2 km	30	40	36	—
		50	35	41	—
		70	39	37	—
	4 km	30	27	49	$p \leqslant 0.02$
		50	30	46	$p \leqslant 0.09$
		70	34	42	—
	6 km	30	36	40	—
		50	38	38	—
		70	39	37	—
Corrected Reflectivity (Zt)	Avg.	30	36	40	—
		50	38	38	—
		70	37	39	—
	2 km	30	42	34	—
		50	37	39	—
		70	40	36	—
	4 km	30	28	48	$p \leqslant 0.03$
		50	30	46	$p \leqslant 0.09$
		70	33	43	—
	6 km	30	34	42	—
		50	40	36	—
		70	38	38	—

Table B.39: Results from the Binomial Analysis of 3-D TRMM-3A25 Conditional Statistics v. Elevation (Part g); The count of positive and negative conditional statistic differences is compared to the binomial distribution to detect significant biases. The ranges are the percentile cutoffs used to create a binary ("high" v. "low") field from the original DEM (e. g., a range of "30" specifies the difference of the statistic between the 30% highest pixels and the 70% lowest.)

Difference Statistic	Level	Range	>0 Counts	<0 Counts	Significance
Stratiform Zm	Avg.	30	28	48	$p \leqslant 0.03$
		50	30	46	$p \leqslant 0.09$
		70	37	39	—
	2 km	30	36	40	—
		50	40	36	—
		70	39	37	—
	4 km	30	31	45	$p \leqslant 0.14$
		50	33	43	—
		70	35	41	—
	6 km	30	32	44	—
		50	36	40	—
		70	42	33	—
Stratiform Zt	Avg.	30	28	48	$p \leqslant 0.03$
		50	30	46	$p \leqslant 0.09$
		70	36	40	—
	2 km	30	37	39	—
		50	40	36	—
		70	41	35	—
	4 km	30	32	44	—
		50	33	43	—
		70	35	41	—
	6 km	30	32	44	—
		50	34	42	—
		70	39	36	—

Table B.40: Results from the Binomial Analysis of 3-D TRMM-3A25 Conditional Statistics v. Elevation (Part h); The count of positive and negative conditional statistic differences is compared to the binomial distribution to detect significant biases. The ranges are the percentile cutoffs used to create a binary ("high" v. "low") field from the original DEM (e. g., a range of "30" specifies the difference of the statistic between the 30% highest pixels and the 70% lowest.)

Difference Statistic	Level	Range	>0 Counts	<0 Counts	Significance
Convective Zm	Avg.	30	41	35	—
		50	41	34	—
		70	33	42	—
	2 km	30	40	36	—
		50	36	39	—
		70	37	38	—
	4 km	30	40	36	—
		50	40	35	—
		70	40	35	—
	6 km	30	37	38	—
		50	40	34	—
		70	39	35	—
Convective Zt	Avg.	30	38	38	—
		50	41	34	—
		70	33	42	—
	2 km	30	38	38	—
		50	40	35	—
		70	35	40	—
	4 km	30	42	34	—
		50	40	35	—
		70	40	35	—
	6 km	30	36	39	—
		50	41	34	—
		70	37	37	—

Table B.41: Results from the Randomization Analysis of 3-D TRMM-3A25 Conditional Statistics v. Elevation (Part a); The count of times that the conditional statistic difference is greater than the upper 99% confidence bound, and the count of the number of times that the difference is less than the lower 99% confidence bound are summarized. The ranges are the percentile cutoffs used to create a binary ("high" v. "low") field from the original DEM (e. g., a range of "30" specifies the difference of the statistic between the 30% highest pixels and the 70% lowest.)

Difference Statistic	Level	Range	>↑99% Limit	<↓99% Limit
Rain Mean	Avg.	30	3	0
		50	1	2
		70	2	2
	2 km	30	3	1
		50	3	2
		70	3	2
	4 km	30	1	0
		50	2	2
		70	2	2
	6 km	30	2	0
		50	2	1
		70	1	0
Rain Std. Dev.	Avg.	30	1	0
		50	3	2
		70	3	1
	2 km	30	2	1
		50	2	2
		70	3	1
	4 km	30	1	0
		50	0	1
		70	3	1
	6 km	30	1	0
		50	2	1
		70	1	0

Table B.42: Results from the Randomization Analysis of 3-D TRMM-3A25 Conditional Statistics v. Elevation (Part b); The count of times that the conditional statistic difference is greater than the upper 99% confidence bound, and the count of the number of times that the difference is less than the lower 99% confidence bound are summarized. The ranges are the percentile cutoffs used to create a binary ("high" v. "low") field from the original DEM (e. g., a range of "30" specifies the difference of the statistic between the 30% highest pixels and the 70% lowest.)

Difference Statistic	Level	Range	>↑99% Limit	<↓99% Limit
Conv. Rain Mean	Avg.	30	2	0
		50	0	2
		70	3	0
	2 km	30	1	1
		50	1	1
		70	1	0
	4 km	30	2	1
		50	1	2
		70	0	1
	6 km	30	3	2
		50	2	2
		70	0	0
Conv. Rain Std. Dev.	Avg.	30	1	0
		50	2	0
		70	2	1
	2 km	30	1	0
		50	3	0
		70	4	0
	4 km	30	0	0
		50	1	1
		70	1	1
	6 km	30	3	2
		50	2	2
		70	0	1

Table B.43: Results from the Randomization Analysis of 3-D TRMM-3A25 Conditional Statistics v. Elevation (Part c); The count of times that the conditional statistic difference is greater than the upper 99% confidence bound, and the count of the number of times that the difference is less than the lower 99% confidence bound are summarized. The ranges are the percentile cutoffs used to create a binary ("high" v. "low") field from the original DEM (e. g., a range of "30" specifies the difference of the statistic between the 30% highest pixels and the 70% lowest.)

Difference Statistic	Level	Range	>↑99% Limit	<↓99% Limit
Strat. Rain Mean	Avg.	30	0	1
		50	0	2
		70	0	1
	2 km	30	0	1
		50	0	3
		70	0	1
	4 km	30	0	0
		50	0	2
		70	0	1
	6 km	30	0	0
		50	1	1
		70	1	0
Strat. Rain Std. Dev.	Avg.	30	1	0
		50	2	1
		70	0	1
	2 km	30	1	0
		50	0	1
		70	0	1
	4 km	30	0	0
		50	0	1
		70	1	2
	6 km	30	2	0
		50	2	0
		70	1	0

Table B.44: Results from the Randomization Analysis of 3-D TRMM-3A25 Conditional Statistics v. Elevation (Part d); The count of times that the conditional statistic difference is greater than the upper 99% confidence bound, and the count of the number of times that the difference is less than the lower 99% confidence bound are summarized. The ranges are the percentile cutoffs used to create a binary ("high" v. "low") field from the original DEM (e. g., a range of "30" specifies the difference of the statistic between the 30% highest pixels and the 70% lowest.)

Difference Statistic	Level	Range	>↑99% Limit	<↓99% Limit
Rain Pixels	Avg.	30	0	2
		50	0	4
		70	0	4
	2 km	30	0	2
		50	0	3
		70	0	6
	4 km	30	0	2
		50	0	3
		70	0	6
	6 km	30	0	0
		50	1	3
		70	0	4

Table B.45: Results from the Randomization Analysis of 3-D TRMM-3A25 Conditional Statistics v. Elevation (Part e); The count of times that the conditional statistic difference is greater than the upper 99% confidence bound, and the count of the number of times that the difference is less than the lower 99% confidence bound are summarized. The ranges are the percentile cutoffs used to create a binary ("high" v. "low") field from the original DEM (e. g., a range of "30" specifies the difference of the statistic between the 30% highest pixels and the 70% lowest.)

Difference Statistic	Level	Range	>↑99% Limit	<↓99% Limit
Conv. Rain Pixels	Avg.	30	1	1
		50	2	1
		70	1	4
	2 km	30	1	1
		50	2	1
		70	1	4
	4 km	30	2	1
		50	2	1
		70	1	3
	6 km	30	2	2
		50	1	1
		70	1	2
Strat. Rain Pixels	Avg.	30	0	2
		50	0	4
		70	0	7
	2 km	30	0	2
		50	0	4
		70	0	6
	4 km	30	0	2
		50	0	5
		70	0	6
	6 km	30	0	3
		50	0	5
		70	1	3

Table B.46: Results from the Randomization Analysis of 3-D TRMM-3A25 Conditional Statistics v. Elevation (Part f); The count of times that the conditional statistic difference is greater than the upper 99% confidence bound, and the count of the number of times that the difference is less than the lower 99% confidence bound are summarized. The ranges are the percentile cutoffs used to create a binary ("high" v. "low") field from the original DEM (e. g., a range of "30" specifies the difference of the statistic between the 30% highest pixels and the 70% lowest.)

Difference Statistic	Level	Range	>↑99% Limit	<↓99% Limit
Measured Reflectivity (Zm)	Avg.	30	1	0
		50	1	2
		70	1	4
	2 km	30	2	0
		50	1	3
		70	0	1
	4 km	30	1	0
		50	1	2
		70	1	6
	6 km	30	3	0
		50	2	1
		70	1	1
Corrected Reflectivity (Zt)	Avg.	30	1	0
		50	1	2
		70	1	4
	2 km	30	2	0
		50	1	3
		70	1	0
	4 km	30	1	0
		50	1	2
		70	1	6
	6 km	30	1	0
		50	1	1
		70	1	1

Table B.47: Results from the Randomization Analysis of 3-D TRMM-3A25 Conditional Statistics v. Elevation (Part g); The count of times that the conditional statistic difference is greater than the upper 99% confidence bound, and the count of the number of times that the difference is less than the lower 99% confidence bound are summarized. The ranges are the percentile cutoffs used to create a binary ("high" v. "low") field from the original DEM (e. g., a range of "30" specifies the difference of the statistic between the 30% highest pixels and the 70% lowest.)

Difference Statistic	Level	Range	>↑99% Limit	<↓99% Limit
Stratiform Zm	Avg.	30	0	1
		50	0	1
		70	1	1
	2 km	30	0	1
		50	0	1
		70	1	1
	4 km	30	0	1
		50	0	2
		70	0	3
	6 km	30	0	0
		50	0	1
		70	1	1
Stratiform Zt	Avg.	30	0	1
		50	0	1
		70	1	1
	2 km	30	0	1
		50	0	1
		70	1	1
	4 km	30	0	1
		50	0	3
		70	0	3
	6 km	30	0	0
		50	0	1
		70	0	1

Table B.48: Results from the Randomization Analysis of 3-D TRMM-3A25 Conditional Statistics v. Elevation (Part h); The count of times that the conditional statistic difference is greater than the upper 99% confidence bound, and the count of the number of times that the difference is less than the lower 99% confidence bound are summarized. The ranges are the percentile cutoffs used to create a binary ("high" v. "low") field from the original DEM (e. g., a range of "30" specifies the difference of the statistic between the 30% highest pixels and the 70% lowest.)

Difference Statistic	Level	Range	>↑99% Limit	<↓99% Limit
Convective Zm	Avg.	30	2	2
		50	1	1
		70	2	0
	2 km	30	1	1
		50	0	3
		70	1	0
	4 km	30	1	1
		50	0	1
		70	0	0
	6 km	30	3	4
		50	1	1
		70	0	1
Convective Zt	Avg.	30	2	2
		50	0	0
		70	2	0
	2 km	30	1	1
		50	0	4
		70	2	1
	4 km	30	2	1
		50	0	1
		70	0	0
	6 km	30	4	4
		50	1	1
		70	0	1

Table B.49: Results from the Binomial Analysis of 3-D TRMM-3A25 Conditional Statistics v. Slope (Part a); The count of positive and negative conditional statistic differences is compared to the binomial distribution to detect significant biases. The ranges are the percentile cutoffs used to create a binary ("steep" v. "gradual") field from the original DEM (e. g., a range of "30" specifies the difference of the statistic between the 30% steepest pixels and the 70% most gradual.)

Difference Statistic	Level	Range	>0 Counts	<0 Counts	Significance
Rain Mean	Avg.	30	46	30	$p \leqslant 0.09$
		50	38	38	—
		70	42	34	—
	2 km	30	47	29	$p \leqslant 0.06$
		50	38	38	—
		70	45	31	$p \leqslant 0.14$
	4 km	30	47	29	$p \leqslant 0.06$
		50	40	36	—
		70	43	33	—
	6 km	30	47	29	$p \leqslant 0.06$
		50	44	32	—
		70	42	34	—
Rain Std. Dev.	Avg.	30	48	28	$p \leqslant 0.03$
		50	44	32	—
		70	45	31	$p \leqslant 0.14$
	2 km	30	49	27	$p \leqslant 0.02$
		50	43	33	—
		70	47	29	$p \leqslant 0.06$
	4 km	30	48	28	$p \leqslant 0.03$
		50	44	32	—
		70	46	30	$p \leqslant 0.09$
	6 km	30	48	28	$p \leqslant 0.03$
		50	44	32	—
		70	45	31	$p \leqslant 0.14$

Table B.50: Results from the Binomial Analysis of 3-D TRMM-3A25 Conditional Statistics v. Slope (Part b); The count of positive and negative conditional statistic differences is compared to the binomial distribution to detect significant biases. The ranges are the percentile cutoffs used to create a binary ("steep" v. "gradual") field from the original DEM (e. g., a range of "30" specifies the difference of the statistic between the 30% steepest pixels and the 70% most gradual.)

Difference Statistic	Level	Range	>0 Counts	<0 Counts	Significance
Conv. Rain Mean	Avg.	30	44	32	—
		50	38	38	—
		70	40	35	—
	2 km	30	44	32	—
		50	41	35	—
		70	44	31	—
	4 km	30	45	31	$p \leqslant 0.14$
		50	46	30	$p \leqslant 0.09$
		70	42	33	—
	6 km	30	42	34	—
		50	45	30	$p \leqslant 0.11$
		70	42	32	—
Conv. Rain Std. Dev.	Avg.	30	41	35	—
		50	43	33	—
		70	37	38	—
	2 km	30	44	32	—
		50	36	40	—
		70	44	31	—
	4 km	30	45	31	$p \leqslant 0.14$
		50	44	32	—
		70	44	31	—
	6 km	30	40	36	—
		50	38	37	—
		70	41	33	—

Table B.51: Results from the Binomial Analysis of 3-D TRMM-3A25 Conditional Statistics v. Slope (Part c); The count of positive and negative conditional statistic differences is compared to the binomial distribution to detect significant biases. The ranges are the percentile cutoffs used to create a binary ("steep" v. "gradual") field from the original DEM (e. g., a range of "30" specifies the difference of the statistic between the 30% steepest pixels and the 70% most gradual.)

Difference Statistic	Level	Range	>0 Counts	<0 Counts	Significance
Strat. Rain Mean	Avg.	30	32	44	—
		50	35	41	—
		70	35	41	—
	2 km	30	32	44	—
		50	34	42	—
		70	36	40	—
	4 km	30	31	45	$p \leqslant 0.14$
		50	33	43	—
		70	32	44	—
	6 km	30	42	34	—
		50	39	37	—
		70	38	38	—
Strat. Rain Std. Dev.	Avg.	30	38	38	—
		50	36	40	—
		70	37	39	—
	2 km	30	33	43	—
		50	39	37	—
		70	34	42	—
	4 km	30	37	39	—
		50	30	46	$p \leqslant 0.09$
		70	31	45	$p \leqslant 0.14$
	6 km	30	44	32	—
		50	44	32	—
		70	39	37	—

Table B.52: Results from the Binomial Analysis of 3-D TRMM-3A25 Conditional Statistics v. Slope (Part d); The count of positive and negative conditional statistic differences is compared to the binomial distribution to detect significant biases. The ranges are the percentile cutoffs used to create a binary ("steep" v. "gradual") field from the original DEM (e. g., a range of "30" specifies the difference of the statistic between the 30% steepest pixels and the 70% most gradual.)

Difference Statistic	Level	Range	>0 Counts	<0 Counts	Significance
Rain Pixels	Avg.	30	37	39	—
		50	42	34	—
		70	40	36	—
	2 km	30	40	36	—
		50	41	35	—
		70	38	38	—
	4 km	30	39	37	—
		50	42	34	—
		70	40	36	—
	6 km	30	37	39	—
		50	42	33	—
		70	40	36	—

Table B.53: Results from the Binomial Analysis of 3-D TRMM-3A25 Conditional Statistics v. Slope (Part e); The count of positive and negative conditional statistic differences is compared to the binomial distribution to detect significant biases. The ranges are the percentile cutoffs used to create a binary ("steep" v. "gradual") field from the original DEM (e. g., a range of "30" specifies the difference of the statistic between the 30% steepest pixels and the 70% most gradual.)

Difference Statistic	Level	Range	>0 Counts	<0 Counts	Significance
Conv. Rain Pixels	Avg.	30	44	32	—
		50	45	31	$p \leqslant 0.14$
		70	48	28	$p \leqslant 0.03$
	2 km	30	44	31	—
		50	45	31	$p \leqslant 0.14$
		70	47	29	$p \leqslant 0.06$
	4 km	30	45	31	$p \leqslant 0.14$
		50	46	30	$p \leqslant 0.09$
		70	45	31	$p \leqslant 0.14$
	6 km	30	46	30	$p \leqslant 0.09$
		50	50	26	$p \leqslant 0.008$
		70	42	34	—
Strat. Rain Pixels	Avg.	30	35	41	—
		50	38	38	—
		70	39	37	—
	2 km	30	35	41	—
		50	37	39	—
		70	41	35	—
	4 km	30	34	42	—
		50	39	37	—
		70	39	37	—
	6 km	30	34	42	—
		50	38	38	—
		70	38	38	—

Table B.54: Results from the Binomial Analysis of 3-D TRMM-3A25 Conditional Statistics v. Slope (Part f); The count of positive and negative conditional statistic differences is compared to the binomial distribution to detect significant biases. The ranges are the percentile cutoffs used to create a binary ("steep" v. "gradual") field from the original DEM (e. g., a range of "30" specifies the difference of the statistic between the 30% steepest pixels and the 70% most gradual.)

Difference Statistic	Level	Range	>0 Counts	<0 Counts	Significance
Measured Reflectivity (Zm)	Avg.	30	43	33	—
		50	40	36	—
		70	40	36	—
	2 km	30	45	31	$p \leqslant 0.14$
		50	43	33	—
		70	38	38	—
	4 km	30	38	38	—
		50	42	34	—
		70	38	38	—
	6 km	30	46	30	$p \leqslant 0.09$
		50	38	38	—
		70	40	36	—
Corrected Reflectivity (Zt)	Avg.	30	43	33	—
		50	42	34	—
		70	40	36	—
	2 km	30	46	30	$p \leqslant 0.09$
		50	43	33	—
		70	40	36	—
	4 km	30	38	38	—
		50	43	33	—
		70	38	38	—
	6 km	30	45	31	$p \leqslant 0.14$
		50	37	39	—
		70	40	36	—

Table B.55: Results from the Binomial Analysis of 3-D TRMM-3A25 Conditional Statistics v. Slope (Part g); The count of positive and negative conditional statistic differences is compared to the binomial distribution to detect significant biases. The ranges are the percentile cutoffs used to create a binary ("steep" v. "gradual") field from the original DEM (e. g., a range of "30" specifies the difference of the statistic between the 30% steepest pixels and the 70% most gradual.)

Difference Statistic	Level	Range	>0 Counts	<0 Counts	Significance
Stratiform Zm	Avg.	30	40	36	—
		50	36	40	—
		70	34	42	—
	2 km	30	42	34	—
		50	41	35	—
		70	34	42	—
	4 km	30	35	41	—
		50	35	41	—
		70	33	43	—
	6 km	30	43	33	—
		50	41	35	—
		70	39	37	—
Stratiform Zt	Avg.	30	38	38	—
		50	37	39	—
		70	38	38	—
	2 km	30	40	36	—
		50	41	35	—
		70	33	43	—
	4 km	30	36	40	—
		50	37	39	—
		70	33	43	—
	6 km	30	42	34	—
		50	39	37	—
		70	42	34	—

Table B.56: Results from the Binomial Analysis of 3-D TRMM-3A25 Conditional Statistics v. Slope (Part h); The count of positive and negative conditional statistic differences is compared to the binomial distribution to detect significant biases. The ranges are the percentile cutoffs used to create a binary ("steep" v. "gradual") field from the original DEM (e. g., a range of "30" specifies the difference of the statistic between the 30% steepest pixels and the 70% most gradual.)

Difference Statistic	Level	Range	>0 Counts	<0 Counts	Significance
Convective Zm	Avg.	30	46	30	$p \leqslant 0.09$
		50	40	36	—
		70	36	39	—
	2 km	30	43	33	—
		50	40	36	—
		70	38	37	—
	4 km	30	43	33	—
		50	47	29	$p \leqslant 0.06$
		70	45	30	$p \leqslant 0.11$
	6 km	30	40	36	—
		50	44	31	—
		70	47	27	$p \leqslant 0.03$
Convective Zt	Avg.	30	45	31	$p \leqslant 0.14$
		50	41	35	—
		70	40	35	—
	2 km	30	45	31	$p \leqslant 0.14$
		50	43	33	—
		70	40	35	—
	4 km	30	43	33	—
		50	47	29	$p \leqslant 0.06$
		70	45	30	$p \leqslant 0.11$
	6 km	30	42	34	—
		50	46	29	$p \leqslant 0.07$
		70	47	27	$p \leqslant 0.03$

Table B.57: Results from the Randomization Analysis of 3-D TRMM-3A25 Conditional Statistics v. Slope (Part a); The count of times that the conditional statistic difference is greater than the upper 99% confidence bound, and the count of the number of times that the difference is less than the lower 99% confidence bound are summarized. The ranges are the percentile cutoffs used to create a binary ("steep" v. "gradual") field from the original DEM (e. g., a range of "30" specifies the difference of the statistic between the 30% steepest pixels and the 70% most gradual.)

Difference Statistic	Level	Range	>↑99% Limit	<↓99% Limit
Rain Mean	Avg.	30	0	0
		50	0	0
		70	0	0
	2 km	30	0	0
		50	0	0
		70	0	0
	4 km	30	0	0
		50	1	0
		70	0	0
	6 km	30	0	0
		50	0	0
		70	0	0
Rain Std. Dev.	Avg.	30	0	0
		50	1	0
		70	0	0
	2 km	30	1	0
		50	1	0
		70	0	1
	4 km	30	0	0
		50	0	0
		70	0	0
	6 km	30	1	1
		50	0	1
		70	0	0

Table B.58: Results from the Randomization Analysis of 3-D TRMM-3A25 Conditional Statistics v. Slope (Part b); The count of times that the conditional statistic difference is greater than the upper 99% confidence bound, and the count of the number of times that the difference is less than the lower 99% confidence bound are summarized. The ranges are the percentile cutoffs used to create a binary ("steep" v. "gradual") field from the original DEM (e. g., a range of "30" specifies the difference of the statistic between the 30% steepest pixels and the 70% most gradual.)

Difference Statistic	Level	Range	$>\uparrow$99% Limit	$<\downarrow$99% Limit
Conv. Rain Mean	Avg.	30	2	0
		50	4	0
		70	1	0
	2 km	30	1	0
		50	2	0
		70	0	0
	4 km	30	1	0
		50	3	0
		70	0	0
	6 km	30	1	0
		50	2	0
		70	1	0
Conv. Rain Std. Dev.	Avg.	30	0	0
		50	1	0
		70	0	0
	2 km	30	1	0
		50	0	1
		70	0	0
	4 km	30	1	0
		50	0	0
		70	0	0
	6 km	30	1	1
		50	1	0
		70	0	1

Table B.59: Results from the Randomization Analysis of 3-D TRMM-3A25 Conditional Statistics v. Slope (Part c); The count of times that the conditional statistic difference is greater than the upper 99% confidence bound, and the count of the number of times that the difference is less than the lower 99% confidence bound are summarized. The ranges are the percentile cutoffs used to create a binary ("steep" v. "gradual") field from the original DEM (e. g., a range of "30" specifies the difference of the statistic between the 30% steepest pixels and the 70% most gradual.)

Difference Statistic	Level	Range	>↑99% Limit	<↓99% Limit
Strat. Rain Mean	Avg.	30	0	0
		50	1	0
		70	0	0
	2 km	30	0	0
		50	0	1
		70	0	0
	4 km	30	0	0
		50	0	0
		70	0	0
	6 km	30	0	0
		50	0	0
		70	0	0
Strat. Rain Std. Dev.	Avg.	30	0	0
		50	1	0
		70	0	0
	2 km	30	0	0
		50	0	0
		70	0	0
	4 km	30	1	0
		50	1	0
		70	0	0
	6 km	30	0	0
		50	0	0
		70	0	0

Table B.60: Results from the Randomization Analysis of 3-D TRMM-3A25 Conditional Statistics v. Slope (Part d); The count of times that the conditional statistic difference is greater than the upper 99% confidence bound, and the count of the number of times that the difference is less than the lower 99% confidence bound are summarized. The ranges are the percentile cutoffs used to create a binary ("steep" v. "gradual") field from the original DEM (e. g., a range of "30" specifies the difference of the statistic between the 30% steepest pixels and the 70% most gradual.)

Difference Statistic	Level	Range	>↑99% Limit	<↓99% Limit
Rain Pixels	Avg.	30	0	0
		50	0	0
		70	0	0
	2 km	30	0	0
		50	0	0
		70	1	0
	4 km	30	0	0
		50	0	0
		70	1	0
	6 km	30	0	0
		50	0	0
		70	1	0

Table B.61: Results from the Randomization Analysis of 3-D TRMM-3A25 Conditional Statistics v. Slope (Part e); The count of times that the conditional statistic difference is greater than the upper 99% confidence bound, and the count of the number of times that the difference is less than the lower 99% confidence bound are summarized. The ranges are the percentile cutoffs used to create a binary ("steep" v. "gradual") field from the original DEM (e. g., a range of "30" specifies the difference of the statistic between the 30% steepest pixels and the 70% most gradual.)

Difference Statistic	Level	Range	>↑99% Limit	<↓99% Limit
Conv. Rain Pixels	Avg.	30	0	0
		50	1	0
		70	0	0
	2 km	30	0	0
		50	1	0
		70	0	0
	4 km	30	0	0
		50	1	0
		70	0	0
	6 km	30	0	0
		50	1	0
		70	0	0
Strat. Rain Pixels	Avg.	30	0	0
		50	0	0
		70	0	0
	2 km	30	0	0
		50	0	0
		70	1	0
	4 km	30	0	0
		50	0	0
		70	0	0
	6 km	30	0	0
		50	0	0
		70	0	0

Table B.62: Results from the Randomization Analysis of 3-D TRMM-3A25 Conditional Statistics v. Slope (Part f); The count of times that the conditional statistic difference is greater than the upper 99% confidence bound, and the count of the number of times that the difference is less than the lower 99% confidence bound are summarized. The ranges are the percentile cutoffs used to create a binary ("steep" v. "gradual") field from the original DEM (e. g., a range of "30" specifies the difference of the statistic between the 30% steepest pixels and the 70% most gradual.)

Difference Statistic	Level	Range	>↑99% Limit	<↓99% Limit
Measured Reflectivity (Zm)	Avg.	30	0	0
		50	0	0
		70	0	0
	2 km	30	0	0
		50	1	0
		70	0	0
	4 km	30	0	0
		50	1	0
		70	0	0
	6 km	30	0	0
		50	0	0
		70	0	0
Corrected Reflectivity (Zt)	Avg.	30	0	0
		50	0	0
		70	0	0
	2 km	30	0	0
		50	1	0
		70	0	0
	4 km	30	0	0
		50	1	0
		70	0	0
	6 km	30	0	0
		50	0	0
		70	0	0

Table B.63: Results from the Randomization Analysis of 3-D TRMM-3A25 Conditional Statistics v. Slope (Part g); The count of times that the conditional statistic difference is greater than the upper 99% confidence bound, and the count of the number of times that the difference is less than the lower 99% confidence bound are summarized. The ranges are the percentile cutoffs used to create a binary ("steep" v. "gradual") field from the original DEM (e. g., a range of "30" specifies the difference of the statistic between the 30% steepest pixels and the 70% most gradual.)

Difference Statistic	Level	Range	$>\uparrow$99% Limit	$<\downarrow$99% Limit
Stratiform Zm	Avg.	30	0	0
		50	0	0
		70	0	0
	2 km	30	0	0
		50	1	0
		70	0	0
	4 km	30	0	0
		50	1	0
		70	0	0
	6 km	30	0	0
		50	0	0
		70	1	0
Stratiform Zt	Avg.	30	0	0
		50	0	0
		70	0	0
	2 km	30	0	0
		50	1	0
		70	0	0
	4 km	30	0	0
		50	1	0
		70	0	0
	6 km	30	0	0
		50	0	0
		70	1	0

Table B.64: Results from the Randomization Analysis of 3-D TRMM-3A25 Conditional Statistics v. Slope (Part h); The count of times that the conditional statistic difference is greater than the upper 99% confidence bound, and the count of the number of times that the difference is less than the lower 99% confidence bound are summarized. The ranges are the percentile cutoffs used to create a binary ("steep" v. "gradual") field from the original DEM (e. g., a range of "30" specifies the difference of the statistic between the 30% steepest pixels and the 70% most gradual.)

Difference Statistic	Level	Range	>↑99% Limit	<↓99% Limit
Convective Zm	Avg.	30	2	0
		50	4	1
		70	2	0
	2 km	30	1	0
		50	3	0
		70	0	0
	4 km	30	2	0
		50	3	1
		70	0	0
	6 km	30	2	0
		50	2	1
		70	0	0
Convective Zt	Avg.	30	2	0
		50	4	1
		70	2	0
	2 km	30	2	0
		50	3	0
		70	0	0
	4 km	30	2	0
		50	3	0
		70	0	0
	6 km	30	2	0
		50	2	0
		70	0	0

APPENDIX C

GOES CALIBRATION

C.1 McIDAS Source Code for Visible Channel Calibration

```
      SUBROUTINE MAIN0
C
C     *** McIDAS Revision History ***
C
C     17 MC.PGM 15-Feb-93,7:53:18,'USER' Released
C     —author/source of this code is unknown—
C
C     16-Jun-2002 Frederic Chagnon — Addition of comments throughout
C                                    code, and change algorithm
C                                                                      10
C     28-jan-2003 Frederic Chagnon — Change algorithm to Minnis et al.
C                                    JAOT 19(9) Sept. 2002 pp 1233-...
C
C
C     *** McIDAS Revision History ***
C
C     HELP FILE
C
C ? Name:
C ?    GOES8_VIS_CALIBRATION - Calculates bidiectional reflectance from      20
C ?                            raw brightness temperature and corrects
C ?                            for solar elevation angle
C ? Input:
C ?    AREA_IN    | Integer Number of AREA file that is to be converted
C ? Output:
C ?    AREA_OUT   | Integer Number ####, output stored in AREA####
C ? Remarks:
C ?    There seem to be many ways that the 0.65 micro-m visible sensor
C ?    on-board GOES-8 can be "calibrated" to reflectance. The empirical
C ?    formula often cited (e.g. Garand, J.Clim., 1988) is as follows:       30
C ?    REFLECANCE = ( a * BRIGHTNESS^2 + b ) / ( I cos(E) ) , where:
C ?    a, b and I are empirically set constants ( determined pre-launch
```

```
C ?    as a=0.00539 W/m^2 b=-2.67 W/m^2 I=336 W/m^2 ) , and E is the
C ?    solar elevation angle, and BRIGHTNESS is the 8-bit count.
C ?    Another formula (Weinreb & Huan, 1997) "calibrates" as follows:
C ?    R=100*0.0019279*0.5501873*r^2*(C10-C0), where r is the sun-earth
C ?    distance in astronomical units (=1 AU), C10 is the 10-bit
C ?    brightness count, and C0 is 29.
C ?    The original code uses the following algorithm:
C ?    new_brit = min(255, old_brit + old_brit (1-cos(sun_angle)))
C ?    The calibration used here will follow Garand, 1988:
C ?    R=(a*8-bit brightness^2+b)/(I cos E)
C ?
C ?    ADDENDUM (02/06/2003) Algorithm in Minnis et al. JAOT 19(9)
C ?    Sept. 2002 improves calibration. Their algorithm is used here:
C ?    R=(g0+dg(DSL))*(C10(SZA,VZA,AZMTH)-C0)/(SOLCNST*COS(SZA)*r(DOY))
C ?  ------
C
C-------------------------------------------------------------
C-------------------------------------------------------------
C
C   FUNCTIONS USED, AND THEIR DESCRIPTION:
C
C-------------------------------------------------------------
C
C-----FUNCTION IPP()
C       Name:
C            ipp - Fetches positional parameter in integer form.
C
C       Interface:
C            integer function
C            ipp(integer position, integer def)
C
C       Input:
C            position - Specifies which argument from argument sequence
C                       to fetch. (1-based), e.g., 1 specifies first
C                       positional param.
C            def - Number to use as missing value.
C
C       Input and Output:
C            none
C
C       Output:
C            none
C
C       Return values:
C            value - The requested argument's integer value,
C                    or 0 if it is invalid.
C
C       Remarks:
C            Obsolete function, replaced by mcargint.
C
C       Categories:
C            user_interface
C
C       Filename:
```

```
C            argold.c
C
C
C------FUNCTION OPNARA(AREA)                                          90
C       OPNARA - Collect list of track groups assigned to an area;
C       place them in the COMMON block
C       Input:
C         AREA = (I) input area
C       Returns:
C         OPNARA = PTR# into area COMMON of area just opened
C         OPNARA = AREA
C
C
C------FUNCTION ARAOPT()                                              100
C       araopt - Sets the options used when a McIDAS area is read.
C
C       Interface:
C            subroutine
C            araopt(integer area, integer nopt, character*(*) copt(*),
C                   integer val(*))
C
C       Input:
C            area     - McIDAS area number.
C            nopt     - Number of options to be set.                  110
C            copt     - Names of the options to be set.
C            val      - Value to set each option to.
C
C       Input and Output:
C            none
C
C       Output:
C            none
C
C       Return values:                                                120
C             none
C
C       Remarks:
C            The valid options and values are:
C            option  value
C            ------  -----
C            'SPAC'  spacing of output data (1, 2 or 4 bytes)
C            'PREC'  precision of stored data (1, 2 or 4 bytes)
C            'UNIT'  output physical quantity ('TEMP','BRIT','RAW',...)
C            'SCAL'  scale factor to apply to data                    130
C            'CALB'  name of package to calibrate data
C                    (1-4 character name)
C
C            Be sure that you have opened the area (OPNARA()) prior to
C            calling this routine.
C
C       Categories:
C            image
C            calibration
C                                                                     140
```

```
C----FUNCTION LIT()
C       Name:
C            lit      - Returns the four bytes of a character string
C                       as an integer.
C
C       Interface:
C            character*4 function
C            lit(integer c)
C
C       Input:                                                          150
C            c        - Character string that is copied to an integer.
C
C       Input and Output:
C            none
C
C       Output:
C            none
C
C       Return values:
C            The four bytes of the character string.                    160
C
C       Remarks:
C            This function is designed to move the four bytes of a
C            character string to an integer variable.  It enables
C            programmers to avoid conversions implicit in replacement
C            statements in which variables of different types are on
C            opposite sides of the equal sign.
C       Categories:
C            converter
C                                                                       170
C----FUNCTION READD()
C       SUBROUTINE READD(ANUM, ENTRY)  (RCD)
C       READS DIRECTORY ENTRY FROM AREA/SOUNDING DIRECTORY 'DATDIR'
C       ANUM = (I) INPUT  AREA NUMBER
C       ENTRY = (I) OUTPUT  64 WORD DIRECTORY ENTRY (INTEGER ARRAY)
C       READD = AREA
C
C----FUNCTION MAKARA()
C       SUBROUTINE MAKARA(AREA,ARADIR) (RCD)
C       MAKARA: AQUIRES STORAGE FOR A NEW AREA AND MAKES AREA DIR ENTRY  180
C               AREA - (I) INPUT  AREA NUMBER
C               ARADIR - (I) INPUT ARRAY CONTAINING NEW AREA DIRECTORY
C       MAKARA = AREA
C
C----FUNCTION ARAGET()
C       Name:
C            araget - Obtains bytes from a McIDAS area file.
C
C       Interface:
C            subroutine                                                 190
C            araget(integer area, integer offset, integer nbyte,
C                   integer outbuf(*))
C
C       Input:
```

```
C           area   - McIDAS area number.
C           offset - First byte to obtain.
C           nbyte  - Number of bytes to obtain.
C
C       Input and Output:
C           none                                                    200
C
C       Output:
C           outbuf - Array containing the requested data.
C
C       Return values:
C           none
C
C       Remarks:
C           This routine may return without the data if the area number
C           is not valid.  You may want to call ARANAM() before calling  210
C           this routine.
C
C           The bytes returned start at the offset.  The data does not
C           start at a scan line, a prefix or a validity code.
C
C       Categories:
C           image
C
C-----FUNCTION ARAPUT()
C       Name:                                                       220
C           araput   - Adds a buffer to an area file.
C
C       Interface:
C           subroutine
C           araput(integer area, integer offset, integer nbyte,
C                  integer iarray(*))
C
C       Input:
C           area   - Number of area which will be receiving data.
C           offset - Byte offset into file. The new data will start here.  230
C           nbyte  - Number of bytes to write.
C           iarray - Array of data to be written.
C
C       Input and Output:
C           none
C
C       Output:
C           none
C
C       Return values:                                              240
C           none
C
C       Remarks:
C           none
C
C       Categories:
C           image
C
```

```
C-----FUNCTION CLSARA()
C       Name:                                                          250
C            clsara - Closes a McIDAS area.
C
C       Interface:
C            subroutine
C            clsara(integer area)
C
C       Input:
C            area    - Number of MCIDAS area to be closed.
C
C       Input and Output:                                              260
C            none
C
C       Output:
C            none
C
C       Return values:
C            none
C
C       Remarks:
C            After calling this routine the only area access routine   270
C            that will work is opnara().
C
C       Categories:
C            image
C            file
C
C-----FUNCTION STAMP()
C       Name:
C            stamp - Builds an audit message and writes it to the area.
C                                                                       280
C       Interface:
C            subroutine
C            stamp(integer anum)
C
C       Input:
C            anum  - Area number.
C
C       Input and Output:
C            none
C                                                                       290
C       Output:
C            none
C
C       Return values:
C            none
C
C       Remarks:
C            Stamp fetches the command being audited, fetches the
C            current date and time, formats the message and writes
C            it to the area.                                           300
C
C       Categories:
```

```
C           image
C
C----FUNCTION FTIME()
C
C       Name:
C           ftime   - Converts a packed integer time value to a real.
C
C       Interface:                                                      310
C           real function
C           ftime(integer m)
C
C       Input:
C           m       - Time, formatted as:
C                     sign hhmmss.
C
C       Input and Output:
C           none
C                                                                       320
C       Output:
C           none
C
C       Return values:
C           The reformatted time.
C
C       Remarks:
C           The reformatted time is in terms of hours and fractions of
C           hours.  93500 is returned as 9.5833.
C                                                                       330
C           The sign can be negative.
C
C       Categories:
C           utility
C           converter
C           day/time
C
C----FUNCTION NVSET()
C       Name:
C           nvset   - Sets up navigation from a codicil.                340
C
C       Interface:
C           integer function
C           nvset(character*(*) copt, integer num)
C
C       Input:
C           copt    - 'AREA'  Navigation parameters will be from
C                             the area file.
C                     'FRAME' Navigation parameters will be from
C                             the frame directory.                      350
C
C       Input and Output:
C           none
C
C       Output:
C           none
```

```
C
C       Return values:
C            0      - Navigation was set up.
C           -1      - Input area or frame didn't exist.                    360
C           -2      - Navigation data couldn't be found.
C           -3      - The option was not correct.
C
C       Remarks:
C            none
C
C       Categories:
C            navigation
C
C-----FUNCTION REDARA()                                                    370
C       SUBROUTINE REDARA (AREA,LINE,ELEM,NELE,BAND,IARRAY)
C       REDARA - Read line from area returning specified subset of line
C       Input:
C         AREA = (I) area number
C         LINE = (I) line to read
C         ELEM = (I) starting element desired. 0 returns first byte
C                    of data
C         NELE = (I) number of elements. Will not return any past line
C                    end
C         BAND = Spectral band of desired data or 'ALL' for all bands      380
C       OUTPUT:
C         IARRAY = (I) array to hold returned data
C         REDARA = AREA
C
C-----FUNCTION WRTARA()
C       SUBROUTINE WRTARA(AREA,LINE,IARRAY)
C       WRTARA - write a line to an area
C       Input:
C         IAREA = (I) area number
C         NREC = (I) line number                                           390
C         IARRAY = (*) source of data, length dependant on area size
C         WRTARA = AREA
C
C-----FUNCTION NVXOPT()
C       FUNCTION NVXOPT(IFUNC,XIN,XOUT)
C
C        IFUNC= 'SPOS'    SUBSATELLITE LAT/LON
C
C          XIN  - NOT USED
C          XOUT - 1. SUB-SATELLITE LATITUDE                                400
C               - 2. SUB-SATELLITE LONGITUDE
C
C        IFUNC= 'ANG '   ANGLES
C
C          XIN - 1. SSYYDDD
C                2. TIME (HOURS)
C                3. LATITUDE
C                4. LONGITUDE (***** WEST NEGATIVE *****)
C          XOUT- 1. SATELLITE ANGLE
C                2. SUN ANGLE                                              410
```

```
C                3. RELATIVE ANGLE
C
C
C
C       IFUNC= 'HGT '   INPUT HEIGHT FOR PARALLAX
C
C          XIN - 1. HEIGHT (KM)
C
C----FUNCTION MPIXEL()
C       Name:                                                          420
C            mpixel - Moves 1,2, or 4 byte data into 1,2, or 4 byte
C                     fields. The data is moved within one array,
C                     not from one array to another.
C
C       Interface:
C            subroutine
C            mpixel (integer n, integer isou, integer ides,
C                    character ibuf)
C
C       Input:                                                         430
C            n       - Number of transfers to be made.
C            isou    - Byte size of the source fields in the buffer.
C            ides    - Byte size of the destination fields in the
C                      buffer.
C
C       Input and Output:
C            ibuf    - Array containing byte fields to be transferred.
C
C       Output:
C            none                                                      440
C
C       Return values:
C            none
C
C       Remarks:
C            none
C
C       Categories:
C            utility
C                                                                      450
C-------------------------------------------------------------
C-------------------------------------------------------------
```

```
      implicit none

      integer MXCDSZ
      parameter (MXCDSZ = 5*128)
      integer*4 navsiz
                                                                       460
      integer iadir(64),navarr(MXCDSZ)
      integer ia
      integer ioa
      integer ipp
```

```
      integer lit

C
C     GET AREAS
C
      IA=IPP(1,0)              ! sets number of input area                    470
      IOA=IPP(2,0)             ! sets number of output area

      CALL OPNARA(IA)          ! "opens" the input area
      CALL ARAOPT(IA,1,'SPAC',4) ! sets spacing of area output = 4bytes
      CALL ARAOPT(IA,1,'UNIT',LIT('RAW')) ! sets output unit
C
C     FORMAT OUPUT AREA
C
      CALL READD(IA,IADIR) ! read area dirctory
      IF(IOA.NE.0) THEN    ! if output area is set                          480
        IADIR(11)=1        ! number of bytes per element (1,2 or 4)
        IADIR(14)=1        ! maximum number of bands / line of area
        IADIR(15)=0        ! byte length of the DATA block line prefix
                           ! sum of W49, W50, W51 (+ 4 if W36
                           ! validity code is present)
        IADIR(19)=1        ! 32-bit filter band map for multichannel
                           ! images; if a bit is set, data exists
                           ! for the band; band 1 is the least
                           ! significant byte (rightmost)
        IADIR(36)=0        ! validity code; contains zeros if this area    490
                           ! does not have validity codes; if these bytes
                           ! are non-zero, they must match the first four
                           ! bytes ofeach DATA block line prefix or the
                           ! line's data is ignored; this word is usually
                           ! constructed from the date and time of the
                           ! Area Directory creation; DDDHHMMSS
        IADIR(49)=0        ! byte-length of the DATA block line prefix
                           ! documentation region
        IADIR(50)=0        ! byte-length of the DATA block line prefix
                           ! calibration region                             500
        IADIR(51)=0        ! byte-length of the DATA block line prefix
                           ! level map region
        IADIR(52)=LIT('VISR')  ! image source type (VISR,VAS,AAA,ERBE,AVHR)
        IADIR(53)=LIT('BRIT')  ! calibration type (RAW, TEMP, BRIT)
        CALL MAKARA(IOA,IADIR) ! makes new area
        CALL OPNARA(IOA)       ! "opens" the output area
      ENDIF

      NAVSIZ=IADIR(63)-IADIR(35) ! size of NAV block calculation:
                           ! byte offset to the beginning of the            510
                           ! area file CAL block - byte offset to
                           ! the start of the area file NAV block
      IF (IADIR(63).EQ.0) THEN   ! if CAL block inexistant:
        NAVSIZ=IADIR(34)-IADIR(35) ! size of NAV block calculation =
                             ! byte offset to the start of the
                             ! area file DATA block - byte offset
                             ! to the start of the area file NAV
                             ! block
```

```
      ENDIF
      CALL ARAGET(IA,IADIR(35),NAVSIZ,NAVARR) ! gets NAV block from input
      CALL ARAPUT(IOA,IADIR(35),NAVSIZ,NAVARR) ! puts it into output

      CALL LEGEND(IA,IOA,IADIR) ! main subroutine (see below)

      IF(IOA.NE.0) CALL CLSARA(IOA) ! closes the output area
      IF(IOA.NE.0) CALL STAMP(IOA)  ! affixes time-stamp to output area
      CALL SDEST('Completed Calibration of Visible Radiance',0)
      RETURN
      END
C
C     SUBROUTINE LEGEND:
C
      SUBROUTINE LEGEND(IA,IOA,IADIR)

      implicit none

      real pi
      real dlat
      real dlon
      real navin(4)
      real navout(3)
      real degrees
      real radians
      real dz
      real idoy
      real idsl
      real gamma
      real delta
      real brit

      integer ia
      integer ioa
      integer iadir(64)
      integer IBUF2(5000)
      integer IREST(5000)
      integer i
      integer ilen
      integer istat
      integer j
      integer element
      integer line
      integer nlins
      integer neles

      integer nv1saegvar
      integer nvset
      integer lit
      integer yyddd
      integer doy
      integer dsl
      real    ftime
```

```
      NLINS=IADIR(9)-1         ! number of lines in the area - 1
      NELES=IADIR(10)          ! number of elements in each line
      ILEN=IADIR(11)           ! number of bytes per element (1,2,4)
      pi = 3.141592654
      istat = nvset('AREA',ia)  ! sets up navigation for input area
      if (istat .lt. 0) then    ! error catch from nvset() call
        if (istat .eq. -1) then
          call sdest('Input area or frame doesn''t exist.',0)
        elseif (istat .eq. -2) then
          call sdest('Navigation data can''t be found.',0)
        elseif (istat .eq. -3) then
          call sdest('The option is not correct.',0)
        endif
        call sdest('return code from nvset=',istat)
        return
      endif

      navin(1) = float(iadir(4)) ! date of image data collection YYDDD
      navin(2) = ftime(iadir(5)) ! time of image data collection HHMMSS
      call sdest('Date = ',iadir(4)) ! Screen print of date
      call sdest('Time = ',iadir(5)) ! Screen print of time

C
C     Get day-of-year from YYDDD for normalized sun-earth distance
C
      yyddd=int(navin(1))

      if (yyddd .lt. 95000) then
        doy=yyddd-94000
      elseif (yyddd .lt. 96000) then
        doy=yyddd-95000
      elseif (yyddd .lt. 97000) then
        doy=yyddd-96000
      elseif (yyddd .lt. 98000) then
        doy=yyddd-97000
      elseif (yyddd .lt. 99000) then
        doy=yyddd-98000
      elseif (yyddd .lt. 100000) then
        doy=yyddd-99000
      elseif (yyddd .lt. 101000) then
        doy=yyddd-100000
      elseif (yyddd .lt. 102000) then
        doy=yyddd-101000
      elseif (yyddd .lt. 103000) then
        doy=yyddd-102000
      elseif (yyddd .lt. 104000) then
        doy=yyddd-103000
      elseif (yyddd .lt. 105000) then
        doy=yyddd-104000
      elseif (yyddd .lt. 106000) then
        doy=yyddd-105000
      elseif (yyddd .lt. 107000) then
        doy=yyddd-106000
      endif
```

```
      print*,'day-of-year =',doy

C                                                                       630
C     Get days since launch from YYDDD for calibration algorithm
C     (LAUNCH=94103)
C

      if (yyddd .lt. 95000) then
        dsl=doy-103
      elseif (yyddd .lt. 96000) then
        dsl=doy+262
      elseif (yyddd .lt. 97000) then
        dsl=doy+627                                                     640
      elseif (yyddd .lt. 98000) then
        dsl=doy+993
      elseif (yyddd .lt. 99000) then
        dsl=doy+1358
      elseif (yyddd .lt. 100000) then
        dsl=doy+1723
      elseif (yyddd .lt. 101000) then
        dsl=doy+2088
      elseif (yyddd .lt. 102000) then
        dsl=doy+2454                                                    650
      elseif (yyddd .lt. 103000) then
        dsl=doy+2819
      elseif (yyddd .lt. 104000) then
        dsl=doy+3184
      elseif (yyddd .lt. 105000) then
        dsl=doy+3549
      elseif (yyddd .lt. 106000) then
        dsl=doy+3915
      elseif (yyddd .lt. 107000) then
        dsl=doy+4280                                                    660
      endif

      print*,'Days Since GOES-8 Launch =',dsl

C
C     trandform to floating point
C
      idoy=float(doy)
      idsl=float(dsl)
C                                                                       670
C     Calculate normalized Earth-Sun distance for DOY
C
      gamma = 2. * pi * (float(doy)-1) / 365
      delta = 1.000110 + ( 0.034221 * cos(gamma) ) +
     &     ( 0.001280 * sin(gamma) ) +
     &     ( 0.000719 * cos(2.*gamma) ) +
     &     ( 0.000077 * sin(2.*gamma) )

      print*,'Earth-Sun Orbital Angle Factor =',gamma
      print*,'Earth-Sun Distance Factor =',delta                        680
```

```
      DO 10 I=0,NLINS
        line=iadir(6)+iadir(12)*i ! image line coordinate of area
                                  ! line 0, element 0 + line resolution
                                  ! number of image lines between
                                  ! consecutive area lines*line-number
        CALL REDARA(IA,I,0,NELES,1,IBUF2) ! read line into IBUF2 array
        DO 5 J=1,NELES
C
C     Calculate albedo corrected for solar zenith angle                    690
C
            brit=ibuf2(j)/32 ! Division by 32 because SSEC GVAR ingester
                             ! shifts imager visible raw values left
                             ! 5 bits to occupy 15 bits. Hence to obtain
                             ! the raw 10-bit (0-1023) McIDAS pixel,
                             ! must divide by 32.
            element=iadir(7)+iadir(13)*j ! image element coordinate of
                                         ! area line 0, element 0 +
                                         ! element resolution; number of
                                         ! image elements between          700
                                         ! consecutive area elements *
                                         ! element number
            istat=nv1saegvar(float(line),float(element),
     &           0.,dlat,dlon,dz) ! converts image coordinates to earth
                                  ! coordinates
            navin(3) = dlat
            navin(4) = -dlon
C
C       perform special navigation services: from date,time,lat,lon
C       to sat angle, solar angle, relative angle calculation              710
C
            call nv1optgvar(lit('ANG '),navin,navout)
            degrees = navout(2)
            radians = (degrees*pi)/180. ! conversion to radians

C     Check to avoid div-by-0
            if (abs(degrees) .ge. 89) then ! SZA greater than 89 deg
              irest(j) = 0.
            else
              irest(j) = 100. * ( ( 0.650+0.0001341*float(dsl) )           720
     &             *(brit-31.) ) /
     &             ( 526.9 * cos(radians) * delta )
            endif

 5      CONTINUE
        CALL MPIXEL(NELES,4,ILEN,IREST) ! move converted data to
                                        ! appropriate position in array
        CALL WRTARA(IOA,I,IREST) ! write line to output area
 10   CONTINUE
      RETURN                                                             730
      END
```